

**Computational Modeling and Multi-Fidelity Uncertainty Analysis for Masonry Walls
Under In-Plane and/or Out-of-Plane Loading: Development and Applications**

by

Bowen Zeng

A thesis submitted in partial fulfillment of the requirements for the degree of

Doctor of Philosophy

in

Structural Engineering

Department of Civil and Environmental Engineering

University of Alberta

© Bowen Zeng, 2024

ABSTRACT

Unreinforced and reinforced masonry walls are essential elements in low-to-medium-rise residential and commercial buildings. They play an indispensable role in both vertical and lateral load-resisting systems, withstanding diverse loads such as seismic loads acting along and perpendicular to the wall during earthquakes, wind loads perpendicular to the wall, and eccentric gravity loads transmitted from floor or roof diaphragms. These loads can be categorized into in-plane (IP) loading and out-of-plane (OOP) loading, which occur simultaneously in most scenarios. Nevertheless, predicting their structural behaviors, including the failure modes and load-resisting capacity under IP and/or OOP loading, poses a considerable challenge considering the composite nature of masonry walls and the intricate interactions among their components, particularly when pertinent uncertainty in material properties is taken into account. In response to this challenge, this thesis consists of two parts: (1) development of 3D constitutive models for mortar joints to facilitate high-fidelity simulations of masonry walls and their applications to study the IP-OOP behavior interaction; and (2) development and application of algorithms and estimators for uncertainty analyses (e.g., mean and variance estimation of load resistance, reliability analysis) of masonry walls using low-fidelity models (e.g., design-code models) assisted by high-fidelity models via multi-fidelity approaches.

To be specific, the first part of this thesis work aims at advancing finite element (FE) modeling techniques for masonry walls and enhancing the understanding of the interactive behavior of masonry walls under combined IP and OOP loading. At the core of this part is the development of two innovative constitutive models for cohesive interfaces to simulate mortar

joints of masonry walls within the micro modeling framework. One model is implemented in a computational plasticity-based framework, while the other is developed within a damage plasticity-based framework, enabling the simulation of both monotonic and cyclic behaviors of masonry mortar joints, respectively. These two models are capable of capturing various failure modes, including tensile cracking, shear sliding, and compressive crushing, which allows for high-fidelity representations of masonry walls under both IP and OOP loading scenarios. A significant application of the developed models is to explore the IP-OOP interaction behavior of masonry walls. Two groups of numerical analyses are conducted, with the focus on the unreinforced and reinforced masonry walls, respectively, to investigate the effects of various design parameters, such as aspect ratio (height-to-length ratio), slenderness ratio (height-to-thickness ratio), pre-compression load, and reinforcement ratio. This application elucidates the intricate failure mechanisms of masonry walls under combined IP and OOP loadings and quantifies the consequent reductions in IP capacity due to the presence of OOP loading. Such insights highlight the criticality of considering IP-OOP interactions in ensuring safe and reliable masonry wall design and evaluation.

The second part of this thesis aims at addressing a practical need for uncertainty analysis of masonry walls as required for reliability-based calibration of design codes and probabilistic performance-based design for masonry buildings. In this context, statistics estimation and reliability analysis are pivotal aspects. At the same time, the second part of this thesis will address a fundamental need in the field of uncertainty quantification: developing efficient algorithms/estimators for mean, variance, and failure probability when quantities of interest involved are obtained using computationally expensive high-fidelity models, such as those

developed in the first part. In the second part, two novel statistics estimators (for mean and variance, respectively) and an innovative reliability analysis algorithm are proposed. The proposed estimators/algorithms leverage limited expensive high-fidelity models (e.g., finite element models) with a large number of cheap low-fidelity models (e.g., design-code models), via a multi-fidelity (MF) approach. This not only enhances computational efficiency but also ensures the accuracy of estimations of mean, variance, and probability of failure in reliability analysis. Case studies on masonry walls under IP or OOP loadings demonstrate the adaptability and practicality of these methods, marking a significant improvement over several existing approaches. Aside from the uncertainty analysis, this research also opens new possibilities for integrating high-fidelity computational models into design-code model enhancements in the masonry community.

PREFACE

This thesis includes original research conducted by Bowen Zeng. Ten journal papers have been published, are under review, or are in preparation for publication on the basis of this thesis. The details of the corresponding chapters are summarized below:

A version of Chapter 2 has been published as **Zeng, B., and Li, Y. 2023. *Towards Performance-Based Design of Masonry Buildings: Literature Review. Buildings, 13(1534)***. For the consistency and coherence of this thesis, contents have been modified, removed, or added from the submitted paper. Bowen Zeng was responsible for conceptualization, methodology development, and paper composition. Yong Li was in charge of conceptualization, methodology development, supervision, funding acquisition, and paper revision.

A version of Chapter 3 has been published as **Zeng, B., Li, Y., and Cruz Noguez, C. 2021. *Modeling and Parameter Importance Investigation for Simulating In-plane and Out-of-plane Behaviors of Un-reinforced Masonry Walls. Engineering Structures, 248: 113233. Elsevier***. For the consistency and coherence of this thesis, contents have been modified, removed, or added from the submitted paper. Bowen Zeng was responsible for conceptualization, methodology development, numerical model development, analysis implementation, and paper composition. Yong Li was in charge of conceptualization, methodology development, supervision, funding acquisition, and paper revision. Carlos 'Lobo' Cruz Noguez was in charge of paper revision.

A version of Chapter 4 has been published as **Li, Y., and Zeng, B. 2023. *Modeling of Masonry Structures using a New 3D Cohesive Interface Material Model considering Dilatancy Softening. Engineering Structures, 277 (December 2022): 115466. Elsevier***. For the consistency and

coherence of this thesis, contents have been modified, removed, or added from the submitted paper. Bowen Zeng was responsible for conceptualization, methodology development, numerical model development, analysis implementation, and paper composition. Yong Li was in charge of conceptualization, methodology development, supervision, funding acquisition, and paper revision.

A version of Chapter 5 is in press as **Zeng, B., and Li, Y. Formulation, Implementation, and Validation of a 3D Damage-plasticity based Cohesive-interface Model with Multi-yield Surfaces for Cyclic Modeling of Mortar Joints. ASCE Journal of Structural Engineering.** For the consistency and coherence of this thesis, contents have been modified, removed, or added from the submitted paper. Bowen Zeng was responsible for conceptualization, methodology development, numerical model development, analysis implementation, and paper composition. Yong Li was in charge of conceptualization, methodology development, supervision, funding acquisition, and paper revision.

A version of Chapter 6 is published as **Zeng, B., and Li, Y. In-plane and out-of-plane one-way vertical bending behavior interaction analysis of unreinforced masonry walls with newly developed load capacity interaction curve. Engineering Structures 305 (2024): 117729.** For the consistency and coherence of this thesis, contents have been modified, removed, or added from the submitted paper. Bowen Zeng was responsible for conceptualization, methodology development, numerical model development, analysis implementation, and paper composition. Yong Li was in charge of conceptualization, methodology development, supervision, funding acquisition, and paper revision.

A version of Chapter 7 is under revision as **Zeng, B., and Li, Y. Numerical Investigation of Reinforced Masonry Walls under Bi-directional Loading: In-plane Capacity Reduction due to Out-of-plane Loading. ASCE Journal of Structural Engineering.** For the consistency and coherence of this thesis, contents have been modified, removed, or added from the submitted paper. Bowen Zeng was responsible for conceptualization, methodology development, numerical model development, analysis implementation, and paper composition. Yong Li was in charge of conceptualization, methodology development, supervision, funding acquisition, and paper revision.

A version of Chapter 8 is under review as **Zeng, B., and Li, Y. Estimating Mean and Variance of In-plane Load Resistance of Masonry Walls Using Inaccurate Design Code Models and Limited High-fidelity Data. ASCE Journal of Structural Engineering.** For the consistency and coherence of this thesis, contents have been modified, removed, or added from the submitted paper. Bowen Zeng was responsible for conceptualization, methodology development, numerical model development, analysis implementation, and paper composition. Yong Li was in charge of conceptualization, methodology development, supervision, funding acquisition, and paper revision.

A version of Chapter 9 is in preparation as **Zeng, B., and Li, Y. Statistics Estimation of Out-of-plane Load Resistance of Masonry Walls Using Empirical Models and Mechanics-based Finite Element Models. Engineering Structures.** For the consistency and coherence of this thesis, contents have been modified, removed, or added from the submitted paper. Bowen Zeng was responsible for conceptualization, methodology development, numerical model development,

analysis implementation, and paper composition. Yong Li was in charge of conceptualization, methodology development, supervision, funding acquisition, and paper revision.

A version of Chapter 10 is in preparation as the following two manuscripts. For the consistency and coherence of this thesis, contents have been modified, removed, or added from the submitted paper. Bowen Zeng was responsible for conceptualization, methodology development, numerical model development, analysis implementation, and paper composition. Yong Li was in charge of conceptualization, methodology development, supervision, funding acquisition, and paper revision.

- ***Zeng, B., and Li, Y. Novel Structural Reliability Methods Using Multi-fidelity Models through Cross-Entropy Importance Sampling and Control Variate Techniques. Structural Safety.***
- ***Zeng, B., and Li, Y. Efficient Finite Element-based Reliability Analysis of Reinforced Masonry Walls under OOP Loading assisted by a Multi-fidelity Approach. ASCE Journal of Engineering Mechanics.***

In addition to the abovementioned manuscripts, the following works published or currently under revision are not included in this thesis:

- ***Metwally, Z., Zeng, B., and Li, Y. Probabilistic Behavior and Variance-Based Sensitivity Analysis of Reinforced Concrete Masonry Walls Considering Slenderness Effect. ASCE-ASME Journal of Risk and Uncertainty in Engineering Systems, Part A: Civil Engineering 8.4 (2022): 04022051.***

- **Metwally, Z., Li, Y., and Zeng, B. Finite element-based reliability analysis of reinforced concrete masonry walls under eccentric axial loading considering slenderness effects. *Engineering Structures* 304 (2024): 117597.**
- **Zeng, B., Cruz Noguez, C., and Li, Y. Enhanced Prediction and Uncertainty Analysis for In-plane and Out-of-plane Resistance of Unreinforced Masonry Walls: a Multi-fidelity Approach. Under Revision. *ASCE-ASME Journal of Risk and Uncertainty in Engineering Systems, Part A: Civil Engineering*.**
- **Li, Y. Metwally, Z., and Zeng, B. Model Error Assessment of Out-of-plane Load Capacity Models for Reinforced Concrete Masonry Walls in CSA S304-14 and TMS 402-16. Under Revision. *ASCE Journal of Structural Engineering*.**

DEDICATION

To

my parents

ACKNOWLEDGMENTS

Completing this PhD has been a life-changing journey, one that I could not have embarked on without the support and encouragement of many. First and foremost, my heartfelt thanks to my supervisor, and also my friend, Professor Yong Li, whose encouragement, guidance, friendship, and support have been pivotal in shaping this thesis. The moments spent debugging over 3000 lines of draft code together are unforgettable and epitomize his commitment to my growth as a researcher.

My gratitude extends to my supervisory committee members, Dr. Samer Adeeb and Dr. Carlos A. “Lobo” Cruz-Noguez, for their invaluable constructive feedback and insights that have significantly enriched my research. I am equally grateful to my PhD defense examiners, Dr. F. Albert Liu and Dr. James Goulet, for their rigorous review and helpful suggestions.

A special thanks to my friends and fellow graduate students from the Structural Modeling and Reliability Analysis (SM&RA) group for all the laughs and memories. I cherish our time together and am grateful for the support and solidarity.

Acknowledgments are also due to the Natural Sciences and Engineering Research Council of Canada (NSERC) and the University of Alberta for their financial support of my research.

In a journey filled with challenges and triumphs, the constant support and love of my girlfriend, Yiwen Zhang, has been a beacon of light. Her patience, understanding, and unwavering faith in my abilities have been a source of strength and inspiration. Her ability to make me smile even on the most stressful days has been invaluable. also, incredibly grateful for her

companionship, empathy, and endless love, which made this journey not just possible but also enjoyable.

Lastly, I would like to thank my parents, who instilled in me a love of learning and whose support and understanding, for all their love and encouragement during the pressures of my Ph.D.

TABLE OF CONTENTS

ABSTRACT.....	III
PREFACE.....	VI
DEDICATION.....	XI
ACKNOWLEDGMENTS.....	XII
TABLE OF CONTENTS.....	XIV
LIST OF TABLES.....	XXV
LIST OF FIGURES.....	XXVIII
CHAPTER 1. INTRODUCTION.....	1
1.1. BACKGROUND.....	1
1.2. RESEARCH MOTIVATION AND PROBLEM STATEMENT.....	5
1.3. RESEARCH OBJECTIVES.....	8
1.4. NOVELTY AND SIGNIFICANCE OF RESEARCH.....	10
1.5. ORGANIZATION OF THESIS.....	12
CHAPTER 2. LITERATURE REVIEW.....	15
2.1. FINITE ELEMENT MODELING FOR MASONRY WALLS.....	15
2.1.1. Micro modeling approach.....	15
2.1.2. Macro modeling strategy.....	25

2.2.	CONSTITUTIVE MODELS OF COHESIVE INTERFACES FOR MASONRY MORTAR JOINTS	33
2.2.1.	Monotonic models	34
2.2.2.	Cyclic models.....	41
2.3.	IN-PLANE AND OUT-OF-PLANE INTERACTION BEHAVIORS OF MASONRY WALLS	44
2.4.	DESIGN CODE-BASED MODELS FOR MASONRY WALLS.....	48
2.5.	UNCERTAINTY IN MASONRY WALLS	51
2.6.	UNCERTAINTY ANALYSIS AND RELIABILITY ANALYSIS OF MASONRY WALLS	53
2.6.1.	Simplified model-based	53
2.6.2.	Micro model-based	55
2.7.	MULTI-FIDELITY METHOD (MODEL)-BASED PROBABILISTIC ANALYSIS	56
2.7.1.	Surrogate model	56
2.7.2.	Multi-fidelity method.....	57
 CHAPTER 3. FINITE ELEMENT MODELING AND PARAMETER IMPORTANCE		
INVESTIGATION OF UNREINFORCED MASONRY WALLS USING OFF-THE-SHELF TECHNIQUES.....		
		63
3.1.	INTRODUCTION.....	63
3.2.	SIMPLIFIED MICRO MODELING STRATEGY	69
3.3.	MATERIAL MODELING FOR EXPANDED BRICK UNITS.....	70

3.4.	CONTACT-BASED COHESIVE SURFACE BEHAVIOR FOR MORTAR JOINTS	72
3.4.1.	Elastic behavior.....	72
3.4.2.	Failure criterion.....	73
3.5.	FINITE ELEMENT MODEL VALIDATION	77
3.5.1.	Unit-mortar-unit assemblages.....	78
3.5.2.	URM walls under in-plane (IP) loading.....	80
3.5.3.	URM walls under out-of-plane (OOP) loading	85
3.6.	FINITE ELEMENT-BASED PARAMETRIC STUDY.....	91
3.6.1.	Masonry unit-related model parameters	92
3.6.2.	Mortar interface-related model parameters.....	95
3.7.	CHAPTER CONCLUSIONS.....	99
	CHAPTER 4. DEVELOPMENT OF A PLASTICITY-BASED 3D MULTI-YIELD SURFACES CONSTITUTIVE MODEL FOR MASONRY MORTAR JOINTS UNDER MONOTONIC LOADING	101
4.1.	INTRODUCTION.....	102
4.2.	REMARKS ON THE OFF-THE-SHELF MODELING TECHNIQUES.....	149
4.3.	CONSTITUTIVE MODEL FORMULATION	108
4.3.1.	Multi-yield surfaces plastic criterion	108
4.3.2.	Flow rule.....	110

4.3.3.	State variables evolution during plastic flow	112
4.4.	PLASTICITY INTEGRATION STRATEGY	116
4.4.1.	Multi-yield surface plasticity integration strategy	117
4.4.2.	Error-based auto-adaptive sub-stepping algorithm.....	120
4.5.	FINITE ELEMENT MODEL VALIDATION	125
4.5.1.	Unit-mortar-unit assemblages.....	125
4.5.2.	URM wall under in-plane (IP) loading	130
4.5.3.	URM walls under out-of-plane (OOP) loading	137
4.6.	CHAPTER CONCLUSIONS.....	142
CHAPTER 5. DEVELOPMENT OF A DAMAGE PLASTICITY-BASED 3D MULTI-YIELD SURFACES CONSTITUTIVE MODEL FOR MASONRY MORTAR JOINTS UNDER CYCLIC LOADING		
		153
5.1.	INTRODUCTION.....	153
5.2.	CONSTITUTIVE MODEL FORMULATION	159
5.2.1.	Coupling of plasticity and damage	159
5.2.2.	Traction-separation relationship	161
5.2.3.	Damage evolution laws.....	171
5.2.4.	Model parameterization	172
5.3.	MODEL IMPLEMENTATION	175

5.3.1.	Tangent stiffness	175
5.3.2.	Semi-implicit stress return algorithm.....	177
5.4.	FINITE ELEMENT VALIDATION	180
5.4.1.	Three-point bending beam under indirect cyclic tensile loading.....	181
5.4.2.	Masonry couplet under compressive-shear loading.....	183
5.4.3.	A short URM wall under cyclic in-plane (IP) loading.....	185
5.4.4.	A tall URM wall under cyclic in-plane (IP) loading.....	191
5.4.5.	A reinforced masonry (RM) wall under cyclic in-plane (IP) loading.....	194
5.5.	CHAPTER CONCLUSION.....	197
CHAPTER 6. NUMERICAL INVESTIGATION OF UNREINFORCED MASONRY		
WALLS UNDER BI-DIRECTIONAL LOADING: IN-PLANE CAPACITY REDUCTION		
DUE TO OUT-OF-PLANE LOADING.....		
		199
6.1.	INTRODUCTION.....	200
6.2.	3D FINITE ELEMENT MODELS OF URM WALLS	204
6.2.1.	Simplified micro modeling strategy.....	204
6.2.2.	Parametric design for the numerical study.....	205
6.3.	PURE IP AND PURE OOP BEHAVIORS OF URM WALLS	210
6.3.1.	Pure IP behavior.....	210
6.3.2.	Pure OOP behavior	214

6.4.	IP AND OOP INTERACTION BEHAVIORS OF URM WALLS.....	218	
6.4.1.	Influence of aspect ratio (AR) and pre-compression load (P_v).....	219	
6.4.2.	Influence of slenderness ratio (SR) and pre-compression load (P_v).....	226	
6.5.	ANALYTICAL MODEL FOR INTERACTION CURVES	230	
6.6.	CHAPTER CONCLUSION.....	234	
 CHAPTER 7. NUMERICAL INVESTIGATION OF REINFORCED MASONRY			
WALLS UNDER BI-DIRECTIONAL LOADING: IN-PLANE CAPACITY REDUCTION			
DUE TO OUT-OF-PLANE LOADING.....			236
7.1.	INTRODUCTION.....	236	
7.2.	3D FINITE ELEMENT MODEL FOR RM WALLS.....	241	
7.2.1.	RM wall under IP loading.....	243	
7.2.2.	RM wall under OOP loading	246	
7.3.	STRATEGY FOR FE-BASED INVESTIGATION OF RM WALLS UNDER COMBINED IP AND		
OOP LOADING		249	
7.4.	PURE IP AND PURE OOP BEHAVIORS OF RM WALLS.....	253	
7.5.	COMBINED IP AND OOP LOADING	258	
7.5.1.	Influence of aspect ratio (AR) and pre-compression load (P_v).....	258	
7.5.2.	Influence of slenderness ratio (SR) and pre-compression load (P_v).....	265	
7.6.	COMPARISON BETWEEN RM AND URM WALLS.....	268	

7.7.	CHAPTER CONCLUSION.....	269
CHAPTER 8. ESTIMATING MEAN AND VARIANCE OF IN-PLANE RESISTANCE		
OF MASONRY WALLS USING INACCURATE DESIGN-CODE MODELS AND		
LIMITED HIGH-FIDELITY DATA.....		
		273
8.1.	INTRODUCTION.....	274
8.2.	CRUDE MONTE CARLO-BASED ESTIMATORS.....	277
8.2.1.	Mean and variance estimators using design-code models.....	278
8.2.2.	Mean and variance estimators using FE models.....	279
8.2.3.	Quality measure of Monte Carlo estimators.....	281
8.3.	IMPROVED ESTIMATORS FOR MEAN AND VARIANCE.....	281
8.3.1.	Mean estimator.....	282
8.3.2.	Variance estimator.....	285
8.4.	MEAN AND VARIANCE ESTIMATORS FOR IP RESISTANCE OF URM WALLS.....	286
8.4.1.	Wall configuration.....	287
8.4.2.	Uncertainties in material parameters.....	288
8.4.3.	Statistics estimation.....	290
8.5.	MEAN AND VARIANCE ESTIMATORS FOR IP RESISTANCE OF RM WALLS.....	303
8.5.1.	Shear-governed RM wall.....	303
8.5.2.	Flexural-governed RM wall.....	312

8.6.	CHAPTER CONCLUSIONS.....	318
CHAPTER 9. STATISTICS ESTIMATION OF OUT-OF-PLANE LOAD RESISTANCE OF MASONRY WALLS USING ANALYTICAL MODELS AND MECHANICS-BASED FINITE ELEMENT MODELS		
		320
9.1.	INTRODUCTION.....	321
9.2.	CRUDE MONTE CARLO STATISTICS ESTIMATION	323
9.2.1.	Finite element model.....	324
9.2.2.	Design-code Model.....	324
9.2.3.	Mean and variance estimations based on crude MC simulation.....	326
9.2.4.	Quality measure of Monte Carlo estimators	328
9.3.	IMPROVED MEAN AND VARIANCE ESTIMATORS.....	328
9.3.1.	Mean estimator.....	329
9.3.2.	Variance estimator	332
9.4.	MEAN AND VARIANCE ESTIMATION OF OOP RESISTANCE OF MASONRY WALLS..	333
9.4.1.	Case study: URM wall.....	334
9.4.2.	Case study: RM wall.....	347
9.5.	CHAPTER CONCLUSION.....	355
CHAPTER 10. NOVEL STRUCTURAL RELIABILITY METHODS USING MULTI-FIDELITY MODELS THROUGH CROSS-ENTROPY IMPORTANCE SAMPLING AND		

CONTROL VARIATE TECHNIQUES WITH APPLICATIONS ON MASONRY WALLS

357

10.1. INTRODUCTION..... 358

10.2. MULTI-FIDELITY RELIABILITY ANALYSIS 365

 10.2.1. Importance sampling (IS) 366

 10.2.2. Cross entropy-based importance sampling (CEIS)..... 367

10.3. MULTI-FIDELITY RELIABILITY ANALYSIS 371

 10.3.1. Mathematical preliminary of control variate (CV) method 371

 10.3.2. Multi-fidelity (MF) reliability estimator..... 372

10.4. NUMERICAL EXAMPLES 375

 10.4.1. Example #1: Cantilever beam..... 377

 10.4.2. Example #2: Cantilever beam (rare event analysis) 381

 10.4.3. Example #3: A ten-bar truss structures..... 383

 10.4.4. Example #4: A three-bay three-story frame structure..... 386

**10.5. RELIABILITY ANALYSIS OF REINFORCED MASONRY WALLS UNDER OUT-OF-
PLANE LOADING 389**

 10.5.1. Details of the RM wall..... 389

 10.5.2. Demand and resistance calculation..... 391

 10.5.3. Reliability analysis..... 393

10.6. RELIABILITY ANALYSIS OF REINFORCED MASONRY WALLS UNDER IN-PLANE LOADING	396
10.6.1. Details of the RM wall.....	396
10.6.2. Reliability analysis.....	398
10.7. CONCLUSIONS.....	403
CHAPTER 11. CONCLUSIONS AND RECOMMENDATIONS.....	405
11.1. SUMMARY AND CONCLUSIONS.....	405
11.2. CONTRIBUTIONS AND DELIVERABLES	411
11.3. LIMITATIONS AND RECOMMENDATIONS FOR FUTURE WORK	414
REFERENCE.....	417
APPENDIX A. DERIVATION OF JACOBIAN MATRICES IN THE 3D MULTI- YIELD SURFACES PLASTICITY-BASED CONSTITUTIVE MODEL.....	470
APPENDIX B. DERIVATION OF TANGENT STIFFNESS MATRIX AND STRESS INCREMENT IN THE 3D MULTI-YIELD SURFACES DAMAGE PLASTICITY-BASED CONSTITUTIVE MODEL.....	481
APPENDIX C. IN-PLANE RESISTANCE PREDICTION OF UNREINFORCED MASONRY WALLS BASED ON CSA S304-14	485
APPENDIX D. IN-PLANE RESISTANCE PREDICTION OF REINFORCED MASONRY WALLS BASED ON CSA S304-14	486

**APPENDIX E. OUT-OF-PLANE RESISTANCE PREDICTION OF UNREINFORCED
MASONRY WALLS BASED ON CSA S304-14 489**

**APPENDIX F. OUT-OF-PLANE RESISTANCE PREDICTION OF REINFORCED
MASONRY WALLS BASED ON CSA S304-14 490**

**APPENDIX G. PYTHON-BASED TOOLS FOR MODELING MASONRY WALLS
BASED ON MICRO MODELING STRATEGY 494**

LIST OF TABLES

Table 2-1. Existing monotonic models of interface elements for masonry mortar joints.....	41
Table 2-2. Existing cyclic models of interface elements for masonry mortar joints	44
Table 3-1. Material parameters of contact-based cohesive surfaces for unit-mortar-unit assemblages.....	80
Table 3-2. Material properties of interfaces of URM walls under IP loading	83
Table 3-3. Material properties of interfaces of URM walls under OOP loading.....	86
Table 4-1. Material parameters for unit-mortar-unit assemblages (Pluijm, 1999)	127
Table 4-2. Dilatancy-related material parameters for the unit-mortar-unit assemblage.....	129
Table 4-3. Material parameters of interface elements for the URM walls	133
Table 5-1. Baseline material parameters used for the parameter influence test	173
Table 5-2. Material parameters for the FE model of masonry couplet.....	184
Table 5-3. Material parameters for the FE model of short URM wall under cyclic IP loading .	188
Table 5-4. Material parameters for the FE model of tall URM wall under cyclic IP loading	192
Table 5-5. Material parameters for the FE model of the RM wall under cyclic IP loading	195
Table 6-1. Material parameters of units and mortar joints (Lourenço, 1996).....	208
Table 6-2. Design cases for FE-based investigation of the IP-OOP interaction behavior of URM walls	209
Table 7-1. Material parameters of concrete block units, grouts, and reinforcements used in the FE model.....	244
Table 7-2. Material parameters of mortar joints (interfaces) used in the FE model.....	245
Table 7-3. Design cases for FE-based investigation of the IP-OOP behavior interaction of RM walls	251

Table 7-4. Failure modes of RM walls under pure IP loading.....	255
Table 8-1. Statistical characterization of material parameters for the URM wall considered....	289
Table 8-2. Pearson correlation coefficient ρ between design-code model and FE model for the IP resistance prediction for the URM wall considered.....	294
Table 8-3. Model evaluation numbers (m_{FE} and m_{CSA}) and coefficient α for the mean estimation of IP resistance for the URM wall considered.....	296
Table 8-4. Model evaluation numbers (m_{FE} and m_{CSA}) and coefficient β for the variance estimation of IP resistance for the URM wall considered.....	299
Table 8-5. Statistical characterization of material parameters for the RM shear wall.....	305
Table 8-6. Model evaluation numbers and coefficient for the mean and variance estimations of IP resistance for the RM shear wall.....	307
Table 8-7. Model evaluation numbers and coefficients for the mean and variance estimations of IP resistance for the RM flexural wall.....	315
Table 9-1. Statistical characterization of material parameters for the URM wall.....	336
Table 9-2. Model evaluation numbers (m_{FE} and m_{CSA}) and coefficient α for the mean estimation of OOP resistance for the URM wall considered.....	340
Table 9-3. Model evaluation numbers (m_{FE} and m_{CSA}) and coefficient β for the variance estimation of OOP resistance for the URM wall considered.....	343
Table 9-4. Statistical characterization of independent random variables.....	348
Table 9-5. Model evaluation numbers and coefficient for the mean and variance estimations of OOP resistance for the RM wall.....	351
Table 10-1. Statistics of random variables for the cantilever beam in Example #1.....	377
Table 10-2. Reliability analysis results for Example #1.....	379
Table 10-3. Reliability analysis results of the cantilever beam in Example #2.....	383
Table 10-4. Reliability analysis results for the ten-bar truss structure in Example #3.....	385

Table 10-5. Statistics of the random variables for the plastic frame in Example #4 388

Table 10-6. Reliability analysis results for the steel frame in Example #4 389

Table 10-7. Nominal values of material parameter considered for the RM wall 391

Table 10-8. Statistical characterization of random variables considered for the RM wall under OOP loading..... 391

Table 10-9. Statistical parameters for loads (Bartlett et al., 2003) 393

Table 10-10. Reliability analysis results for the RM wall under OOP loading 396

Table 10-11. Statistical characterization of material parameters for the RM wall under IP loading 399

Table 10-12. Empirical relationships of material parameters for the RM wall under IP loading400

Table 10-13. Statistical characterization of material parameters for the RM wall under IP loading 400

Table 10-14. Reliability analysis results for the RM wall under OOP loading 401

LIST OF FIGURES

Figure 1-1. Failure modes of masonry walls under IP loading: (a) diagonal tension cracking (Celano et al., 2021), (b) shear sliding (Saatcioglu et al., 2006), and (c) flexural rocking (Celano et al., 2021).....	2
Figure 1-2. Failure modes of masonry walls under OOP loading: (a) overturning failure (Giaretton et al., 2016), (b) one-way bending failure (Giaretton et al., 2016), and (c) two-way bending failure (Astroza et al., 2012)	2
Figure 1-3. In-plane and out-of-plane failure at corner regions: (a) field observations, and (b) corresponding schematic sketch (Vlachakis et al., 2020)	3
Figure 1-4. Out-of-plane collapse of in-plane damaged masonry walls: (a) field observation, and (b) corresponding schematic sketch (Vlachakis et al., 2020)	4
Figure 1-5. Organization of the thesis.....	14
Figure 2-1. FE micro modeling strategies for masonry structures (a) masonry specimen, (b) detailed micro modeling approach, and (c) simplified micro modeling approach	16
Figure 2-2. FE models for URM walls under IP loading by Lourenço (1996).....	17
Figure 2-3. Flexural rocking failure and corresponding hysteretic behaviors of URM walls predicted by the micro modeling strategy: (a) D’Altri et al. (2019), and (b) Minga et al. (2018)	19
Figure 2-4. (a) Micro modeling strategy for PGRM walls, and (b-c) numerical-experimental comparison in terms of the crack pattern and load-deformation behavior by Calderón et al. (2019).....	21
Figure 2-5. Improved micro modeling scheme for FGRM walls by Koutras and Shing (2021a)	23
Figure 2-6. Numerical-experimental comparison of crack pattern of URM walls by Macorini and Izzuddin (2012).....	24
Figure 2-7. Detailed micro modeling approach for URM structures proposed by D’ Altri et al. (2018).....	25

Figure 2-8. Numerical predictions based on the macro continuum models (Stankowski et al., 1993b)	28
Figure 2-9. Macro element modeling strategy and numerical validation for: (a-b) flexural-governed RM walls by Cheng and Shing (2022b), and (c-d) shear-governed RM walls by Cheng and Shing (2022a).....	31
Figure 2-10. Experimental-numerical comparison in terms of crack pattern for confined masonry wall under OOP loading from Noor-E-Khuda and Thambiratnam (2021).....	32
Figure 2-11. Failure modes considered in the cohesive interfaces for mortar joints: (a) tensile cracking, (b) shear sliding, (c) compressive-shear failure, and (d) compressive crushing (Kumar et al., 2014).....	35
Figure 2-12. Multi-yield surfaces plasticity model proposed by Lourenco and Rots (1996; 1997)	36
Figure 2-13. Single yield surface model to consider tensile cracking and shear sliding (a) Hyperbolic yield surface and plastic potential surface, (b) evolution of yield surface (Carol et al., 1997)	36
Figure 2-14. Single yield surface model to consider tensile cracking, shear sliding, and compressive crushing (Kumar et al., 2014)	37
Figure 2-15. Failure surface for cohesive interfaces proposed by D'Altri et al. (2018): (a) Mohr-Coulomb surface with tension cut-off, (b) post-peak tensile response, and (c) post-peak shear response.....	38
Figure 2-16. Hypothetic motion of the unloading surface in stress space to: (a) tension, and (b) compression (D. V. Oliveira and Lourenço, 2004).....	42
Figure 2-17. Uniaxial behavior of interface model: (a) loading and unloading, and (b) reloading	42
Figure 2-18. URM panel under combined IP and OOP loading tested by Najafgholipour et al. (2013) (a) test specimen, and (b) IP-OOP capacity interaction curve	45
Figure 2-19. Load sequence of URM walls under combined IP and OOP loading tested by Dolatshahi and Aref (2016)	46

Figure 2-20. URM wall tested by Krishnachandran and Menon (2023): (a) IP loading, and (b) OOP loading.....	47
Figure 2-21. Comparison of OOP capacity by design codes and FE model by Noor-E-Khuda and Dhanasekar (2020).....	50
Figure 2-22. (a) Experimental results versus the predicted in-plane shear strength, and (b) statistical comparisons between the accuracy of shear equations for predicting in-plane shear strength of fully grouted reinforced masonry walls (Seif EIDin et al., 2019)	51
Figure 2-23. General framework for surrogate model-based uncertainty quantification	57
Figure 2-24. General framework for multi-fidelity model-based uncertainty quantification.....	58
Figure 2-25. Multi-fidelity method used for the simulation-based seismic reliability analysis for a reinforced concrete frame: (a) high-fidelity model, and (b) low-fidelity model (Skandalos et al., 2022)	60
Figure 3-1. Simplified micro modeling strategy for URM structures: (a) masonry assemblage sample, and (b) FE modeling strategy	70
Figure 3-2. Yield surface of DP model.....	71
Figure 3-3. Stress-displacement response of interfaces under pure tension	74
Figure 3-4. Stress-displacement response of interfaces under shear: (a) cohesion model, (b) frictional model, and (c) cohesive-frictional model.....	76
Figure 3-5. Comparisons between numerical and experimental results for unit-mortar-unit assemblages: (a) pure tensile loading, and (b) shear loading under different pre-compression load levels	80
Figure 3-6. URM walls considered for IP loading: (a) pre-compression applied at the top of the walls, and (b) monotonic displacement-controlled in-plane loading.....	81
Figure 3-7. Load-displacement curve comparison between FE simulations and experiments for the three URM walls under IP loading	84
Figure 3-8. Failure crack pattern (J4D): (a) FE simulation, and (b) experiment (Raijmakers, 1992; Vermeltfoort and Raijmakers, 1993)	84
Figure 3-9. Comparison of load-displacement curves of URM walls under OOP loading	87

Figure 3-10. OOP displacement distribution for Wall 8 at 20 kPa: (a) vertical center line, and (b) horizontal center line.....	88
Figure 3-11. OOP displacement distribution for Wall 10 at 5 kPa: (a) free right edge, and (b) horizontal center line.....	88
Figure 3-12. Crack pattern comparison: (a) (b) (c) FE simulations for Wall 4, Wall 8 and Wall 10, and (d) (e) (f) experimental studies for Wall 4, Wall 8, and Wall 10 ((C. L. Ng, 1996)).....	90
Figure 3-13. Effects of elastic modulus E on the: (a) IP load-deformation behaviors, and (b) OOP load-deformation behaviors	93
Figure 3-14. Effects of compressive strength f_c on the: (a) IP load-deformation behaviors, and (b) OOP load-deformation behaviors	94
Figure 3-15. Effects of dilation angle ψ on the: (a) IP load-deformation behaviors, and (b) OOP load-deformation behaviors	95
Figure 3-16. Effects of frictional angle β on the: (a) IP load-deformation behaviors, and (b) OOP load-deformation behaviors	95
Figure 3-17. Effects of tensile failure displacements δ_n^f on the: (a) IP load-deformation behaviors, and (b) OOP load-deformation behaviors.....	96
Figure 3-18. Effects of tensile strength f_t on the: (a) IP load-deformation behaviors, and (b) OOP load-deformation behaviors	97
Figure 3-19. Effects of shear failure displacement δ_t^f on the: (a) IP load-deformation behaviors, and (b) OOP load-deformation behaviors.....	98
Figure 3-20. Effects of cohesion c on the: (a) IP load-deformation behaviors, and (b) OOP load-deformation behaviors	98
Figure 3-21. Effects of frictional coefficient μ on the: (a) IP load-deformation behaviors, and (b) OOP load-deformation behaviors	99
Figure 4-1. Schematic view of yield surfaces of proposed constitutive material model	110
Figure 4-2. Relationship between dilatancy coefficient and (a) plastic shear displacement, and (b) compressive normal stress	111

Figure 4-3. Relationship between mode II fracture energy and compressive normal stress	113
Figure 4-4. Evolution law of the compressive yield stress σ_c	116
Figure 4-5. Graphical representation for the predictor-corrector strategy for the multi-yield surface model.....	119
Figure 4-6. Schematic illustration of the general idea for the sub-stepping backward integration used in the proposed constitutive model.....	122
Figure 4-7. Comparison between numerical and experimental results for unit-mortar-unit assemblages under compression-shear loading: (a) CS-brick90, and (b) CS-block96.....	128
Figure 4-8. Comparison of plastic normal displacement-plastic shear displacement relationship for specimen CS-block96 between the experimental and FE simulation results.....	128
Figure 4-9. Masonry triplet under direct shear tested by Amadei et al. (1989).....	129
Figure 4-10. Comparison of <i>unp-utp</i> curves for different normal compressive stress levels between the experimental results and FE simulation results.....	130
Figure 4-11. URM wall considered for the IP loading: (a) pre-compression applied at the top of the quasi-rigid beam, and (b) IP displacement-controlled loading	131
Figure 4-12. Load-displacement curve comparison for the URM wall under IP loading	134
Figure 4-13. Final crack pattern: (a) experiment (da Porto, 2005), (b) deformed shape of wall from FE simulation, (c) equivalent plastic displacements for mortar joints from FE simulation, and (d) tensile damage scalar (DAMAGET) and compressive damage scalar (DAMAGEC) plots for units from FE simulation. Note: SDV1, SDV2, SDV3 represent the equivalent plastic displacements for tension, shear, and compression (i.e., κ_1 , κ_2 , κ_3), respectively	136
Figure 4-14. Load-displacement curve comparison for the URM walls under OOP loading: (a) Wall s1, and (b) Wall s2	139
Figure 4-15. Comparison of crack pattern for Wall s1: (a) experimental tests (Vaculik, 2012), (b) deformed shape from FE simulation, (c) equivalent plastic displacements for mortar joints from FE simulation, and (d) tensile damage scalar (DAMAGET) and compressive damage scalar (DAMAGEC) plots for units from FE simulation. Note: SDV1, SDV2, SDV3 represent the equivalent plastic displacements for tension, shear, and compression (i.e., κ_1 , κ_2 , κ_3), respectively	140

Figure 4-16. Comparison of crack pattern for Wall s2: (a) experimental tests (Vaculik, 2012), (b) deformed shape from FE simulation, (c) equivalent plastic displacements for mortar joints from FE simulation, and (d) tensile damage scalar (DAMAGET) and compressive damage scalar Note: SDV1, SDV2, SDV3 represent the equivalent plastic displacements for tension, shear, and compression (i.e., κ_1 , κ_2 , κ_3), respectively (DAMAGEC) plots for units from FE simulation.....	141
Figure 5-1. Constitutive material ($\sigma - \varepsilon$) relationship in different computational frameworks: (a) plasticity-based, (b) damage-based, and (c) damage plasticity-based	160
Figure 5-2. Illustration of 8-node zero-thickness interface element in the 3D space: (a) undeformed shape, and (b) deformed shape.....	162
Figure 5-3. Stress evolutions of the proposed constitutive model: (a) normal stress evolution, (b) shear stress evolution ($\sigma_n \geq 0$), and (c) shear stress evolution ($\sigma_n < 0$)	163
Figure 5-4. Normal stress evolution with stiffness recovery effects ($\omega_c = 1$, $\omega_t = 0$).....	166
Figure 5-5. Yield surfaces of the proposed constitutive model: (a) tension-shear yield surface, and (b) compression-cap surface	167
Figure 5-6. Evolution of yield surfaces in the 3D space.....	168
Figure 5-7. Relationship between dilatancy coefficient and: (a) plastic shear displacement, and (b) compressive normal stress	171
Figure 5-8. Effects of parameter η_t and η_c on the stress-displacement responses: (a) pure tension behavior, (b) pure shear behavior, and (c) pure compressive behavior	173
Figure 5-9. Effects of parameter α , β , and γ on the stress-displacement responses: (a) pure tension behavior, (b) pure shear behavior, and (c) pure compressive behavior	173
Figure 5-10. Graphical representation of stress return in the multi-yield surfaces model.....	179
Figure 5-11. Experimental-numerical comparison of normalized stress-displacement curve under cyclic tension loading	183
Figure 5-12. Masonry couplet specimen by Atkinson et al. (1989).....	184
Figure 5-13. Numerical-experimental comparison of shear stress-displacement responses	185

Figure 5-14. URM wall considered for the cyclic IP loading: (a) pre-compression applied at the top of the steel rigid beam, and (b) cyclic IP displacement-controlled loading.....	186
Figure 5-15. Load-history for the tested wall (Salmanpour, 2017; Salmanpour et al., 2015)	186
Figure 5-16. Numerical-experimental comparison of IP force-displacement curve for the short URM wall.....	189
Figure 5-17. Crack patterns and deformed shapes of the short URM wall obtained through the FE simulation at different stages (SDV1 and SDV2 represent the damage scalars D_t and D_c , respectively): (a) Point A, (b) Point B, (c) Point C, and (d) Point D	191
Figure 5-18. Failure mode of short URM wall in the experimental study by Salmanpour (2017)	191
Figure 5-19. Failure mode of tall URM wall obtained from the FE simulation: (a) deformed shape, (b) damage variable D_t , and (c) damage variable D_c	193
Figure 5-20. Numerical-experimental comparison of IP force-displacement curve for the tall URM wall.....	194
Figure 5-21. Failure modes of the RM wall: (a) experimental test (Shing et al. (1991)), (b) deformed shape of wall, (c) tensile damage of mortar joints, and (d) plastic strain distribution of reinforcements.....	196
Figure 5-22. Experimental-numerical comparison in terms of the load-deformation behavior of RM wall under cyclic IP loading	197
Figure 6-1. Schematic view of the FE modeling strategy using the simplified micro approach for URM walls	205
Figure 6-2. Numerical-experimental comparison for URM walls under IP loading: (a) IP load-deformation behavior, (b) experimental crack pattern for the wall with a pre-compression load of 0.3 MPa, (c) damage distribution in mortar joints (interfaces) from FE simulation, and (d) damage distribution in units from FE simulation	207
Figure 6-3. Loading sequence considered for URM walls under combined IP and OOP loading: (a) apply a pre-compression load P_v , (b) apply a predetermined uniformly distributed OOP load p_{oop} , and (c) apply an IP load F_{ip} until wall failure	210

Figure 6-4. Failure modes of URM walls: (a) wall AR1.00_SR9.92 with a pre-compression load of 0.0 MPa, (b) wall AR0.75_SR9.92 with a pre-compression load of 2.0 MPa, and (c) wall AR1.00_SR32.24 with a pre-compression load of 0.0 MPa.....	211
Figure 6-5. Influence of (a) AR, (b) SR, and (c) P_v on the IP load-deformation behaviors of URM walls	213
Figure 6-6. Variation of IP capacity of URM walls in terms of the (a) AR, (b) SR, and (c) pre-compression load	214
Figure 6-7. Failure mode of URM wall subject to one-way vertical bending	215
Figure 6-8. Influence of (a) AR, (b) SR, and (c) P_v on the OOP load-deformation behaviors ..	217
Figure 6-9. Variation of OOP capacity of URM walls in terms of the (a) AR, (b) SR, and (c) pre-compression load	218
Figure 6-10. Failure modes of wall AR0.75_SR9.92 under a pre-compression load of 2.00 MPa with different pre-applied OOP load levels: (a) 0%, (b) 20%, (c) 40%, (d) 60%, and (e) 80% of pure OOP capacity (deformation scale factor: 15)	220
Figure 6-11. IP load-deformation curves with different levels of pre-applied OOP loading for the wall AR0.75_SR9.92 with $P_v = 2.00$ MPa.....	221
Figure 6-12. Failure modes of wall AR2.25_SR9.92 under a pre-compression load of 2.00 MPa with different pre-applied OOP load levels: (a) 0%, (b) 20%, (c) 40%, (d) 60%, and (e) 80% of pure OOP capacity (deformation scale factor: 10)	222
Figure 6-13. IP load-deformation curves with different levels of pre-applied OOP loading for the wall AR2.25_SR9.92 with $P_v = 0.00$ MPa	222
Figure 6-14. IP-OOP capacity interaction curves for URM walls with different AR under a pre-compression load of: (a) 0.00 MPa, and (b) 2.00 MPa	223
Figure 6-15. Failure modes of wall AR0.75_SR9.92 with pre-applied OOP load levels at 80% of pure OOP capacities under a pre-compression load of : (a) 0 MPa (deformation scale factor: 100), (b) 0.25 MPa, (c) 0.50 MPa, (d) 1.00 MPa, (e) 1.50 MPa, and (f) 2.00 MPa (deformation scale factor for (b-f): 15).....	225
Figure 6-16. IP-OOP capacity interaction curves under different pre-compression loads for: (a) wall AR0.75_SR9.92 and (b) wall AR2.25_SR9.92	226

Figure 6-17. Evolution of OOP deformations (mm) due to IP loads for the: (a) wall AR1.00_SR9.92 with $P_v = 0.0$ MPa, and (b) wall AR1.00_SR9.92 with $P_v = 0.0$ MPa (deformation scale factor: 500).....	228
Figure 6-18. IP-OOP capacity interaction curves for URM walls with different SR under a pre-compression load of: (a) 0.00 MPa, and (b) 2.00 MPa	229
Figure 6-19. IP-OOP capacity interaction curves for URM walls with different P_v for the wall: (a) AR1.00_SR9.92 and (b) AR1.00_SR32.24	230
Figure 6-20. Range of interaction curves of URM walls considered	231
Figure 6-21. Comparison of interaction curves between the proposed model, the model proposed by Kesavan and Menon. (2022), and ASCE 41-17 (ASCE, 2017) for masonry infill walls: (a) AR0.75_SR9.92 with $P_v = 0.00$ MPa, (b) AR2.25_SR9.92 with $P_v = 0.00$ MPa, (c) AR0.75_SR9.92 with $P_v = 2.00$ MPa, (d) AR2.25_SR9.92 with $P_v = 2.00$ MPa, (e) AR1.00_SR9.92 with $P_v = 0.00$ MPa, (f) AR1.00_SR32.24 with $P_v = 0.00$ MPa, (g) AR1.00_SR9.92 with $P_v = 2.00$ MPa, and (h) AR1.00_SR32.24 with $P_v = 2.00$ MPa	234
Figure 7-1. Schematic view of the FE modeling strategy using simplified micro approach for RM walls	242
Figure 7-2. Experimental and FE-predicted load-deformation curves for the RM wall under IP loading.....	246
Figure 7-3. Comparison of the failure mode of the RM wall under IP loading: (a) experiment (Seif Eldin, 2016) and (b) FE simulation.....	246
Figure 7-4. Tested RM wall under OOP loading.....	247
Figure 7-5. Experimental and FE-predicted load-displacement curve of RM wall under OOP loading.....	249
Figure 7-6. OOP deformation (mm) of RM wall at the peak OOP load stage	249
Figure 7-7. Loading sequence for RM walls under combined IP and OOP loading: (a) apply a pre-compression load, (b) apply a predetermined uniformly distributed OOP load, and (c) apply an IP load until wall failure.....	252
Figure 7-8. FE simulation results for RM walls under pure IP loading: (a) the long wall AR0.67_SR8.42 with $P_v = 2.50$ MPa, and (b) the short wall AR2.00_SR8.42 with $P_v = 0.00$	

MPa (Left: deformed shapes of RM walls; Right: the plastic strain distributions of reinforcements)	254
Figure 7-9. Load-deformation curves of RM walls under pure IP loading with different pre-compression load levels for: (a) the long wall AR 0.67_SR8.42 and (b) the short wall AR2.00_SR8.42	255
Figure 7-10. IP capacities of RM walls: (a) influence of AR and P_v and (b) influence of SR and P_v	256
Figure 7-11. FE simulation results for Wall AR1.33_SR12.63 with $P_v = 1.00$ MPa under pure OOP loading: (a) deformed shape and (b) equivalent plastic strain of reinforcements.....	257
Figure 7-12. Load-deformation curves of RM walls under pure OOP loading with different pre-compression load levels for: (a) wall AR1.33_SR8.42 and (b) AR1.33_SR29.47.....	257
Figure 7-13. OOP capacities of RM walls with different slenderness ratios (with a fixed AR = 1.33) and pre-compression loads	258
Figure 7-14. IP load-deformation curves with different levels of pre-applied OOP loading for: (a) wall AR2.00_SR8.42 with $P_v = 0.00$ MPa and (b) wall AR1.60_SR8.42 with $P_v = 1.50$ MPa	260
Figure 7-15. IP-OOP capacity interaction curves under different pre-compression loads for: (a) wall AR2.00_SR8.42 and (b) wall AR1.60_SR8.42	260
Figure 7-16. Failure modes of wall AR2.00_SR8.42 under a pre-compression load of 0.00 MPa with different pre-applied OOP load levels: (a) 20%, (b) 40%, (c) 60%, and (d) 80% of OOP capacity obtained under pure OOP loading condition (deformation scale factor: 15).....	261
Figure 7-17. IP-OOP capacity interaction curves for flexural governed RM walls considered .	262
Figure 7-18. Failure modes of wall AR0.67_SR8.42 under a pre-compression load of 2.50 MPa with different pre-applied OOP load levels: (a) 20%, (b) 40%, (c) 60%, and (d) 80% of OOP capacity obtained under pure OOP loading (Deformation scale factor: 15).....	263
Figure 7-19. IP-OOP capacity interaction curves for the shear governed RM walls: (a) walls of different AR with $P_v = 2.0$ MPa and (b) the wall AR1.33_SR8.42 under different pre-compression loads	264

Figure 7-20. Comparison of IP-OOP capacity interaction curves for the flexural and shear governed walls	265
Figure 7-21. Evolution of OOP deformations (mm) due to IP loads for: (a) wall AR1.33_SR8.42 with $P_v = 0.0$ MPa, (b) AR1.33_SR29.47 with $P_v = 0.0$ MPa, and (c) wall AR1.33_SR29.47 with $P_v = 2.5$ MPa (defomation scale factor:15).....	267
Figure 7-22. IP-OOP capacity interaction curves of RM walls: (a) walls with different SR when pre-compression load $P_v = 0.0$ MPa, and (b) wall AR1.33_SR29.47 with different pre-compression load levels	268
Figure 7-23. Comparison of the IP-OOP capacity interaction curves for RM walls and their URM counterparts: (a) the most ‘flexural’ and the most ‘shear’ walls considered, and (b) the wall considered with strongest IP-OOP interaction effects	269
Figure 8-1. FE model for the IP resistance prediction of RM walls	280
Figure 8-2. URM wall considered for the case study	287
Figure 8-3. Histograms and probability distributions of random variables: (a) compressive strength of masonry units f'_c , (b) tensile strength of mortar joints f_t , (c) frictional coefficient $\tan\psi$, (d) initial dilation coefficient $\tan\psi_0$, (e) peak cohesion c_0 , and (f) compressive strength of masonry f'_m	291
Figure 8-4. Emperical cumulative probability functions of IP resistances for the URM wall considered	292
Figure 8-5. Comparison of IP resistances obtained by FE model and design-code model for URM walls governed by (a) flexural rocking, (b) diagonal tension cracking, and (c) shear sliding failure	293
Figure 8-6. Relationship between MSE reduction e and Pearson correlation coefficient ρ with different computational cost ratios w_{CSA} / w_{FE}	295
Figure 8-7. MSE of FE model-based crude MC estimator, design-code model-based crude MC estimator, and proposed estimator for the mean value of IP resistance for the URM wall considered	297
Figure 8-8. Distributions of FE model-based crude MC mean estimator and proposed mean estimator obtained by 500 replicates with different computational costs	298

Figure 8-9. MSE of crude MC estimators, and proposed estimators (mean-optimal and variance-optimal) for the variance of IP resistance for the URM wall considered 300

Figure 8-10. Distributions of FE model-based crude MC variance estimator and proposed variance estimator (variance-optimal) obtained by 500 replicates with different computational costs 302

Figure 8-11. RM shear wall considered for the case study..... 304

Figure 8-12. Emperical cumulative probability function of IP resistance for the RM shear wall 307

Figure 8-13. Comparison of IP resistance obtained by FE model and design-code model for the RM shear wall..... 308

Figure 8-14. MSE of FE model-based crude MC estimator, design code-based crude MC estimator, and proposed estimator for the (a) mean, and (b) variance of IP resistance of the RM shear wall..... 309

Figure 8-15. Distributions of FE model-based crude MC mean estimator and proposed mean estimator for the IP resistance of the RM shear wall obtained by 500 replicates with different computational costs..... 310

Figure 8-16. Distributions of FE model-based crude MC variance estimator and proposed variance estimator (variance-optimal) obtained by 500 replicates with different computational costs 311

Figure 8-17. RM flexural wall considered for the case study..... 312

Figure 8-18. Emperical cumulative probability function of IP resistance for the RM flexural wall considered 314

Figure 8-19. Comparison of IP resistance obtained by FE model and design-code model for the RM flexural wall considered..... 314

Figure 8-20. MSE of FE model-based crude MC estimator, design code-based crude MC estimator, and proposed estimator for the (a) mean, and (b) variance of IP resistance of the RM flexural wall..... 315

Figure 8-21. Distributions of FE model-based crude MC mean estimator and proposed mean estimator for the IP resistance of the RM flexural wall obtained by 500 replicates with different computational costs 316

Figure 8-22. Distributions of FE model-based crude MC variance estimator and proposed variance estimator (variance-optimal) obtained by 500 replicates with different computational costs 317

Figure 9-1. URM wall considered for the case study 334

Figure 9-2. Empirical cumulative probability functions of OOP resistances for the URM wall considered 337

Figure 9-3. Comparison of OOP resistances obtained by the FE model and design-code model for URM walls 338

Figure 9-4. MSE of FE model-based crude MC estimator, design-code model-based crude MC estimator, and proposed estimator for the mean value of OOP resistance for the URM wall considered 341

Figure 9-5. Distributions of FE model-based crude MC mean estimator and proposed mean estimator obtained by 500 replicates with different computational costs 342

Figure 9-6. MSE of FE-based crude MC estimator, design code-based crude MC estimator, and proposed estimators (mean-optimal and variance-optimal) for the variance of OOP resistance for the URM wall considered..... 344

Figure 9-7. Distributions of FE model-based crude MC variance estimator and proposed variance estimator (variance-optimal) obtained by 500 replicates with different computational costs 346

Figure 9-8. Empirical cumulative probability function of OOP resistance for the RM wall..... 350

Figure 9-9. Comparison of OOP capacity obtained by design-code and FE models for RM walls 350

Figure 9-10. MSE of FE model-based crude MC estimator, design code-based crude MC estimator, and proposed estimator for the (a) mean, and (b) variance of OOP resistance of the RM wall 352

Figure 9-11. Distributions of FE model-based crude MC mean estimator and proposed mean estimator obtained by 500 replicates with different computational costs	353
Figure 9-12. Distributions of FE model-based crude MC variance estimator and proposed variance estimator (variance-optimal) obtained by 500 replicates with different computational costs	354
Figure 10-1. Flowchart of the proposed reliability analysis method	375
Figure 10-2. Cantilever beam under a concentrated vertical load at the free end: (a) HF model with a finer mesh, and (b) LF model with a coarser mesh	377
Figure 10-3. Illustration of proposed method: (a) generated samples on the LF model at different intermediate levels, and (b) corresponding probability densities of beam deformation at different intermediate levels for LF and HF models in Example #1	379
Figure 10-4. Comparison of reliability analysis results for Example #1 in terms of: (a) RMSE, and (b) COV	380
Figure 10-5. Illustration of proposed method: (a) generated samples on the LF model at different intermediate levels, and (b) corresponding probability densities of beam deformation on LF and HF models in Example #2	382
Figure 10-6. Comparison of reliability analysis results for Example #2 in terms of: (a) RMSE, and (b) COV	383
Figure 10-7. A ten-bar truss structure	384
Figure 10-8. Comparison of reliability analysis results for Example #3 in terms of: (a) RMSE, and (b) COV	386
Figure 10-9. A three-bay by three-story frame structure	386
Figure 10-10. Stress-strain curve for the steel member considered in Example #4	387
Figure 10-11. Comparison of reliability analysis results for Example #4 in terms of: (a) RMSE, and (b) COV	389
Figure 10-12. Probabilistic load effects and resistance of RM wall under OOP loading using crude MCS on the HF model	394

Figure 10-13. Biasing PDFs at intermediate levels in the cross-entropy adaptive sampling procedure for the RM wall under OOP loading: (a) Young’s modulus of reinforcements, (b) yield strength of reinforcements, (c) compressive strength of masonry, and (d) reinforcement location..... 395

Figure 10-14. Comparison of reliability analysis results for the RM wall under OOP loading in terms of: (a) RMSE, and (b) COV 396

Figure 10-15. Biasing PDFs at intermediate levels in the cross-entropy adaptive sampling procedure for the RM wall under IP loading: (a) Young’s modulus of reinforcements, (b) yield strength of reinforcements, (c) compressive strength of masonry, and (d) reinforcement location . 402

Figure 11-1. Contribution and deliverables of this research work..... 414

Chapter 1. INTRODUCTION

1.1. BACKGROUND

Masonry has transitioned from basic stone constructions to complex architectural feats across millennia. This time-honored construction material is exemplified in historical landmarks such as the Egyptian pyramids, the Roman Colosseum, and the majestic cathedrals of Gothic architecture. These architectural wonders are not only testaments to human ingenuity but also stand as timeless symbols of ancient and medieval civilizations. In the modern construction industry, masonry continues to play a crucial role and maintains its relevance through the integration of traditional craftsmanship with modern technological innovations. This fusion has led to masonry being used not only for its aesthetic appeal but also for its practical benefits, such as energy efficiency, durability, and cost-effectiveness. The widespread application of masonry in global construction is underscored by a report from the Mason Contractors Association of America (MCAA), noting that over 70% of the world's buildings are built of masonry. Modern masonry structures, contrasted with traditional unreinforced masonry (URM), often include reinforcements to augment strength and ductility, leading to the development of reinforced masonry (RM) structures.

Masonry walls serve as an integral component in both vertical and lateral load-resisting systems in masonry buildings, providing resistance against various loads such as earthquake loads along and perpendicular to the wall, wind loads perpendicular to the wall, and eccentric gravity loads transferred from diaphragms supported on the wall. Consequently, the structural behaviors of masonry walls are typically characterized by two distinct loading modes: in-plane (IP) loading and out-of-plane (OOP) loading. The vulnerability of masonry walls has been highlighted in post-

earthquake surveys in several notable earthquakes, including the 2011 Christchurch earthquake (Dizhur et al. 2011), 2013 Kaki earthquake (Sherafati and Sohrabi 2016a), 2017 Lesvos earthquake (Vlachakis et al. 2020). Due to masonry's heterogeneity and anisotropy, masonry walls may exhibit various failure modes. Under IP loading, for example, masonry walls are governed by three main failure mechanisms, as shown in Figure 1-1 (a-c): diagonal tension cracking, shear sliding, and flexural rocking. OOP failure modes include overturning failure, one-way bending (i.e., vertical bending), and two-way bending, as illustrated in Figure 1-2 (a-c).

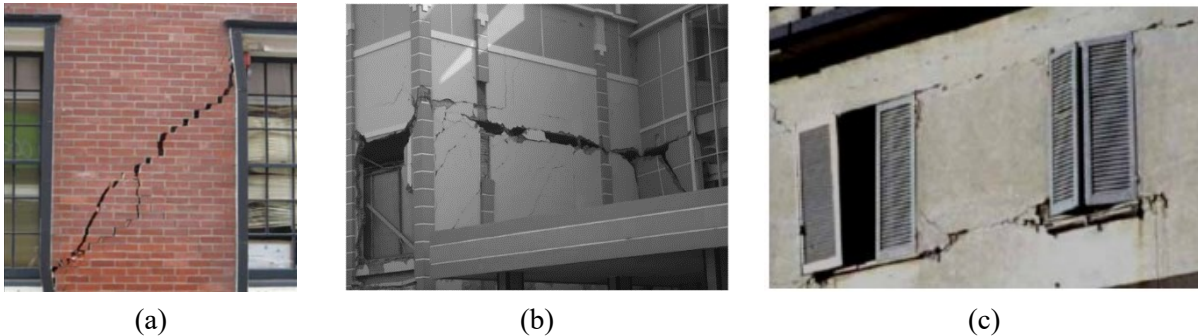


Figure 1-1. Failure modes of masonry walls under IP loading: (a) diagonal tension cracking (Celano et al. 2021), (b) shear sliding (Saatcioglu et al. 2006), and (c) flexural rocking (Celano et al. 2021)

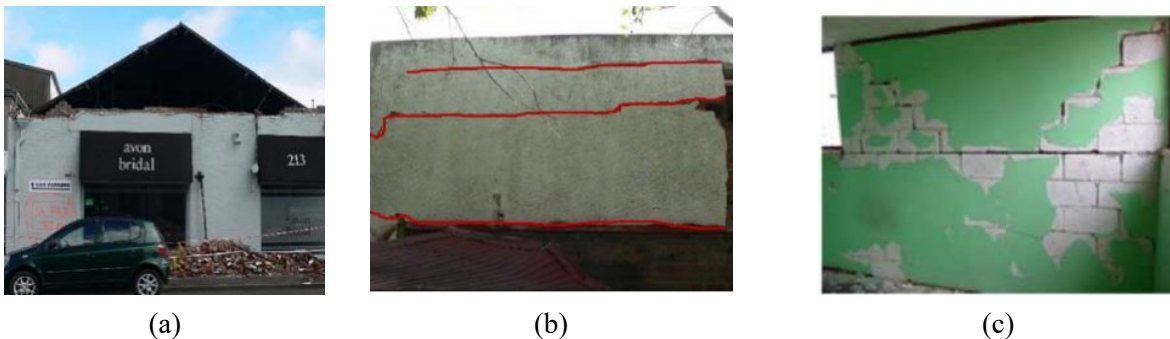


Figure 1-2. Failure modes of masonry walls under OOP loading: (a) overturning failure (Giaretton et al. 2016), (b) one-way bending failure (Giaretton et al. 2016), and (c) two-way bending failure (Astroza et al. 2012)

In addition to the distinct occurrence of IP or OOP failure, combined IP and OOP failure modes were also frequently observed in earthquake events, e.g., the 2017 Lesvos earthquake

(Vlachakis et al. 2020). Specifically, corner regions of masonry buildings (i.e., wedges) are typically highly stressed by the biaxial actions under combined IP and OOP loading. Such an effect often leads to a ‘bursting’ collapse phenomenon, as shown in Figure 1-3. A similar pattern was observed in the aforementioned earthquake survey, where OOP strength in masonry walls was compromised due to existing IP damage, leading to the isolation and overturning of walls under OOP forces, as shown in Figure 1-4. This IP-OOP interaction behavior is exemplified by the effects of axial load and bi-directional bending moment (P-M-M) interaction diagrams for reinforced concrete columns (Shen et al. 2023; Del Zoppo et al. 2017; Zuhair Murad 2021), as well as the IP and OOP capacity interaction relationships for masonry infill walls as specified in ASCE 41-17 (2017).

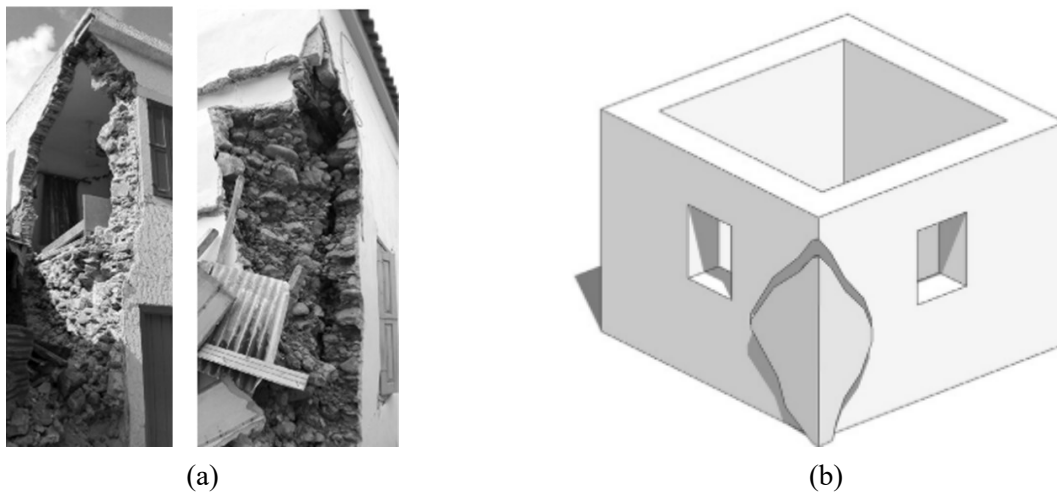


Figure 1-3. In-plane and out-of-plane failure at corner regions: (a) field observations, and (b) corresponding schematic sketch (Vlachakis et al. 2020)

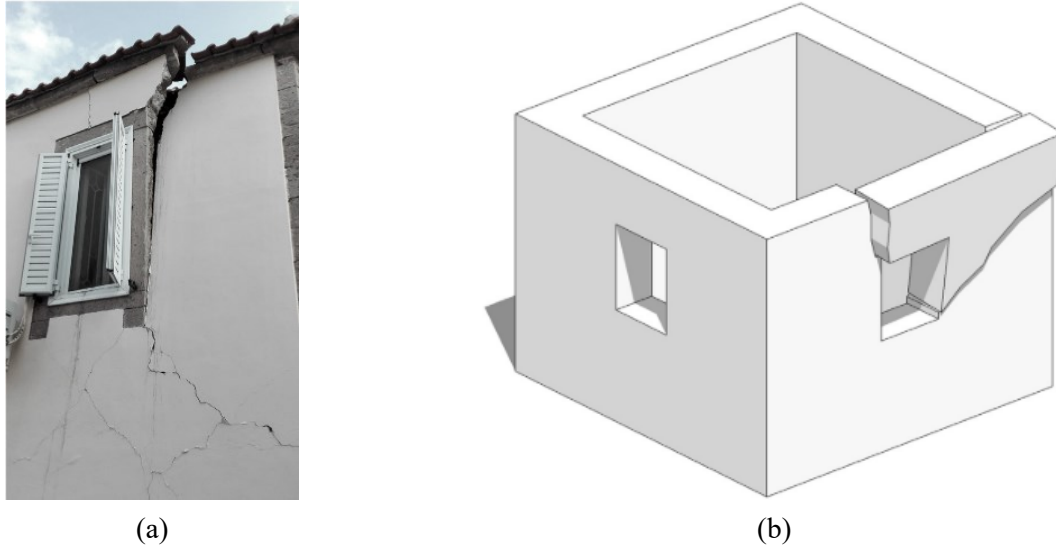


Figure 1-4. Out-of-plane collapse of in-plane damaged masonry walls: (a) field observation, and (b) corresponding schematic sketch (Vlachakis et al. 2020)

The prediction of structural behaviors in masonry walls (e.g., wall resistances, crack initiation and propagation, failure modes) faces significant challenges due to complex failure modes under various loading scenarios. Currently, masonry walls are primarily designed to adhere to prescriptive code regulations based on the limit-state design philosophy. In North America, several codes are available for the design of masonry walls, including CSA S304-14 (2014), TMS 402-16 (2016), and NBCC (2015). These prescriptive codes generally provide guidelines on material properties, detailing requirements, minimum and/or maximum reinforcements, allowable stresses, and other considerations. Experimental, analytical, and numerical research efforts have played a vital role in shaping the development of masonry design and construction, contributing to the evolution of design regulations, and fostering a deeper understanding of the complex behaviors of masonry walls (Zeng and Li 2023). Over the past few decades, a scientific basis has been laid on what originated as a purely heuristic code development process, enabling the incorporation of research findings. However, design codes for the prediction of IP or OOP

behaviors of masonry walls in the current versions do not still lead to rational design outcomes, with many being overly conservative (Bolhassani et al. 2016; Izquierdo 2021; Samy et al. 2012; Seif EIDin et al. 2019). Moreover, current design practices for masonry walls often neglect the IP and OOP capacity interaction effects, and this aspect also remains largely unexplored in the research community, particularly in the case of RM walls.

The composite nature of masonry walls not only results in challenges in the structural behavior prediction of masonry walls but also introduces substantial variabilities associated with masonry material. For instance, Müller and Graubner (2021) and Sherafati and Sohrabi (2016b) conducted the field studies regarding the compressive strength of masonry and the shear-sliding strength of mortar joints, respectively. The test results revealed that the coefficient of variation (COV) for these two material properties is extremely high: 30% ~ 40% and 56%, respectively. Despite these uncertainties, contemporary design guidelines for masonry walls still heavily rely on deterministic approaches with partial safety factors, which need to be calibrated using reliability-based approaches to ensure that masonry walls achieve the desired level of reliability (Isfeld et al. 2023; Lawrence and Stewart 2015; Moosavi and Korany 2014; Rota et al. 2014; Stewart and Lawrence 2007; Zhai et al. 2012; Zhai and Stewart 2010). In this context, uncertainty quantification (e.g., statistics estimation and reliability analysis) play crucial roles.

1.2. RESEARCH MOTIVATION AND PROBLEM STATEMENT

To facilitate a reliable prediction of the structural behavior of masonry walls (including both URM and RM walls) under various loading conditions, a high-fidelity finite element (FE) model is of paramount importance. The first part of this thesis is dedicated to addressing this challenge.

In the realm of FE modeling for masonry structures, the research community broadly classifies modeling strategies into two main categories, as per Lourenço (1995a): micro modeling strategy and macro modeling strategy. The micro modeling approach provides an elaborate representation of masonry components, such as brick units or concrete blocks, mortar, grouts, and reinforcements. This technique facilitates an extensive analysis of both local and global behaviors of masonry walls. Notably, it provides essential local-level insights, particularly for phenomena like crack initiation and propagation. Despite its flexibility in accommodating complex loading conditions such as combined IP and OOP loading, its intricate nature entails considerable computational demands, posing challenges in simulating large-scale masonry structures.

In contrast, the macro modeling strategy conceptualizes masonry as a homogenized continuum. This method is more efficient and practical for analyzing larger structures or for preliminary design phases, as it reduces computational demands and streamlines model configurations. Despite its efficacy in large-scale structural analysis, macro modeling strategy tends to overlook complex interactions between masonry constituents, potentially leading to the omission of critical local failure events. This generalization may lead to inaccuracies in capturing specific localized behaviors, such as distinctive crack patterns or stress concentrations.

Recognizing the distinctive advantages and disadvantages inherent in both strategies, this thesis relies on the micro modeling approach to develop high-fidelity computational models for masonry walls. The efficacy of the micro modeling strategy in simulating structural behavior is heavily dependent on the constitutive model of cohesive interfaces for mortar joints, typically the most vulnerable part of masonry walls. An extensive literature review on this subject (Sections 2.1 and 2.2), complemented by an investigation of public studies on the structural behavior of masonry

walls under combined IP and OOP loadings (Section 2.3), is presented. The review highlights several research gaps that motivate the first half of this thesis:

- Existing constitutive models of cohesive interfaces in simulating mortar joints were mostly limited to two-dimensional (2D) stress domains. In scenarios when investigating the structural behavior of masonry walls subject to OOP loading or combined IP and OOP loading, a three-dimensional constitutive material model is essential.
- The constitutive formulation for cohesive interfaces should encompass various potential failure modes of mortar joints under complex loadings, including tensile cracking, shear sliding, and compressive crushing. Furthermore, an important micro-mechanical phenomenon, ‘dilatancy’, was not adequately addressed in existing models.
- The complex failure mechanisms of mortar joints under cyclic loading, characterized by stiffness degradation and irreversible deformations, were not satisfactorily modeled by existing models relying solely on computational plasticity or damage mechanics.
- Public studies on the IP and OOP interaction behaviors of masonry walls are notably scarce, resulting in a significant knowledge gap. This deficiency in the literature can be attributed to the challenges and costs associated with testing masonry walls under complex loading conditions and the computational complexities of modeling masonry walls in 3D space.

To promote modern limit-state design and foster the evolution of next-generation performance-based design in the masonry community, the second part of this thesis is dedicated to formulating robust strategies to address the material uncertainty of masonry. This entails two main tasks: statistics estimation and reliability analysis. The research problems addressed in this part are to

formulate effective strategies for the statistics estimation of IP and OOP resistances of masonry walls and to establish a comprehensive framework for the reliability analysis of masonry walls. A literature review presented in Section 2.5 and Section 2.6 indicates that in the existing research, two types of deterministic models are commonly integrated into the Monte Carlo (MC) simulation framework for these purposes, namely low-fidelity (LF) model (e.g., design-code model, simple analytical model) and high-fidelity (HF) model (e.g., micro model). However, exclusively relying on either model may present challenges. LF model-based studies might incur substantial model error due to the inherent assumptions and simplifications. On the other hand, HF model-based studies are often associated with intense computational costs, and limited samples within the MC simulation framework do not ensure accurate results for uncertainty quantification. This motivates the second part of this thesis: multi-fidelity uncertainty quantification (including statistics estimation and reliability analysis) for masonry walls. Accordingly, research objectives are detailed in the subsequent section.

1.3. RESEARCH OBJECTIVES

In light of the identified research gaps and motivations, the overarching objective of this thesis is twofold: (1) to develop 3D constitutive models for mortar joints to facilitate high-fidelity simulation of masonry walls and their applications in investigation of masonry walls under complex loading scenarios (e.g., combined IP and OOP loadings), and (2) to develop sophisticated algorithms for uncertainty quantification and their applications on masonry walls. To this end, this research is coordinated with the following four primary sub-objectives:

(1) Sub-objective #1: Development of 3D constitutive models for mortar joints to facilitate the high-fidelity modeling of masonry walls

This sub-objective starts with an assessment of readily available modeling techniques for the modeling of mortar joints in the General-purpose Finite Element (FE) software ABAQUS (Dassault Systemes 2017). It involves evaluating their effectiveness and identifying the limitations of off-the-shelf modeling techniques. Following this, a new 3D multi-yield surfaces plasticity-based constitutive model is developed for simulating the monotonic behavior of mortar joints. This model is subsequently extended to a damage plasticity-based framework, resulting in a second newly developed damage-plasticity constitutive model for simulating the cyclic behavior of mortar joints. Theoretical formulations and numerical implementations are detailed. The developed two constitutive models are validated against experimental tests in the public literature on small-scale masonry specimens (i.e., unit-mortar-unit assemblages) and URM and RM walls under IP or OOP loadings.

(2) Sub-objective #2: Investigation of IP-OOP interaction behavior of unreinforced and reinforced masonry walls

Expanding upon the constitutive model from Sub-objective #1, this sub-objective entails a comprehensive numerical investigation of 252 unreinforced masonry (URM) walls and 288 reinforced masonry (RM) walls under combined IP and OOP loadings. The focus is to thoroughly analyze the failure mechanisms of masonry walls and to quantitatively assess the impact of pre-existing OOP loading on the IP capacity. This involves an in-depth exploration of various potential influential factors: aspect ratio, slenderness ratio, and pre-compression load. Furthermore, IP-OOP interaction behaviors of URM and RM walls are compared to show the effects of reinforcements. Additionally, considering the complexity of model setup associated with the micro modeling strategy, automated modeling tools are needed to streamline this procedure.

(3) Sub-objective #3: Development of methodologies for statistics estimation using a multi-fidelity approach and its application to the IP and OOP resistances of masonry walls with uncertain material properties

This sub-objective addresses the first of two primary goals in the uncertainty quantification aspect of this research: statistics estimation. Accordingly, two novel statistics estimators for mean and variance are developed, respectively. The developed estimators integrate limited high-fidelity models (e.g., the FE models developed in Sub-objective #1) with a large number of low-fidelity models (e.g., design-code models), namely multi-fidelity (MF) approaches. The effectiveness of these estimators is demonstrated through case studies involving masonry walls subjected to IP or OOP loadings, showcasing their superior performance.

(4) Sub-objective #4: Development of multi-fidelity reliability analysis algorithm and its application to masonry walls with uncertain material properties

This sub-objective tackles the second goal of the uncertainty quantification part: reliability analysis. A novel MF reliability analysis algorithm is proposed, and its applicability is validated through four numerical examples. The algorithm is then applied to conduct reliability analyses for reinforced masonry walls under IP and OOP loadings, respectively.

1.4. NOVELTY AND SIGNIFICANCE OF RESEARCH

This research contributes to the masonry community by developing innovative computational techniques and algorithms of uncertainty quantification for masonry walls. In the first part of this thesis, two novel 3D constitutive models for masonry mortar joints are introduced to facilitate the high-fidelity modeling of masonry walls. Contrasting with existing models in the public literature

that were mainly limited to 2D stress space and thus restricted to in-plane (IP) loading conditions, this research introduces more versatile models that can be applied in complex loading scenarios (e.g., combined IP and OOP loading). The newly developed models effectively incorporate critical micro-mechanical phenomena such as “dilatancy” and reasonably depict the complex failure mechanisms of mortar joints under cyclic loading, characterized by stiffness degradation and irreversible deformations. The research thoroughly addresses these aspects, filling a significant gap in existing modeling approaches. Furthermore, this thesis sheds light on the IP-OOP interaction effects in masonry walls, a topic previously largely unexplored in the literature. This exploration has direct implications for the practical design of masonry structures, offering insights into how different wall configurations influence the structural behaviors of masonry walls under combined IP and OOP loading. Additionally, the quantitative assessment of IP-OOP capacity interaction curves is vital for practical designs, improving the safety of masonry walls.

The second part of the thesis takes a pioneering role in the advancement of multi-fidelity (MF) approaches within the realm of uncertainty quantification in the masonry community. It entails the development of innovative methods for statistics estimation and reliability analysis that integrate high-fidelity models (e.g., advanced computational models) and low-fidelity models (e.g., design-code models). This integration leads to more efficient and accurate estimations compared to other available methods.

The significance of this research extends to enhancing the structural safety of masonry walls. The improved modeling capabilities provide more accurate predictions, aiding in the design of masonry buildings. By addressing notable gaps in existing literature and practices, the research enriches the body of knowledge about masonry structures, guiding future research and practical

applications. Moreover, the findings have the potential to influence the development of future building codes and standards for masonry structures. This contribution is critical in shaping more accurate and effective design guidelines, thereby enhancing the safety and resilience of masonry buildings. Moreover, the pioneering work in MF approaches for uncertainty quantification aligns with the principles of next-generation probabilistic performance-based design. This area of design, increasingly recognized for its potential to model the uncertainties inherent in structural behavior and loading conditions accurately, is enhanced by the integration of high-fidelity and low-fidelity models. Such integration leads to more reliable probabilistic analyses, which are crucial for developing design strategies that are not only safe but also adaptable to the variability and unpredictability of real-world conditions.

1.5. ORGANIZATION OF THESIS

This thesis is structured into eleven chapters, each covering specific aspects as outlined below and shown in Figure 1-5:

- **Chapter 1** offers an introduction to this research, providing an overview of the background, problem statement, research motivation, objectives, and methodology. It also highlights the novelty and significance of the study.
- **Chapter 2** provides a comprehensive literature review pertinent to this thesis, focusing on computational modeling approaches for masonry walls, constitutive models for mortar joints in various computational frameworks, IP-OOP interaction behaviors of masonry walls, and aspects of uncertainty quantification on masonry walls.
- **Chapter 3** presents a finite element (FE) modeling strategy using off-the-shelf techniques to simulate the IP and OOP behavior of URM walls, accompanied by a parametric analysis to

assess parameter importance. Moreover, the limitations of off-the-shelf modeling techniques in modeling mortar joints are identified.

- **Chapter 4** presents a newly developed a 3D plasticity-based multi-yield surfaces constitutive model for monotonic modeling of mortar joints by addressing the limitations previously identified. Validation of this model is conducted with small-scale masonry specimens and large-scale masonry walls under IP or OOP loadings.
- Building on the computational plasticity framework, **Chapter 5** extends the monotonic model from **Chapter 4** to a cyclic model, introducing a novel damage-plasticity based 3D multi-yield surfaces constitutive model for simulating the cyclic behavior of masonry mortar joints.
- **Chapter 6** and **Chapter 7** present two comprehensive numerical studies exploring the structural behavior of URM and RM walls under combined IP and OOP loadings. The IP capacity reductions due to the OOP loading are quantified, and the critical scenarios most susceptible to the combined IP and OOP loadings are identified.
- **Chapter 8** and **Chapter 9** introduce two innovative statistical estimators for mean and variance, respectively. This is achieved by leveraging efficient design-code models and expensive high-fidelity micro models using the control variate (CV) method. The performance of the proposed estimators compared to the crude Monte Carlo (MC) estimators relying solely on either model is demonstrated through several case studies.
- In **Chapter 10**, a novel multi-fidelity reliability analysis algorithm is presented. Several numerical examples are presented to show its robustness. Subsequently, this novel algorithm is applied for the reliability analysis of masonry walls.

- **Chapter 11** concludes the thesis work with a summary, conclusions, contributions, and highlights of this research, as well as the recommendation for future work.

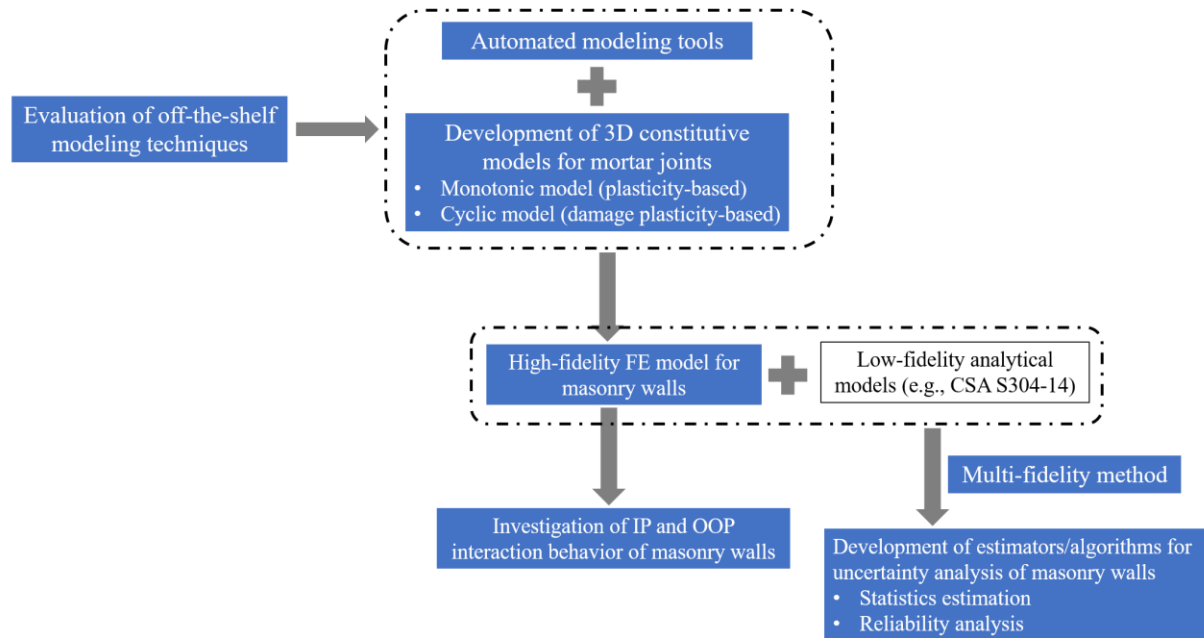


Figure 1-5. Organization of the thesis

Chapter 2. LITERATURE REVIEW

2.1. FINITE ELEMENT MODELING FOR MASONRY WALLS

Depending on different levels of sophistication and complexity, finite element (FE) modeling approaches for masonry walls are broadly characterized into two types: the micro modeling approach and the macro modeling approach (Lourenço et al. 1995a). This section reviews relevant works on using these strategies in the FE modeling of masonry walls.

2.1.1. Micro modeling approach

The micro modeling approach for masonry structures can be subdivided into detailed and simplified micro modeling strategies. For the masonry specimen shown in Figure 2-1 (a), all components are explicitly simulated in the detailed micro modeling approach: units and mortar are represented with solid continua, while contact surfaces between units and mortar are modeled by discontinuous cohesive interfaces, as shown in Figure 2-1 (b). In the simplified micro modeling approach, mortar and unit-mortar contact surfaces are lumped into mortar joints modeled by zero-thickness interfaces, as illustrated in Figure 2-1 (c). This simplification reduces the number of interface elements considered, thereby leading to computational costs. In this subsection, the FE model strategies for investigating the IP and OOP behaviors of masonry walls are reviewed, encompassing both unreinforced masonry (URM) walls and reinforced masonry (RM) walls.

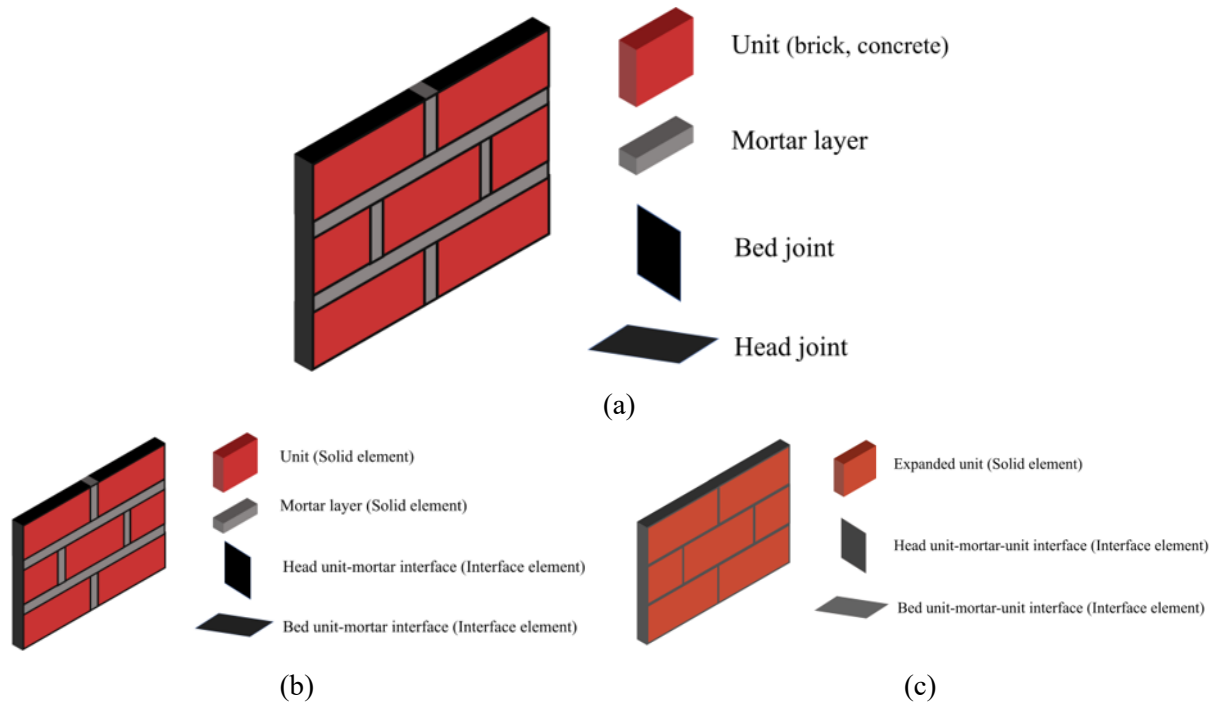


Figure 2-1. FE micro modeling strategies for masonry structures: (a) masonry specimen, (b) detailed micro modeling approach, and (c) simplified micro modeling approach

2.1.1.1 In-plane behavior

Micro models for masonry walls are typically validated against existing experimental results. Remarkable success was achieved in reproducing the structural behaviors of URM walls under IP loading, including the load-deformation behaviors and failure modes. A significant number of studies based on the micro modeling approach focused solely on the monotonic IP behavior of URM walls, see for example (Abdulla et al. 2017; Anand and Yalamanchili 1996; Berto et al. 2004; Chaimoon and Attard 2007; Citto 2008; D’Altri et al. 2018; Dolatshahi and Aref 2011; Drougkas et al. 2019; Fouchal et al. 2009; Giambanco et al. 2001, 2018; Greco et al. 2016; Kumar et al. 2014; Kumar and Barbato 2019; Li and Zeng 2023; Lotfi and Shing 1994; Lourenço 1996; Lourenço and Rots 1997; Macorini and Izzuddin 2011; Marfia and Sacco 2012; Nazir and Dhanasekar 2014; da Porto et al. 2010; Vandoren et al. 2013; Wambacq et al. 2022; Xu et al. 2012; Zeng et al. 2021;

van Zijl 2004). For instance, URM walls tested in the monotonic IP loading condition (Raijmakers 1992), characterized by a typical diagonal tension failure mode shown in Figure 2-2, were widely used as validation examples in a large number of studies, e.g., (Abdulla et al. 2017; Lourenço 1996; Macorini and Izzuddin 2011; Zeng et al. 2021). These studies demonstrate the capability of the micro modeling strategy to accurately predict the initial stiffness, peak strength, and post-peak behavior.

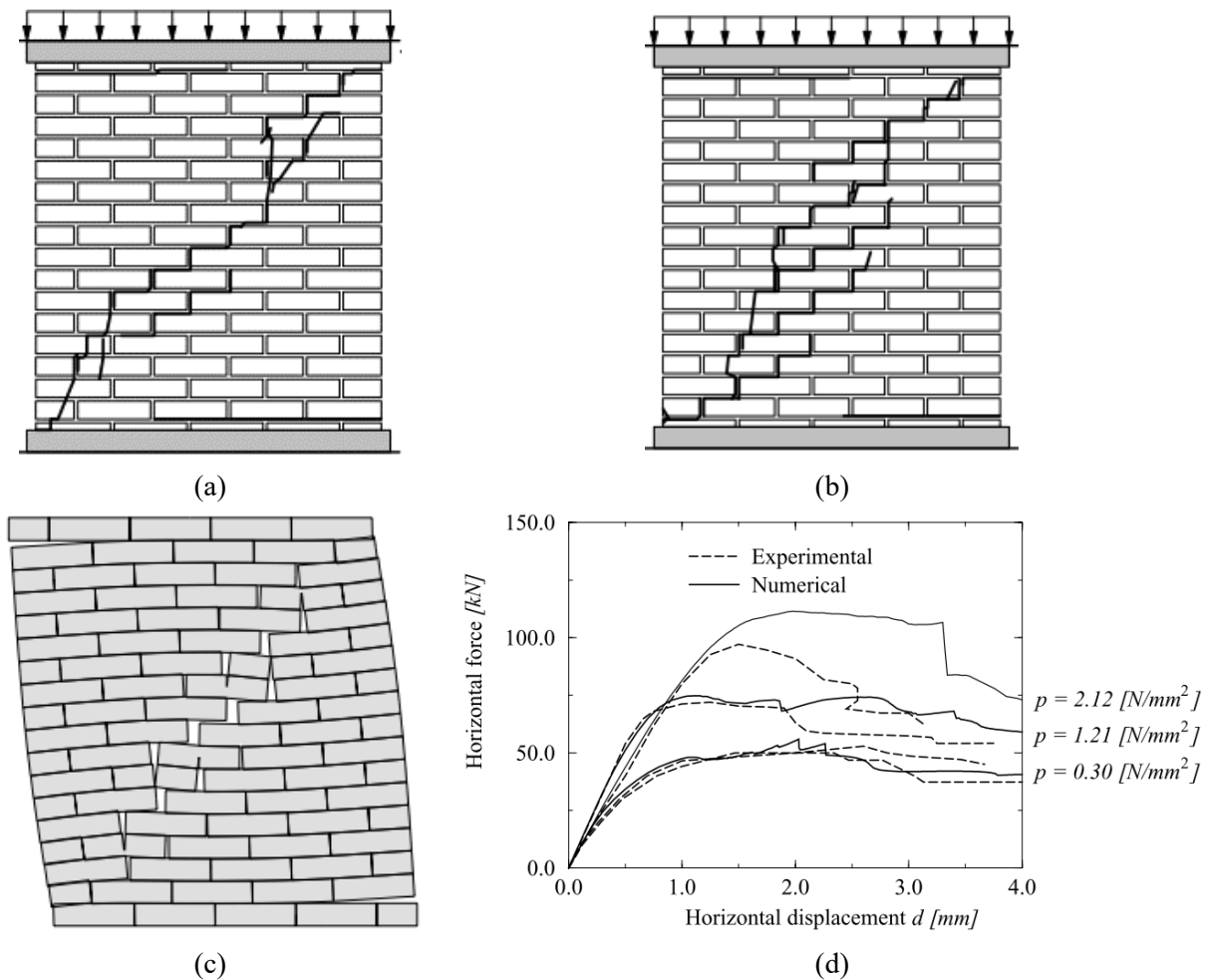


Figure 2-2. FE models based on the micro modeling strategy for URM walls under IP loading by Lourenço (1996)

Nonetheless, comparatively fewer studies have addressed the cyclic behavior of URM walls under IP loading (Aref and Dolatshahi 2013; D’Altri et al. 2019; Gambarotta and Lagomarsino 1997a; Koutromanos and Shing 2012; Minga et al. 2018; Nie et al. 2022b; a; Oliveira and Lourenço 2004; Xie et al. 2021b; Yavartanoo and Kang 2022). This gap is partly attributed to the significant numerical complexity of the theoretical implementations involved in the model development. Effective cyclic constitutive models of mortar joints must encapsulate key characteristics of the material's hysteretic stress–strain loop, including energy dissipation during a cycle, plastic strains at the zero-stress level, crack closure under compressive stresses, and degradation of strength and stiffness in both tensile and compressive regimes. For instance, the flexural failure mode of URM walls tested in (Anthoine et al. 1994; Messali et al. 2020) and corresponding hysteretic behaviors were reasonably predicted using micro modeling strategy as evidenced by Minga et al. (2018) and D’Altri et al. (2019), as illustrated in Figure 2-3 (a-b).

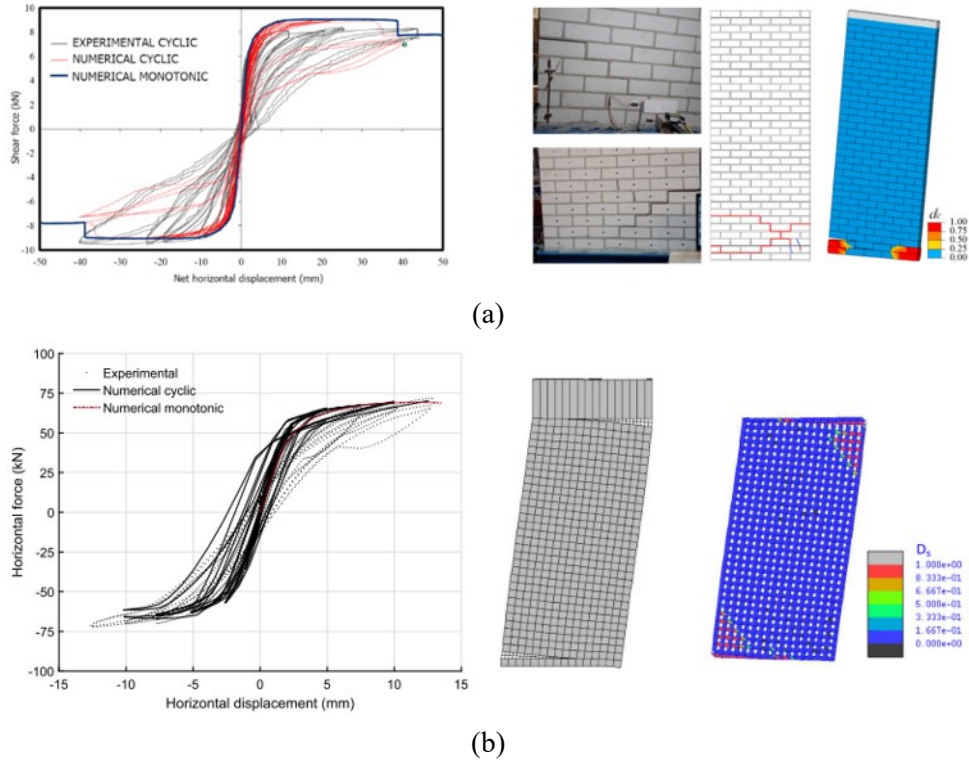


Figure 2-3. Flexural rocking failures and corresponding hysteretic behaviors of URM walls predicted by the micro modeling strategy: (a) D'Altri et al. (2019), and (b) Minga et al. (2018)

In recent decades, more high-fidelity micro models have been developed by researchers for the modeling of IP behaviors of RM walls. An early attempt by Shing and Cao (1997) involved simulating partially grouted reinforced masonry (PGRM) walls using the micro modeling strategy. In this model, masonry units were simulated using a plane-stress smeared crack formulation, and mortar joints were modeled by an elastic-plastic interface model proposed by Lotfi and Shing (1994). The validation results illustrated that the lateral strengths obtained were higher than those shown by tests. The discrepancies were attributed to the different load histories (i.e., monotonic or cyclic) and partly due to the assumption in the bond strength between the wall panels and concrete head beams.

Maleki (2008) simulated the PGRM walls in a discrete manner by using smear-crack plane stress elements to represent the grouted parts and cohesive interface elements to model the ungrouted parts and mortar joints, respectively. The proposed modeling scheme was capable of capturing the cracking pattern but was only applicable to monotonic loading scenarios.

Calderón et al. (2017, 2019, 2021a) developed detailed micro models for PGRM walls, as shown in Figure 2-4. The nonlinear behaviors of units, mortar, and grout were considered by means of a total strain-based crack model, accounting for tensile cracking and compressive crushing. The steel reinforcement was assumed to be perfectly bonded with the surrounding grout parts and represented with beam elements and the Von Mises plasticity model. The proposed modeling strategy involved the nonlinear behaviors of the following interactions: unit to head-joint, bed-joint to head-joint, bed-joint to reinforcement, unit to grout, and bed-joint to grout. Numerical validations included several PGRM walls with or without openings, and reasonable agreements were achieved in terms of failure modes, lateral resistances, and deformation capacities. The developed micro models by Calderón et al. (2017, 2019, 2021a) were subsequently used for a parametric study to assess the influence of aspect ratio, axial load level, and horizontal reinforcement ratio on the behaviors of PGRM walls (Calderón et al. 2021b). The analysis results indicated that increasing the horizontal reinforcement ratio could be associated with spreader damage and narrower cracks. Meanwhile, increasing the aspect ratio results in higher deformation capability but reduced strength.

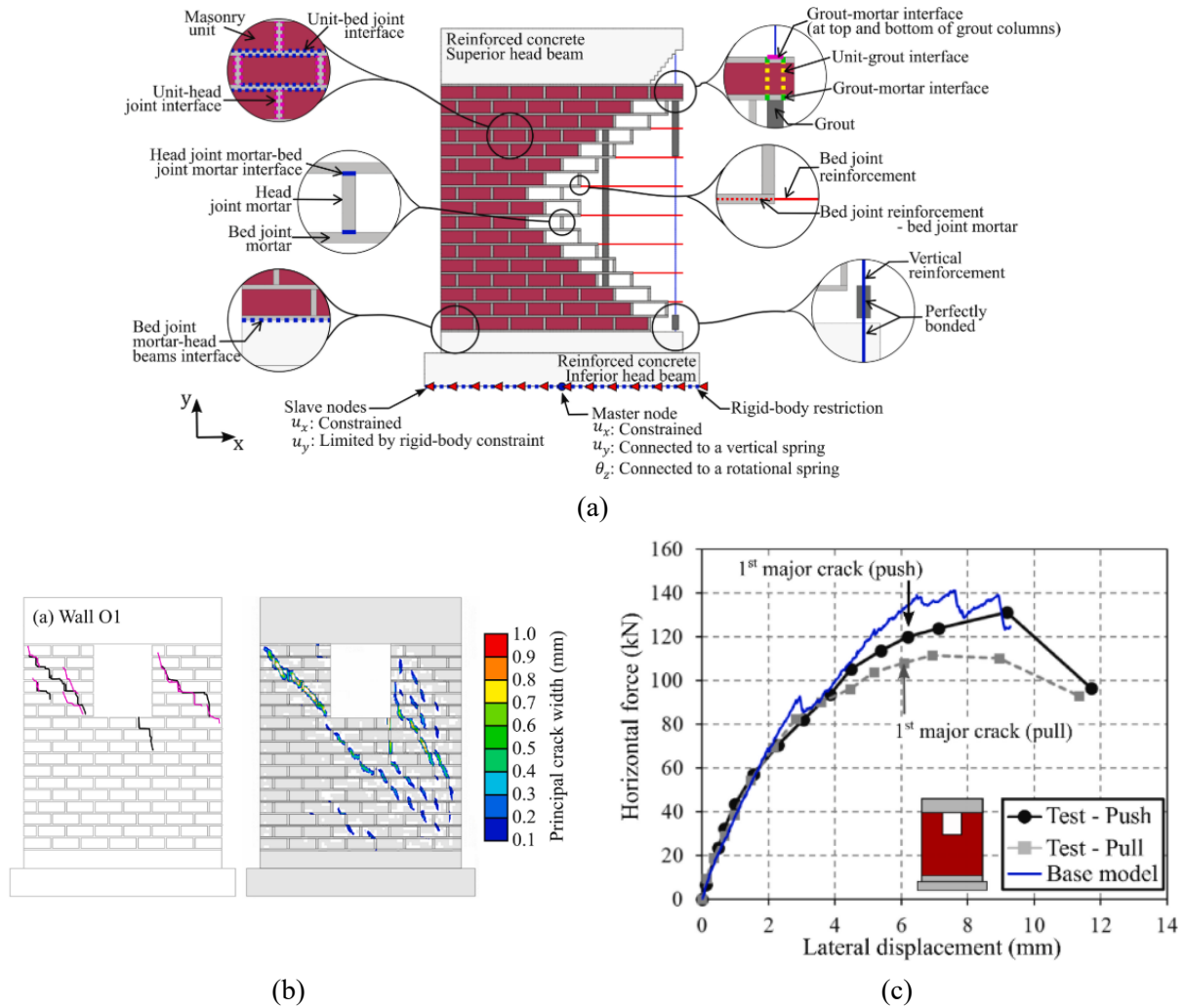


Figure 2-4. (a) Micro modeling strategy for PGRM walls, and (b-c) numerical-experimental comparison in terms of the crack pattern and load-deformation behavior by Calderón et al. (2019)

Mavros (2015) proposed a novel discretization scheme for the micro modeling of fully grouted reinforced masonry (FGRM) walls. This approach utilized smear-crack shell elements to simulate the compressive behavior of concrete units, and cohesive discrete crack interface elements were placed at 45 and 135 degrees to capture the possible diagonal shear cracks in the units. Reinforcing steel was modeled using truss elements that were connected to the smear-crack shell elements through the nonlinear bond-slip and dowel action interface elements. The developed

model was validated using existing experimental walls, including flexural- and shear-governed FGRM walls. The simulation results were in good agreement with the experimental results in terms of failure mechanisms, hysteretic behaviors, energy dissipation capacities, stiffness, and strengths.

Koutras and Shing (2019; 2021a) enhanced the modeling scheme proposed by Mavros (2015) in the following ways: 1) adding horizontal and vertical cohesive interfaces to account for possible sliding and splitting failure of masonry, respectively; 2) using beam elements instead of truss elements to better account for the reinforcement buckling and flexural deformation. The modeling discretization proposed by Koutras is shown in Figure 2-5, leading to accurate predictions for the structural performance of FGRM wall components under static cyclic loading. Moreover, Koutras and Shing (2019; 2021b) extended the applicability of the proposed modeling scheme from FGRM walls to PGRM walls. The grouted part of PGRM walls was modeled in the same way as that of FGRM walls, while the ungrouted units were represented by quadrilateral three-layered shell elements with vertical and horizontal interfaces inserted. It is worth noting that only the thickness of the face shells of units was considered in the shell elements. The validation results indicated the significant potential of the proposed modeling scheme to accurately capture the performance details of PGRM walls, including the hysteretic behaviors, failure modes, drift ratio time history, etc.

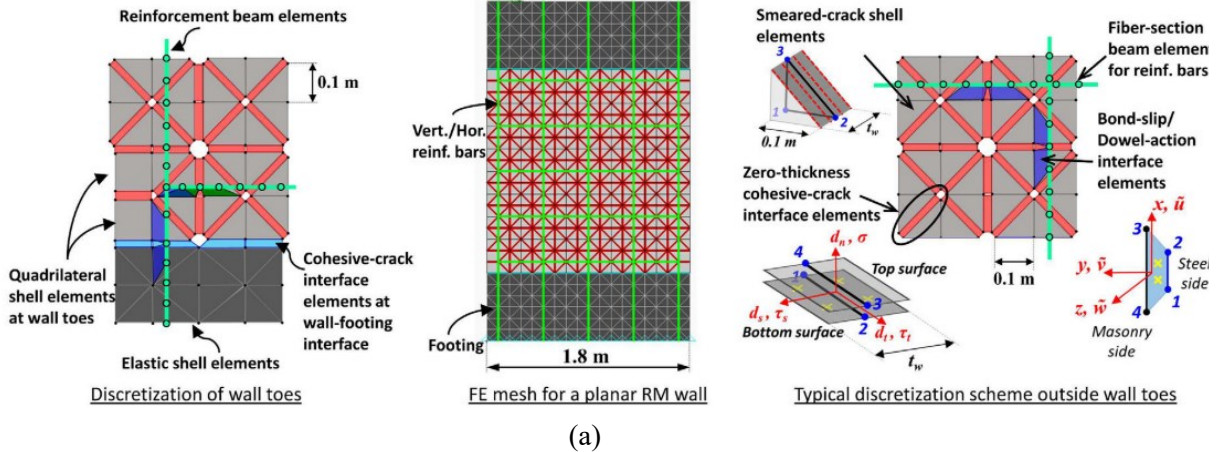


Figure 2-5. Improved micro modeling strategy for FGFRM walls by Koutras and Shing (2021a)

2.1.1.2 OOP behavior

The majority of research discussed in the previous section on the IP behaviors of masonry walls predominantly utilized two-dimensional (2D) FE models, thus not applicable to the three-dimensional FE modeling of masonry walls. In such scenarios, when investigating the wall behavior under OOP loading, three-dimensional (3D) FE models are required. Such studies remain notably scarce on URM walls, and there is a lack of such research on RM walls in public literature.

Macorini and Izzuddin (2012) introduced a micro modeling strategy in which the masonry units were modeled using 3D continuum solid elements, whereas the mortar and brick-mortar interfaces were modeled by means of nonlinear interface elements. This enables the representation of any 3D arrangement for brick-masonry, accounting for the through-thickness geometry, and importantly, it allows the investigation of both the IP and OOP responses of URM panels. Good agreements were observed between the numerical and experimental results in terms of the crack pattern (shown in Figure 2-6) and load-deformation behavior.

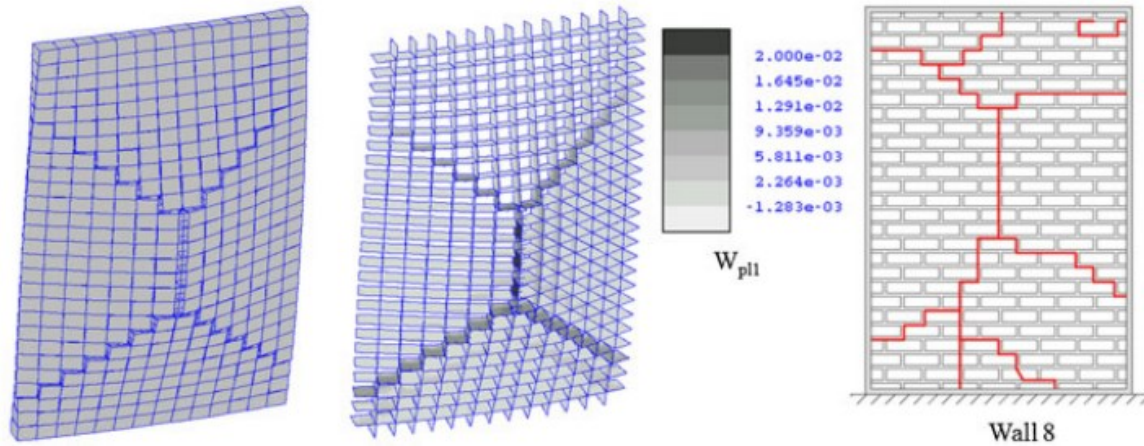


Figure 2-6. Numerical-experimental comparison of crack pattern of URM walls by Macorini and Izzuddin (2012)

Abdulla et al. (2017) presented a simplified micro model strategy that integrated plasticity-based constitutive models with the extended finite element method (XFEM). The constitutive models include surface-based cohesive behavior to capture the elastic and plastic behavior of masonry joints and a Drucker Prager (DP) plasticity model to simulate the crushing of masonry under compression. A notable aspect of this research is the detailed application of XFEM in simulating crack propagation within masonry units without requiring a pre-defined crack location. The efficacy of the proposed modeling strategy was validated through a study of a four-sided supported URM wall subjected to OOP loading.

D'Altri et al. (2018) presented a novel 3D detailed micro-model to analyze the mechanical response of URM panels under IP and OOP loading conditions. The modeling approach, shown in Figure 2-7, features textured units composed of one brick and several mortar layers, each represented by 3D solid elements obeying plastic-damage constitutive laws. Textured units are assembled to accurately reflect the actual 3D through-thickness configurations of URM structures

and are interconnected using zero-thickness rigid-cohesive-frictional interfaces, and these interfaces were governed by a Mohr-Coulomb failure surface with tension cut-off.

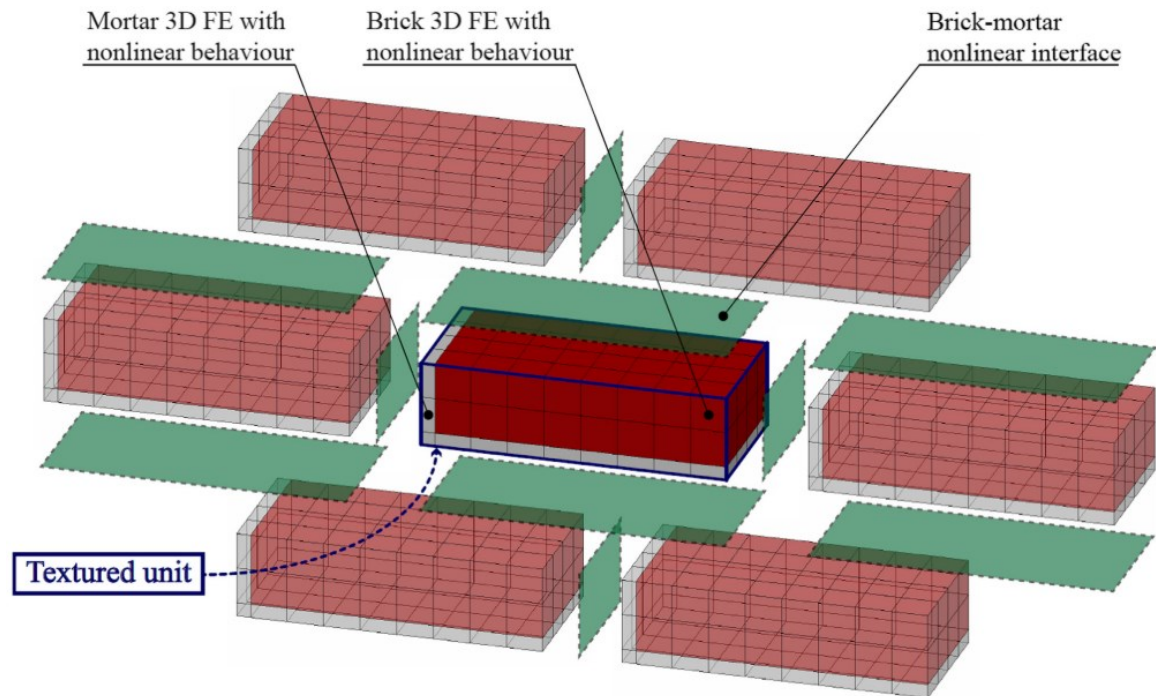


Figure 2-7. Detailed micro modeling approach for URM structures proposed by D’Altri et al. (2018)

2.1.2. Macro modeling strategy

Macro models for masonry structures can be generally categorized into two types: macro continuum and macro element models. Macro continuum models treat masonry as a continuum deformable body with a fictitious homogenized isotropic or orthotropic constitutive law. The constitutive law is typically formulated in the various computational mechanics frameworks, such as damage-based (Berto et al. 2002; Calderini and Lagomarsino 2008; Gambarotta and Lagomarsino 1997b; Karapitta et al. 2011; Pelà et al. 2011, 2013; Zucchini and Lourenço 2004), plasticity-based (De Buhan and De Felice 1997; Lotfi and Shing 1991; Lourenço et al. 1997, 1998; Lourenço 2000a), and damage plasticity-based (Biye et al. 2022; Chisari et al. 2023; Gatta et al.

2018; Lopez et al. 1999; Shen et al. 2022; Yacila et al. 2019). Consequently, the mesh discretization in macro continuum models does not need to describe the actual masonry texture. The computational cost is moderate and generally lower than that of micro models, enabling a more efficient procedure for large-scale masonry structural analysis.

On the other hand, macro element models intend to idealize masonry systems into several components using structural elements/connectors (e.g., spring, hinge, interface, truss, beam, frame). Each component is represented with a phenomenological (e.g., from experimental data) or mechanical-based (e.g., from Euler Bernoulli beam formulation) material response, facilitating a more focused and component-specific analysis of masonry structures.

2.1.2.1 IP behavior

Macro continuum models were initially developed for URM walls, focusing on predicting the IP peak strength (i.e., failure envelope). The first group of available studies involves only the investigation of monotonic behaviors for URM walls under IP loading, such as (De Buhan and De Felice 1997; Lopez et al. 1999; Lourenço et al. 1997, 1998; Lourenço 2000a; Pelà et al. 2013). The primary objective is to validate the capability of macro continuum models to predict peak strength, while ductility, stiffness degradation, and post-peak behavior received less attention due to the inadequacy of monotonic models.

With the increasing availability of experimental data on the hysteretic behavior of masonry materials, more sophisticated macro continuum models emerged (Berto et al. 2002; Biye et al. 2022; Calderini and Lagomarsino 2008; Gambarotta and Lagomarsino 1997b; Gatta et al. 2018; Karapitta et al. 2011; Shen et al. 2022). These models have been instrumental in predicting the structural behavior of URM walls under cyclic IP loading. For example, two URM walls with

different height-to-width ratios, tested by Anthoine and Magonette (Anthoine et al. 1994), served as benchmark cases for validation. Experimental hysteretic behavior of the flexural-governed URM wall indicated a nonlinear response with limited energy dissipation and significant ductility, which was reasonably predicted in studies (Calderini and Lagomarsino 2008; Gatta et al. 2018; Shen et al. 2022). Shear-governed failure, characterized by an abrupt strength degradation and a larger energy dissipation, was also well captured in these studies. However, macro continuum models' inherent limitation in representing discrete crack patterns, typically characterized by localized cracking in masonry, was evident due to their assumption of smeared damage. To address this issue, Saloustros et al. (2018) enhanced the macro continuum model with a local crack-tracking algorithm, improving the representation of localized tensile crack propagation. The proposed model was capable of capturing the multiple flexural and shear failure modes of a large-scale URM wall.

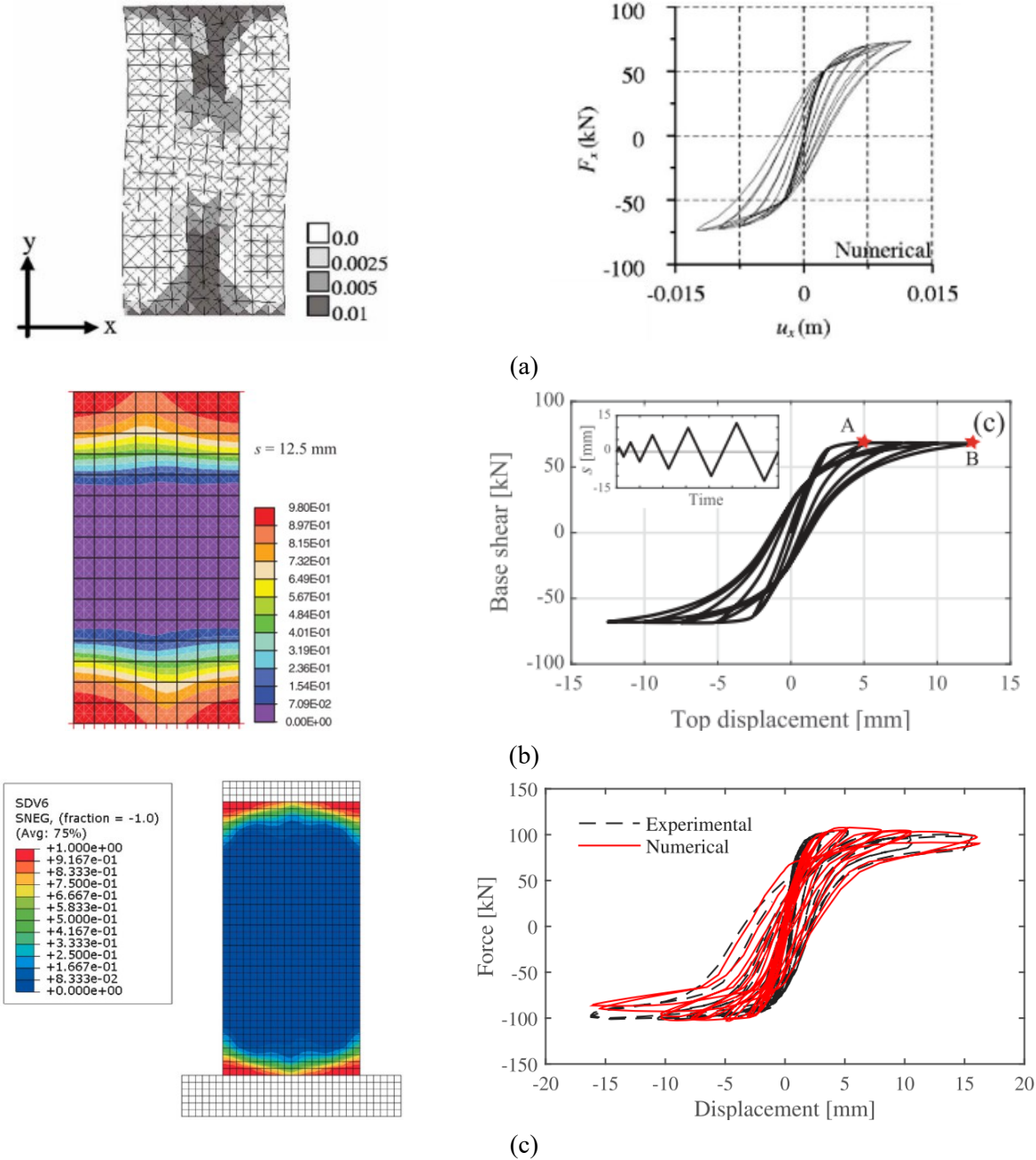


Figure 2-8. Numerical predictions based on the macro continuum models: (a) Karapitta et al. (2011), (b) Shen et al. (2022), and (c) Gatta et al. (2018)

In addition to macro continuum models, macro element models have wider applicability in practice-oriented assessments for URM walls. Examples include monotonic behavior estimation with a primary interest in the initial stiffness and peak strength (Addessi et al. 2014, 2015; Chen

et al. 2008; Kesavan and Menon 2023; Liberatore and Addessi 2015; Pirsabehe et al. 2020; Roca et al. 2005) and cyclic response assessment focusing on more structural characteristics (Bracchi et al. 2021; Bracchi and Penna 2021; Penelis 2006; Penna et al. 2014; Rinaldin et al. 2016; Vanin et al. 2020), e.g., stiffness degradation, energy dissipation capability. Based on the assumption that damage could be approximately concentrated in particular structural sections, macro elements can be modeled through lumped plasticity behaviors at specified locations (e.g., at the end and/or midpoint of structural elements). However, due to the simplification in the idealization of masonry walls, the crack location and damage distribution cannot be generally obtained explicitly but can be qualitatively inferred through the violation of plastic material laws (e.g., flexural or shear strength).

Despite the extensive applicability of macro models on URM walls, particularly in the context of historic masonry structures, their potential for modeling the IP behaviors of RM walls has not been fully explored. Current studies on RM walls using macro continuum models, such as those by Lotfi and Shing (1991), Dhanasekar and Haider (2008), Abdellatif et al. (2019), Yacila et al. (2019), and Noor-E-Khuda and Thambiratnam (2021), focus primarily on monotonic behavior. Furthermore, the effects of reinforcements have not been adequately addressed, using either a smeared approach (Lotfi and Shing 1991) or assuming perfect bonding between the reinforcing bar and block/grout (Abdellatif et al. 2019; Dhanasekar and Haider 2008; Noor-E-Khuda and Thambiratnam 2021; Yacila et al. 2019). Other effects, such as nonlinear bond slip behavior and dowel effects, are typically neglected, even though these effects have been shown to significantly impact the IP behaviors of RM walls.

Macro element models have only been introduced to RM walls very recently (Cheng and Shing 2022a; b; Peruch et al. 2019b), despite their considerable success in modeling reinforced concrete members. Peruch et al. (2019a) explored the use of distributed plasticity Timoshenko frame elements with fiber cross sections for analyzing the FGRM walls. Cheng and Shing (2022b) presented a modeling method based on a fiber-section beam-column element idealization to capture the nonlinear IP cyclic behavior of flexural-dominated RM walls illustrated in Figure 2-9 (a), with a highlight of considering the buckling and low-cycle fatigue of vertical reinforcing bars using a phenomenological material law. Later, Cheng and Shing (2022a) developed a more advanced beam-column element capable of capturing the axial-flexural-shear interaction, as shown in Figure 2-9 (c). The proposed model was validated against tested RM walls, and the validation results showed a lower shear strength compared to the test results, but the hysteretic character was reasonably captured.

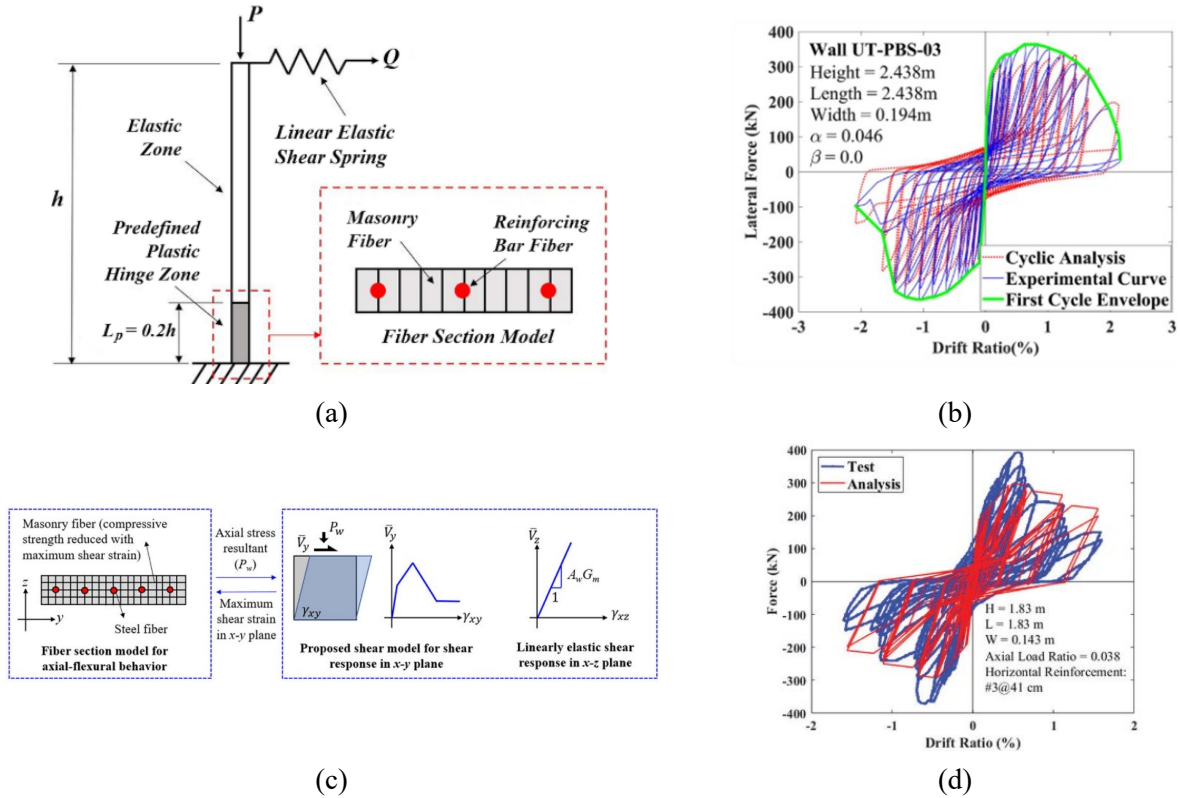


Figure 2-9. Macro element modeling strategy and numerical validation for: (a-b) flexural-governed RM walls by Cheng and Shing (2022b), and (c-d) shear-governed RM walls by Cheng and Shing (2022a)

2.1.2.2 OOP behavior

Studies utilizing macro continuum models for analyzing the out-of-plane (OOP) behavior of masonry walls are relatively limited. These models typically treat masonry as a homogenized material with orthogonal properties. For instance, Lourenço (2000a) proposed an anisotropic model for masonry plates and shells characterized by a composite plasticity criterion that is able to reproduce elastic and inelastic behavior in two orthogonal directions coinciding with the orientation of the bed and head joints of masonry. Further validation of the model with experimental results on masonry panels subjected to OOP loading demonstrates the accuracy of the proposed models.

Noor-E-Khuda et al. (2016a) developed a macro modeling strategy for masonry walls in which masonry is modeled as a layer with macroscopic orthotropic properties and external reinforcing render, grout, and reinforcing bars are modeled as distinct layers within the shell element. The model was successfully validated using the OOP response of seven walls comprising unreinforced masonry, internally reinforced masonry, confined masonry (see Figure 2-10), and externally surface reinforced masonry walls. A subsequent parametric study by Noor-E-Khuda and Thambiratnam (2021) employed this macro modeling strategy to explore the impact of reinforcement ratio on the OOP behavior of FGRM walls.

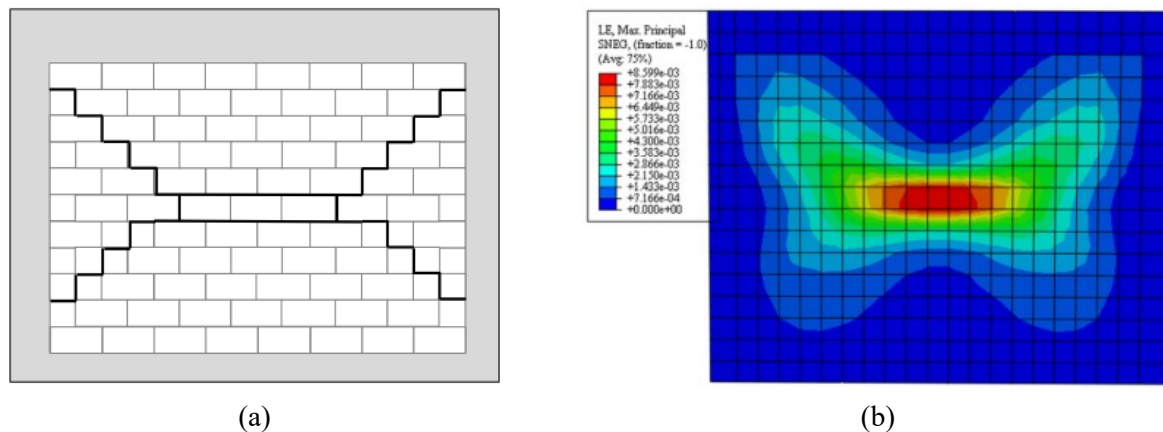


Figure 2-10. Experimental-numerical comparison in terms of crack pattern for confined masonry wall under OOP loading from Noor-E-Khuda and Thambiratnam (2021)

EI-Hashimy et al. (2019) developed a three-dimensional model in the Open-source FE software framework *OpenSees* (Mazzoni et al. 2006) to simulate the OOP response of masonry walls. This approach, namely the ‘layered finite-element model (LFEM)’, employed the SHELLMITC4 shell element (Lu et al. 2015), allowing for the incorporation of the properties of reinforcements and concrete units. The LFEM demonstrated its effectiveness in accurately predicting initial stiffness, peak load, and corresponding displacements for various FGRM walls.

In addition to macro continuum models, the other type of macro model in studying the OOP behavior of masonry walls is the macro element model. A significant example in this category is the section fiber-based-beam model, as illustrated in studies by Metwally et al. (2022), Pantò et al. (2017), Vanin et al. (2020). The section fiber-based-beam model adeptly integrates heterogeneous material properties and complex failure mechanisms, providing a realistic representation of masonry wall behaviors. Its flexibility in characterizing different masonry compositions and computational efficiency make it an advantageous tool for comprehensive studies, particularly when resources are constrained. However, the section fiber-based-beam model's assumption of material homogeneity along the beam's length can introduce inaccuracies, especially in walls with notable material heterogeneity. This limitation poses challenges in accurately capturing localized effects such as cracking or spalling at the micro-level, which are crucial for understanding damage initiation and propagation.

2.2. CONSTITUTIVE MODELS OF COHESIVE INTERFACES FOR MASONRY MORTAR JOINTS

The capability of the micro modeling approach to simulate the structural behavior of masonry walls relies heavily on the constitutive models of cohesive interfaces for mortar joints. Cohesive interfaces were first introduced for the modeling of concrete structures by Ngo and Scordelis (1967), and also in the area of rock mechanics by Goodman et al. (1968). It was first introduced for the modeling of masonry mortar joints by Page (1978) and later has received great attention in the micro modeling of masonry structures. This section reviews significant contributions to the development of constitutive models for cohesive interfaces in masonry mortar joints. The review

categorizes the models into two groups: the first focuses on monotonic behavior, while the second group addresses more advanced cyclic (hysteretic) behaviors.

2.2.1. Monotonic models

In the monotonic model formulation of cohesive interfaces, a crucial factor is to represent various failure modes of mortar joints under different loading conditions. Generally, there are two primary categories of interface models: the first category includes models that account for tensile cracking and shear sliding with shear-compression hardening, as explored in studies (Abdulla et al. 2017; Giambanco et al. 2001; Giambanco and Di Gati 1997; Lotfi and Shing 1994; Stankowski et al. 1993b; a; Zhai et al. 2017), and the second category extends the model by additionally considering compression failure mode, as demonstrated by (Aref and Dolatshahi 2013; Citto 2008; Dolatshahi and Aref 2011; Kumar et al. 2014; Kumar and Barbato 2019; Lourenço 1996; Lourenço and Rots 1997; Nazir and Dhanasekar 2014; da Porto et al. 2010; Remacle et al. 2012; van Zijl 2004). Constitutive material models for interfaces should ideally incorporate all possible failure modes, as shown in Figure 2-11.

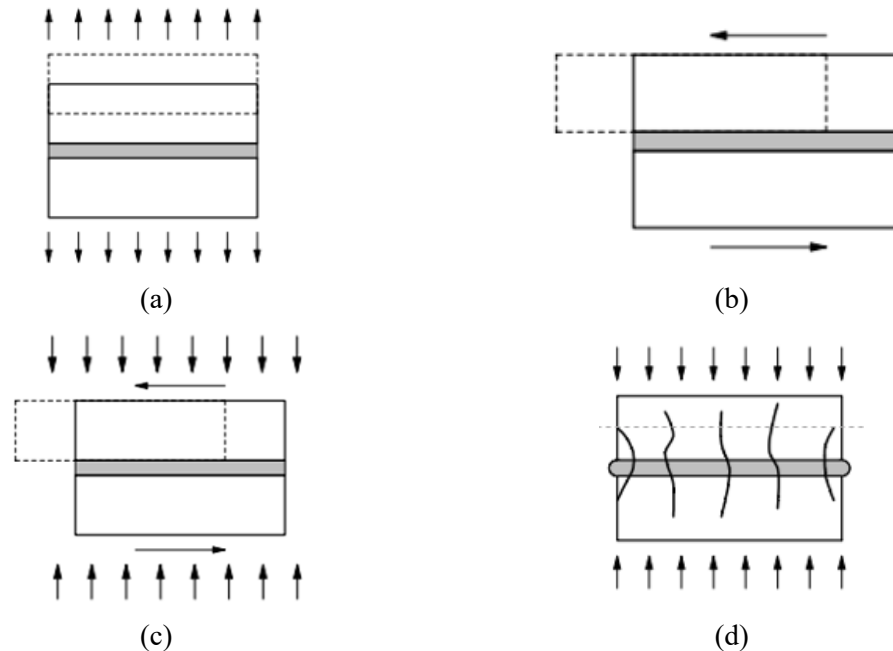


Figure 2-11. Failure modes considered in the cohesive interfaces for mortar joints: (a) tensile cracking, (b) shear sliding, (c) compressive-shear failure, and (d) compressive crushing (Lourenco 1996)

Lourenco and Rots (1996; 1997) pioneered the development of a multi-yield surfaces model to encompass all three primary failure modes and criteria: tensile cracking, shear sliding, and masonry or mortar crushing. This model has been extensively adopted and further refined by other researchers (Dolatshahi and Aref 2011; Giambanco and Di Gati 1997; Nazir and Dhanasekar 2014; van Zijl 2004). However, these plasticity-based constitutive models are known to encounter a well-known singularity issue due to non-smooth corners at the intersection of different yield surfaces, as depicted in Figure 2-12. To address this challenge in the numerical integration, some researchers proposed a single yield surface failure criterion, e.g., (Citto 2008; Kumar et al. 2014, 2015), as illustrated in Figure 2-13 and Figure 2-14. While the single yield surface model offers mathematical elegance, it suffers from a lack of clear physical interpretation of tension-shear failure, which represents a unit-mortar interfacial phenomenon (e.g., tensile cracking and shear

sliding), and the compression cap, which represents a masonry or mortar crushing failure mode. Accordingly, cohesive interface elements with single yield surface models often require complex yield function expressions that include some non-physical parameters that are difficult to quantify. Notably, using a single yield function to represent the tension-shear failure mode is more acceptable using hyperbolic (Kumar and Barbato 2019; Lotfi and Shing 1994; Remacle et al. 2012), elliptical (Nazir and Dhanasekar 2014), and parabolic (Stankowski et al. 1993b; a) yield surfaces.

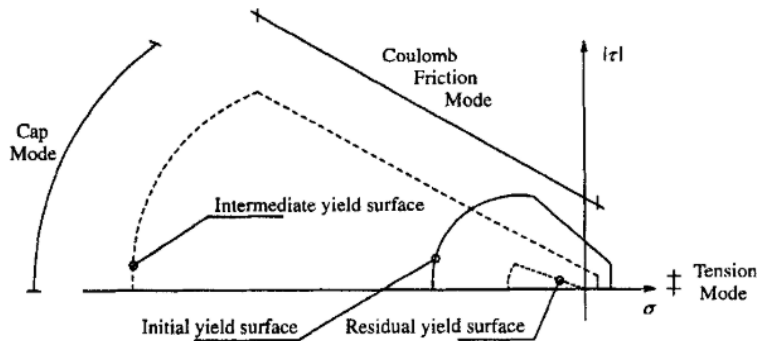


Figure 2-12. Multi-yield surfaces plasticity model proposed by Lourenco and Rots (1996; 1997)

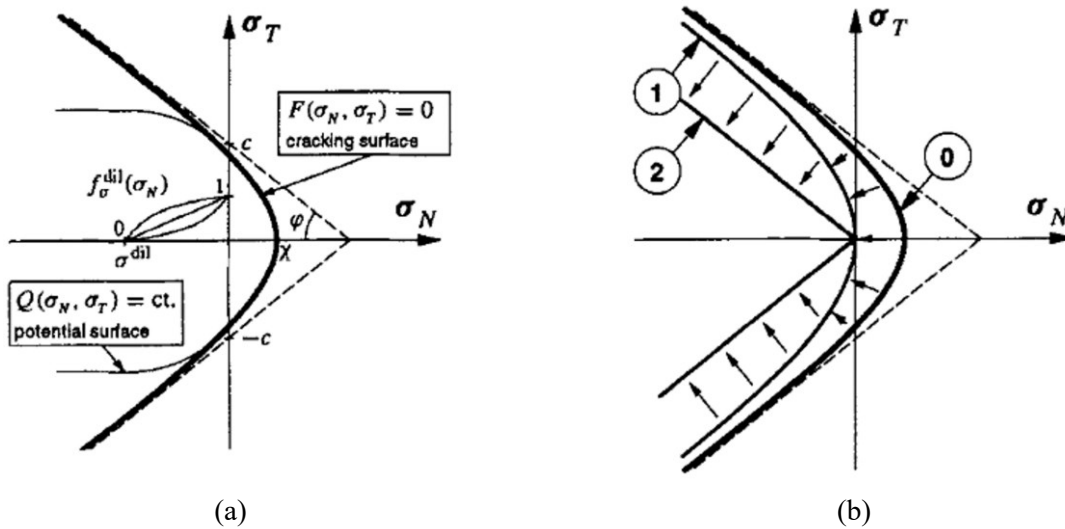


Figure 2-13. Single yield surface model to consider tensile cracking and shear sliding (a) Hyperbolic yield surface and plastic potential surface, (b) evolution of yield surface (Carol et al. 1997)

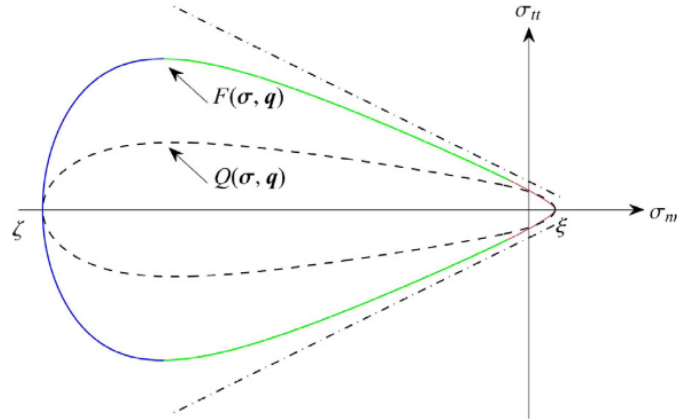


Figure 2-14. Single yield surface model to consider tensile cracking, shear sliding, and compressive crushing (Kumar et al. 2014)

The aforementioned constitutive models were all implemented in the 2D stress space, thus having the only possibility of being applied in the IP loading scenario. Recognizing the need for more versatile models for masonry walls under complex loading scenarios, such as OOP loading, researchers started to put focus on the 3D constitutive model formulation.

Caballero et al. (2008) extended the 2D model developed by Carol et al. (1997) into 3D space. In addition, a backward-Euler integration strategy was developed in this study combined with a local/global Newton Solver, incorporating a consistent tangent operator compatible with an adaptive sub-stepping strategy. This innovation significantly enhanced numerical efficiency and accuracy.

Macorini and Izzuddin (2012) adopted a co-rotational approach for interface elements, which shifts the treatment of geometric nonlinearity to the level of discrete entities. This approach facilitated material nonlinearity handling within a simplified local framework using first-order kinematics. In this respect, internal interface forces were modeled by means of elasto-plastic material laws based on work-softening plasticity and employing a multi-surface plasticity criterion.

Serpieri et al. (2017) developed a microstructured 3D composite Cohesive-Zone Model (CZM) to describe the behavior of joints of adhesive quasi-brittle materials. The developed model was capable of reproducing an initial linear elastic response, corresponding to the elastic parameters of a thin adhesive quasi-brittle layer of finite thickness and stiffness, followed by a post-elastic response of the joint featuring progressive crack formation and the onset of frictional and dilating responses. The proposed model was validated through a small-scale unit-mortar-unit assemblage and a masonry wallette subjected to OOP bending.

D'Altri et al. (2018) developed a zero-thickness rigid-cohesive-frictional interface model based on the contact penalty method. The developed model was governed by a Mohr-Coulomb failure surface with a tension cut-off. The experimental-numerical comparisons were performed on the small-scale masonry assemblages and URM walls under IP and OOP loading, respectively, showing its great potential.

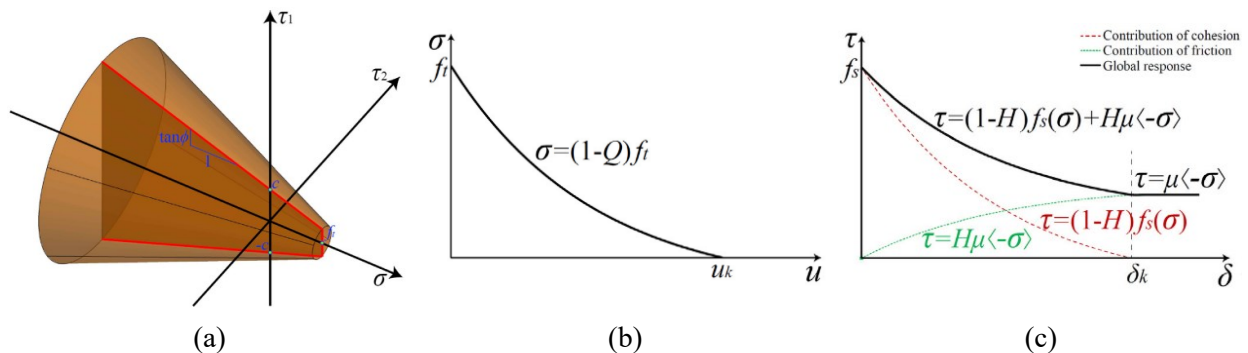


Figure 2-15. Failure surfaces for cohesive interfaces proposed by D'Altri et al. (2018): (a) Mohr-Coulomb surface with tension cut-off, (b) post-peak tensile response, and (c) post-peak shear response

To overcome the numerical stability issues, Pari et al. (2021) proposed the use of numerically robust sequentially linear procedures and a suitable discretized tension-shear-compression failure model for cohesive interfaces. The sequentially linear procedures described

the nonlinear response of a specimen/structure through a sequence of scaled linear analyses, each of which represents locally applied damage increments, using secant-stiffness based discretized constitutive relations called saw-tooth laws.

Compared with the consideration of various failure modes in the constitutive models of interface elements for masonry joints, there is an important phenomenon that has attracted less attention. As identified by Andreotti et al. (2019), the micromechanical behavior of the mortar layer and the two mortar-unit interfaces has inherent dilatancy, as a result of a crack surface that is not perfectly smooth: the mortar joint specimen will deform with an uplift under compression and shear loading, thus leading to a volume increase. As evidenced by the experimental results (Andreotti et al. 2019; Jafari et al. 2020; Pluijm 1999), the dilatancy effects become pronounced under lower compression, and will diminish with the increase of normal compressive stress and plastic shear displacement. Inappropriate description of dilatancy can produce an increase in normal stress, resulting in a considerable overestimate of shear capacity for pressure-dependent materials or specimens.

Two main methods have been developed to integrate the dilatancy effects into the numerical description of the constitutive material model for mortar joints. The first approach is to incorporate the dilatancy into the Mohr-Coulomb yield criterion (Giambanco et al. 2001; Giambanco and Di Gati 1997). As a result, it can reflect the increase in shear strength due to the dilatancy effects. However, the volume increase and the uplift of the specimen upon shearing cannot be captured. The other approach is to adopt an unassociated flow rule in the formulation of the constitutive material model to consider the influence of dilatancy. However, most studies assumed the constant dilatancy angle (Lourenço 1996; Lourenço and Rots 1997; Oliveira and

Lourenço 2004; da Porto et al. 2010; Stankowski et al. 1993b; a) in a simplified manner, which would result in an inaccurate estimation of shear capacity. Although some researchers considered the variation of dilation angle, the dependence of compressive stress (Koutromanos and Shing 2012; Kumar and Barbato 2019; Remacle et al. 2012; Zhai et al. 2017) or plastic shear displacement (Citto 2008) on the dilatancy effects was neglected. Few 2D interface models (Lotfi and Shing 1994; van Zijl 2004) formulated the decreased dilatancy angle with the increase of compressive stress and plastic shear displacement. These 2D models, however, failed to address the OOP behavior prediction of masonry walls, as mentioned earlier. Meanwhile, although the diminishment of dilatancy is observed at large shear sliding due to the wear and damage to the asperities along the unit-mortar interface, the dilatancy becomes stable at a non-zero value based on some experimental evidence, e.g., (Andreotti et al. 2019; Jafari et al. 2020), which is not taken into account in current models.

Table 2-1 offers a comprehensive overview of existing constitutive models in the public literature for interface elements in masonry mortar joints. It summarizes key features of these models, including yield criteria, failure mechanisms considered, model implementation space (whether 2D or 3D), consideration of dilatancy variation, and their application in various contexts. This encompasses both small-scale masonry assemblages and large-scale masonry walls under IP and/or OOP loading.

Table 2-1. Existing monotonic models of interface elements for masonry mortar joints

Reference	Yield Criterion	Failure Mechanisms	Dimension	Dilatancy	Application	
Stankowski et al. (1993b; a)	SYS	TC, SS	2D	No	UMU	
Lotfi and Shing (1994)	SYS	TC, SS		Yes	UMU, IP	
Lourenço and Rots (1997)	MYS	TC, SS, CC		No	IP	
Giambanco and Di Gati (1997)	MYS	TC, SS		Yes	IP	
Giambanco et al. (2001)	MYS	TC, SS		Yes	UMU	
Giambanco et al. (2001)	MYS	TC, SS		Yes	IP	
van Zijl (2004)	MYS	TC, SS, CC		Yes	UMU	
Citto (2008)	SYS	TC, SS, CC		Yes	IP	
Da Porto (2010)	MYS	TC, SS, CC		No	IP	
Dolatshahi and Aref (2011)	MYS	TC, SS, CC		No	IP	
Koutromanos and Shing (2012)	SYS	TC, SS		Yes	UMU, IP	
Kumar et al. (2014)	SYS	TC, SS, CC		Yes	IP	
Nazir and Dhanasekar (2014)	MYS	TC, SS, CC		No	UMU, IP	
Zhai et al. (2017)	SYS	TC, SS		Yes	IP	
Kumar and Barbato (2019)	MYS	TC, SS, CC		Yes	IP	
Caballero et al. (2008)	SYS	TC, SS		3D	No	NA
Macorini and Izzuddin (2012)	MYS	TC, SS, CC			Yes	IP, OOP
Aref and Dolatshahi (2013)	MYS	TC, SS, CC	No		IP, OOP	
Abdulla et al. (2017)	MYS	TC, SS	No		IP, OOP	
D'Altri et al. (2018)	MYS	TC, SS	No		UMU, IP, OOP	
Pari et al. (2021)	MYS	TC, SS, CC	No		IP	

TC: Tensile cracking; SS: Shear sliding; CC: Compressive crushing

MYS: Multi-yield surface; SYS: Single-yield surface

UMU assemblage: Unit-mortar-unit assemblage

IP: masonry walls under IP loading

OOP: masonry walls under OOP loading

2.2.2. Cyclic models

The cyclic behavior of mortar joints is much more complex than the monotonic behavior. In addition to the initial stiffness and strength softening that should be well addressed in the monotonic behavior, more factors should be well considered to lead to a rational constitutive formulation: stiffness degradation, stiffness recovery upon stress reversal (e.g., from tension to compression), residual displacement at zero-stress level, etc.

To this aim, Oliveira and Lourenco (2004) improved the interface model proposed by Lourenço and Rots (1997) and introduced two auxiliary yield surfaces during the unloading process, as shown in Figure 2-16. The motion of the unloading surfaces is controlled by a mixed

hardening law. Although the stiffness reduction effects were captured, the total of six possibilities for unloading/reloading movements resulted in a complex implementation framework.

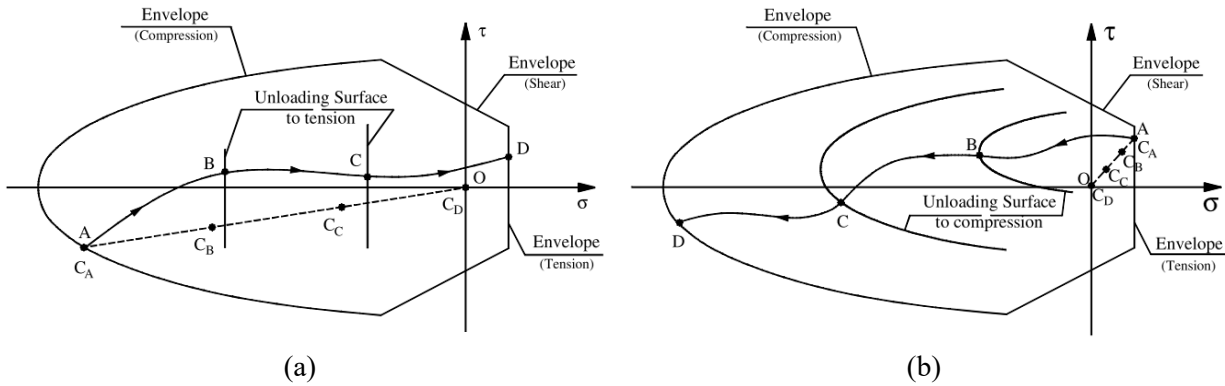


Figure 2-16. Hypothetic motion of the unloading surface in stress space to: (a) tension, and (b) compression (Oliveira and Lourenço 2004)

Aref and Dolatshahi (2013) developed a 3D plasticity-based interface model within the explicit integration procedure, and the stiffness degradation was considered in the positive normal direction using a single scalar in a simplified manner. Koutromanos and Shing (2012) adopted a modified elastoplastic formulation to simulate mixed-mode fracture, crack opening and closing, reversible shear dilatation, and joint compaction under cyclic loading conditions, and the corresponding cyclic stress-displacement response is shown in Figure 2-17.

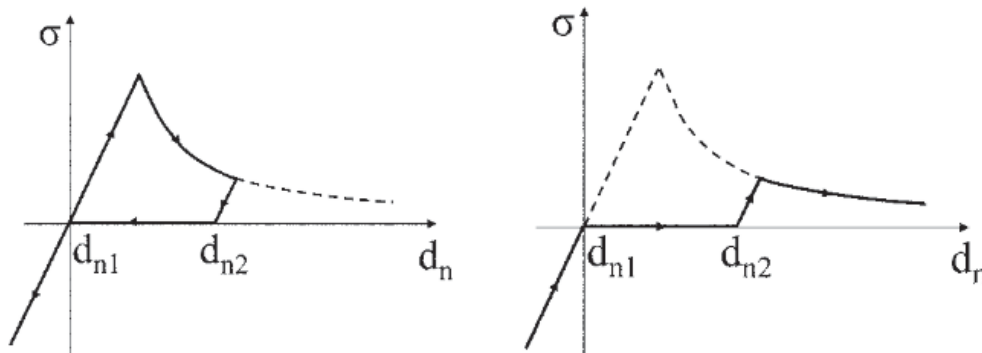


Figure 2-17. Uniaxial behavior of interface model: (a) loading and unloading, and (b) reloading

In addition to the plasticity-based framework, damage mechanics theory has also been applied to formulate the constitutive material model for cohesive interface elements. Parrinello et al. (2009) proposed an interface constitutive model, which couples a cohesive behavior based on the damage mechanics with a frictional one defined in a non-associated plasticity framework. D'Altri et al. (2019) developed a damaging block-based model for the numerical analysis of the cyclic behavior of masonry structures. For the modeling of mortar joints, the cohesive-frictional contact-based formulation is adopted with an elastic-damage procedure assumed in the tensile regime, while stiffness degradation is neglected in the compressive regime. Similar numerical simplification methods can be found in (Gambarotta and Lagomarsino 1997a; Sacco and Lebon 2012). However, the aforementioned pure damage-based models result in the absence of irreversible deformation (i.e., the unloading curve is pointing to the origin), which appears contradictory to the experimental findings for the quasi-brittle materials.

As discussed above, general plasticity-based models are incapable of capturing the stiffness degradation observed in experimental results, whereas pure damage-based models are inadequate for describing irreversible deformation. Furthermore, the inelastic volumetric expansion of mortar joints under compression caused by the dilatancy effects cannot be accounted for with pure damage theory. Consequently, the combination of plasticity and damage might be an effective approach to modeling the cyclic behavior of mortar joints. This framework has gained popularity for the macroscopic modeling of quasi-brittle materials (Comi and Perego 2001; Grassl et al. 2013; Jason et al. 2006; Lee and Fenves 1998). However, its applications on the cohesive interface for the modeling of mortar joints are rare (Minga et al. 2018; Nie et al. 2022b; a; Yuen et al. 2019). Minga et al. (2018) introduced stiffness degradation via an anisotropic damage tensor based on the

evolution of plastic work produced. However, a simplified multi-surface plasticity criterion with two flat yield surfaces (i.e., compressive cap and tension cut-off) was employed, in which two sharp singularity corners could possibly result in a convergence issue. Yuen et al. (Yuen et al. 2019) presented a fracture-energy based damage-plasticity model in the explicit Euler integration scheme. Thus, a sufficient small loading increment is required to guarantee numerical accuracy. More recently, Nie et al. (2022b; a) proposed two interfacial damage-plasticity based models for mortar joints characterized by a smooth hyperbolic yield surface. However, the failure mode associated with compressive crushing was not considered, leading to a possible overestimation of the masonry wall's capacity. A summary of existing cyclic models for mortar joints in the public literature is presented in Table 2-2.

Table 2-2. Existing cyclic models of interface elements for masonry mortar joints

Reference	Failure mechanisms	Dimension	Computational framework	Application
Gambarotta and Lagomarsino (1997a)	TC, SS	2D	Damage	IP
Oliveira and Lourenco (2004)	TC, SS, CC		Plasticity	UMU, IP
Koutromanos and Shing (2012)	TC, SS		Plasticity	UMU, IP
Parrinello et al. (2009)	TC, SS		Damage	IP
Sacco and Lebon (2012)	TC, SS		Damage	UMU
Aref and Dolatshahi (2013)	TC, SS, CC		3D	Plasticity
Minga et al. (2018)	TC, SS, CC	Damage-plasticity		UMU, IP, OOP
Yuen et al. (2019)	TC, SS	Damage-plasticity		UMU, IP
Nie et al. (2022b; a)	TC, SS	Damage-plasticity		UMU, IP

TC: Tensile cracking; SS: Shear sliding; CC: Compressive crushing

UMU assemblage: Unit-mortar-unit assemblage

IP: masonry walls under IP loading

OOP: masonry walls under OOP loading

2.3. IN-PLANE AND OUT-OF-PLANE INTERACTION BEHAVIORS OF MASONRY WALLS

Experimental programs that test masonry walls under combined IP and OOP loadings are rare (Dolatshahi and Aref 2016; Krishnachandran and Menon 2023; Najafgholipour et al. 2013), and the majority of the numerical models developed are either limited to the simulation of pure IP or

OOP behavior, as reviewed in the previous sections. This deficiency in the literature could be attributed to the challenges and costs associated with testing masonry walls under complex loading conditions, as well as the technical complexities and computational costs involved in modeling masonry walls in 3D space.

Najafgholipour et al. (2013) tested a series of URM wall panels subjected to simultaneous IP and OOP loading, as shown in Figure 2-18 (a). The experimental results highlighted a significant reduction in IP shear capacity as OOP load increased, and the corresponding results were expressed in terms of the capacity interaction curves illustrated in Figure 2-18 (b). It should be noted, however that in this test program, the IP capacity was obtained through diagonal compression tests, which did not capture the other possible IP failure modes (e.g., flexural rocking, shear sliding), and the coupling effects between axial load and flexure or shear capacity were also neglected.

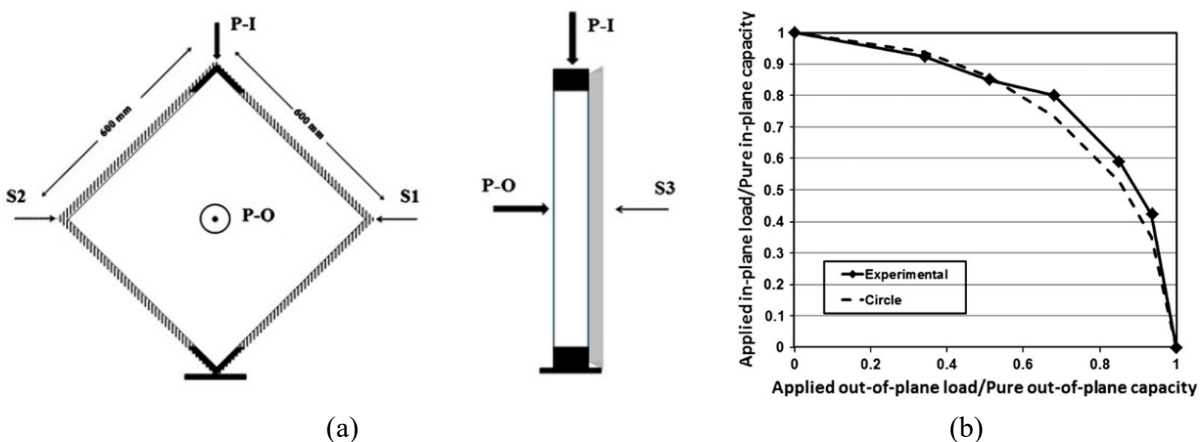


Figure 2-18. URM panel under combined IP and OOP loading tested by Najafgholipour et al. (2013): (a) test specimen, and (b) IP-OOP capacity interaction curve

Dolatshahi and Aref (2016) conducted tests to explore the multi-directional behavior of URM walls under simultaneous IP and OOP loadings, using both monotonic and cyclic quasi-

static loading protocols. It was observed that, due to the pre-applied OOP loading, the URM wall easily collapsed because of the accumulative OOP deformation under subsequent IP loading. The IP and OOP interaction effects were found to be strongly influenced by the aspect ratio (i.e., height-to-length ratio) and the IP failure modes of URM walls when no OOP load exists.

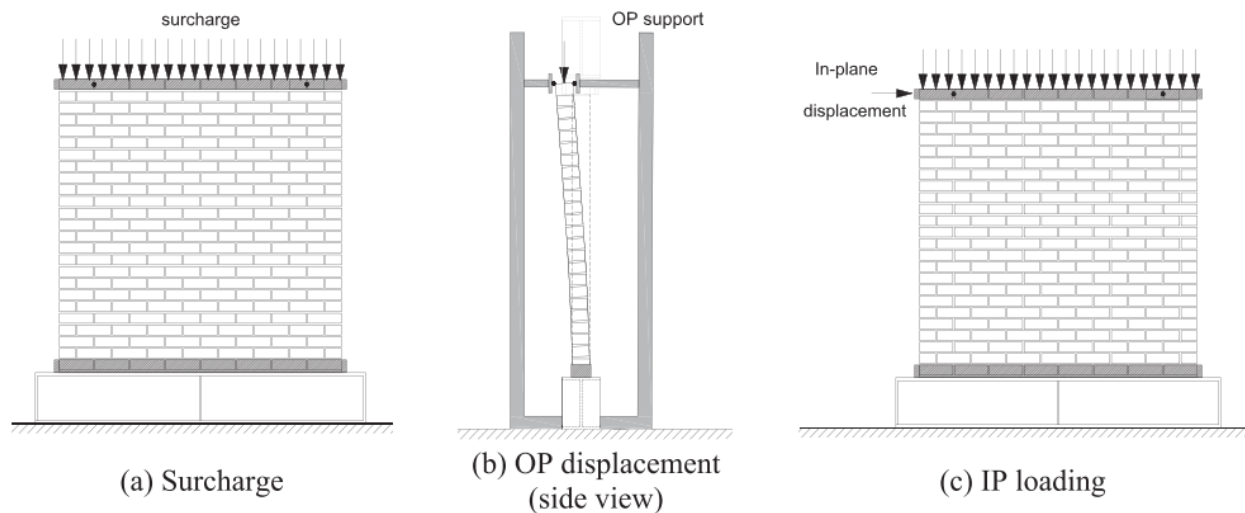


Figure 2-19. Load sequence of URM walls under combined IP and OOP loading tested by Dolatshahi and Aref (2016)

A recent experimental study by Krishnachandran and Menon (2023) examined the IP flexural capacity of URM piers with varying aspect ratios in the presence of OOP displacements. The test results also demonstrated a reduction in both stiffness and strength of URM piers when subjected to inelastic OOP displacements.

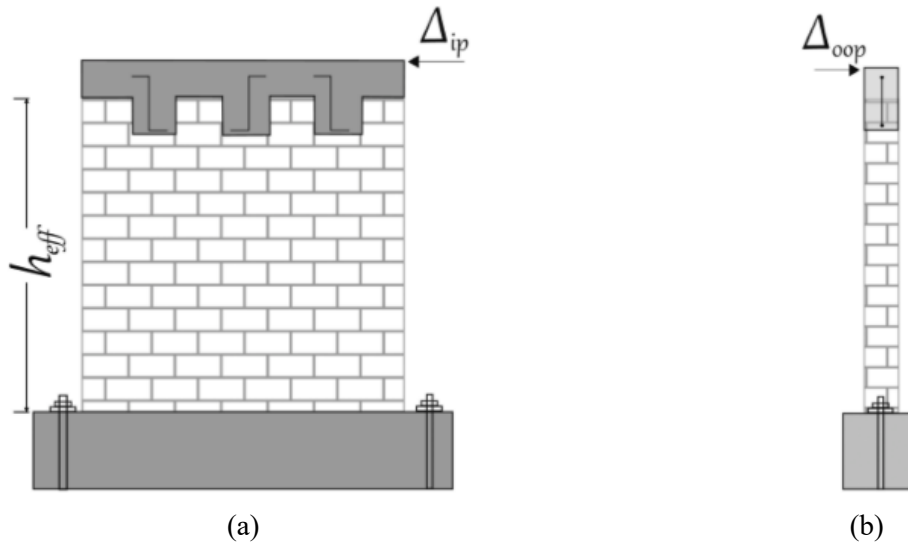


Figure 2-20. URM wall tested by Krishnachandran and Menon (2023): (a) IP loading, and (b) OOP loading

Several researchers have complemented the previously discussed experimental studies by exploring IP-OOP interaction effects in URM walls through numerical approaches. The first set of studies focused on simplified models, including macro and analytical models (Agnihotri et al. 2013; Dolatshahi et al. 2015; Malomo and DeJong 2022; Najafgholipour et al. 2014; Noor-E-Khuda and Dhanasekar 2018a; b). Nonetheless, these models are insufficient for accurately characterizing the inherent composite nature of masonry, and the intricate failure modes of URM walls cannot be well captured. The current use of micro modeling approach in examining IP-OOP interactions in URM walls is relatively limited (Dolatshahi and Yekrangnia 2015; Kesavan and Menon 2022). Dolatshahi and Yekrangnia (2015) examined the IP-OOP interaction effects utilizing the simplified micro models. The results revealed that the OOP strength could be reduced by up to 72% for URM walls under simultaneous IP and OOP loading. More recently, Kesavan and Menon (Kesavan and Menon 2022) relied on the so-called ‘block-based modeling approach’, in which units and mortar were modeled explicitly while the unit-mortar contacts were assumed to be rigidly

connected. It was generally concluded that the IP-OOP interaction effects were more significant in the shear-controlled URM piers than the flexural-controlled ones.

In contrast to the URM walls, the relevant research on RM walls can only be found by Noor-E-Khuda and Dhanasekar (2018a), in which a macro continuum model was used by representing masonry (units plus mortar joints) as a homogeneous material. This numerical investigation identified a critical value of OOP load (as a percentage of OOP capacity), beyond which the IP capacity decreased rapidly. However, the influence of various parameters (e.g., geometrical parameters) on the IP and OOP interaction behaviors of RM walls was not reported due to the limited number of RM walls simulated. Moreover, the detailed failure modes of RM walls were not adequately captured through the macro modeling approach, causing a lack of comprehension regarding the IP and OOP interaction behaviors.

2.4. DESIGN CODE-BASED MODELS FOR MASONRY WALLS

In current engineering practice, masonry walls are primarily designed to adhere to prescriptive code regulations, which establish specific construction practices to ensure performance satisfaction. In North America, several design codes are available for the design of masonry structures, including CSA S304-14 “Design of Masonry Structures” (2014), TMS 402 “Building Code Requirements and Specification for Masonry Structures” (2016), etc. These prescriptive codes generally provide guidelines on material properties, detailing requirements, minimum reinforcements, allowable stresses, and other considerations. The applicability and appropriateness of design codes to masonry walls are mainly studied by comparing the design code-model predictions and experimental results. In this section, the available studies on this topic for masonry

walls are reviewed. It should be noted that only unreinforced masonry (URM) walls and fully grouted reinforced masonry (RM) walls are included in the review.

Hwang et al. (2022) found that the design equations specified by the New Zealand Society for Earthquake Engineering (NZSEE) and Federal Emergency Management Agency (FEMA) 273 (Applied Technology Council 1997) result in quite conservative evaluations of the IP resistance of URM walls with a large deviation, particularly when the pre-compression stress is less than 0.5 MPa. Haach et al. (2013) compiled an experimental database and evaluated the performance of Eurocode 6 (2005), finding that both design code models yielded overly-conservative results with a large scatter. Celano et al. (2021) collected the experimental tests from the public literature, and a comparison between theoretical and experimental results was carried out. The results revealed that the design code predictions and experimental results on the flexural capacity of URM walls were in good agreement, with the design code predictions slightly underestimated. Noor-E-Khuda and Dhanasekar (2020) compared the design code predictions and FE predictions on the OOP capacity of RM walls, with the results shown in Figure 2-21. It was concluded that the design provisions in the AS3700 (2018) and Euro (2005) are shown to be overly-conservative for RM walls under vertical compression higher than or equal to 1 MPa, while design provisions for walls supported at top and bottom are safe in all four design standards considered. In addition, OOP capacities of the three sides supported and longer/taller walls predicted with the code equations are overly-conservative.

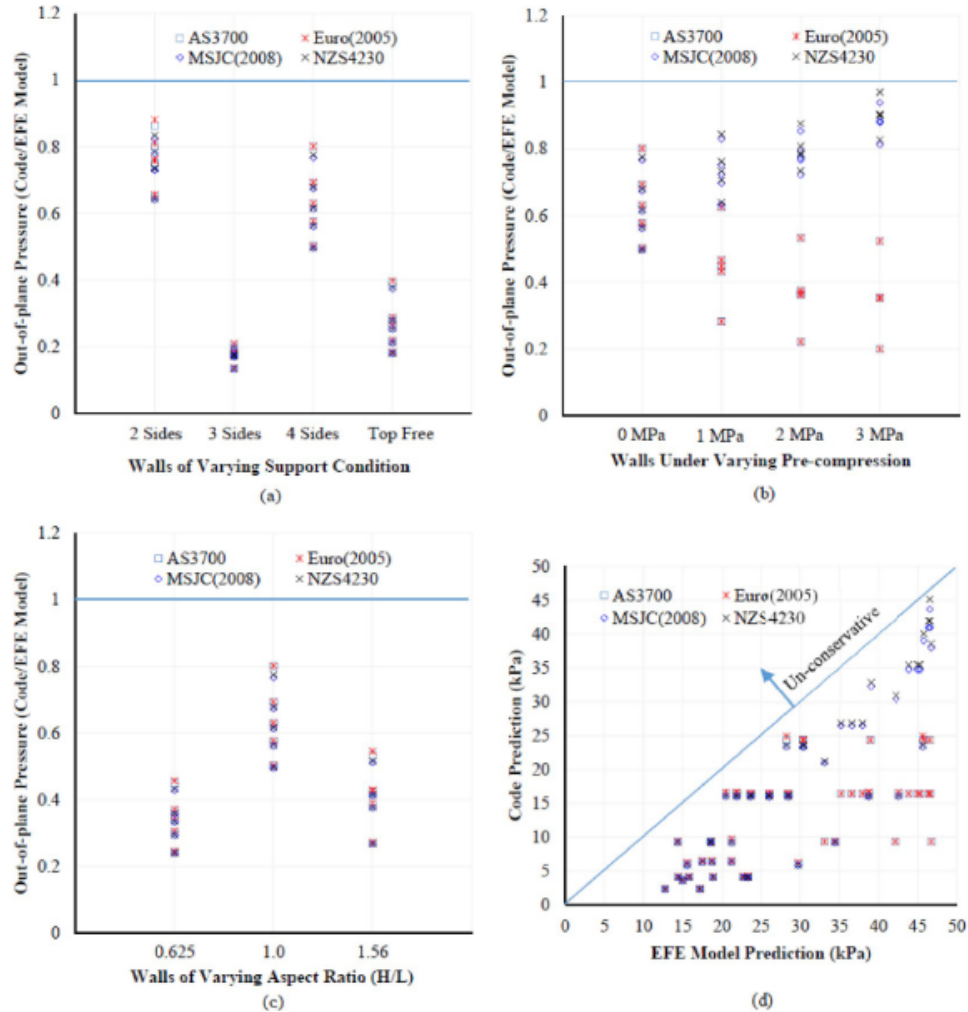


Figure 2-21. Comparison of OOP capacity by design codes and FE model by Noor-E-Khuda and Dhanasekar (2020)

Samy et al. (2012) compiled an experimental database of 173 flexural tests on RM beams and walls. CSA S304-14 flexural design provisions were checked against the compiled database. It was concluded that the mean value of the experimental-to-predicted ratio in terms of flexural strength is 1.13. Seif Eldin et al. (2019) performed a statistical analysis to evaluate the accuracy of various design equations of shear strength of fully grouted RM walls, including Matsumura (1988), Shing et al. (1990a), CSA (2014), TMS (2016), Voon and Ingham (2007), and the one proposed by Seif Eldin et al. (2019). The results of the statistical analysis showed that the given

equations by Matsumura (1988), TMS (2016), and the proposed equation were the most precise equations in terms of the smallest values for the coefficient of variation (COV). For the data set that includes all the studied walls, they have COV values of 15.3%, 13.6%, and 14.6%, respectively. Whereas, the proposed equation by Seif EIDin et al. (2019) has a COV ranging from 9.8% to 15.2% for the different data sets, compared to 11.3% ~ 17.5% and 11% ~ 19.5% for the equations provided by Matsumura (1988) and TMS (2016). Regarding the CSA S304-14 (2014), a consistent overestimate of shear strength was observed, as shown in Figure 2-22. The equation given in CSA S304-14 (2014) led to a 95th percentile value of the experimental-to-predicted ratio, which is higher than one. However, using the equation given in CSA S304-14 (2014) results in conservative values with a significantly large variation (COV = 25.1%).

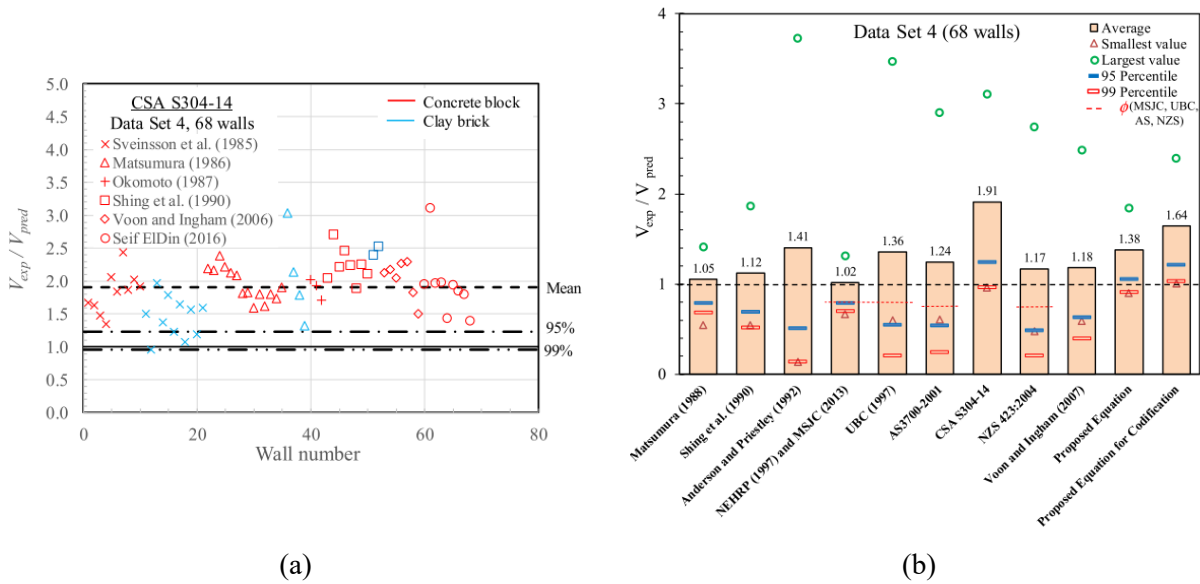


Figure 2-22. (a) Experimental results versus the predicted in-plane shear strength, and (b) statistical comparisons between the accuracy of shear equations for predicting in-plane shear strength of fully grouted reinforced masonry walls (Seif EIDin et al. 2019)

2.5. UNCERTAINTY IN MASONRY WALLS

Uncertainties in engineering systems are typically classified as either aleatoric or epistemic (Kiureghian and Ditlevsen 2009). Aleatoric uncertainty stems from inherent randomness of natural systems or processes and is commonly irreducible. This type of uncertainty, encompassing the intrinsic randomness in phenomena like material properties and loading conditions, is often addressed through probabilistic models. Epistemic uncertainty, on the other hand, arises from incomplete knowledge about the system or process. Characterized by measurement inaccuracies and model inadequacies, this uncertainty can diminish with enhanced information or understanding.

Epistemic uncertainty is often linked to limited data on masonry's behavior, simplifications in structural modeling, or uncertainties in future environmental conditions. Bartoli et al. (2017) investigated the importance of epistemic uncertainties in the structural modeling of masonry structures. Different analytical models and/or numerical techniques, including macro element, equivalent frame, finite element, and energy approach, were used for assessing the structural behavior of a series of slender masonry elements under increasing horizontal loads. All these approaches, especially those adopting a damage model, provide estimations of the ultimate load quite different from each other, highlighting a very strong dependence of the collapse displacement on the employed constitutive model. Rota et al. (2014) introduced a probabilistic methodology for incorporating diverse epistemic uncertainty sources in seismic assessments of masonry buildings. Similarly, Mucedero et al. (2022) studied the influence of modeling uncertainty in existing masonry-infill RC frames. It was concluded that a robust estimation of modeling uncertainty plays an important role on the collapse capacity of existing masonry-infilled RC frames;

when the modeling uncertainty was considered in a more integrated manner, a stronger reduction of the median collapse intensity was observed to almost 50% of that obtained considering only aleatory uncertainty.

Aleatoric uncertainty in masonry walls pertains to the inherent variability in these structures' behavior and properties. Sahu et al. (2020) investigate the statistical variations of the compressive strength of fly ash bricks. Twenty-six distributions were selected to find the best fit probabilistic model that closely describes the compressive strength of the bricks. Mendoza-Puchades (2021) focused on the variability and uncertainty present in the brick-to-mortar interface under dynamic loading, contributing valuable experimental data on masonry joint strength variations. Heffler et al. (2008) developed an experimental program to examine the extent of spatial correlation between unit flexural bond strengths within clay brick walls, taking into account mortar type, batch location, and mason workmanship. Such statistical quantification of aleatoric uncertainty is essential for the uncertainty analysis of masonry walls, and relevant studies will be reviewed in the next section.

2.6. UNCERTAINTY ANALYSIS AND RELIABILITY ANALYSIS OF MASONRY WALLS

2.6.1. Simplified model-based

Uncertainty analyses of masonry walls can be classified into two primary categories. The first involves the use of simplified models, such as design code-based models, as exemplified by studies by Iannacone et al. (2021) and Metwally et al. (2022). A crucial aspect of these studies is the probabilistic quantification of model error, which is often significant in simplified models. For instance, Iannacone et al. (2021) developed probabilistic capacity models for URM walls under IP loading. The models were constructed using existing physics-based models, which attempt to

capture the underlying physics, together with correction terms used to improve the accuracy of the models and remove the inherent bias. Unknown parameters for the proposed models were calibrated using a Bayesian updating approach. The proposed models are probabilistic and encompass relevant uncertainties and have been applied to assess the fragility functions of URM walls.

Metwally et al. (2022) incorporated uncertainties in material and geometric properties into the macro FE model to analyze the probabilistic OOP behavior of RM walls. Furthermore, the model error inherent in the macro model was quantified using a compiled experimental database. A sensitivity analysis indicated that a significant portion of the OOP load capacity variance was contributed by the uncertainty associated with model error.

In the realm of reliability analysis, a large number of researchers relied on the design code for the reliability evaluation of masonry walls under various loading conditions. The initial attempt at applying the modern limit state design philosophy to the masonry structure was made by Ellingwood and Tallin (1985). They demonstrated how probability-based design criteria might be developed for strength limit states of brick and concrete masonry construction, and the focus was paid on masonry walls loaded in combinations of axial compression and OOP flexure. Stewart and Lawrence (2007) compared design strengths with experimental test data to estimate a model error in probabilistic terms, for slender and non-slender URM walls in compression. This information, in conjunction with probabilistic models for material properties and loads, was used to calculate the structural reliability of masonry walls in compression. Zhai and Stewart (2010) developed a probabilistic model to calculate the structural reliability of typical FGRM walls designed to Chinese standards, loaded concentrically and eccentrically in compression. The effect of the

probability distribution of model error, material strengths, live load type, structural safety class, live-to-dead ratio, reinforcement ratio, discretization of wall thickness, eccentricity and load effect combination were considered. Moosavi and Korany (2014) performed a reliability analysis on concrete masonry under axial compression using the First Order Reliability Method (FORM) to assess the reliability levels of the Canadian masonry design standard. The Hasofer–Lind reliability index was evaluated at different live-to-dead load and snow-to-dead load ratios using the Rackwitz–Fiessler procedure. Similar to the simplified model-based uncertainty analysis, the reliability analysis relying on the simplified models might involve significant model error, which necessitates careful quantification.

2.6.2. Micro model-based

In recent years, with the increasing availability of computational resources, there has been a growing focus among researchers on using the high-fidelity model (e.g., micro model) to quantify the uncertainty associated with masonry walls (Gonen et al. 2021, 2022; Gooch et al. 2021; Isfeld et al. 2021; Li et al. 2014, 2016, 2017; Muhit et al. 2022; Pulatsu et al. 2022; Tabbakhha and Deodatis 2017).

Gooch et al. (2021) performed a stochastic FE analysis on perforated URM walls under IP loading conditions using the micro modeling strategy. The uncertainties were quantified in terms of IP capacities and ductility factors, as reflected in the load-deformation curves. Pulatsu et al. (2022) and Gonen et al. (2021, 2022) evaluated the probabilistic behavior of URM walls under IP loading using a discrete rigid block model, wherein the rigid blocks were utilized for masonry units, and mortar joints were represented as zero-thickness interfaces. Isfeld et al. (2021) investigated the uncertain behavior of URM walls subjected to uniformly distributed OOP loads

in a one-way vertical bending condition. Li et al. (2014, 2016, 2017) explored the impact of material uncertainty on the OOP capacity of URM walls under one-way (horizontally or vertically) and two-way bending conditions. Muhit et al. (2022) conducted a stochastic assessment of URM veneer walls subjected to OOP loading with variable constituent material properties. These studies utilized the micro modeling strategy that effectively replicates the inherent heterogeneity characteristics of URM walls, encompassing localized effects such as damage and cracking as well as corresponding IP or OOP capacity. However, it is notable that there are no existing uncertainty studies using micro modeling strategies specifically focused on RM walls.

2.7. MULTI-FIDELITY METHOD (MODEL)-BASED PROBABILISTIC ANALYSIS

2.7.1. Surrogate model

The main challenge in quantifying probabilistic behavior when using the micro model for masonry walls, as discussed above, can be attributed to the intense computational cost. In fact, this is also one of the biggest challenges in the general uncertainty quantification field. In order to address this challenge, surrogate models (aka metamodels) have been proposed to replace the original expensive model to approximate the input-output relationship. The construction of surrogate models is usually based on a certain amount of high-fidelity (HF) model data, through data-based approaches, as shown in Figure 2-23. Various surrogate models have been developed during recent decades, for example, response surface models (Bucher and Bourgund 1990; Gupta and Manohar 2004; Li and Wang 2021), Kriging models (Hong et al. 2022; Sacks et al. 1989), polynomial chaos expansion (Clermont and Sudret 2007; Schöbi et al. 2017; Sudret 2008), artificial neural networks (Deng et al. 2005), etc. Most surrogate models are expressed analytically, making them an attractive option in uncertainty studies involving computational complexity.

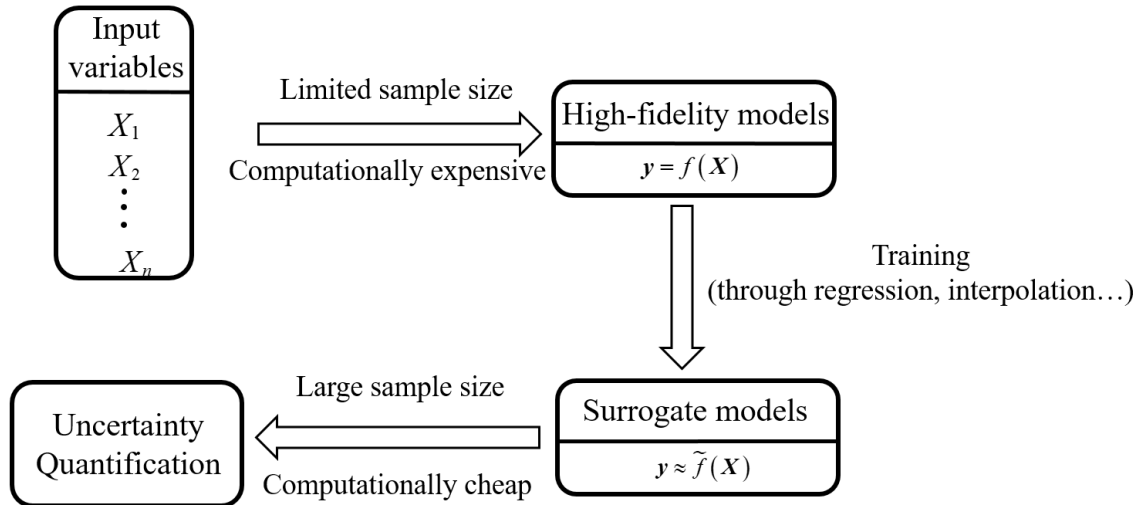


Figure 2-23. General framework for surrogate model-based uncertainty quantification

Efforts to apply the SM to the probabilistic analysis for masonry structures are limited, see Tubaldi et al. (2020) for the masonry arch bridge, Zhu et al. (2017) for hollow concrete block masonry wall, Mukherjee et al. (2011) for the URM shear wall, and Metwally et al. (2022) for the RM wall under OOP loading. Although SM showed the potential in these works, its applicability still remains questionable. This is because the accuracy of SM is highly dependent on the expensive data points available. The quality of SM should be evaluated in terms of some metrics (e.g., bias, variance, efficiency, problem size). However, these factors, in the aforementioned SM-based studies, were not discussed. In fact, the number of samples needed for an accurate approximation to construct a SM still requires an unaffordable computation cost, particularly for high-dimensional and highly nonlinear problems (Li and Jia 2020; Paiva et al. 2010; Skandalos et al. 2022).

2.7.2. Multi-fidelity method

To further alleviate the computational burden, the concept of the multi-fidelity (MF) method has been recently proposed. In structural engineering problems, the use of high-fidelity (HF) computational models is paramount to characterizing the structural performance (e.g., micro model for masonry walls). On the other hand, computationally cheaper low-fidelity (LF) models are generally accessible. MF methods seek to leverage information from models of varying fidelities and computational costs to achieve an accurate approximation. The general procedure for MF method-based uncertainty quantification is shown in Figure 2-24.

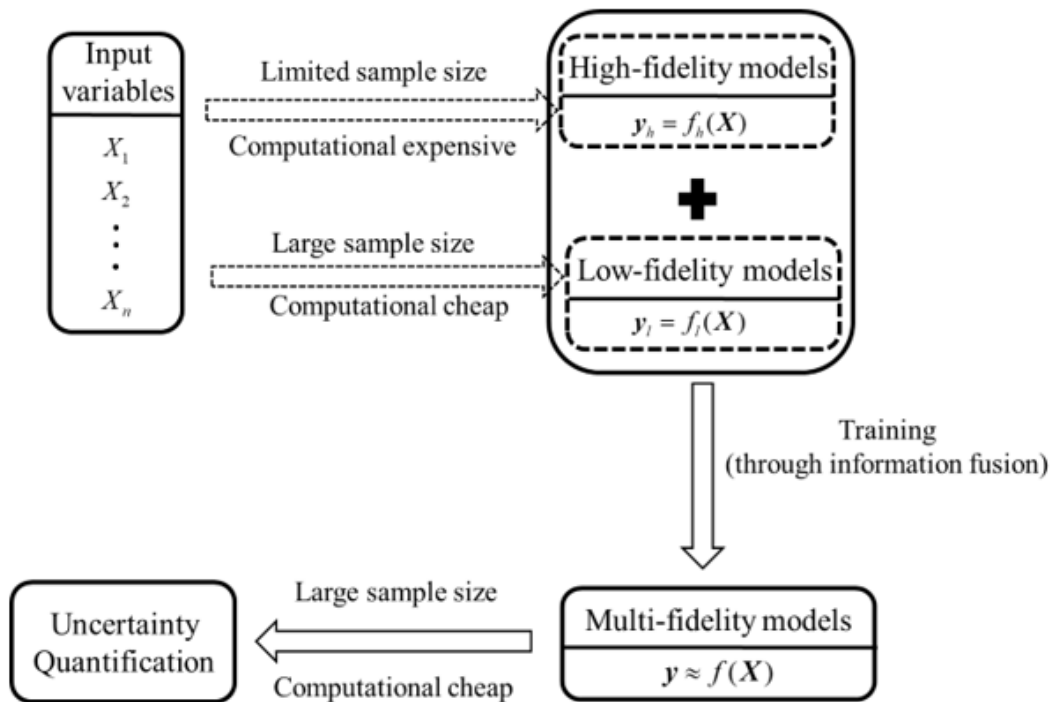


Figure 2-24. General framework for multi-fidelity model-based uncertainty quantification

The first category of MF methods and/or models has been developed using data-driven approaches. The core idea is to ‘correct’ the LF model data by constructing a surrogate model to represent the difference or ratio between the HF and LF models, typically termed ‘additive or

multiplicative corrections'. Furthermore, this type of modeling approach can be broadly divided into deterministic and non-deterministic methods. In deterministic approaches, the correction terms are expressed in terms of deterministic basis functions, whose coefficients are determined by minimizing discrepancies between HF and LF data, for example (Alexandrov et al. 2001; Forrester et al. 2006; Vitali et al. 2002). In contrast, non-deterministic approaches assume uncertainty in either the basis functions or coefficients, and this uncertainty is reduced by incorporating the available sample data. A prominent example in this context is the Multi-fidelity Gaussian Process, also known as the Co-Kriging model (Kennedy and O'Hagan 2000). The applications of the Co-Kriging model in the civil engineering field can be found (Chen et al. 2022; Dey et al. 2021; Li and Jia 2020; Skandalos et al. 2022). Li and Jia (2020) developed an MF Gaussian Process model in the context of Bayesian updating for problems when only a limited number of HF data are available. The proposed model was then applied to establish a predictive model for the deformation capacity of reinforced concrete columns. Skandalos et al. (2022) performed the simulation-based seismic reliability analysis for a reinforced concrete frame by employing the MF surrogate model. The HF model was developed in OpenSees involving a distributed plasticity model for reinforced concrete primary buildings illustrated in Figure 2-25 (a), while the LF model was a linear-elastic stick model with one horizontal degree of freedom per floor shown in Figure 2-25 (b). Dey et al. (2021) evaluated the applicability of the Co-Kriging surrogate model for pipelines undergoing fault rupture displacements. The HF model is a well-validated 3D nonlinear FE model, whereas in the LF model, the beam elements were used for pipelines and soil-pipeline interactions were represented as spring elements. Chen et al. (2022) presented an experimental study for the Co-Kriging surrogate model in the Real Time Hybrid

Simulation (RTHS) framework to explicitly account for structural uncertainty. The results indicate that Co-Kriging can achieve greater accuracy through less expensive HF information.

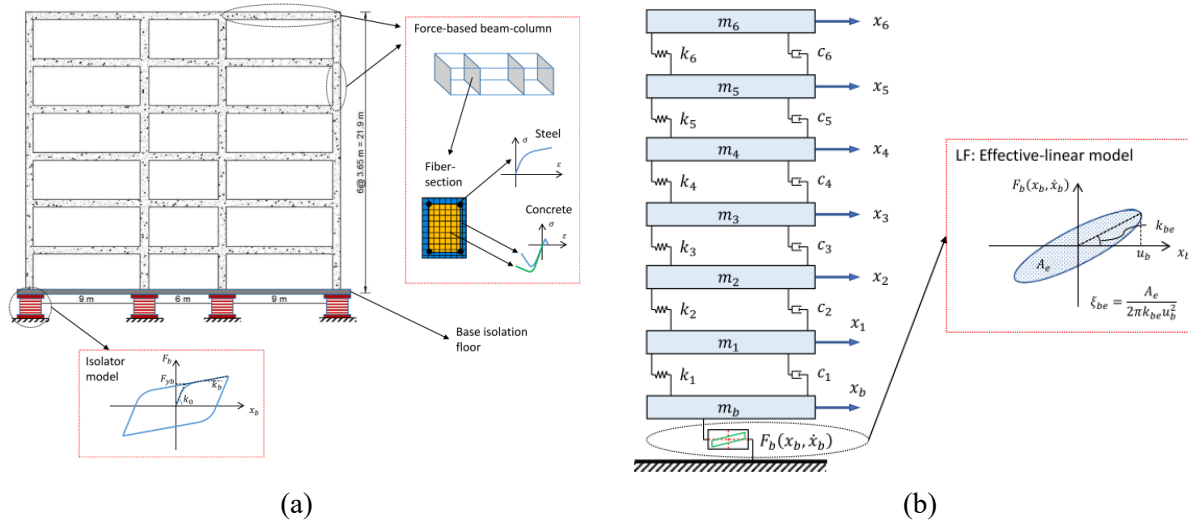


Figure 2-25. Multi-fidelity method used for the simulation-based seismic reliability analysis for a reinforced concrete frame: (a) high-fidelity model, and (b) low-fidelity model (Skandalos et al. 2022)

The underlying mathematical principle of the second category MF method is the control variate (CV) method (Nelson 1987, 1990). Those estimations built based on the CV method, namely CV estimators (e.g., statistics estimators, reliability estimators), have two important properties: (1) unbiasedness; and (2) potential variance reductions. These properties allow CV-based MF methods to perform the uncertainty analysis with both accuracy and efficiency. The key ingredient of CV-based MF methods is an optimization problem to distribute the computational budget among the expensive HF model and the cheap LF model such that the error (e.g., mean square error with respect to the true value) of the estimator is minimized for a given computational budget.

This idea first emerged in Monte Carlo (MC) statistical estimation, such as mean and variance estimations, highlighted by relevant works in Multi-Level Monte Carlo (MLMC)

estimation (Giles 2008, 2015; Gruber et al. 2023), Multi-Fidelity Monte Carlo (MFMC) estimation (Peherstorfer et al. 2016b; Qian et al. 2018), as well as some engineering applications in aerospace engineering (Gianluca et al. 2017; Ng and Willcox 2016; Peherstorfer et al. 2018a), and additive manufacturing engineering (Xu and Liu 2019). Particularly, in the field of structural engineering, Patsialis et al. (2022; 2021) investigated the use of the CV-based MF method in probabilistic seismic risk assessment. In their work, an efficient but inaccurate reduced order model was integrated, in conjunction with the nonlinear time-history analyses on the HF FE model, into the CV-based MF framework, and the results indicated its significant potential in predicting the engineering demand parameters in terms of efficiency and accuracy.

Different from statistical estimation, reliability assessments pose greater challenges, given the significance of extreme percentiles in probability distribution functions. Rashki et al. (2018) introduced a strategy that integrated coarse- and fine-mesh FE models for reliability analysis. In this study, the failure probability integral was broken down into two separate terms using the CV technique. The first term provided a low-cost estimate of the failure probability using a model with coarse mesh density, whereas the second term regulated the failure probability based on fewer FE analyses with fine mesh density. Hamdia and Ghasemi (2023) presented a reliability analysis for fracture toughness estimation using a multi-level refinement on a hierarchy of computational models. The probability of failure was estimated by expanding it into a telescoping sum of an initial approximation at the coarsest mesh and a series of incremental corrections between the subsequent levels. Li and Xiu (2010) proposed a hybrid approach by sampling the cheap LF model in a ‘large’ portion of the probability space and the expensive HF model in a ‘small’ portion. Nonetheless, these approaches typically assumed a certain type of LF model, without showing

generality. Lately, Peherstorfer et al. (2016a) incorporated the importance sampling strategy to facilitate the reliability analysis relying on both HF and LF models. Notably, the failure domain was captured using cheap LF models via an expectation-maximization method. However, a relatively large number of HF evaluations were still required, especially for rare event analyses.

Chapter 3. FINITE ELEMENT MODELING AND PARAMETER IMPORTANCE INVESTIGATION OF UNREINFORCED MASONRY WALLS USING OFF-THE-SHELF TECHNIQUES

The mechanical behavior of unreinforced masonry (URM) walls is complex due to the masonry heterogeneity and anisotropy, and thus finite element (FE) prediction of their structural response under in-plane (IP) and/or out-of-plane (OOP) loading conditions remains a challenging task for engineers. In this chapter, three-dimensional (3D) FE models were developed in the commercial FE software ABAQUS using off-the-shelf continuum elements for units and contact-based cohesive surfaces for between- or within-brick interfaces. This FE strategy was validated as a unified modeling approach that is capable of predicting the response of unit-mortar-unit assemblages and URM walls under IP and OOP loadings. The numerical-experimental comparisons showed the accuracy and potential of the FE models developed. A parametric study was then conducted to investigate the relative importance of influencing material parameters on the URM behavior under IP and OOP loadings. The results of the parametric study indicated that the OOP behavior was affected by the tension-related interface parameters, while the IP behavior was affected by both shear-related and tension-related interface parameters.

3.1. INTRODUCTION

The structural behavior of unreinforced masonry (URM) walls depends on the properties of the masonry constituents (e.g., units, mortar) and their interaction. Due to the heterogeneity and anisotropy of masonry as well as the periodic arrangement of URM walls, the simulation or prediction of masonry wall behavior under in-plane (IP) and/or out-of-plane (OOP) loading conditions remains a challenging task (Xu et al. 2012). This has been evidenced by the uncertainty

in predicting the strength, stiffness, and ductility as typically reflected by overall load-deflection curves and the lack of accuracy in simulating the failure mechanisms as implied by crack patterns and/or unit crushing (Dymiotis and Gutleiderer 2002; Tabbakhha and Deodatis 2017).

In the past few decades, a wide range of finite element (FE) modeling approaches have been proposed with different levels of sophistication, accuracy, and efficiency. FE modeling approaches for masonry walls can be mainly classified into two broad categories (Lourenço et al. 1995a): generalized macro modeling and detailed micro modeling. The generalized macro models can be further divided into macro continuum models and macro element models (D’Altri et al. 2020). The generalized macro modeling approach treats masonry as an averaged continuum using homogeneous constitutive laws (Casapulla et al. 2013; Noor-E-Khuda and Dhanasekar 2018a), without explicit modeling of the geometry and material of individual constituents. As such, generalized macro modeling for masonry is computationally efficient and applicable for walls with sufficiently large dimensions. However, the macro modeling approach is incapable of capturing the detailed failure modes of masonry structures, such as tensile cracking and shear sliding of masonry mortar interfaces (Lourenço et al. 1995a; Lourenço 1996). On the other hand, the detailed micro modeling approach is characterized by a detailed representation of masonry on the basis of explicit modeling of each constituent and interfaces. The units and mortar are modeled using continuum elements, while the interface is modeled using discontinuous elements. This approach allows for the description of characteristic failure modes of URM structures, including unit crushing and potential crack propagation (e.g., along the joints, through the mortar and units), but at high computational costs.

As a compromise option between macro and detailed micro modeling, simplified micro modeling has been proposed and extensively developed in the masonry community (Abdulla et al. 2017; Kumar and Barbato 2019; Lourenço 1996; da Porto et al. 2010) to achieve a balance between computation efficiency and accuracy. Different from the detailed micro modeling strategy, in the simplified micro modeling strategy, mortar joints and unit-mortar contacts are lumped into interfaces, while units are modeled with size expansion to maintain the overall geometry of a wall, leading to a reduced number of interface elements. The simplified micro modeling approach, which has been mainly used for IP behavior simulation (Kumar and Barbato 2019; Lourenço 1996; da Porto et al. 2010) in a two-dimensional (2D) domain, is adopted in this chapter to simulate both the IP and OOP behavior of tested URM walls from the literature.

As the key aspects of the simplified micro modeling approach, material constitutive models for units and interface models have led to various modeling strategies, as found in the literature. Specifically, significant efforts have been devoted to developing interface models, e.g., single-yield surface models (Lotfi and Shing 1994; Stankowski et al. 1993a), and multi-yield surface models (Lourenço 1996; Lourenço and Rots 1997). However, most of the surveyed material models are proprietary and unavailable to the majority of researchers and engineers. Instead, this study takes advantage of off-the-shelf materials and elements in the commercial FE software ABAQUS (Simulia 2017), adopting the contact-based surface approach to model the cohesive-frictional behavior of interfaces. For cracking modeling of units, there are two main approaches: discrete (Lourenço 1996) and smeared crack models (Lotfi and Shing 1994). The former approach relies on simulating individual cracks as geometrical discontinuities localized at interfaces between continuum elements, while the latter one treats the cracked unit as a continuum with damage and

material deterioration spread across the elements. As noted by Lourenço (1996), the latter approach is better suited for larger-scale structures with distributed crack patterns, such as those made with reinforced concrete, while the localized cracks exhibited by masonry between the units are better described by the discrete crack model. Therefore, this chapter adopts the former approach, which is more computationally robust, in conjunction with the Drucker-Prager (DP) model to capture the possible compressive failure of masonry units.

In spite of the aforementioned advantages of the simplified micro modeling approach, the relatively large number of micro-level mechanical parameters can be intimidating for numerical studies. As such, knowledge of their importance in simulating the structural behavior of masonry structures is essential. Many numerical studies were conducted to study the material parameter sensitivity to the structural behavior of masonry systems. Much attention has been focused on the FE simulations of small masonry tests such as triplet-shear tests, compressive tests for masonry prisms, and diagonal compression tests (for small masonry panels). Zhang et al. (2018) and Ferretti et al. (2018) performed parametric studies in terms of the elastic stiffness of mortar joints and dilatancy-related parameters based on the developed FE models for the triplet-shear test setup. Álvarez-Pérez et al. (2020) carried out a sensitivity analysis to conclude that the most influential material parameters for the masonry prism compression strength are the compressive strength of concrete block and the tensile strength of mortar. Sousa et al. (2015) developed a micro-FE model that was capable of simulating the European Standard Compressive Test and further studied the influence of compression-related parameters of units and mortar on the compressive strength of masonry prisms. Similar research conducted by Roca et al. (2016) indicated that the increase of the Young's modulus and the decrease of the Poisson's ratio of the units resulted in an increase in

the compressive strength of masonry, while the opposite effect of the relevant material parameters of the mortar was observed. The sensitivities of material parameters in the diagonal compression tests for small masonry panels were investigated in (Calderini et al. 2010; Sousa et al. 2013; Zhang et al. 2017), in which the material parameters of different constituents, including the brick-mortar interfaces, were studied.

Regarding the large-scale masonry structure, some related numerical sensitivity studies can be found with a focus on masonry arch structures (Zhang et al. 2016), masonry domes (Li and Atamturktur 2014), masonry cross vaults (Gaetani et al. 2017), and large masonry columns (Qamar and Qin 2021). However, relatively less attention has been paid to the material parameter sensitivity or their importance to masonry walls through modeling the lateral-load tests and out-of-plane loading bending tests. Specifically, to the best knowledge of the authors, no studies examined the importance of micro FE modeling parameters on both IP and OOP behaviors of masonry walls, and existing studies typically only focused on either IP (Stavridis and Shing 2010) or OOP (La Mendola et al. 2014) behaviors of masonry walls. Stavridis and Shing (2010) studied the IP behavior of masonry-infilled walls using a 2D simplified micro FE modeling approach and assessed the importance of material parameters for mortar joints and bricks. Among all the material parameters studied, the frictional coefficient for mortar joints was found to be the most influential for IP behaviors. La Mendole et al. (2014) studied the influence of material parameters on the OOP behavior of URM walls, in which only mode I failure-related material parameters were considered for mortar interfaces, such as elastic stiffness in the normal direction, tensile strength, and mode I fracture energy. However, mode II failure-related material parameters for mortar interfaces were not studied, even though they can be potentially important for URM walls under OOP loading

since they are related to shear sliding failure of interfaces (Pluijm 1999). Additionally, it is also unclear how the mode I failure-related material parameters affect the wall behavior under IP loading, particularly for URM walls that are prone to overturning and excessive cracking. This entails the need for further study of the relative importance of micro-level mechanical parameters on the IP and OOP behaviors of URM walls.

In this chapter, the integrated use of off-the-shelf three-dimensional (3D) continuum elements and 3D contact-based cohesive surfaces leads to a unified modeling strategy for predicting both the IP and OOP behaviors of masonry walls. Thus, this unified approach allows for the assessment of the relative importance of different micro-level modeling parameters for the IP and OOP behaviors of URM walls, respectively. To this end, this chapter first validated the unified modeling approach through unit-mortar-unit assemblages and tested URM walls well-documented in the literature, after a detailed description of the modeling strategy. With the validated FE models developed for the URM walls, this chapter then conducted a parametric study to investigate the importance of micro-level modeling parameters for the behavior prediction of URM walls under IP and OOP loadings. This is different from most parametric studies of URM walls, which focused on engineering design or wall configuration parameters such as aspect ratios, slenderness ratios, and pre-compression levels. The information on the relative importance of the micro model parameters could provide valuable guidance on (1) planning the material tests for experimental studies and (2) micro modeling of masonry walls under complex loadings for numerical studies.

3.2. SIMPLIFIED MICRO MODELING STRATEGY

In the simplified micro modeling approach, the geometrical configuration of masonry walls is simplified by: (1) expanding the brick units to the middle surfaces of mortar layers, and (2) bonding the expanded units through zero-thickness interfaces, as shown in Figure 3-1. The zero-thickness interfaces between expanded units, referred to as between-brick interfaces hereafter, are modeled as contact-based cohesive surfaces that are defined by node-to-surface discretization. As evidenced by experimental observations (Aref and Dolatshahi 2013; Dolatshahi 2012), cracks in masonry walls can form vertically through the middle surface of units. As such, a vertical contact-based cohesive surface is inserted at the middle of each brick shown in Figure 3-1 (b), referred to as a within-brick interface hereafter, to provide a potential path for crack propagation. It is worth mentioning that the cracks can develop arbitrarily along different paths with inclinations in brick units. Insertion of vertical contact-based cohesive surfaces to model crack propagation through brick units is a practical simplification, which was used in existing works (Aref and Dolatshahi 2013; Kumar and Barbato 2019; Lourenço 1996; Remacle et al. 2012). Finite sliding tracking is enabled to allow arbitrary separation, sliding, and rotation of the contact surfaces (Dassault Systemes 2017). The material models for expanded units and interfaces are detailed in the following sections, respectively.

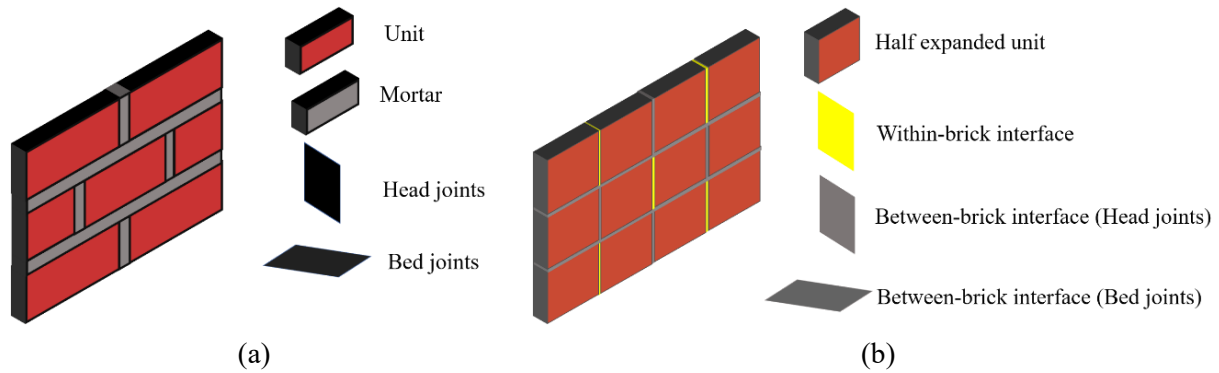


Figure 3-1. Simplified micro modeling strategy for URM structures: (a) masonry assemblage sample, and (b) FE modeling strategy

3.3. MATERIAL MODELING FOR EXPANDED BRICK UNITS

In the case of URM walls under IP loading, the crushing behavior at the toe of URM walls has a significant influence on determining the ultimate shear capacity (Nazir 2015; Shing et al. 1989a). Since the interfacial behavior of contact-based cohesive surfaces does not include a compression-cap failure surface as in the simplified micro modeling strategy proposed by Lourenco and Rots (1997), brick units are modeled using the Drucker-Prager (DP) model in order to take into account the compression failure mechanism of URM walls. In this model, the yield surface f can be considered a generalization of the von Mises criterion with hydro-static pressure dependence or a generalization of the Mohr-Coulomb criterion (Drucker and Prager 1952), defined by the frictional angle β and cohesion d , as defined in Eq. (3-1). A non-associated flow rule was selected, with the plastic potential defined by a dilation angle ψ , which is different from the frictional angle β .

$$f = t - p \tan \beta - d = 0 \quad (3-1)$$

where $t = \frac{1}{2}q \left(1 + \frac{1}{R} - \left(1 - \frac{1}{R} \right) \left(\frac{r}{q} \right)^3 \right)$, q is von Mises equivalent stress, defined as $q = \sqrt{\frac{3}{2}(\mathbf{S}:\mathbf{S})}$, in which \mathbf{S} is the stress deviator, given by $\mathbf{S} = \boldsymbol{\sigma} + p\mathbf{I}$; p is the equivalent stress, defined as $p = -\frac{1}{3}\text{trace}(\boldsymbol{\sigma})$; R is the ratio of the flow stress in tri-axial tension to the flow stress in tri-axial compression (referred to as the flow stress ratio ranging from 0.778 to 1.0); β is the frictional angle, d is the cohesion of the material with $d = \left(1 - \frac{1}{3}\tan\beta \right) \sigma_c$ when hardening is defined by the uniaxial compressive yield stress f_c , and r is the third deviatoric stress invariant. The yield surface plot is shown in Figure 3-2.

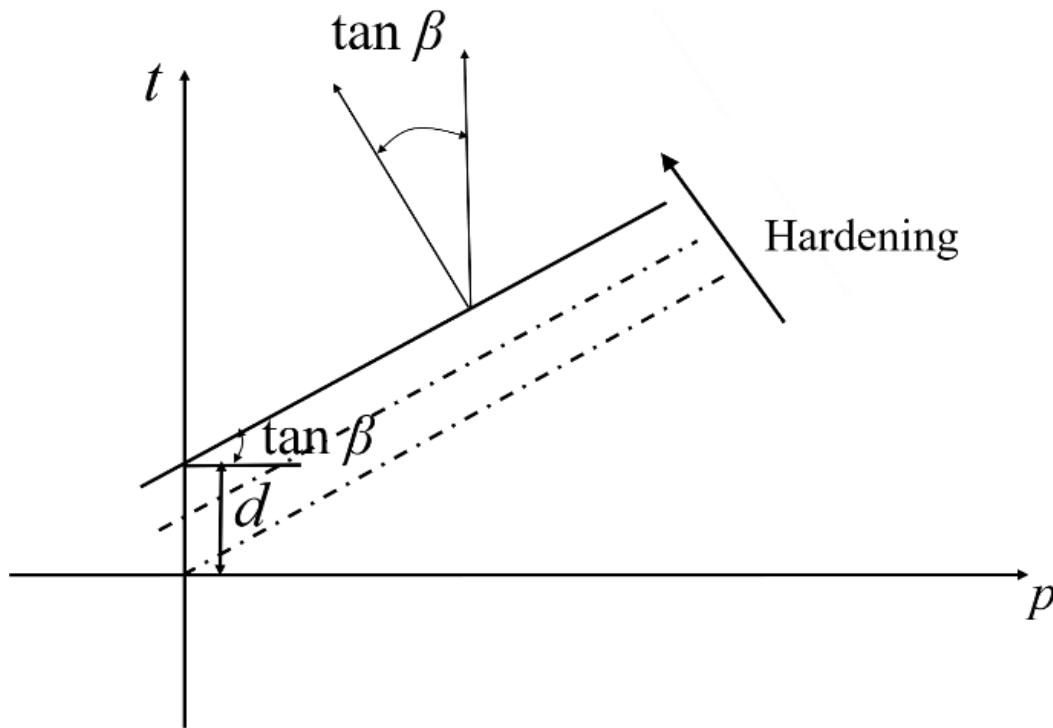


Figure 3-2. Yield surface of DP model

To summarize, in the DP model described above, two inelastic parameters (i.e., frictional angle β , dilation angle ψ) are needed together with the uniaxial compressive stress-strain curve, in addition to two elastic parameters (i.e., elastic modulus E , Poisson ratio γ).

3.4. CONTACT-BASED COHESIVE SURFACE BEHAVIOR FOR MORTAR JOINTS

3.4.1. Elastic behavior

The commonly used linear traction-separation relationship is utilized to characterize the interaction stiffness of contact-based cohesive interfaces prior to damage. Specifically, three stiffness constants k_{nn} , k_{ss} and k_{tt} are assumed to relate three stress components (i.e., σ_n , τ_s , τ_t) and three displacement separations (i.e., u_n , u_s , u_t), see Eq. (3-2):

$$\begin{bmatrix} \sigma_n \\ \tau_s \\ \tau_t \end{bmatrix} = \begin{bmatrix} k_{nn} & & \\ & k_{ss} & \\ & & k_{tt} \end{bmatrix} \begin{bmatrix} u_n \\ u_s \\ u_t \end{bmatrix} \quad (3-2)$$

where for the stress and displacement components, subscript ‘ n ’ denotes the normal direction, ‘ s ’ and ‘ t ’ represent the first and second tangential directions.

For the within-brick interfaces, three stiffness constants are treated as dummy parameters with relatively large values to avoid the non-physical penetration. For the between-brick interfaces, stiffness constants are determined under the assumption of stack bond, e.g., a series connection of the masonry constituents (i.e., brick units and mortar layers), and uniform stress distribution in both the brick unit and mortar (Lourenço 1996), as detailed in Eq. (3-3) and Eq. (3-4):

$$k_{nn} = \frac{E_u E_m}{h_m (E_u - E_m)} \quad (3-3)$$

$$k_{ss} = k_{tt} = \frac{G_u G_m}{h_m (G_u - G_m)} \quad (3-4)$$

where E and G are Young's and shear moduli, respectively; the subscripts u and m indicate the unit and mortar, respectively; and h_m is the mortar thickness.

3.4.2. Failure criterion

The elastic traction-separation relationship discussed above is used with a certain failure criterion for cohesive interfaces. A built-in modified Mohr-Coulomb yield criterion combined with tension cut-off surface available in ABAQUS (Dassault Systemes 2017) is used to represent the shear and tensile strengths of mortar joints, which can be mathematically expressed as Eq. (3-5):

$$\max \left\{ \frac{\langle \sigma_n \rangle}{f_t}, \frac{\tau}{f_s} \right\} = 1 \quad (3-5)$$

where the symbol $\langle \rangle$ represents the Macaulay bracket, i.e., $\langle x \rangle = (|x| + x) / 2$; σ_n and $\tau = \sqrt{\tau_s^2 + \tau_t^2}$ are the normal stress (i.e., tensile as positive) and the resultant shear stress of interfaces, respectively; f_t and f_s are the tensile and shear strengths, respectively. This implies that a pure compressive deformation or stress state does not initiate damage in interfaces, and the compressive behavior is described as a linear pressure-overclosure relationship with a large contact stiffness to ensure negligible penetration of the slave surface to the master surface in contacts. It is also assumed that the pressure-overclosure relationship only governs compressive behavior, which is independent of the cohesive behavior and is deactivated when contact is lost.

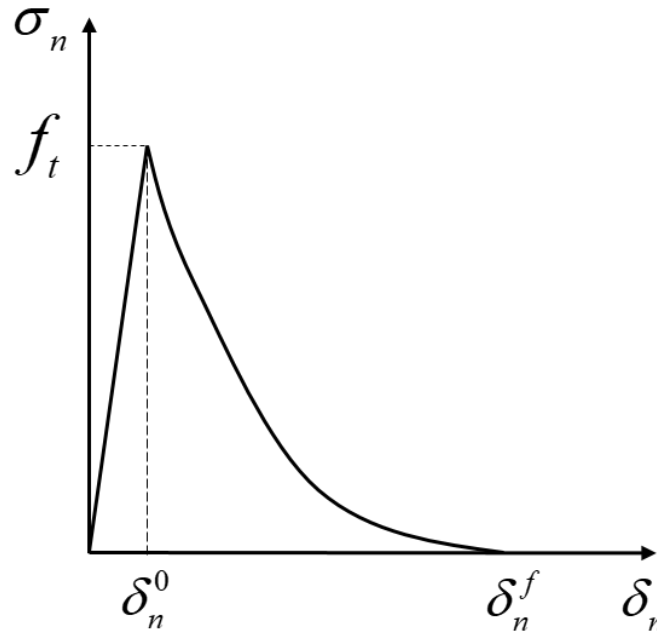


Figure 3-3. Stress-displacement response of interfaces under pure tension

As can be seen in Eq. (3-5), damage initiates when the tensile strength f_t is reached under the pure tension condition (i.e., $\tau_s = \tau_t = 0$), corresponding to a damage initiation displacement $\delta_n^0 > 0$ in the normal direction. An exponential softening branch is defined as damage evolves until the tensile stress reduces to zero with an ultimate failure displacement δ_n^f (shown in Figure 3-3). As such, a scalar damage variable D , ranging from 0 to 1, is used to account for the stiffness degradation with respect to the initial stiffness, as shown in Eq. (3-6) for the normal direction:

$$\sigma_n = k_m (1 - D) \delta_n \quad (3-6)$$

In analogy to the definition of resultant shear stress (i.e., $\tau = \sqrt{\tau_s^2 + \tau_t^2}$), the resultant shear displacement δ_τ is determined as $\delta_\tau = \sqrt{\delta_s^2 + \delta_t^2}$. Under pure shear loading condition, damage initiates when the cohesive strength c is reached, corresponding to a damage initiation

displacement δ_τ^0 . Once the stiffness starts degrading, the frictional model activates and begins contributing to the shear stress. The elastic stick stiffness of frictional model (i.e., frictional coefficient $\mu = \tan \varphi_u$, in which φ_u is the initial frictional angle) is ramped up in proportion to the degradation of the elastic cohesive stiffness (i.e., k_{ss} , k_{tt}). Prior to the ultimate failure of the cohesive bond, and following the damage evolution, the shear stress is a combination of the contribution from cohesive stress (i.e., τ_{coh}) and the frictional stress (i.e., τ_{fric}). At the peak point, corresponding to a shear displacement δ_τ^{peak} , peak shear stress f_s is determined by Eq. (3-7):

$$f_s = \tau_{coh} + \tau_{fric} = c \times (1 - D) + \sigma_n \times \tan \varphi_u \times D \quad (3-7)$$

Consequently, this built-in cohesive-interfacial model underestimates the peak shear strength compared with the conventional Mohr-Coulomb model (D'Altri et al. 2018; Lourenço 1996) that is not available for contact-based surfaces or interfaces in ABAQUS (Dassault Systemes 2017).

Similar to the damage-induced softening for the tensile regime, a softening branch under pure shear loading condition is followed. The post-peak behavior is also determined based on Eq. (3-6) with the increase of the damage variable D until the maximum degradation of interface is reached. Once maximum damage is achieved (i.e., $D = 1$), starting at a failure displacement δ_τ^f , the cohesive contribution to the shear stresses is zero, and the only contribution comes from the frictional component, resulting in a residual stress $f_r = \sigma_n \tan \varphi_r$, where φ_r is the residual frictional angle. The stress-displacement response under shear condition for the cohesive-friction model is illustrated in Figure 3-4.

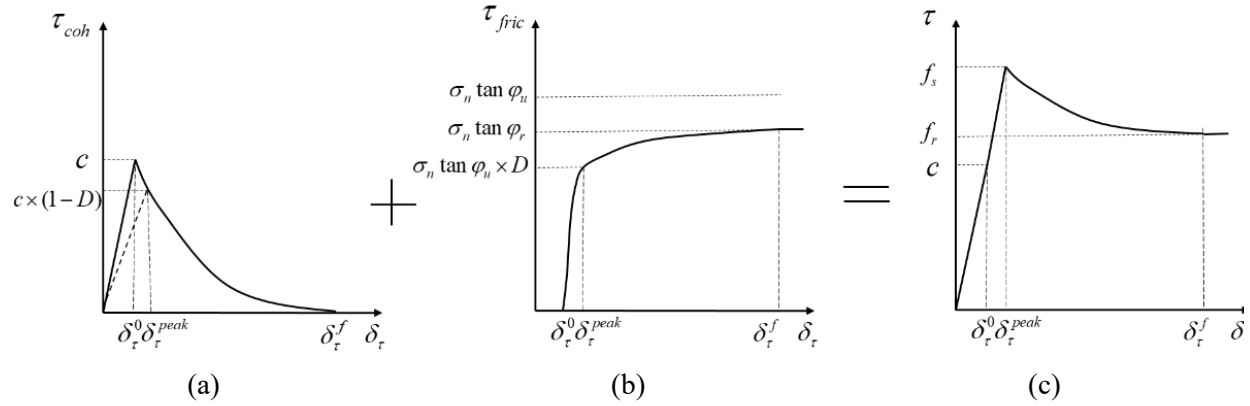


Figure 3-4. Stress-displacement response of interfaces under shear: (a) cohesion model, (b) frictional model, and (c) cohesive-frictional model

The damage evolution presented above for both tensile and shear regimes is attributed to the cementation of mortar (Aref and Dolatshahi 2013). As a result, the damage-induced softening behavior is fully coupled in both tension and cohesion component (not the frictional component) of shear, which means that the stiffness loss percentages for them are equal through the entire degradation process (Abdulla et al. 2017; Aref and Dolatshahi 2013; D’Altri et al. 2018; Lourenço 1996). The single damage variable D in Eqs. (3-6) and (3-7) is calculated as Eq. (3-8):

$$D = 1 - \left\{ \frac{\delta^0}{\delta} \right\} \left\{ 1 - \frac{1 - \exp\left(-\alpha \left(\frac{\delta - \delta^0}{\delta^f - \delta^0} \right)\right)}{1 - \exp(-\alpha)} \right\} \quad (3-8)$$

where δ^0 is the displacement at damage initiation and δ^f is the failure displacement at the complete stiffness loss; δ is the maximum displacement reached during the entire loading history; and α is a non-dimensional parameter that determines the shape of soften branch of stress-displacement curve. It should be noted that all symbols in Eq. (3-8) have subscripts ‘ n ’ or ‘ τ ’, corresponding to normal or tangential directions, respectively.

To summarize, to define the contact-based cohesive surfaces for interfaces, a total of 11 model parameters are needed. They are three elastic stiffness coefficients (i.e., k_{nn} , k_{ss} and k_{tt}), six nonlinear material parameters such as tensile strength f_t , cohesion C , frictional coefficient μ , residual frictional angle φ_r , failure displacements in the normal and tangential direction (δ_n^f and δ_t^f), and two non-dimensional parameters (α_n and α_t). These parameters can be defined as described earlier in this section. The relative importance for these parameters or associated parameters will be studied later for IP and OOP behavior of URM walls studied in this chapter.

3.5. FINITE ELEMENT MODEL VALIDATION

To validate the simplified micro modeling strategy used in this chapter, two unit-mortar-unit assemblages, three masonry walls under IP loading, and three masonry walls under OOP loading are simulated and compared with the experimental data available in the public literature. Geometrical nonlinearity is considered in all numerical models to account for the large deformation effects occurring in unit-mortar-unit assemblages and URM walls subjected to different loading conditions. General standard static steps are used in the analysis to achieve convergence in each substep by means of the Newton-Raphson method. Since the developed model exhibits various forms of softening behavior (e.g., units and interfaces) and stiffness reduction, viscous regularization is introduced to overcome some severe convergence difficulties. A value of 0.002 for the viscosity coefficient is employed, as suggested by Abdulla et al. (2017). The modeling process, material model parameter determination, and simulation results are presented next, together with a concise summary of the experiments.

3.5.1. Unit-mortar-unit assemblages

Two unit-mortar-unit assemblages simulated here were described in (Van der Pluijm 1992, 1993). One specimen was under pure tension, and the other one was under shear with various levels of pre-compression load (0.1 MPa, 0.5 MPa, and 1.0 MPa). These tests were conducted to understand the tensile and shear behavior of the mortar joints between bricks and were thus appropriate for validating the modeling of the between-brick interfaces adopted in this chapter. The experimental tensile and shear behaviors are shown in Figure 3-5 as shaded areas, respectively. Large variations in the stress-displacement curves were observed in the experiments due to the inherent variations in the material properties across different specimens. However, as the general stress-displacement behavior is characterized in both the tensile and shear behaviors with an exponential softening branch after the peak stress points in the model, it is rational to assume that the tensile strength would eventually deteriorate to zero, while the shear strength would remain at a certain level, depending on the pre-compression stress. With a focus on the interface behavior, the test specimens are modeled by assuming only elastic behavior for the brick units with an elastic modulus of 16700 MPa and a Poisson ratio of 0.15 (Van der Pluijm 1992, 1993) since experimental reports indicated that damage was concentrated on the mortar joints. The cohesive surface-based contact approach is used for the interface modeling between the two brick units, with the mechanical properties of the cohesive interface for small masonry specimens listed in Table 3-1. The cohesion c , tensile strength f_t , tensile failure displacement δ_n^f , and shear failure displacement δ_r^f are determined directly from the experimental results. The frictional coefficient μ was measured, ranging from 0.7 to 1.2 (Lourenço 1996). The residual friction angle $\tan \varphi_r$ was determined as 0.8, which is the ratio of the residual stress to the pre-compression stress. Non-

dimensional parameters α_n and α_τ are calibrated to make the descending branch fit the experimental envelopes. Consequently, the areas under the tension-displacement curve and the shear-displacement curves are approximately equal to the mode I fracture energy $G_I = 0.012$ N/mm and the mode II fracture energy $G_{II} = 0.058 - 0.13\sigma_c$ N/mm (Lourenço 1996), in which mode II fracture energy is related to pre-compression σ_c . It should be noted that elastic stiffness for cohesive interfaces was not reported in existing studies (D'Altri et al. 2018; Lourenço 1996; Van der Pluijm 1992, 1993). Hence, a default contact enforcement method available in ABAQUS (Dassault Systemes 2017) was used to automatically determine the cohesive stiffness in both normal and shear directions. In this context, the stiffness would be set as 10 times a representative underlying element stiffness.

The simulated tensile and shear stress-displacement curves are compared with the experimental ones, as included in Figure 3-5. It can be observed that good agreements with the experimental results are achieved regarding the joint behavior under both pure tension and compressive-shear loading, except for the descending branch in Figure 3-5 (b) for $\sigma_c = 1.0$ MPa. As evidenced by the experimental results (Van der Pluijm 1992, 1993), the ductility and energy dissipation capacity of mortar joints (i.e., interfaces) are increased under higher pre-compressive stresses. As a result, the mode II fracture energy G_{II} increases with the increase in the pre-compressive stress, corresponding to a less steep softening branch. The variation of G_{II} is neglected in the current FE model, which means that the brittleness parameter α_τ is a constant. Although some discrepancies can be observed between the FE simulation and experimental results for the higher pre-compression stress cases, the main characteristics of interfaces under shear loading can still be reproduced with reasonable accuracy. As such, it can be concluded that interface modeling

can well represent the tensile behavior and the shear behavior under different loading conditions. Thus, such an interface modeling approach can potentially be used for the between-brick interfaces in the modeling of masonry walls. For the within-brick interfaces, the same modeling strategy is used but with different model parameters, as described later.

Table 3-1. Material parameters of contact-based cohesive surfaces for unit-mortar-unit assemblages

f_t (MPa)	c (MPa)	μ	$\tan \varphi_r$	δ_n^f (mm)	δ_r^f (mm)	α_n	α_r
0.3	1.0	1.08	0.8	0.22	0.8	5.5	9.5

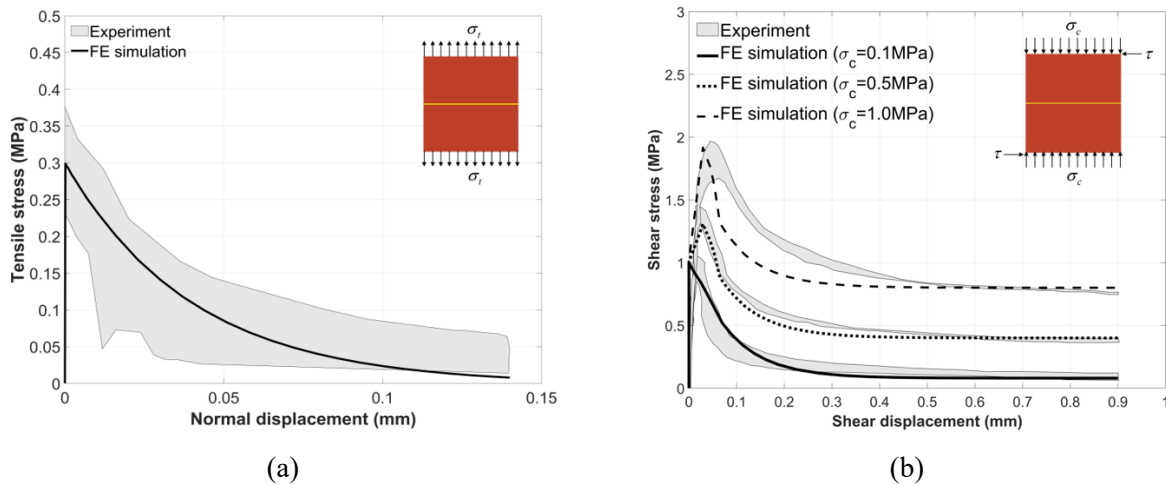


Figure 3-5. Comparisons between numerical and experimental results for unit-mortar-unit assemblages: (a) pure tensile loading, and (b) shear loading under different pre-compression load levels

3.5.2. URM walls under in-plane (IP) loading

The IP behavior of three URM walls considered in this chapter was experimentally investigated at the Eindhoven University of Technology (Raijmakers 1992; Vermeltoort and Raijmakers 1993). The dimensions, configurations, and test procedures for three walls (referred to as J4D, J5D and J6D) are the same except for the pre-compressive pressure: 0.3 MPa for the first two and 1.21 MPa for the third. They were solid (without openings) with the same dimensions: height = 1000 mm,

width = 990 mm, and thickness = 100 mm. Each wall was built up with 18 courses, composed of wire-cut solid clay bricks (210 mm × 52 mm × 100 mm) and 10 mm thick mortar layers. The top and bottom courses of the walls were clamped in steel beams, and the walls were tested to failure subjected to a monotonically increasing horizontal load shown in Figure 3-6 (b), after an initial pre-compression p_c applied at the top of masonry walls, as shown in Figure 3-6 (a).

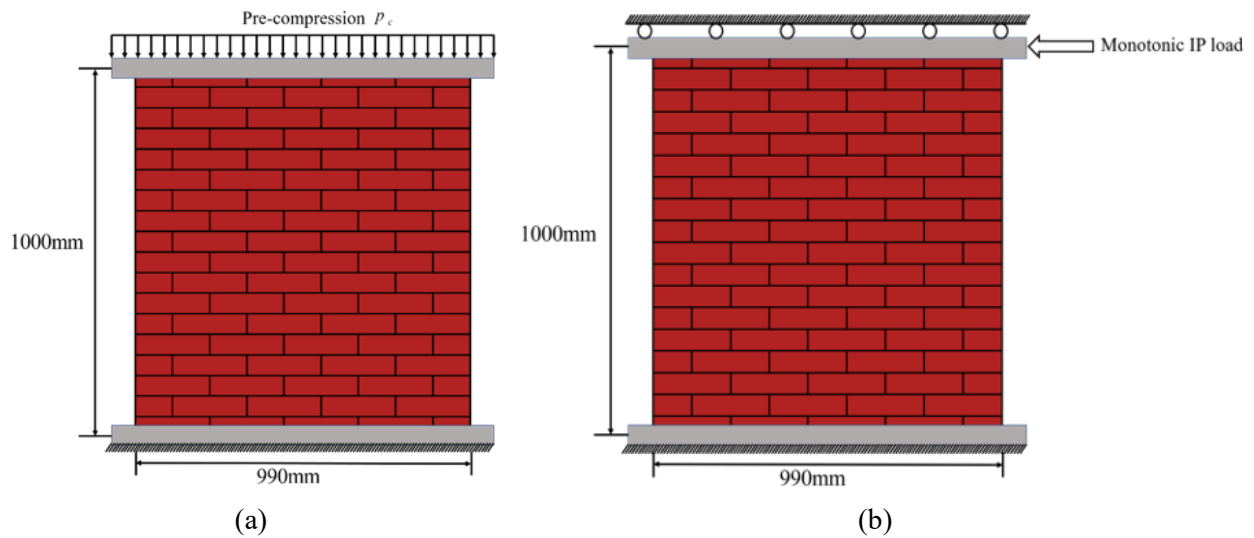


Figure 3-6. URM walls considered for IP loading: (a) pre-compression applied at the top of the walls, and (b) monotonic displacement-controlled in-plane loading

These walls are selected for model validation and used for further study because their behaviors and material parameters were well documented and used by a number of other researchers (D’Altri et al. 2018; Dolatshahi 2012; Lourenço 1996; Lourenço and Rots 1997). In contrast to the modeling approach employed in this work, only elastic behavior was taken into consideration for units in (Lourenço 1996; Lourenço and Rots 1997), where the damage in the units (e.g., crushing of masonry toes) was not captured. Conversely, Dolatshahi (2012) and D’Altri et al. (2018) used CDP to model units but without within-brick interfaces. Different modeling approaches were used for the mortar joints in these works: interface elements based on energy-

based softening laws (Dolatshahi 2012; Lourenço 1996; Lourenço and Rots 1997), and rigid contact-based cohesive surfaces with a user-defined Mohr-Coulomb model (D'Altri et al. 2018). It is worth mentioning that these strategies are not readily available to engineers since they are proprietary to the developers.

Based on the simplified micro modeling approach presented earlier, one FE model is developed for J4D and J5D, which were designed to be identical, and the other FE model is developed for wall J6D. Regarding the DP model used for brick units, the elastic modulus and the Poisson ratio are 16700 MPa and 0.15, respectively. The frictional angle β , dilation angle ψ are determined as 10.0° and 5.0° , respectively (Pina-Henriques and Lourenço 2003; Zucchini and Lourenço 2007). The uniaxial stress strain curves as measured from tests are used, the compressive strengths of units for J4D/J5D and J6D are 10.5 MPa and 11.5 MPa, respectively.

For the between-brick interfaces, elastic stiffness constants (k_{nn} , k_{ss} , and k_{tt}), tensile strength f_t , cohesion c , frictional coefficient μ and residual frictional φ_r are determined directly from experimental results. The non-dimensional parameters (α_n and α_t) are determined so that reasonable failure displacements (δ_n^f and δ_t^f) can be calibrated based on the fracture energies (G_I and G_{II}) reported in the experiment (Raijmakers 1992; Vermeltfoort and Raijmakers 1993). For the within-brick interfaces, elastic stiffness constants (k_{nn} , k_{ss} , and k_{tt}) are assumed with a dummy elastic stiffness (Lourenço 1996), frictional coefficient μ and residual angle φ_r are selected as the same as the between-brick interfaces, and the tensile strength of interface f_t is set to be equal to the tensile strength of units, cohesion c is determined as 1.4 times of tensile strength f_t (Abdulla et al. 2017; Lourenço 1996). Similarly, the failure displacements (δ_n^f and δ_t^f) and non-dimensional

parameters (α_n and α_t) are calibrated following the same way as for the between-brick interfaces. The material properties for interfaces are given in Table 3-2.

Table 3-2. Material properties of interfaces of URM walls under IP loading

		Elastic properties			Nonlinear properties						
					Tension-related			Shear-related			
Wall		k_{nn} (N/mm ³)	k_{ss}, k_{tt} (N/mm ³)	f_t (MPa)	δ_n^f (mm)	α_n	c (MPa)	μ	δ_τ^f (mm)	$\tan \phi_r$	α_τ
Between -brick	J4D/ J5D	82	36	0.25	0.34	4	0.35	0.75	0.93	0.75	1.4
	J6D	110	52	0.16	0.31	4	0.22	0.75	0.5	0.75	1.4
Within -brick	All	10000	10000	2	0.82	4	2.8	0.75	1.2	0.75	1.4

The simulation results obtained from the FE models for walls J4D/J5D and J6D are compared with the corresponding experimental results. Figure 3-7 shows the comparison of the global behavior in terms of the load-displacement curves. It should be noted that walls J4D and J5D, which were designed to be identical, showed a slight difference in the post peak behavior during the tests, primarily due to the heterogeneity of the mortar and brick materials (Dolatshahi 2012). Overall, the FE-predicted load-displacement curves agree well with the experimental results in terms of initial stiffness, peak strength, and post-peak behavior under different pre-compressive stresses.

Figure 3-8 (a) shows the cracking propagation of the URM walls (e.g., J4D) from the FE simulation: starting from horizontal tensile cracking developed at the bottom and top of the wall, respectively (denoted as region A in Figure 3-8 (a)), to stepped cracking along the between-brick interfaces at the center of the wall (denoted as region B in Figure 3-8 (a)), and finally to stepped diagonal cracking along both between-brick and within-brick interfaces (denoted as region C in Figure 3-8 (a)). Figure 3-8 is associated with the four critical stages (A, B, C, and D) indicated in

Figure 3-7. Note that the failure mode of the URM wall obtained by the FE model has a good agreement with the experimental one in terms of diagonal cracks passing through mortar joints and brick units, as highlighted red in Figure 3-8 (a). Additionally, crushing of masonry toes as indicated by the plastic damage in terms of PEEQ (i.e., the equivalent plastic strain) is also well captured, as illustrated in region D in Figure 3-8 (a).

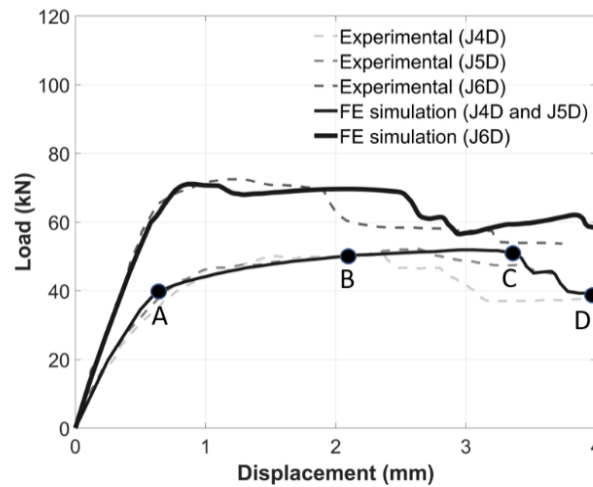


Figure 3-7. Load-displacement curve comparison between FE simulations and experiments for the three URM walls under IP loading

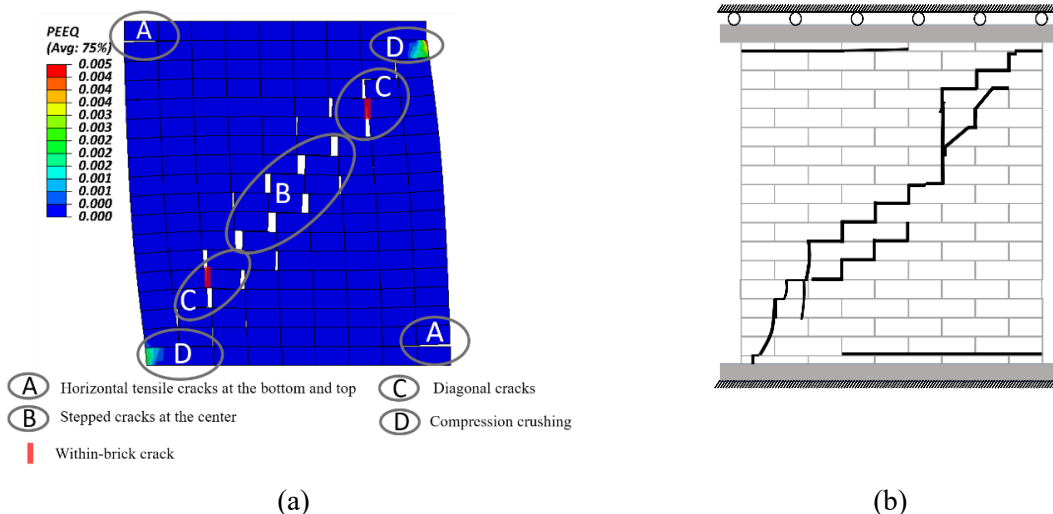


Figure 3-8. Failure crack pattern (J4D): (a) FE simulation, and (b) experiment (Raijmakers 1992; Vermeltoort and Raijmakers 1993)

3.5.3. URM walls under out-of-plane (OOP) loading

The OOP behavior of the three URM walls considered in this chapter was experimentally investigated by Ng (1996). The tested three walls, referred to as Wall 4, Wall 8, and Wall 10 in (Ng 1996), had different aspect ratios and were tested with various boundary conditions under OOP loading. Specifically, Wall 4 had an aspect ratio of 1.0 (i.e., 1140 mm long \times 1140 mm tall), and the other two walls had an aspect ratio of 0.67 (i.e., 795 mm long \times 1140 mm tall). Wall 4 and Wall 10 were simply supported on three sides with top edge and right edge free, respectively, while Wall 8 was simply supported on all four sides.

The three single-wythe walls were built with 112 mm \times 53 mm \times 36 mm brick and 10 mm thick mortar. The walls were modeled using the same strategy as adopted in this chapter. The elastic moduli of brick units and mortar for Wall 8 are 16700 MPa and 2300 MPa, respectively, and the Poisson ratio is 0.15 (D'Altri et al. 2018). The same elastic properties are assumed for Wall 4 and Wall 10. The nonlinear material parameters used for the DP model (i.e., frictional angle β , dilation angle ψ) are the same as defined in the previous section, with the experimentally determined uniaxial compressive strength 36 MPa (Ng 1996). The model parameters for within-brick interfaces are the same as those in the IP model, while the material parameters for between-brick interfaces are summarized in Table 3-3.

To be specific for the between-brick interfaces, the stiffness constants (k_{nn} , k_{ss} , and k_{tt}) are determined based on Eq. (3-3) and Eq. (3-4). The tensile strength of between-brick interfaces f_t is determined as one-third of the flexural tensile strength along the weak axis (Lourenço 2000b; Milani et al. 2006), and cohesion $c = 1.4 f_t$ (Abdulla et al. 2017; Lourenço 1996). The frictional coefficient μ and residual friction angle ϕ_r are both 0.58 and 30.1° ($\tan\phi_r = 0.58$), respectively

(Macorini and Izzuddin 2011). The additional parameters, failure displacements (δ_n^f and δ_τ^f) and non-dimension parameters (α_n and α_τ), are calibrated following the same procedure mentioned earlier in the IP model.

Table 3-3. Material properties of interfaces of URM walls under OOP loading

Wall	Elastic properties		Nonlinear properties							
	k_{nn} (N/mm ³)	k_{ss}, k_{tt} (N/mm ³)	Tension-related			Shear-related				
			f_t (MPa)	δ_n^f (mm)	α_n	c (MPa)	μ	δ_τ^f (mm)	$\tan \phi_r$	α_τ
Wall 4			0.25	0.31	4	0.35	0.58	0.91	0.58	1.4
Wall 8	266	116	0.3	0.31	4	0.42	0.58	0.91	0.58	1.4
Wall 10			0.37	0.31	4	0.52	0.58	0.91	0.58	1.4

The FE models developed above are used to simulate the OOP behaviors of URM walls. The comparisons of load-displacement curves are shown in Figure 3-9. Note that OOP displacements were measured at the locations with maximum bending moment, e.g., the midpoint of the top free edge for Wall 4, the central point of the surface for Wall 8, and the midpoint of the right free edge for Wall 10. The deflections were measured up to about 80% - 90% of the failure pressure for Wall 8 and Wall 4 and 65% for Wall 10 due to deflection gauge damage (Ng 1996). The comparison of the load-displacement curves shows that the FE models developed predicted well about the OOP behavior of URM walls, and the comparison of the maximum pressure obtained by the FE simulations (i.e., 8.50 KPa, 26.69 KPa, 11.66 KPa for Wall 4, Wall 8, and Wall 10, respectively) and experimental results (i.e., 8.54 KPa, 25.00 KPa, 12.20 KPa for Wall 4, Wall 8, and Wall 10, respectively) further confirms this conclusion.

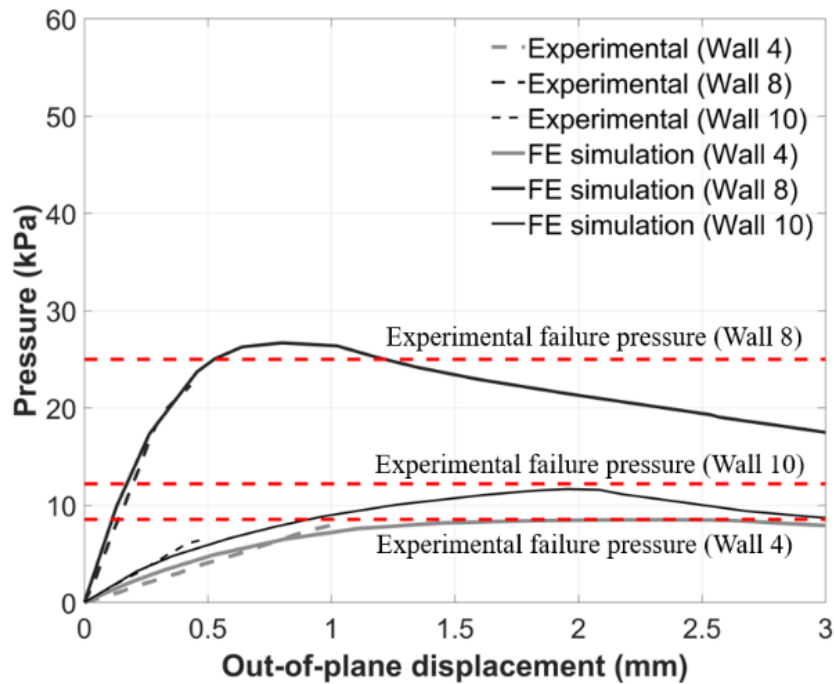


Figure 3-9. Comparison of load-displacement curves of URM walls under OOP loading

Figure 3-10 to Figure 3-11 show the comparison of FE simulations and experimental tests in terms of the OOP displacement distribution along the height and length directions of the tested walls at a certain load level. Figure 3-10 shows that the simulation results of Wall 8 are in excellent agreement with the experimental results, while slight and moderate difference are observed, respectively, for Wall 4 and Wall 10, as shown in Figure 3-10 and Figure 3-11, respectively. This can be attributed to lack of experimental data on the elastic parameters for units in Wall 4 and Wall 10 and the possible non-uniformly distributed pressure loading applied through the airbag in the experiment.

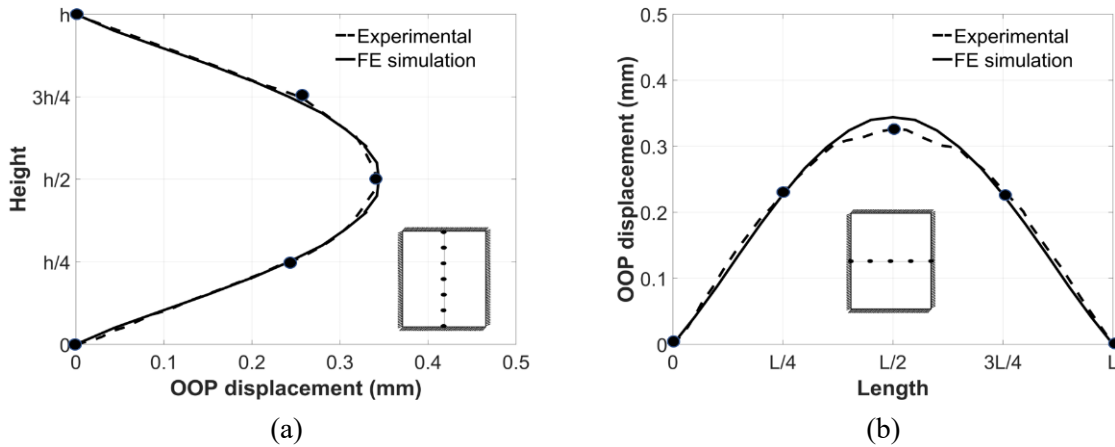


Figure 3-10. OOP displacement distribution for Wall 8 at 20 kPa: (a) vertical center line, and (b) horizontal center line

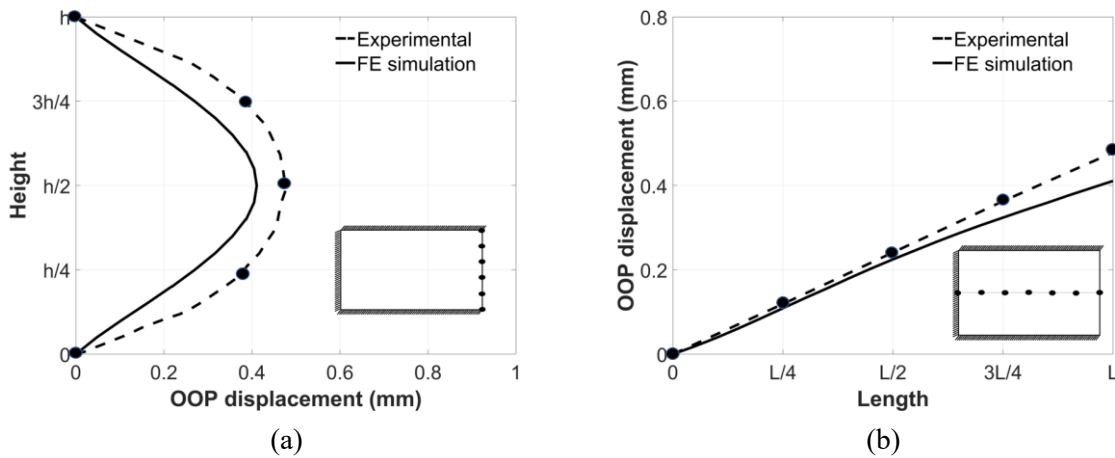


Figure 3-11. OOP displacement distribution for Wall 10 at 5 kPa: (a) free right edge, and (b) horizontal center line

The crack patterns obtained by the proposed models are also compared with the experimental results, as shown in Figure 3-12. Reasonably good agreements can be observed for these walls. Specifically, the FE simulations for Wall 4 and Wall 10, which have three edges simply supported and one edge free, reveal that the crack initiates at the mid-span of the free edge. With the increase of load pressure, the crack propagates vertically downwards (e.g., Wall 4) or horizontally leftwards (e.g., Wall 10) until reaching the center of the wall panel and then bifurcates

diagonally to the bottom corners (Figure 3-12 (a)) or left corners (Figure 3-12 (c)). The collapse mechanisms of Wall 4 and Wall 10 are both characterized by Y-shaped cracking. For Wall 4, the FE simulation results correlate well with the experimental observations except for the right branch of the diagonal crack in the experiment shown in Figure 3-12 (d). For Wall 10, its FE simulation fails to capture the cracking pattern observed in the experiment, which can be attributed to boundary effects, i.e., the OOP displacement was not strictly constrained at the left side illustrated Figure 3-12 (f). The FE model for Wall 8 predicts crack initiation in the center of the wall panel and further development vertically (Figure 3-12 (b)). The wall failure predicted features a symmetrical crack pattern (X-shaped), i.e., several vertical cracks with four diagonal cracking branches, while in the test, only two diagonal cracking branches at the bottom of the wall were observed.

Note that the models presented in this chapter did not capture the failure pattern accurately. To be specific, the vertical failure lines were not exactly captured by the FE models. This is due to the lack of information on the tensile strength parameter for the within-brick interfaces. Thus, a more representative value of 2.0 MPa for the tensile strength of units from (Lourenço 1996) was adopted in this chapter for the URM walls under OOP loading. It is worth mentioning that this parameter value was not tuned to have a perfect match with the tests to achieve the vertical failure line, e.g., by using an extremely low value, e.g., 1.0 MPa (2.8% of the compressive strength of the brick unit). More importantly, it was found that the models with different tensile strength parameter values (e.g., between 1.0 MPa and 2.5 MPa) predicted the load-carrying capacities reasonably well, i.e., close to the experimental result (25.0 kPa) with a maximum difference of 7.0%. Furthermore, the crack propagation path highly depends on the spatial variation of materials

(Ng 1996) and the boundary conditions. For example, the uncertainty in the boundary conditions in the experiments, such as insufficient constraints on the OOP displacements at the boundaries, can affect the crack propagation path and thus the crack pattern (e.g., walls failed with “rigid” zones bounded by horizontal crack paths). This could explain why no analytical studies, to the knowledge of the authors, were capable of predicting the accurate crack patterns, especially for Wall 8 and Wall 10 (D’Altri et al. 2018; Macorini and Izzuddin 2011; Milani and Taliercio 2016). As an alternative to showing the validity of the FE models, the crack patterns predicted by the yield line theory are included for numerical-theoretical comparison. It is observed that the idealized crack patterns predicted by the yield line theory are consistent with the FE predicted OOP deformation fields, characterized by three or four “quasi-rigid” zones.

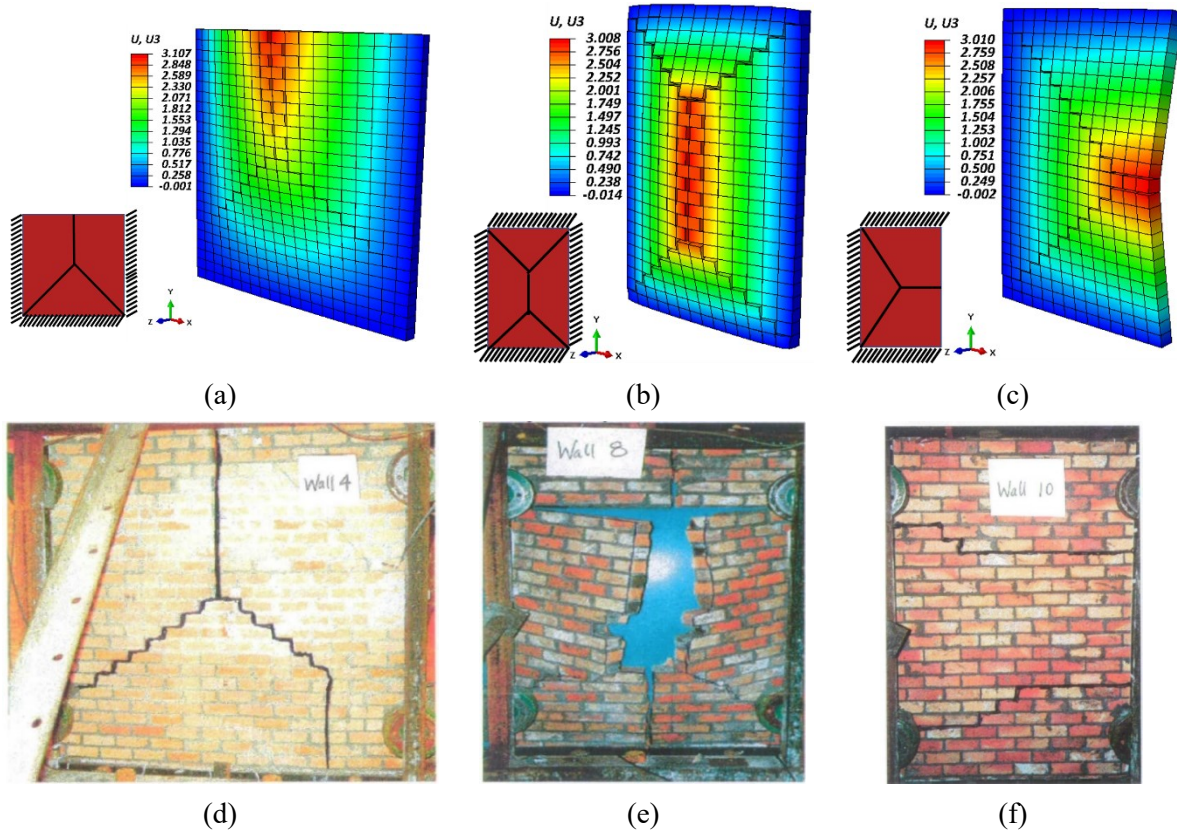


Figure 3-12. Crack pattern comparison: (a) (b) (c) FE simulations for Wall 4, Wall 8 and Wall 10, and (d) (e) (f) experimental studies for Wall 4, Wall 8, and Wall 10 (Ng 1996)

Based on the presented results, the FE modeling strategy used in this chapter shows to be a valid approach for small and large-scale specimens, and more importantly, for URM walls under both IP and OOP loadings. In the next section, a parametric study will be conducted to investigate the importance of different material parameters (i.e., unit and interface parameters) on the IP and OOP behavior of URM walls, respectively.

3.6. FINITE ELEMENT-BASED PARAMETRIC STUDY

In order to identify the relative importance of material parameters for IP and OOP behavior of URM walls, the FE models developed for wall J4D under IP loading and Wall 8 under OOP loading are used to conduct a parametric analysis, respectively, with a focus on the load-

displacement behavior and failure modes (e.g., crack pattern). Note that the failure modes will only be emphasized in this section if they are different from those presented earlier.

Based on the FE models developed, one-at-a-time sensitivity analysis is performed in this section. The studied parameters are unit-related model parameters and interface-related model parameters. Specifically, they are the elastic modulus E , dilation angle ψ , frictional angle β , compressive strength f_c of masonry units, and the tensile strength f_t , cohesion c , frictional coefficient μ , tensile and shear failure displacements (δ_n^f and δ_r^f) of interfaces. The parameter values are varied within reasonable ranges for their use in URM walls.

The FE simulation results in the preceding section indicate that although some cracks went through within-brick interfaces, the failure modes depend largely on the damage of the between-brick interface damage (Figure 3-8 and Figure 3-12). The fact that mortar joints always act as planes of weakness in URM structures has also been confirmed in (Dolatshahi 2012; Lourenço 1996). As a result, the between-brick, instead of the within-brick, interface parameters are considered in the parametric study.

3.6.1. Masonry unit-related model parameters

Figure 3-13 (a) and Figure 3-13 (b) show the load-displacement curves for the URM walls under IP and OOP loadings, respectively, with different values for the elastic modulus E of masonry units. It is observed that the initial stiffness and the load capacity of the wall increase with the increase of E , especially for the OOP case. The URM walls under OOP loading with different elastic moduli E all fail with the same X-shaped crack pattern, as shown in Figure 3-12 (b). However, the URM wall under IP loading with a low elastic modulus (i.e., $E = 5000$ MPa) for the

units fails with shear sliding of mortar joints at the bottom, which is associated with point A in Figure 3-13 (a). Note that shear sliding mode is in contrast to the failure with a diagonal crack pattern (i.e., Figure 3-8 (b)). The main reason is that the low stiffness of URM wall would promote the development of the flexural cracks located at the corner, which resultantly reduces the resistance capacity along the bed joints of URM walls. Note that shear sliding failure is another typical failure mode (Calderini et al. 2009; Haider 2007) for URM walls under IP loading. In this context, the URM wall behaves in a more brittle manner, and the IP capacity decreases rapidly to zero, as shown in Figure 3-13 (a).

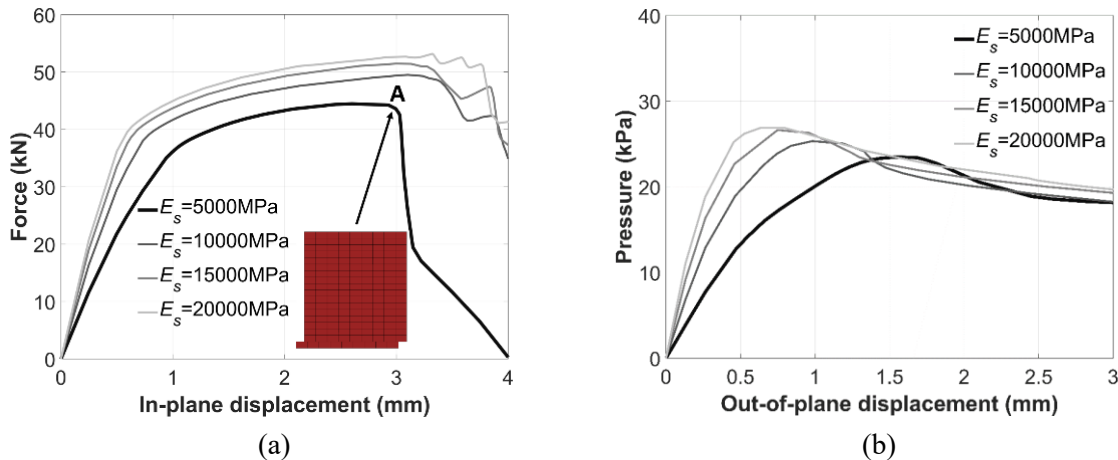


Figure 3-13. Effects of elastic modulus E on the: (a) IP load-deformation behaviors, and (b) OOP load-deformation behaviors

The effects of the compressive strength of masonry units are illustrated in Figure 3-14 (a). It can be seen that it has limited influence on the load-displacement curves. For the IP case, the crushing of compression toes was observed (Raijmakers 1992; Vermeltfoort and Raijmakers 1993). However, the crushing zones are only restricted to a small region shown in Figure 3-8 (a). As a result, although compressive crushing failure is necessary to form a collapse mechanism (i.e., diagonal crack and toe crushing) for the URM wall considered, the effects of compressive strength

are not significant in the global load-displacement relationship of URM walls under IP loading. For the OOP case, the URM wall behavior is barely affected by the compressive strength of the masonry units. However, it should be noted that URM walls bounded by relatively rigid structural elements, such as reinforced concrete and steel frame members, may form a compressive strut arching mechanism under OOP loading, generally resulting in an increase of the OOP strength (Liberatore et al. 2020; Walsh et al. 2018). For the URM with timber diaphragms or insufficient boundary constraints (e.g., simply supported boundary, roller condition), the compressive arching effects have little influence on the OOP capacity, such as the Wall 8 in the current parametric study.

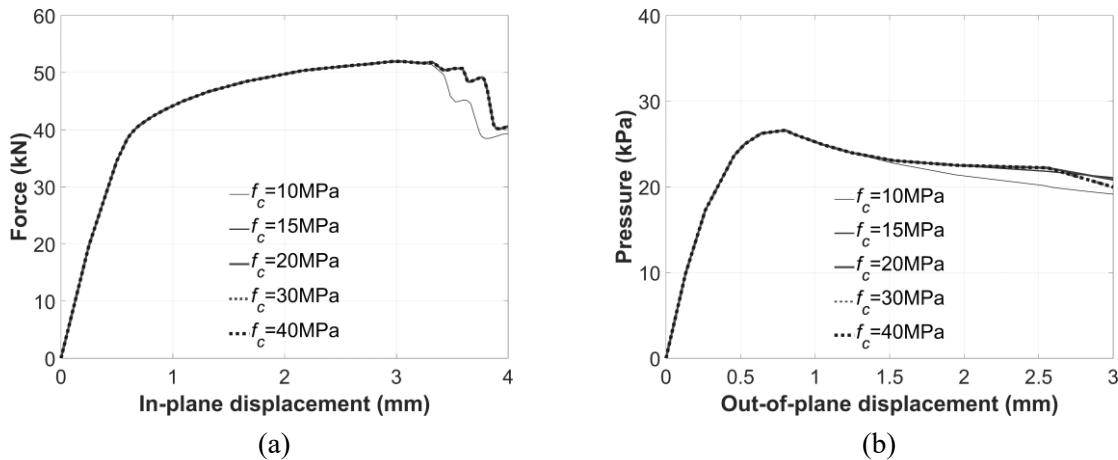


Figure 3-14. Effects of compressive strength f_c on the: (a) IP load-deformation behaviors, and (b) OOP load-deformation behaviors

The effects of the nonlinear material parameters (i.e., the dilation angle ψ and friction angle β) of the masonry units are also examined. Figure 3-15 and Figure 3-16 show the corresponding load-displacement curves for the URM walls under IP and OOP loadings. It can be observed that the two nonlinear material model parameters have a negligible effect on the URM wall behavior.

Only some slight differences can be found in the post-peak behavior for the OOP behavior of URM walls with the variation of frictional angle β .

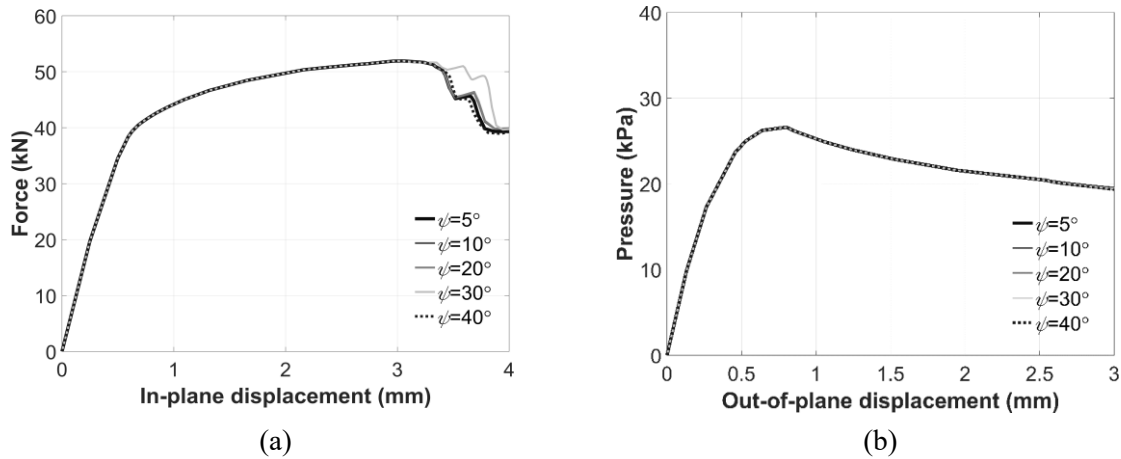


Figure 3-15. Effects of dilation angle ψ on the: (a) IP load-deformation behaviors, and (b) OOP load-deformation behaviors

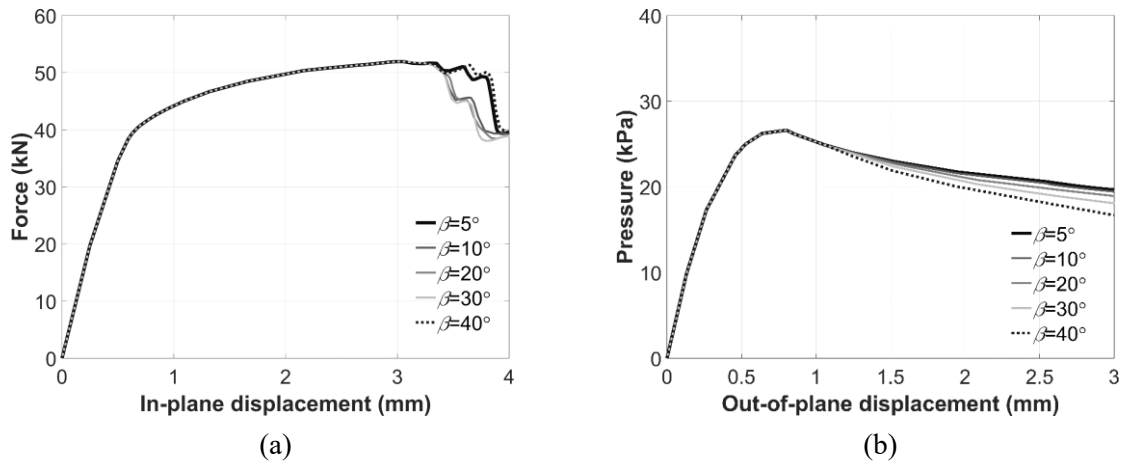


Figure 3-16. Effects of frictional angle β on the: (a) IP load-deformation behaviors, and (b) OOP load-deformation behaviors

3.6.2. Mortar interface-related model parameters

The material model parameters of interfaces can be categorized into: (1) tension-related parameters (i.e., tensile strength f_t , tensile failure displacement δ_n^f) and (2) shear-related parameters (i.e.,

cohesion c , frictional coefficient μ , shear failure displacement δ_r^f). The failure displacements are calibrated according to fracture energies, as mentioned earlier and thus various failure displacements considered in the parametric study are physically related to fracture energies as shown later.

Figure 3-17 and Figure 3-18 present the effects of two tension-related parameters on load-displacement curves for URM walls under IP and OOP loadings. It is observed that tension-related parameters have a great influence on the OOP behavior (Figure 3-17 (b) and Figure 3-18 (b)) than on the IP behavior of URM walls (Figure 3-17 (a) and Figure 3-18 (a)). Higher tensile strength and larger tensile failure displacement (larger fracture energies) increase the OOP capacities of URM walls. On the contrary, results indicate that tension-related parameters have little effect on the IP behavior of URM walls. This shows that the tensile properties are significant for a reliable prediction of the OOP behavior.

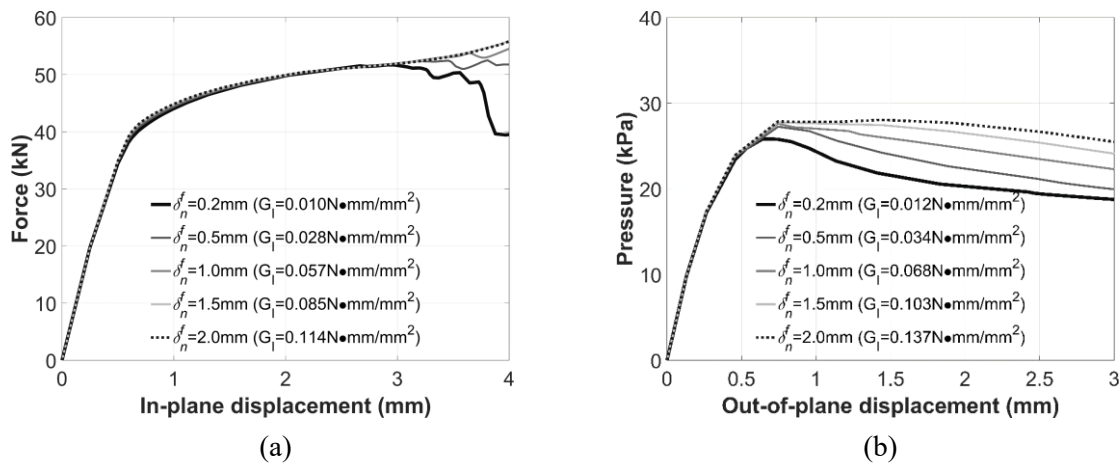


Figure 3-17. Effects of tensile failure displacements δ_n^f on the: (a) IP load-deformation behaviors, and (b) OOP load-deformation behaviors

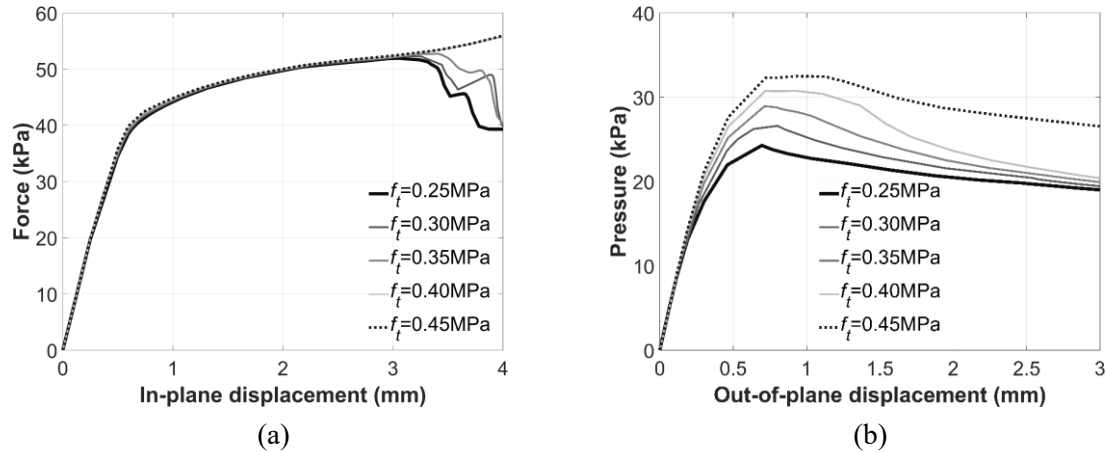


Figure 3-18. Effects of tensile strength f_t on the: (a) IP load-deformation behaviors, and (b) OOP load-deformation behaviors

Figure 3-19 to Figure 3-21 show the effects of three shear-related parameters on load-displacement curves for URM walls under IP and OOP loadings. The results show that shear-related parameters affect both the IP and OOP behaviors of URM walls, but they have a greater influence on the IP behavior. Specifically, the higher shear failure displacement (or model II fracture energy), the larger cohesion, and the higher frictional coefficient lead to higher strength and ductility for URM walls under IP loading. In particular, the ductility of URM walls under IP loading reduces significantly with lower shear failure displacements (or mode II fracture energies), e.g., $\delta_r^f = 0.2\text{mm}$ and $\delta_r^f = 0.5\text{mm}$, and lower frictional coefficient, e.g., $\mu = 0.5$. As shown in Figure 3-19 (a) and Figure 3-21 (a), sudden drops in lateral loads are observed for these cases, which are related to a different failure mode, namely shear sliding along horizontal mortar joints (Figure 3-13 (a)). It is worth mentioning that the shear sliding of mortar joints does not necessarily occur at the bottom mortar interface. Regarding the OOP behavior, the peak strength increases with stronger cohesion of interfaces, while the other two parameters (shear failure displacement and frictional coefficient) barely influence the peak strength of URM walls. The post-peak

behavior is highly sensitive to the shear failure displacement: the higher value will yield greater ductility, as shown in Figure 3-19 (b), and insensitive to the frictional coefficient, as shown in Figure 3-21 (b).

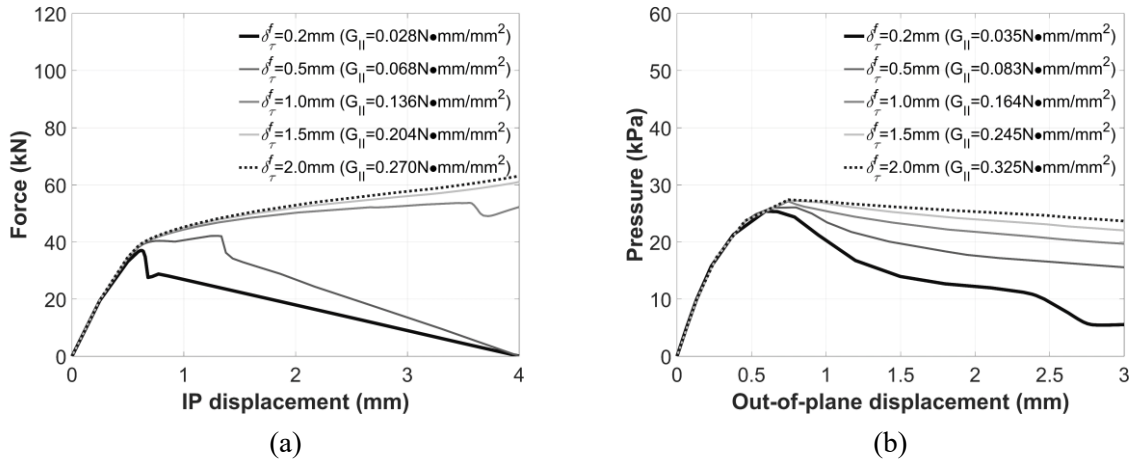


Figure 3-19. Effects of shear failure displacement δ_{τ}^f on the: (a) IP load-deformation behaviors, and (b) OOP load-deformation behaviors

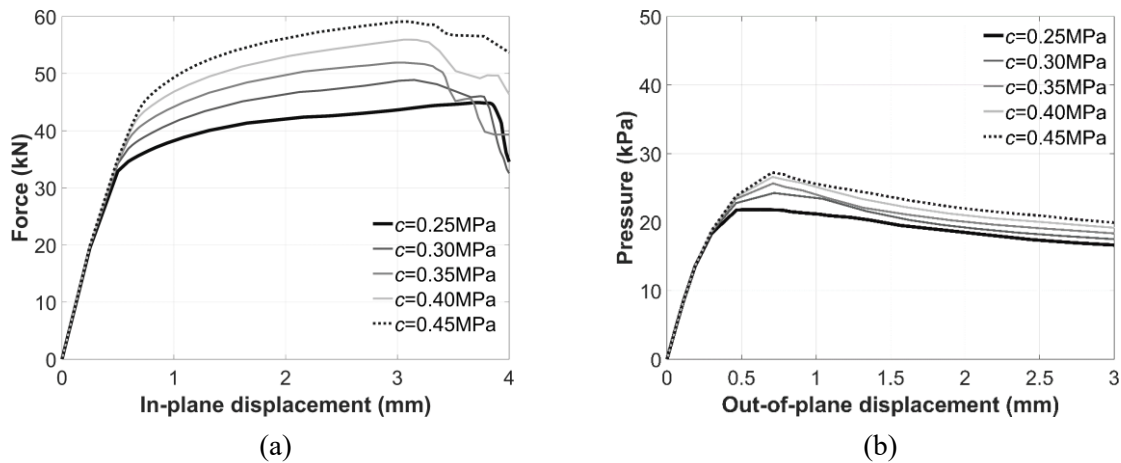


Figure 3-20. Effects of cohesion c on the: (a) IP load-deformation behaviors, and (b) OOP load-deformation behaviors

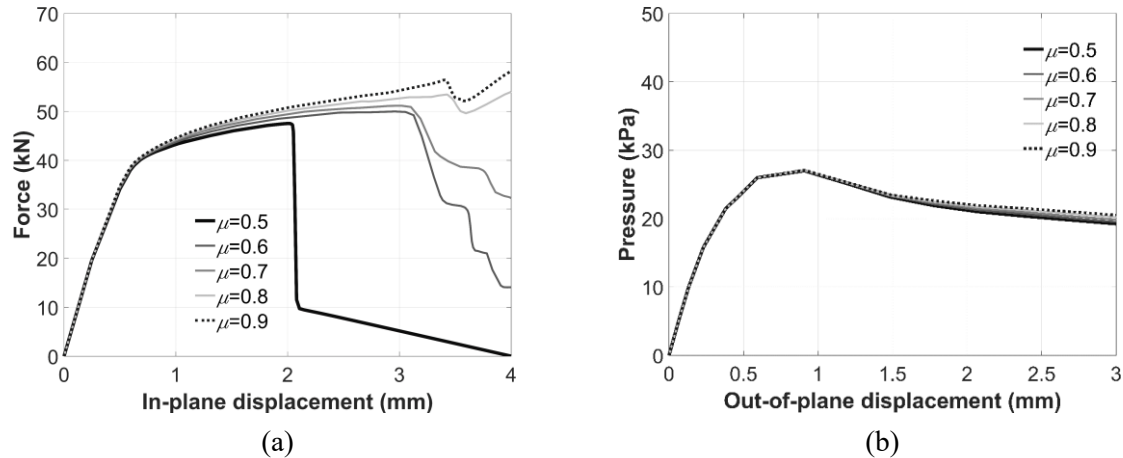


Figure 3-21. Effects of frictional coefficient μ on the: (a) IP load-deformation behaviors, and (b) OOP load-deformation behaviors

3.7. CHAPTER CONCLUSIONS

A finite element model using 3D continuum elements and contact-based cohesive surfaces was presented for unreinforced masonry (URM) walls in this chapter, taking advantage of readily available modeling techniques in ABAQUS (Dassault Systemes 2017). Numerical-experimental comparisons were conducted in terms of load-displacement curves and failure crack patterns. Reasonable agreement was achieved in terms of initial stiffness, in-plane (IP) /out-of-plane (OOP) capacity, post-peak behavior, as well as the crack pattern. This allows a unified approach to model the masonry walls under IP and OOP loading and boundary conditions.

A parametric study was subsequently conducted to investigate the influence of material parameters on URM wall behavior. For material parameters of units, elastic modulus has a considerable influence on the initial stiffness and the wall strength, other parameters such as compressive strength, dilation angle, and frictional angle have negligible effects on the URM wall behavior. Regarding the material parameters of mortar joint interfaces, the tension-related parameters have a greater influence on OOP behavior in terms of peak load and ductility, while

both shear- and tension-related interface parameters affect the IP behavior of masonry walls. Different failure modes (i.e., diagonal cracking, shear sliding) are captured, and under shear sliding failure, the URM wall behaves in a more brittle manner. Such information on the relative importance of the micro model parameters is valuable to both experimental and numerical studies of masonry walls under complex loadings.

Chapter 4. DEVELOPMENT OF A PLASTICITY-BASED 3D MULTI-YIELD SURFACES CONSTITUTIVE MODEL FOR MASONRY MORTAR JOINTS UNDER MONOTONIC LOADING

This chapter presents a new 3D multi-yield surfaces constitutive model for masonry mortar joints, which can be used with interface elements for finite element (FE) modeling of masonry structures to capture various failure mechanisms. This model is featured with (1) two hyperbolic yield surfaces capable of capturing various failure modes of mortar joints, including tensile cracking, shear sliding, and compressive crushing; (2) an unassociated flow rule to capture the ‘dilatancy’ phenomenon in the mortar joints; and (3) the dilatancy softening and variation of mode II fracture energy under different normal stress levels. An implicit Euler backward integration algorithm, combined with a local-global Newton-Raphson (NR) solver, is adopted to achieve the predictor-corrector return mapping in the numerical formulation. The error-based auto-adaptive sub-stepping algorithm is employed to achieve robustness and efficiency in the integration procedure. The developed model is implemented in the general-purpose FE software ABAQUS, with the specialized capability of modeling masonry structures. The developed model is validated through three unit-mortar-unit assemblages and three unreinforced masonry (URM) walls under in-plane (IP) loading or out-of-plane (OOP) loading. The importance of appropriate modeling of dilatancy in simulating the IP and OOP behavior of URM walls is highlighted. The validation results show that the developed constitutive model is capable of modeling masonry structures at various scales with improved accuracy by considering dilatancy softening.

4.1. INTRODUCTION

Masonry structures are commonly used in historical and modern building construction, with attractive aesthetics arising from the periodic arrangement of masonry units (e.g., bricks, concrete blocks) and mortar joints. Under extreme loadings, extensive cracking and other damage can occur between units and within mortar layers (Khansefid et al. 2022). The structural behavior and failure of masonry structures under in-plane (IP) and/or out-of-plane (OOP) loadings highly depend on the mechanical properties of the masonry constituents (e.g., unit, mortar) and their interactions. As such, one of the leading challenges in computational mechanics for predicting masonry structural behavior lies in the appropriate treatment of the interaction between masonry units through mortar layers.

Depending on the desired simulation accuracy and expected detail of the mechanical behavior, different modeling approaches have been developed and used for computational simulation of masonry structures in the literature, e.g., limit analysis (LA) approaches (Gilbert et al. 2006; Livesley 1992; Portioli and Cascini 2016), discrete element model (DEM)-based approaches (Pantò et al. 2021; Savalle et al. 2022), finite element (FE) approaches. A comprehensive review of the formulation and application of these approaches can be found in (Ghiassi and Milani 2019). LA and DEM-based approaches assume rigid blocks connected with contacts/interfaces to represent the non-linear behaviors of mortar joints, which have been proven to be efficient in predicting the structural behavior of masonry. In the recent decade, FE approaches have received more attention in masonry simulation. FE-based approaches can be broadly categorized into macro modeling, simplified micro modeling, and detailed micro modeling (Lourenço 1996). In these approaches, different strategies are taken to address the masonry joints.

Specifically, macro modeling treats masonry as a homogeneous material with the smeared properties of unit-mortar composites without explicitly modeling the interactions between masonry units. In contrast, detailed micro models represent masonry units and mortar layers explicitly using continuum elements and consider two unit-mortar interfaces. Compared to macro models that are oversimplified with less accuracy, detailed micro models are more accurate but computationally prohibitive. To achieve a balance between computation efficiency and modeling capability, simplified micro models were introduced by Page (1978) by making use of the concept of zero-thickness interface elements, representing the compounded behavior of mortar layers and unit-mortar contacts. Although Poisson's effect of mortar is neglected in the simplified micro modeling strategy, it is proven to be capable of predicting the structural behavior of masonry at a high level of accuracy, which is widely used in the masonry community (Abdulla et al. 2017; Citto 2008; Dolatshahi and Aref 2011; Giambanco et al. 2001; Kumar et al. 2014; Kumar and Barbato 2019; Lotfi and Shing 1994; Lourenço 1996; Lourenço and Rots 1997; Nazir and Dhanasekar 2014; da Porto et al. 2010; Zeng et al. 2021).

In the simplified micro modeling approach, units are modeled with size expansion to maintain the overall geometry of masonry structures, and the discontinuity between expanded masonry units is then represented by interface elements. The capability of the simplified micro modeling approach to simulate the structural behavior of masonry structures relies heavily on the accuracy of the interface elements.

Large efforts have been devoted to developing interface models to consider different failure modes (e.g., tensile cracking, shear sliding, and/or compressive crushing), and a comprehensive review can be found in (Shadlou et al. 2020). In general, there exist mainly three groups of interface

elements: the first group assuming zero tensile strength and shear sliding based on Coulomb's law (Lemos 2017; Yavartanoo and Kang 2022), second group considering tension cracking and shear sliding with shear-compression hardening (Abdulla et al. 2017; Giambanco et al. 2001; Giambanco and Di Gati 1997; Koutromanos and Shing 2012; Lotfi and Shing 1994; Stankowski et al. 1993b; a; Zeng et al. 2021; Zhai et al. 2017), and the third group considering compression crushing failure in addition to the two aforementioned failure modes (Aref and Dolatshahi 2013; Citto 2008; Dolatshahi and Aref 2011; Kumar et al. 2014; Kumar and Barbato 2019; Lourenço 1996; Lourenço and Rots 1997; Macorini and Izzuddin 2011; Nazir and Dhanasekar 2014; Oliveira and Lourenço 2004; da Porto et al. 2010; van Zijl 2004). The first group of interface elements is mainly applicable to dry-stack masonry structures (i.e., the bonding effects of mortar play a limited role (Casapulla and Portioli 2016; Elvin and Uzoegbo 2011; Martínez and Atamturktur 2019)). For the scenario in which the mortar layer provides a certain bonding strength, all possible failure modes should be considered in the constitutive material model for interfaces. For example, Lourenço (Lourenço 1996) made an early attempt to develop a multi-yield surfaces model to consider all three failure modes/criteria, which has later been extensively used and refined by other researchers, e.g., see (Dolatshahi and Aref 2011; Giambanco and Di Gati 1997; Nazir and Dhanasekar 2014; van Zijl 2004). However, a well-known singularity issue in plasticity-based constitutive models exists due to non-smooth corners at the intersection of different yield surfaces. In order to overcome this potential issue in the numerical integration process, other researchers proposed a single yield surface failure criterion (Citto 2008; Kumar et al. 2014, 2015). In spite of the mathematical beauty introduced by defining a single yield surface, it suffers from a lack of clear physical interpretation of tension-shear failure, which represents a unit-mortar interfacial phenomenon (e.g., tensile

cracking, shear sliding), and the compression cap, which represents a masonry or mortar crushing failure mode. Accordingly, to describe different softening and hardening behaviors in the tension and compression conditions, the single yield surface model usually results in quite lengthy yield function expressions, with some non-physical parameters hard to be determined. Note that it is more acceptable to use a single yield function to represent the tension-shear failure mode, e.g., hyperbolic (Kumar and Barbato 2019; Lotfi and Shing 1994; Macorini and Izzuddin 2011), elliptical (Nazir and Dhanasekar 2014), parabolic (Stankowski et al. 1993b; a) yield surfaces.

Among the aforementioned constitutive models for interface elements, a majority of them were implemented in the two-dimensional (2D) stress space (Citto 2008; Dolatshahi and Aref 2011; Giambanco et al. 2001; Giambanco and Di Gati 1997; Kumar et al. 2014; Kumar and Barbato 2019; Lotfi and Shing 1994; Lourenço 1996; Lourenço and Rots 1997; Nazir and Dhanasekar 2014; Oliveira and Lourenço 2004; da Porto et al. 2010; Stankowski et al. 1993a; b; Zeng et al. 2021; van Zijl 2004) for masonry walls under IP loading conditions. Thus, they are not applicable to three-dimensional (3D) FE modeling of masonry walls under complex loading and boundary conditions. In such scenarios when investigating the wall behavior under OOP loading, or combined OOP and IP loading, 3D constitutive models for interface elements are required. In view of this research need, a few 3D interface models have been successfully developed in public literature (Aref and Dolatshahi 2013; Macorini and Izzuddin 2011), but each of them has its own limitations. Specifically, in Macorini's model (Macorini and Izzuddin 2011), two yield surfaces are employed to account for all the possible failure modes, including compression failure. However, Kumar and Barbato (2019) showed that the work softening hypothesis negatively influences the accuracy of the simulation results compared with the results obtained by a strain

softening/hardening hypothesis. Aref and Dolatshahi (2013) proposed a 3D cyclic meso-scale interface model in an explicit integration framework in which a small loading increment is required to improve numerical accuracy.

Compared with the consideration of various failure modes in the constitutive models of interface elements for masonry joints, there is an important phenomenon that has attracted less attention. The micromechanical behavior of the mortar layer and the two mortar-unit interfaces has inherent dilatancy (Andreotti et al. 2019), as a result of a crack surface that is not perfectly smooth. The mortar joint specimen will deform with an uplift under compression and shear loading, thus leading to a volume increase. As evidenced by the experimental results (Andreotti et al. 2019; Jafari et al. 2020; Pluijm 1999), the dilatancy effects are evident under lower compression, and will diminish with the increase of normal compressive stress and plastic shear displacement. An inappropriate description of dilatancy can produce an increase in normal stress, resulting in a considerable overestimate of shear capacity for pressure-dependent materials or specimens. Most current studies assumed the constant dilatancy angle (Lourenço 1996; Lourenço and Rots 1997; Oliveira and Lourenço 2004; da Porto et al. 2010; Stankowski et al. 1993b; a) in a simplified manner, which would result in an inaccurate estimation of shear capacity. Although some researchers considered the variation of dilation angle, the dependence of compressive stress (Koutromanos and Shing 2012; Kumar and Barbato 2019; Macorini and Izzuddin 2011; Zhai et al. 2017) or plastic shear displacement (Citto 2008) on the dilatancy effects was neglected. Few 2D interface models (Lotfi and Shing 1994; van Zijl 2004) formulated the decreased dilatancy angle with the increase of compressive stress and plastic shear displacement. These 2D models, however, failed to address the OOP behavior prediction of masonry walls as mentioned earlier. Meanwhile,

although the diminishment of dilatancy is observed at large shear sliding due to the wear and damage to the asperities along the unit-mortar interface, the dilatancy becomes stable at a non-zero value based on some experimental evidences (Andreotti et al. 2019; Jafari et al. 2020), which is not taken into account in current models. In addition, previous interface models have not dealt with the dependence of mode II fracture energy (i.e., the energy required to create a unit area of a shear crack) on the compressive stress. It is observed that the higher compressive stress would improve the ductility and energy dissipation capacity (Pluijm 1999), inducing a mode II fracture energy, which should also be considered in the constitutive material model formulation.

This chapter proposes a newly developed plasticity-based 3D constitutive material model for interface elements used in FE simulation of masonry structures considering dilation. The dilatancy softening and variation of mode II fracture energy are incorporated into the proposed model. Three failure modes (i.e., tensile cracking, shear sliding, compressive crushing) are all considered using two hyperbolic yield surfaces: one for compression and one for shear-tension. The proposed model is implemented in the commercial software ABAQUS (Dassault Systemes 2017) via the user subroutine UMAT. A fully implicit Euler Backward integration algorithm, combined with a local-global Newton-Raphson (NR) solver, is adopted to achieve the predictor-corrector return mapping procedure in the numerical formulation. The error-based auto-adaptive sub-stepping algorithm is used to enhance accuracy, robustness, and efficiency. After the description of the theoretical formulation and numerical implementation, the developed model is validated against tested unit-mortar-unit assemblages and three unreinforced masonry (URM) walls under IP and OOP loading, respectively, with a highlight on the effect of dilatancy on the behavior of URM walls.

4.2. CONSTITUTIVE MODEL FORMULATION

The elastic regime for the proposed interface model is characterized based on the traction-separation relationship. Specifically, three stiffness constants k_{nn} , k_{ss} , and k_{tt} are used respectively to relate the three stress components (i.e., σ_n , τ_s , τ_t) and three corresponding displacement separations (i.e., u_n , u_s , u_t). Note that subscripts n , s , and t denote normal and two tangential directions of the interface, respectively. Negative values of σ_n indicate the interface element is under compressive while positive values correspond to the tensile stress states. The elastic behavior can be written in the matrix form shown in Eq. (4-1):

$$\begin{bmatrix} \sigma_n \\ \tau_s \\ \tau_t \end{bmatrix} = \begin{bmatrix} k_{nn} & & \\ & k_{ss} & \\ & & k_{tt} \end{bmatrix} \begin{bmatrix} u_n \\ u_s \\ u_t \end{bmatrix} = \mathbf{K}\mathbf{u} \quad (4-1)$$

where \mathbf{K} and \mathbf{u} represent the initial stiffness matrix and the relative displacement vector. The stiffness constants are determined experimentally as the slopes of pre-peak branches in traction-separation curves obtained from experiments tests. The plastic regime is elaborated as follows in this section.

4.2.1. Multi-yield surfaces plastic criterion

The proposed multi-yield surface criterion consists of two hyperbolic surfaces: tension-shear failure surface f_1 and compression cap f_2 . The tension-shear failure surface f_1 is inspired by Ignacio Carol's model (Carol et al. 1997), which was used to describe the concrete fracture at the meso-scale. Compared with the Mohr-Coulomb and tension cut-off yield surfaces commonly used in the masonry interface model (Lourenço 1996), this continuous and differentiable hyperbolic yield surface provides a smooth transition between the Mohr-Coulomb surface and tension cut-off

surface, which can overcome the computational singularity in the non-smooth corner of tension-shear failure region. Later, Carol's model (Carol et al. 1997) was improved by introducing a hyperbolic cap to describe the compressive crushing failure mode (Macorini and Izzuddin 2011). However, two yield functions in (Macorini and Izzuddin 2011) are quadratic and thus have two branches, only one of which has actual physical meaning. This may cause the misidentification of yield surfaces in the numerical integration process, especially when the elastic stiffness constants are relatively large, resulting in the trial stress state being far away from the correct yield surfaces. Therefore, in the proposed interface model, two yield criteria are adjusted to Eq. (4-2) and Eq. (4-3), respectively, such that each of them has only one correct branch considered in both failure regions:

$$f_1(\sigma_n, \tau_s, \tau_t) = -(c - \sigma_n \tan \varphi) + \sqrt{\tau_s^2 + \tau_t^2 + (c - \sigma_n \tan \varphi)^2} \quad (4-2)$$

$$f_2(\sigma_n, \tau_s, \tau_t) = -(f_c + \sigma_n \tan \theta) + \sqrt{\tau_s^2 + \tau_t^2 + (f_c - \sigma_n \tan \theta)^2} \quad (4-3)$$

where c , σ_t , and $\tan \varphi$ denote the cohesion, the tensile yield stress, and the frictional coefficient, respectively; σ_c is the compressive yield stress, f_c is the compressive strength; $\tan \theta$ is the asymptote slope of compressive cap surface.

The yield surface plot in the 3D space is schematically shown in Figure 4-1.

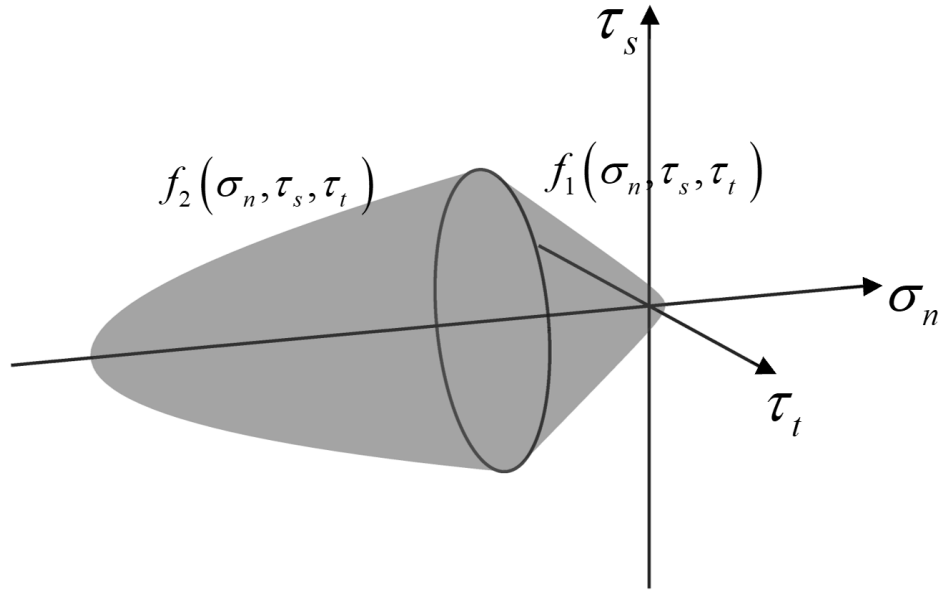


Figure 4-1. Schematic view of yield surfaces of proposed constitutive material model

4.2.2. Flow rule

The associated flow rule is assumed for the compression cap yield surface f_2 , i.e., plastic potential $g_2 = f_2$, while non-associated flow rule is used for the yield surface f_1 to consider shear dilatancy in the masonry mortar interface, i.e., plastic potential $g_1 \neq f_1$. A similar but different function from the yield function f_1 is assumed for the plastic potential g_1 as per Eq. (4-4):

$$g_1(\sigma_n, \tau_s, \tau_t) = -(c_q - \sigma_n \tan \psi) + \sqrt{\tau_s^2 + \tau_t^2 + (c_q - \sigma_n \tan \psi)^2} \quad (4-4)$$

where c_q is the apparent cohesion, $\tan \psi$ is the dilatancy coefficient. Note that ψ should not be constant, as observed in experiments where the dilatancy coefficient reduces from the initial value to the residual one (Almeida et al. 2016; Atkinson et al. 1988; Vasconcelos et al. 2008). The evolution law for the dilatancy coefficient is defined in terms of the compressive stress and plastic shear displacement, conforming to the experimental evidence (Andreotti et al. 2019; Jafari et al. 2020; Pluijm 1999). The experimental results indicate that with the increase of plastic shear

displacement and compressive normal stress (absolute value), the dilatancy coefficient reduces gradually. Despite the large scatter in the experimental data, a linear relationship could be a good representation for this dilatancy softening behavior, as shown in Figure 4-2. Thus, the following model was proposed to incorporate the softening dilatancy effects into the unassociated flow rule, as shown in Eq. (4-5):

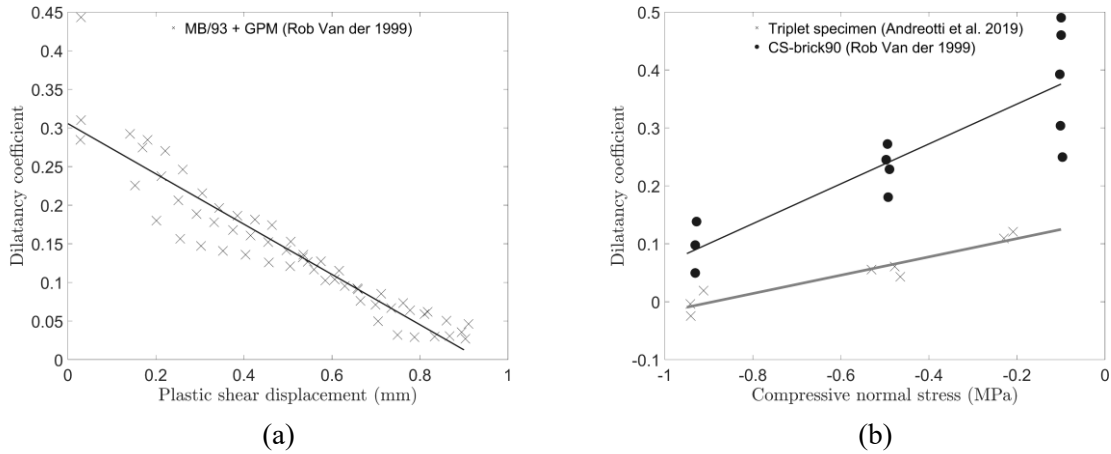


Figure 4-2. Relationship between dilatancy coefficient and (a) plastic shear displacement, and (b) compressive normal stress

$$\tan \psi = \begin{cases} \tan \psi_r + (\tan \psi_0 - \tan \psi_r) \left\langle 1 - \frac{\sqrt{(u_s^p)^2 + (u_t^p)^2}}{u_\tau} \right\rangle & \sigma_n \geq 0 \\ \tan \psi_r + (\tan \psi_0 - \tan \psi_r) \left(1 - \frac{\sigma_n}{\sigma_u} \right) \left\langle 1 - \frac{\sqrt{(u_s^p)^2 + (u_t^p)^2}}{u_\tau} \right\rangle & \sigma_u \leq \sigma_n < 0 \\ \tan \psi_r & \sigma_n < \sigma_u \end{cases} \quad (4-5)$$

where $\langle \rangle$ represents the Macaulay bracket (i.e., $\langle x \rangle = (|x| + x) / 2$); u_s^p and u_t^p are plastic displacements on the first and second tangential directions, respectively; $\tan \psi_0$ and $\tan \psi_r$ are the

initial (i.e., corresponding to $u_s^p = u_t^p = 0$ when $\sigma_n = 0$) and residual dilatancy coefficient, respectively; u_τ is ‘critical shear plastic displacement’ and σ_u is ‘critical dilatancy compressive stress’. It is apparent from Eq. (4-5) that when the applied compressive stress σ_n is less than σ_u or the resultant plastic shear displacement (i.e., $\sqrt{(u_s^p)^2 + (u_t^p)^2}$) is greater than u_τ , the dilatancy coefficient $\tan\psi$ is reduced to the residual level (i.e., $\tan\psi = \tan\psi_r$).

4.2.3. State variables evolution during plastic flow

4.2.3.1 State variables in the yield surface f_I

The mechanical behaviors of mortar joints under tension and shear show a similar softening phenomenon to those of other quasi-brittle materials (e.g., concrete). The evolution laws of tensile strength σ_t and cohesion c are based on strain softening (Lourenço 1996) defined as Eq. (4-6) and Eq. (4-7), respectively:

$$\sigma_t = f_t \exp\left(-\frac{f_t \kappa_1}{G_I}\right) \quad (4-6)$$

$$c = c_0 \exp\left(-\frac{c_0 \kappa_2}{G_{II}}\right) \quad (4-7)$$

where f_t is the tensile strength, G_I is the mode I fracture energy, c_0 is the peak cohesion, and G_{II} is the mode II fracture energy. The apparent cohesion c_q in Eq. (4-7) has the same evolution law as c but with a different peak value c_q^0 . These four material parameters (i.e., f_t , G_I , c_0 , G_{II}) have explicit physical meaning, which can typically be obtained from laboratory experiments. Previous experimental results, such as (Pluijm 1999; Raijmakers and Vermeltoort 1992), showed the dependence of mode II fracture energy G_{II} on the compressive normal stress σ_n . Although the

experimental data showed relatively large scatter, it is still apparent that G_{II} increases with the increase of the compressive stress level (Jafari et al. 2020; Lourenço 1996). A regression analysis, illustrated in Figure 4-3, indicated that the relationship between G_{II} and σ_n can be described using two parameters $a_{G_{II}}$ and G_{II}^0 , shown in Eq. (4-8):

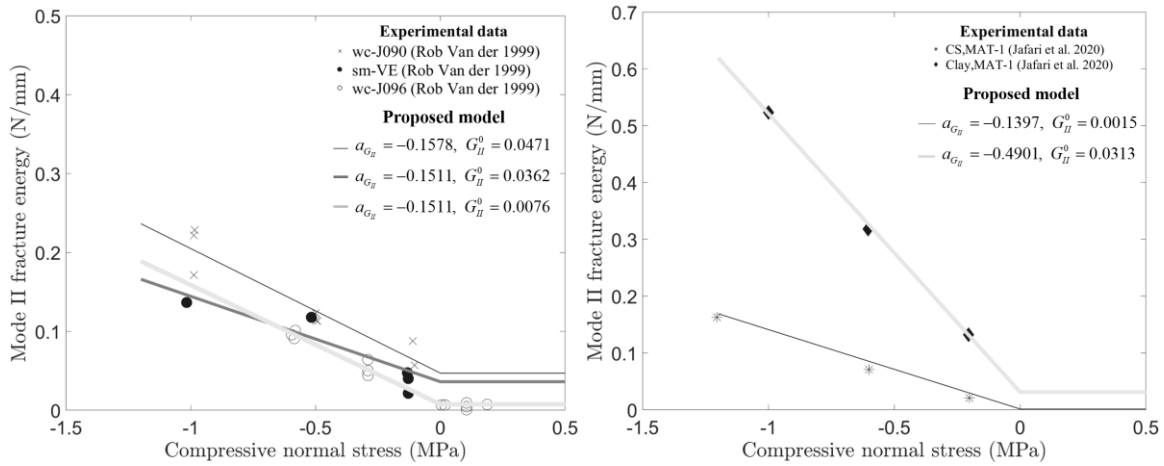


Figure 4-3. Relationship between mode II fracture energy and compressive normal stress

$$G_{II} = \begin{cases} a_{G_{II}} \sigma_n + G_{II}^0 & \sigma_n < 0 \quad \text{under compression} \\ G_{II}^0 & \sigma_n \geq 0 \quad \text{under tension} \end{cases} \quad (4-8)$$

where $a_{G_{II}}$ is a negative constant parameter, G_{II}^0 is the mode II fracture energy when $\sigma_n = 0$. In Eq. (4-6) and Eq. (4-7), κ_1 and κ_2 are two softening scalars, formulated in the rate form using plastic displacements, see Eq. (4-9) and Eq. (4-10):

$$\dot{\kappa}_1 = \sqrt{\left\langle \dot{u}_n^p \right\rangle^2 + \left(\frac{G_I}{G_{II}} \times \frac{c_0}{f_t} \sqrt{(\dot{u}_s^p)^2 + (\dot{u}_t^p)^2} \right)^2} \quad (4-9)$$

$$\dot{\kappa}_2 = \sqrt{\left\langle \frac{G_{II}}{G_I} \times \frac{f_t}{c_0} \times \dot{u}_n^p \right\rangle^2 + (\dot{u}_s^p)^2 + (\dot{u}_t^p)^2} \quad (4-10)$$

where u_n^p , u_s^p , and u_t^p are the plastic displacements in the normal, first tangential, and second tangential directions, respectively. The Macaulay bracket $\langle \ \rangle$ implies that a compressive stress state in the normal direction has no contribution to the softening scalar variables (i.e., κ_1 , κ_2). The quadratic combinations of plastic displacements in Eq. (4-9) and Eq. (4-10) ensure that the loss percentages for tensile yield stress σ_t and cohesion c are equal through the entire softening process. This fully coupled tension-shear softening model is consistent with the fact that both softening behaviors are related to the interfacial debonding at the micro level (Lourenço 1996).

The frictional coefficient $\tan\phi$ would have a gradual change during the plastic deformation process, which is coupled with cohesion softening, as given in Eq. (4-11):

$$\tan \phi = \tan \phi_0 + \frac{c - c_0}{c_0} (\tan \phi_0 - \tan \phi_r) \quad (4-11)$$

The residual frictional coefficient $\tan\phi_r$ can be obtained directly from experimental results, defined as the ratio between the residual shear stress and the compressive normal stress after the cohesion c is fully exhausted. It is worth noting that the residual frictional coefficient $\tan\phi_r$ is not necessarily less than the initial frictional coefficient $\tan\phi_0$, which is related to the mortar type and the roughness of the unit-mortar interaction surface. Some experimental data with $\tan\phi_r > \tan\phi_0$ can be found in (Almeida et al. 2016; Atkinson et al. 1988; Vasconcelos et al. 2008).

4.2.3.2 State variables in the yield surface f_2

The compressive yield stress σ_c evolves with the increase of equivalent plastic displacement κ_3 , defined as the quadratic combinations of three plastic displacement components in the rate form, as given in Eq. (4-12):

$$\dot{\kappa}_3 = \sqrt{\left(\langle -\dot{u}_n^p \rangle\right)^2 + \left(\dot{u}_s^p\right)^2 + \left(\dot{u}_t^p\right)^2} \quad (4-12)$$

The evolution law of σ_c is divided into three segments, similar to the those used by (Kumar and Barbato 2019; Lourenço 1996), shown in Eq. (4-13) and Figure 4-4. The compressive yield stress first experiences hardening from the initial value σ_c^i to the peak value σ_c^p , i.e., compressive strength f_c in Eq. (4-3). Then it reduces to the intermediate stress level σ_c^m . An exponential softening branch is subsequently followed to the residual compressive stress σ_c^r . The whole σ_c - κ_3 curve is determined based on several controlling values, which should be calibrated based on the experimental results. When relevant experimental data is not available, the values of controlling points can be assumed empirically. The displacement κ_3^p , corresponding to the compressive strength, is assumed to be equal to σ_c^p/k_m according to (Nazir and Dhanasekar 2014). To make sure the numerical stability, the initial and residual compressive yield stress (i.e., σ_c^i and σ_c^r) are defined as $\sigma_c^p/4$ (Nazir and Dhanasekar 2014) and $\sigma_c^p/7$ (Lourenço 1996), respectively. The intermediate point (κ_3^m, σ_c^m) is set to be $(5\kappa_3^p, 0.55\sigma_c^p)$ to provide a smooth transition between different segments (Lourenço 1996).

$$\sigma_c = \begin{cases} \sigma_c^i + (\sigma_c^p - \sigma_c^i) \left(\frac{2\kappa_3}{\kappa_3^p} - \frac{\kappa_3^2}{(\kappa_3^p)^2} \right) & \kappa_3 \leq \kappa_3^p \\ \sigma_c^p + (\sigma_c^m - \sigma_c^p) \left(\frac{\kappa_3 - \kappa_3^p}{\kappa_3^m - \kappa_3^p} \right)^2 & \kappa_3^p < \kappa_3 \leq \kappa_3^m \\ \sigma_c^r + (\sigma_c^m - \sigma_c^r) \exp\left(2 \frac{\sigma_c^m - \sigma_c^p}{\kappa_3^m - \kappa_3^p} \frac{\kappa_3 - \kappa_3^m}{\sigma_c^m - \sigma_c^r} \right) & \kappa_3 > \kappa_3^m \end{cases} \quad (4-13)$$

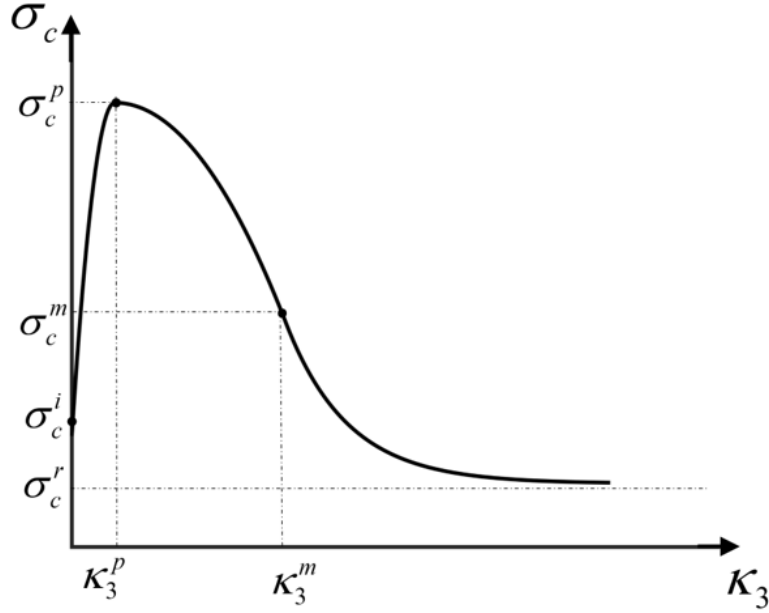


Figure 4-4. Evolution law of the compressive yield stress σ_c

4.3. PLASTICITY INTEGRATION STRATEGY

In the context of finite element implementation, plasticity integration is required since the rate form is used in the evolutionary rules for the abovementioned hardening/softening and the flow rule, in addition to the strain rate decomposition. The plasticity integration problem can be stated as follows: Given the known stress (i.e., $\sigma_n = [\sigma_n, \tau_s, \tau_t]^T$) and softening/hardening scalars (i.e., $\kappa_n = [\kappa_{1,n}, \kappa_{2,n}, \kappa_{3,n}]^T$) at load step n and the displacement increment $du = [du_n, du_s, du_t]^T$ at load step $n+1$, update all the stress and state variables (i.e., $\sigma_{n+1}, \kappa_{n+1}$) at load step $n+1$. This section deals with the plastic integration of the proposed constitutive material model for the interface element in a general finite element framework. Specifically, a fully implicit Euler Backward integration algorithm is adopted to achieve the predictor-corrector return mapping procedure (Simo et al. 1988). The Newton-Raphson (NR) method is utilized to provide the nonlinear equation solutions at the constitutive level, and the consistent tangent matrix is derived to guarantee the quadratic rate of convergence at the finite element (FE) level. In addition, an error-based auto-adaptive sub-

stepping algorithm is employed to enhance numerical accuracy, robustness, and efficiency. Details are provided as follows.

4.3.1. Multi-yield surface plasticity integration strategy

For the sake of generality, the specific case in which both yield criteria are violated is discussed here. The non-smooth corner is defined by the intersection region of tension-shear yield surface f_1 and compression cap f_2 .

With the displacement increment \mathbf{du} at load step $n+1$, the trial stress state $\boldsymbol{\sigma}^{tri}$ can be obtained as Eq. (4-14):

$$\boldsymbol{\sigma}^{tri} = \boldsymbol{\sigma}_n + \mathbf{K}\mathbf{du} \quad (4-14)$$

where $\boldsymbol{\sigma}_n$ is the last converged stress state (at step n), and \mathbf{K} is the elastic stiffness matrix defined in Eq. (4-1).

According to the multi-yield surface plasticity integration strategy proposed by Simo (1988), in the presence of yielding, the plastic strain increment is obtained as a linear combination of the plastic strain rates of the two yield surfaces, given in Eq. (4-15):

$$\mathbf{du}^p = \dot{\lambda}_1 \frac{\partial \mathbf{g}_1}{\partial \boldsymbol{\sigma}_{n+1}} + \dot{\lambda}_2 \frac{\partial \mathbf{g}_2}{\partial \boldsymbol{\sigma}_{n+1}} \quad (4-15)$$

where $\mathbf{du}^p = [du_n^p, du_s^p, du_t^p]^T$ is the plastic displacement vector, $\dot{\lambda}_1$ and $\dot{\lambda}_2$ are two plastic multipliers.

As a result, the predictor-corrector return mapping strategy based on the Euler Backward algorithm gives a set of nonlinear equations (a total of $8 = 3 + 3 + 2$), as given in Eq. (4-16):

$$\begin{cases} \boldsymbol{\sigma}_{n+1} - \boldsymbol{\sigma}_n - \mathbf{K} \left(d\mathbf{u} - \dot{\lambda}_1 \frac{\partial \mathbf{g}_1}{\partial \boldsymbol{\sigma}_{n+1}} - \dot{\lambda}_2 \frac{\partial \mathbf{g}_2}{\partial \boldsymbol{\sigma}_{n+1}} \right) = \mathbf{0} \\ \boldsymbol{\kappa}_{n+1} - \boldsymbol{\kappa}_n - \Delta \boldsymbol{\kappa}_{n+1} = \mathbf{0} \\ \mathbf{f}(\boldsymbol{\sigma}_{n+1}, \boldsymbol{\kappa}_{n+1}) = \mathbf{0} \end{cases} \quad (4-16)$$

where the first sub-equation relates to the stress increment, the second sub-equation relates to the increments of scalar variables from load step n to load step $n+1$, and the third sub-equation imposes the yield constraints in the plasticity theory.

The eight unknowns in the nonlinear Eq. (4-16) are three stress components in $\boldsymbol{\sigma}_{n+1}$, three state variables in $\boldsymbol{\kappa}_{n+1}$, and two plastic multipliers (i.e., $\dot{\lambda}_{n+1} = [\dot{\lambda}_1, \dot{\lambda}_2]^T$). It is unlikely to find a closed-form solution for this set of nonlinear equations. Therefore, a standard NR method is adopted to solve the nonlinear system to ensure quadratic convergence, provided that the initial solution is sufficiently close to the exact one. The residuals of Eq. (4-16) can be linearized as Eq. (4-17):

$$\mathbf{r}^{k+1}(\boldsymbol{\sigma}_{n+1}^{k+1}, \boldsymbol{\kappa}_{n+1}^{k+1}, \dot{\lambda}_{n+1}^{k+1}) = \mathbf{r}^k(\boldsymbol{\sigma}_{n+1}^k, \boldsymbol{\kappa}_{n+1}^k, \dot{\lambda}_{n+1}^k) + \mathbf{J}(\boldsymbol{\sigma}_{n+1}^k, \boldsymbol{\kappa}_{n+1}^k, \dot{\lambda}_{n+1}^k) \begin{bmatrix} d\boldsymbol{\sigma}_{n+1}^{k+1} & d\boldsymbol{\kappa}_{n+1}^{k+1} & d\dot{\lambda}_{n+1}^{k+1} \end{bmatrix}^T \quad (4-17)$$

where \mathbf{r}^k represents the residual vector for NR iteration k , and \mathbf{J} is the Jacobian matrix of Eq. (4-16).

By letting the left-hand side of Eq. (4-17) be equal to $\mathbf{0}$, the increments of the unknown variables are derived as Eq. (4-18):

$$\begin{bmatrix} d\boldsymbol{\sigma}_{n+1}^{k+1} & d\boldsymbol{\kappa}_{n+1}^{k+1} & d\dot{\lambda}_{n+1}^{k+1} \end{bmatrix}^T = -\mathbf{J}^{-1}(\boldsymbol{\sigma}_{n+1}^k, \boldsymbol{\kappa}_{n+1}^k, \dot{\lambda}_{n+1}^k) \mathbf{r}(\boldsymbol{\sigma}_{n+1}^k, \boldsymbol{\kappa}_{n+1}^k, \dot{\lambda}_{n+1}^k) \quad (4-18)$$

The solution can be achieved iteratively by Eq. (4-18) until the Euclidean norm of the residual vector $\|r\| = \|r^{k+1}(\sigma_{n+1}^{k+1}, \kappa_{n+1}^{k+1}, \dot{\lambda}_{n+1}^{k+1})\|$ in Eq. (4-17) reaches a prescribed tolerance. The initial guess for stress vector σ_{n+1}^0 and state variables κ_{n+1}^0 are determined as the trial stress σ^{tri} and the converged values in the previous load step κ_n , respectively. The initial guess for plastic multipliers is $\dot{\lambda}_{n+1}^0 = \mathbf{0}$.

The graphical representation for the predictor-corrector strategy for the multi-yield surface model is illustrated in Figure 4-5, in which Point A denotes the elastic stress state at the step n , Point B denotes the trial stress state at step $n+1$, and Point C is reached through NR method, denoting the converged stress state at step $n+1$.

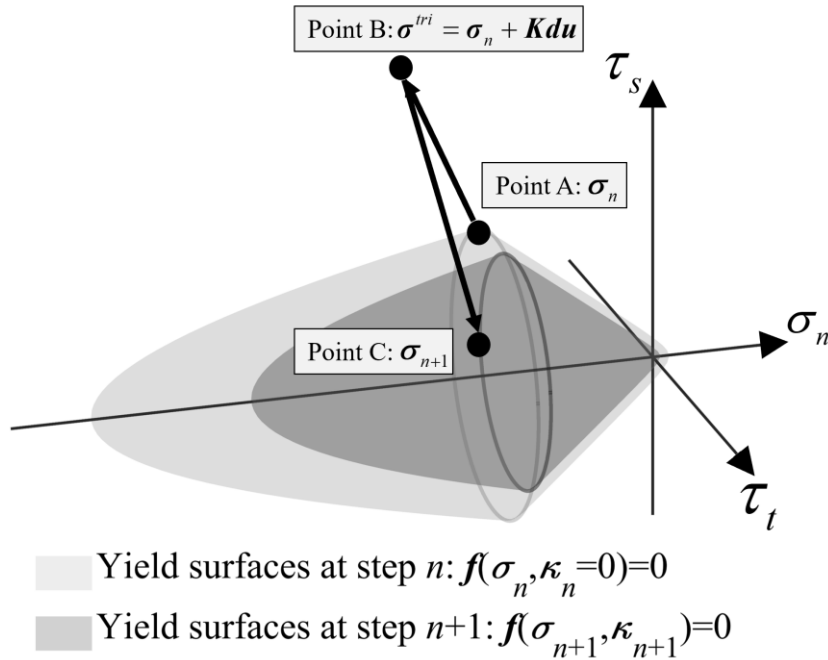


Figure 4-5. Graphical representation for the predictor-corrector strategy for the multi-yield surface model

4.3.2. Error-based auto-adaptive sub-stepping algorithm

The implicit solver in the FE software, e.g., ABAQUS Standard (Dassault Systemes 2017), permits the use of large displacement increments. Thus, to ensure the robustness of NR iteration procedure at the constitutive level when a relatively large displacement increment is imposed at the structural level, an error-based auto-adaptive sub-stepping algorithm based on the error-tolerance ratio is introduced to control the step size.

In the context of sub-stepping strategy, a single load step is discretized into several sub-steps, resulting in a sub-incremental displacement $\omega_{i,n+1} \mathbf{du}$ ($0 < \omega_{i,n+1} < 1$) in each sub-step, as given in Eq. (4-19):

$$\mathbf{du} = \sum_{i=1}^m \mathbf{du}_i = \sum_{i=1}^m \omega_{i,n+1} \mathbf{du} \quad \text{with} \quad \sum_{i=1}^m \omega_{i,n+1} = 1 \quad (4-19)$$

where $\omega_{i,n+1}$ is the reduction factor at sub-step i within global step $n+1$, m is the number of sub-steps. A large value of $\omega_{i,n+1}$ may cause the divergence of NR, resulting in numerical instability. On the contrary, a small value of $\omega_{i,n+1}$ would increase the computational cost with more sub-steps. To address this issue, the auto-adaptive step size control strategy proposed by Gupta et al. (2020) is used to adjust the reduction factor $\omega_{i,n+1}$ such that the residual error is close to the prescribed tolerance, as shown in Eq. (4-20):

$$\frac{\omega_{i,n+1}}{\omega_{i-1,n+1}} = \left(\frac{Tol}{error} \right)^{1/\alpha} \quad (4-20)$$

where Tol is the prescribed tolerance, $error$ is the residual $\|\mathbf{r}\|$ and will be updated in each NR iteration, and α is a constant ($\alpha = 0.2$ is used in this study). As shown in Eq. (4-20), if the NR

iteration fails to converge (i.e., $Tol < error$) within a specified number of iterations, $\omega_{i,n+1}$ is reduced accordingly. Conversely, if the NR iteration converges (i.e., $Tol > error$), $\omega_{i,n+1}$ is increased as per the sub-step controller, i.e., Eq. (4-20), to save computational cost.

For the plasticity integration problems involved in the sub-stepping strategy, the nonlinear system at sub-step $i+1$ within load step $n+1$ can be written as Eq. (4-21):

$$\begin{cases} \sigma_{i,n+1} - \sigma_{i-1,n+1} - \mathbf{K} \left(\omega_{i,n+1} \mathbf{d}\mathbf{u} - \dot{\lambda}_{1,i} \frac{\partial \mathbf{g}_1}{\partial \sigma_{i,n+1}} - \dot{\lambda}_{2,i} \frac{\partial \mathbf{g}_2}{\partial \sigma_{i,n+1}} \right) = \mathbf{0} \\ \boldsymbol{\kappa}_{i,n+1} - \boldsymbol{\kappa}_{i-1,n+1} - \Delta \boldsymbol{\kappa}_{i,n+1} = \mathbf{0} \\ \mathbf{f}(\sigma_{i,n+1}, \boldsymbol{\kappa}_{i,n+1}) = \mathbf{0} \end{cases} \quad (4-21)$$

It should be noted that the independent variables of the nonlinear system in Eq. (4-21) are $\sigma_{i,n+1}$, $\boldsymbol{\kappa}_{i,n+1}$, and $\dot{\lambda}_i = [\dot{\lambda}_{1,i}, \dot{\lambda}_{2,i}]$. Similarly, Eq. (4-21) can be solved iteratively, as given in Eq. (4-22):

$$\begin{bmatrix} d\sigma_{i,n+1}^{k+1} & d\boldsymbol{\kappa}_{i,n+1}^{k+1} & d\dot{\lambda}_i^{k+1} \end{bmatrix}^T = -\mathbf{J}_i^{-1}(\sigma_{i,n+1}^k, \boldsymbol{\kappa}_{i,n+1}^k, \dot{\lambda}_i^k) \mathbf{r}(\sigma_{i,n+1}^k, \boldsymbol{\kappa}_{i,n+1}^k, \dot{\lambda}_i^k) \quad (4-22)$$

where k and $k+1$ are NR iteration cycles. Plastic multipliers $\dot{\lambda}_i = [\dot{\lambda}_{1,i}, \dot{\lambda}_{2,i}]$ are set to zero at the first iteration cycle at each sub-step because they only take account of the plastic procedure incrementally. Thus, plastic displacements accumulate through all the sub-steps.

The general idea for the sub-stepping backward integration is schematically illustrated in Figure 4-6, in which σ_n and σ_{n+1} are the stress states at steps n and $n+1$, $\sigma_{i,n+1}^{tri}$ and $\sigma_{i,n+1}$ ($i=1,2,\dots,m$) are the trial and converged stress states at sub-step i .

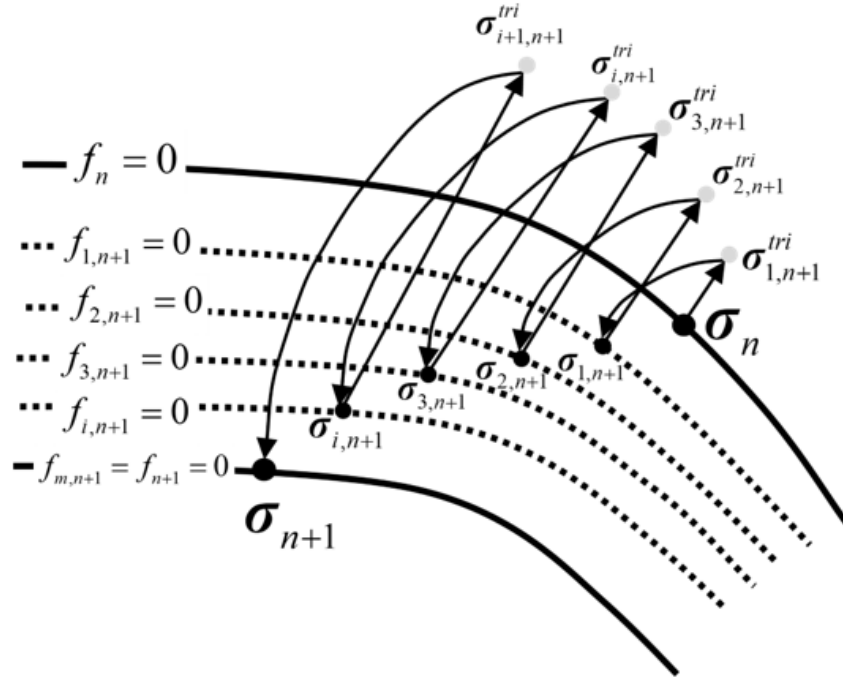


Figure 4-6. Schematic illustration of the general idea for the sub-stepping backward integration used in the proposed constitutive model

For the global NR iteration at the structural level, the consistent tangent stiffness matrix at each Gaussian point, defined as $\frac{\partial \sigma}{\partial du}$, is needed for the current load step. Following the method provided in (Caballero et al. 2008; Pérez-Foguet et al. 2001), $\frac{\partial \sigma}{\partial du}$ can be computed by differentiating Eq. (4-21) with respect to du by applying the chain rule, leading to Eq. (4-23):

$$\mathbf{J}_i \begin{bmatrix} \frac{\partial \sigma_{i,n+1}}{\partial du} & \frac{\partial \kappa_{i,n+1}}{\partial du} & \frac{\partial \lambda_i}{\partial du} \end{bmatrix}^T = \begin{bmatrix} \frac{\partial \sigma_{i-1,n+1}}{\partial du} + \omega_{i,n+1} \mathbf{K} & \frac{\partial \kappa_{i-1,n+1}}{\partial du} & \mathbf{0} \end{bmatrix}^T \quad (4-23)$$

where \mathbf{J}_i has the same structure as the Jacobian matrix in the local NR iteration procedure shown in Eq. (4-22). Accordingly, the consistent tangent stiffness matrix $\frac{\partial \sigma_{i,n+1}}{\partial du}$ at sub-step level i can be thus obtained by pre-multiplying the inverse of the Jacobian matrix \mathbf{J}_i on both sides of Eq. (4-23).

The recursive structure in Eq. (4-23) indicates that the consistent tangent stiffness matrix from the previous sub-step (i.e., sub-step $i-1$) has to be considered for the update at the current sub-step (i.e., sub-step i). The initial conditions for Eq. (4-23) are corresponding to the case $i = 1$, given in Eq. (4-24):

$$\frac{\partial \sigma_{0,n+1}}{\partial \mathbf{du}} = \mathbf{0}, \frac{\partial \kappa_{0,n+1}}{\partial \mathbf{du}} = \mathbf{0} \quad (4-24)$$

At the end of the sub-stepping process for each load level, i.e., until the summation of sub displacement increments is equal to the total displacement increments ($\sum_{i=1}^m \omega_{i,n+1} = 1$), the stress and state variables as well as the consistent tangent stiffness matrix will be obtained as given in Eq. (4-25):

$$\sigma_{n+1} = \sigma_{m,n+1}, \kappa_{n+1} = \kappa_{m,n+1}, \frac{\partial \sigma_{n+1}}{\partial \mathbf{du}} = \frac{\partial \sigma_{m,n+1}}{\partial \mathbf{du}} \quad (4-25)$$

where $n+1$ and m represent the load step level and last sub-step level, respectively.

For the other two cases in which only a single yield surface (e.g., f_1 or f_2) is violated, the general procedure to obtain the solutions is almost identical to the case elaborated above. The only difference lies in the softening variables that are calculated in the plasticity integration procedure: $\kappa_{1,n}$ and $\kappa_{2,n}$ for the case when f_1 is violated, and $\kappa_{3,n}$ when f_2 is violated. It is also worth mentioning that at the end of each integration process, the *Kuhn-Tucker conditions* as detailed in Eq. (4-26) must be satisfied. If the *Kuhn-Tucker conditions* are violated after the return mapping procedure (i.e., $\dot{\lambda}_i < 0$ or $f_i > 0$), the correct number of active yield surfaces must be identified, and thus the plasticity integration procedure will be restarted. The implicit Euler backward integration strategy within the sub-stepping framework is illustrated in the following algorithm.

$$\dot{\lambda}_i \geq 0, \quad f_i \leq 0, \quad \dot{\lambda}_i f_i = 0 \quad (i=1,2) \quad (4-26)$$

Algorithm: Implicit Euler Backward integration algorithm with error-based auto-adaptive sub-stepping strategy

```

1 Obtain stress state and state variables  $\sigma_n$  and  $\kappa_n$  from last converged step
2 Obtain the displacement increment  $du$  at the current step
3 Compute the trial stress state  $\sigma_{trial} = \sigma_n + K du$ 
4 if  $F_1(\sigma_{trial}) \leq 0$  and  $F_2(\sigma_{trial}) \leq 0$  then
5   Elastic state
6    $\sigma_{n+1} = \sigma_{trial}$ ;  $\kappa_{n+1} = \kappa_n$ 
7 else if  $F_1(\sigma_{trial}) > 0$  and  $F_2(\sigma_{trial}) \leq 0$  then
8   Plastic state: Only  $F_1$  is violated
9   for  $i \leftarrow 1$  to  $m$  do
10    while  $r(\sigma_i^k, \kappa_{1,i}^k, \kappa_{2,i}^k, \dot{\lambda}_{1,i}^k) > tolerance$  do
11      Calculate Jacobian matrix  $J_1$ 
12      Calculate  $[d\sigma_i^k, d\kappa_{1,i}^k, d\kappa_{2,i}^k, d\dot{\lambda}_{1,i}^k]$  according to Eq.(4-22)
13      Calculate  $[\sigma_i^k, \kappa_{1,i}^k, \kappa_{2,i}^k, \dot{\lambda}_{1,i}^k] = [\sigma_i^{k-1}, \kappa_{1,i}^{k-1}, \kappa_{2,i}^{k-1}, \dot{\lambda}_{1,i}^{k-1}] + [d\sigma_i^k, d\kappa_{1,i}^k, d\kappa_{2,i}^k, d\dot{\lambda}_{1,i}^k]$ 
14    end
15    Update  $\sigma_i = \sigma_i^k$ ;  $\kappa_{1,i} = \kappa_{1,i}^k$ ;  $\kappa_{2,i} = \kappa_{2,i}^k$ 
16    Calculate  $\frac{\partial \sigma_i}{\partial du}$  according to Eq.(4-23)
17    Calculate the next sub-step reduction factor  $\omega_{i+1}$  according to Eq.(4-20)
18  end
19  Update  $\sigma_{n+1} = \sigma_m$ ;  $\kappa_{1,n+1} = \kappa_{1,m}$ ;  $\kappa_{2,n+1} = \kappa_{2,m}$ 
20  Check if  $F_2$  is violated:
21    If  $F_2(\sigma_{n+1}, \kappa_{1,n+1}, \kappa_{2,n+1}) > 0$ , go to line 38
22 else if  $F_1(\sigma_{trial}) \leq 0$  and  $F_2(\sigma_{trial}) > 0$  then
23   Plastic state: Only  $F_2$  is violated
24   for  $i \leftarrow 1$  to  $m$  do
25    while  $r(\sigma_i^k, \kappa_{3,i}^k, \dot{\lambda}_{2,i}^k) > tolerance$  do
26      Calculate Jacobian matrix  $J_2$ 
27      Calculate  $[d\sigma_i^k, d\kappa_{3,i}^k, d\dot{\lambda}_{2,i}^k]$  according to Eq.(4-22)
28      Calculate  $[\sigma_i^k, \kappa_{3,i}^k, \dot{\lambda}_{2,i}^k] = [\sigma_i^{k-1}, \kappa_{3,i}^{k-1}, \dot{\lambda}_{2,i}^{k-1}] + [d\sigma_i^k, d\kappa_{3,i}^k, d\dot{\lambda}_{2,i}^k]$ 
29    end
30    Update  $\sigma_i = \sigma_i^k$ ;  $\kappa_{3,i} = \kappa_{3,i}^k$ 
31    Calculate  $\frac{\partial \sigma_i}{\partial du}$  according to Eq.(4-23)
32    Calculate the next sub-step reduction factor  $\omega_{i+1}$  according to Eq.(4-20)
33  end
34  Update  $\sigma_{n+1} = \sigma_m$ ;  $\kappa_{3,n+1} = \kappa_{3,m}$ ;  $\frac{\partial \sigma}{\partial du(n+1)} = \frac{\partial \sigma_m}{\partial du}$ 
35  Check if  $F_1$  is violated:
36    If  $F_1(\sigma_{n+1}, \kappa_{3,n+1}) > 0$ , goto 38
37 else if  $F_1(\sigma_{trial}) > 0$  and  $F_2(\sigma_{trial}) > 0$  then
38   for  $i \leftarrow 1$  to  $m$  do
39    while  $r(\sigma_i^k, \kappa_{1,i}^k, \kappa_{2,i}^k, \kappa_{3,i}^k, \dot{\lambda}_{1,i}^k, \dot{\lambda}_{2,i}^k) > tolerance$  do
40      Calculate Jacobian matrix  $J_3$ 
41      Calculate  $[d\sigma_i^k, d\kappa_{1,i}^k, d\kappa_{2,i}^k, d\kappa_{3,i}^k, d\dot{\lambda}_{1,i}^k, d\dot{\lambda}_{2,i}^k]$  according to Eq.(4-22)
42      Calculate  $[\sigma_i^k, \kappa_{1,i}^k, \kappa_{2,i}^k, \kappa_{3,i}^k, \dot{\lambda}_{1,i}^k, \dot{\lambda}_{2,i}^k] = [\sigma_i^{k-1}, \kappa_{1,i}^{k-1}, \kappa_{2,i}^{k-1}, \kappa_{3,i}^{k-1}, \dot{\lambda}_{1,i}^{k-1}, \dot{\lambda}_{2,i}^{k-1}] + [d\sigma_i^k, d\kappa_{1,i}^k, d\kappa_{2,i}^k, d\kappa_{3,i}^k, d\dot{\lambda}_{1,i}^k, d\dot{\lambda}_{2,i}^k]$ 
43    end
44    Update  $\sigma_i = \sigma_i^k$ ;  $\kappa_{1,i} = \kappa_{1,i}^k$ ;  $\kappa_{2,i} = \kappa_{2,i}^k$ ;  $\kappa_{3,i} = \kappa_{3,i}^k$ 
45    Calculate  $\frac{\partial \sigma_i}{\partial du}$  according to Eq.(4-23)
46    Calculate the next sub-step reduction factor  $\omega_{i+1}$  according to Eq.(4-20)
47  end
48  Update  $\sigma_{n+1} = \sigma_m$ ;  $\kappa_{1,n+1} = \kappa_{1,m}$ ;  $\kappa_{2,n+1} = \kappa_{2,m}$ ;  $\kappa_{3,n+1} = \kappa_{3,m}$ ;  $\frac{\partial \sigma}{\partial du(n+1)} = \frac{\partial \sigma_m}{\partial du}$ 
49  Check if the plastic multipliers are negative:
50    If  $\dot{\lambda}_{1,m} < 0$ , goto line 23
51    If  $\dot{\lambda}_{2,m} < 0$ , goto line 8
52 end

```

4.4. FINITE ELEMENT MODEL VALIDATION

The proposed constitutive material model is implemented via the user-defined subroutine UMAT in ABAQUS (Dassault Systemes 2017). This empowers the general-purpose FE software ABAQUS with the specialized capability of modeling masonry structures, considering complex mechanisms under different loading and boundary conditions. For the purpose of demonstration, the implemented material model is used together with the interface element in ABAQUS within the simplified micro modeling strategy (Lourenço 1996) to simulate three unit-mortar-unit assemblages under compression-shear loading and three unreinforced masonry (URM) walls under IP and OOP loading. The FE simulation results are compared with the experimental results reported in the literature to validate the effectiveness of the proposed model. Note that an implicit dynamic procedure is utilized to enhance the convergence performance, without affecting the accuracy, considering various forms of softening behavior exhibited in units and interfaces.

4.4.1. Unit-mortar-unit assemblages

Different unit-mortar-unit assemblages were tested by Pluijm (1999). Two representative experimental specimens under compression-shear loading, referred to as ‘CS-brick90’ and ‘CS-block96’, are simulated in this section. ‘CS-brick90’ and ‘CS-block96’ were constructed with 212 mm × 100 mm × 53 mm calcium silicate brick units plus 12 mm thick mortar, and 439 mm × 100 mm × 198 mm calcium silicate block units plus 2 mm thick mortar, respectively. The pre-compression stresses were applied at the top of the masonry specimens, while the bottom sides were fully constrained. The shear loads were applied at the top surface in a displacement-control manner.

With a focus on the mortar joint behavior, the test specimens are modeled by considering elastic brick units with a commonly used Poisson ratio of 0.15 (Abdulla et al. 2017; Aref and Dolatshahi 2013) and the elastic moduli reported in the experimental tests (Pluijm 1999), i.e., 13.40 GPa and 12.19 GPa for ‘CS-brick90’ and ‘CS-block96’, respectively.

For the parameters of the material model for the interface element, elastic stiffness constants (k_m , k_{ss} , and k_u) are determined as 400 N/mm³, 200 N/mm³, and 200 N/mm³ to represent the quasi-rigid behavior with small deformation before the onset of damage, as observed from the experimental results (denoted by shade areas) in Figure 4-7. The plastic material parameters for tension and shear are determined directly from the experimental report (Pluijm 1999), such as: tension-related parameters (tensile strength f_t , mode I fracture energy G_I), shear-related parameters (peak cohesion c_0 , mode II fracture energy under zero compressive stress G_{II}^0 , constant parameter $a_{G_{II}}$, initial frictional coefficient $\tan\phi_0$, residual frictional coefficient $\tan\phi_r$), as summarized in Table 4-1. The dilatancy-related parameters (initial dilatancy coefficient $\tan\psi_0$, residual dilatancy coefficient $\tan\psi_r$, critical shear plastic displacement u_τ , critical dilatancy compressive stress σ_u) are also included. Specifically, the critical shear plastic displacement u_τ is obtained directly from the test report. The values of $\tan\psi_0$ and $\tan\psi_r$ are determined from the relationships between the dilatancy coefficient and the compressive normal stress σ_n (Pluijm 1999): $\tan\psi = 0.35\sigma_n + 0.41$ for ‘CS-brick90’ and $\tan\psi = 0.68\sigma_n + 0.86$ for ‘CS-block96’. Note that the normal compressive stress level remained constant during the experiment for each of the unit-mortar-unit specimen tested, but different compressive normal stress levels were considered during the experiments. The stress level threshold σ_u is determined by letting $\tan\psi = 0$: -1.17 MPa and -1.26 MPa for two specimens, respectively. The initial dilatancy coefficients $\tan\psi_0$ are equal to 0.41 and 0.86, respectively,

corresponding to the cases when $\sigma_n = 0$. At the residual state, the dilatancy effects can be negligible according to the experimental results (Pluijm 1999), resulting in a zero dilatancy coefficient at the residual level (i.e., $\tan\psi_r = 0$). Note that the yield surface f_2 is assumed to be inactive in the unit-mortar-unit assemblage models since the test specimens were under relatively low compressive stress.

Table 4-1. Material parameters for unit-mortar-unit assemblages (Pluijm 1999)

Specimen	Tension-related		Shear-related					Dilatancy-related		
	f_t (MPa)	G_t (N/mm)	c_0 (MPa)	c_q^0 (MPa)	G_n^0 (N/mm)	α_{G_n}	$\tan\phi_0 / \tan\phi_r$	$\tan\psi_0 / \tan\psi_r$	σ_u (MPa)	u_r (mm)
CS-brick90	0.02	0.5	0.14	$100c_0$	0.005	-0.02	0.75/ 0.73	0.41/ 0	-1.26	0.75
CS-block96	0.42	1.1	1.1	$100c_0$	0.02	-0.14	0.82/ 0.85	0.86/ 0	-1.17	0.3

The simulated shear stress-displacement curves are compared with the experimental ones, as shown in Figure 4-7. It can be observed that good agreements with the experimental results are achieved. The shear strengths, post peak branches and residual behaviors under different compressive normal stresses are well reproduced. As such, it can be concluded that the developed constitutive material model for the interface element can well represent the tangential interfacial behavior of the mortar joint in the unit-mortar-unit assemblages.

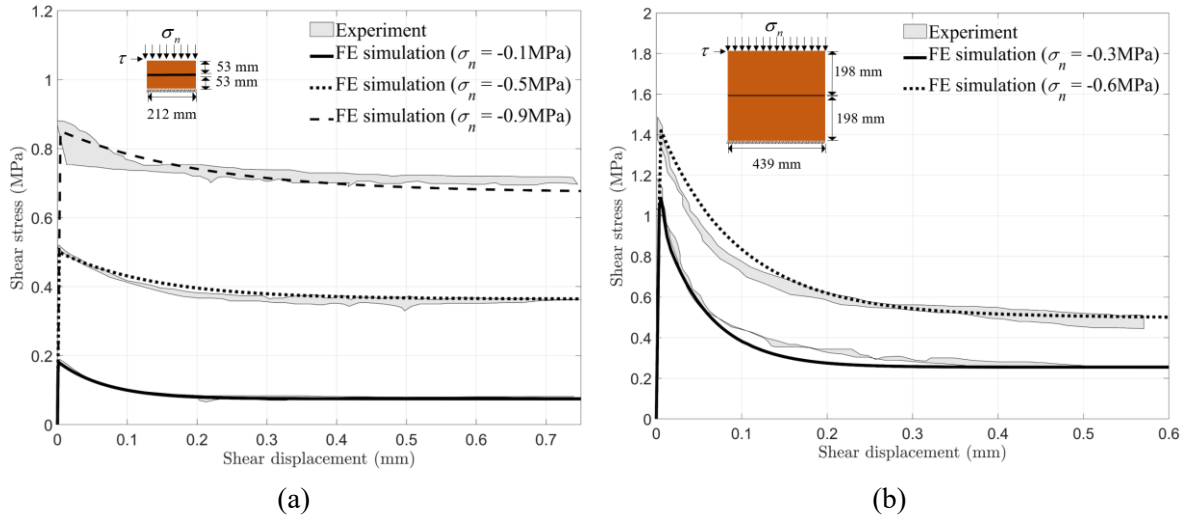


Figure 4-7. Comparison between numerical and experimental results for unit-mortar-unit assemblages under compression-shear loading: (a) CS-brick90, and (b) CS-block96

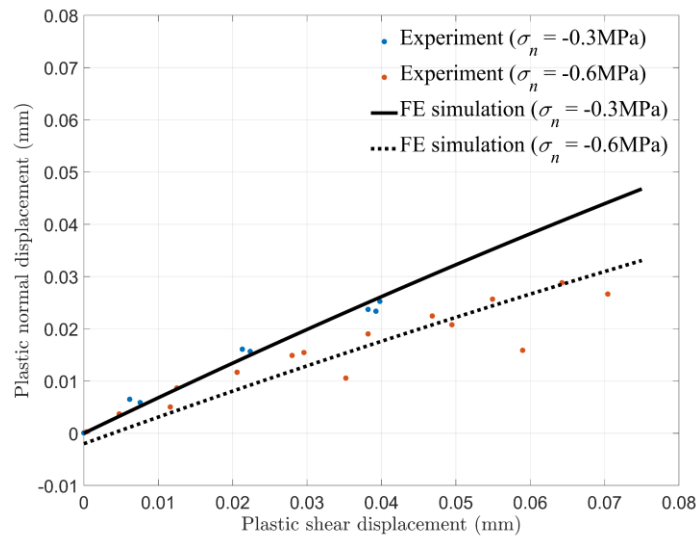


Figure 4-8. Comparison of plastic normal displacement-plastic shear displacement relationship for specimen CS-block96 between the experimental and FE simulation results

The dilatancy behaviors of specimen CS-block96 were illustrated in Figure 4-8 by the relationship between the plastic normal and shear displacements. Although there are some scatters, a good agreement is achieved between the simulation results and the experimental results. In this section, a masonry triplet under direct shear shown in Figure 4-9, tested by Amadei et al. (1989),

was also simulated to quantify the dilatancy behavior. The strength-related parameters are obtained directly from the experimental report (Amadei et al. 1989). The two critical dilatancy coefficients (i.e., $\tan\varphi_0$ and $\tan\varphi_r$) are determined as the slopes of $u_n^p-u_\tau^p$ curve when $u_\tau^p = 0$ and u_τ^p is large enough such that the dilatancy coefficient reaches a stable residual value. The u_τ and σ_u are calibrated as the critical plastic shear displacement and compressive stress at which the dilatancy effects reach the residual level. Particularly, the value of σ_u is determined through the linear interpolation of $\tan\psi$ (slopes of curves shown in Figure 4-10)- σ_n relationship when the plastic shear displacement is zero. The parameters are summarized in Table 4-2. The experimental results are indicated by the dashed lines in the Figure 4-10. The comparisons between the experimental results and FE simulation results indicated the good fitness of the proposed constitutive model considering dilatancy softening.

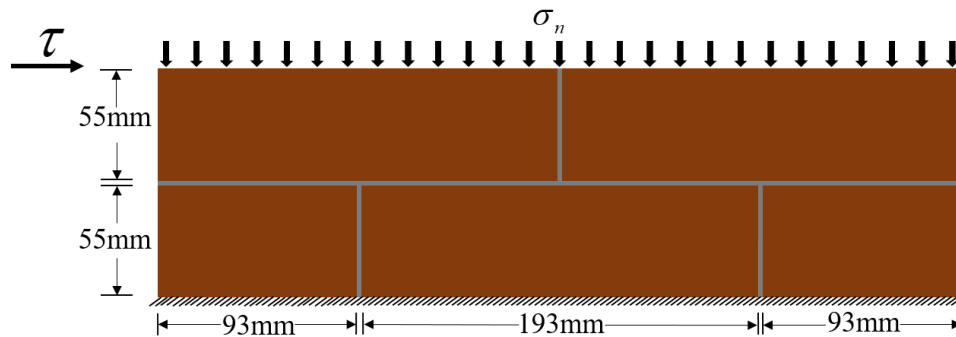


Figure 4-9. Masonry triplet under direct shear tested by Amadei et al. (1989)

Table 4-2. Dilatancy-related material parameters for the unit-mortar-unit assemblage

Parameter	$\tan\psi_0$	σ_u (MPa)	$\tan\psi_r$	u_τ (mm)
Value	0.35	2.5	0	25

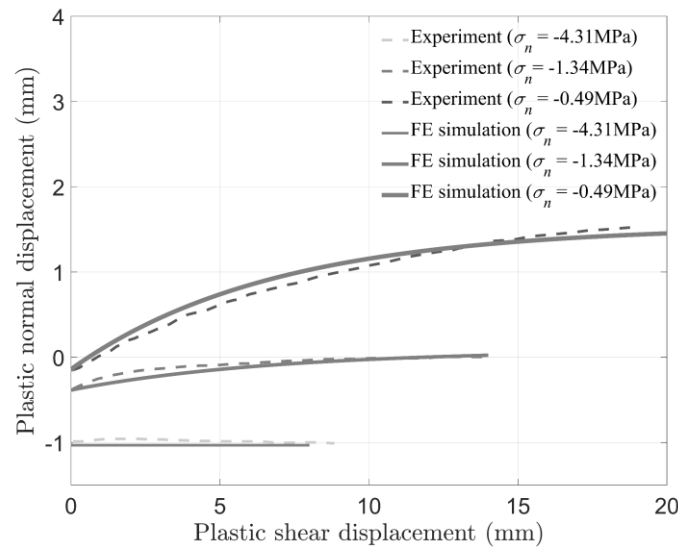


Figure 4-10. Comparison of u_n^p - u_t^p curves for different normal compressive stress levels between the experimental results and FE simulation results

4.4.2. URM wall under in-plane (IP) loading

A single-leaf unreinforced masonry (URM) wall under in-plane (IP) loading, referred to as ‘TMM’, was tested by da Porto (2005). The URM wall was built with perforated clay units with dimensions of 984 mm long, 1250 mm high, and 300 mm thick. The mortar thickness of the bed joints was 1.3 mm. The gross dimension of the units was 240 mm × 250 mm × 300 mm with holes inside. Due to the 43% percentage of holes, the effective thickness of the URM wall was 171 mm (da Porto 2005). A relatively stiff (quasi-rigid) reinforced concrete beam was placed at the top of the wall, which was used to enable uniform distribution of the applied vertical pre-compression load and to minimize the chances for local failure of the loaded corner of the wall. The base slab at the bottom of the wall was bolted down to the strong floor to prevent any horizontal sliding. The wall was first loaded with the pre-compression stress of 1.90 MPa. Then, the IP displacement-controlled loading imposed on the top rigid beam was monotonically increased until the wall failed. The details of the URM wall and test procedure are illustrated in Figure 4-11.

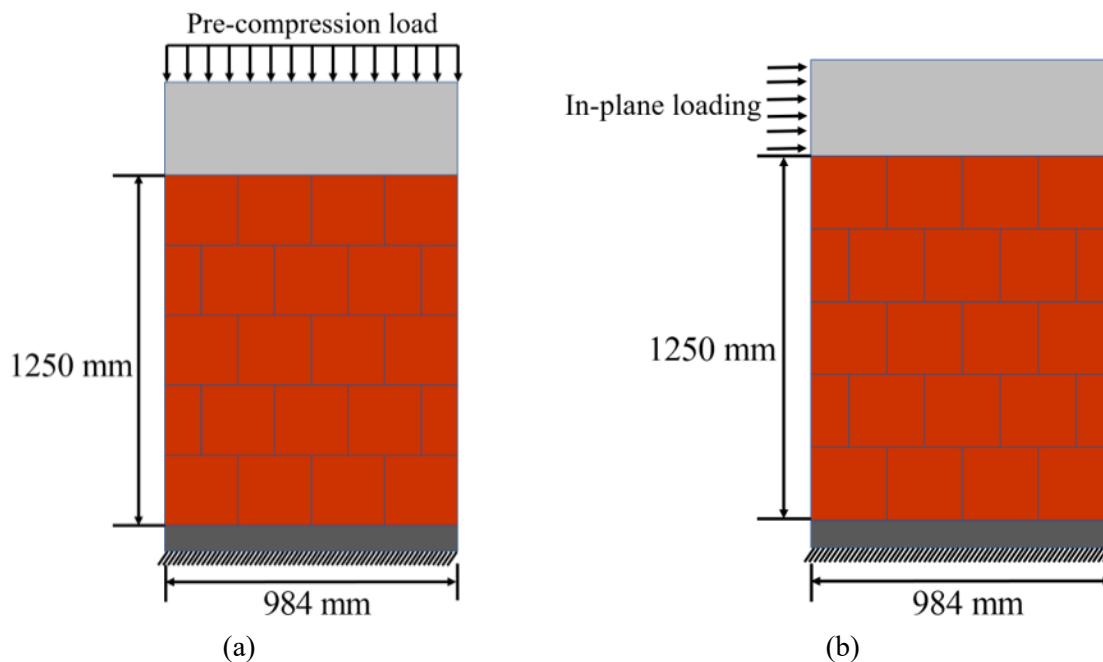


Figure 4-11. URM wall considered for the IP loading: (a) pre-compression applied at the top of the quasi-rigid beam, and (b) IP displacement-controlled loading

The FE model was developed based on the aforementioned simplified micro modeling strategy. The top reinforced concrete beam is represented with rigid elements, and the brick units are modeled with full integration 8-node solid element (C3D8), instead of C3D8R with reduced integration that is susceptible to non-physical hourglass modes. The mesh convergence study was first performed, and the adopted mesh density is $8 \times 8 \times 6$ elements for one single unit in order to reach a balance between the computational efficiency and accuracy.

The Concrete Damage Plasticity (CDP) model was employed for brick units, similar to the modeling strategy used in (Nazir and Dhanasekar 2014; da Porto et al. 2010) which allows to simulate the damage in units, in particular the tensile cracking (Dolatshahi 2012; da Porto 2005). The elastic modulus $E = 9328$ MPa and Poisson's ratio $\gamma = 0.15$ reported in the experimental tests (da Porto 2005) are used for the CDP model. The nonlinear material parameters required to define the CDP model include dilation angle ψ_b , the ratio between the biaxial initial compressive strength

and the initial uniaxial compressive strength σ_{b0}/σ_{c0} , the ratio of the second stress invariant on the tensile meridian to that on the compressive meridian K_c , and flow potential eccentricity ϵ . Typical values of these four nonlinear parameters for the quasi-brittle materials suggested by (Dassault Systemes 2017; Nguyen and Livaoğlu 2020) are adopted: $\psi_b = 35^\circ$, $\sigma_{b0}/\sigma_{c0} = 1.16$, $K_c = 2/3$, and $\epsilon = 0.1$. In addition, the tensile and compressive uniaxial stress-strain relationships and two corresponding damage scalars (i.e., d_t , d_c) are required to reproduce two failure mechanisms of brick units: tensile cracking and compressive crushing. The compressive strength σ_{cu} and tensile strength σ_{tu} of brick units are 20.43 MPa and 1.391 MPa according to the experimental results (da Porto 2005). The nonlinear branches of uniaxial stress-strain behavior are determined according to (Nguyen and Livaoğlu 2020).

The material parameters for interface elements to simulate the mortar joints were obtained directly from the FE study (da Porto et al. 2010) by the same author, including the stiffness constants (k_{nn} , k_{ss} , k_{tt}), tensile strength f_t , peak cohesion c_0 , mode I fracture energy G_I , mode II fracture energy G_{II}^0 when $\sigma_n = 0$ MPa, initial and residual frictional coefficients $\tan\varphi_0$ and $\tan\varphi_r$, initial and residual dilatancy coefficients $\tan\psi_0$ and $\tan\psi_r$, and compressive strength σ_c^p . For the other parameters, $a_{G_{II}}$ is determined as -0.08, i.e., the mean value of the upper bound (-0.14) and the lower bound (-0.02) experimentally determined (Pluijm 1999). The asymptote slope of the compressive yield surface $\tan\theta$ is assumed according to the numerical study (Macorini and Izzuddin 2011) in which a similar compressive yield surface was employed. The values of the controlling points on the compressive are calculated based on the assumptions previously detailed. All material parameters for the interface elements are summarized in Table 4-3.

Table 4-3. Material parameters of interface elements for the URM walls

Parameter	In-plane model	Out-of-plane models
k_{nn}, k_{ss}, k_{tt} (N/mm ³)	34.90, 14.42, 14.42 (da Porto et al. 2010)	42,17,17 (Abdulla et al. 2017)
f_t (MPa)	0.36 (da Porto 2005; da Porto et al. 2010)	0.12 (Abdulla et al. 2017)
c_0 (MPa)	0.44 (da Porto 2005; da Porto et al. 2010)	0.17 (Abdulla et al. 2017)
G_I (N/mm)	0.026 (da Porto et al. 2010)	0.012 (Abdulla et al. 2017)
G_{II}^0 (N/mm)	0.044 (da Porto et al. 2010)	0.04 (Abdulla et al. 2017)
$a_{G_{II}}$	-0.08 (Pluijm 1999)	-0.08 (Pluijm 1999)
c_q^0 (MPa)	100 c_0 (assumed)	100 c_0 (assumed)
$\tan\phi_0$	0.4 (da Porto 2005; da Porto et al. 2010)	0.576 (Vaculik 2012)
$\tan\phi_r$	0.4 (da Porto 2005; da Porto et al. 2010)	0.576 (Vaculik 2012)
$\tan\psi_0 / \tan\psi_r$	0/0 (da Porto et al. 2010)	0/0 (assumed)
σ_u (MPa)	-2 (assumed)	-2 (assumed)
u_r (mm)	25 (assumed)	25 (assumed)
$\tan\theta$	0.045 (Macorini and Izzuddin 2011)	0.045 (Macorini and Izzuddin 2011)
κ_3^p, κ_3^m (mm)	0.716 (calculated), 3.58 (calculated)	0.381 (calculated), 1.905 (calculated)
$\sigma_c^i, \sigma_c^p, \sigma_c^r$ (MPa)	6.25 (calculated), 25 (da Porto et al. 2010), 3.57 (calculated)	4 (calculated), 16 (Vaculik 2012), 1.6 (calculated)

The FE simulation results are compared with the experimental results, including the load-displacement curves in Figure 4-12 and the damage (cracking and crushing) pattern comparison in Figure 4-13. It can be observed from Figure 4-12 that the FE model with zero dilatancy (i.e., $\tan\psi = 0$) is able to reproduce the experimental test fairly well in terms of the initial stiffness and the post peak behavior. However, the IP load capacity is underestimated, i.e., 138.20 kN for the FE simulation and 168.05 kN for the experimental test. This can be attributed to the zero dilatancy assumption made in the FE analysis, which leads to a conservative prediction about the shear resistance of mortar joints and URM walls.

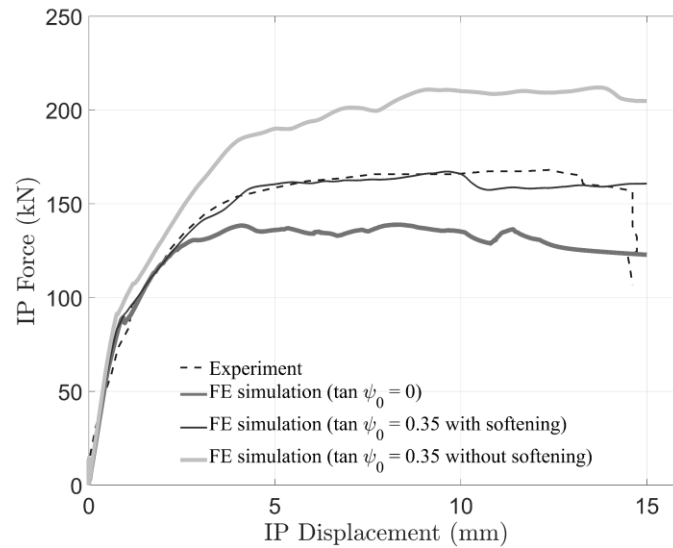


Figure 4-12. Load-displacement curve comparison for the URM wall under IP loading

Even though the influence of dilatancy effects on the wall capacity may be significant, dilatancy-related parameters are usually difficult to obtain. There is no general agreement about the experimental standard methodology for these parameters. Thus, dilatancy-related parameters are mostly determined empirically (Andreotti et al. 2019). In this chapter, dilatancy-related parameters are assumed to be equal to those in the previous unit-mortar-unit assemblages validation model. Note that the mortar joint in this wall was on the thin side. The dilatancy-related parameters may be strongly influenced by the mortar thickness. However, the general trend of dilatancy effects is identical, i.e., the dilatancy coefficient decreased with the increase in the plastic shear displacement and compressive normal stress (absolute value). To expose the effects of dilatancy on wall responses, two additional cases are considered here: softening dilatancy (i.e., $\tan\psi_0 = 0.35$, $\tan\psi_r = 0$), and constant dilatancy with non-zero value (i.e., $\tan\psi_0 = 0.35$, $\tan\psi_r = 0.35$). Compared with the case considering zero dilatancy, the load-displacement curve obtained from the FE model considering softening dilatancy has improved agreement with the experimental

one in terms of the IP capacity (i.e., 167.18 kN for the FE simulation and 168.05 kN for the experimental test). In contrast, a considerable overestimation of the IP load capacity was observed when no softening is considered with $\tan\psi_0 = 0.35$ (i.e., 210.7 kN for the FE simulation). In this case, the shear stresses of mortar joints keep increasing even in the relatively high compressive stress regime, resulting in an overestimation of the IP capacity of the URM wall. This comparison further affirms the need for appropriate modeling of dilatancy behavior.

Figure 4-13 summarizes the damage pattern comparison. The diagonal crack, denoted by the white line in Figure 4-13 (a), occurred and then developed toward the compressed toe following the inclined compressed struts, extending through both joint interfaces and units. The deformed shape and crack pattern obtained by the FE simulation are illustrated in Figure 4-13 (b) and Figure 4-13 (c). The diagonal cracks are well captured in terms of the equivalent plastic displacements κ_1 and κ_2 in the interfaces. The compressive struts, developed through units and mortar, are represented by the plastic displacement/damage in interfaces/units. Furthermore, the tensile damage through the units and compressive damage at the compressed toe, identified in the FE simulations, as shown in Figure 4-13 (d), conform with the findings reported in the experimental test (da Porto 2005). Overall, the damage patterns obtained by FE simulations are in fairly good agreement with the experimental ones.

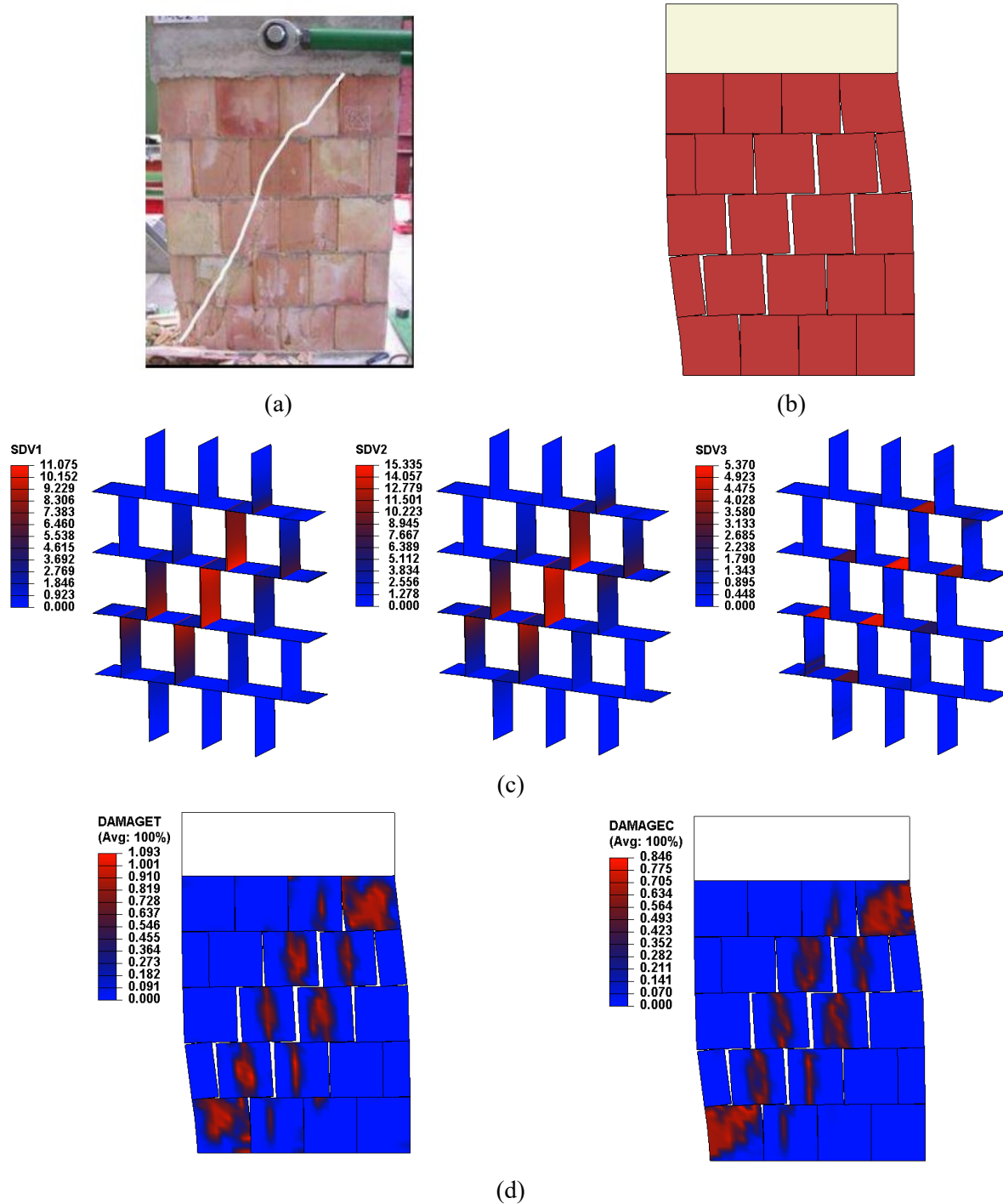


Figure 4-13. Final crack pattern: (a) experiment (da Porto 2005), (b) deformed shape of wall from FE simulation, (c) equivalent plastic displacements for mortar joints from FE simulation, and (d) tensile damage scalar (DAMAGET) and compressive damage scalar (DAMAGEC) plots for units from FE simulation. Note: SDV1, SDV2, SDV3 represent the equivalent plastic displacements for tension, shear, and compression (i.e., κ_1 , κ_2 , κ_3), respectively

4.4.3. URM walls under out-of-plane (OOP) loading

Two URM walls experimentally investigated by Vaculik (2012) under OOP loading are considered in this section to investigate the effect of dilatancy on OOP behavior. The two walls, referred to as ‘Wall s1’ and ‘Wall s2’, differed only in that Wall s2 was tested without pre-compression, while Wall s1 was tested with a 0.1 MPa pre-compression. Two walls were constructed using half-overlap stretcher-bonded masonry and built with clay brick units of 230 mm (length) \times 76 mm (height) \times 110 mm (width) and 10 mm thick mortar. The main leaf of the walls was 4000 mm long, 2500 mm high, and 110 mm thick. Two 450 mm long retaining walls were rigidly connected with the main wall on the left and right sides. The top and bottom sides of walls were simply supported, while the left and right sides were fixed. The uniform OOP loading was applied through the airbag.

Similarly, simplified micro models are developed using 3D full integration element (C3D8) for brick units and interface elements for mortar bedding. The mesh sensitivity study leads to an optimal mesh density of $4 \times 2 \times 2$ elements for one single brick unit. For the material parameters of mortar joints, the initial and residual frictional coefficients are both equal to 0.576, and the compressive strength of σ_c^p is 16 MPa, according to the experimental report (Vaculik 2012). The stiffness constants, tensile strength, peak cohesion, mode I fracture energy, and mode II fracture energy when $\sigma_n=0$ are determined based on Abdulla et al. (2017), in which the same URM wall was simulated. The rest of the material parameters are assumed to be identical to those in the URM wall under IP loading, as detailed in Table 4-3. For the material parameters required to define the CDP model, commonly used empirical relationships (Nguyen and Livaoglu 2020) are used to determine the compressive strength of brick units from $E = 300\sigma_{cu}$, and the tensile strength is 12%

of the compressive strength. The inelastic strains and damage scalars of the CDP model are determined following the same procedure as used for the IP model presented earlier. The material parameters of interface elements for the walls under OOP loading are detailed in Table 4-3.

According to the experimental procedure reported in Vaculik (2012), the OOP displacements were measured at the middle position of the wall. Both walls displayed a relatively constant post-peak strength plateau; this apparent ‘plastic’ behavior occurred due to the redistribution of diagonal bending moment resistance at the retaining walls. The load-displacement curves are compared between the FE simulations and experimental tests shown in Figure 4-14. Due to the applied pre-compression load, Wall s1 has a larger initial stiffness and OOP strength compared with Wall s2, which is well captured in the FE simulations.

For comparison, three different FE models are developed when considering three different dilatancy scenarios as studied for the IP model. It is found that when a constant dilation angle of $\tan\psi_0 = 0.35$ without softening is used, the OOP load capacities are over-predicted. In contrast, considering a dilation angle of $\tan\psi_0 = 0.35$ with softening can significantly improve the prediction accuracy. Note that considering a dilation angle of $\tan\psi_0 = 0.35$ with softening can be approximated by considering a constant dilation angle of $\tan\psi_0 = 0$, though the accuracy can be slightly sacrificed, particularly for Wall s1 with pre-compression, where dilatancy plays a greater role.

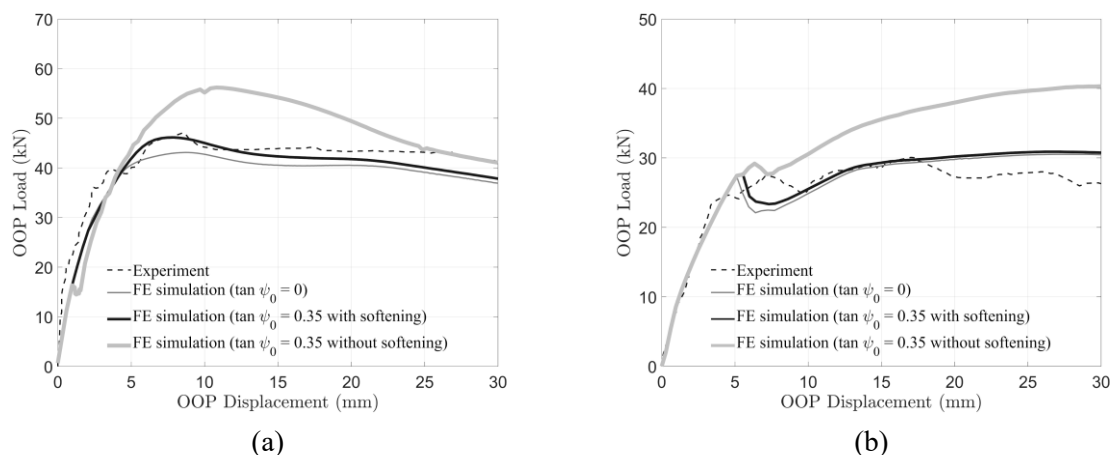


Figure 4-14. Load-displacement curve comparison for the URM walls under OOP loading: (a) Wall s1, and (b) Wall s2

The crack patterns obtained by the experimental results and FE simulations (i.e., when considering a dilation angle with softening) are also compared. The diagonal (X-shaped) cracks were fully developed due to the bending tension failure of the bed joints for both walls and are well captured by the FE models, as verified by the deformed shapes. The plastic displacement distributions in the interface elements are shown in Figure 4-15 (b-c) and Figure 4-16 (b-c). Moreover, the discrepancy in crack propagation between Wall s1 and Wall s2 is accurately reproduced by the FE simulations: Wall s1 does not exhibit the horizontal tensile cracking along the bed joints at the middle height position due to the applied pre-compression load, as illustrated in Figure 4-15 (b-c); on the contrary, Wall s2 does exhibit the horizontal tensile cracking along the bed joints, as shown in Figure 4-16 (b-c). In addition, the vertical cracks along the intersection corner between the main wall and retaining wall, as found in the experimental test (Vaculik 2012), are well captured through the unit damage contour plots, shown in Figure 4-15 (d) and Figure 4-16 (d).

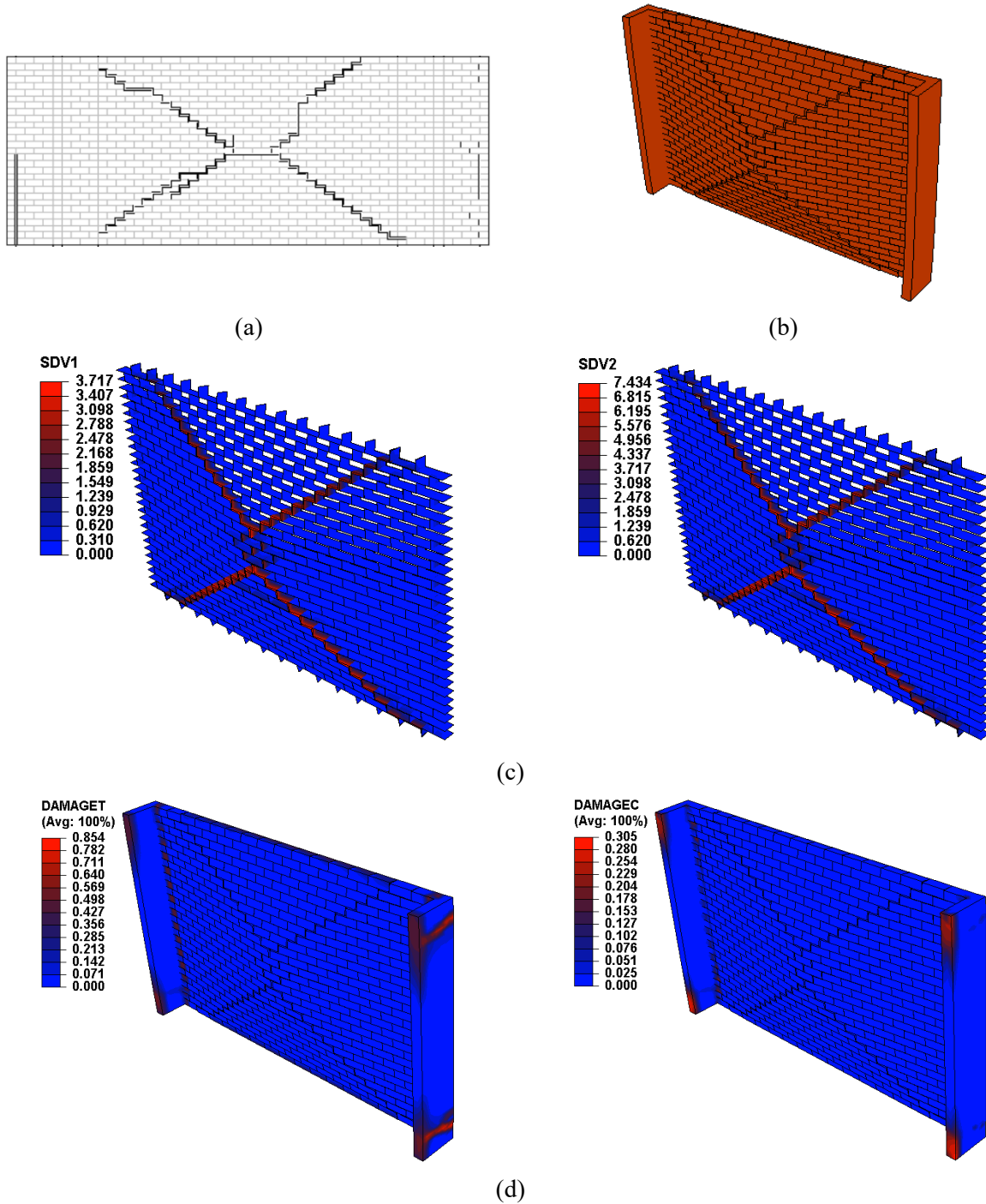


Figure 4-15. Comparison of crack pattern for Wall s1: (a) experimental tests (Vaculik 2012), (b) deformed shape from FE simulation, (c) equivalent plastic displacements for mortar joints from FE simulation, and (d) tensile damage scalar (DAMAGET) and compressive damage scalar (DAMAGEC) plots for units from FE simulation. Note: SDV1, SDV2, SDV3 represent the equivalent plastic displacements for tension, shear, and compression (i.e., κ_1 , κ_2 , κ_3), respectively

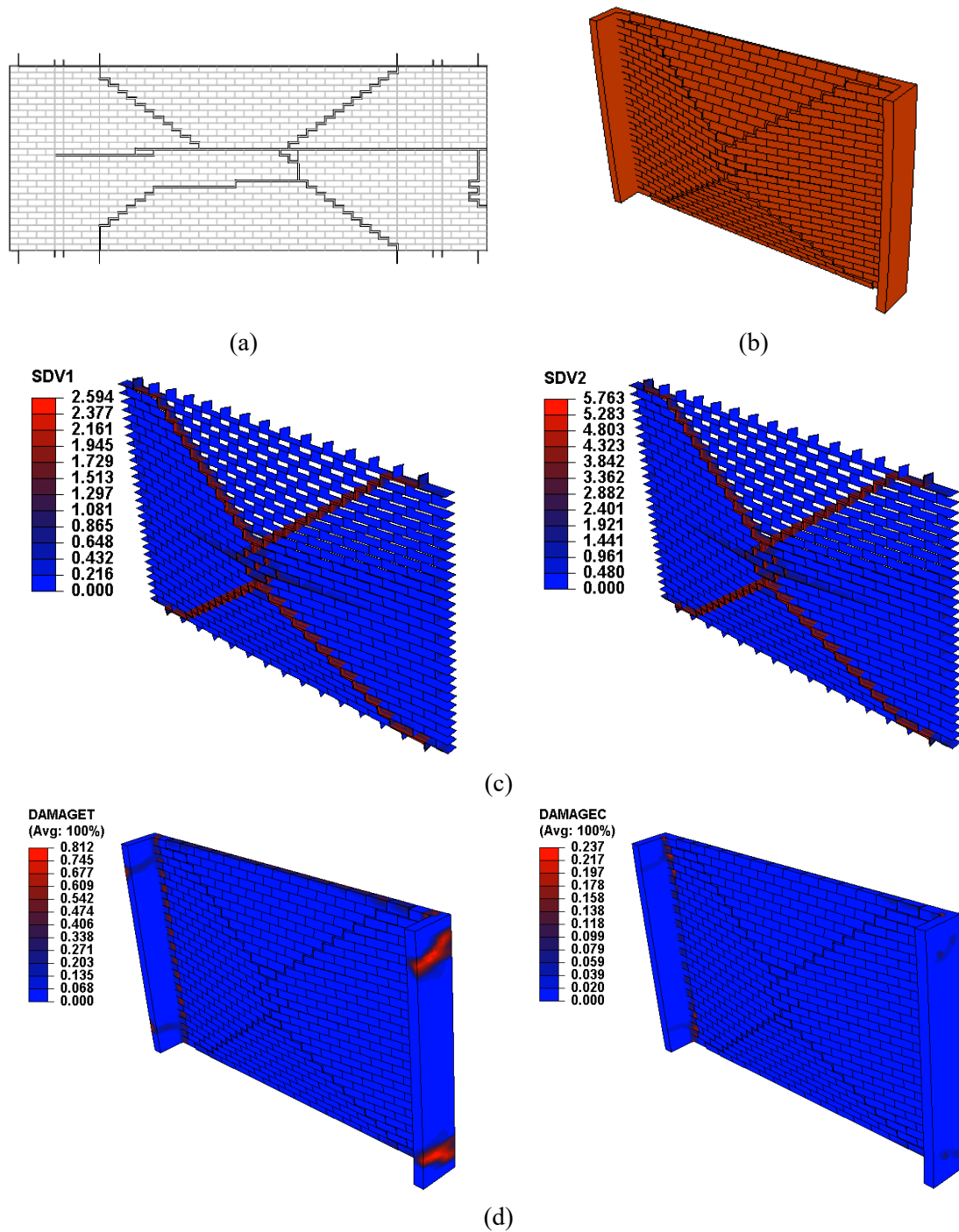


Figure 4-16. Comparison of crack pattern for Wall s2: (a) experimental tests (Vaculik 2012), (b) deformed shape from FE simulation, (c) equivalent plastic displacements for mortar joints from FE simulation, and (d) tensile damage scalar (DAMAGET) and compressive damage scalar Note: SDV1, SDV2, SDV3 represent the equivalent plastic displacements for tension, shear, and compression (i.e., κ_1 , κ_2 , κ_3), respectively (DAMAGEC) plots for units from FE simulation

4.4.4. RM walls under IP loading

Three RM walls (W-Ref, W- ρ_h0 , W- $\sigma_n1.5$), tested under IP loading (Seif Eldin 2016; Seif Eldin and Galal 2017), are simulated using the FE modeling scheme mentioned above. They had dimensions of 1.8 m (length) \times 1.6 m (height) \times 0.19 m (thickness). Concrete masonry units had standard dimensions of 390 mm \times 190 mm \times 190 mm. The RM walls W-Ref and W- $\sigma_n1.5$ were vertically reinforced with 20M bars (with a 300 mm² cross-section area) in each cell and horizontally reinforced with uniformly distributed 10M bars (with a 100 mm² cross-sectional area) spaced at 400 mm. The corresponding horizontal and vertical reinforcement ratios were 0.13% and 0.79%, respectively. On the other hand, W- ρ_h0 had a same vertical reinforcement ratio but did not have horizontal reinforcements. Note that the tested walls were designed with sufficient vertical reinforcements to fail in diagonal shear, thus eliminating possible sliding failure. A uniformly distributed pre-compression pressure load of 1.0 MPa was applied to the W-Ref and W- ρ_h0 , while W- $\sigma_n1.5$ was subjected to a pre-compression load of 1.5 MPa. The pre-compression loads were applied in a force-controlled manner and were kept constant throughout the testing procedure, followed by displacement-controlled IP loads until the wall failures. An automated load increment control scheme is used in the FE model. The sensitivity of mesh (or element size) is investigated until convergence of load-deformation behavior is achieved. This leads to an optimal mesh size of $8 \times 4 \times 5$ for one single concrete unit.

According to the experimental program loading (Seif Eldin 2016; Seif Eldin and Galal 2017), the compressive strengths of the concrete block units and grout were $f_{u,c} = 16.7$ MPa and $f_{g,c} = 29.4$ MPa, respectively. The steel reinforcements have an elastic modulus of $E_s = 196$ GPa, a yield strength of $f_y = 430$ MPa, and an ultimate strength of $f_u = 536$ MPa with an ultimate strain

of 0.2. Additionally, the compressive strength of masonry f_{mc} is 13.1 MPa as per the prism compression test, and the flexural tensile strength of masonry along the weak axis is $f_{mt} = 1.8$ MPa. These key properties reported in the tests are summarized here and used as the basis for determining other modeling parameters with reference to the literature. It is noted that the values of stiffness constants for interfaces are calibrated so that the initial stiffness of load-deformation curve is consistent with the experimental one. Moreover, the compressive-related properties (e.g., compressive strength) presented in Table 4-5 represent the composite behavior of masonry, instead of mortar material. Thus, compressive strength of masonry is used as the compressive strength in the constitutive model for interfaces, following the well-established practice when using the simplified micro modeling strategy (Abdulla et al. 2017; Kumar and Barbato 2019; Lourenço 1996). All parameters are detailed in Table 4-4 and Table 4-5.

Table 4-4. Material parameters of concrete block units, grouts, and reinforcements

Material	Parameter	Value	
		IP (Seif Eldin 2016)	OOP (Hamid and Abboud 1989)
Concrete block unit	Elastic modulus E_u (MPa)	938 $f_{u,c}$ (Barbosa et al. 2010)	
	Tensile strength $f_{u,t}$ (MPa)	0.09 $f_{u,c}$ (Barbosa et al. 2010)	1.93 (Hamid and Abboud 1989)
	Compressive strength $f_{u,c}$ (MPa)	16.7 (Seif Eldin 2016)	20.13 (Hamid and Abboud 1989)
Grout	Elastic modulus E_g (MPa)	500 $f_{g,c}$ (TMS 2016)	
	Tensile strength $f_{g,t}$ (MPa)	0.24 $f_{g,c}$ (Calderón et al. 2019)	
	Compressive strength $f_{g,c}$ (MPa)	29.4 (Seif Eldin 2016)	38.54 (Hamid and Abboud 1989)
Vertical Reinforcement	Elastic modulus E_s (GPa)	196/196 (Seif Eldin 2016)	174/207 (Wall1) (Hamid and Abboud 1989)
	Yield strength f_y (MPa)	430/430 (Seif Eldin 2016)	460/547 (Wall 1) 448/547 (Wall 4) 436/547 (Wall (Hamid and Abboud 1989)
	Ultimate strength f_u (MPa)	536/536 (Seif Eldin 2016)	758/724 (Hamid and Abboud 1989)
	Ultimate strain ϵ_u	0.2/0.2 (Seif Eldin 2016)	0.125/0.117 (Hamid and Abboud 1989)
	Horizontal Reinforcement	Elastic modulus E_s (GPa)	196 (Hamid and Abboud 1989)
	Yield strength f_y (MPa)	430 (Hamid and Abboud 1989)	547 (Hamid and Abboud 1989)
	Ultimate strength f_u (MPa)	536 (Hamid and Abboud 1989)	827 (Hamid and Abboud 1989)
	Ultimate strain ϵ_u	0.2 (Hamid and Abboud 1989)	0.117 (Hamid and Abboud 1989)

Table 4-5. Material parameters of mortar joints (interfaces) used in the FE model

Parameter	Value (Reference)	
	IP (Seif Eldin 2016)	OOP (Hamid and Abboud 1989)
Stiffness constants k_{mm}, k_{ss}, k_{tt} (N/mm ³)	75, 50, 50 (Calibrated)	26, 7, 7 (Calibrated)
Tensile strength f_t (MPa)	$f_t = f_{mt} / 3$ (Li and Zeng 2023)	
Peak cohesion c_0 (MPa)	$1.4 f_t$ (Lourenço 1996)	
Mode I fracture energy G_I (N/mm)	$0.01571 f_t + 0.0004882$ (Isfeld et al. 2021)	
Mode II fracture energy G_{II}^0 (N/mm)	$10 G_I$ (Lotfi and Shing 1994)	
Initial/Residual frictional coefficient $\tan \phi_0 / \tan \phi_r$	0.7 (Canadian Standards Association 2014; Mavros 2015)	
Initial/residual dilation coefficient $\tan \psi_0 / \tan \psi_r$	0 (Li and Zeng 2023)	
Compressive strength of masonry f'_m (MPa)	13.1 (Seif Eldin 2016)	14.1 (Hamid and Abboud 1989)
Initial/intermediate/residual compressive yield strength $\sigma_c^i, \sigma_c^m, \sigma_c^r$ (MPa)	$0.25 f'_m, 0.55 f'_m, 0.143 f'_m$ (Li and Zeng 2023)	
Controlling displacements κ_3^p, κ_3^m (mm)	$f'_m / k_{mm}, 5 \kappa_3^p$ (Li and Zeng 2023)	

Figure 2 illustrates the comparisons of experimental and FE-predicted IP load-displacement curves. The ‘IP displacement’ represents the deformation in the horizontal direction. Overall, the FE simulations capture the load-deformation behaviors of the walls well when compared with the experimental results, particularly concerning the wall capacities. Compared to the tested IP capacities of 418 kN, 365 kN, and 458 kN for these three walls, the FE-predicted IP capacities are (i.e., 426 kN, 364 kN, and 450 kN) indicated errors of 1.9%, 0.3%, and 1.6%, respectively. Note that the onset of stiffness degradation, caused by the flexural cracking at the bed joints, and the yielding of vertical reinforcements were not accurately captured. This could be attributed to the perfect bond assumption for vertical reinforcements. However, the diagonal tension cracking observed in the tested wall is also well predicted, as demonstrated in Figure 3. Severe diagonal cracking can be observed in the top right corner for both the experimental test and the FE simulation results.

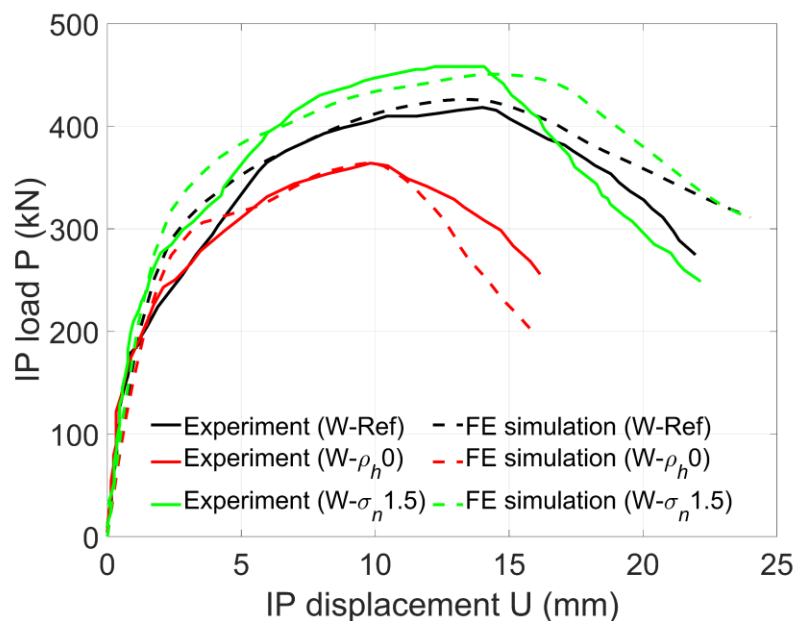
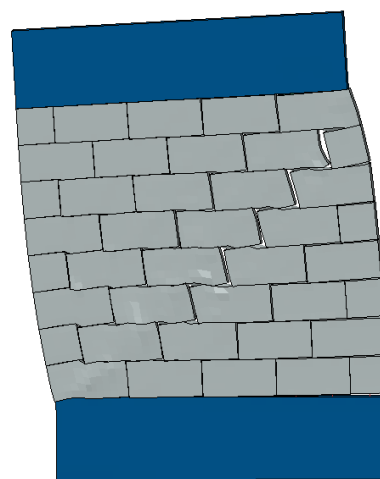


Figure 4-17. Experimental and FE-predicted load-deformation curves for the RM wall under IP loading



(a)



(b)

Figure 4-18. Comparison of the failure mode of the RM wall under IP loading: (a) experiment (Seif Eldin 2016) and (b) FE simulation for W-Ref

4.4.5. RM walls under OOP loading

Three RM walls (W1, W4, and W6) tested under OOP loading in the TCCMAR research program (Hamid and Abboud 1989) are modeled to validate the capability of the modeling strategy

mentioned above. The RM walls were fully grouted, 3 units long and 13 courses high, with dimensions of 1.2 m (length) \times 2.6 m (height) \times 0.193 m (thickness). The concrete masonry units used in the tests were 393 mm long, 193 mm high, and 193 mm wide. These RM walls were tested with simple supports at the bottom and top in a four-point bending manner. The vertical reinforcement configurations of three walls are different: Two No. 5 rebars (with a 200 mm² cross-section area), No.4 rebars (with a 129 mm² cross-section area), and No.7 rebars (with a 387 mm² cross-section area) were used for Wall 1, Wall 4, and Wall 6, respectively. The vertical reinforcements were placed at a spacing of 610 mm, and No. 3 rebars (with a cross-section area of 71 mm²) were used every third course to provide a minimum horizontal reinforcement ratio of 0.07% for all three walls. Two equal line loads ($P + P$) were applied to the face of the wall panels at the two third points to provide a pure bending zone in the middle region, as shown in Figure 4-19. All required material parameters are summarized in Table 4-4 and Table 4-5.

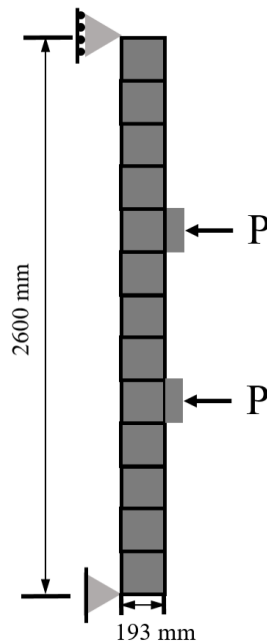


Figure 4-19. Tested RM wall under OOP loading

Figure 4-20 presents the comparisons of the experimental and FE-predicted OOP load-displacement curves. It is worth mentioning that the OOP load in Figure 4-20 represents the point load ‘P’ in Figure 4-19, and the OOP displacement was measured at the mid-height position. The OOP load capacities obtained through FE simulations are 13.54 kN, 7.82 kN, and 20.3 kN for W1, W4, and W6, respectively. Compared to the experimental tested capacities (13.31 kN, 7.79 kN, 19.42 kN), the FE simulation results indicate relative errors of 1.7%, 0.39%, and 4.5%. The OOP deformation for W1 corresponding to the peak OOP load is shown in Figure 4-21, with the largest crack openings concentrated at the two load application locations. Overall, the FE model is capable of predicting the OOP behavior of RM walls well, particularly the load capacity of primary interest in this study.

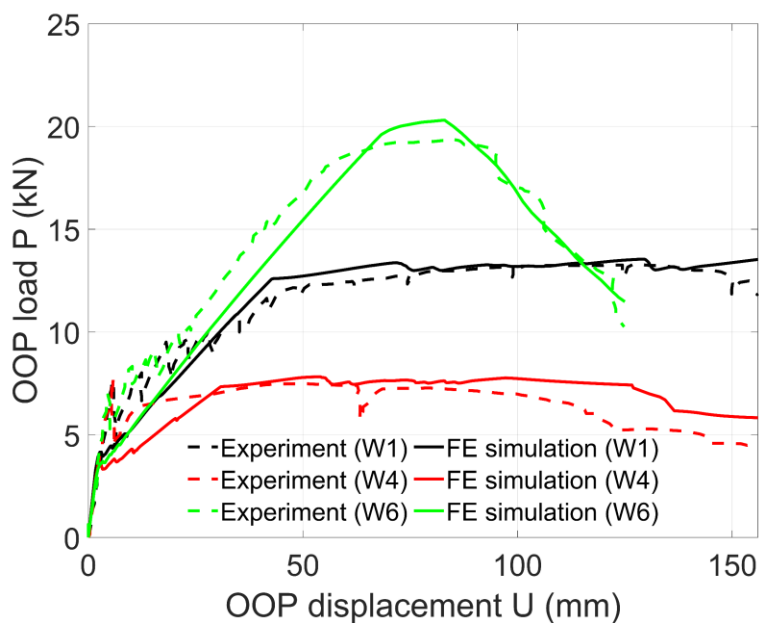


Figure 4-20. Experimental-numerical comparison of load-displacement curve of RM walls under OOP loading

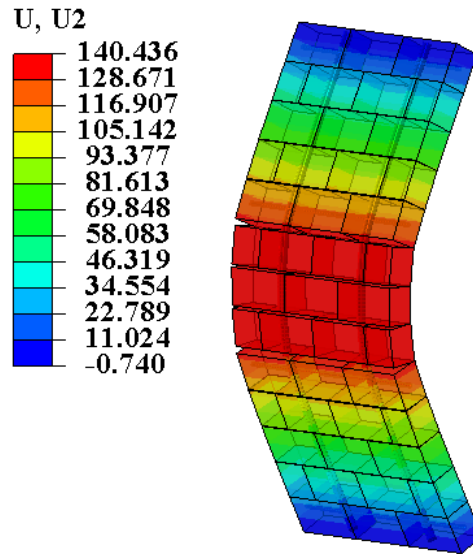


Figure 4-21. OOP deformation (mm) of RM wall at the peak OOP load stage

4.5. COMPARISON BETWEEN THE DEVELOPED MODEL AND OFF-THE-SHELF MODELING TECHNIQUES

The off-the-shelf modeling technique for simulating mortar joints presented in Chapter 3, namely contact-based cohesive surfaces, demonstrates satisfactory performance in certain scenarios. However, there are some limitations associated with this technique. Firstly, the modified Mohr-Coulomb criterion would lead to an underestimation of shear strength, particularly under high pre-compressive load. Secondly, the micromechanical phenomenon of ‘dilatancy’, as previously discussed, is not accounted for. More critically, the unloading behavior is inadequately addressed, characterized by stiffness degradation and irreversible deformation. However, the material modeling of contact-based cohesive surfaces in ABAQUS adheres to a general damage-based computational mechanics framework, within which these characteristics are not well interpreted. A detailed discussion on cyclic modeling will be presented in Chapter 5, while this section will compare the simulation results obtained by the off-the-shelf modeling technique and the one developed in this chapter.

Two examples are included in this section: one masonry triplet under compressive-shear loading tested by Hatch (2009), and one URM wall under IP loading tested by da Porto (2005). These two examples are selected here to show the effects of strength criterion employed in the off-the-shelf modeling technique and the developed model. The shear displacement curve for the masonry triplet and the IP load-deformation curve are shown in Figure 4-22 (a-b), respectively. It can be seen that the built-in model underestimates the shear strengths for both examples. As discussed earlier, this is mainly due to the modified Mohr-Coulomb strength criterion employed in the built-in model. This effect is more evident in the cases with high compressive loads. Conversely, the developed model utilizes a Mohr-Coulomb criterion, providing an accurate estimation.

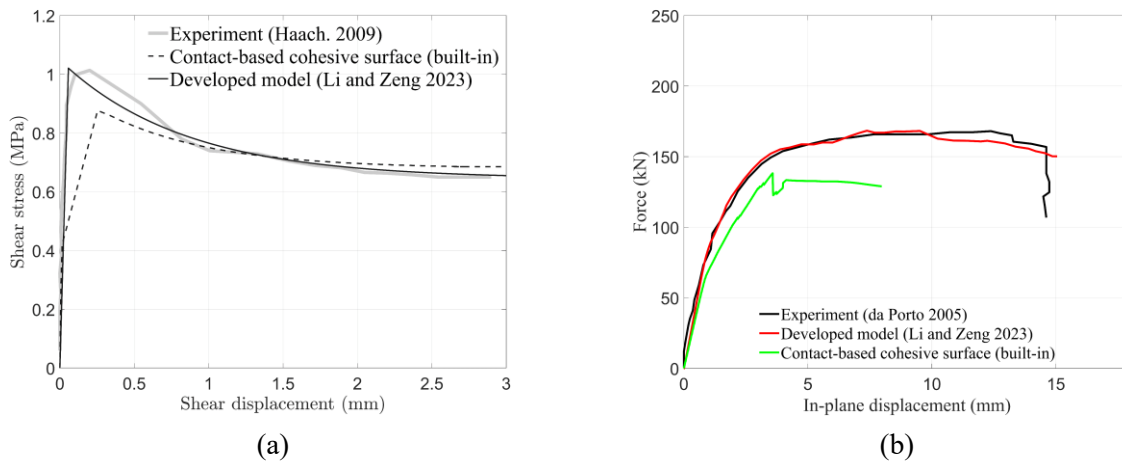


Figure 4-22. Experimental-numerical comparison for (a) masonry triplet, and (b) masonry wall under IP loading

4.6. CHAPTER CONCLUSIONS

A newly developed 3D constitutive material model for mortar joints in masonry structures was presented in this chapter. This plasticity-based model was featured with (1) two hyperbolic yield surfaces capable of capturing various failure modes (i.e., tensile cracking, shear sliding,

compressive crushing) of mortar joints; (2) an unassociated flow rule to capture the ‘dilatancy’ phenomenon in the mortar joints; and (3) dilatancy softening and variation of model II fracture energy under different normal stress levels. The newly developed model was implemented in the commercial FE software ABAQUS using a fully implicit Euler Backward integration algorithm, enhanced with an error-based adaptive sub-stepping strategy. This empowers the general-purpose FE software ABAQUS with the specialized capability of modeling masonry structures, considering complex mechanisms under different loading and boundary conditions.

The developed constitutive material model was validated against the experimental results at both assemblage and wall component levels. Three unit-mortar-unit assemblages tested in the literature were simulated. Results indicated that the stress-displacement response and volume increase/specimen uplift under compression-shear loading were both well captured. Three unreinforced masonry walls tested under in-plane and out-of-plane loading were simulated as well. Reasonable agreement was achieved in terms of initial stiffness, in-plane/out-of-plane capacity, and post-peak behavior, as well as the damage patterns.

Particularly, the effect of the dilatancy model on the simulated load-displacement curves was discussed. The simulation results indicated that considering dilatancy without softening led to a considerable overestimation of IP or OOP capacity, while a constant zero dilatancy led to an underestimation of masonry wall capacities. In contrast, the simulation results obtained by the proposed model with dilatancy softening had the best predictability when compared with the experimental results.

It is worth mentioning that very limited experimental studies exist for the characterization of dilatancy in the mortar joints in public literature. Moreover, different testing methods (e.g.,

triplet test, shove test, core test) may result in different results about dilatancy. The study of uncertain dilatancy-related parameters in the proposed constitutive material model and their importance on the masonry wall behavior prediction requires further investigation. The developed constitutive model with dilatancy softening, which is more realistic, can be potentially used in this regard.

Chapter 5. DEVELOPMENT OF A DAMAGE PLASTICITY-BASED 3D MULTI-YIELD SURFACES CONSTITUTIVE MODEL FOR MASONRY MORTAR JOINTS UNDER CYCLIC LOADING

The mechanical behavior of mortar joints can be described by means of the cohesive interface element in the mesoscale modeling of masonry structures. In this chapter, a novel 3D constitutive model for the cohesive interface element under cyclic loading is presented. The proposed constitutive model is formulated in the damage-plasticity theoretical framework with the following unique features: (1) two smooth hyperbolic yield surfaces capable of capturing various failure modes of mortar joints; (2) two damage scalars D_t and D_c to characterize the stiffness degradation; (3) two damage functions $\xi_t(D_t)$ and $\xi_c(D_c)$ to describe the strength softening; and (4) an unassociated flow rule to capture the dilatancy behavior. The proposed constitutive model is implemented in the general-purpose Finite Element package ABAQUS using the user subroutine UMAT. The developed model is first validated at the masonry component level, through a mortar-jointed specimen under indirect cyclic tensile loading and three masonry couplets under compressive-shear loading, and then at the structural level through two unreinforced masonry walls characterized by two distinct failure modes. The validation results show that the developed constitutive model is capable of modeling mortar joints and masonry structures with good performance.

5.1. INTRODUCTION

Masonry, mainly composed of units and mortar layers, is one of the oldest construction materials and is still widely used in engineered structures due to its durability, energy efficiency, and fire resistance. However, masonry structures are sensibly vulnerable to earthquake excitations,

particularly unreinforced masonry walls. Compared to modern reinforced concrete and steel structures, unreinforced masonry structures are susceptible to a high level of damage even in light seismic events (Algoi 2013). The composite nature and induced complex failure modes pose a significant challenge when predicting the nonlinear mechanical behavior of masonry structures against cyclic seismic loading. With the advent of high computational technologies and resources, finite element (FE) simulation has emerged as a viable alternative and gained more and more popularity in the masonry community. The structural evaluation of masonry under complex loading conditions can be performed through a FE-based framework.

FE modeling approaches for masonry structures can be roughly categorized as the macro modeling approach and the micro modeling approach (Lourenço et al. 1995a) depending on the different levels of sophistication and simplification. The macro modeling approach can be further subdivided into the macro element approach (Addessi et al. 2014; Chen et al. 2008; Di Trapani et al. 2018) and the macro block-based approach (Addessi et al. 2021; Lourenço 2000b; Zucchini and Lourenço 2004). The macro modeling approach, in which the masonry is treated as a fictitious homogeneous material with a uniform stress-strain relationship, is more applicable to large-scale masonry structures due to its computational efficiency. However, the local failure behavior (i.e., damage and cracking) of masonry structures cannot be adequately addressed by the macro model. In contrast, in the micro modeling approach, units and mortar are represented by the solid continuum, while the contact surfaces between the units and mortar are modeled by the discontinuous cohesive interface elements. As such, the micro modeling approach allows a more generic representation of masonry structure at the mesoscale. Although it requires a higher computational demand, the micro modeling approach can capture the complicated crack patterns

of masonry structures under complex loadings. Recently, the concept of simplified micro modeling was proposed and widely adopted by researchers (Lotfi and Shing 1994; Macorini and Izzuddin 2011). In this approach, mortar layer and block-mortar contact surfaces are lumped into mortar joints modeled by zero-thickness interface elements. As a result, the number of interface elements considered in the simplified micro model was decreased, resulting in a reduced computational cost. Meanwhile, the failure modes of masonry structures under various loading scenarios can be described with a high degree of accuracy. Therefore, the simplified micro modeling strategy will be employed in this section.

In the simplified micro modeling strategy, particular interest lies in the constitutive model of cohesive interface elements for mortar joints, which are the primary sources of structural weakness and material nonlinearity. The material formulations of cohesive interfaces should account for all possible failure modes observed in the experimental tests, such as tensile cracking, shear sliding, and compressive crushing. Pioneering works to apply the cohesive interface elements to simulate the cracking behavior of masonry structures were from Rots (1991). Later, Lotfi and Shing (1994) developed a 2D interface model characterized by a three-parameter hyperbolic yield criterion that provided a smooth transition between the Mohr-Coulomb and tension cut-off yield criteria, validated by the tested small-scale masonry specimens and unreinforced concrete masonry panels. Lourenco and Rots (1997) made the first attempt to include a compression cap surface in the constitutive material model of interface elements to represent the compression crushing behavior of masonry composite, and the proposed interface model was implemented in a multi-yield surfaces plasticity framework. Recent efforts have been devoted to the better applicability of interface elements to masonry structures. Giambanco et al. (2001)

adopted an asperity model in the numerical formulation that can describe the evolution of the block-mortar contact surface shape during the loss of cohesion. Carol et al. (2001) formulated a 2D interface model conforming to work-softening elastoplastic theory, and a sub-stepping scheme was utilized to reduce the integration errors in the implementation procedure. Carol's model (Carol et al. 2001) was later extended to 3D space by Caballero et al. (2008). Macorini and Izzuddin (2011) employed a co-rotational approach for the interface element formulation, which shifts the treatment of geometric non-linearity to the level of discrete entities and enables the consideration of material non-linearity within a simplified local framework.

The constitutive material models for the cohesive interface element discussed above were based on plasticity theory and demonstrated good potential for the modeling of masonry structures under monotonic loading. These models, however, have a significant drawback when dealing with repeated loading-unloading conditions: the stiffness degradation effects cannot be well accounted for. To this aim, Oliveira and Lourenco (2004) improved the interface model proposed in (Lourenço 1996; Lourenço and Rots 1997) and introduced two auxiliary yield surfaces during the unloading process. Although the stiffness reduction effects were captured, a total of six possibilities for unloading and reloading movements resulted in a complex implementation framework. Aref and Dolatshahi (2013) developed a 3D plasticity-based interface model within the explicit integration procedure, and the stiffness degradation was considered in the positive normal direction using a single scalar in a simplified manner. Koutromanos and Shing (2012) adopted a modified elastoplastic formulation to simulate the cyclic response of joints for concrete and masonry structures; however, the gradual decrease in unloading stiffness was not accurately modeled.

In addition to the plasticity-based framework, damage mechanics theory has also been applied to formulate the constitutive material model for cohesive interface elements. Parrinello et al. (2009) proposed an interface constitutive model, which couples a cohesive behavior based on the damage mechanics with a frictional one defined in a non-associated plasticity framework. D'Altri et al. (2019) developed a damaging block-based model for the numerical analysis of the cyclic behavior of masonry structures. For the modeling of mortar joints, the cohesive-frictional contact-based formulation is adopted with an elastic-damage procedure assumed in the tensile regime, while the stiffness degradation is neglected in the compressive regime. Similar numerical simplification methods can be found in (Gambarotta and Lagomarsino 1997a; Sacco and Lebon 2012). However, the aforementioned pure damage-based models result in the absence of irreversible deformation (i.e., the unloading curve is pointing to the origin), which appears contradictory to the experimental findings for quasi-brittle materials, e.g., concrete (Gopalaratnam and Shah 1985), mortar (Jefferson and Mills 1998).

As discussed above, general plasticity-based models are incapable of capturing the stiffness degradation observed in experimental results, whereas pure damage-based models are inadequate for describing irreversible deformation. Furthermore, the inelastic volumetric expansion of mortar joints under compression caused by the dilatancy effects cannot be accounted for with pure damage theory. Consequently, the combination of plasticity and damage might be an effective approach to modeling the cyclic behavior of mortar joints. This framework has gained popularity for the macroscopic modeling of quasi-brittle materials (Comi and Perego 2001; Grassl et al. 2013; Jason et al. 2006; Lee and Fenves 1998). However, its applications on the cohesive interface for the modeling of mortar joints are rare, and each has its own limitations (Minga et al. 2018; Nie et al.

2022b; a; Yuen et al. 2019). Minga et al. (2018) introduced stiffness degradation via an anisotropic damage tensor based on the evolution of plastic work produced. However, a simplified multi-surface plasticity criterion with two flat yield surfaces (i.e., compressive cap and tension cut-off) was employed, in which two sharp singularity corners could possibly result in a convergence issue. Yuen et al. (2019) presented a fracture-energy based damage-plasticity model in the explicit Euler integration scheme. Thus, a sufficient small loading increment is required to guarantee numerical accuracy. More recently, Nie et al. (2022b; a) proposed two interfacial damage-plasticity based models for mortar joints characterized by a smooth hyperbolic yield surface. However, the failure mode associated with compressive crushing was not considered, leading to a possible overestimation of the masonry wall's capacity.

To this end, a novel 3D cohesive interface constitutive model for the cyclic modeling of mortar joints was developed (i.e., formulated, implemented, and validated) in this chapter. The proposed model followed the damage-plasticity framework with two yield surfaces characterizing different failure modes (i.e., tension cracking, shear sliding, compressive crushing). Two damage scalars, D_t and D_c , are introduced, associated with two yield surfaces, respectively. Both damage and plasticity, and their coupling, are considered in a unified form of loading function. The formulation, together with the numerical implementation, is presented in detail. The capability of the proposed model was validated against several experimental tests, including an indirect tensile test on the mortar-jointed cylinder specimen, masonry couplets under compressive-shear loading, and two URM walls under in-plane loading with different aspect ratios.

5.2. CONSTITUTIVE MODEL FORMULATION

In the simplified micro modeling strategy, the zero-thickness interface element represents the compound mechanical behavior of mortar joints, including mortar and unit-mortar interactions. Relevant experimental and numerical works (Atkinson et al. 1989; Gopalaratnam and Shah 1985; Jefferson and Mills 1998; Lourenço 1996; Lourenco and Ramos 2004; Oliveira 2003; Reinhardt 1984) indicated that cyclic behavior modeling of mortar joints should consider the following crucial aspects: 1) strength softening in both normal (i.e., in tension and compression) and shear loading scenarios; 2) normal stiffness degradation under both tension and compression loading regimes; 3) residual shear strength under compressive-shear loading; 4) unchanged shear stiffness under compressive-shear loading; and 5) stiffness recovery in the normal direction as a result of crack closure from tension to compression loading conditions. The proposed model in this chapter tackles all these aspects based on a rational formulation, as detailed below.

5.2.1. Coupling of plasticity and damage

Plasticity-based models are typically developed by defining yield criteria to bound elastic domains in the stress space, compounded with plastic strain-dependent softening and hardening laws, as shown in Figure 5-1 (a). The plasticity-based models generally show good potential to describe the irreversible deformation upon loading. On the contrary, damage-based models are not suitable for the description of irreversible deformations but reproduce the stiffness degradation well shown in Figure 5-1 (b). With plasticity or damage mechanics alone, the complex failure process of mortar joints, characterized by stiffness degradation and irreversible deformations, cannot be satisfactorily modeled. Thus, a combination of plasticity and damage mechanics, for example, see Figure 5-1 (c), might be a possible solution.

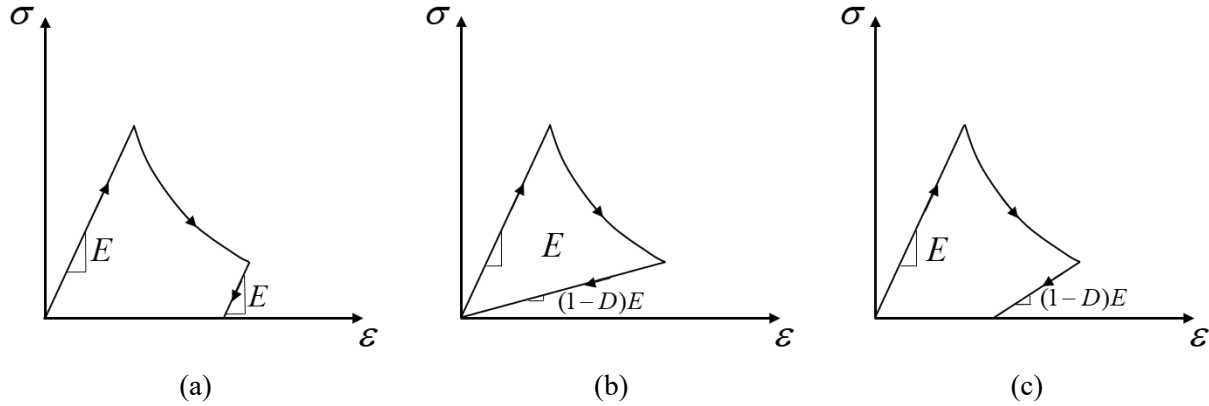


Figure 5-1. Constitutive material ($\sigma - \varepsilon$) relationship in different computational frameworks: (a) plasticity-based, (b) damage-based, and (c) damage plasticity-based

Plasticity with hardening and/or softening, enriched by various damage evolution laws, constitutes the basic theoretical framework of damage-plasticity models. Two general approaches have been developed to couple plasticity and damage in stress-based constitutive models. In the first type of damage-plasticity models, yield functions are expressed in terms of the effective stress; see for instance (Grassl et al. 2013; Grassl and Rempling 2008; Lee and Fenves 1998; Minga et al. 2018; Simo and Ju 1987a; b). In this context, effective stress is meant as the average stress acting in the undamaged area between defects, defined as force divided by the undamaged part of the area. As such, plastic effects, governed by the effective stresses, are described separately from damage effects and vice versa. The other group of material models is formulated in the nominal stress space, also termed the ‘strong coupled damage-plasticity’ model (Jason et al. 2006). Here, the nominal stress is defined as force divided by the total area. Relevant numerical implementations can be found in (Luccioni et al. 1996; Nguyen 2005; Salari et al. 2004). The damage is implicitly embedded in the yield and plastic criteria, and a strong coupling between plasticity and damage is achieved through a simultaneous solution of the plastic and damage problems. In this chapter, the latter approach is adopted considering the fact that stiffness

degradation and plastic displacement in the mortar joints generally occur simultaneously. As a result, the damage effects are explicitly embedded in the plastic yield criteria, leading to one single loading function for plasticity and damage.

5.2.2. Traction-separation relationship

The configuration of the 3D 8-node zero-thickness interface element available in ABAQUS (Dassault Systemes 2017) is illustrated in Figure 5-2. The constitutive relationship of zero-thickness interface elements is expressed in terms of the traction-separation relationship, relating the three stress components to relative displacements between top and bottom surfaces in three directions (i.e., one normal direction n , the first tangential direction s , the second tangential direction t shown in Figure 5-2). In the proposed model, the traction-separation law is given in Eq. (5-1):

$$\begin{bmatrix} \sigma_n \\ \tau_s \\ \tau_t \end{bmatrix} = \begin{bmatrix} 1-D & 0 & 0 \\ 0 & 1-D & 0 \\ 0 & 0 & 1-D \end{bmatrix} \begin{bmatrix} k_{nn} & 0 & 0 \\ 0 & k_{ss} & 0 \\ 0 & 0 & k_{tt} \end{bmatrix} \begin{bmatrix} \langle u_n - u_{n,1}^p \rangle - \langle u_{n,2}^p - u_n \rangle \\ u_s - u_s^p \\ u_t - u_t^p \end{bmatrix} \quad (5-1)$$

where $\langle \rangle$ represents the Macaulay bracket, i.e., $\langle x \rangle = (|x| + x) / 2$. σ , u , u^p , and k are used together with the subscripts n , s , and t , denoting the stress component, displacement jump, plastic displacement, and initial stiffness constant under undamaged conditions. nn , ss , and tt represent three mutually orthogonal directions in 3D space: normal, first tangential, and second tangential directions. Specially, the plastic displacements in the normal direction are distinguished by the tensile one ($u_{n,1}^p$) and the compressive one ($u_{n,2}^p$). Negative values of stress and (plastic) displacement components indicate that the cohesive interface is under compression, while positive

values correspond to the tensile regime. D is a damage scalar used to indicate the material degradation state, which takes the value from 0 to 1. $D = 0$ represents the material state where mortar joint behavior is in the elastic range without any damage, while $D = 1$ represents a fully damaged state where stiffness is completely degraded.

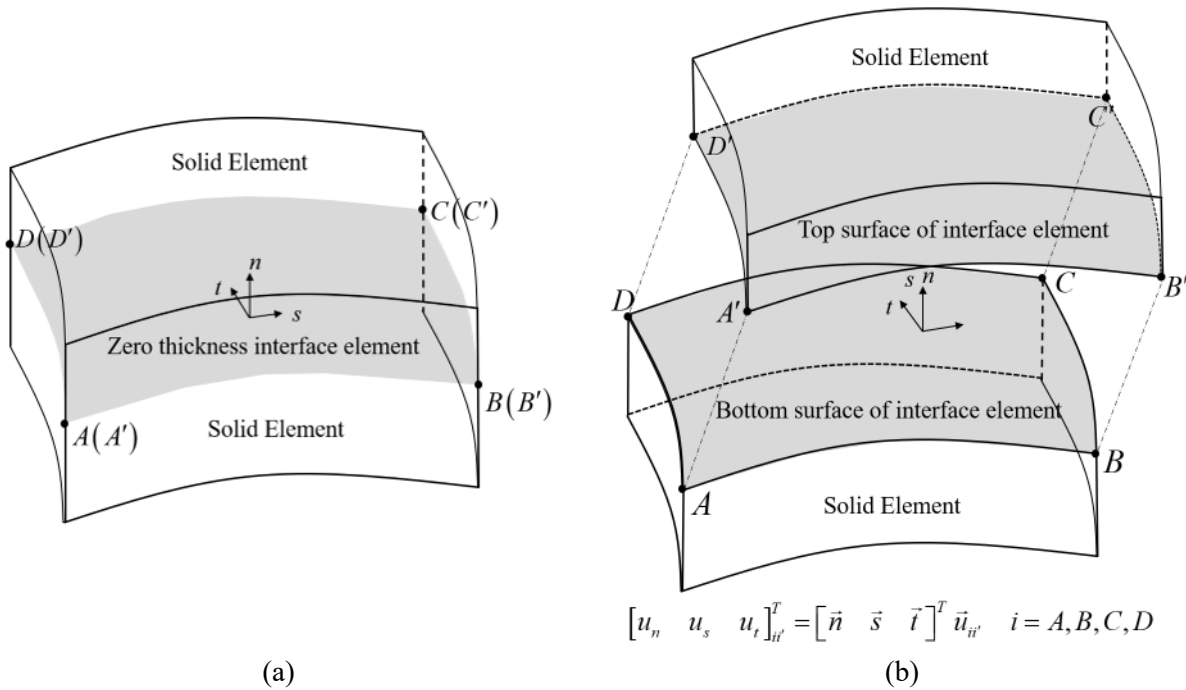


Figure 5-2. Illustration of 8-node zero-thickness interface element in the 3D space: (a) undeformed shape, and (b) deformed shape

The definition of normal stress σ_n in Eq. (5-1) allows distinguishing the tensile and compressive behaviors separately. The normal stress evolution with load-unloading-reloading is presented in Figure 5-3. With this definition, tensile and compressive stress can develop only upon crack opening (i.e., $u_n > u_{n,1}^p$) and closure (i.e., $u_n < u_{n,2}^p$), respectively. When the normal displacement is between two plastic displacements (i.e., $u_{n,1}^p \leq u_n \leq u_{n,2}^p$), the normal stress remains zero, as depicted in Figure 5-3 (a). The shear stress evolution differs in the tensile and compressive

regimes, as shown in Figure 5-3 (b) and Figure 5-3 (c), respectively. This is related to the failure mechanisms activated. Under tensile loading, shear failure is only related to the cohesion loss, while under compressive loading, both cohesion and frictional effects contribute to the shear resistance. With the increase of shear displacement, cohesion would eventually be exhausted but frictional effects still play an important role. Therefore, in the compressive regime, higher shear strength is expected, and the residual shear resistance exists (τ_{res}) even under large shear displacement, as shown in Figure 5-3 (c).

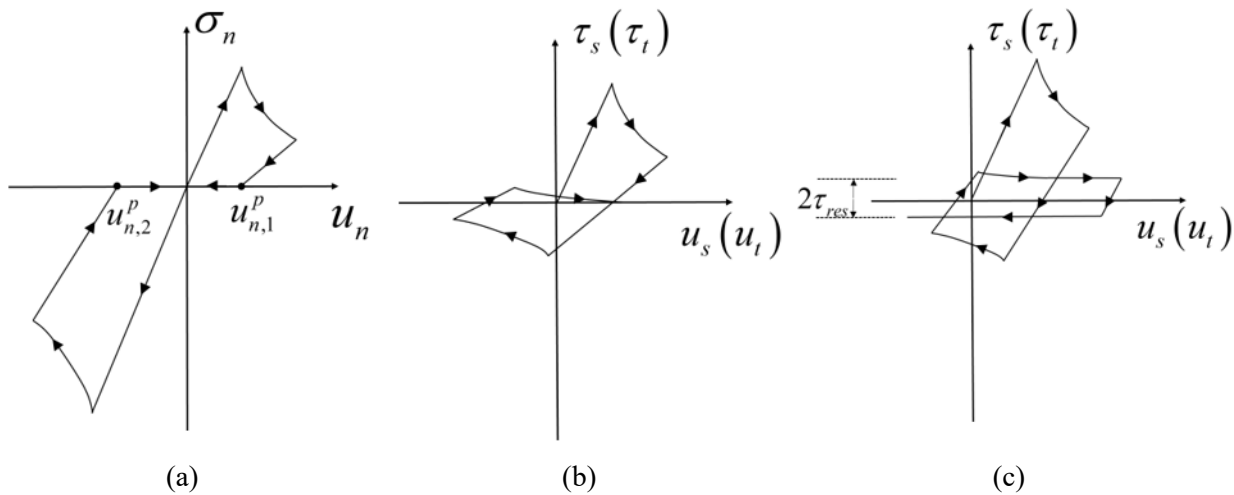


Figure 5-3. Stress evolutions of the proposed constitutive model: (a) normal stress evolution, (b) shear stress evolution ($\sigma_n \geq 0$), and (c) shear stress evolution ($\sigma_n < 0$)

The mechanism of stiffness degradation of mortar joints under cyclic loading is complex. Initial invisible microcracks induced by thermal expansion, shrinkage, and other factors would develop into noticeable cracks as the load increases. For typical quasi-brittle materials, e.g., mortar (Minga et al. 2018), concrete (Nguyen 2005), cement bond material (Senanayake et al. 2022), failure in compression (e.g., crushing of mortar) has significant effects on the tensile behavior. Conversely, tensile failure has limited influence on the compressive behavior due to the re-closure

of tensile crack up on load reversal from tension to compression. In order to consider this characteristic, two damage scalars (D_t and D_c) and two functions (s_t and s_c) related to the stress states are introduced to define the single damage scalar D in Eq. (5-1), as shown in Eq. (5-2):

$$(1 - D) = (1 - s_t D_c)(1 - s_c D_t) \quad (5-2)$$

In Eq. (5-2), D_t and D_c denote two damage scalars, ranging from 0 to 1, which describe the material deteriorations caused by tensile cracking and compressive crushing, respectively. As described earlier, mortar joints exhibit different stiffness behaviors in the tensile and compressive regimes. To achieve this, two functions s_t and s_c are introduced, reading Eq. (5-3) and Eq. (5-4), respectively:

$$s_t = 1 - \omega_t H(\sigma_n) \quad (5-3)$$

$$s_c = 1 - \omega_c (1 - H(\sigma_n)) \quad (5-4)$$

where ω_c and ω_t are two stiffness recovery factors ranging from 0 to 1, describing the compression-to-tension and tension-to-compression stiffness recovery effects, respectively. $H(x)$

is the Heaviside step function, defined as: $H(x) = \begin{cases} 1 & x \geq 0 \\ 0 & x < 0 \end{cases}$.

A typical case for mortar joints (Gatta et al. 2018; Koutromanos and Shing 2012; Oliveira and Lourenço 2004) is a complete stiffness recovery from tension to compression (i.e., $\omega_c = 1$) and no stiffness recovery from compression to tension (i.e., $\omega_t = 0$). In this case, by substituting Eq. (5-3) and Eq. (5-4) into Eq. (5-2), damage scalar D then becomes:

$$(1-D) = \begin{cases} (1-D_c)(1-D_t) & \sigma_n \geq 0 \\ (1-D_c) & \sigma_n < 0 \end{cases} \quad (5-5)$$

It can be seen from Eq. (5-5) that D_t has an influence on the material state only in the tensile regime, while D_c contributes to the stiffness degradation in both tension and compression. Figure 5-4 presents a full cycle of normal stress-displacement response corresponding to the case $\omega_c = 1$ and $\omega_t = 0$. The load path for the complete stiffness recovery case is $O-A-B-C-O-D-E-F-O-C-G-H$. Starting from Point O , tensile normal stress develops along the pre-peak path until Point A , which corresponds to the tensile strength, and the softening branch is subsequently followed with further loading (segment AB). On the tensile unloading branch (segment BC), the unloading stiffness has decreased compared with the initial one. Then, the normal stress remains zero until cracks fully close (segment CO). In the compressive regime, the stiffness fully recovers until reaching the compressive strength (Point D). After that, strength softening (segment DE) and stiffness degradation (segment EF) are followed due to compressive crushing. After a complete cycle, the stress state reverts to the tensile regime. The damage and plasticity deformation continue to accumulate in the next loading cycle (segment GH).

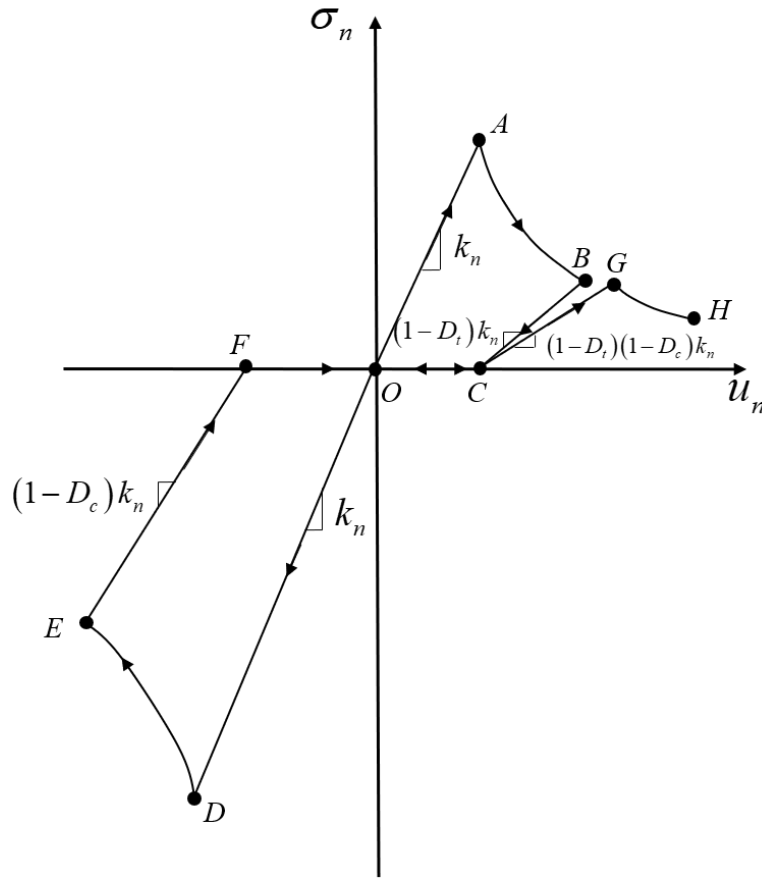


Figure 5-4. Normal stress evolution with stiffness recovery effects ($\omega_c = 1, \omega_t = 0$)

5.2.2.1 Multi-yield surfaces plastic criterion

The yield criterion is critical in determining the true stress state upon loading, aiming to capture material strength. In the proposed model, two yield criteria are introduced to consider different failure modes: tension-shear failure surface f_1 and compression cap failure surface f_2 , as shown in Figure 5-5 (a) and Figure 5-5 (b), respectively. The continuous and differentiable hyperbolic yield surface f_1 , initially proposed by Carol et al. (1997) to describe the concrete fracture at the meso-scale, provides a smooth transition between the Mohr-Coulomb surface and tension cut-off surface. This model was later refined by introducing a hyperbolic cap to describe the compressive

crushing failure mode (Li and Zeng 2023; Macorini and Izzuddin 2011). In this work, they are adjusted as Eq. (5-6) and Eq. (5-7) in a computational damage-plasticity framework:

$$f_1(\sigma_n, \sigma_s, \sigma_t, D_t) = -[c_0 \xi_t(D_t) - \sigma_n \tan \varphi] + \sqrt{\sigma_s^2 + \sigma_t^2 + [c_0 \xi_t(D_t) - f_t \xi_t(D_t) \tan \varphi]^2} \quad (5-6)$$

$$f_2(\sigma_n, \sigma_s, \sigma_t, D_c) = -[f_c + \sigma_n \tan \theta] + \sqrt{\sigma_s^2 + \sigma_t^2 + [f_c - ((f_c - f_r) \xi_c(D_c) + f_r) \tan \theta]^2} \quad (5-7)$$

where $\xi_t(D_t)$ and $\xi_c(D_c)$ are two damage functions characterizing strength softening. In the yield function f_1 , f_t and c_0 are the tensile strength and peak cohesion. $\tan \varphi$ denotes the frictional coefficient. In the yield function f_2 , f_c , and f_r are the peak and residual compressive strengths, respectively. $\tan \theta$ is the asymptote slope of compressive cap surface.

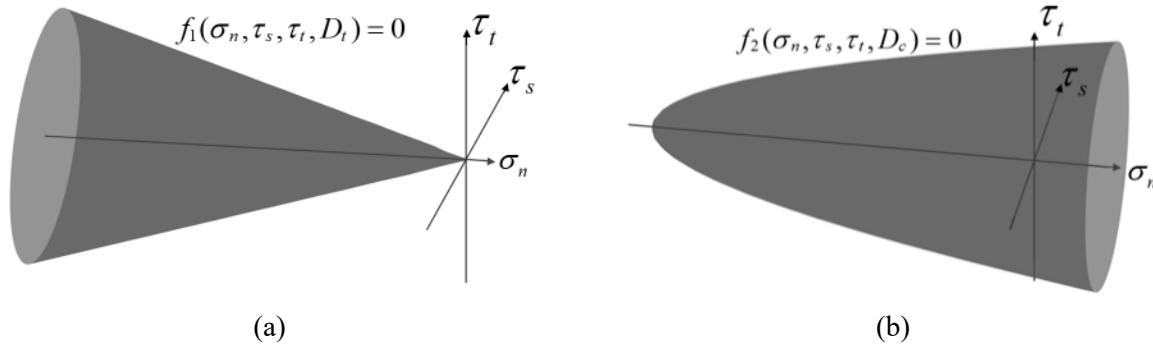


Figure 5-5. Yield surfaces of the proposed constitutive model: (a) tension-shear yield surface, and (b) compression-cap surface

The experimental findings (Lourenço 1996) indicate that the frictional coefficient $\tan \varphi$ would undergo a progressive softening during the plastic deformation process. The softening of frictional coefficient is coupled with damage function $\xi_t(D_t)$, given in Eq. (5-8):

$$\tan \varphi = (\tan \varphi_0 - \tan \varphi_r) \xi_t(D_t) + \tan \varphi_r \quad (5-8)$$

where $\tan \varphi_0$ and $\tan \varphi_r$ represent the frictional coefficients at the initial state and residual state, respectively.

As can be seen from Eq. (5-6), Eq. (5-7), and Eq. (5-8), $\xi_t(D_t)$ and $\xi_c(D_c)$ play an important role in the yield criteria. The special feature of $\xi_t(D_t)$ and $\xi_c(D_c)$ is that they are equal to one at an undamaged state. The yield surfaces then shrink as damage variables increase until the fully damaged state, corresponding to $\xi_t(D_t) = \xi_c(D_c) = 0$. More specifically, yield surface f_1 intersects the normal stress axis at $\sigma_n = f_t \xi_t(D_t)$ (when $\tau_s = \tau_t = 0$) in the tensile regime and asymptotically approaches the well-known Mohr-Coulomb strength criterion in the compressive regime. At a fully damaged state, tensile strength and cohesion would be fully exhausted. The yield surface f_1 then degrades to $f_1(\sigma_n, \tau_s, \tau_t, D_t) = \sigma_n \tan \varphi_r + \sqrt{\tau_s^2 + \tau_t^2}$. The yield surface f_2 intersects the normal stress axis at $\sigma_n = -(f_c - f_r) \xi_c(D_c) - f_r$: the absolute value of normal stress is equal to compressive strength f_c when $\xi_c(D_c) = 1$ and reduces to the residual strength f_r when $\xi_c(D_c) = 0$. The initial undamaged and ultimate fully damaged states of yield surfaces in the 3D space are schematically shown in Figure 5-6.

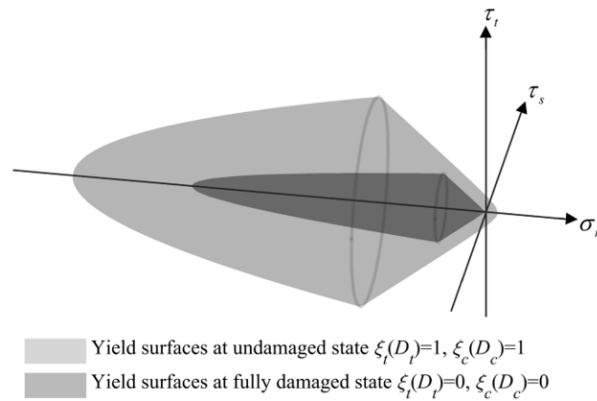


Figure 5-6. Evolution of yield surfaces in the 3D space

The formulation of $\xi_t(D_t)$ and $\xi_c(D_c)$ should satisfy the conditions that the values of $\xi_t(D_t)$ and $\xi_c(D_c)$ are 1 when $D_t = 0$ and $D_c = 0$ at the initial undamaged state, while at the fully damage state, $\xi_t(D_t)$ and $\xi_c(D_c)$ are equal to 0 when $D_t = 1$ and $D_c = 1$. To this aim, $\xi_t(D_t)$ and $\xi_c(D_c)$ are defined as Eq. (5-9) and Eq. (5-10), respectively:

$$\xi_t(D_t) = (1 - D_t)^{\eta_t} \quad (5-9)$$

$$\xi_c(D_c) = (1 - D_c)^{\eta_c} \quad (5-10)$$

where η_t and η_c are two positive constants, which can be calibrated based on the experimental data. The effects of η_t and η_c on the model behaviors are illustrated later.

5.2.2.2 Plastic flow rule

The definition of flow rule is crucial for a reasonable description of plastic deformation evolution. For the yield surface f_2 , an associated flow rule is assumed, i.e., plastic potential function $g_2 = f_2$. However, for the yield surface f_1 , a non-associated flow rule should be adopted for considering dilatancy effects as recognized in the relevant studies (Li and Zeng 2023; Nie et al. 2022b). The plastic potential function g_1 is defined as Eq. (5-11):

$$g_1(\sigma_n, \tau_s, \tau_t, D_t) = -[c_q \xi_t(D_t) - \sigma_n \tan \psi] + \sqrt{\tau_s^2 + \tau_t^2 + [c_q \xi_t(D_t) - f_t \xi_t(D_t) \tan \psi]^2} \quad (5-11)$$

where c_q is the apparent cohesion, $\tan \psi$ is the tangent of dilatancy angle ψ (i.e., dilatancy coefficient). Based on the experimental observations (Andreotti et al. 2019; Jafari et al. 2020; Pluijm 1999), dilatancy angle ψ reduces from the initial value to the residual one with the increase of plastic shear displacements and compressive normal stress (absolute value). The evolution law

for the dilatancy coefficient is adopted from (Li and Zeng 2023), defined in terms of the compressive stress and plastic shear displacement, as given in Eq. (4-5).

5.2.3. Damage evolution laws

As evidenced by the experimental findings (Le et al. 2018; Lee and Fenves 1998; Senanayake et al. 2022), the stiffness degrades rapidly right after reaching the yielding state, and the degradation rate reduces with further loading for quasi-brittle materials. Therefore, in the proposed model, the evolution laws for damage scalars D_t and D_c are defined as exponential decay functions shown in Eq. (5-12) and Eq. (5-13), respectively:

$$1 - D_t = e^{-(u^{pt})} \quad \text{with} \quad \dot{u}^{pt} = \sqrt{\left(\frac{\alpha \langle \dot{u}_{n,1}^p \rangle}{u_{t0}}\right)^2 + \left(\frac{\beta \dot{u}_s^p}{u_{t0}}\right)^2 + \left(\frac{\beta \dot{u}_t^p}{u_{t0}}\right)^2} \quad (5-12)$$

$$1 - D_c = e^{-(u^{pc})} \quad \text{with} \quad \dot{u}^{pc} = \frac{\gamma \langle -\dot{u}_{n,2}^p \rangle}{u_{c0}} \quad (5-13)$$

where u^{pt} and u^{pc} are two displacement parameters formulated in the non-dimensional form; α , β , and γ are three non-dimensional constant parameters controlling the contribution of plastic displacement increments to the damage evolution; $\langle \rangle$ represents the Macaulay bracket, indicating that compressive and tensile normal plastic displacements contribute to D_c and D_t , respectively; u_{t0} and u_{c0} are displacements corresponding to the tensile and compressive strengths, (i.e., $u_{t0} = f_t / k_m$, $u_{c0} = f_c / k_m$). It should be noted that u_{t0} and u_{c0} are introduced only for the purpose of making the damage variables non-dimensional.

Following Eq. (5-12) and Eq. (5-13), the increments of two damage variables can then be obtained as Eq. (5-14) and Eq. (5-15), respectively:

$$\dot{D}_t = (1 - D_t) \dot{u}^{pt} \quad (5-14)$$

$$\dot{D}_c = (1 - D_c) \dot{u}^{pc} \quad (5-15)$$

5.2.4. Model parameterization

The proposed model represents the mesoscale mechanical behaviors of mortar joints subject to cyclic loading. Therefore, more advanced experimental procedures would be required to obtain the required parameters. The first type of parameters includes tensile-related parameters (k_{nn} and f_t), shear-related parameters (k_{ss} , k_{tt} , c_0 , $\tan\phi_0$ and $\tan\phi_r$), compressive-related parameters (f_c and f_r), and dilatancy related parameters ($\tan\psi_0$, $\tan\psi_r$, u_τ and σ_u). All these parameters have explicit physical meaning, thus can be identified easily through experimentation. The other type of non-physical parameters includes α , β , γ , η_t , and η_c , which are defined to adapt the model to different stiffness degradation and strength softening effects. To illustrate the effects of these parameters on the model behavior, stress-displacement responses on a single Gaussian integration point under pure tensile, pure shear, and pure compressive loading are shown in Figure 5-7 and Figure 5-8. The baseline materials used for this illustration are listed in Table 5-1. Parameters α , β , γ , η_t , and η_c are varied one-at-a-time while keeping others fixed as the baseline values.

Table 5-1. Baseline material parameters used for the parameter influence test

Tension		Shear			Compression	Dilatancy			Non-physical				
k_{nn} (N/mm ³)	f_t (MPa)	k_{ss} (N/mm ³)	c_0 (MPa)	$\tan\phi_0 / \tan\phi_r$	f_c / f_r (MPa)	$\tan\psi_0 / \tan\psi_r$	σ_u (MPa)	u_τ (mm)	α	β	γ	η_t	η_c
60	1.5	30	1.8	0.9/0.9	7.7/1.1	0/0	-2	1	0.2	0.2	0.5	1	1

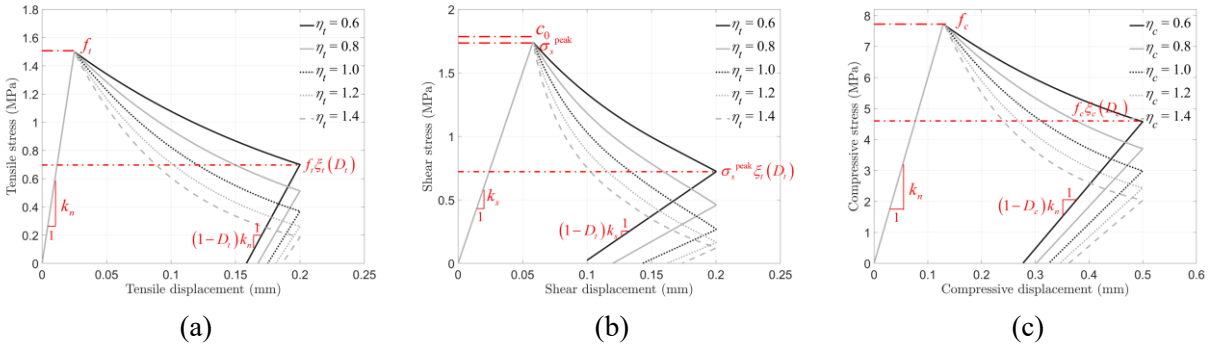


Figure 5-7. Effects of parameter η_t and η_c on the stress-displacement responses: (a) pure tension behavior, (b) pure shear behavior, and (c) pure compressive behavior

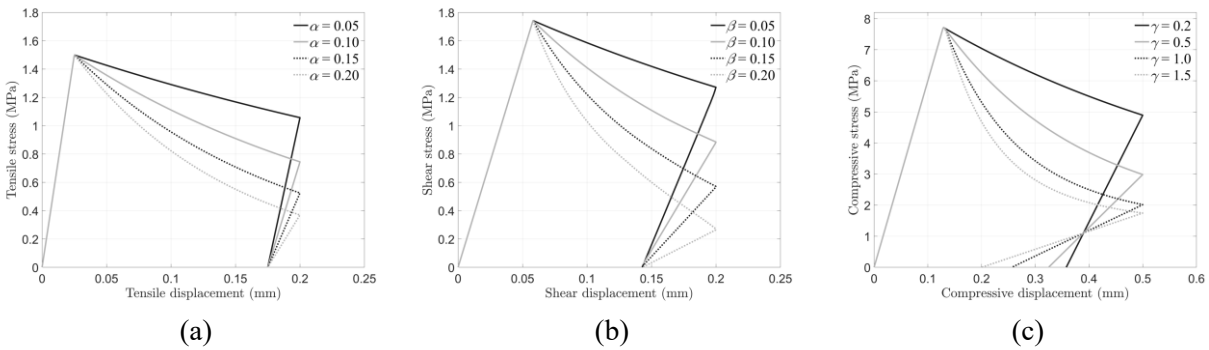


Figure 5-8. Effects of parameter α , β , and γ on the stress-displacement responses: (a) pure tension behavior, (b) pure shear behavior, and (c) pure compressive behavior

The parameter η_t introduced in Eq. (5-9) aims to describe the relationship between the strength softening function $\xi_t(D_t)$ and the stiffness degradation scalar D_t . When η_t is greater than 1, the strength softening amount is greater than the stiffness loss. Conversely, the stiffness degradation effect is more severe if η_t is less than 1. It should be noted that η_t is assumed to be 1 (i.e., loss percentage of strength and stiffness is equal) in many damage-plasticity based models, see for example, (Nie et al. 2022a) for mortar joints, (Le et al. 2017, 2018) for rock. This has proved to be a reasonable option in the absence of experimental data. In the proposed model, the inclusion of η_t and η_c provides a certain level of flexibility when dealing with different material behaviors.

Figure 5-7 (a) and Figure 5-7 (b) present different post-peak behaviors under pure tensile and shear loading with different values of parameter η_t , whereas Figure 5-7 (c) demonstrates such behaviors under pure compression with different values of parameter η_c . It is evident from Figure 5-7 (a) and Figure 5-7 (b) that for a given displacement, the stiffness degradation amount is identical, but the post-peak strengths vary, with higher values of η_t indicating greater ductility. Furthermore, the proposed formulation of $\xi_t(D_t)$ ensures that the loss percentages for tensile strength f_t and shear strength σ_s^{peak} are identical throughout the entire softening procedure. This fully coupled tension-shear softening model is consistent with the fact that both softening behaviors are related to the interfacial debonding at the micro level (Lourenço 1996). It is also worth mentioning that the shear strength σ_s^{peak} is slightly less than the peak cohesion c_0 , as shown in Figure 5-7 (b), due to the smooth hyperbolic yield function f_1 employed in the proposed model. The effect of parameter η_c on the compressive stress evolution is similar to that of parameter η_t , as evidenced in Figure 5-7 (c). Note that for the plotting purpose, the compressive stress and displacement are converted to positive values.

The parameters α , β , and γ are directly correlated with the damage scalar evolutions given in Eq. (5-12) and Eq. (5-13), thereby affecting both stiffness degradation and strength softening. As per Eq. (5-12) and Eq. (5-13), larger values of α , β , and γ indicate a greater contribution of plastic displacements to the damage evolutions. This is consistent with the observations presented in Figure 5-8, which illustrates the effects of these three parameters on the pure tension, pure shear, and pure compressive behaviors, respectively. When the post-peak behavior is available, parameters α , β , and γ should be first determined to fit the stiffness degradation amount acquired

through FE simulation with the experimental one at a certain displacement. Subsequently, parameters η_t and η_c can be determined by conforming to the experimental post-peak stress softening behaviors.

5.3. MODEL IMPLEMENTATION

This section deals with the formulation of the tangent stiffness and stress return algorithm in the general FE framework. In the proposed model, two yield criteria are defined to account for different failure modes of mortar joints. For the sake of generality, the special case in which both yield criteria are violated is detailed below.

5.3.1. Tangent stiffness

To facilitate the mathematical formulation, the stress, displacement, and plastic displacement components are written in the vector form: $\boldsymbol{\sigma} = [\sigma_n, \tau_s, \tau_t]^T$, $\mathbf{u} = [u_n, u_s, u_t]^T$, $\mathbf{u}^p = [u_{n,1}^p, u_{n,2}^p, u_s^p, u_t^p]^T$.

Accordingly, Eq. (5-1) for the stress state is reformulated in a compact vector form as Eq. (5-16):

$$\boldsymbol{\sigma} = \boldsymbol{\sigma}(\mathbf{u}, \mathbf{u}^p, D_t, D_c) \quad (5-16)$$

By taking the derivative of Eq. (5-16), the stress is updated in the rate form, reading Eq. (5-17):

$$\dot{\boldsymbol{\sigma}} = \frac{\partial \boldsymbol{\sigma}}{\partial \mathbf{u}} \dot{\mathbf{u}} + \frac{\partial \boldsymbol{\sigma}}{\partial \mathbf{u}^p} \dot{\mathbf{u}}^p + \frac{\partial \boldsymbol{\sigma}}{\partial D_t} \dot{D}_t + \frac{\partial \boldsymbol{\sigma}}{\partial D_c} \dot{D}_c \quad (5-17)$$

The determination of updated yield surfaces is based on *Kuhn-Tucker conditions*:

$$\dot{\lambda}_i \geq 0, \quad f_i \leq 0, \quad \dot{\lambda}_i f_i = 0 \quad (i=1,2) \quad (5-18)$$

where i represents the yield surface specified, $\dot{\lambda}_i$ is the plastic multiplier.

Upon yielding, Eq. (5-17) can be written as the consistency equation: $\dot{\lambda}_i > 0$ and $\dot{f}_i = 0$, resulting in:

$$\dot{f}_1 = \frac{\partial f_1}{\partial \boldsymbol{\sigma}} \left(\frac{\partial \boldsymbol{\sigma}}{\partial \mathbf{u}} \dot{\mathbf{u}} + \frac{\partial \boldsymbol{\sigma}}{\partial \mathbf{u}^p} \dot{\mathbf{u}}^p + \frac{\partial \boldsymbol{\sigma}}{\partial D_t} \dot{D}_t \right) + \frac{\partial f_1}{\partial D_t} \dot{D}_t = 0 \quad (5-19)$$

$$\dot{f}_2 = \frac{\partial f_2}{\partial \boldsymbol{\sigma}} \left(\frac{\partial \boldsymbol{\sigma}}{\partial \mathbf{u}} \dot{\mathbf{u}} + \frac{\partial \boldsymbol{\sigma}}{\partial \mathbf{u}^p} \dot{\mathbf{u}}^p + \frac{\partial \boldsymbol{\sigma}}{\partial D_c} \dot{D}_c \right) + \frac{\partial f_2}{\partial D_c} \dot{D}_c = 0 \quad (5-20)$$

According to the multi-yield surfaces plasticity integration strategy proposed by Simo (1988), the plastic strain increment can be obtained as a linear combination of the plastic strain rates of the two yield surfaces, determined as Eq. (5-21):

$$\dot{\mathbf{u}}^p = \dot{\lambda}_1 \frac{\partial \mathbf{g}_1}{\partial \boldsymbol{\sigma}} + \dot{\lambda}_2 \frac{\partial \mathbf{g}_2}{\partial \boldsymbol{\sigma}} \quad (5-21)$$

By substituting Eq. (5-1), Eq. (5-12), Eq. (5-13), Eq. (5-14), Eq. (5-15), and Eq. (5-21) into Eq. (5-19) and Eq. (5-20), and solving for two plastic multipliers, one can obtain:

$$\dot{\lambda}_1 = \frac{-\frac{\partial f_1}{\partial \boldsymbol{\sigma}} \frac{\partial \boldsymbol{\sigma}}{\partial \mathbf{u}} \dot{\mathbf{u}}}{\frac{\partial f_1}{\partial \boldsymbol{\sigma}} \frac{\partial \boldsymbol{\sigma}}{\partial \mathbf{u}^p} \frac{\partial \mathbf{g}}{\partial \boldsymbol{\sigma}} + \sqrt{\left(\frac{\left\langle \alpha \frac{\partial \mathbf{g}}{\partial \sigma_n} \right\rangle}{u_{t0}} \right)^2 + \left(\frac{\beta \frac{\partial \mathbf{g}}{\partial \sigma_s}}{u_{t0}} \right)^2 + \left(\frac{\beta \frac{\partial \mathbf{g}}{\partial \sigma_t}}{u_{t0}} \right)^2} \left[\frac{\partial f_1}{\partial \boldsymbol{\sigma}} \frac{\partial \boldsymbol{\sigma}}{\partial D_t} (1 - D_t) + \frac{\partial f_1}{\partial D} (1 - D_t) \right]} = P_1 \dot{\mathbf{u}} \quad (5-22)$$

$$\dot{\lambda}_2 = \frac{-\frac{\partial f_2}{\partial \boldsymbol{\sigma}} \frac{\partial \boldsymbol{\sigma}}{\partial \mathbf{u}} \dot{\mathbf{u}}}{\frac{\partial f_2}{\partial \boldsymbol{\sigma}} \frac{\partial \boldsymbol{\sigma}}{\partial \mathbf{u}^p} \frac{\partial \mathbf{g}_2}{\partial \boldsymbol{\sigma}} + \sqrt{\left(\frac{\left\langle -\gamma \frac{\partial \mathbf{g}}{\partial \sigma_n} \right\rangle}{u_{c0}} \right)^2} \left[\frac{\partial f_2}{\partial \boldsymbol{\sigma}} \frac{\partial \boldsymbol{\sigma}}{\partial D_c} (1 - D_c) + \frac{\partial f_2}{\partial D_c} (1 - D_c) \right]} = P_2 \dot{\mathbf{u}} \quad (5-23)$$

Once $\dot{\lambda}_1$ and $\dot{\lambda}_2$ are obtained, the increments of other state variables (i.e., $\dot{\mathbf{u}}^p$, \dot{D}_c , \dot{D}_t) can be computed and then substituted into the rate form formula for the stress, i.e., Eq. (5-17), the tangent stiffness \mathbf{K}^{tan} can be formulated as Eq. (5-24):

$$\dot{\boldsymbol{\sigma}} = \left[\frac{\partial \boldsymbol{\sigma}}{\partial \mathbf{u}} + \frac{\partial \boldsymbol{\sigma}}{\partial \mathbf{u}^p} \left(P_1 \frac{\partial g_1}{\partial \boldsymbol{\sigma}} + P_2 \frac{\partial g_2}{\partial \boldsymbol{\sigma}} \right) + \frac{\partial \boldsymbol{\sigma}}{\partial D_t} P_1 (1 - D_t) \sqrt{\left(\frac{\alpha \frac{\partial g}{\partial \sigma_n}}{u_{t0}} \right)^2 + \left(\frac{\beta \frac{\partial g}{\partial \sigma_s}}{u_{t0}} \right)^2 + \left(\frac{\beta \frac{\partial g}{\partial \sigma_t}}{u_{t0}} \right)^2} + \frac{\partial \boldsymbol{\sigma}}{\partial D_c} P_2 (1 - D_c) \sqrt{\left(\frac{\gamma \frac{\partial g}{\partial \sigma_n}}{u_{c0}} \right)^2} \right] \dot{\mathbf{u}} \quad (5-24)$$

$$= \mathbf{K}^{\text{tan}} \dot{\mathbf{u}}$$

5.3.2. Semi-implicit stress return algorithm

The stress return problem can be stated as follows: Given the known stress $\boldsymbol{\sigma}_{(m)}$ at load step m and the displacement increment $\dot{\mathbf{u}}_{(m+1)}$ at load step $m+1$, update the stress $\boldsymbol{\sigma}_{(m+1)}$ at load step $m+1$. Although the formulation of tangent stiffness provides a simple way to calculate the stress increment, the state variables used in Eq. (5-24) are derived from the load step m . This fully explicit integration strategy, although adopted in some existing studies (Aref and Dolatshahi 2013; Yuen et al. 2019), only guarantees numerical accuracy provided that the displacement increment is sufficiently small. Therefore, to ensure the numerical robustness, a semi-implicit stress return algorithm is employed in the present study, detailed as follows.

The trial stress state is firstly computed as Eq. (5-25), by assuming the strain/displacement increment from load step m to the trial stress state is elastic:

$$\boldsymbol{\sigma}^{\text{trial}} = \boldsymbol{\sigma}_m + \mathbf{DK}\dot{\mathbf{u}} \quad (5-25)$$

where \mathbf{D} and \mathbf{K} are damage and stiffness matrix defined in Eq. (5-1):

$$\mathbf{D} = \begin{bmatrix} 1-D & 0 & 0 \\ 0 & 1-D & 0 \\ 0 & 0 & 1-D \end{bmatrix}, \mathbf{K} = \begin{bmatrix} k_n & 0 & 0 \\ 0 & k_s & 0 \\ 0 & 0 & k_t \end{bmatrix}. \dot{\mathbf{u}} \text{ is the displacement increment vector.}$$

If the trial stress state does not violate neither yield criterion, i.e., $f_1(\boldsymbol{\sigma}^{\text{trial}}, D_t) \leq 0$ and $f_2(\boldsymbol{\sigma}^{\text{trial}}, D_c) \leq 0$, the stress at step $m+1$ can be updated as the trail stress $\boldsymbol{\sigma}_{(m+1)} = \boldsymbol{\sigma}^{\text{trial}}$. The stress correction is needed when the trial stress state violates the yield criteria. Similarly, the specific case when both yield criteria are violated is discussed here, as shown in Figure 5-9.

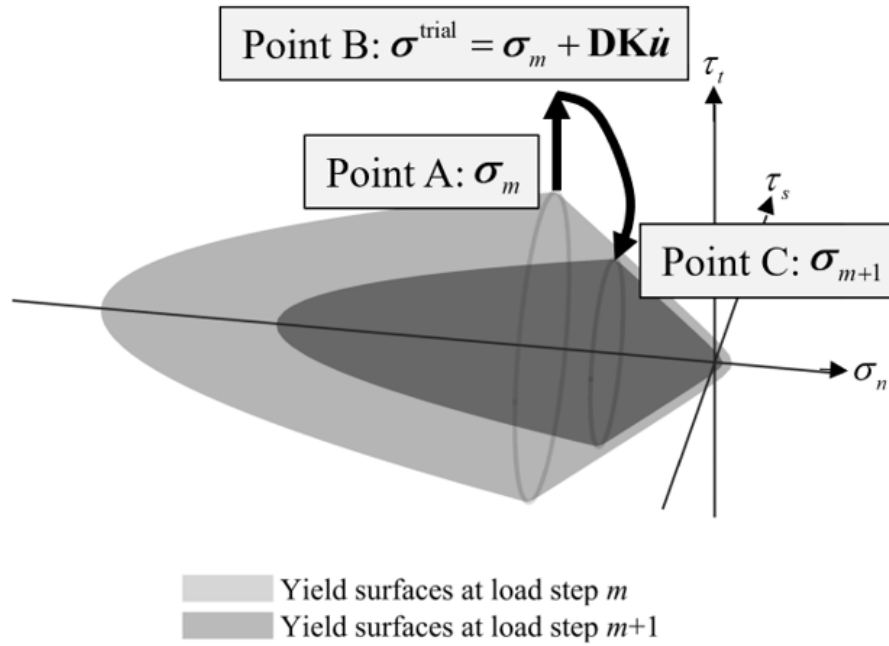


Figure 5-9. Graphical representation of stress return in the multi-yield surfaces model

The adopted stress return algorithm is a special form of the one proposed in Simo and Hughes (2006). The yield functions at the load step $m+1$ (Point C in Figure 5-9) are approximated using first-order Taylor Expansion around the trial stress state (Point B in Figure 5-9):

$$f_{1,C} = f_{1,B} + \frac{\partial f_{1,B}}{\partial \boldsymbol{\sigma}} \dot{\boldsymbol{\sigma}} + \frac{\partial f_{1,B}}{\partial D_t} \dot{D}_t \quad (5-26)$$

$$f_{2,C} = f_{2,B} + \frac{\partial f_{2,B}}{\partial \boldsymbol{\sigma}} \dot{\boldsymbol{\sigma}} + \frac{\partial f_{2,B}}{\partial D_c} \dot{D}_c \quad (5-27)$$

The stress increment can be obtained similarly to Eq. (5-17). The only difference is that the contribution of total displacement increments to the stress increment, i.e., $\frac{\partial \boldsymbol{\sigma}}{\partial \mathbf{u}} \dot{\mathbf{u}}$ in Eq. (5-17), has already been considered in the trail stress state. Thus, the stress increments in Eq. (5-26) and (5-27) can be written as:

$$\dot{\boldsymbol{\sigma}} = \frac{\partial \boldsymbol{\sigma}}{\partial \mathbf{u}^p} \dot{\mathbf{u}}^p + \frac{\partial \boldsymbol{\sigma}}{\partial D_t} \dot{D}_t \quad \text{for Eq. (5-26)} \quad (5-28)$$

$$\dot{\boldsymbol{\sigma}} = \frac{\partial \boldsymbol{\sigma}}{\partial \mathbf{u}^p} \dot{\mathbf{u}}^p + \frac{\partial \boldsymbol{\sigma}}{\partial D_c} \dot{D}_c \quad \text{for Eq. (5-27)} \quad (5-29)$$

Substituting Eq. (5-12), Eq. (5-13), Eq. (5-14), Eq. (5-15), and Eq. (5-21) into Eq. (5-28) and Eq. (5-29), and then enforcing the yield functions Eq. (5-26) and Eq. (5-27) to be zero, two plastic multipliers $\dot{\lambda}_1$ and $\dot{\lambda}_2$ can be solved as follows:

$$\dot{\lambda}_1 = - \frac{f_{1,B}}{\frac{\partial f_1}{\partial \boldsymbol{\sigma}} \frac{\partial \boldsymbol{\sigma}}{\partial \mathbf{u}^p} \frac{\partial g_1}{\partial \boldsymbol{\sigma}} + \sqrt{\left(\frac{\langle \alpha \frac{\partial g_1}{\partial \sigma_n} \rangle}{u_{t0}} \right)^2 + \left(\frac{\beta \frac{\partial g_1}{\partial \sigma_s}}{u_{t0}} \right)^2 + \left(\frac{\beta \frac{\partial g_1}{\partial \sigma_t}}{u_{t0}} \right)^2} \left[\frac{\partial f_1}{\partial \boldsymbol{\sigma}} \frac{\partial \boldsymbol{\sigma}}{\partial D_t} (1-D_t) + \frac{\partial f_1}{\partial D_t} (1-D_t) \right] \quad (5-30)$$

$$\dot{\lambda}_2 = - \frac{f_{2,B}}{\frac{\partial f_2}{\partial \boldsymbol{\sigma}} \frac{\partial \boldsymbol{\sigma}}{\partial \mathbf{u}^p} \frac{\partial g}{\partial \boldsymbol{\sigma}} + \sqrt{\left(\frac{\gamma \langle -\dot{u}_n^p \rangle}{u_c} \right)^2} \left[\frac{\partial f_2}{\partial \boldsymbol{\sigma}} \frac{\partial \boldsymbol{\sigma}}{\partial D_c} (1-D_c) + \frac{\partial f_2}{\partial D_c} (1-D_c) \right]} \quad (5-31)$$

With the values of $\dot{\lambda}_1$ and $\dot{\lambda}_2$, the increment of state variables can be easily computed from Eq. (5-12), Eq. (5-13), Eq. (5-14), Eq. (5-15), and Eq.(5-21). Subsequently, stress increments can be computed as per Eq. (5-32):

$$\dot{\sigma} = \dot{\sigma}^{\text{trial}} + \frac{\partial \sigma}{\partial \mathbf{u}^p} \dot{\mathbf{u}}^p + \frac{\partial \sigma}{\partial D_t} \dot{D}_t + \frac{\partial \sigma}{\partial D_c} \dot{D}_c \quad (5-32)$$

5.4. FINITE ELEMENT VALIDATION

The proposed constitutive material model is implemented via the user-defined subroutine UMAT and used together with the 3D interface element COH3D8 in the general-purpose FE package ABAQUS (Dassault Systemes 2017). It is worth mentioning that the non-iterative stress update strategy employed in the numerical implementation improves the numerical efficiency at the local level, although the explicit strategy at the global level requires a small load increment. To demonstrate the potential of the developed constitutive model, four FE model validation examples were presented in this section: (1) a three-point bending beam under indirect cyclic tensile loading; (2) three masonry couplets under cyclic shear loading; (3) a short URM wall under cyclic in-plane (IP) loading; and (4) a tall URM wall under cyclic in-plane (IP) loading. The previous two validation models aim to test the capability of the proposed model to represent the small-scale behavior of mortar joints, and the two URM walls are selected to examine the proposed model at the structural scale to capture different failure modes. The simplified micro model (Lourenço et al. 1995a) is employed for the development of FE models. Without compromising accuracy, a quasi-static implicit dynamic procedure was utilized to enhance the convergence performance of the FE simulation.

5.4.1. Three-point bending beam under indirect cyclic tensile loading

Experimental data about the cyclic tensile behavior of mortar joints is quite limited due to the difficulty in applying the reversible tensile loading to the mortar specimen. A mortar-jointed notched cylinder specimen with cyclic loading was carried out at the University of Wales Cardiff (Jefferson and Mills 1998). The mortar joint was formed with a 5 mm thickness mortar in a preformed gap between the two halves of the concrete cylinder. The experimental result was expressed in terms of the load-crack mouth opening displacement curve. The purpose of the test was to investigate the cyclic tensile behavior of mortar joints. Recognizing the fact that the nonlinear behavior of the cylinder specimen was governed by the notched mortar joint as described in the experimental report (Jefferson and Mills 1998), a single interface element model under pure tensile loading was developed to test the capability of the proposed constitutive material to reproduce the loading-unloading behavior. For the validation purposes, the experimental peak load was normalized to one.

Required material parameters include the normal stiffness k_n , tensile strength f_t , and two non-physical parameters α and η_t . The tensile strength f_t is taken as 1.5 MPa as experimentally reported, and the normal stiffness k_n is set as the slope of the pre-peak branch at 60 N/mm³. α is determined as 0.23 to match the unloading stiffness to fit the experimental one and η_t is adjusted as 0.6 to fit the post-peak softening branch.

Figure 5-10 presents the comparison between the normalized experimental and FE-simulated stress-displacement curves. It can be observed that the FE simulation result matches well with the experimental one. During each loading-unloading cycle, characteristic features,

including stiffness degradation and tensile strength softening, are captured in an appropriate manner.

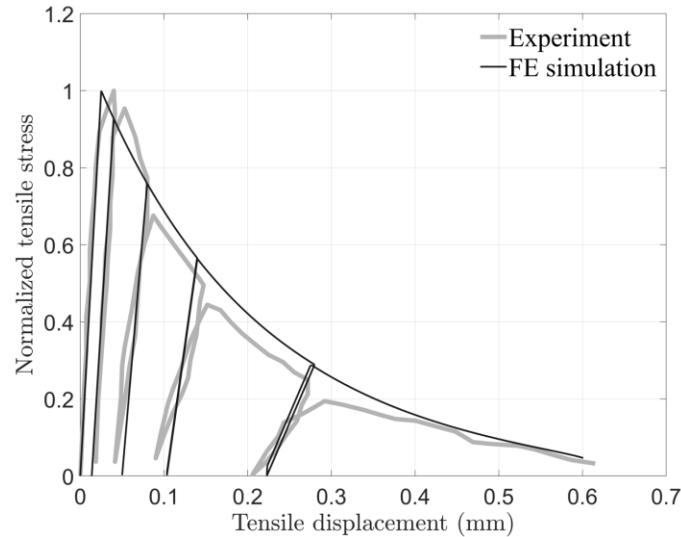


Figure 5-10. Experimental-numerical comparison of normalized stress-displacement curve under cyclic tension loading

5.4.2. Masonry couplet under compressive-shear loading

In reference (Atkinson et al. 1989), three masonry couplets were tested under combined compressive and shear loading. The geometries of three specimens are identical, and the unit dimension is illustrated in Figure 5-11. The mortar thickness was 7 mm. Three specimens were first loaded with different pre-defined compressive stresses (0.49 MPa, 1.34 MPa, and 4.39 MPa), and then the cyclic shear displacement-control loading was applied on the top surface of couplets while keeping the pre-compressive stresses constant. The bottom surfaces of the specimens were fully restrained. The tests were designed to investigate the shear behavior of mortar joints under compressive stresses. Therefore, the material behavior of masonry units was assumed to be elastic in the FE models. The elastic modulus and Poisson ratio of units are 14701 MPa and 0.22, respectively, according to the experimental data (Atkinson et al. 1989). The compressive crushing

failure surface f_2 is not active in the FE model since no crushing-related failure was observed in the test. The value of η_t is assumed to be equal to 1, while α and β are calibrated to fit the experimental post-peak responses. The material parameters required for the mortar joints are summarized in Table 5-2.

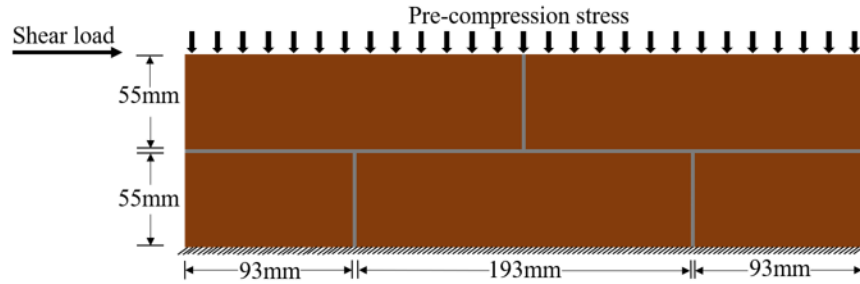


Figure 5-11. Masonry couplet specimen by Atkinson et al. (1989)

Table 5-2. Material parameters for the FE model of masonry couplet

Tension		Shear			Dilatancy			Non-physical				
k_n (N/mm ³)	f_t (MPa)	k_s, k_t (N/mm ³)	c_0 (MPa)	$\tan\phi_0 / \tan\phi_r$	$\tan\psi_0 / \tan\psi_r$	σ_u (MPa)	u_r (mm)	α	β	γ	η_t	η_c
3.8	0.65	11.5	0.811	0.745/ 0.747	0.01/ 0	-2	1	0.05	0.1	0.5	1	1

Figure 5-12 compares the simulated shear force-displacement curves with the experimental ones. It can be observed that good agreements are achieved. Based on the experimental data, the unloading shear stiffnesses have no obvious degradation compared with the initial ones, even under large shear displacements with cohesion strength being fully exhausted. Under higher pre-compressive stresses, both peak and residual capacities increase due to the enhanced sliding resistance. The peak capacities, post-peak behaviors, residual strengths, and unloading behaviors under different compressive normal stresses are well reproduced. As such, it can be concluded that the developed constitutive material model for the interface element can well represent the tangential cyclic behavior of the mortar joint.

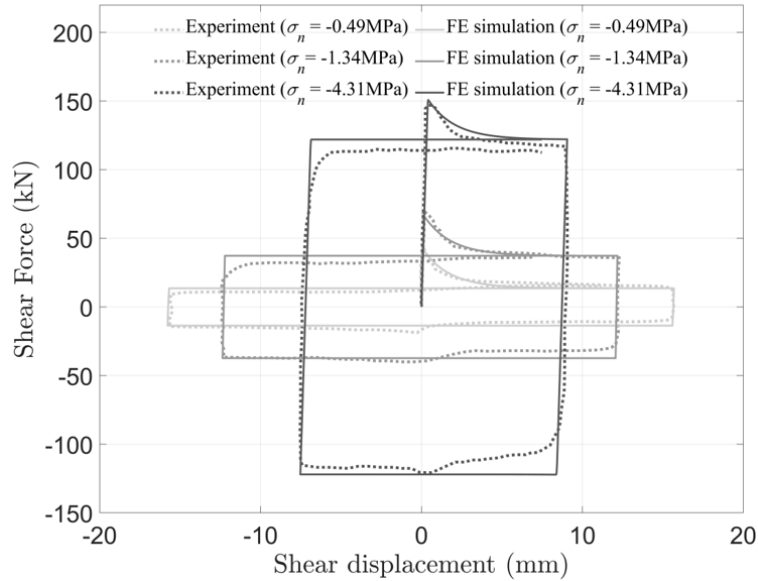


Figure 5-12. Numerical-experimental comparison of shear stress-displacement responses

5.4.3. A short URM wall under cyclic in-plane (IP) loading

In this validation example, a short URM wall tested by Salmanpour (2015) and Salmanpour et al. (2017) was simulated. The tested wall was constructed of calcium-silicate units and general-purpose cement mortar with dimensions of 1550 mm long, 1600 mm high, and 150 mm thick. The dimension for units was 250 mm × 190 mm × 145 mm, with a void ratio of 25%. Thus, in the FE model, the thickness of the URM wall was reduced to 112.5 mm due to the hole inside. The wall was built in a running bond pattern, and the mortar thickness was 10 mm.

The tested wall was first subjected to the 269 kN pre-compression load through a stiff steel loading beam on the top of the walls. Then, quasi-static cyclic IP loading was applied. The loading beam was connected to the walls by a layer of the same mortar used for the construction of the walls. The wall was tested with a two-end fixed boundary condition. The details of the wall specimen and test procedure are presented in Figure 5-13. The load history is illustrated in Figure 5-14, in which the horizontal axis denotes the pseudo-time utilized in the FE simulation.

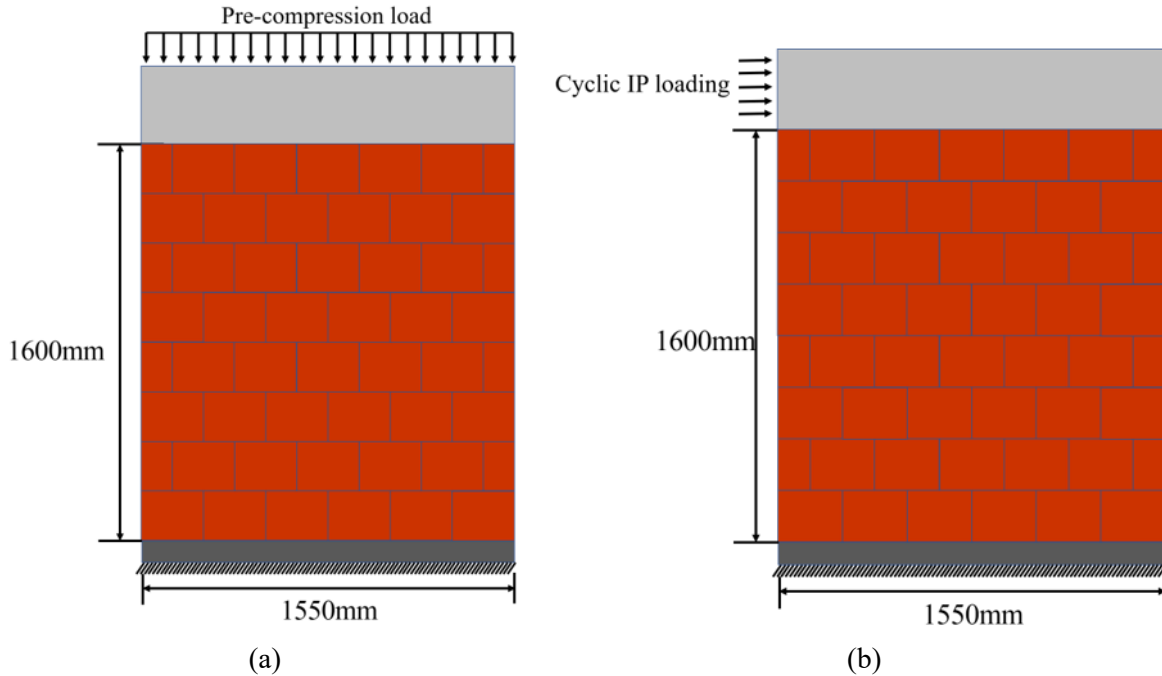


Figure 5-13. URM wall considered for the cyclic IP loading: (a) pre-compression applied at the top of the steel rigid beam, and (b) cyclic IP displacement-controlled loading

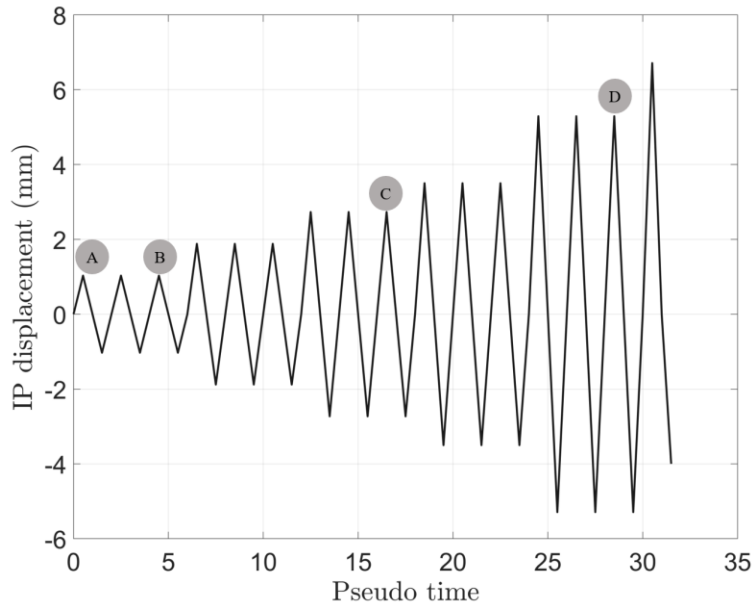


Figure 5-14. Load-history for the tested wall (Salmanpour 2017; Salmanpour et al. 2015)

In the FE model, the top steel beam and brick units are modeled using an 8-node solid element with reduced integration (C3D8R). A preliminary mesh convergence study leads to a mesh

size of $10 \times 8 \times 5$ elements for one single unit in order to reach a balance between computational efficiency and accuracy. The mechanical behavior of units is assumed to be elastic, and all nonlinearities are concentrated in the mortar joints. The elastic modulus of brick units was not reported in the experimental test (Salmanpour 2017), and it was calibrated at 8000 MPa to fit the initial stiffness of the load-deformation curve obtained from the FE simulation to the experimental one. For the material parameters of mortar joints, the peak cohesion c_0 was determined as 0.26 MPa, the initial and residual frictional coefficients $\tan\phi_0$ and $\tan\phi_r$ are both 0.48, and the compressive strength f_c is 7.7 MPa, according to the experimental tests (Salmanpour 2017; Salmanpour et al. 2015). The empirical relationship between tensile strength and cohesion $c_0 = 1.4f_t$ (Zeng et al. 2021) was adopted to determine the tensile strength f_t . The dilatancy coefficient was assumed to be zero to avoid an overestimation of the shear capacity, and the residual compressive yield stress was determined as 1/7 of compressive strength, as suggested by Li and Zeng (2023). For the other modeling parameters, two stiffness recovery factors ω_t and ω_c are determined as 0 and 1, respectively, as being reasonable for quasi-brittle materials. Due to the lack of small-scale experimental data, η_t and η_c are assumed to be 1, which implies that the amount of strength softening, and stiffness degradation is identical. The values of α , β , and γ are determined such that post-peak behaviors under pure tension, shear, and compression are characterized by the same fracture energies as those in Nie et al. (2022a), in which the same wall was modeled. The material parameters used for the mortar joints are summarized in Table 5-3.

Table 5-3. Material parameters for the FE model of short URM wall under cyclic IP loading

Tension		Shear			Compression	Dilatancy			Non-physical				
k_n (N/mm ³)	f_t (MPa)	k_s (N/mm ³)	c_0 (MPa)	$\tan\phi_0 / \tan\phi_r$	f_c / f_r (MPa)	$\tan\psi_0 / \tan\psi_r$	σ_u (MPa)	u_r (mm)	α	β	γ	η_t	η_c
48	0.1	21	0.23	0.58/ 0.58	6.2/0.89	0/ 0	-2	1	0.0013	0.0011	0.03	1	1

The comparison of load-displacement curves is presented in Figure 5-15. The results from Nie et al. (2022a), in which the same wall was modeled, are also included. The wall capacity obtained by the FE simulation (i.e., 133 kN) is slightly less than the experimental one (i.e., 148 kN). This is deemed a satisfactory result considering the lack of detailed information about several material parameters (e.g., elastic modulus of units, dilatancy coefficient), for which typical values from the literature were assumed. The progressively increasing degradation of stiffness is observed in both positive and negative directions. The amount of degradation is in reasonably good agreement with the experimental data. However, under large displacement cycles, the FE predicted results have an underestimation of energy dissipation. This can be partially attributed to the simplified elastic unloading-reloading behavior assumed in the model formulation.

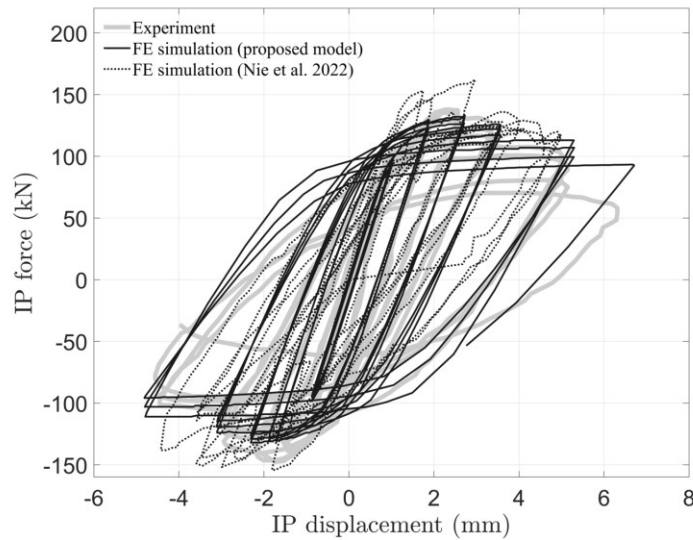
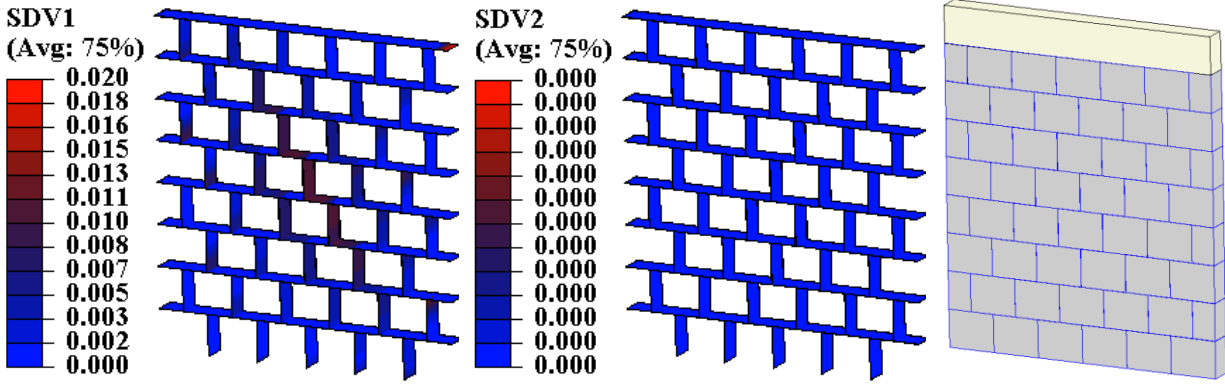
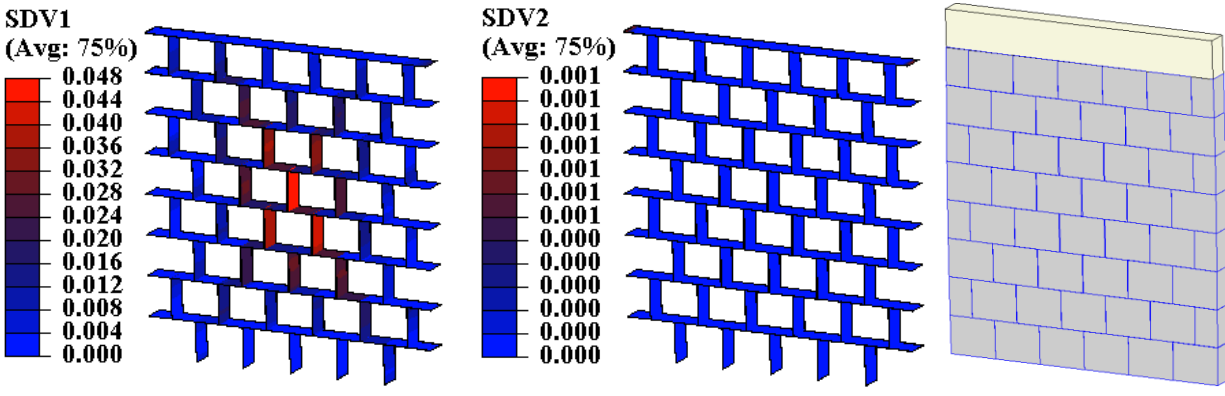


Figure 5-15. Numerical-experimental comparison of IP force-displacement curve for the short URM wall

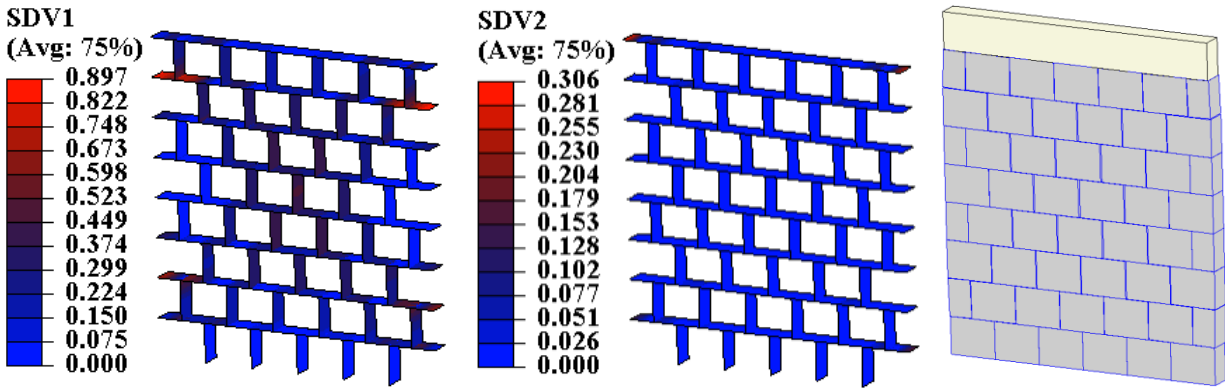
The failure mode of the wall is characterized by a diagonal crack pattern. Figure 5-16 shows crack patterns and deformed shapes at four different stages (indicated by Points A, B, C and D in Figure 5-14) in the FE simulation, in which SDV1 and SDV2 represent the damage scalars D_t and D_c respectively. In the first half cycle at the first displacement level (Point A in Figure 5-14), only a small portion of mortar joints experienced shear sliding and tensile cracking along the diagonal line, and no compressive crushing was observed. Meanwhile, some horizontal tensile cracks developed at the top of the wall. With further loading, the cracks developed significantly at the center of the wall. At the third displacement level (Point C in Figure 5-14), the crushing induced by the high compressive stress at the toe of the wall was captured in Figure 5-16 (c). At a larger displacement level, the typical staircase-shaped crack pattern formed, as illustrated in Figure 5-16 (d). It can be seen that the FE predicted crack pattern matches well with the experimental one, as shown in Figure 5-17.



(a)



(b)



(c)

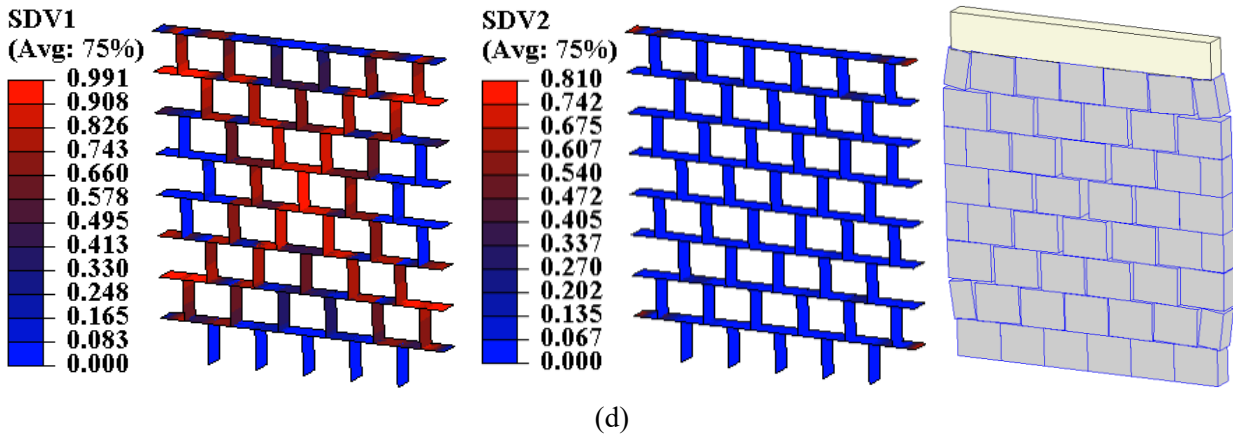


Figure 5-16. Crack patterns and deformed shapes of the short URM wall obtained through the FE simulation at different stages (SDV1 and SDV2 represent the damage scalars D_t and D_c , respectively): (a) Point A, (b) Point B, (c) Point C, and (d) Point D



Figure 5-17. Failure mode of short URM wall in the experimental study by Salmanpour (2017)

5.4.4. A tall URM wall under cyclic in-plane (IP) loading

In this section, a tall URM wall with a larger aspect ratio, tested by Anthoine and Magonette (1995), is simulated. The tested URM wall was 1000 mm long and 2000 mm high, built with 250 mm × 120 mm × 55 mm units and 10 thickness hydraulic lime mortar, and arranged in a two-wythe thick English bonding pattern. The boundary conditions and loading procedure are identical to those of

the short wall illustrated in Section 5.4.3. An average compressive normal stress of 0.6 MPa was initially applied on the top of the wall. Subsequently, the displacement-control cyclic IP loading was applied. Similar to the FE model developed for the short URM wall, the top loading beam and brick units are modeled with an 8-node solid element with reduced integration (C3D8R). The mesh convergence study leads to $8 \times 2 \times 4$ elements for one single unit. Limited information about the material parameters is available in the test (Anthoine and Magonette 1995). Therefore, material parameters are determined from the numerical works (Gambarotta and Lagomarsino 1997a; Minga et al. 2018) in which the same wall was modeled. Similar to the short URM wall, non-physical parameters η_t and η_c are assumed to be 1, while α , β , and γ are determined such that the fracture energies are equal to those reported in works (Gambarotta and Lagomarsino 1997a; Minga et al. 2018). The elastic modulus and Poisson ratio of units are 3000 MPa and 0.15, respectively. The parameters for mortar joints in the tall URM wall are summarized in Table 5-4.

Table 5-4. Material parameters for the FE model of tall URM wall under cyclic IP loading

Tension		Shear			Compression	Dilatancy			Non-physical				
k_n (N/mm ³)	f_t (MPa)	k_s (N/mm ³)	c_0 (MPa)	$\tan\phi_0 / \tan\phi_r$	f_c / f_r (MPa)	$\tan\psi_0 / \tan\psi_r$	σ_u (MPa)	u_r (mm)	α	β	γ	η_t	η_c
50	0.185	25	0.26	0.48 / 0.48	7.7 / 1.1	0 / 0	-2	1	0.00 / 1428	0.00 / 0832	0.05	1	1

The main purpose of including the tall URM wall is to examine the capability of the proposed model to capture different IP failure modes of URM walls. The experimentally observed failure mode for the tall wall is significantly different from that of the short wall illustrated in Section 5.4.3. An in-plane rocking failure was observed, with flexural cracks concentrating on the top and bottom bed joints. The governed failure mode was well captured through the FE simulation shown in Figure 5-18.

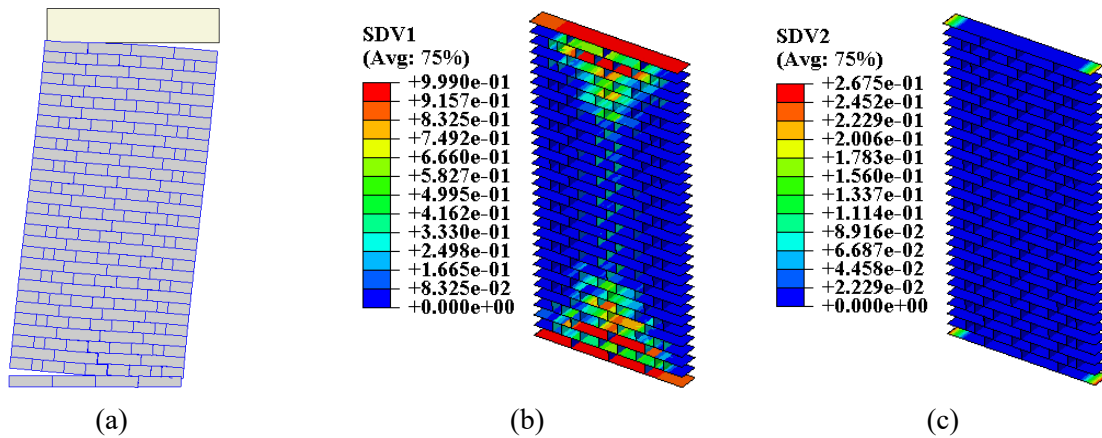


Figure 5-18. Failure mode of tall URM wall obtained from the FE simulation: (a) deformed shape, (b) damage variable D_t , and (c) damage variable D_c

The numerical-experimental comparison in terms of the load-deformation curve is presented in Figure 5-19. The tested tall wall exhibited low energy dissipation during load-unloading-reloading cycles, and no obvious strength degradation was observed from the test. This is a direct consequence of the activated failure mechanism. Although some discrepancies can be observed between the FE simulation and test results, a reasonably good agreement is achieved in terms of the maximum strength and the rocking mechanism.

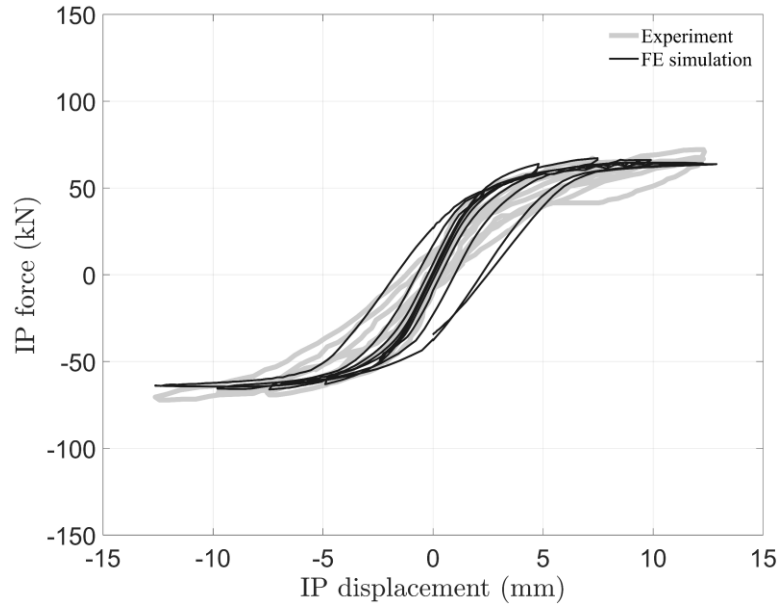


Figure 5-19. Numerical-experimental comparison of IP force-displacement curve for the tall URM wall

5.4.5. A reinforced masonry (RM) wall under cyclic in-plane (IP) loading

The reinforced masonry (RM) wall considered in this section was experimentally studied by Shing et al. (1991). The tested RM wall was fully grouted and had a dimension of 1828 mm high and 1828 mm long, thus an aspect ratio of 1.0. It was constructed using $152 \times 203 \times 406$ mm hollow concrete blocks. The tested wall had five vertical and five horizontal reinforcing bars, with a center-to-center spacing of 406 mm. The vertical steel ran continuously from the base slab to the top beam with 180-degree anchoring hooks. The horizontal reinforcement had 180-degree hooks around the extreme vertical steel. This led to a vertical and horizontal reinforcement ratio of 0.74% and 0.14%, respectively. A pre-compression load of 0.69 MPa was first applied on the top of the wall, and then an IP load was applied in a cantilever condition.

The FE modeling strategy used for this validation example is similar to that for URM walls discussed previously. The concrete blocks and grouts are modeled with C3D8 element, plus the

nonlinear behaviors represented via the Concrete Damage Plasticity (CDP) model (Lee & Fenves, 1998), in which the tensile cracking and compressive crushing can be well described using different parameters for concrete and grouts. Reinforcing bars are modeled using truss elements T3D2 with the von Mises plasticity model and a bilinear hardening law. Note that a perfect bond is assumed for grout-reinforcement and grout-concrete unit contacts. Mortar joints are simulated using zero-thickness interface elements (COH3D8) in conjunction with the developed constitutive model in this chapter. The horizontal and vertical reinforcements have a yield strength of 383 MPa and 496 MPa, respectively. The material parameters of mortar joints are summarized in Table 5-5.

Table 5-5. Material parameters for the FE model of the RM wall under cyclic IP loading

Tension		Shear			Compression	Dilatancy			Non-physical				
k_n (N/mm ³)	f_t (MPa)	k_s (N/mm ³)	c_0 (MPa)	$\tan\phi_0/\tan\phi_r$	f_c/f_r (MPa)	$\tan\psi_0/\tan\psi_r$	σ_u (MPa)	u_r (mm)	α	β	γ	η_i	η_c
50	0.3	25	0.42	0.8/ 0.8	18.18/2.60	0.3/0.3	-2	0.5	0.00 43	0.00 12	0.05	1	1

The failure mode of the tested RM wall was characterized by diagonal tension cracking, as shown in Figure 5-20(a). This is consistent with the FE predictions illustrated in Figure 5-20(b). Moreover, the tensile damage distributions of mortar joints and concrete units (represented by the damage scalar DAMAGET) are shown in Figure 5-20(c) and Figure 5-20(d). It is evident that significant damage is distributed along the two diagonal paths, and horizontal reinforcement experiences significant damage. The numerical-experimental comparison in terms of the load-deformation behavior is shown in Figure 5-21. It can be observed that the peak IP load is well predicted. Meanwhile, the pinching effects and stiffness degradation of the tested wall under large displacement amplitudes are well captured. However, the FE prediction has more rapid strength softening compared to the tested data. Moreover, the load-capacity in the negative loading

direction (i.e., when the displacement is negative) is higher than that in the positive direction. This is mainly because full compressive stress develops when loaded in the negative direction. As a result, when loaded back to the positive direction, irreversible compressive crushing damage reduces the wall capacity.

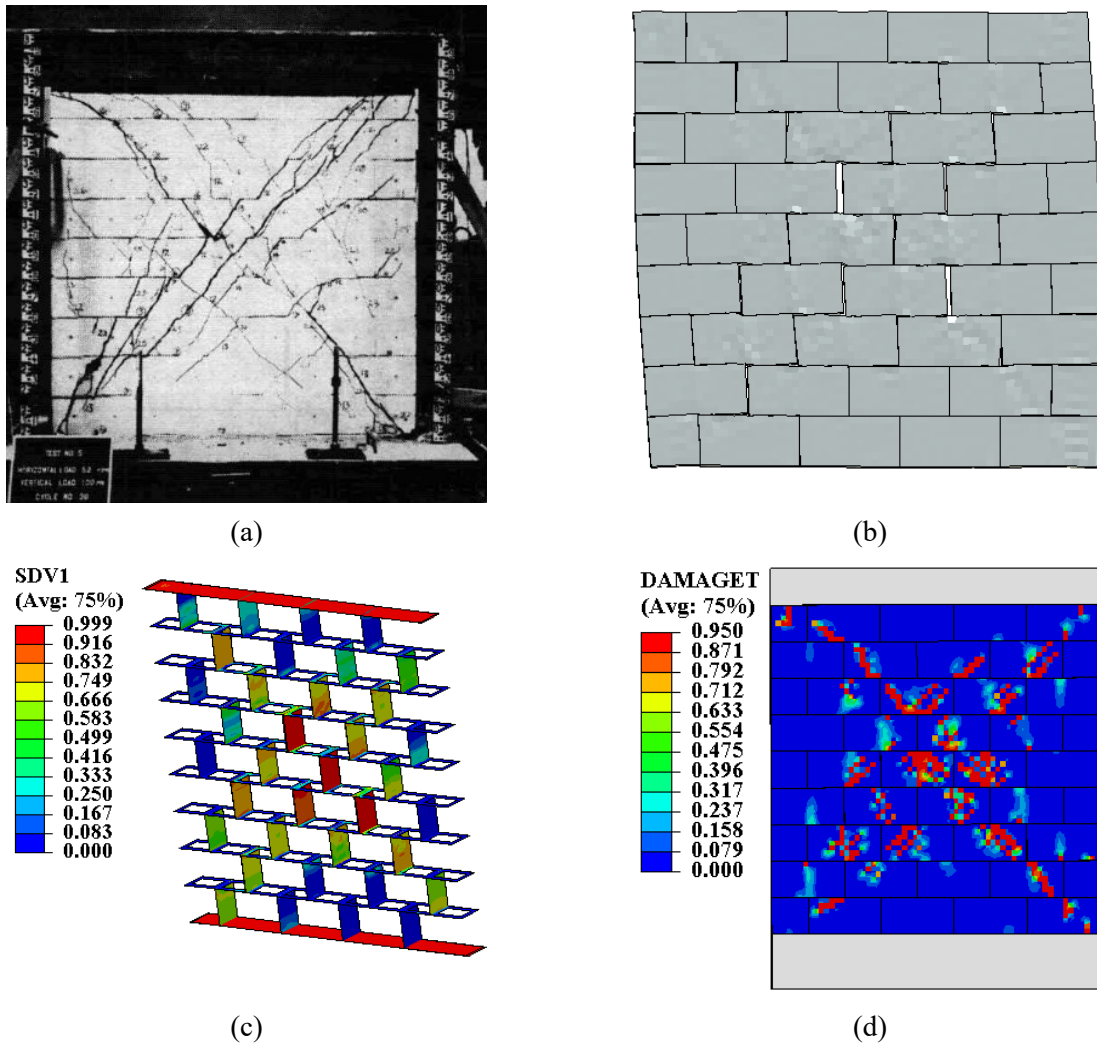


Figure 5-20. Failure modes of the RM wall: (a) experimental test by Shing et al. (1991), (b) deformed shape of wall, (c) tensile damage of mortar joints, and (d) tensile damage of concrete units

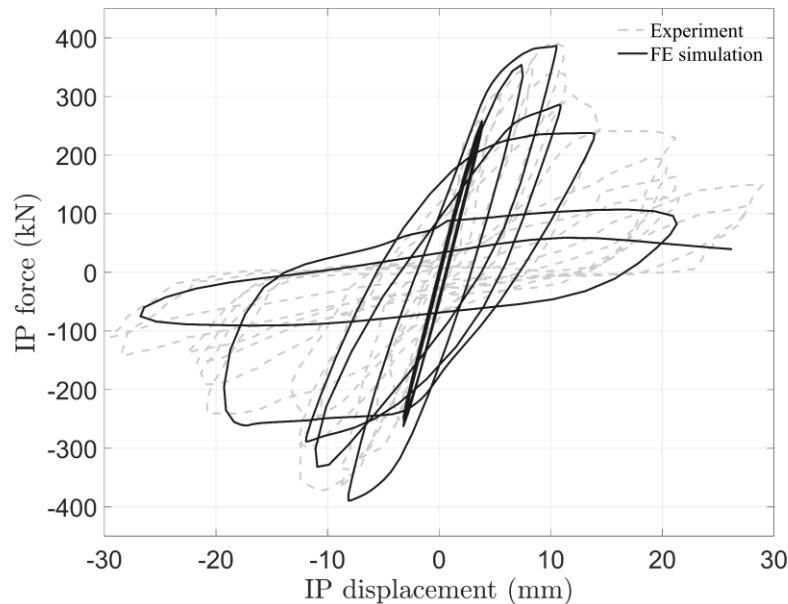


Figure 5-21. Experimental-numerical comparison in terms of the load-deformation behavior of RM wall under cyclic IP loading

5.5. CHAPTER CONCLUSION

A novel three-dimensional constitutive model for cohesive interfaces was proposed in this chapter for the cyclic modeling of mortar joints in masonry structures. The proposed novel model was formulated in the damage-plasticity framework with the following unique features: (1) two smooth hyperbolic yield surfaces capable of capturing various failure modes (i.e., tensile cracking, shear sliding, compressive crushing) of mortar joints; (2) single damage scalar D to model various stiffness recovery effects; (3) two damage scalars D_t and D_c to characterize the normal (including the tensile and compressive) and tangential stiffness degradation; and (4) two damage functions $\xi_t(D_t)$ and $\xi_c(D_c)$ to represent the strength softening (e.g., tensile strength, cohesion, compressive strength). The model formulation enables a high degree of flexibility in dealing with various modeling aspects (e.g., stiffness recovery, post-peak behavior), verified by illustrating the influence of parameters on the model behavior.

The newly developed constitutive material model was implemented in the commercial finite element software ABAQUS. Several experimental tests available in the literature were simulated to demonstrate the reliability of the proposed model. At the masonry component level, an indirect cyclic tensile test on a mortar-jointed cylinder specimen and three masonry couplets under compression-shear loading were simulated, respectively. Comparison results indicated that peak capacity, strength softening, and stiffness degradation were accurately captured. At the structural level, two unreinforced masonry (URM) walls with different aspect ratios were simulated, aiming to test the capacity of the proposed model to reproduce different failure modes of URM walls under in-plane loading. Two distinct failures, namely diagonal cracking and flexural rocking, were well predicted. Moreover, a reinforced masonry (RM) wall was also validated. Discrepancies in the load-deformation behaviors can be attributed to the uncertainty in some material parameters. This entails parameter sensitivity analysis when the proposed model is applied to the masonry wall. In conclusion, the proposed 3D model can be utilized in conjunction with a simplified micro modeling strategy to investigate the structural behavior of URM walls under complex loading scenarios (e.g., cyclic seismic loading) consider both in-plane and out-of-plane loadings.

Chapter 6. NUMERICAL INVESTIGATION OF UNREINFORCED MASONRY WALLS UNDER BI-DIRECTIONAL LOADING: IN-PLANE CAPACITY REDUCTION DUE TO OUT-OF-PLANE LOADING

The structural behavior of unreinforced masonry (URM) walls under in-plane (IP) or out-of-plane (OOP) loading in masonry buildings has been extensively investigated in public literature. However, studies focusing on the URM walls subjected to concurrent IP and OOP loadings are limited. Neglecting IP and OOP interaction effects may lead to unsafe design practices. As such, this study conducts a comprehensive numerical investigation into the behavior of URM walls under combined IP and OOP loading, focusing on the influence of aspect ratio (i.e., height-to-length ratio), slenderness ratio (i.e., height-to-thickness ratio), and pre-compression load levels. To capture the possible failure modes of URM walls under various loading scenarios, the simplified micro modeling approach is employed. The analysis results indicate that the presence of OOP loading leads to a substantial reduction in IP capacities. Longer walls, characterized by smaller aspect ratios (AR), exhibit more pronounced IP and OOP interaction effects. Additionally, highly slender walls show significant additional moments due to second-order effects under OOP loading, thereby negatively affecting the IP capacity. Low-level pre-compression loads are beneficial for diminishing capacity interaction effects, while high pre-compression loads exert a negative influence. To facilitate the consideration of IP and OOP capacity interaction effects in an efficient manner, a simplified analytical model is developed through curve fitting, in which the effects of aspect ratio, slenderness ratio, and pre-compression load are incorporated.

6.1. INTRODUCTION

Unreinforced masonry (URM) walls are an essential structural component of numerous buildings, encompassing residential, commercial, industrial, and cultural heritage structures. The widespread use of URM walls in various architectural styles and construction applications can be attributed to their inherent durability, thermal efficiency, aesthetic versatility, as well as their advantageous architectural and structural roles. However, URM walls are vulnerable to earthquake loads, including loads applied parallel to the wall (i.e., in-plane), and loads applied perpendicular to the wall (i.e., out-of-plane), along with simultaneous loads from other sources, like vertical gravity loads. This susceptibility has raised concerns regarding the safety and effectiveness of URM walls, prompting ongoing research aimed at understanding their behavior further and bolstering their ability to withstand adverse loading conditions.

In the literature, the structural behavior of URM walls is commonly characterized under two distinct loading scenarios: in-plane (IP) and out-of-plane (OOP) loadings. Researchers and practicing engineers have devoted considerable efforts to investigating the load capacities and failure mechanisms of URM walls under either pure IP loading (Gonen et al. 2021; Hwang et al. 2022; Pulatsu et al. 2023; Salmanpour et al. 2015; Zeng and Li 2023) or pure OOP loading (Doherty et al. 2002; Godio and Beyer 2019; Noor-E-Khuda et al. 2016a). However, the behavior of URM walls under combined IP and OOP loading scenarios (e.g., during earthquakes) needs to be better understood to consider the potential interplay between IP and OOP behaviors. Such a need is highlighted by a post-earthquake survey (Vlachakis et al. 2020), which pointed out that a URM wall can become more vulnerable under combined IP and OOP loading.

While it is unquestionable that an interaction between IP and OOP behaviors is present, existing engineering practices, e.g., CSA S304-14 (Canadian Standards Association 2014), often overlook the consideration of the interaction effect for URM structural walls. By contrast, the IP-OOP interaction effects for masonry infill walls are provided for seismic evaluation and retrofit of existing buildings in ASCE 41-17 (ASCE 2017), which specifies the IP-OOP strength interaction relationships to account for the IP capacity reduction due to the presence of OOP loading and vice versa. The applicability of these relationships to URM structural walls is unclear since URM structural walls are often subjected to axial loading or pre-compression, which is considered an important factor affecting the failure modes of URM walls under both IP and OOP loadings.

In the research community, in contrast to numerous studies conducted experimentally (De Risi et al. 2019; Xie et al. 2021a) and numerically (Mazza and Donnici 2022; Di Trapani et al. 2018) to examine the accuracy of design provisions pertaining to the interaction behaviors of masonry infill walls, studies on the IP-OOP interactions of URM structural walls are scarce. Najafgholipour et al. (2013) tested a series of URM wall panels subjected to simultaneous IP and OOP loading. The experimental results highlighted a significant decrease in IP shear capacity as the OOP load increased, and corresponding IP-OOP interaction behaviors were expressed in terms of the capacity interaction curves. However, it is worth mentioning that in the test by Najafgholipour et al (2013), the IP capacity was obtained through diagonal compression tests, which did not capture the coupling between axial load and flexure. Dolatshahi and Aref (2012) performed tests on the bi-directional behavior of URM walls with both IP and OOP loadings imposed simultaneously. It was concluded that due to the pre-applied OOP loading, the URM wall easily collapsed because of the accumulative OOP deformation under subsequent IP loading. The

IP and OOP interaction effects were found to be strongly influenced by the aspect ratio (AR) (i.e., height-to-length ratio) and the IP failure modes of URM walls when no OOP load existed. A recent experimental study by Krishnachandran and Menon (2023) examined the IP flexural capacity of URM piers with varying aspect ratios in the presence of OOP displacements. The test results also indicated that the URM pier would experience a stiffness and strength reduction in the presence of inelastic OOP displacements.

In addition to the previously discussed experimental studies, several researchers explored the IP-OOP interaction effects in URM walls using numerical approaches. Based on the macro continuum finite element (FE) or distinct element (DE) model with homogenized masonry material, (Agnihotri et al. 2013; Dolatshahi et al. 2015; Malomo and DeJong 2022; Najafgholipour et al. 2014; Noor-E-Khuda and Dhanasekar 2018a; b) studied the IP-OOP interaction of URM walls, considering different influencing factors. These works confirmed the IP-OOP interaction of URM walls. Nonetheless, the models used were insufficient for accurately characterizing the inherent composite nature of masonry, and thus the intricate failure modes and IP-OOP interaction of URM walls cannot be well captured. To address this issue, other researchers took the simplified micro modeling approach, and intended to explicitly represent masonry units and mortar joints using discontinuous interfaces. For example, Dolatshahi and Yekrangnia (2015) examined the IP-OOP interaction effects utilizing this micro modeling approach. Their results revealed that the OOP strength could be reduced up to 72% for URM walls under simultaneous IP and OOP loading. More recently, Kesavan and Menon (2022) used the ‘block-based modeling approach’, in which units and mortar were explicitly modeled, while the unit-mortar contacts were assumed to be

rigidly connected. It was generally concluded that the IP-OOP interaction effects were more significant in the shear-controlled URM piers than the flexural-controlled ones.

Upon reviewing the existing studies on the IP-OOP interaction behaviors of URM walls, it is evident that the OOP load detrimentally affects the IP capacity and vice versa. However, such interaction effects remain largely unexplored or rarely quantified using reliable models. The use of the micro modeling strategy is of paramount importance to characterizing the intricate structural behaviors of URM walls under combined IP and OOP loading, as stressed in (Dolatshahi and Yekrangnia 2015), which, however, only examined the effects of boundary conditions (cantilever or fixed) and loading patterns (monotonic or cyclic). It is well known that other geometric factors, including AR and SR and pre-compression load P_v , have substantial influences on the structural behavior of URM walls under IP loading (e.g., AR and P_v) or OOP loading (e.g., SR and P_v). Their effects on the IP and OOP interaction behaviors of URM walls have not been well understood. As such, the present study contributes to a numerical investigation of the IP-OOP interaction behaviors of URM walls using the simplified micro modeling approach. Detailed failure modes and corresponding load-deformation behaviors of URM walls under combined IP and OOP loadings are discussed, with a particular emphasis on IP capacity reduction due to the presence of OOP loading. The influences of AR, SR, and P_v are quantified in terms of the IP-OOP capacity interaction curves. Finally, based on the FE simulation data, an analytical model is proposed to account for the IP-OOP capacity interactions, considering the effects of AR, SR, and P_v , in comparison to the existing models in the literature and the ASCE 41-17 design provisions for masonry infill walls.

6.2. 3D FINITE ELEMENT MODELS OF URM WALLS

6.2.1. Simplified micro modeling strategy

The FE modeling strategy employed in this chapter for URM walls is illustrated in Figure 6-1. Mortar joints are modeled using the zero-thickness interface element COH3D8 available in ABAQUS (Dassault Systemes 2017), in conjunction with a 3D plasticity-based multi-yield surfaces model recently developed by the authors (Li and Zeng 2023), capable of capturing various failure modes (e.g., tensile cracking, shear sliding, compressive crushing). The constitutive model used was implemented via the user subroutine UMAT in ABAQUS. An implicit Euler backward integration algorithm, combined with a local-global Newton-Raphson solver, was employed to achieve the predictor-corrector return mapping in the numerical formulation. Other than that, off-the-shelf elements and material constitutive models are used for the modeling of URM walls. For example, brick units are simulated using the 3D full integration element C3D8 and the Concrete Damage Plasticity (CDP) model (Lee and Fenves 1998), which allows for the simulation of the nonlinear damage behavior in units, in particular the tensile cracking commonly observed in the experimental tests. This modeling strategy was validated using small-scale masonry specimens (e.g., unit-mortar-unit assemblages) and large-scale URM walls under IP or OOP loadings (Li and Zeng 2023) and thus used in this chapter. For more details about the modeling strategy and its validations, interested readers are referred to Li and Zeng (2023).

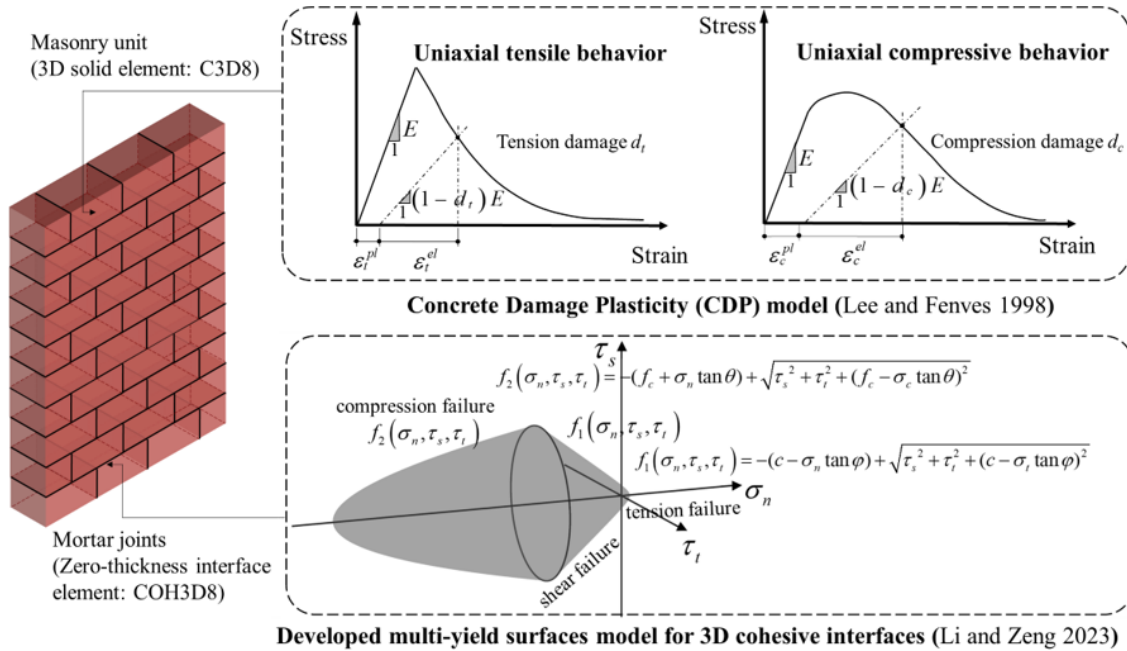


Figure 6-1. Schematic view of the FE modeling strategy using the simplified micro approach for URM walls

6.2.2. Parametric design for the numerical study

The parametric design aims to cover factors that could affect the structural behavior of URM walls subjected to IP and/or OOP loading conditions. The baseline model employed in this study is a URM wall that was experimentally tested in (Raijmakers 1992). This wall is selected due to its extensive use as a benchmark or application example under IP loading in numerous studies (Abdulla et al. 2017; Zeng et al. 2021), as well as for its well-documented material parameters, which are summarized in Table 1.

Table 6-1. Material parameters of units and mortar joints (Lourenço 1996)

Material	Parameters	Value
Units	Tensile strength f_u^t (MPa)	2
	Compressive strength f_u^c (MPa)	16.6*
	Elastic modulus E_u (MPa)	16700
Mortar joints (interfaces)	Stiffness constants k_{nn}, k_{ss}, k_{tt} (N/mm ³)	82, 36, 36
	Tensile strength f_i (MPa)	0.25
	Peak cohesion c_0 (MPa)	0.35
	Mode I fracture energy G_I (N/mm)	0.012
	Mode II fracture energy G_{II}^0 (N/mm)	0.125
	Initial frictional coefficient $\tan \varphi_0$	0.75
	Residual frictional coefficient $\tan \varphi_r$	0.75
	Initial dilation coefficient $\tan \psi_0$	0.4
	Residual dilation coefficient $\tan \psi_r$	0
	Compressive strength of masonry f_m' (MPa)	10.5
	Initial/intermediate/residual compressive yield strength $\sigma_c^i, \sigma_c^m, \sigma_c^r$ (MPa)	2.625, 5.775, 1.5
	Controlling displacements κ_3^p, κ_3^m (mm)	0.128, 0.64

*Compressive strength of units f_u^c is empirically determined by the relationship: $f_u^c = f_u^t / 0.12$ (Li and Zeng 2023)

The tested URM wall was a 16-course solid wall built with wire-cut solid clay bricks (210 mm × 52 mm × 100 mm) and 10 mm thick mortar layers. To verify the effectiveness of the employed modeling strategy in capturing the influence of different pre-compression load levels, the URM walls tested with pre-compression loads of 0.3 MPa and 1.21 MPa (Rajmakers 1992) were simulated, although the modeling strategy was validated by the authors based on other experimental studies (Li and Zeng 2023). Figure 6-2 (a) shows the numerical-experimental comparison in terms of IP load-deformation behaviors. Note that two walls were tested under a pre-compression load of 0.3 MPa and they showed slight difference in the post-peak behavior during the tests primarily due to the heterogeneity of the mortar and brick materials (Rajmakers 1992). The increase in pre-compression load leads to an increase in the initial stiffness, peak

strength, and post-peak behavior, as evidenced by the experimental results. Overall, the FE-predicted load–displacement curves agree well with the experimental ones, although some minor discrepancies in the post-peak behavior are observed for the case of 1.21 MPa. On the other hand, all tested walls were governed by the diagonal tensile cracking, and thus the crack pattern is presented only for the case of 0.3 MPa. Figure 6-2 (c) and Figure 6-2 (d) present the damage distributions in mortar joints (interfaces) and units, respectively. It can be observed that the failure modes predicted by the FE model closely resemble that of experimental observation as illustrated in Figure 6-2 (b).

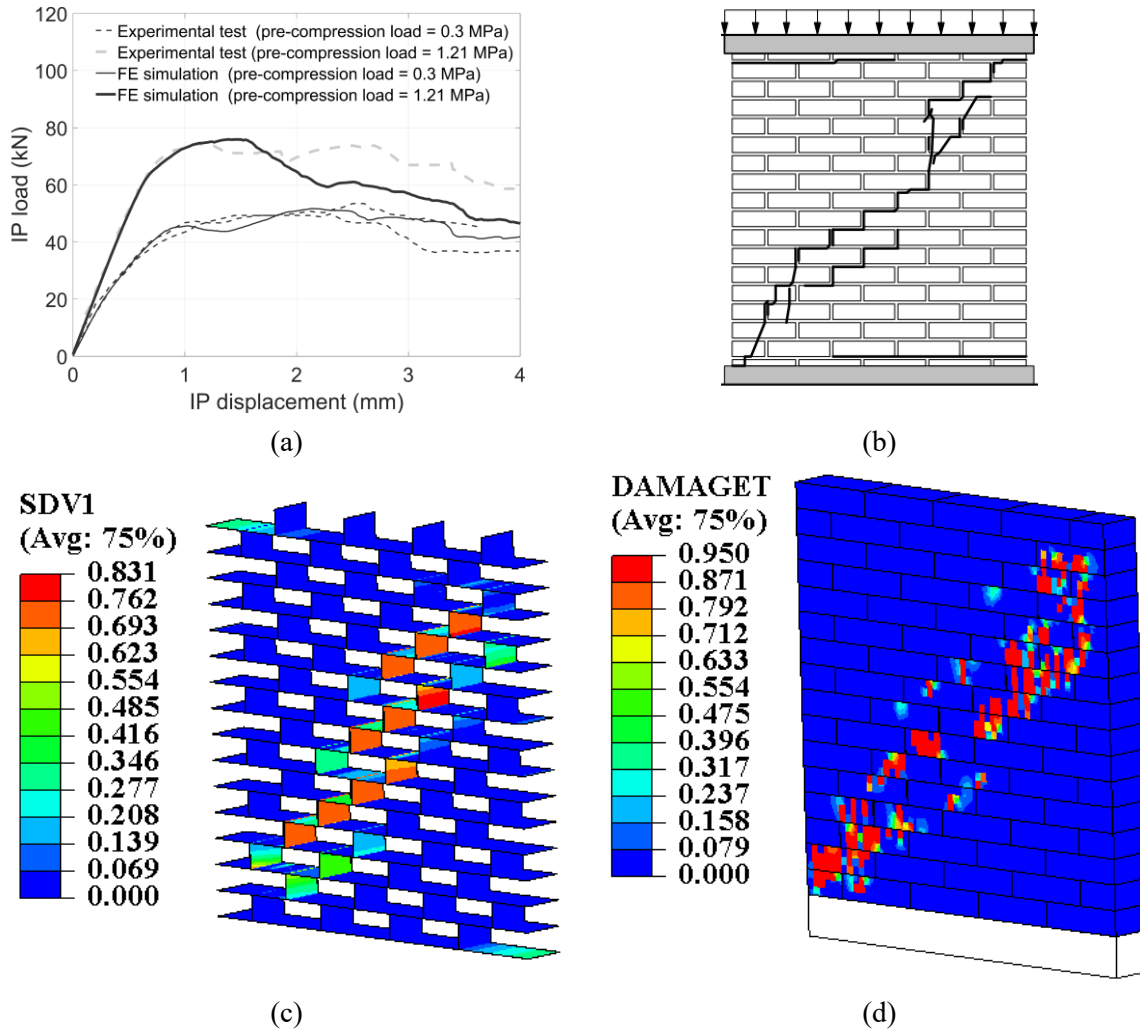


Figure 6-2. Numerical-experimental comparison for URM walls under IP loading: (a) IP load-deformation behavior, (b) experimental crack pattern for the wall with a pre-compression load of 0.3 MPa, (c) damage distribution in mortar joints (interfaces) from FE simulation, and (d) damage distribution in units from FE simulation

It is well recognized that the aspect ratio AR (i.e., height-to-length ratio) and pre-compression P_v exert considerable influence on the failure modes (e.g., flexural, diagonal shear, sliding) and associated capacities of URM walls under pure IP loading. On the other hand, the structural responses of URM walls under pure OOP loading are largely influenced by SR (i.e., height-to-thickness ratio) and P_v . Therefore, the influencing factors AR , SR , and P_v are considered

as variables in the parametric design in this study. Four different values of AR (0.75, 1.00, 1.5, and 2.25), combined with six different levels of P_v (0, 0.25, 0.5, 1.0, 1.5, and 2.0 MPa), are considered for URM walls to encompass different failure modes. Notably, AR is varied by changing the wall length while keeping the wall height constant. Furthermore, while keeping AR fixed as the same as the baseline wall, four different values of SR (9.92, 15.50, 21.08, and 32.24) are considered by adjusting the wall height, while the wall thickness remains the same as the unit thickness. This leads to a total of 42 cases with distinct geometrical configurations, or P_v levels, as summarized in Table 6-2. In the parametric design, the minimum and maximum values for AR and SR are selected in accordance with the design guidelines specified in the Canadian Masonry Design Code (Canadian Standards Association 2014), and the largest P_v is determined to be approximately 20% of the compressive strength of masonry (10.5 MPa), deemed a reasonable maximum axial load applied to URM walls (Kesavan and Menon 2022). In Table 6-2, the notations used to distinguish different wall geometries include the values of AR and SR. For instance, ‘AR0.75_SR9.92’ refers to the URM wall with an AR of 0.75 and a SR of 9.92.

Table 6-2. Design cases for FE-based investigation of the IP-OOP interaction behavior of URM walls

Wall	Length (mm)	Height (mm)	AR	SR	P_v (MPa)
AR0.75_SR9.92	1320	992	0.75	9.92	0.0, 0.25, 0.5, 1.0, 1.5, and 2.0
AR1.00_SR9.92	990	992	1.00	9.92	0.0, 0.25, 0.5, 1.0, 1.5, and 2.0
AR1.50_SR9.92	660	992	1.50	9.92	0.0, 0.25, 0.5, 1.0, 1.5, and 2.0
AR2.25_SR9.92	440	992	2.25	9.92	0.0, 0.25, 0.5, 1.0, 1.5, and 2.0
AR1.00_SR15.50	1540	1550	1.00	15.50	0.0, 0.25, 0.5, 1.0, 1.5, and 2.0
AR1.00_SR21.08	2090	2108	1.00	21.08	0.0, 0.25, 0.5, 1.0, 1.5, and 2.0
AR1.00_SR32.24	3190	3224	1.00	32.24	0.0, 0.25, 0.5, 1.0, 1.5, and 2.0

The IP boundary condition of URM walls is considered to be cantilever, and the OOP boundary condition is characterized by simple supports with the wall subjected to a typical one-way bending, representing a common boundary condition for masonry walls in low-rise buildings.

In the FE analysis, a pre-compression load P_v is initially applied at the top of the wall and remains constant throughout the analysis. Following this, a uniformly distributed OOP pressure p_{OOP} with a predetermined load level is applied. The analysis then proceeds with the application of an IP load F_{IP} until the wall fails. The pre-applied OOP load p_{OOP} is determined as 20%, 40%, 60%, and 80% of the OOP capacity for the examined URM wall under pure OOP loading. These four OOP loading levels represent the slight, moderate, intermediate, and near collapse stages under pure OOP loading (i.e., with no IP load). The loading sequence considered in this study is illustrated in Figure 6-3.

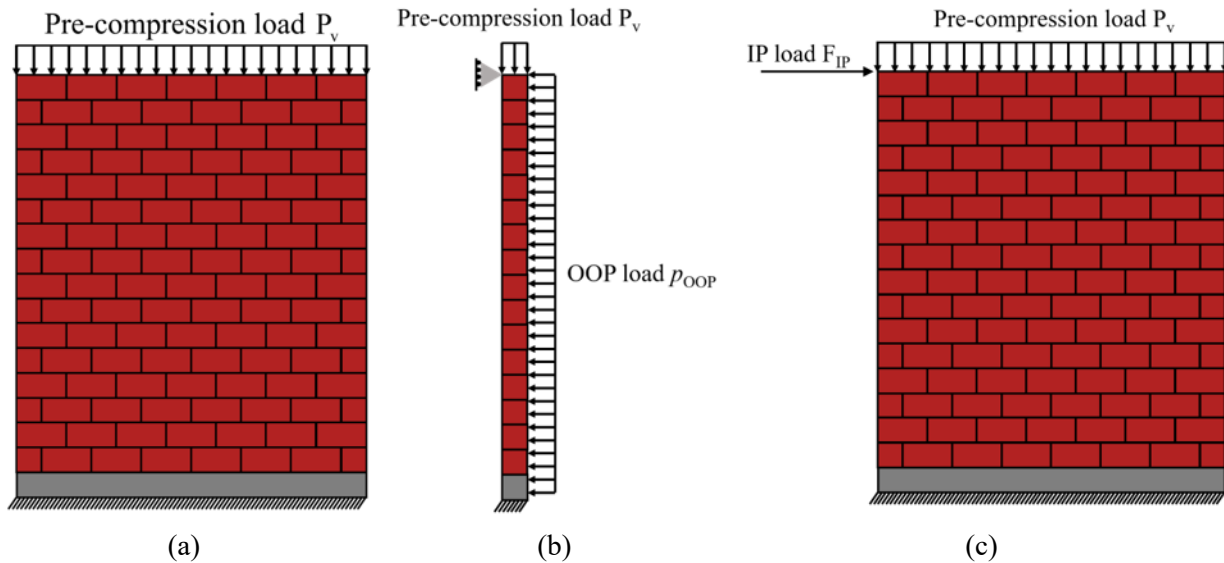


Figure 6-3. Loading sequence considered for URM walls under combined IP and OOP loading: (a) apply a pre-compression load P_v , (b) apply a predetermined uniformly distributed OOP load p_{OOP} , and (c) apply an IP load F_{IP} until wall failure

6.3. PURE IP AND PURE OOP BEHAVIORS OF URM WALLS

In this section, pure IP and pure OOP behaviors of URM walls are presented. Load-deformation behaviors, with a particular emphasis of IP and OOP capacities, and failure modes, are discussed to reflect the influence of AR, SR, and P_v .

6.3.1. Pure IP behavior

Predicting the IP failure mode of URM walls is a rather challenging task due to the heterogeneity of the masonry material. Figure 6-4 (a) and Figure 6-4 (b) present the flexural and shear governed URM walls observed in the FE analyses. It can be deduced that flexural failure is initiated in cases with low pre-compression load and high aspect ratio, e.g., Figure 6-4 (a), while shear failure is commonly observed in squat walls under high pre-compression loads, e.g., Figure 6-4 (b). Moreover, slenderness ratio has negligible influence on the IP failure modes in all involved FE cases, as demonstrated by comparing Figure 6-4 (a) and Figure 6-4 (c).

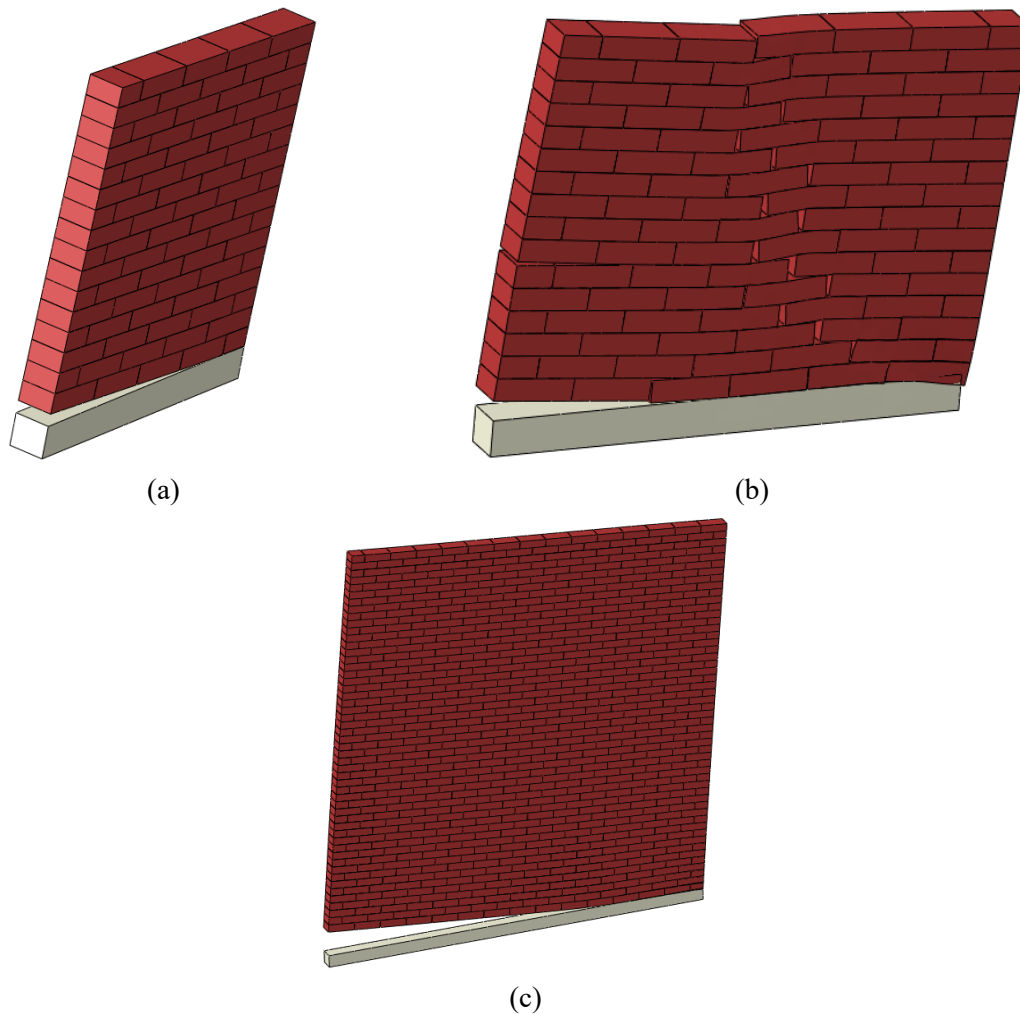
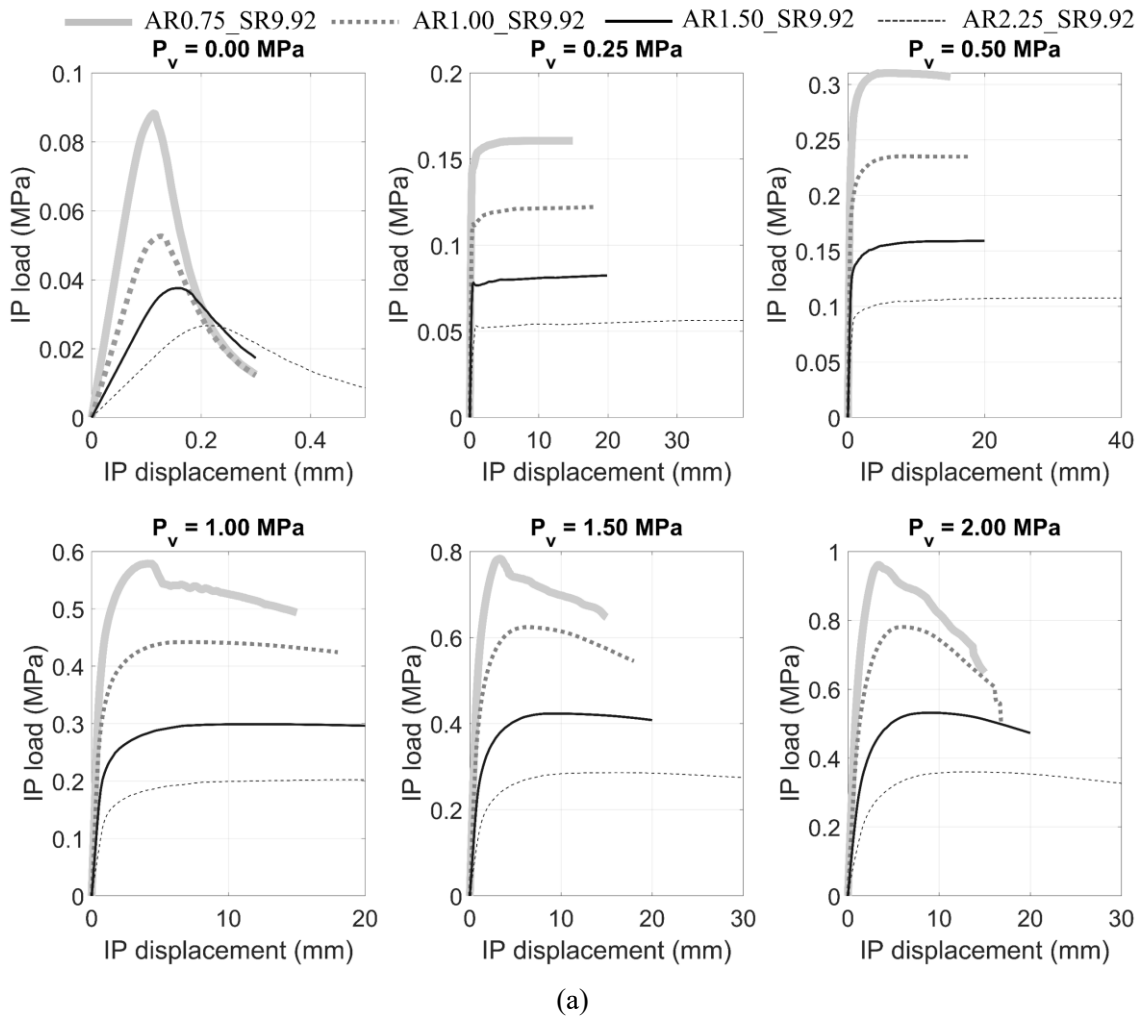
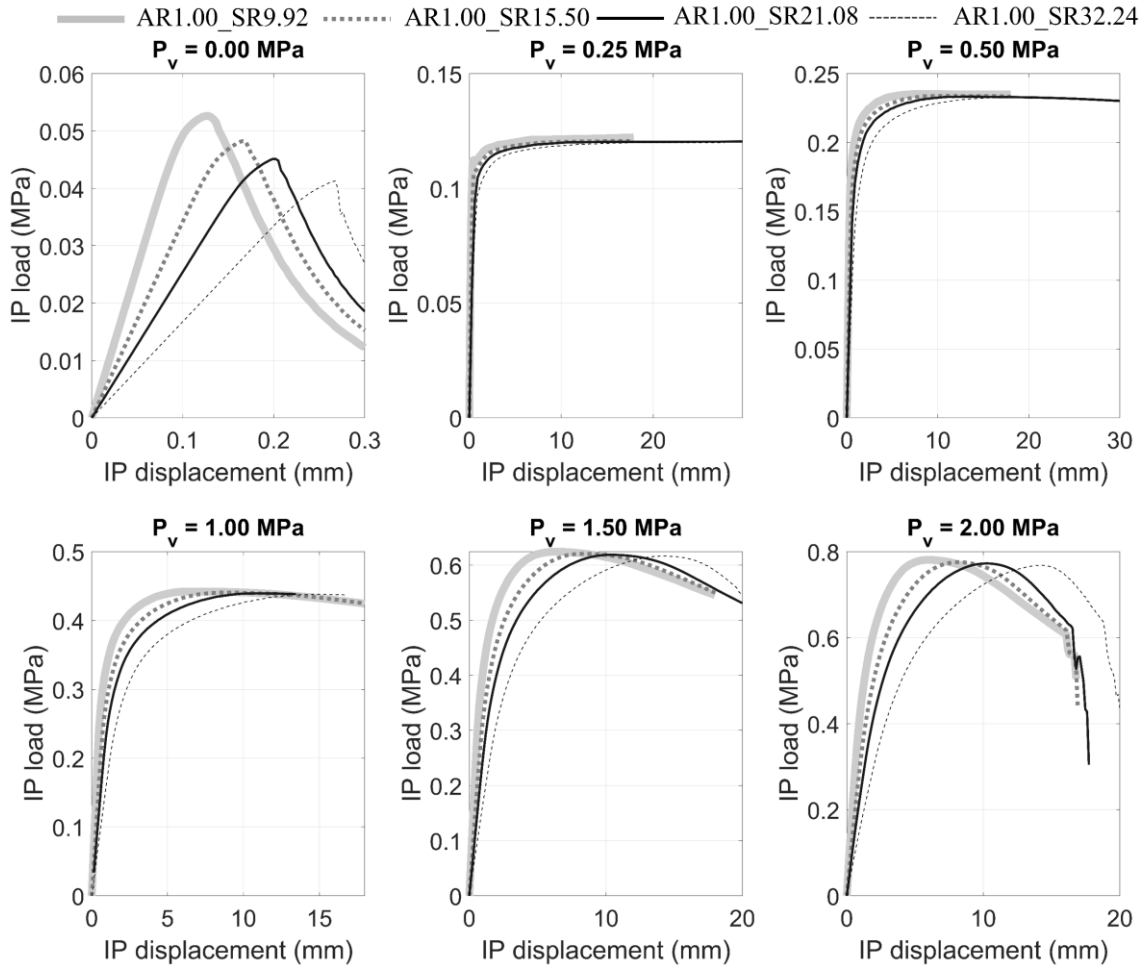


Figure 6-4. Failure modes of URM walls: (a) wall AR1.00_SR9.92 with a pre-compression load of 0.0 MPa, (b) wall AR0.75_SR9.92 with a pre-compression load of 2.0 MPa, and (c) wall AR1.00_SR32.24 with a pre-compression load of 0.0 MPa

The variation of load-deformation curves for different values of AR, SR, and P_v is demonstrated in Figure 6-5. It should be noted that the displacement referenced here represents the horizontal drift at the top of the walls. As observed in Figure 6-5 (a), the IP capacity and stiffness increase with the reduction of AR. This is reasonable and consistent with experimental and/or numerical findings, as more compressive struts along the diagonal path and a larger compressive zone at the toe regions are expected in squat walls (i.e., walls with smaller ARs) under large pre-compression loads. Nevertheless, the ductility is diminished for squat walls, indicating a more

pronounced strength loss during the post-peak stage. A similar trend is observed for the influence of pre-compression load, as illustrated in Figure 6-5 (c). As for the SR, its influence on the wall capacity is negligible but affects the pre-peak stiffness, as evidenced in Figure 6-5 (b). In this study, of particular interest is the IP capacity, whose variations are shown in Figure 6-6.





(b)

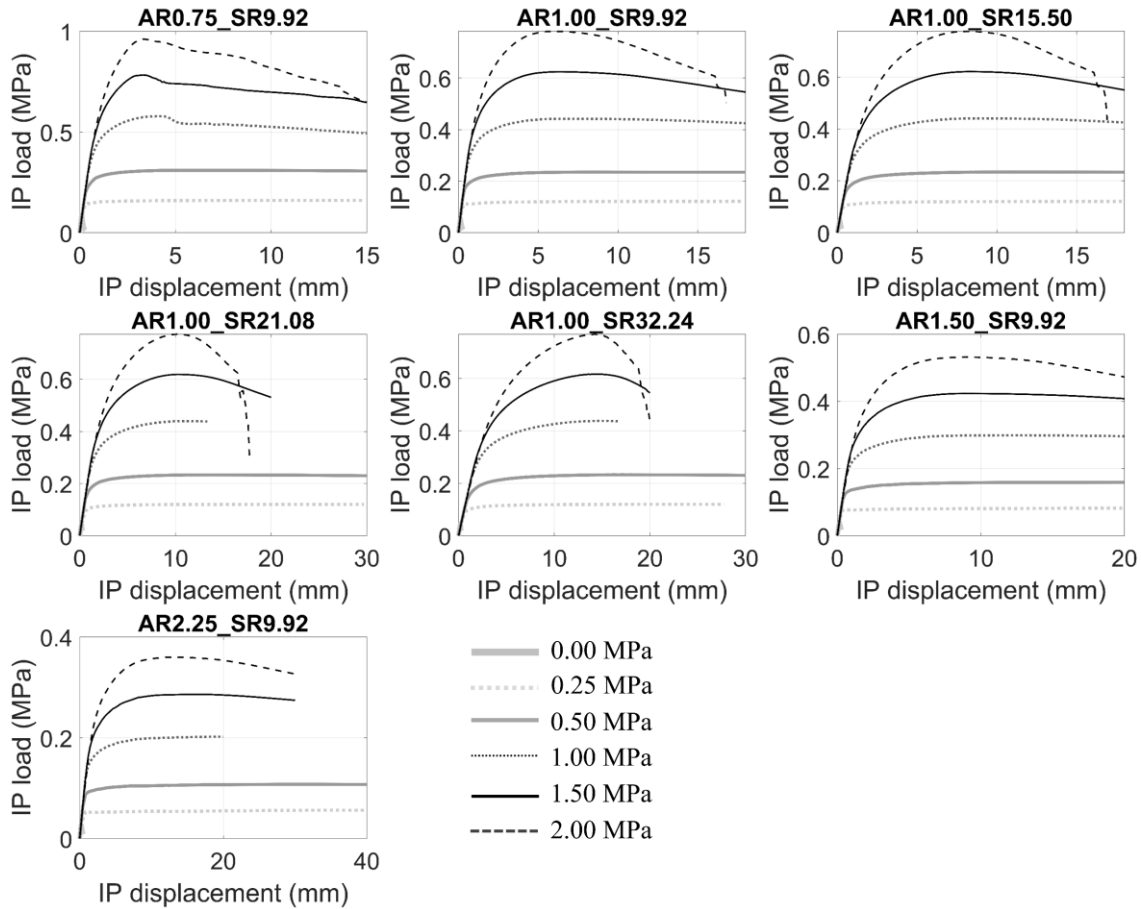


Figure 6-5. Influence of (a) AR, (b) SR, and (c) P_v on the IP load-deformation behaviors of URM walls

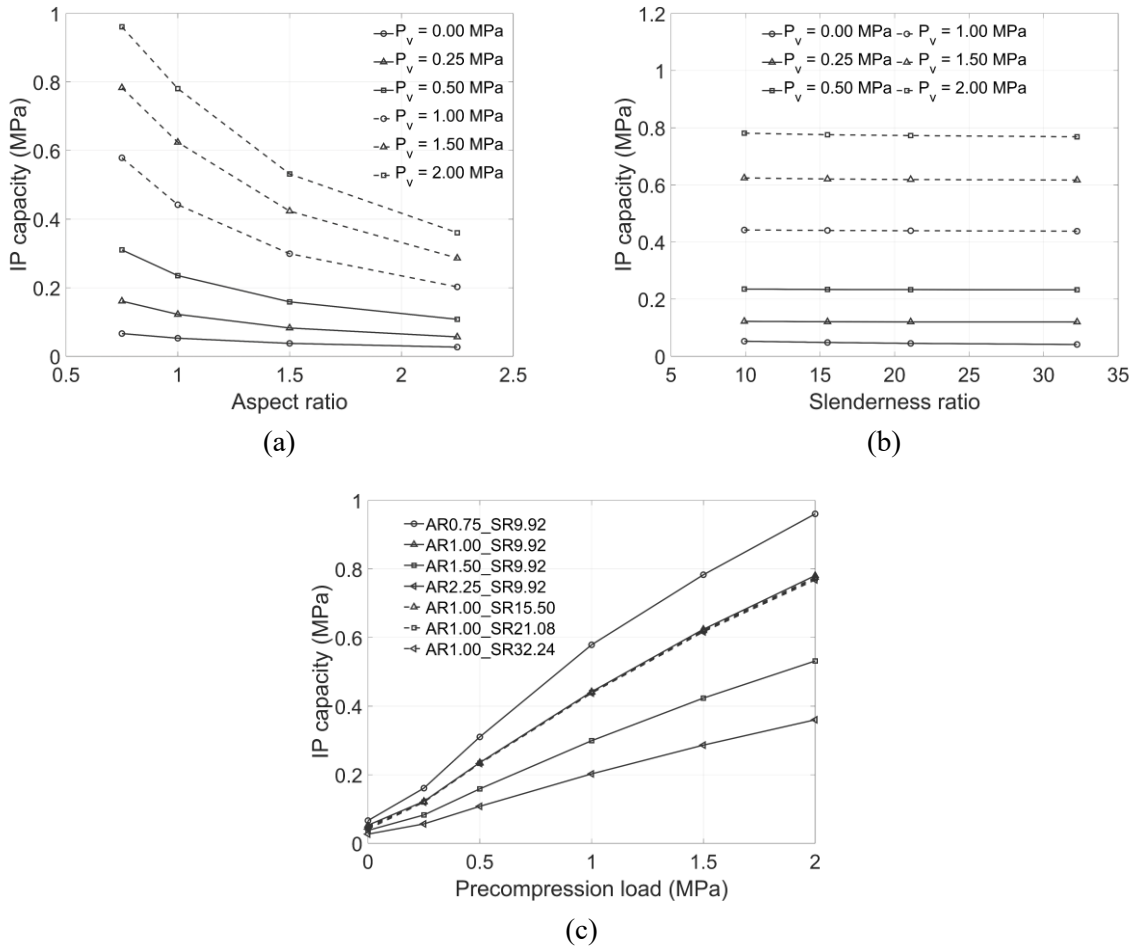


Figure 6-6. Variation of IP capacity of URM walls in terms of the (a) AR, (b) SR, and (c) pre-compression load

6.3.2. Pure OOP behavior

The structural behavior of URM walls subject to one-way vertical bending can be easily interpreted. It should be noted that failure modes of URM walls under OOP loading are not affected by factors discussed in this study (i.e., AR, SR, P_v). The bending moments developed along the wall section would lead to crack propagation at the base section and approximately mid-height position, as shown in Figure 6-7.

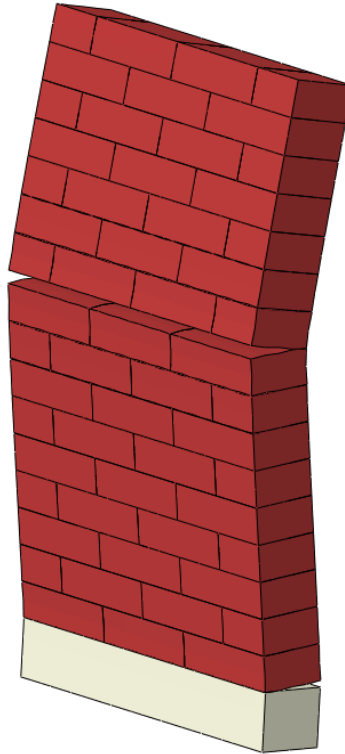
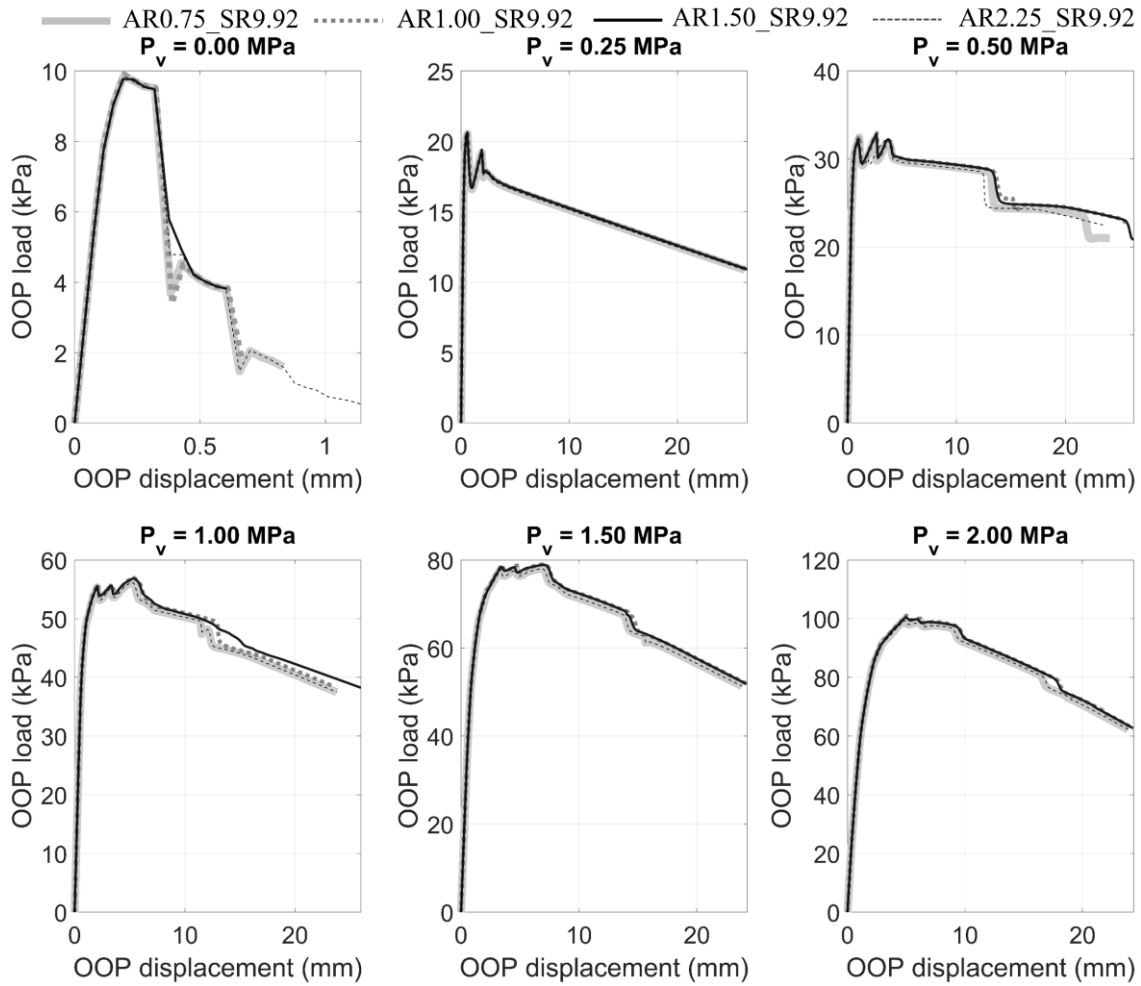


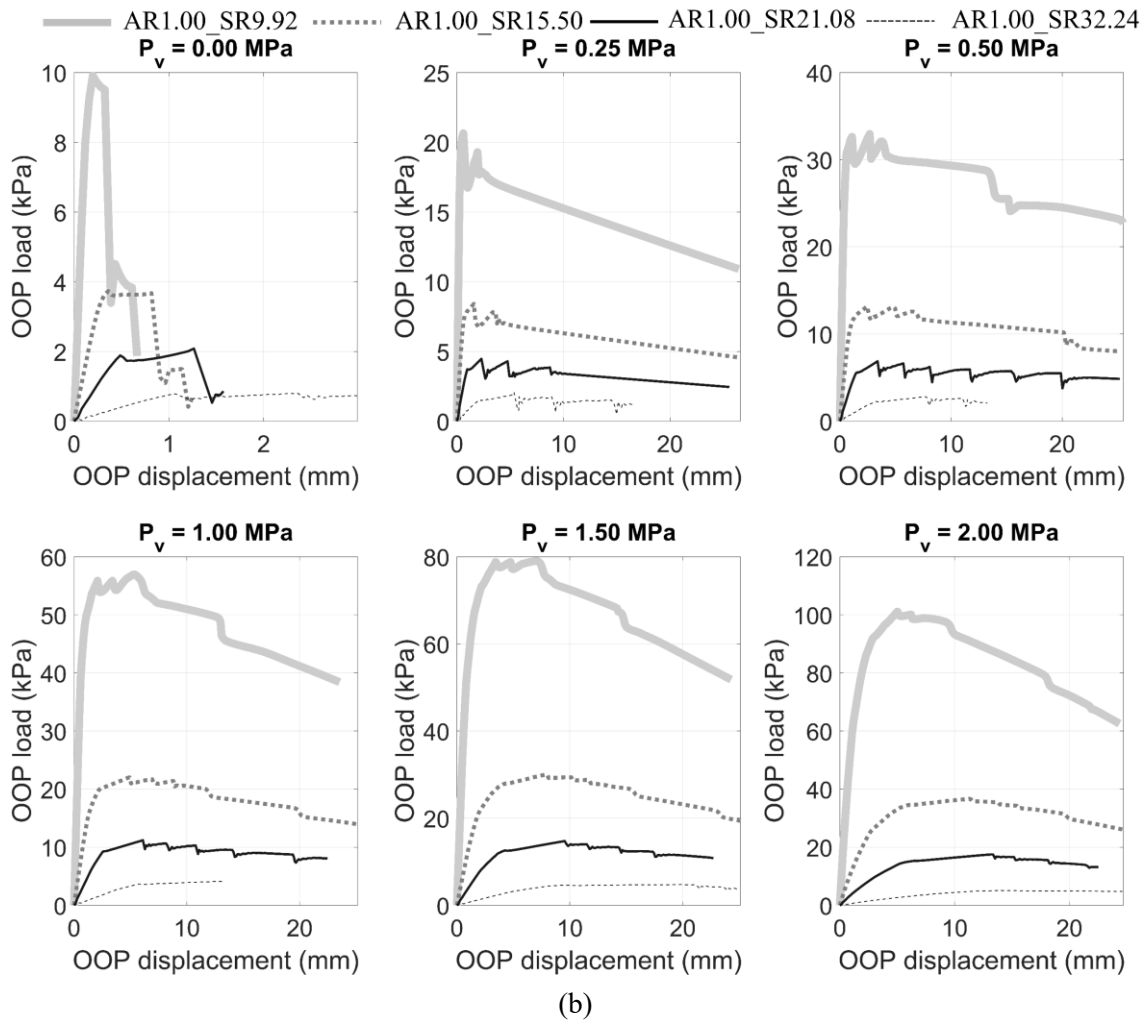
Figure 6-7. Failure mode of URM wall subject to one-way vertical bending

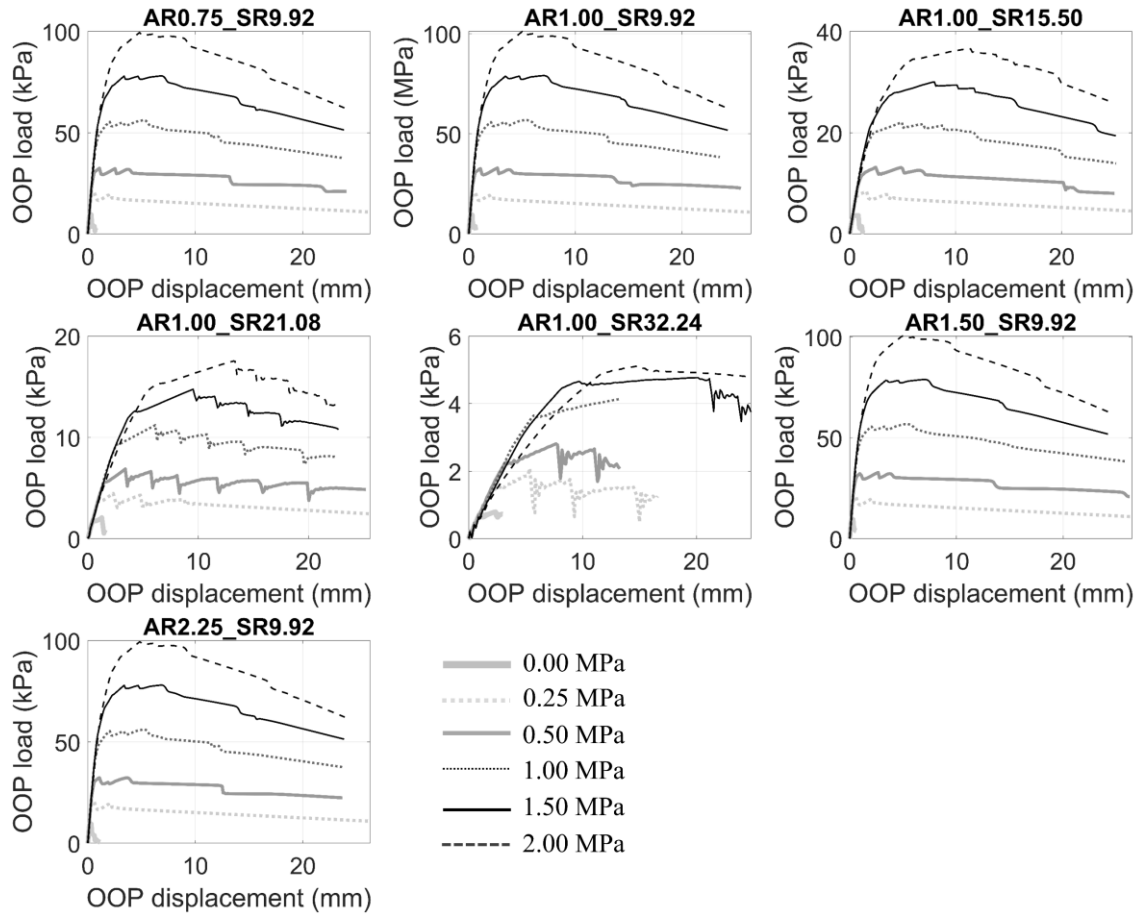
Figure 6-8 illustrates the impact of AR, SR, and P_v on the load-deformation behaviors of URM walls under OOP loading, respectively. OOP displacements are measured at the central positions of the load-applied faces. As observed in Figure 6-8 (a), AR has a negligible influence on the OOP behavior, including stiffness, peak capacity (shown in Figure 6-9 (a)), and post-peak behavior. A larger SR generally leads to decreased OOP stiffness and capacity, as shown in Figure 6-8 (b), since taller walls are more susceptible to buckling and secondary moments caused by larger deflections under OOP lateral loads. The variation curves of OOP capacity in terms of the SR under different pre-compression load levels, displayed in Figure 6-9 (b), indicate different slopes, which implies that the influence of pre-compression load and SR can be interdependent. An increase in the pre-compression load could counteract the tensile stress generated by OOP forces, thereby enhancing the OOP capacity (Figure 6-8 (c)). A linear relationship can be used to

describe the relationship between the OOP capacity and pre-compression load, shown in Figure 6-9 (c). However, it should be noted that for highly slender walls (e.g., SR = 32.24) shown in Figure 6-8 (c), a higher pre-compression load would be detrimental to the wall's stiffness.



(a)





(c)

Figure 6-8. Influence of (a) AR, (b) SR, and (c) P_v on the OOP load-deformation behaviors

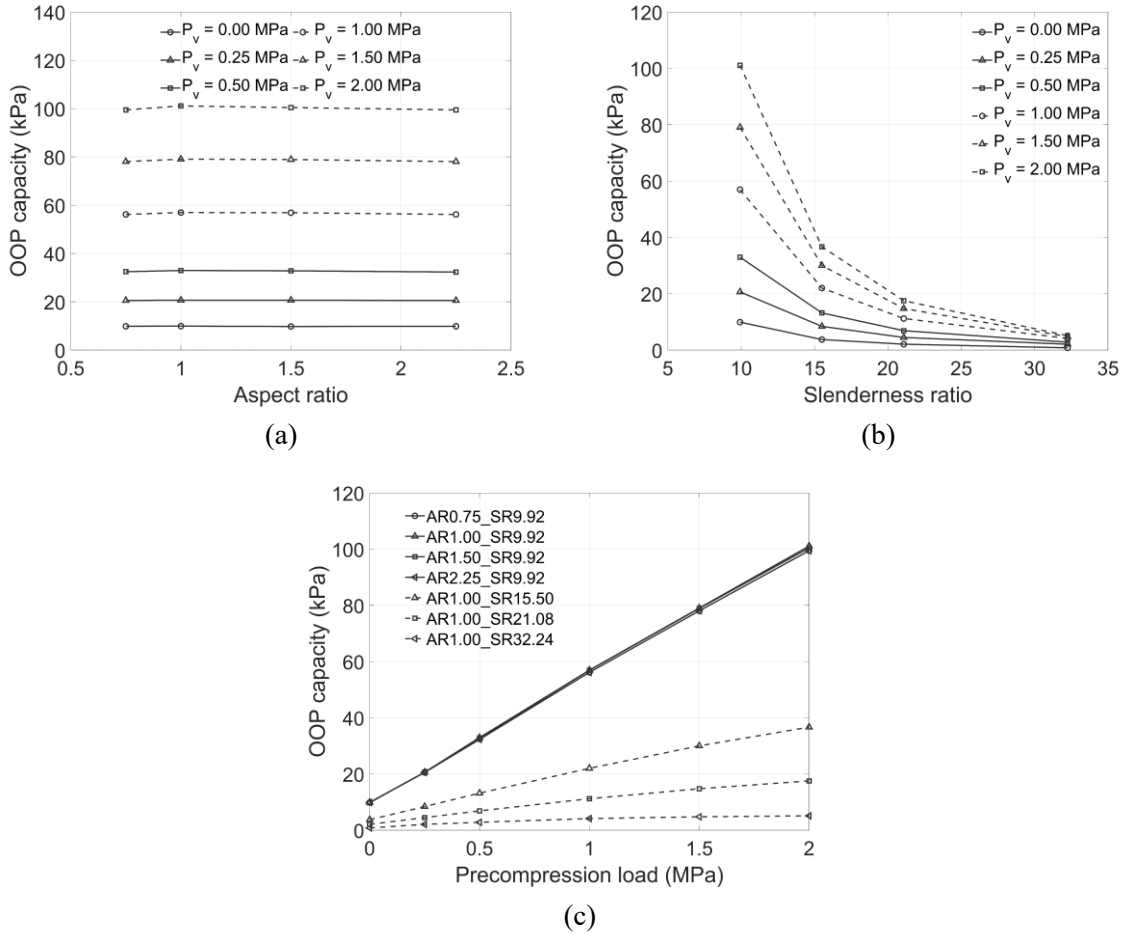


Figure 6-9. Variation of OOP capacity of URM walls in terms of the (a) AR, (b) SR, and (c) pre-compression load

6.4. IP AND OOP INTERACTION BEHAVIORS OF URM WALLS

This section presents the simulation results for URM walls subjected to combined IP and OOP loading. The reduction in IP capacity caused by the presence of OOP loading is quantified across various geometrical configurations and pre-compression load levels. The effects of AR, SR, and P_v on the capacity interaction are investigated. To facilitate the discussion, pure IP and pure OOP capacities (i.e., capacities under pure IP and pure OOP loading) of URM walls are denoted as F_{IP}^{pure}

and $p_{\text{OOP}}^{\text{pure}}$, respectively. Conversely, IP and OOP capacities under combined IP and OOP conditions are denoted as F_{IP} and p_{OOP} , respectively.

6.4.1. Influence of aspect ratio (AR) and pre-compression load (P_v)

To obtain insights into the IP-OOP interaction behaviors of URM walls with different AR, two walls with the smallest and largest AR values are considered to examine the failure modes: wall AR0.75_SR9.92 and wall AR2.25_SR9.92. Note that under pure IP loading, wall AR0.75_SR9.92 (a long wall) demonstrates a diagonal shear failure mode, whereas wall AR2.25_SR9.92 (a short wall) exhibits the flexural failure. Under combined IP and OOP loading, the failure modes are affected by the pre-applied OOP loads.

Figure 6-10 presents the different failure modes of wall AR0.75_SR9.92 when the peak IP loads are attained under IP loading after a pre-compression $P_v = 2.00$ MPa and different levels of OOP loads are pre-applied. As shown in Figure 6-10 (a), under the pure IP condition (i.e., no OOP load), IP flexural cracks can be observed at the bottom, but the IP capacity is governed by the formation of diagonal shear cracking and the crushing at the toe region. With the escalation of pre-applied OOP loads to 20% of the pure OOP capacity, the failure mode remains largely unaltered, see Figure 6-10 (b). However, with OOP loads attaining 40% and 60% of the pure OOP capacity, more OOP flexural cracks develop at the bottom course and the middle height, and under combined IP-OOP loading, additional OOP shear sliding deformations can be observed with less diagonal shear cracking, see Figure 6-10 (c-d). The further increase in OOP load leads to a weakened section at the base, induced by the combined effects of OOP bending and OOP sliding, while no diagonal shear cracks are visible when the wall fails, as illustrated in Figure 6-10 (e).

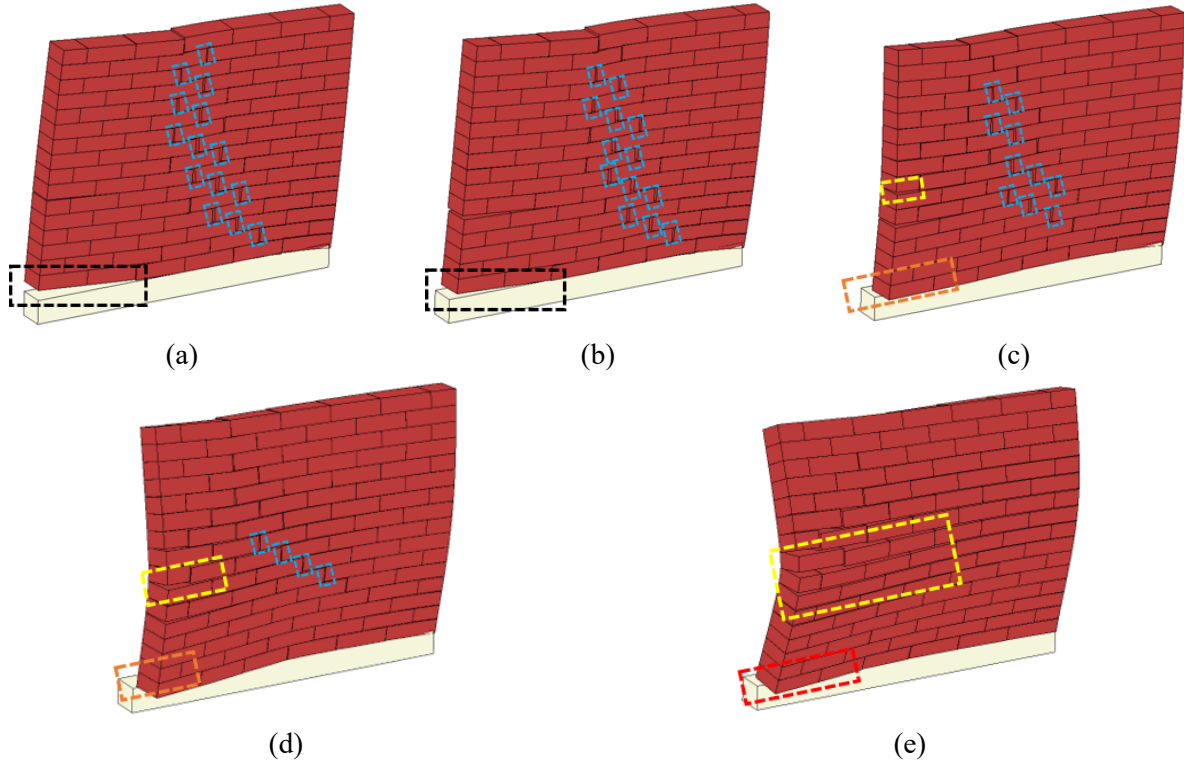


Figure 6-10. Failure modes of wall AR0.75_SR9.92 under a pre-compression load of 2.00 MPa with different pre-applied OOP load levels: (a) 0%, (b) 20%, (c) 40%, (d) 60%, and (e) 80% of pure OOP capacity (deformation scale factor: 15)

- IP flexural cracking
- Diagonal tension cracking
- OOP shear sliding
- OOP flexural cracking
- OOP flexural cracking + OOP shear sliding

The associated IP load-deformation curves are shown in Figure 6-11. It is worth noting that the IP loads are normalized by the wall lengths to reflect the load per unit wall length. In addition to the ductility reduction, an obvious decrease in IP capacities is observed due to the presence of the OOP load. When the pre-applied OOP load levels are at 60% and 80% of the pure OOP capacity, the IP capacities are 86.13 kN/m and 72.99 kN/m, respectively, corresponding to reductions of 10.37% and 24.04% with respect to the pure IP capacity of 96.09 kN/m.

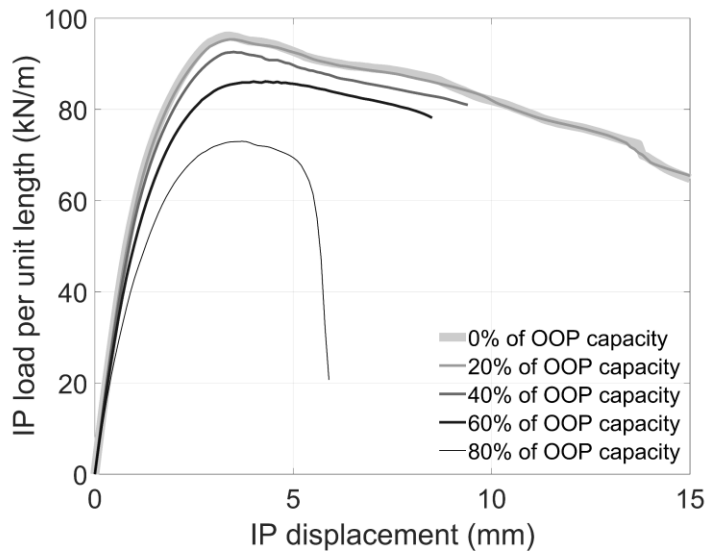


Figure 6-11. IP load-deformation curves with different levels of pre-applied OOP loading for the wall AR0.75_SR9.92 with $P_v = 2.00$ MPa

Similarly, Figure 6-12 illustrates the failure modes for the wall AR2.25_SR9.92 subjected to IP loading with $P_v = 2.00$ MPa and different pre-applied OOP loads. It can be observed that the failure modes with pre-applied OOP loads at 20%, 40%, and 60% of the pure OOP capacity closely resemble that of the wall without pre-applied OOP load, characterized by the IP flexural cracking, i.e., cracking opening at the mortar joints below the bottom course shown in Figure 6-12(a). When the pre-applied OOP load reaches 80% of the pure OOP capacity, the critical section shifts to the mid-height section due to the extensive OOP flexural cracks developed. Notably, there is no evident shear sliding developed for this wall, even with high pre-applied OOP loads. This is essentially different from the failure mechanism of wall AR0.75_SR9.92 with $P_v = 2.00$ MPa discussed earlier. Correspondingly, the IP load-deformation curves for the wall AR2.25_SR9.92 with $P_v = 2.00$ MPa are shown in Figure 6-13. Note that the IP capacity with a pre-applied load equal to 80% of the pure OOP capacity is reduced by 30.3% compared to the pure IP capacity.

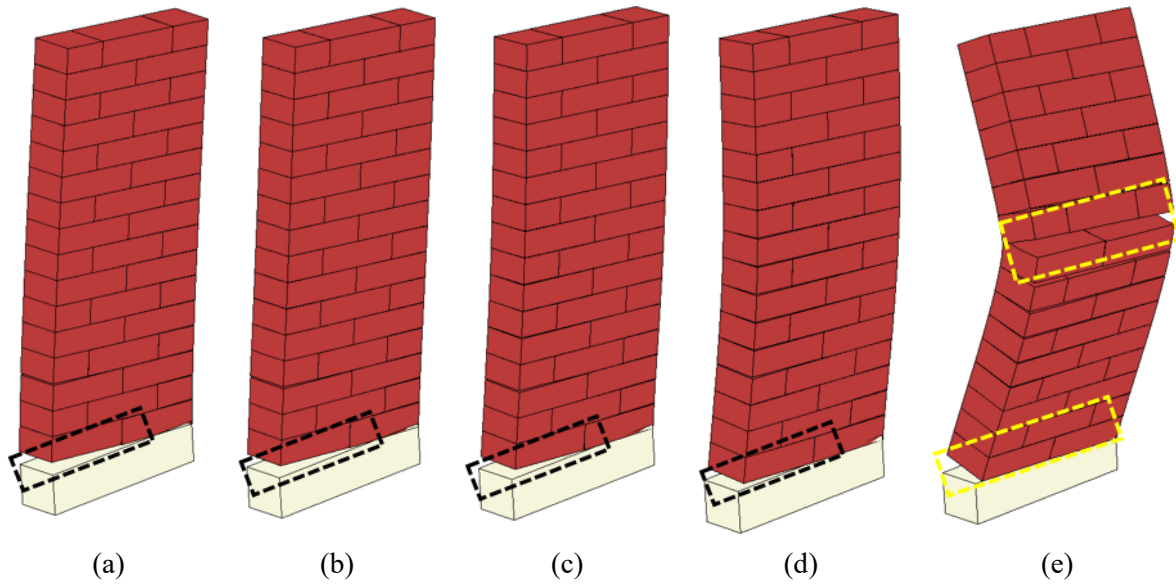


Figure 6-12. Failure modes of wall AR2.25_SR9.92 under a pre-compression load of 2.00 MPa with different pre-applied OOP load levels: (a) 0%, (b) 20%, (c) 40%, (d) 60%, and (e) 80% of pure OOP capacity (deformation scale factor: 10)

IP flexural cracking
 OOP flexural cracking

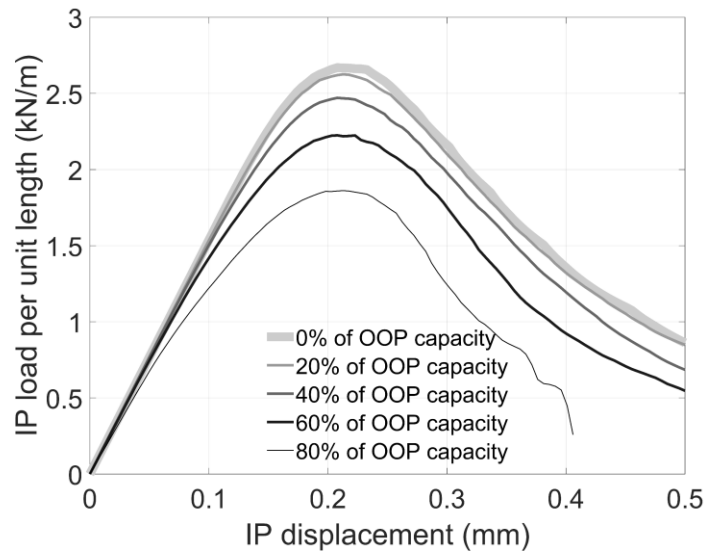


Figure 6-13. IP load-deformation curves with different levels of pre-applied OOP loading for the wall AR2.25_SR9.92 with $P_v = 0.00$ MPa

To quantify the IP-OOP capacity interaction effects, or the influence of OOP load on the IP capacity, interaction curves are developed by normalizing the IP and OOP capacities F_{IP} and p_{OOP} using the pure IP and OOP capacities F_{IP}^{pure} and p_{OOP}^{pure} . Figure 6-14 presents the influence of AR on the interaction curves. As AR decreases, the interaction effects become stronger, leading to more pronounced reductions in IP capacities due to the presence of OOP loading. That is to say, longer walls exhibit more pronounced IP capacity reductions, which is attributed to the failure mechanisms discussed previously.

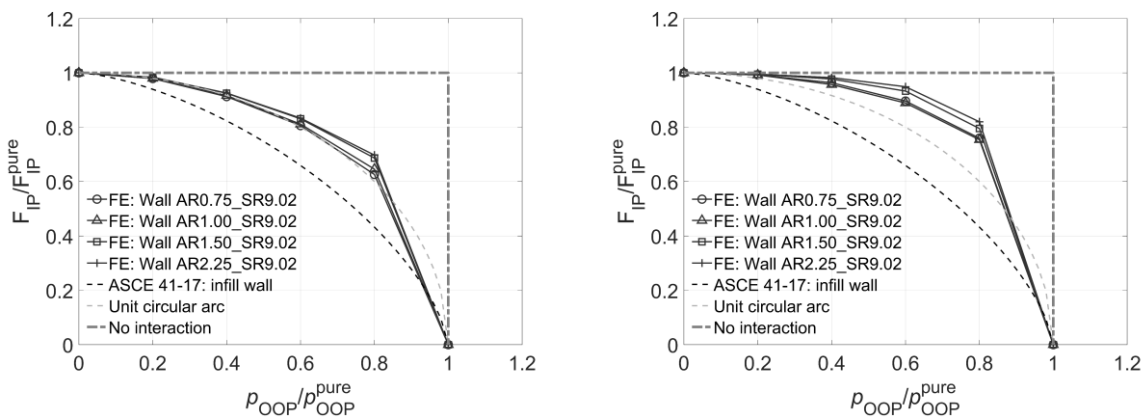


Figure 6-14. IP-OOP capacity interaction curves for URM walls with different AR under a pre-compression load of: (a) 0.00 MPa, and (b) 2.00 MPa

In addition, three reference interaction curves are included in Figure 6-14 for comparison purposes: one suggested by ASCE 41-17 (ASCE 2017) for masonry infill walls, one depicted by a unit circular arc, and another one indicating no interaction. Notably, the unit circular arc correlates better with the interaction curves derived based on FE simulations for the URM walls considered. For the URM wall exhibiting the most pronounced IP-OOP interaction effects shown in Figure 6-14 (i.e., wall AR0.75_SR9.92 with $P_v = 0.00$ MPa), there is a 37% reduction relative

to the IP capacity of the wall without OOP loads. This reduction is considerably less than that suggested by ASCE 41-17 for masonry infill walls (i.e., 58%).

A comparison between Figure 6-14 (a) and Figure 6-14 (b) indicates that the walls without a pre-compression load exhibit greater IP capacity reduction than those with a 2.00 MPa pre-compression load. To have more insights on the influence of pre-compression load on the IP-OOP interactions, the failure modes of the wall AR0.75_SR9.92 with pre-applied OOP loads at 80% of the pure OOP capacities subjected to different pre-compression load levels are presented as an example in Figure 6-15. For the cases of $P_v = 0$ MPa and $P_v = 0.25$ MPa, as shown in Figure 6-15 (a-b), the combined IP and OOP loading results in the detachment of the corner region and a noticeable wall twist, largely attributed to the low OOP sliding resistance of the walls. This type of failure is commonly observed in low-rising URM buildings, for instance, see a post-earthquake survey referenced in (Vlachakis et al. 2020). Consequently, this would lead to a substantial reduction in IP capacity. An increase in pre-compression load would alleviate the IP-OOP interaction effects given its positive role in enhancing sliding resistance, and the OOP bending deformation would become more prominent, as shown in Figure 6-15 (b-d). However, as the pre-compression load further increases, additional OOP flexural cracks would develop around the mid-height region, as seen in Figure 6-15 (e-f). This can compromise the IP capacity due to the reduced effective thickness of the wall.

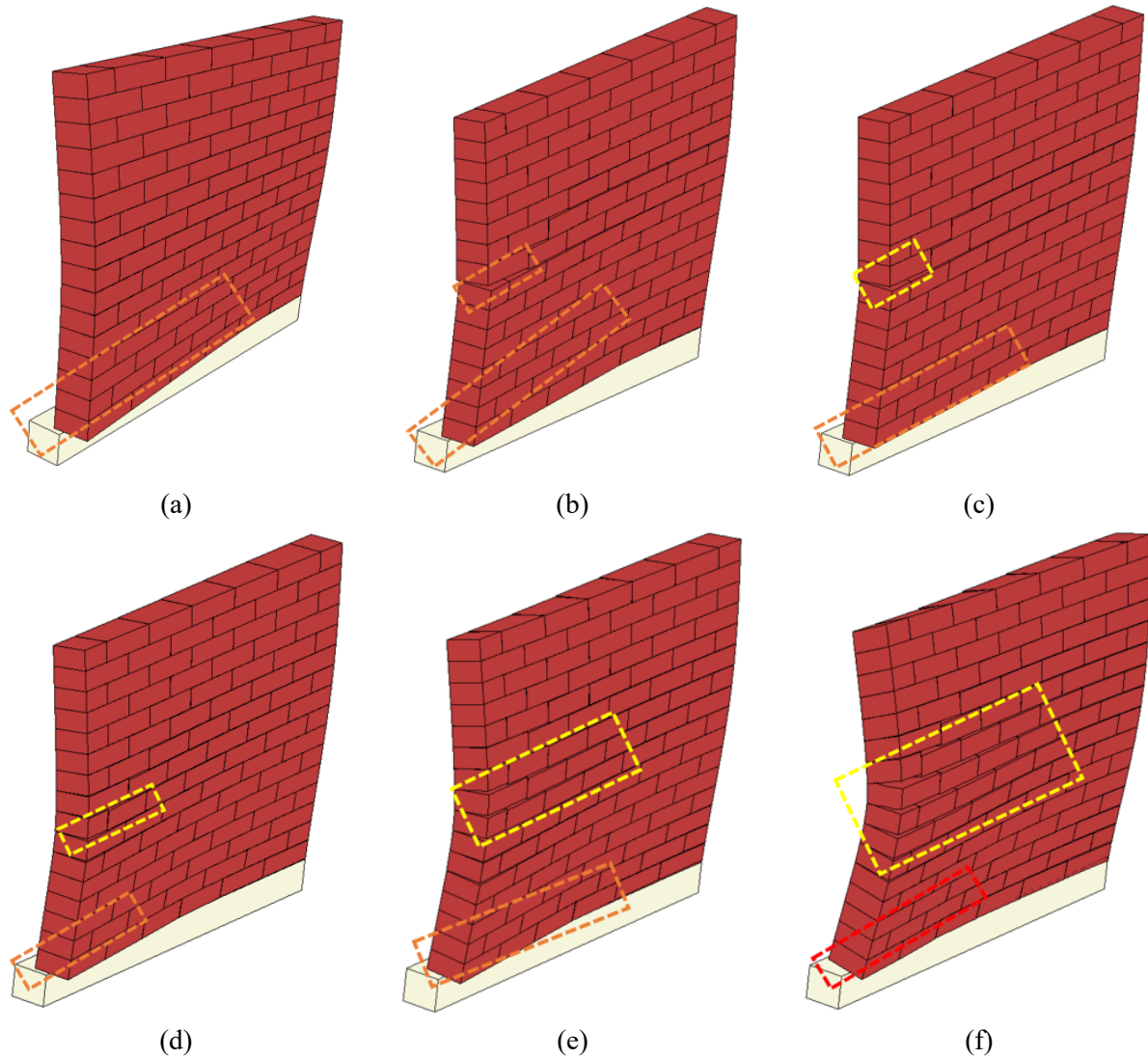


Figure 6-15. Failure modes of wall AR0.75_SR9.92 with pre-applied OOP load levels at 80% of pure OOP capacities under a pre-compression load of : (a) 0 MPa (deformation scale factor: 100), (b) 0.25 MPa, (c) 0.50 MPa, (d) 1.00 MPa, (e) 1.50 MPa, and (f) 2.00 MPa (deformation scale factor for (b-f): 15)

- OOP shear sliding
- OOP flexural cracking
- OOP flexural cracking + OOP shear sliding

Figure 6-16 illustrates the IP-OOP capacity interaction curves for both walls discussed. It is observed that pre-compression loads in a relatively lower range are beneficial for mitigating the capacity interaction effects for the walls. To be specific, this range is $0.00 \text{ MPa} < P_v < 0.25 \text{ MPa}$

for the wall AR0.75_SR9.92, and $0.00 \text{ MPa} < P_v < 0.5 \text{ MPa}$ for the wall AR2.25_SR9.92. However, at higher pre-compression load levels, an increase in P_v adversely impacts the IP-OOP interaction effects. Notably, walls with $P_v = 0.00 \text{ MPa}$ exhibit the most significant IP capacity reductions when the pre-applied OOP loads are 80% of the pure OOP capacities, primarily due to their limited OOP sliding resistance. However, these reductions are still less than those suggested by ASCE 41-17 for masonry infill walls. On the other hand, the unit circular arc is much better correlated with the ones obtained by FE simulations.

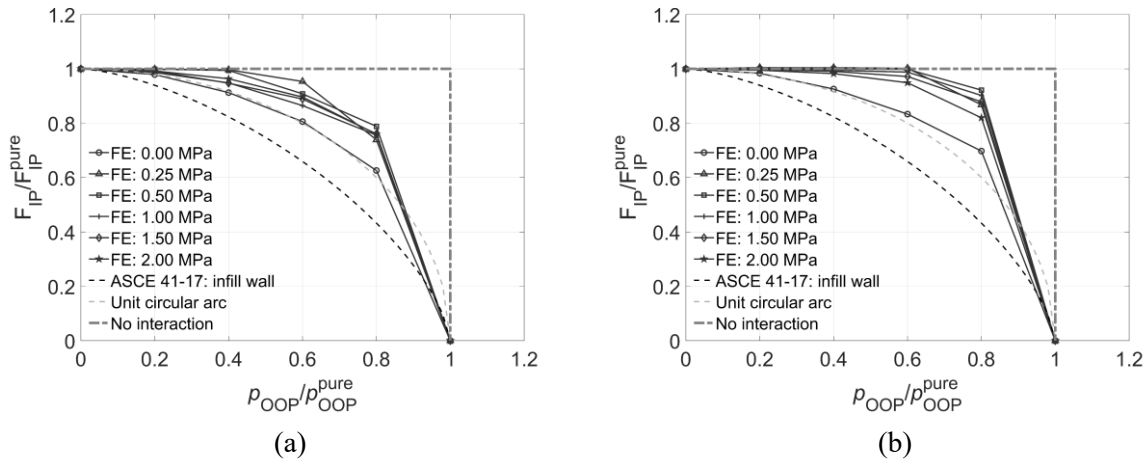


Figure 6-16. IP-OOP capacity interaction curves under different pre-compression loads for: (a) wall AR0.75_SR9.92 and (b) wall AR2.25_SR9.92

6.4.2. Influence of slenderness ratio (SR) and pre-compression load (P_v)

Figure 6-17 presents the OOP deformation contours of wall AR1.00_SR9.92 and wall AR1.00_SR32.24, representing two walls with the smallest and largest SR considered, respectively. Both walls are subjected to a pre-compression load of 0.0 MPa. To illustrate the effects of IP loads on the OOP deformations, two IP loading levels are involved in Figure 6-17: no IP load (i.e., only with pre-applied OOP loads at 80% of the pure OOP capacities) and peak IP load. It is worth emphasizing that when assessing the influence of SR, the length and height of

walls are varied proportionally to maintain a fixed value of AR, as indicated by the dimensions (at undeformed stages) shown in Figure 6-17. The contour plots reveal that the IP load induces a greater additional OOP deformation for the highly slender wall (i.e., wall with SR = 32.24). The increased OOP deformations cause more extensive tensile crack openings, leading to more reductions in the effective thickness of the wall. In turn, walls with larger SR are prone to greater IP capacity reductions, thereby resulting in stronger IP and OOP interaction effects. This is corroborated by the IP-OOP capacity interaction curves shown in Figure 6-18, in which the influence of SR is illustrated with $P_v = 0.0$ MPa and $P_v = 2.0$ MPa. At both pre-compression load levels, the walls with maximum SR (i.e., wall AR1.00_SR32.24) demonstrate the most substantial IP capacity reductions due to the presence of OOP loading. For instance, with $P_v = 0.00$ MPa, the IP capacity of wall AR1.00_SR32.24 reduces by 61.5% when the pre-applied OOP load reaches 80% of its pure OOP capacity, surpassing the 58% reduction suggested in ASCE 41-17 for masonry infill walls. In contrast, this reduction is only 35.4% for wall AR1.00_SR9.92. With $P_v = 2.00$ MPa, the IP capacity reductions for wall AR1.00_SR32.24 and wall AR1.00_SR9.92 are 45% and 25%, respectively.

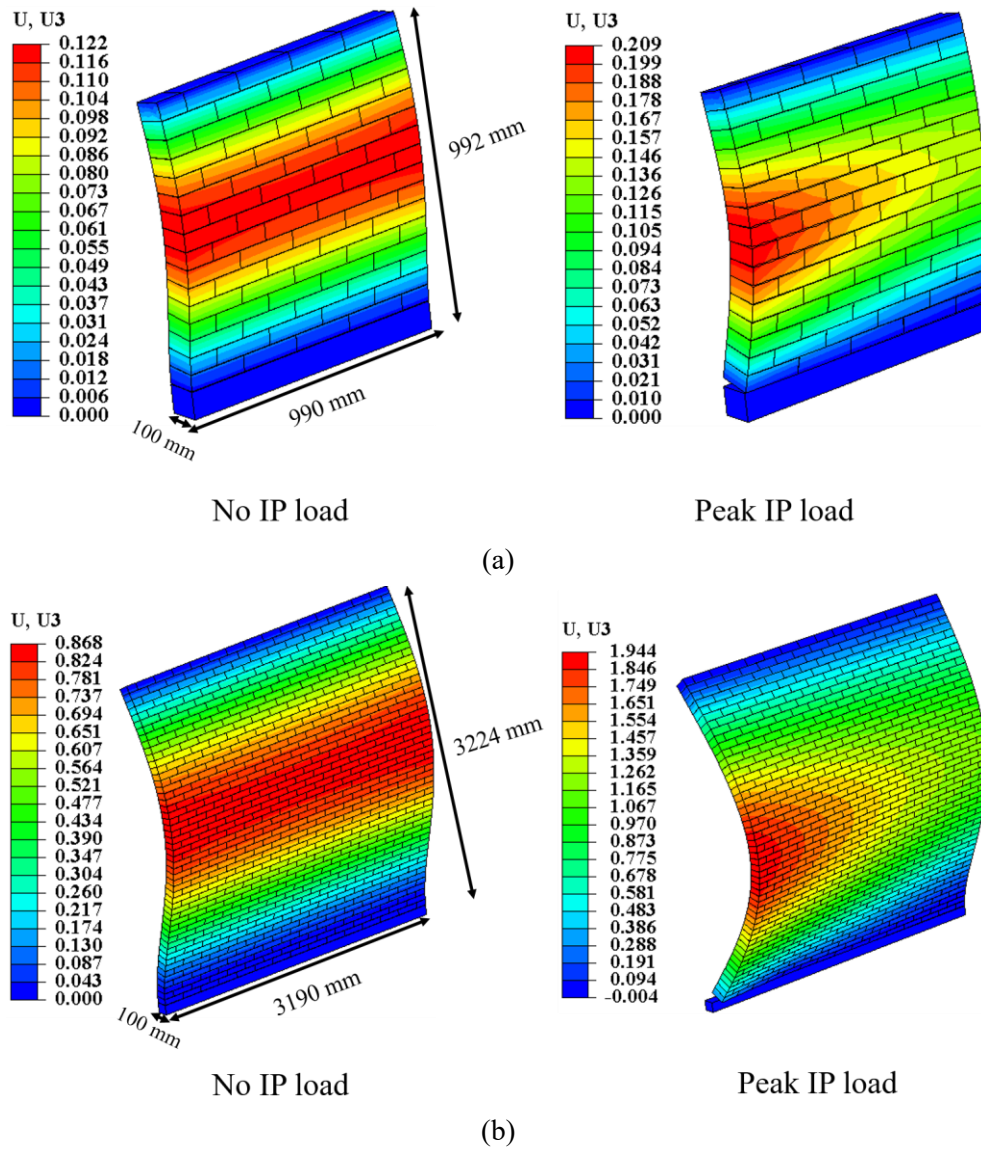


Figure 6-17. Evolution of OOP deformations (mm) due to IP loads for the: (a) wall AR1.00_SR9.92 with $P_v = 0.0$ MPa, and (b) wall AR1.00_SR9.92 with $P_v = 0.0$ MPa (deformation scale factor: 500)

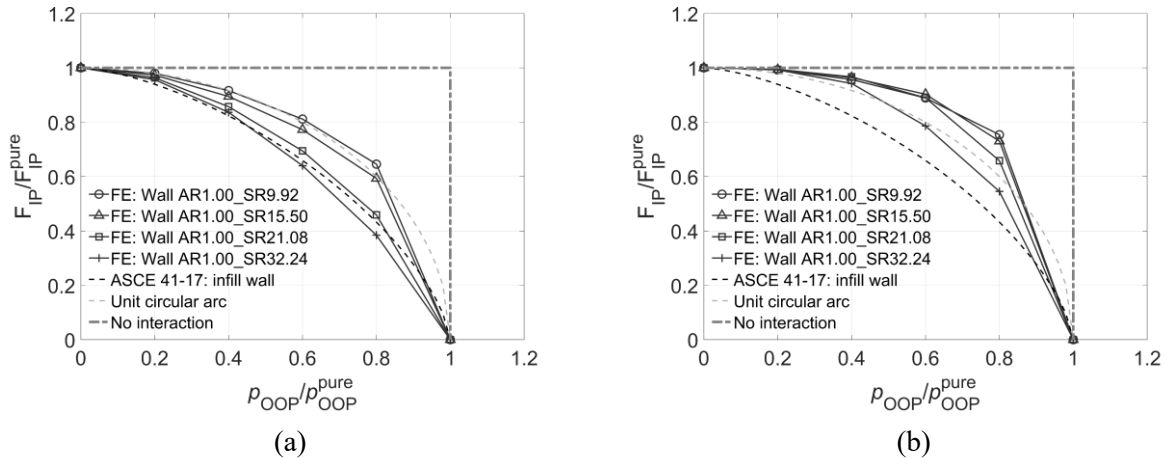


Figure 6-18. IP-OOP capacity interaction curves for URM walls with different SR under a pre-compression load of: (a) 0.00 MPa, and (b) 2.00 MPa

To show the influence of pre-compression loads on the walls with different SR, the IP-OOP interaction curves of two walls, AR1.00_SR9.92 and AR1.00_SR32.24, are shown in Figure 6-19. The observation here is consistent with the discussion presented in Section 6.4.1. At relatively lower magnitudes, increasing the pre-compression load proves beneficial in mitigating the IP-OOP capacity interactions. However, a further increase in pre-compression load becomes detrimental, especially for highly slender walls. This is due to the additional moments generated from second-order effects, which would negatively impact the IP-OOP interactions, i.e., more reductions of IP capacities due to the pre-applied OOP loading. Specifically, it can be obtained from Figure 6-19 that the pre-compression load has beneficial effects in reducing the IP and OOP interaction within the range of 0 ~ 0.5 MPa while exhibiting adverse effects when the pre-compression load exceeds 0.5 MPa.

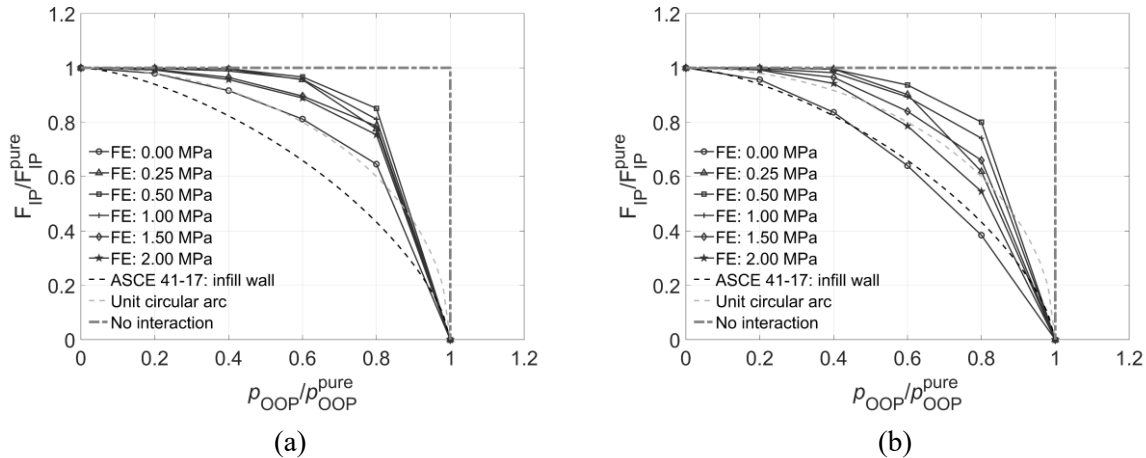


Figure 6-19. IP-OOP capacity interaction curves for URM walls with different P_v for the wall: (a) AR1.00_SR9.92 and (b) AR1.00_SR32.24

6.5. ANALYTICAL MODEL FOR INTERACTION CURVES

A total of 42 URM walls with varying values of AR, SR, and P_v are examined in this study, as detailed in Table 6-2. Figure 6-20 shows the range of interaction curves for the considered walls. Notably, the interaction curve suggested by ASCE 41-17 for masonry infill walls serves as the lower bound for the curves of URM walls considered in this study. However, due to the variation of geometrical parameters and pre-compression loads, a large scatter in interaction curves is observed for URM walls. The greatest IP-OOP interaction (i.e., the largest IP capacity reduction due to the pre-applied OOP loading) is observed in the wall AR1.00_SR32.24 with $P_v = 0.00$ MPa, while the least significant effects are identified in the wall AR2.25_SR9.92 with $P_v = 0.50$ MPa. Thus, it is valuable to develop an analytical model for the IP-OOP capacity interaction curves to account for the influence of AR, SR, and P_v , instead of using one unified relationship such as the one suggested by ASCE 41-17 for masonry infill walls or the unit circular arc. Such a relationship is proposed in the form of Eq. (6-1):

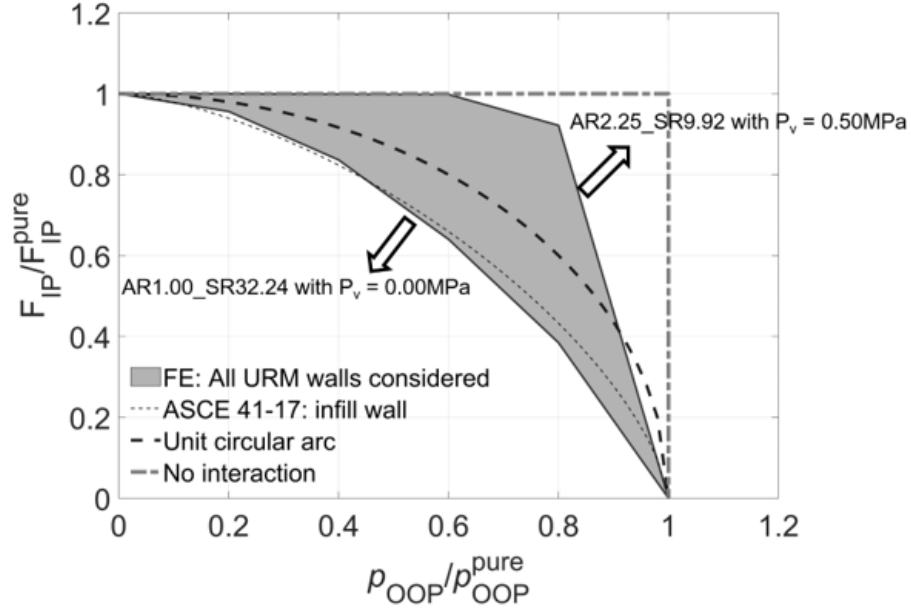


Figure 6-20. Range of interaction curves of URM walls considered

$$\left(\frac{F_{IP}}{F_{IP}^{pure}} \right)^a + \left(\frac{p_{OOP}}{p_{OOP}^{pure}} \right)^b = 1 \quad (6-1)$$

where the parameters ‘*a*’ and ‘*b*’ determine the shape of the interaction curves.

The results derived from curve fitting imply that parameter ‘*a*’ depends on AR and P_v , while parameter ‘*b*’ is influenced by SR and P_v . The general trends regarding the impact of AR, SR, and P_v on interaction curves can be summarized as follows. A lower AR and a higher SR lead to more IP capacity reductions. Consequently, decreasing AR and increasing SR result in decreases in parameters ‘*a*’ and ‘*b*’, respectively. As for the pre-compression load P_v , an increase at a lower magnitude level proves advantageous in mitigating IP-OOP capacity interaction effects, while a further increase at a higher magnitude level negatively impacts IP-OOP interactions. Thus, increasing P_v initially leads to increases in parameters ‘*a*’ and ‘*b*’, followed by an inverse trend

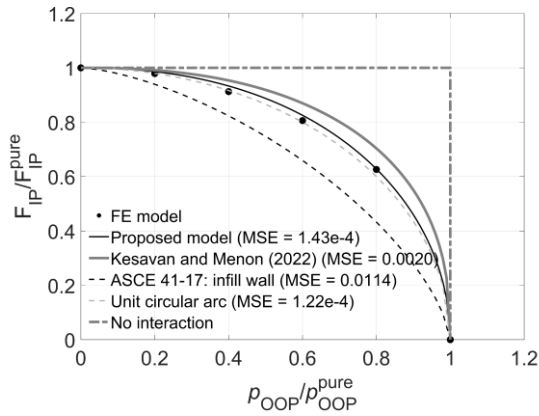
upon further increases in P_v . The curve fitting leads to the expressions of parameters ‘ a ’ and ‘ b ’ in non-dimensional forms, given in Eq. (6-2) and Eq. (6-3):

$$a = (0.57 \times AR - 0.21) \times \exp \left[-160.7 \times \left(\frac{P_v}{f'_m} \right)^2 + 38.3 \times \frac{P_v}{f'_m} \right] + 1.8 > 0 \quad (6-2)$$

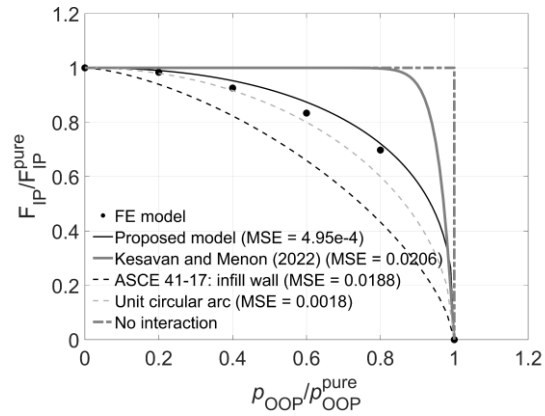
$$b = (-0.05 \times SR + 2.11) + \exp \left[-123.9 \times \left(\frac{P_v}{f'_m} \right)^2 + 20.91 \times \frac{P_v}{f'_m} - 0.49 \right] > 0 \quad (6-3)$$

Here, f'_m is the compressive strength of masonry.

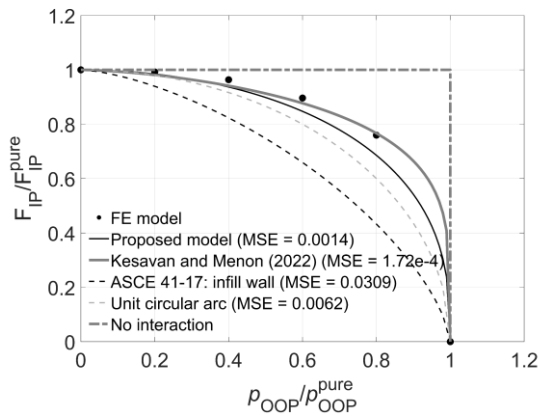
To verify the effectiveness of the proposed model, the interaction curves predicted by Eq. (6-1), Eq. (6-2), and (6-3) are compared with the model proposed by Kesavan and Menon (2022), the design provision in ASCE 41-17 for masonry infill walls, and the unit circular arc. Figure 6-21 (a-d) presents the validation results, demonstrating the capability of the proposed analytical model to capture the effects of AR under different pre-compression loads. Figure 6-21 (e-h), on the other hand, aims to examine whether the impacts of SR can be well described. It is worth mentioning that the design provision in ASCE 41-17 assumes no variation of IP and OOP interaction curves, and constant values are used for parameters ‘ a ’ and ‘ b ’ in Eq. (6-1), both set equal to 1.5. Additionally, the model proposed by Kesavan and Menon (2022) does not account for the effects of SR, leading to identical interaction curves shown in Figure 6-21 (e) and (f), and Figure 6-21 (g) and (h). The model’s accuracy is evaluated in terms of the mean square error (MSE). It can be seen that the proposed model generally outperforms the other models, although it presents a marginally larger MSE in some cases than other models.



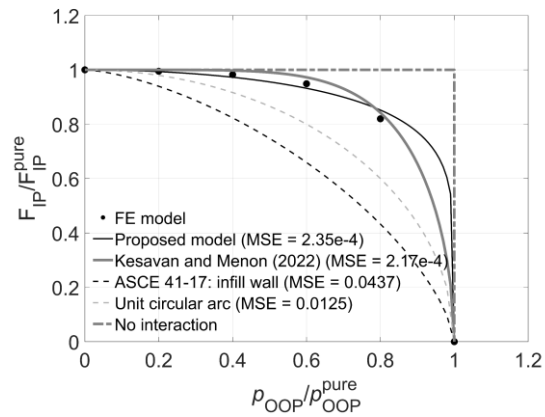
(a)



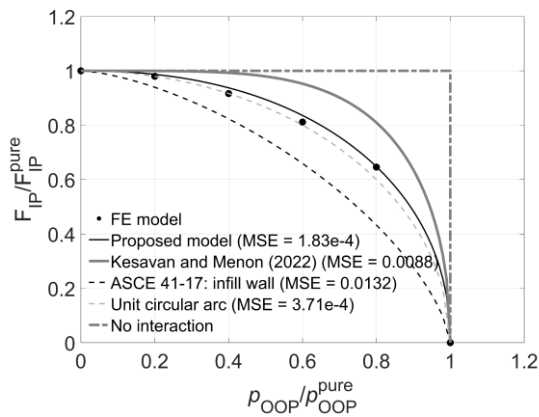
(b)



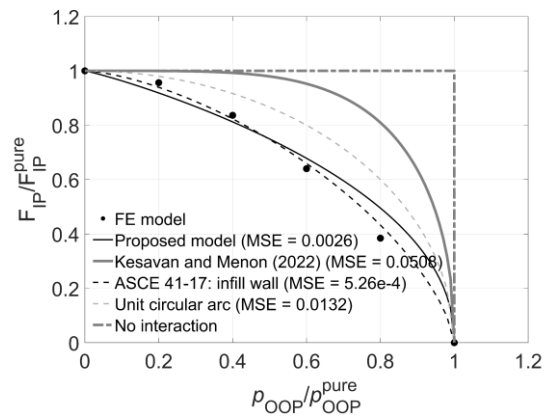
(c)



(d)



(e)



(f)

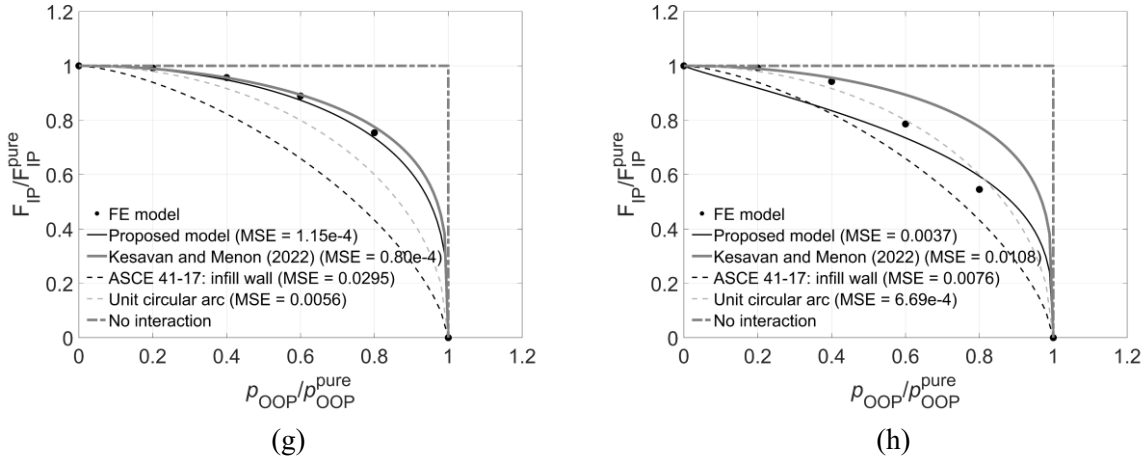


Figure 6-21. Comparison of interaction curves between the proposed model, the model proposed by Kesavan and Menon. (2022), and ASCE 41-17 (ASCE 2017) for masonry infill walls: (a) AR0.75_SR9.92 with $P_v = 0.00$ MPa, (b) AR2.25_SR9.92 with $P_v = 0.00$ MPa, (c) AR0.75_SR9.92 with $P_v = 2.00$ MPa, (d) AR2.25_SR9.92 with $P_v = 2.00$ MPa, (e) AR1.00_SR9.92 with $P_v = 0.00$ MPa, (f) AR1.00_SR32.24 with $P_v = 0.00$ MPa, (g) AR1.00_SR9.92 with $P_v = 2.00$ MPa, and (h) AR1.00_SR32.24 with $P_v = 2.00$ MPa

6.6. CHAPTER CONCLUSION

In this chapter, the complex structural behavior of unreinforced masonry (URM) walls under combined in-plane (IP) and out-of-plane (OOP) loading was investigated using the simplified micro modeling approach. The effects of aspect ratio (AR), slenderness ratio (SR), and pre-compression load (P_v) on the IP-OOP interaction behaviors of URM walls were explored with regard to failure modes, load-deformation behaviors, and IP-OOP capacity interaction curves.

The finite element (FE) analysis results highlighted the sensitivity of the IP capacity reduction in the presence of OOP loading. Longer walls, characterized by smaller AR, exhibit more pronounced IP and OOP interaction effects. Additionally, highly slender walls show significant additional moments due to second-order effects under OOP loading, thereby negatively affecting the IP capacity. Lower-level pre-compression loads are beneficial in diminishing capacity interaction effects, while higher pre-compression loads exert a negative influence. An

analytical model was developed based on the FE simulation data to predict the IP and OOP capacity interaction curves of URM walls more efficiently. The proposed analytical model incorporates the effects of AR, SR, and P_v . A comparison between the proposed analytical model and other models available in the public literature and design code demonstrates its outperformance.

The findings of this study highlight the importance of considering IP and OOP interaction effects, as well as the influences of AR, SR, and P_v , when assessing the structural behaviors of URM walls. This contributes to the underexplored area in the literature. The newly developed IP-OOP capacity interaction curves are complementary to the existing ones for masonry infill walls in ASCE 41-17 for seismic evaluation and retrofit of existing buildings. Note that the results are applicable to safety assessment of typical masonry walls in new and existing low-rise buildings. However, it is well worth noting the restriction in the applicability. For example, the vertical one-way bending under OOP loading is considered, and thus it is not applicable to walls subjected to two-way bending under OOP loading. Moreover, material parameters of masonry walls and its components are taken as constants to represent a typical brick masonry wall with strong unit and weak mortar. Further research is needed to explore the effects of different masonry material properties on the IP and OOP interaction behaviors of URM walls. In addition, the loading sequence considered in this study aims for the investigation of influence of pre-applied OOP loading on the IP capacity reduction. However, the existence of IP load may be detrimental to the OOP capacity as well, which is worth further investigation.

Chapter 7. NUMERICAL INVESTIGATION OF REINFORCED MASONRY WALLS UNDER BI-DIRECTIONAL LOADING: IN-PLANE CAPACITY REDUCTION DUE TO OUT-OF-PLANE LOADING

The structural behavior of reinforced masonry (RM) walls subjected to either pure in-plane (IP) or pure out-of-plane (OOP) loading has been thoroughly examined in public literature. However, in certain circumstances (e.g., seismic loading), RM walls could be subjected to combined IP and OOP loads. This study conducts a comprehensive numerical investigation into the structural behaviors of RM walls under combined IP and OOP loading, focusing on the influence of geometric parameters (aspect ratio and height-to-thickness ratio) and pre-compression load. To capture the possible failure modes of RM walls under bi-directional loading scenarios, a simplified micro modeling approach is employed in this study. The simulation results indicate that the presence of OOP loads can induce substantial IP capacity reductions, especially for flexural governed walls characterized by a larger aspect ratio and a low level of pre-compression load. For flexural governed walls, IP and OOP capacity interactions are found to be less sensitive to geometrical parameters and pre-compression load than shear governed walls. The most interaction is observed for highly slender walls without pre-compression loads, indicating a reduction in IP capacity by 45% when OOP loading is at 80% of its corresponding capacity. A further comparison between the RM walls and their counterparts, unreinforced masonry (URM) walls, suggests that the incorporation of reinforcements is effective in mitigating the IP-OOP interaction effects.

7.1. INTRODUCTION

In North America, reinforced masonry (RM) walls have been successfully used in a variety of construction applications, including low-to-medium-rise residential, commercial, and school

buildings. Typically, the construction of an RM wall entails the utilization of vertical steel reinforcing bars within hollow concrete blocks filled with grout, accompanied by horizontal steel reinforcements. The incorporation of steel reinforcement enhances the structural performance of masonry walls effectively. A RM wall can be used as an integral component of both vertical and lateral load-resisting systems to provide resistance against loads applied in-plane (IP) or out-of-plane (OOP), such as earthquake loads along and perpendicular to the wall, wind loads perpendicular to the wall, and eccentric gravity loads transferred from diaphragms supported on the wall.

The structural behavior of RM walls under IP or OOP loading has been extensively investigated through experimental tests and numerical models of different fidelity levels. Specifically for RM walls under IP loading, the recent advancements have been well documented in relevant review papers (El-Dakhkhni and Ashour 2017; Zeng and Li 2023). A notable research program launched during the 1980s by the US-Japan Technical Coordinated Committee for Masonry Research (TCCMAR) contributed a vast experimental database for RM walls (Kaminosono et al. 1988; Shing et al. 1989, 1990a, b; Takashi et al. 1986). This research initiative laid the basis for the contemporary prescriptive masonry design codes in North America (Canadian Standards Association 2014; TMS 2016), which regulate current design practices for masonry structures. As a complement to the experimental studies, various computational models were developed and applied for RM walls using commercial software or proprietary computer programs to facilitate the understanding and/or prediction of IP behaviors (Cheng and Shing 2022a, b; Peruch et al. 2019). The experimental and analytical findings reveal that RM walls can be categorized into two fundamental types under IP loading according to the behavior or failure mechanism: flexural

governed and shear governed. Failure of flexural governed walls, referred to as IP-flexure herein, is generally associated with bed-joint opening and yielding of flexural reinforcements at the bottom course on the tension side and masonry crushing at the toe region on the compression side. By contrast, the failure of shear governed walls is typically characterized by the formation of diagonal cracks and the yielding of horizontal reinforcements, or the horizontal sliding along the bed joint surface. The complex behavior of masonry shear walls, e.g., either flexure governed or shear governed, is influenced by the boundary condition, aspect ratio (i.e., height-to-length ratio), axial load, the ratio of vertical to horizontal reinforcement, etc (Kingsley et al. 2014b).

Compared to RM walls under IP loading, the behavior of RM walls under OOP loading is relatively less complicated and better understood. When spanned in one-way, RM walls bend in the OOP direction, behaving like beams under lateral loading and/or columns under eccentric vertical loading. RM walls initially behave similarly to unreinforced masonry (URM) walls prior to cracking and then experience a stiffness reduction. However, they could still carry loads up to and beyond the yield of longitudinal (flexural) reinforcements. As such, the OOP failure mode is characterized by the presence of crack openings at bed joints on the tension face and spalling of the mortar and face shells of the masonry unit on the compression side. Such phenomenon was well reported in experimental testing of RM walls under OOP loading (Hamid et al. 1990a, 1990b; Hamid and Abboud 1989). Similarly, numerical models were developed to simulate the OOP-flexural behavior of RM walls (Noor-E-Khuda et al. 2016b; Noor-E-Khuda and Dhanasekar 2020; da Porto et al. 2011; Salem et al. 2019). It is worth noting that the axial load on walls also contributed to the OOP-flexure failure or stability failure due to the second-order effect, particularly for slender RM walls (Metwally et al. 2022).

As noted above, the IP and OOP behaviors have been well studied in an uncoupled manner. Experimental programs rarely tested RM walls under both IP and OOP loadings, and the majority of the numerical models developed are either limited to the simulation of pure IP or OOP behavior. Contemporary design codes only provide models for the IP and OOP capacities of RM walls without mentioning the interaction for RM walls. In engineering practice, IP and OOP capacities are evaluated individually against the corresponding load demands with (partial) safety factors to ensure the desired safety margin, assuming either IP and OOP loads do not co-exist, or IP and OOP capacities are independent from each other. Nonetheless, it is not uncommon that in certain circumstances, such as during earthquakes, RM walls could be subjected to both IP and OOP loads. Note that the OOP loads here include both seismic loads applied perpendicular to the walls and the pre-existing OOP loads arising from winds or eccentric vertical loads. Additionally, it is well acknowledged that concurrent load in one direction could potentially lead to load capacity reduction in the other direction, known as “capacity interaction effects”. This is exemplified by the effects of axial load and bi-directional bending moment (P-M-M) interaction diagrams for columns (Shen et al. 2023; Del Zoppo et al. 2017) and the IP and OOP capacity interaction relationships for masonry infill walls as specified in ASCE 41-17 (ASCE 2017). Lack of accounting for the IP and OOP behavior interaction of RM walls, e.g., the reduction in IP capacity caused by the presence of OOP loading, can potentially result in unexpected performance of RM walls under complex loading conditions.

In contrast to the research focusing solely on the IP or OOP behaviors of RM walls, experimental or numerical works on the behaviors of RM walls under combined IP and OOP loading are notably scarce. This deficiency in the literature could be attributed to the difficulties

and cost concerns associated with testing masonry walls under complex loading conditions, and/or the technical complexities and computational costs involved in modeling masonry walls in three-dimensional (3D) space. A few experimental attempts were made in this aspect regarding URM walls (Dolatshahi 2012; Krishnachandran and Menon 2023; Najafgholipour et al. 2013), with all results indicating substantial IP and OOP capacity interaction effects. In addition, several numerical studies were conducted as well for URM walls (Agnihotri et al. 2013; Dolatshahi et al. 2015; Dolatshahi and Yekrangnia 2015; Kesavan and Menon 2022; Najafgholipour et al. 2014; Noor-E-Khuda and Dhanasekar 2018a, 2018b), resulting in insights about the influence of various design parameters (i.e., geometry, pre-compression load) on the capacity interaction behavior of URM walls. A general conclusion made from these works is that shear-dominated URM walls (i.e., walls with lower aspect ratios under higher pre-compression loads) exhibited more IP capacity reductions with the presence of OOP loading compared to flexural-dominated walls (i.e., walls with higher aspect ratios under lower pre-compression loads). However, the relevant research on RM walls can only be found in Noor-E-Khuda and Dhanasekar (2018a), in which a macro continuum model was used by representing masonry (units plus mortar joints) as a homogeneous material. This numerical investigation identified a critical value of OOP load (as a percentage of OOP capacity), beyond which the IP capacity decreased rapidly. However, the influence of various parameters (e.g., geometrical factors) on the IP and OOP interaction behaviors of RM walls was not informed due to the limited number of RM walls simulated. Moreover, the detailed failure modes of RM walls were not adequately captured through the macro modeling approach, causing a lack of comprehension regarding the IP and OOP interaction behaviors. To reliably predict the masonry wall behavior under both IP and OOP loadings, 3D micro modeling that simulates the

individual masonry units and mortar joints under complex loadings is favored. Such a preference stems from the potential IP shear failure of RM walls, which adds complexity to the interaction between IP and OOP behaviors. This interaction extends beyond the simple bi-directional bending (IP-flexure and OOP-flexure) interaction observed in the P-M-M interaction of reinforced concrete columns.

To address the inadequate research on the IP and OOP interaction behaviors of RM walls, this chapter presents a comprehensive numerical investigation based on the simplified micro modeling strategy introduced by Page (1978) and the recently developed multi-yield surfaces model for mortar joints (Li and Zeng 2023). Detailed failure modes and corresponding load-deformation curves are discussed with a particular emphasis on IP and OOP capacities. The IP capacity reductions due to the presence of different levels of OOP loads are quantified. The primary objective herein is to identify the most critical scenario (i.e., strongest interaction effects) and investigate the influence of three important factors, namely the aspect ratio (AR), slenderness ratio (SR), and pre-compression load (P_v), on the level of reductions in IP capacity due to OOP loading. Moreover, the influence of reinforcement in RM walls is also addressed through a contrast between RM walls and their counterparts, URM walls, in terms of their susceptibility to IP capacity reduction under combined IP and OOP loadings.

7.2. 3D FINITE ELEMENT MODEL FOR RM WALLS

The 3D FE models for RM walls are developed using the simplified micro modeling approach in the general-purpose FE package ABAQUS (Dassault Systemes 2017), as shown in Figure 7-1. Off-the-shelf elements and material constitutive models are used for masonry units, except for mortar joints, which are modeled utilizing a recently developed 3D plasticity-based multi-yield surfaces

constitutive model (Li and Zeng 2023). The modeling strategy was validated using small-scale masonry specimens (e.g., unit-mortar-unit assemblages), large-scale URM walls under IP or OOP loadings (Li and Zeng 2023), and RM walls under IP and OOP loadings presented in Chapter 4.

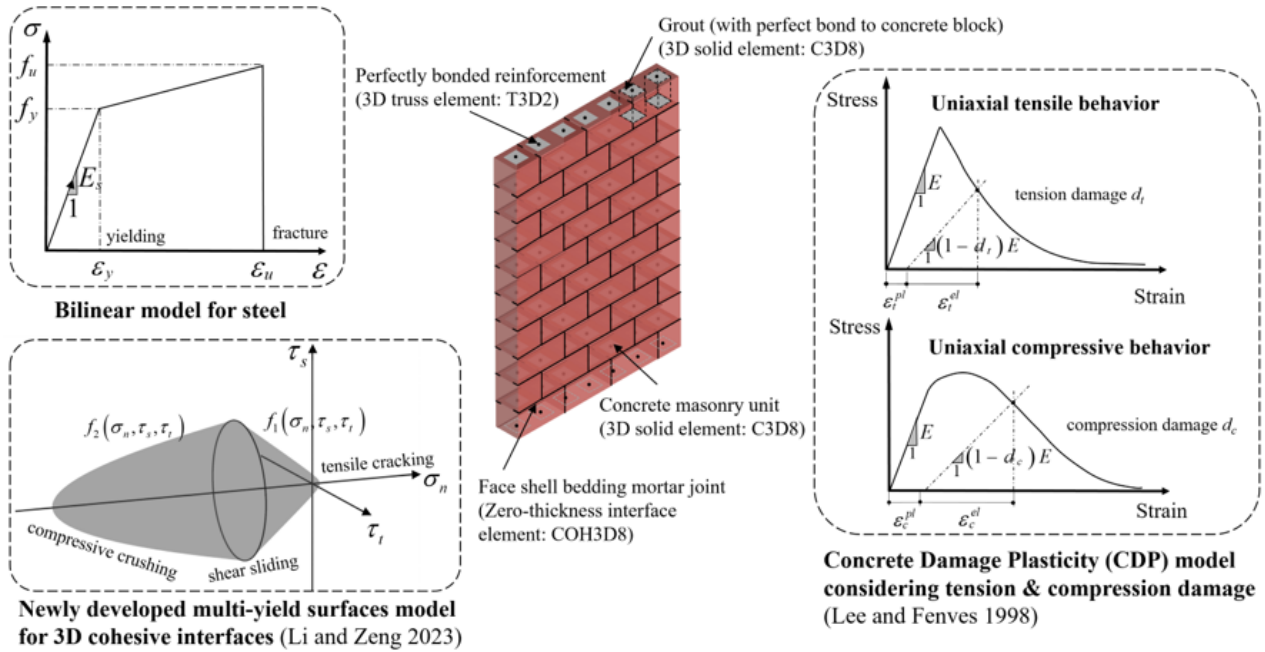


Figure 7-1. Schematic view of the FE modeling strategy using simplified micro approach for RM walls

7.3. STRATEGY FOR FE-BASED INVESTIGATION OF RM WALLS UNDER COMBINED IP AND OOP LOADING

The modeling strategy for RM walls validated for both IP and OOP capacity predictions is used in this section. This section aims to plan for the FE-based investigation of RM walls under combined IP and OOP loading, encompassing the baseline RM wall as a reference for variation, the varied parameters considered, the boundary condition, and the loading protocol for analysis.

The RM wall validated earlier (Seif Eldin 2016; Seif Eldin and Galal 2017) serves as the point of departure, i.e., the baseline model for investigating the IP and OOP interaction behavior of RM walls. This RM wall, designed in accordance with the CSA (2014), represents a typical masonry construction practice. Note that the tested RM wall was shear governed. In this study, the baseline model is varied to provide more cases to encompass both flexural and shear failures. As revealed by the experimental (Hamid et al. 1990a, b; Hamid and Abboud 1989; Shing et al. 1989, 1990a) and numerical studies (Calderón et al. 2021a; Noor-E-Khuda and Dhanasekar 2020; Noor-E-Khuda and Thambiratnam 2021), the IP behavior of RM walls is largely influenced by the aspect ratio (AR), defined as height-to-length ratio, and pre-compression load (P_v). On the other hand, OOP behaviors are greatly sensitive to the slenderness ratio (SR), defined as the height-to-thickness ratio, and pre-compression load (P_v). Thus, AR, SR, and P_v are varied, as the primary focuses of this study, to investigate the behaviors of RM walls under combined IP and OOP loading, while the horizontal and vertical reinforcement ratios in these models are kept identical to those in the baseline model.

Table 7-1. Design cases for FE-based investigation of the IP-OOP behavior interaction of RM walls

Wall	Length (mm)	Height (mm)	Thickness (mm)	AR	SR	P_v (MPa)
AR2.00 SR8.42	800	1600	190	2.00	8.42	0.0, 0.5, 1.0, 1.5, 2.0, and 2.5
AR1.60 SR8.42	1000	1600	190	1.60	8.42	0.0, 0.5, 1.0, 1.5, 2.0, and 2.5
AR1.33 SR8.42	1200	1600	190	1.33	8.42	0.0, 0.5, 1.0, 1.5, 2.0, and 2.5
AR0.89 SR8.42	1800	1600	190	0.89	8.42	0.0, 0.5, 1.0, 1.5, 2.0, and 2.5
AR0.67 SR8.42	2400	1600	190	0.67	8.42	0.0, 0.5, 1.0, 1.5, 2.0, and 2.5
AR1.33 SR12.63	1800	2400	190	1.33	12.63	0.0, 0.5, 1.0, 1.5, 2.0, and 2.5
AR1.33 SR21.05	3000	4000	190	1.33	21.05	0.0, 0.5, 1.0, 1.5, 2.0, and 2.5
AR1.33 SR29.47	4200	5600	190	1.33	29.47	0.0, 0.5, 1.0, 1.5, 2.0, and 2.5

Note: All RM walls have a horizontal reinforcement ratio of 0.13% and a vertical reinforcement ratio of 0.79%

To be specific, AR is varied by changing the wall length while keeping the same height; SR is varied by changing the wall height while keeping the thickness the same as the unit thickness. Note that when varying SR, AR is fixed the same as the baseline wall. A total of eight geometrical configurations, as summarized in Table 7-1, are considered, with AR ranging from 0.67 to 2.00 and SR ranging from 8.42 to 29.47. The lower and upper bounds for AR and SR are determined in accordance with the design guidelines specified in CSA (2014). In Table 7-1, the notations distinguishing different walls include the values of AR and SR. For instance, ‘AR2.00_SR8.42’ refers to the wall with an AR of 2.00 and a SR of 8.42. For each wall, six levels of P_v are considered: 0, 0.5, 1.0, 1.5, 2.0, and 2.5 MPa. The maximum pre-compression is chosen to be approximately 20% of the compressive strength of masonry (13.1 MPa), deemed an appropriate maximum axial load level applied to masonry walls (Kesavan and Menon 2022). With the analysis results obtained from above walls considered, several RM walls with the strongest IP and OOP interaction effects

are identified and used to explore the effects of reinforcements by simulating their counterpart URM walls, as detailed in Section 7.6.

The IP and OOP boundary conditions of RM walls are considered to be identical to those in the validation cases, i.e., cantilever for the IP case and one-way vertical bending for the OOP case. During the FE analyses, a pre-compression load P_v is applied at the top of the wall and kept constant throughout subsequent load steps to simulate the vertical load supported by the wall. Subsequently, a predetermined uniformly distributed OOP pressure (p_{OOP}) is then imposed and maintained to represent the OOP load at a predetermined level. Finally, an IP load (F_{IP}) is applied monotonically with an increasing amplitude until the wall collapses. The predetermined OOP load levels (p_{OOP}) considered are 20%, 40%, 60%, and 80% of the OOP capacity of the examined wall. The FE modeling details, including the boundary conditions and loading sequences, are illustrated in Figure 7-2.

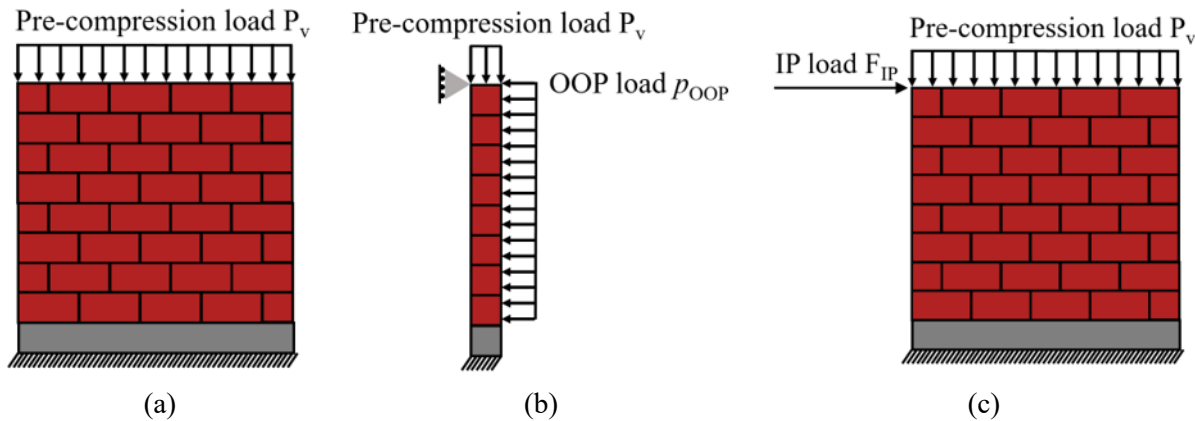
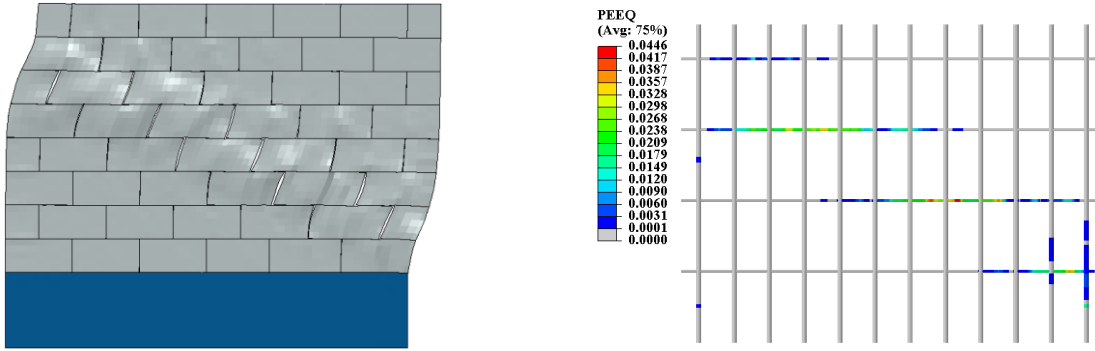


Figure 7-2. Loading sequence for RM walls under combined IP and OOP loading: (a) apply a pre-compression load, (b) apply a predetermined uniformly distributed OOP load, and (c) apply an IP load until wall failure

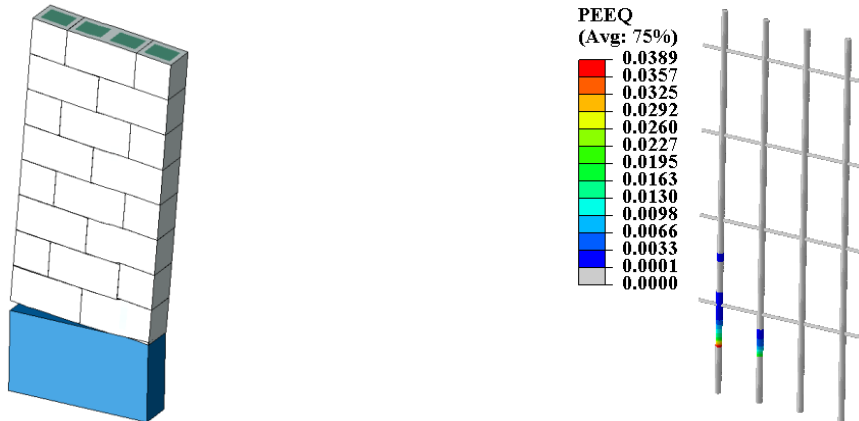
7.4. PURE IP AND PURE OOP BEHAVIORS OF RM WALLS

The failure mechanism of RM walls under pure IP loading is complex, as revealed by extensive studies in the literature, which may further be complicated by the IP and OOP interaction behaviors when concurrent OOP load exists. As a reference, the IP behaviors and capacities are simulated (i.e., under pure IP loading with zero OOP loading). In addition, to quantify the OOP load level as a certain percentage of OOP capacity, the OOP behaviors and capacities of RM walls (under pure OOP loading) are also simulated. The pure IP and pure OOP behaviors can also facilitate the understanding of their interaction behaviors. Thus, in this section, a brief discussion on the pure IP and pure OOP behaviors, including failure modes, of RM walls considered is provided.

Regarding the RM walls under pure IP loading, the simulation results show that longer walls (i.e., those with smaller values of AR) subjected to larger pre-compression stresses are primarily governed by shear failure, characterized by diagonal tensile cracking and yielding of horizontal reinforcements. Conversely, taller walls (i.e., those with larger AR values) under lower pre-compressive loads primarily undergo flexural failure. In such instances, cracking at the bottom course, yielding vertical reinforcements, and crushing of the toe region form a collapse mechanism. These two different failure modes are illustrated in Figure 7-3, in which the deformed shapes and plastic strain of reinforcements (represented by the equivalent plastic strain PEEQ) are included. The RM walls studied are characterized into two groups based on failure modes exhibited under pure IP loading: flexural governed and shear governed walls, depending on the AR and P_v . Such information is detailed in , in which ‘F’ and ‘S’ represent flexural and shear failures, respectively. It should be noted that SR, when varying height with AR is fixed, namely the wall size, does not influence the IP failure modes.



(a)



(b)

Figure 7-3. FE simulation results for RM walls under pure IP loading: (a) the long wall AR0.67_SR8.42 with $P_v = 2.50$ MPa, and (b) the short wall AR2.00_SR8.42 with $P_v = 0.00$ MPa (Left: deformed shapes of RM walls; Right: the plastic strain distributions of reinforcements)

Table 7-2. Failure modes of RM walls under pure IP loading

AR \ P _v (MPa)	0.0	0.5	1.0	1.5	2.0	2.5
2.00	F	F	F	F	F	S
1.60	F	F	F	F	S	S
1.33	S	S	S	S	S	S
0.89	S	S	S	S	S	S
0.67	S	S	S	S	S	S

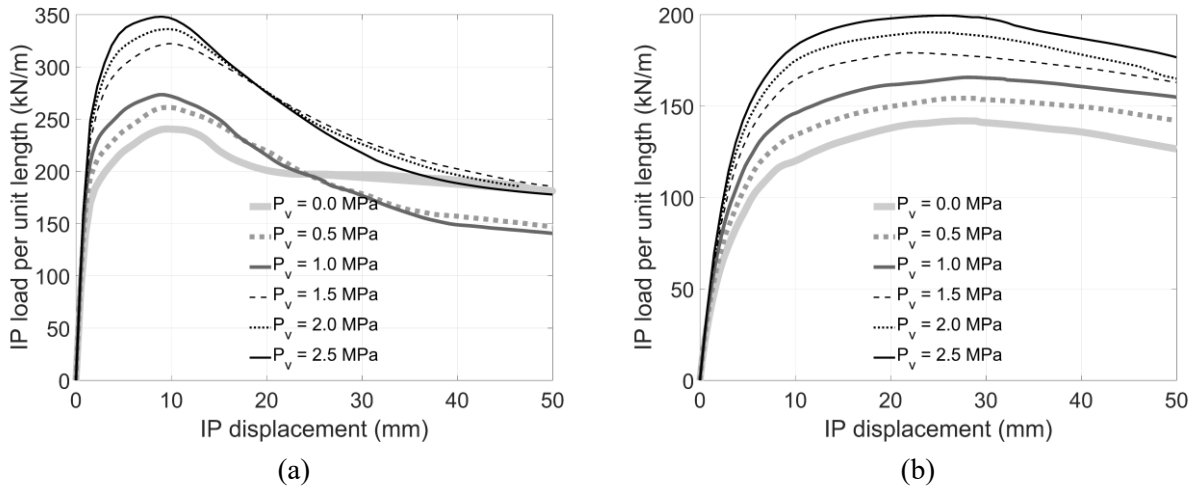


Figure 7-4. Load-deformation curves of RM walls under pure IP loading with different pre-compression load levels for: (a) the long wall AR 0.67_SR8.42 and (b) the short wall AR2.00_SR8.42

Figure 7-4 (a-b) displays the load-deformation curves for the long wall and short wall under different pre-compression load levels, respectively. Correspondingly, the change in IP capacities with respect to the aspect ratio (i.e., wall length here) is reported in Figure 7-5 (a). It is worth mentioning that the IP load is normalized by the wall length. Notably, the IP capacity per unit wall length decreases with the increase in AR (i.e., decrease of wall length here) and the decrease in P_v, in other words, shear governed walls exhibit higher IP capacities than flexural governed walls. When SR is varied with fixed AR, namely varying the wall height and length proportionally, the IP capacities per wall length remain largely unaffected, as shown in Figure 7-5 (b).

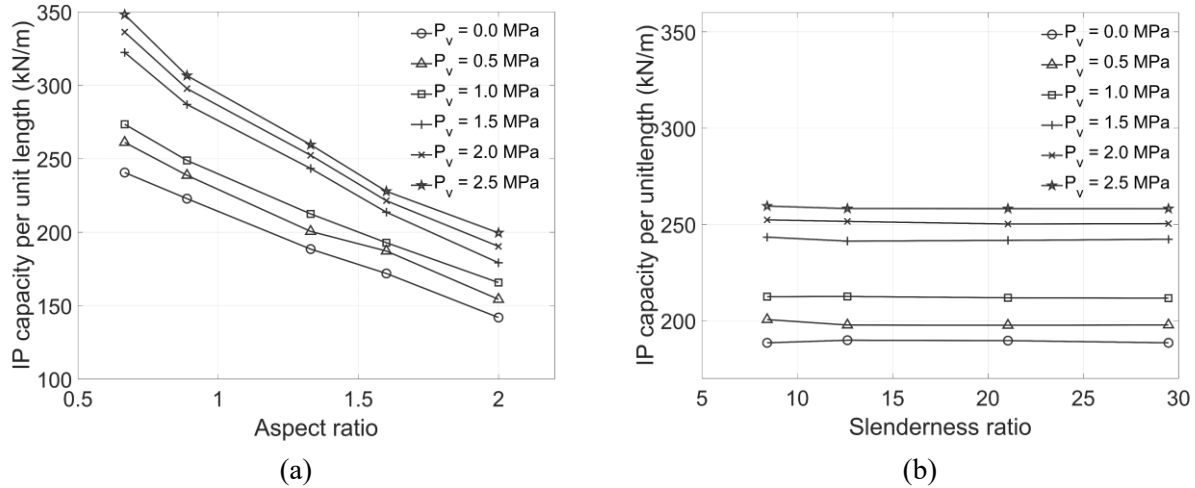


Figure 7-5. IP capacities of RM walls: (a) influence of AR and P_v and (b) influence of SR and P_v

The structural behavior of RM walls under pure OOP loading is characterized by the cracking opening at the mortar joints below the bottom course and around the mid-height position, along with the yielding of vertical reinforcements at the peak OOP load point. This is exemplified in Figure 7-6, including the deformed shape and PEEQ distribution of reinforcements for wall AR1.33_SR12.63 with $P_v = 1.00$ MPa. Figure 7-7 shows the load-deformation behaviors of RM walls under pure OOP loading, and the change of OOP capacity with respect to SR and P_v are presented in Figure 7-8. It is noted that OOP capacity here denotes the OOP resistance against lateral pressure load. As SR or wall height increases, a significant decrease in OOP capacity is observed, which is mainly because the cross-sectional moment is approximately proportional to the square of the wall height. In addition, pre-compression load is beneficial in improving the OOP capacity of RM walls with lower values of SR, while for walls with relatively higher SR, an increase in the pre-compression load adversely affects OOP capacity for walls with larger SR due to P-delta effects, as illustrated in Figure 7-7 (b).

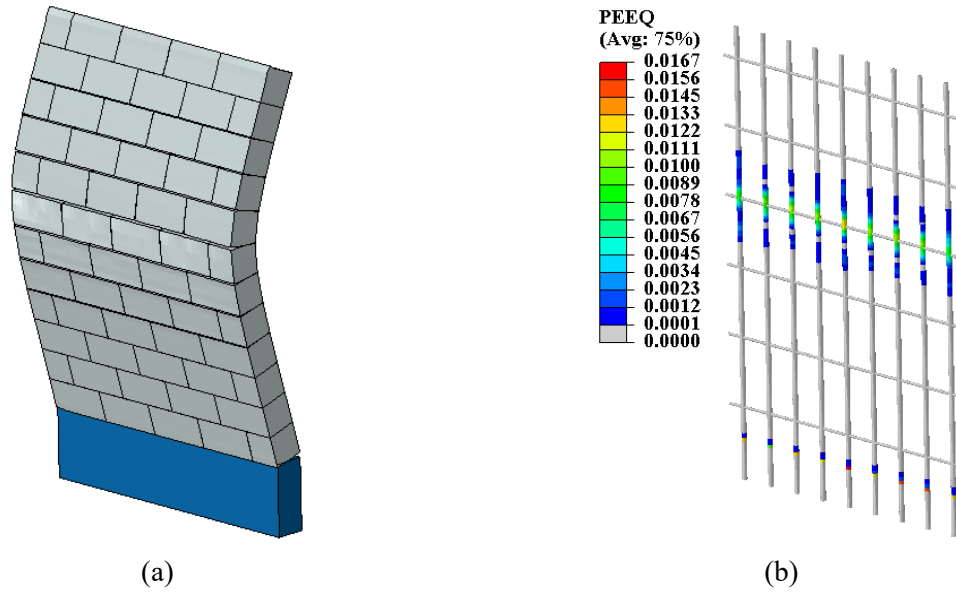


Figure 7-6. FE simulation results for Wall AR1.33_SR12.63 with $P_v = 1.00$ MPa under pure OOP loading: (a) deformed shape and (b) equivalent plastic strain of reinforcements

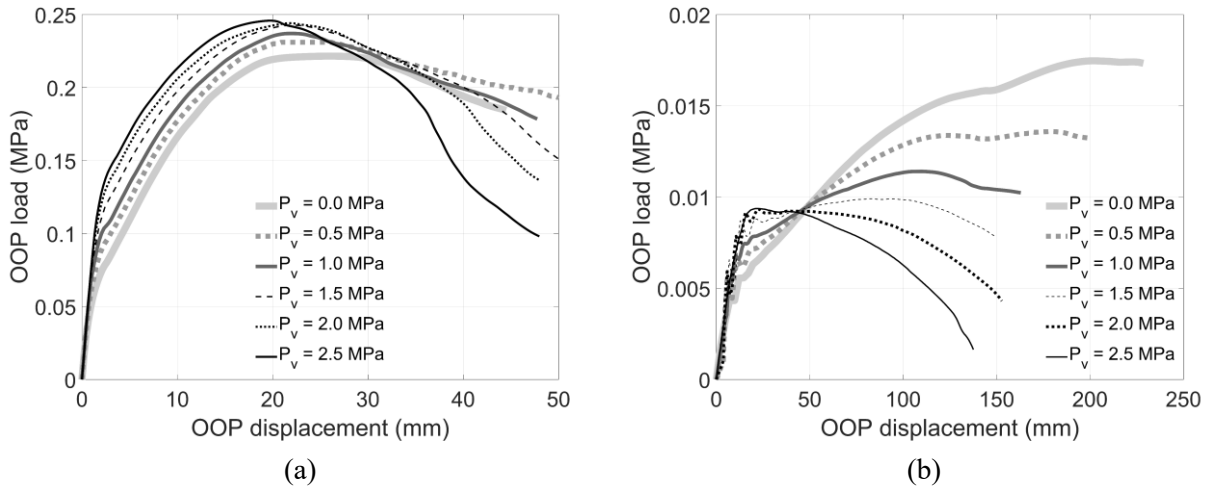


Figure 7-7. Load-deformation curves of RM walls under pure OOP loading with different pre-compression load levels for: (a) wall AR1.33_SR8.42 and (b) AR1.33_SR29.47

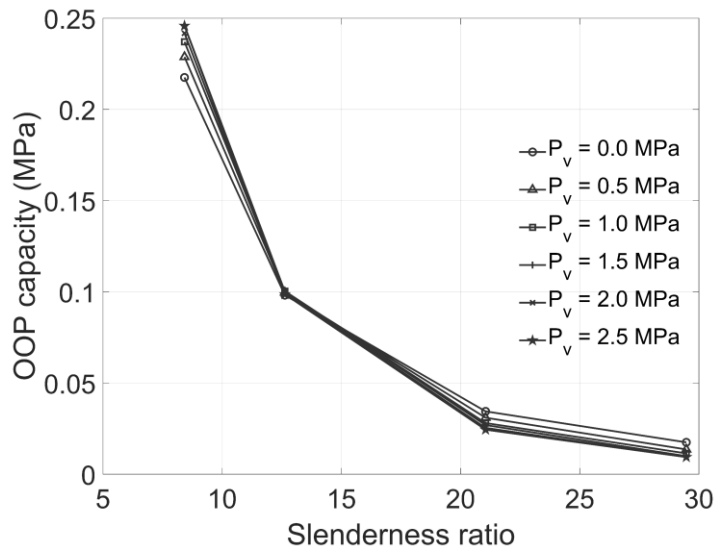


Figure 7-8. OOP capacities of RM walls with different slenderness ratios (with a fixed AR = 1.33) and pre-compression loads

7.5. COMBINED IP AND OOP LOADING

This section presents the simulation results for RM walls subjected to combined IP and OOP loading. The IP capacity reduction caused by the pre-applied OOP loading is quantified, with a focus on the effect of AR and SR, as well as P_v .

7.5.1. Influence of aspect ratio (AR) and pre-compression load (P_v)

As discussed earlier, the failure of RM walls under IP loading is complex and can be primarily categorized into flexure and shear governed walls. Their IP behaviors, including IP capacity, can be further influenced by the OOP load level. Thus, the influence of OOP loads on the IP capacity is discussed here by dividing the walls into two groups. The first group of RM walls comprises flexural governed walls under pure IP loading, including all RM walls with AR = 2.0 except the one with $P_v = 2.5$ MPa and all RM walls with AR = 1.6 except the ones with $P_v = 2.0$ MPa and 2.5

MPa (as shown in Table 7-2). The remaining walls fall into the second group, comprising shear governed walls under pure IP loading.

7.5.1.1 Flexural governed walls under pure IP loading

Among the RM walls in the first group, wall AR2.00_SR8.42 under a pre-compression load of 0.00 MPa and wall AR1.60_SR8.42 under a pre-compression load of 1.50 MPa represent the two extreme cases in terms of failure mechanism under pure IP loading. Their IP load-deformation curves with different levels of pre-applied OOP loading are shown in Figure 7-9. In addition to the ductility reduction, an obvious decrease in IP capacities is observed due to the presence of the OOP load. Specifically, the IP capacities of wall AR2.00_SR8.42 decrease by 10% and 26% with the pre-applied OOP loads equal to 60% and 80% of OOP capacity under pure OOP loading condition, respectively, when compared with the IP capacity of the RM wall subjected to no OOP load. A similar trend is observed for other flexural governed walls under IP loading in the first group, including AR1.60_SR8.42. Such observations highlight the importance of considering the IP and OOP capacity interactions for RM walls.

To quantify the capacity interaction effect, or the influence of the OOP load on the IP capacity, the IP and OOP capacities are normalized by the pure IP and OOP capacities (i.e., capacities under pure IP and pure OOP loading conditions), denoted as F_{IP}^{pure} and p_{OOP}^{pure} , respectively. Interaction curves for wall AR2.00_SR8.42 and wall AR1.60_SR8.42 under different pre-compression levels are reported in Figure 7-10. Here, F_{IP} and p_{OOP} represent the IP and OOP capacities under combined IP and OOP loadings, respectively. Note that pre-compression levels have limited influence on the interaction behavior (see Figure 7-10), although they affect the load-deformation behavior under IP or OOP loading.

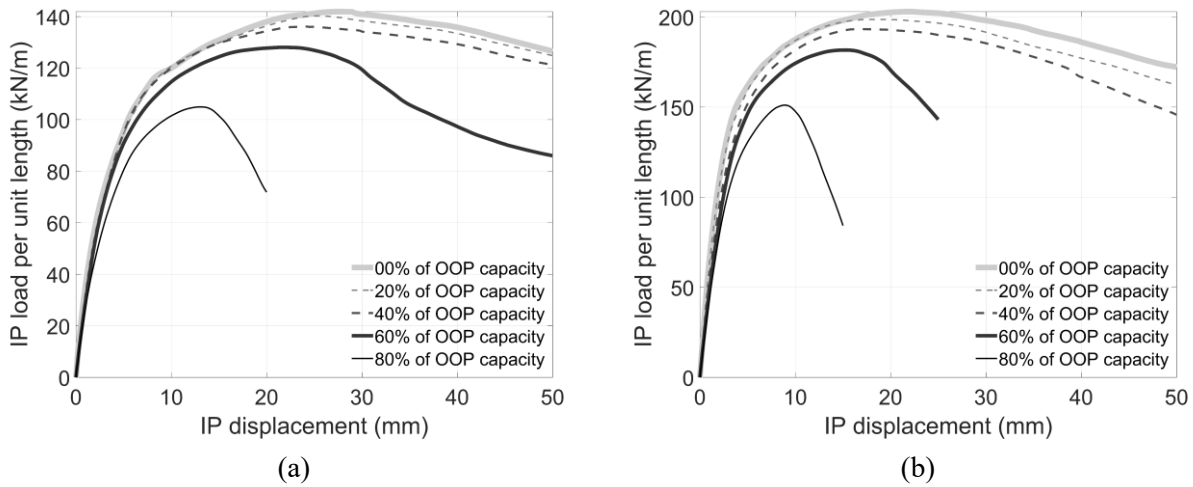


Figure 7-9. IP load-deformation curves with different levels of pre-applied OOP loading for: (a) wall AR2.00_SR8.42 with $P_v = 0.00$ MPa and (b) wall AR1.60_SR8.42 with $P_v = 1.50$ MPa

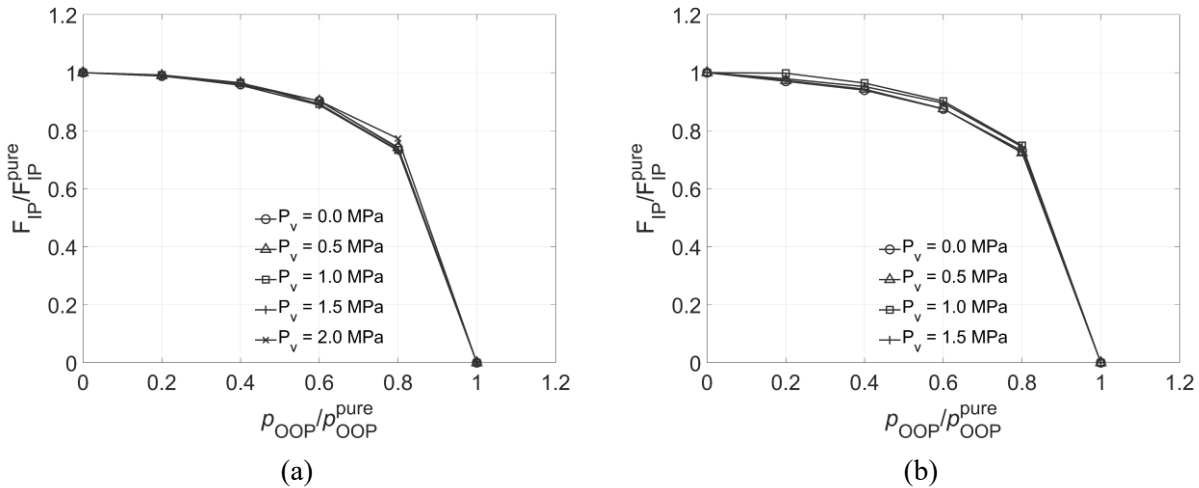


Figure 7-10. IP-OOP capacity interaction curves under different pre-compression loads for: (a) wall AR2.00_SR8.42 and (b) wall AR1.60_SR8.42

To gain more insights into the influence of OOP load on the IP behavior, as an example, Figure 7-11 presents the failure modes of wall AR2.00_SR8.42 under a pre-compression load of 0.00 MPa subjected to IP loading with various pre-applied OOP load levels. At low OOP load levels (e.g., 20% and 40% of the OOP capacity p_{OOP}^{pure}), the failure modes largely resemble those

observed in the pure IP case, as shown in Figure 7-3 (b), with failure mechanisms predominantly characterized by IP flexural rocking. Therefore, the critical section is still located at the bottom for lower levels of the pre-applied OOP load. Nonetheless, as the OOP loads escalate to higher levels, i.e., 60% and 80% of the OOP capacity $p_{\text{OOP}}^{\text{pure}}$, OOP bending deformations become considerably more impactful, as revealed by the deformed shapes shown in Figure 7-14. In such a scenario, the critical section shifts to the mid-height section due to the extensive OOP bending deformation.

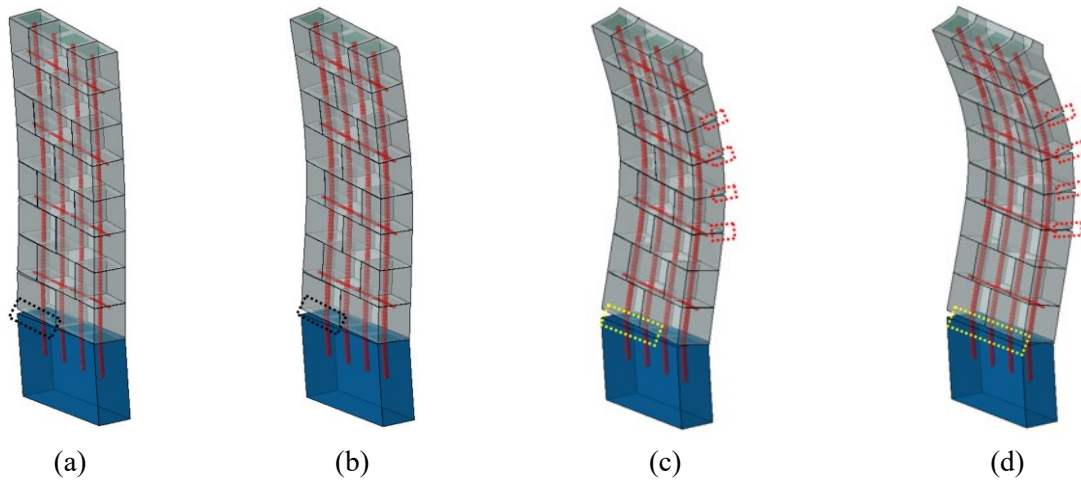
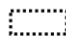




Figure 7-11. Failure modes of wall AR2.00_SR8.42 under a pre-compression load of 0.00 MPa with different pre-applied OOP load levels: (a) 20%, (b) 40%, (c) 60%, and (d) 80% of OOP capacity obtained under pure OOP loading condition (deformation scale factor: 15)

-  IP flexural induced cracking opening
-  OOP bending induced cracking opening
-  OOP bending + IP flexural induced cracking opening

As evident from Figure 7-10, the interaction curves of flexural governed walls AR2.00_SR8.42 and AR1.60_SR8.42 exhibit minimal scatter, which is further shown in Figure 7-12 by the narrow bounds of these interaction curves for all flexural governed RM walls. Namely, different values of AR and P_v have little impact on the interaction curves for the flexural governed

walls in the first group. This can be attributed to the similar failure mechanisms in these walls (see Figure 7-11).

In addition, three reference interaction curves are included for comparison purposes: one suggested by ASCE 41-17 (ASCE 2017) for masonry infill walls, one represented by a unit circular arc, and one indicating no interaction. When the OOP loads reach 80% of OOP capacities, IP capacity reductions lie between 25% and 27% compared to the IP capacities of walls subjected to no OOP load. Such a reduction is only half of that (i.e., 58%) for masonry infill walls suggested by ASCE 41-17. Compared to the interaction curve suggested by ASCE 41-17, the unit circular arc correlates better with the interaction curves obtained for the RM walls considered.

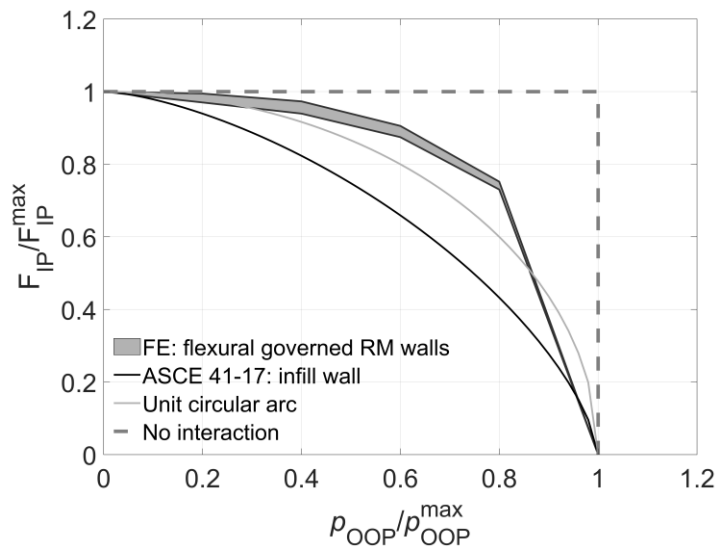


Figure 7-12. IP-OOP capacity interaction curves for flexural governed RM walls considered

7.5.1.2 Shear governed walls under pure IP loading

Among RM walls in the second group characterized by shear failure under pure IP loading, wall AR0.67_SR8.42 under a pre-compression load of 2.50 MPa represents the extreme case, i.e., the most susceptible to shear failure. Figure 7-13 depicts the deformed shapes (including cracking) of

this wall under combined IP and OOP loading with different OOP load levels. Notably, at the 20% OOP load level, the failure mode is similar to the one observed in the pure IP loading scenario, i.e., diagonal shear cracking shown in Figure 7-3 (a), and the pre-applied OOP load has negligible influence on the failure mechanism. As the OOP load level increases, flexural cracks manifest at both the bottom and mid-height locations of walls due to OOP bending, which consequently reduces the effective thickness of the wall and leads to a reduction in IP capacity. At the 80% OOP load level shown in Figure 7-13 (d), the flexural cracks induced by OOP bending become more pronounced, while no diagonal tension cracks are visible when the wall reaches its peak capacity.

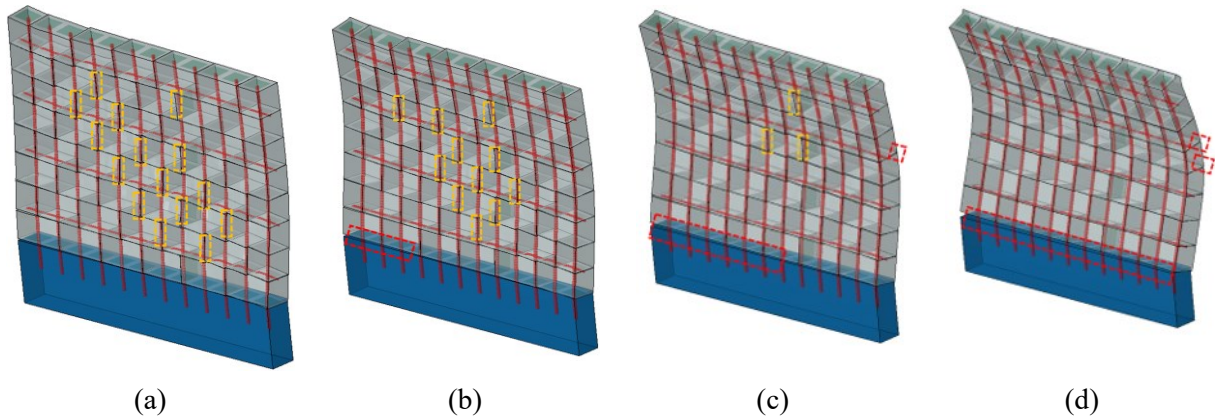


Figure 7-13. Failure modes of wall AR0.67_SR8.42 under a pre-compression load of 2.50 MPa with different pre-applied OOP load levels: (a) 20%, (b) 40%, (c) 60%, and (d) 80% of OOP capacity obtained under pure OOP loading (Deformation scale factor: 15)

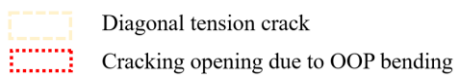


Figure 7-14 presents the influence of AR and P_v on the interaction curves for shear governed walls. As AR increases, the interaction effects become stronger, leading to more pronounced reductions in IP capacities due to the presence of OOP loading, as shown in Figure 7-14 (a). For the walls with a pre-compression load of 2.0 MPa, RM walls with AR of 0.67, 0.89, 1.33 and 1.60 exhibit IP capacity reductions of 12.8%, 16.3%, 20.8%, and 22.5%, respectively,

when pre-applied OOP load levels are at 80% of the pure OOP capacity. Namely, the IP capacity of longer walls is less influenced by the pre-applied OOP load compared with shorter walls. This is primarily because longer walls (those with smaller AR) feature more substantial cross sections under compression, thereby forming wider compressive struts and displaying less IP capacity reduction compared to shorter walls. This also explains the beneficial effects of P_v on mitigating the interaction effects: higher pre-compression loads would lead to less IP capacity reduction, as seen in Figure 7-14 (b). Similar to the flexural governed RM walls, the interaction observed here is less than that specified in the design provision in ASCE 41-17 (ASCE 2017) for masonry infill walls, and the unit circular arc are better correlated with the interaction curves obtained for the shear governed RM walls considered.

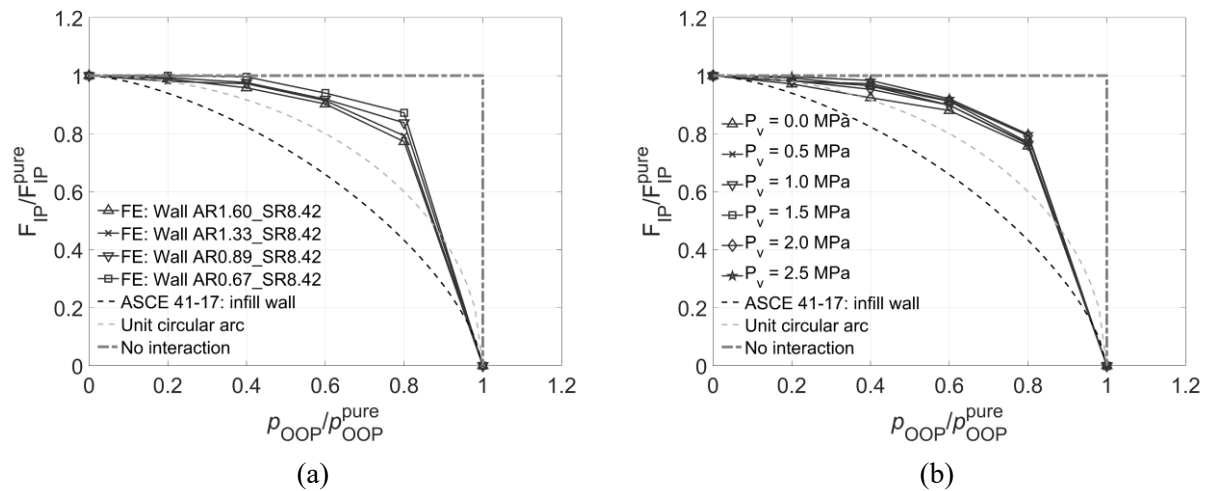


Figure 7-14. IP-OOP capacity interaction curves for the shear governed RM walls: (a) walls of different AR with $P_v = 2.0$ MPa and (b) the wall AR1.33_SR8.42 under different pre-compression loads

Figure 7-15 presents a further comparison of interaction curves between the walls in two groups: flexural and shear governed RM walls under pure IP loading. More scatter is observed for shear governed RM walls considered, and the interaction curves for flexural governed RM walls

are essentially the lower bound of those for shear governed walls. That is to say, the presence of OOP loads can induce more substantial IP capacity reductions for flexural governed walls than shear governed walls.

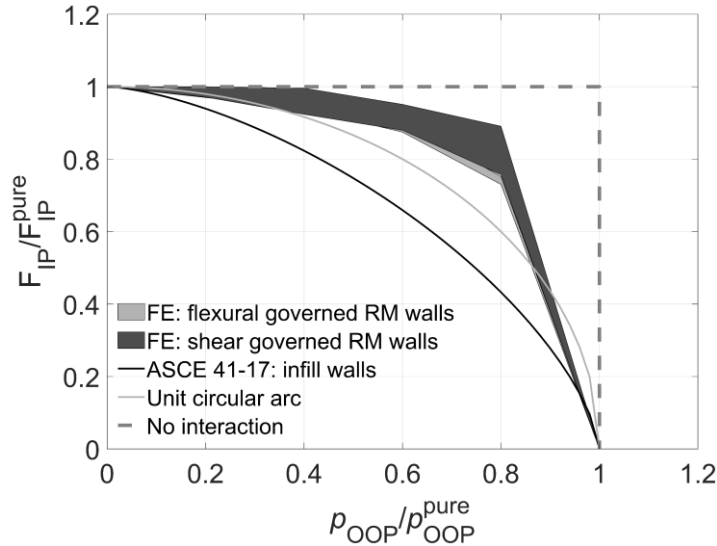


Figure 7-15. Comparison of IP-OOP capacity interaction curves for the flexural and shear governed walls

7.5.2. Influence of slenderness ratio (SR) and pre-compression load (P_v)

Figure 7-16 (a-b) presents the OOP deformations of the wall AR1.33_SR8.42 and the wall AR1.33_SR29.47 (i.e., walls with smallest and largest SR considered) without pre-compression load (i.e., $P_v = 0.0$ MPa). To show how IP loads affect the OOP deformations, OOP deformation contour plots are reported at three IP loading levels: no IP load (i.e., only with pre-applied OOP loads at 80% of the pure OOP capacities), intermediate IP load, and peak IP load. It is worth re-emphasizing that when considering the influence of SR, the length and height of walls are varied proportionally to fix AR, as indicated by the dimensions (at undeformed stages) shown in Figure 7-16. It can be observed from Figure 7-16 (b) that for the wall AR1.33_SR29.47 with $P_v = 0.0$

MPa, the maximum OOP deformation induced by the IP load is localized at the mid-height end zone above the crushed region of the wall. This behavior is indicative of a typical OOP instability phenomenon, as reported in relevant experimental studies on RM walls (Robazza et al. 2018) and reinforced concrete walls (Dashti et al. 2018). Such instability leads to a substantial decrease in the OOP stiffness of the wall (Robazza et al. 2018), thus inducing a significantly large OOP deformation or OOP instability. In turn, this would result in a pronounced reduction in IP capacity. The OOP instability is not observed in the non-slender wall (i.e., wall AR1.33_SR8.42), and the OOP deformation is mainly concentrated at the tension zone considering the IP loading direction. On the other hand, pre-compression load can be beneficial in mitigating the issue of OOP instability as shown in Figure 7-16 (c) for the wall AR1.33_SR29.47 with $P_v = 2.5$ MPa. This is also reported in relevant experimental studies (Dashti et al. 2018; Robazza et al. 2018).

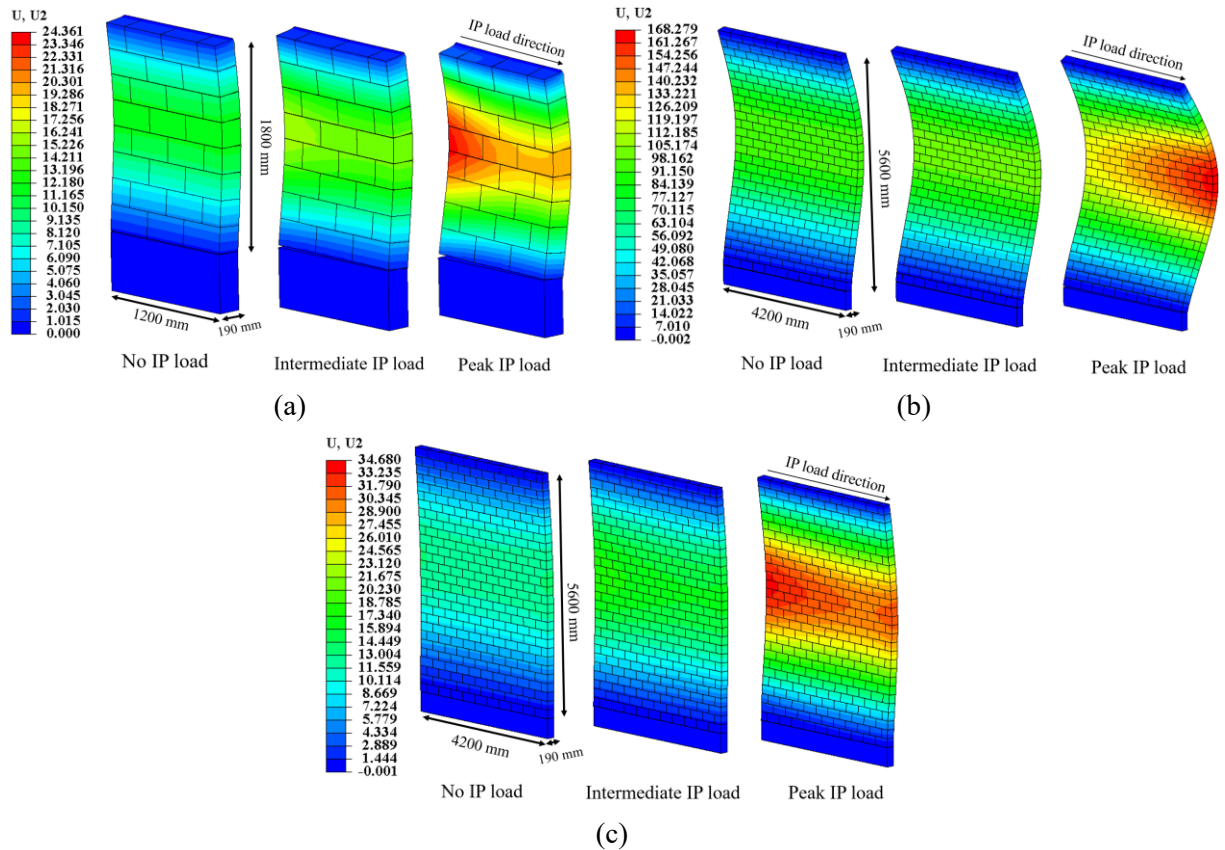


Figure 7-16. Evolution of OOP deformations (mm) due to IP loads for: (a) wall AR1.33_SR8.42 with $P_v = 0.0$ MPa, (b) AR1.33_SR29.47 with $P_v = 0.0$ MPa, and (c) wall AR1.33_SR29.47 with $P_v = 2.5$ MPa (deformation scale factor:15)

Figure 7-17 (a-b) presents the IP and OOP interaction curves for RM walls with different SR and P_v . Figure 7-17 (a) shows that the IP-OOP interaction of RM walls is not largely influenced by SR (when SR = 8.42, 12.63, 21.05), except when the wall has a relatively high SR (e.g., SR = 29.47) with an instability issue. Specifically, when the pre-applied OOP load level is at 80% of the pure OOP capacity, there is approximately 24% reduction in IP capacity for RM walls with lower SR values; nevertheless, the reduction increases up to 45% for the wall with a relatively higher SR = 29.47 due to the instability failure. As explained earlier, an increase in pre-compression load leads to less IP-OOP interaction, namely less reduction in the IP capacity due to OOP load. This is confirmed by the results shown in Figure 21 (b).

According to Figure 7-17 (a-b), it is further confirmed that the interaction observed for RM walls considered is less than that specified in the design provision in ASCE 41-17 (ASCE 2017) for masonry infill walls. For example, the IP capacity reduction is 58% when the OOP load is 80% of the corresponding pure OOP capacity as prescribed in ASCE 41-17; however, this reduction is between 18% and 45% for RM walls considered here.

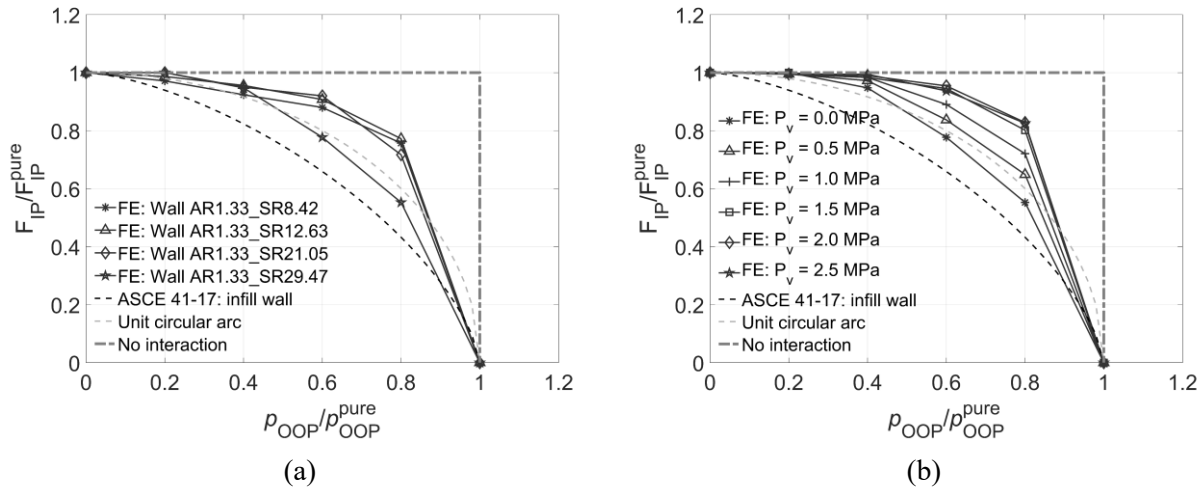


Figure 7-17. IP-OOP capacity interaction curves of RM walls: (a) walls with different SR when pre-compression load $P_v = 0.0$ MPa, and (b) wall AR1.33_SR29.47 with different pre-compression load levels

7.6. COMPARISON BETWEEN RM AND URM WALLS

This section investigates the potential benefits of reinforcements in alleviating the IP and OOP interaction effects. To be representative, three RM walls are considered: the most ‘flexural’ wall (AR2.00_SR8.42 with $P_v = 0.0$ MPa), the most ‘shear’ wall (AR0.67_SR8.42 with $P_v = 2.5$ MPa), and the wall with most IP-OOP interaction (AR1.33_SR29.47 with $P_v = 0.0$ MPa) that is associated with the OOP instability issue. For comparison, the IP-OOP interaction of their counterparts, URM walls with no reinforcements, are studied.

Figure 7-18 illustrates the capacity interaction curves for both URM and RM walls, highlighting the advantageous effects of reinforcements in reducing the IP and OOP interaction effects. The analysis results reveal that all three representative RM walls exhibit less capacity reduction in comparison to their URM counterparts. Additionally, it is also noted that the interaction curve derived for the URM wall with strongest interaction is relatively well correlated with the one suggested in ASCE 41-17 for masonry infill walls, as shown in Figure 7-18 (b).

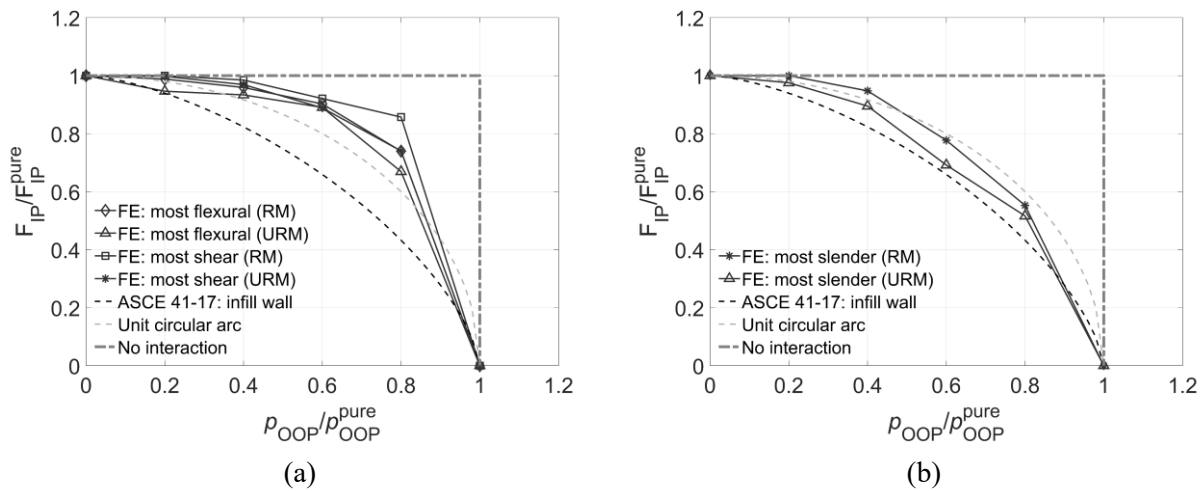


Figure 7-18. Comparison of the IP-OOP capacity interaction curves for RM walls and their URM counterparts: (a) the most ‘flexural’ and the most ‘shear’ walls considered, and (b) the wall considered with strongest IP-OOP interaction effects

7.7. CHAPTER CONCLUSION

This study explored the structural behavior of fully grouted reinforced concrete masonry (RM) walls subjected to combined in-plane (IP) and out-of-plane (OOP) loading using a simplified micro modeling approach. A series of IP-OOP interaction curves were developed to quantify the IP capacity reductions due to the presence of OOP loadings. The influences of aspect ratio (AR), slenderness ratio (SR), and pre-compression load (P_v) on the IP-OOP interaction behaviors of RM walls were investigated.

The numerical simulation results in this study revealed that the presence of OOP loads can induce substantial IP capacity reductions, especially for flexural governed walls, characterized by a larger aspect ratio and a low level of pre-compression load. For flexural governed walls, IP and OOP capacity interactions are found to be less sensitive to geometrical parameters and pre-compression load than shear governed walls. The most interaction is observed for highly slender walls without pre-compression loads, indicating a reduction in IP capacity by 45% when OOP loading reaches 80% of its corresponding capacity. This greatest reduction was attributed to the issue of OOP instability. However, increasing the pre-compression load would help mitigate such capacity reductions for highly slender walls. For the RM walls considered in this study, the IP-OOP interaction is less than that specified in the design provision in ASCE 41-17 for masonry infill walls, and the unit circular arc are better correlated with the interaction curves obtained in this study. For example, for a wall potentially being stressed to about 60% of its OOP capacity, its IP capacity is reduced to approximately 80% and 66% using the circular interaction diagram and design provision in ASCE 41-17, respectively. According to this study, this reduction would be smaller, i.e., still around 90% of the pure IP capacity. Such a reduction is not very significant, particularly considering that most masonry walls have IP capacities well beyond what are required. The findings of this study can serve as a valuable reference and offer guidance for an informed consideration of IP-OOP interaction effects in designing RM walls, contributing to the advancement of current engineering standards and practices. The findings of this study aim to serve as a valuable reference and offer guidance for an informed consideration of IP-OOP interaction effects in the designing of RM walls, contributing to the advancement of current engineering standards and practices.

An additional comparison was conducted to compare the capacity interaction effects between the RM walls and their counterparts, unreinforced masonry walls. The results highlighted that incorporating reinforcements is effective in mitigating the IP-OOP interaction. For the most 'shear' wall, the IP capacity reduction in the RM wall when the OOP load is equal to 80% of its OOP capacity is 11.6% less than that in the URM wall.

Chapter 8. ESTIMATING MEAN AND VARIANCE OF IN-PLANE RESISTANCE OF MASONRY WALLS USING INACCURATE DESIGN-CODE MODELS AND LIMITED HIGH-FIDELITY DATA

Analyzing uncertainty or estimating statistics of structures' load resistance is crucial for reliability-based code calibrations, forming the foundation for modern limit state design. While design-code models can be used to estimate the load resistance of masonry walls against in-plane (IP) loading, it is widely recognized that these models are inherently inaccurate due to their simplifications, assumptions, or empirical features. Therefore, employing them for uncertainty analysis or statistics estimation can be challenging. On the other hand, detailed mechanics-based finite element (FE) models and physical experimental tests are typically more accurate. Nevertheless, their application for uncertainty analysis or statistic estimation is often impractical due to high computational or economic cost. To address this challenge, this study introduces improved estimators for the mean and variance of the OOP resistance of masonry walls after considering parameter uncertainties, by leveraging efficient design-code models and limited high-fidelity data generated from detailed FE models by using the control variate method (Nelson 1987, 1990). In the proposed estimators, a large number of design-code model evaluations are introduced to improve the computational efficiency, while only a limited number of FE model evaluations are integrated to ensure accuracy. Three case studies are presented to illustrate the applicability of the proposed estimators: one on unreinforced masonry (URM) walls and two on reinforced masonry (RM) walls. The results indicate that the proposed estimators for mean and variance outperform the estimators that rely solely on the FE and design-code models regarding accuracy and efficiency, respectively.

8.1. INTRODUCTION

Masonry walls are commonly used as primary vertical load-bearing elements in low- and mid-rise buildings, resisting gravity loads and seismic or wind loads. Therefore, understanding and/or predicting their structural behaviors under in-plane (IP) loading is of paramount importance. Particularly, it is essential to assess the ultimate IP resistance of masonry walls with confidence in practice.

However, despite extensive experimental studies undertaken over recent decades to study IP behaviors (El-Dakhakhni and Ashour 2017; Zeng and Li 2023), design-code models are inherently inaccurate due to their simplifications, assumptions, or empirical features, and are often associated with substantial model error. For instance, Hwang et al. (2022) noted that the design equations specified by the New Zealand Society for Earthquake Engineering (NZSEE) and FEMA 273 (Applied Technology Council 1997) resulted in conservative assessments of the IP resistance of unreinforced masonry (URM) walls with a significant level of deviation when compared with test data. Shedid et al. (2008) compared the experimental results and design code predictions for the IP flexural capacity of reinforced masonry (RM) walls and found that both CSA S304.1-04 (2004) and MSJC code (2005) resulted in conservative estimations. Seif Eldin et al. (2019) also noted that CSA S304-14 (2014) predictions for the IP shear strength of fully grouted RM walls were consistently conservative, with experimental-to-predicted IP shear strength ratios ranging from 1.35 to 3.11. Similar conclusions were made by Aguilar et al., (2016), and CSA S304-14 is overly conservative in predicting the IP shear strength of RM walls. Recent studies (Celano et al. 2021; Tariq et al. 2023) also indicated that the design codes are not entirely effective in accurately predicting the failure modes of masonry walls under IP loading and associated wall capacities.

This inadequacy arises from the fact that multiple failure modes could co-exist and potentially interact.

The issue of predicting the IP resistance of masonry walls is further exacerbated by the pronounced variability of masonry material (Iannacone et al. 2021). Contemporary design guidelines for masonry structures, such as Canadian masonry design code CSA S304-14 (2014), are rooted in the Limit State Design (LSD) philosophy but still heavily rely on deterministic approaches with partial safety factors, which need to be calibrated using reliability-based approaches to ensure that masonry structures achieve the desired level of reliability (Isfeld et al. 2023; Lawrence and Stewart 2015; Moosavi and Korany 2014; Rota et al. 2014; Stewart and Lawrence 2007; Zhai et al. 2012; Zhai and Stewart 2010). In this context, uncertainty quantification of IP load resistance, such as its statistics like mean and variance, plays crucial roles.

In the research community, there is a notable interest in understanding how material uncertainty impacts the IP resistance of masonry walls through stochastic sampling methods, such as the Monte Carlo (MC) simulation method (Metropolis and Ulam 1949). MC simulation is non-intrusive and does not intervene deterministic models. This flexibility allows MC simulation to be integrated seamlessly with various analytical and numerical models, making it a versatile tool for uncertainty analyses. Notably, design-code models provide an efficient means for the uncertainty analysis of IP resistance for masonry walls within the MC simulation framework, in which a large number of model evaluations are necessary (Iannacone et al. 2021; Peng et al. 2020; Zhai et al. 2012). However, relying solely on design-code models is not advisable, despite their computational efficiency, because of the inherent bias or inaccuracy as mentioned earlier. As such, model error must be quantified probabilistically using the high-fidelity experimental data before

their use for reliability calibration (Lawrence and Stewart 2015; Stewart and Lawrence 2007; Zhai and Stewart 2010), though it is noteworthy that such data are often limited and heterogeneous from different experimental sources.

To address these limitations, researchers have shifted their attention to utilizing more accurate models, such as mechanics-based finite element (FE) models with realistic constitutive material models, to assess the IP behavior of masonry walls. For instance, the micro modeling strategy was proposed (Lourenço et al. 1995b) and received great popularity in the masonry research community. In the micro modeling strategy, individual components (e.g., units, mortar, reinforcements, grouts, unit-mortar contacts) are explicitly represented. This approach is generally perceived to be significantly more reliable than design-code models, with remarkable success in the prediction of IP resistance, as well as failure modes, for URM walls (Li and Zeng 2023; Zeng et al. 2021) and RM walls (Koutras and Shing 2021a; Mavros 2015). However, directly integrating the micro models for uncertainty analysis using the MC simulation for estimating the mean and variance of the IP resistance of masonry walls would lead to prohibitive computational cost.

As previously highlighted, when evaluating the IP resistance of masonry walls, micro FE models are more accurate but computationally expensive, while design-code models are more accessible and efficient, but generally associated with larger mode errors. The objective of this chapter is to propose an improved methodology by leveraging the strengths of both models, namely by incorporating only a few high-fidelity data, generated from evaluations of expensive FE models, and a large number of cheap design-code model evaluations into the MC simulation framework. This is achieved by using the control variate method (Nelson 1987, 1990). The main focus is on estimating the mean and variance of IP resistance of both reinforced and unreinforced masonry

walls. The proposed approach promises more precise and efficient results than those stemming from sole reliance on either model, providing a new venue for utilizing computational models for design-code model enhancement. In what follows, the MC simulation-based statistical estimators for the IP resistance of masonry walls are introduced first, using solely design-code models or FE models. Next, improved estimators are introduced by using both design-code models and FE models, assuming FE models can provide high-fidelity data. The advantage of proposed estimators is then illustrated using three case studies: one on URM walls, and two on RM walls.

8.2. CRUDE MONTE CARLO-BASED ESTIMATORS

The quantity of interest, such as the IP resistance of masonry walls $f(\mathbf{x})$, is a derived random variable, as a function of basic random variables \mathbf{x} , such as masonry or its constituents' properties, described by probability density functions $g(\mathbf{x})$. The goal is to estimate its expectation and variance, defined as Eq. (8-1) and Eq. (8-2), respectively:

$$\mathbb{E}[f(\mathbf{x})] = \int f(\mathbf{x})g(\mathbf{x})d\mathbf{x} \quad (8-1)$$

$$\mathbb{V}[f(\mathbf{x})] = \int [f(\mathbf{x}) - \mathbb{E}[f(\mathbf{x})]]^2 g(\mathbf{x}) d\mathbf{x} \quad (8-2)$$

where $\mathbb{E}[\cdot]$ and $\mathbb{V}[\cdot]$ are the expectation and variance operators. The integrals in Eq. (8-1) and Eq. (8-2) can be estimated using MC simulation, by involving deterministic IP resistance models such as finite element models $f_{FE}(\mathbf{x})$, or design-code models $f_{CSA}(\mathbf{x})$ specified in the Canadian masonry design code CSA S304-14 (Canadian Standards Association 2014).

8.2.1. Mean and variance estimators using design-code models

When design-code models for the IP resistance of masonry walls are used, the mean and variance of IP resistance can be estimated as Eq. (8-3) and Eq. (8-4), respectively:

$$\hat{\mathbb{E}}_{\text{CSA}} = \frac{1}{m_{\text{CSA}}} \sum_{i=1}^{m_{\text{CSA}}} f_{\text{CSA}}(\mathbf{x}_i) \quad (8-3)$$

$$\hat{\mathbb{V}}_{\text{CSA}} = \frac{1}{m_{\text{CSA}} - 1} \sum_{i=1}^{m_{\text{CSA}}} \left(f_{\text{CSA}}(\mathbf{x}_i) - \hat{\mathbb{E}}_{\text{CSA}} \right)^2 \quad (8-4)$$

where $\hat{\mathbb{E}}_{\text{CSA}}$ and $\hat{\mathbb{V}}_{\text{CSA}}$ are unbiased MC estimators of $\mathbb{E}[f_{\text{CSA}}(\mathbf{x})]$ and $\mathbb{V}[f_{\text{CSA}}(\mathbf{x})]$; \mathbf{x}_i ($i = 1, 2, \dots, m_{\text{CSA}}$) are independent identically distributed samples drawn from $g(\mathbf{x})$; and m_{CSA} is the number of samples, and thus the evaluation number of design-code model.

Masonry walls under IP loading may exhibit three different failure modes: flexural rocking, diagonal tension cracking, and shear sliding. In the design practices, IP resistance corresponding to each of these three modes is typically evaluated individually based on (semi-) empirical or simplified analytical models, with the one presenting the lowest value being the governing failure mode. In CSA S304-14 (Canadian Standards Association 2014), shear sliding resistance is evaluated based on the Mohr-Coulomb relationship, and the IP resistance of masonry walls governed by diagonal tension cracking is assessed using a semi-empirical relationship. On the other hand, the flexural capacity is evaluated based on the cross-sectional capacity, using the equivalent rectangular block by assuming zero tensile strength of masonry. The code provisions of CSA S304-14 for the prediction of IP resistances of URM and RM walls are detailed in Appendix C and Appendix D, respectively.

8.2.2. Mean and variance estimators using FE models

FE models for masonry walls employed in this study are developed based on the simplified micro modeling strategy (Page 1978), as shown in Figure 6-1 . In this modeling approach, mortar layer plus unit-mortar interaction are lumped into a single zero-thickness interface. Mortar joints are simulated using zero-thickness interface elements COH3D8 in ABAQUS (Dassault Systemes 2017), in conjunction with a recently developed constitutive model by the authors (Li and Zeng 2023). This newly developed constitutive model is characterized by two yield surfaces (i.e., tension-shear yield surface f_1 and compression cap surface f_2) and is capable of capturing various failure modes, including tensile cracking, shear sliding, and compressive crushing. Concrete blocks and grouts are modeled using the C3D8 element plus the nonlinear behaviors represented via the Concrete Damage Plasticity (CDP) model (Lee and Fenves 1998), in which tensile cracking and compressive crushing can be well described using different parameters for concrete and grouts. Reinforcing bars in RM walls are modeled using the truss element T3D2 with the von Mises plasticity model and a bilinear hardening law. A perfect bond is assumed for grout and steel reinforcement in RM walls. The modeling strategy was validated for URM walls (Li and Zeng 2023) and RM walls under IP loading.

When FE models are used, MC estimators for the mean and variance of the IP resistance of masonry walls are expressed in a similar way as those when design-code models are used. Suppose the FE model is denoted by $f_{FE}(\mathbf{x})$, the expectation $\mathbb{E}[f_{FE}(\mathbf{x})]$ and variance $\mathbb{V}[f_{FE}(\mathbf{x})]$ can be estimated as Eq. (8-5) and Eq. (8-6), respectively:

$$\hat{\mathbb{E}}_{FE} = \frac{1}{m_{FE}} \sum_{i=1}^{m_{FE}} f_{FE}(\mathbf{x}_i) \quad (8-5)$$

$$\hat{V}_{FE} = \frac{1}{m_{FE} - 1} \sum_{i=1}^{m_{FE}} \left(f_{FE}(\mathbf{x}_i) - \hat{\mathbb{E}}_{FE} \right)^2 \quad (8-6)$$

Here, $\hat{\mathbb{E}}_{FE}$ and \hat{V}_{FE} are the unbiased MC estimators of $\mathbb{E}[f_{FE}(\mathbf{x})]$ and $\mathbb{V}[f_{FE}(\mathbf{x})]$; \mathbf{x}_i ($i = 1, 2, \dots, m_{FE}$) are independent identically distributed samples drawn from $g(\mathbf{x})$; and m_{FE} is the evaluation number of FE model.

8.2.3. Quality measure of Monte Carlo estimators

The quality of MC estimators can be evaluated by the mean square error (MSE) with respect to the true values. In this study, the true values of expectation and variance are assumed to be obtained by the high-fidelity FE model, i.e., $\mathbb{E}[f_{FE}(\mathbf{x})]$ and $\mathbb{V}[f_{FE}(\mathbf{x})]$, considering the true values are generally unavailable. Error measurement of $\hat{\mathbb{E}}_{FE}$ and \hat{V}_{FE} can be derived as Eq. (8-7) and Eq. (8-8), respectively:

$$\text{MSE}(\hat{\mathbb{E}}_{FE}) = \mathbb{E} \left[\left(\mathbb{E}[f_{FE}(\mathbf{x})] - \hat{\mathbb{E}}_{FE} \right)^2 \right] = \mathbb{V}[\hat{\mathbb{E}}_{FE}] = \frac{\mathbb{V}[f_{FE}(\mathbf{x})]}{m_{FE}} \quad (8-7)$$

$$\text{MSE}(\hat{V}_{FE}) = \mathbb{E} \left[\left(\mathbb{V}[f_{FE}(\mathbf{x})] - \hat{V}_{FE} \right)^2 \right] = \mathbb{V}[\hat{V}_{FE}] = \frac{1}{m_{FE}} \left[\mu_4[f_{FE}(\mathbf{x})] - \frac{m_{FE} - 3}{m_{FE} - 1} \mathbb{V}[f_{FE}(\mathbf{x})]^2 \right] \quad (8-8)$$

In Eq. (8-8), $\mu_4[f_{FE}(\mathbf{x})]$ is the fourth central moment of $f_{FE}(\mathbf{x})$. It can be observed from Eq. (8-7) and Eq. (8-8) that a large value of m_{FE} is required to reach a reasonable accuracy for $\mathbb{E}[f_{FE}(\mathbf{x})]$ and $\mathbb{V}[f_{FE}(\mathbf{x})]$. However, this is generally impractical since evaluating a FE model is expensive, and this necessitates the use of design-code models. Evidently, the estimators using

design-code models shown in Eq. (8-3) and Eq. (8-4) would lead to inaccurate results due to the inherent bias associated with the model $f_{CSA}(\mathbf{x})$ compared to $f_{FE}(\mathbf{x})$.

8.3. IMPROVED ESTIMATORS FOR MEAN AND VARIANCE

The fundamental idea of the proposed estimators is to use the control variate (CV) method, a classical variance reduction technique in statistics (Nelson 1987). The proposed estimators leverage the information from a very limited number of FE evaluations for accuracy enhancement and a large number of design code evaluations (i.e., $m_{CSA} \gg m_{FE}$) for efficiency. The improved estimators for mean and variance for the IP resistance of masonry walls are described as follows.

8.3.1. Mean estimator

The proposed mean estimator for the IP resistance of masonry walls, denoted as $\hat{\mathbb{E}}_{IM}$, is formulated as Eq. (8-9):

$$\hat{\mathbb{E}}_{IM} = \frac{1}{m_{FE}} \sum_{i=1}^{m_{FE}} f_{FE}(\mathbf{x}_i) + \alpha \left(\frac{1}{m_{CSA}} \sum_{i=1}^{m_{CSA}} f_{CSA}(\mathbf{x}'_i) - \frac{1}{m_{FE}} \sum_{i=1}^{m_{FE}} f_{CSA}(\mathbf{x}''_i) \right) \quad (8-9)$$

It is clear that both design-code and FE models are integrated in $\hat{\mathbb{E}}_{IM}$. In Eq. (8-9), the first term of right-hand side (RHS) is related to the FE estimation, the latter two terms are based on the design-code predictions, and α is a coefficient determined by minimizing the MSE of the estimator $\hat{\mathbb{E}}_{IM}$. More details about α are presented later. It is noted that the samples \mathbf{x}_i , \mathbf{x}' , and \mathbf{x}'' are independently and randomly generated. One notable advantage of the proposed mean estimator is that $\hat{\mathbb{E}}_{IM}$ is unbiased with respect to the true value $\mathbb{E}[f_{FE}(\mathbf{x})]$: $\mathbb{E}[\hat{\mathbb{E}}_{IM}] = \mathbb{E}[f_{FE}(\mathbf{x})]$.

This provides significant benefits than the MC estimator when only using design-code models, i.e.,

Eq. (8-3). The other critical feature of $\hat{\mathbb{E}}_{\text{IM}}$ is that the discrepancy between the FE model and design-code model (i.e., $|f_{\text{FE}}(\mathbf{x}_i) - f_{\text{CSA}}(\mathbf{x}_i)|$) does not affect its accuracy. This is demonstrated by the MSE of $\hat{\mathbb{E}}_{\text{IM}}$ with respect to the true value, as derived in Eq. (8-10). Due to the unbiasedness of $\hat{\mathbb{E}}_{\text{IM}}$, $\text{MSE}(\hat{\mathbb{E}}_{\text{IM}})$ is equal to the variance of $\hat{\mathbb{E}}_{\text{IM}}$: $\mathbb{V}[\hat{\mathbb{E}}_{\text{IM}}] = \mathbb{E}\left[\left(\hat{\mathbb{E}}_{\text{IM}} - \mathbb{E}[\hat{\mathbb{E}}_{\text{IM}}]\right)^2\right]$, derived as Eq.

(8-10):

$$\text{MSE}(\hat{\mathbb{E}}_{\text{IM}}) = \frac{\mathbb{V}[f_{\text{FE}}(\mathbf{x})]}{m_{\text{FE}}} + \left(\frac{1}{m_{\text{FE}}} - \frac{1}{m_{\text{CSA}}}\right) \left(\mathbb{V}[f_{\text{FE}}(\mathbf{x})]\mathbb{V}[f_{\text{CSA}}(\mathbf{x})] - 2\rho\sqrt{\mathbb{V}[f_{\text{FE}}(\mathbf{x})]\mathbb{V}[f_{\text{CSA}}(\mathbf{x})]}\right) \quad (8-10)$$

Here, ρ is the Pearson correlation coefficient between the FE model and design-code model, defined in Eq. (8-11):

$$\rho = \frac{\text{Cov}[f_{\text{FE}}(\mathbf{x}), f_{\text{CSA}}(\mathbf{x})]}{\sqrt{\mathbb{V}[f_{\text{FE}}(\mathbf{x})]\mathbb{V}[f_{\text{CSA}}(\mathbf{x})]}} \quad (8-11)$$

where $\text{Cov}[\cdot]$ is the covariance operator. Given a dataset with sample size N , Pearson correlation coefficient estimation $\hat{\rho}$ is estimated as per Eq. (8-12):

$$\hat{\rho} = \frac{\sum_{i=1}^N [f_{\text{FE}}(\mathbf{x}_i) - \overline{f_{\text{FE}}(\mathbf{x})}][f_{\text{CSA}}(\mathbf{x}_i) - \overline{f_{\text{CSA}}(\mathbf{x})}]}{\sqrt{\sum_{i=1}^N [f_{\text{FE}}(\mathbf{x}_i) - \overline{f_{\text{FE}}(\mathbf{x})}]^2} \sqrt{\sum_{i=1}^N [f_{\text{CSA}}(\mathbf{x}_i) - \overline{f_{\text{CSA}}(\mathbf{x})}]^2}} \quad (8-12)$$

where $\overline{f_{\text{FE}}(\mathbf{x})}$ and $\overline{f_{\text{CSA}}(\mathbf{x})}$ are the sample mean values: $\overline{f_{\text{FE}}(\mathbf{x})} = \sum_{i=1}^N f_{\text{FE}}(\mathbf{x}_i)$ and

$$\overline{f_{\text{CSA}}(\mathbf{x})} = \sum_{i=1}^N f_{\text{CSA}}(\mathbf{x}_i).$$

Based on Eq. (8-9), the proposed mean estimator for the IP resistance of masonry walls depends on the evaluation numbers of the FE and design-code models, i.e., m_{FE} and m_{CSA} , as well as the coefficient α . In this study, the close-form solution for the determination of m_{FE} , m_{CSA} , and α derived by Peherstorfer et al. (2016b) is used, by minimizing the $MSE(\hat{E}_{IM})$ given a prescribed computational cost p , i.e., $C_t \leq p$. Here, the total cost C_t is formulated as Eq. (8-13):

$$C_t = m_{FE} w_{FE} + m_{CSA} w_{CSA} \quad (8-13)$$

where w_{FE} and w_{CSA} are the computational costs associated with one single FE model and design-code model evaluation, respectively. The constrained optimization leads to Eqs. (8-14)(8-15)(8-16), which are used to determine the three parameters, respectively.

$$\alpha = \frac{\rho \nabla [f_{FE}(\mathbf{x})]}{\nabla [f_{CSA}(\mathbf{x})]} \quad (8-14)$$

$$m_{FE} = \frac{p}{w_{FE} + w_{CSA} r_{CSA}} \quad (8-15)$$

$$m_{CSA} = m_{FE} r_{CSA} \quad (8-16)$$

where $r_{CSA} = \sqrt{\frac{w_{FE} \rho^2}{w_{CSA} (1 - \rho^2)}}$. One mild condition that needs to be met for the model

management scheme is:

$$\frac{w_{FE}}{w_{CSA}} > \frac{1 - \rho^2}{\rho^2} \quad (8-17)$$

The advantage of the proposed mean estimator $\hat{\mathbb{E}}_{\text{IM}}$ than the design-code based estimator $\hat{\mathbb{E}}_{\text{CSA}}$ is evident, since $\hat{\mathbb{E}}_{\text{IM}}$ is unbiased. On the other hand, the ratio e between $\text{MSE}(\hat{\mathbb{E}}_{\text{IM}})$ and $\text{MSE}(\hat{\mathbb{E}}_{\text{FE}})$ can indicate the performance of $\hat{\mathbb{E}}_{\text{IM}}$ compared to the FE model-based estimator $\hat{\mathbb{E}}_{\text{FE}}$. By assuming the identical computational cost p , the FE model evaluation number in the FE model-based estimator is p / w_{FE} . Thus, the ratio e between $\text{MSE}(\hat{\mathbb{E}}_{\text{IM}})$ and $\text{MSE}(\hat{\mathbb{E}}_{\text{FE}})$ can be derived as Eq. (8-18):

$$e = \frac{\text{MSE}(\hat{\mathbb{E}}_{\text{IM}})}{\text{MSE}(\hat{\mathbb{E}}_{\text{FE}})} = \left(\sqrt{(1-\rho^2)} + \sqrt{\frac{w_{\text{CSA}}\rho^2}{w_{\text{FE}}}} \right)^2 \quad (8-18)$$

From Eq. (8-18), it is evident that a decrease in $w_{\text{CSA}} / w_{\text{FE}}$ leads to a greater error reduction. In addition, with the increase of the square of the correlation coefficient ρ^2 , e would be smaller, considering that design-code model is computationally much cheaper than the FE model.

8.3.2. Variance estimator

The proposed variance estimator $\hat{\mathbb{V}}_{\text{IM}}$ is formulated analogously to the mean estimator, as expressed in Eq. (8-19):

$$\hat{\mathbb{V}}_{\text{IM}} = \frac{1}{m_{\text{FE}} - 1} \sum_{i=1}^{m_{\text{IF}}} \left[f_{\text{FE}}(\mathbf{x}_i) - \frac{1}{m_{\text{FE}}} \sum_{i=1}^{m_{\text{FE}}} f_{\text{FE}}(\mathbf{x}_i) \right]^2 + \beta \left[\frac{1}{m_{\text{CSA}} - 1} \sum_{i=1}^{m_{\text{CSA}}} \left(f_{\text{CSA}}(\mathbf{x}'_i) - \frac{1}{m_{\text{CSA}}} \sum_{i=1}^{m_{\text{CSA}}} f_{\text{CSA}}(\mathbf{x}'_i) \right)^2 - \frac{1}{m_{\text{FE}} - 1} \sum_{i=1}^{m_{\text{FE}}} \left(f_{\text{CSA}}(\mathbf{x}''_i) - \frac{1}{m_{\text{FE}}} \sum_{i=1}^{m_{\text{FE}}} f_{\text{CSA}}(\mathbf{x}''_i) \right)^2 \right] \quad (8-19)$$

where β is a coefficient to be determined. Based on the linearity of expectation operator, $\hat{\mathbb{V}}_{\text{IM}}$ is also an unbiased estimator for $\mathbb{V}[f_{\text{FE}}(\mathbf{x})]$, i.e., $\mathbb{E}[\hat{\mathbb{V}}_{\text{IM}}] = \mathbb{V}[f_{\text{FE}}(\mathbf{x})]$. Consequently, the

MSE of \hat{V}_{IM} is equal to its variance $\mathbb{V}[\hat{V}_{IM}]$. The variance of a sum of random variables is computed by summing the variances of each variable and twice the sum of their pairwise covariances. Accordingly, the MSE of \hat{V}_{IM} can be derived in Eq. (8-20):

$$\begin{aligned} \text{MSE}[\hat{V}_{IM}] = & \frac{1}{m_{HF}} \left(\mu_4[f_{FE}(\mathbf{x})] - \frac{m_{FE}-3}{m_{FE}-1} \mathbb{V}[f_{FE}(\mathbf{x})]^2 \right) \\ & + \beta^2 \left(\frac{1}{m_{CSA}} \left(\mu_4[f_{CSA}(\mathbf{x})] - \frac{m_{FE}-3}{m_{FE}-1} \mathbb{V}[f_{CSA}(\mathbf{x})]^2 \right) - \frac{1}{m_{CSA}} \left(\mu_4[f_{CSA}(\mathbf{x})] - \frac{m_{CSA}-3}{m_{CSA}-1} \mathbb{V}[f_{CSA}(\mathbf{x})]^2 \right) \right) \\ & + 2\beta \left(\frac{1}{m_{CSA}} \left(\text{Cov}[\mathbb{V}[f_{CSA}(\mathbf{x})], \mathbb{V}[f_{CSA}(\mathbf{x})]] + \frac{2}{m_{CSA}-1} (\text{Cov}[f_{FE}(\mathbf{x}), f_{CSA}(\mathbf{x})])^2 \right) \right. \\ & \left. - \frac{1}{m_{FE}} \left(\text{Cov}[\mathbb{V}[f_{CSA}(\mathbf{x})], \mathbb{V}[f_{CSA}(\mathbf{x})]] + \frac{2}{m_{FE}-1} (\text{Cov}[f_{FE}(\mathbf{x}), f_{CSA}(\mathbf{x})])^2 \right) \right) \end{aligned} \quad (8-20)$$

By comparing $\text{MSE}[\hat{V}_{IM}]$ and Eq. (8-8), the quality of the proposed variance estimator can be deduced. In Eq. (8-19), the determination of model evaluation numbers m_{FE} and m_{CSA} , and coefficient β is crucial. Qian et al. (2018) suggested that these quantities be assumed to be identical to those in the mean-optimal model management scheme, as referenced in Eqs. (8-14)(8-15)(8-16). The primary reason for this recommendation is that fourth-order moments are involved in $\text{MSE}[\hat{V}_{IM}]$, which are typically more challenging to estimate than second-order moments. The second approach is to determine these quantities by minimizing $\text{MSE}[\hat{V}_{IM}]$ with a given computational budget p within a numerical optimization procedure. In this study, these two schemes are used and compared based on the estimation results for the study cases considered later.

8.4. MEAN AND VARIANCE ESTIMATORS FOR IP RESISTANCE OF URM WALLS

The design-code model and FE model for the prediction of IP resistances of URM and RM walls introduced previously are incorporated into the proposed estimators. This section presents a case study for URM walls to demonstrate the efficacy of the proposed estimator. For comparison, three

estimators are examined: estimators that rely solely on the design-code model (\hat{E}_{CSA} , \hat{V}_{CSA}), estimators that rely solely on the FE model (\hat{E}_{FE} , \hat{V}_{FE}), and the proposed estimators (\hat{E}_{IM} , \hat{V}_{IM}).

8.4.1. Wall configuration

The URM wall considered in this study was experimentally investigated by Raijmakers (1992). It was constructed using solid clay bricks (210 mm × 52 mm × 100 mm) and 10 mm-thick mortar layers. The wall was 1000 mm high, 990 mm long, and 100 mm thick, as shown in Figure 8-1. The IP wall was tested under a fixed-fixed boundary condition, accompanied by a pre-compression load of 1.2 MPa. A displacement-controlled IP load was imposed on the top rigid beam until wall failure.

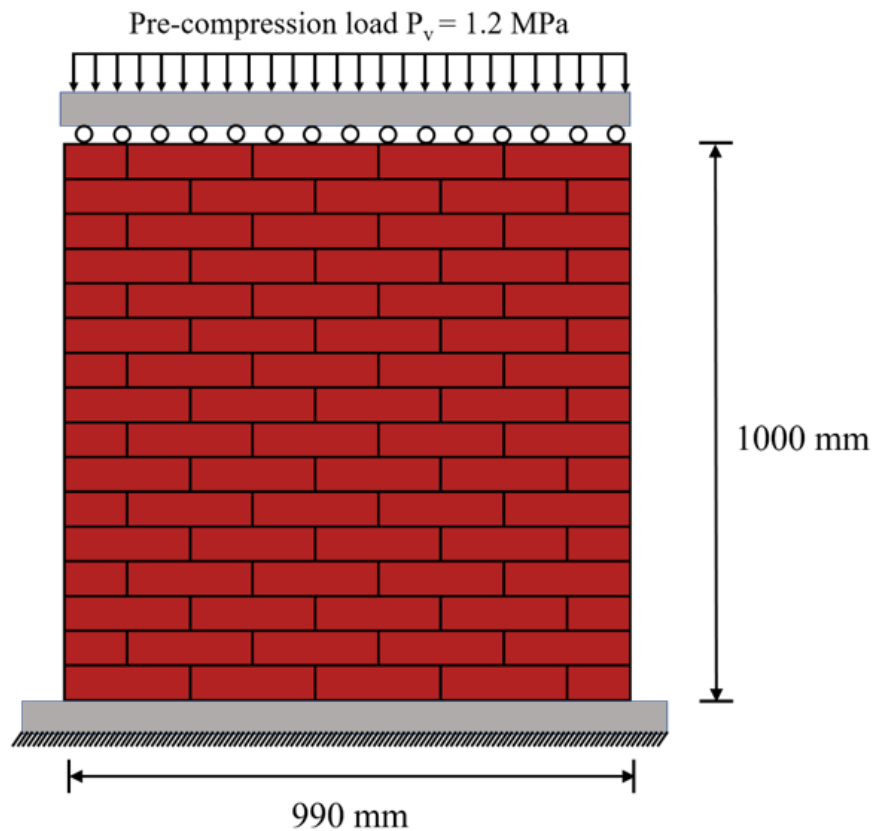


Figure 8-1. URM wall considered for the case study

8.4.2. Uncertainties in material parameters

Four statistically independent variables are considered for the URM wall: compressive strength of brick units f_u^c , tensile strength f_t , frictional coefficient $\tan \varphi$ and initial dilatancy coefficient $\tan \psi_0$ of interfaces (mortar joints). The mean values of these four parameters are assumed to be those reported by Raijmakers (1992). The probability distributions and coefficient of variations (COVs) are determined based on either field observations (Li et al. 2014) or laboratory tests (Pluijm 1999). Other variables are determined based on these four independent variables following the deterministic empirical relationships as prescribed in the public literature. Accordingly, corresponding statistical information can be derived, as summarized in Table 8-1.

Table 8-1. Statistical characterization of material parameters for the URM wall considered

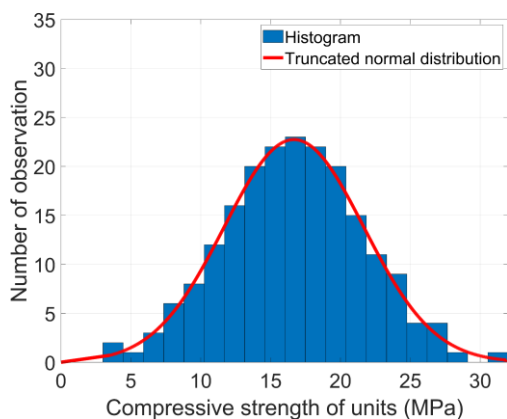
Parameters	Mean	Distribution	COV	Reference
Masonry Units				
Tensile strength f_t^u (MPa)	2 ($f_t^u = 0.12f_c^u$)	Truncated Normal ^(a)	0.3	(Li et al. 2014; Raijmakers 1992)
Compressive strength f_c^u (MPa)	16.67	Truncated Normal	0.3 ^(b)	(Li and Zeng 2023)
Elastic modulus E_u (MPa)	16700 ($E_u = 1002f_c^u$)	Truncated Normal	0.3	(Li and Zeng 2023; Raijmakers 1992)
Mortar				
Compressive strength f_c^m (MPa)	12.10 ($f_t = \frac{0.031}{1.5}f_c^m$)	Truncated Normal	0.3	(Isfeld et al. 2021; Li et al. 2014; Lumantarna et al. 2014)
Elastic modulus E_m (MPa)	2420 ($E_m = 200f_c^m$)	Truncated Normal	0.3	(Kaushik et al. 2007)
Mortar joints (interfaces)				
Tensile strength f_t (MPa)	0.16	Truncated Normal ^(a)	0.3	(Li et al. 2014; Raijmakers 1992)
Mode I fracture energy G_I (N/mm)	0.003 ($G_I = 0.01571f_t + 0.0004882$)	Truncated Normal	0.25	(Isfeld et al. 2021; Li et al. 2014)
Peak cohesion c_0 (MPa)	0.224 ($c_0 = 1.4f_t$)	Truncated Normal	0.3	(Isfeld et al. 2021; Li et al. 2014)
Frictional coefficient $\tan \psi$	0.75	Lognormal	0.1	(Pluijm 1999; Raijmakers 1992)
Mode II fracture energy when the normal stress is equal to zero G_{II}^0 (N/mm)	0.03 ($G_{II}^0 = 10G_I$)	Truncated Normal	0.25	(Lotfi and Shing 1994)
Initial dilation coefficient $\tan \psi_0$	0.36	Truncated Normal ^(a)	0.25	(Pluijm 1999; Raijmakers 1992)
Compressive strength of masonry f_m' (MPa)	$f_m' = 0.55(f_c^u)^{0.7} (f_c^m)^{0.3}$	Derived	Derived	(European Committee for Standardization (CEN) 2005)
Stiffness constants k_{nn}, k_{ss}, k_{tt} (N/mm ³)	$k_{nn} = \frac{E_u E_m}{h_m (E_u - E_m)}$; $k_{ss} = k_{tt} = \frac{k_{nn}}{2(1+0.15)}$	Derived	Derived	(Lourenço 1996)

^(a) f_c^u and f_t have a lower bound of 0.0, $\tan \psi_0$ has lower and upper bounds of 0.27 and 0.57, respectively.

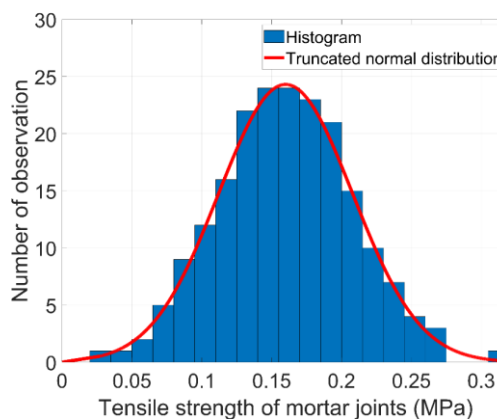
^(b) The value of COV is assumed to be 0.3 due to the lack of experimental information.

8.4.3. Statistics estimation

An essential aspect in the construction of proposed estimators lies in the computation of model statistics and Pearson correlation coefficient, since these quantities subsequently inform the determination of model evaluation numbers m_{FE} and m_{CSA} , as well as the coefficients (α and β for mean and variance, respectively). Given the significant computational demands associated with the FE model, accurate assessments of these quantities are often impractical. In this study, a pilot run on 200 MC samples is performed for this purpose. Figure 8-2 (a-d) presents probability distributions of four statistically independent parameters on the pilot sample, while Figure 8-2 (e-f) shows two examples of derived parameters, including peak cohesion of interfaces and compressive strength of masonry.



(a)



(b)

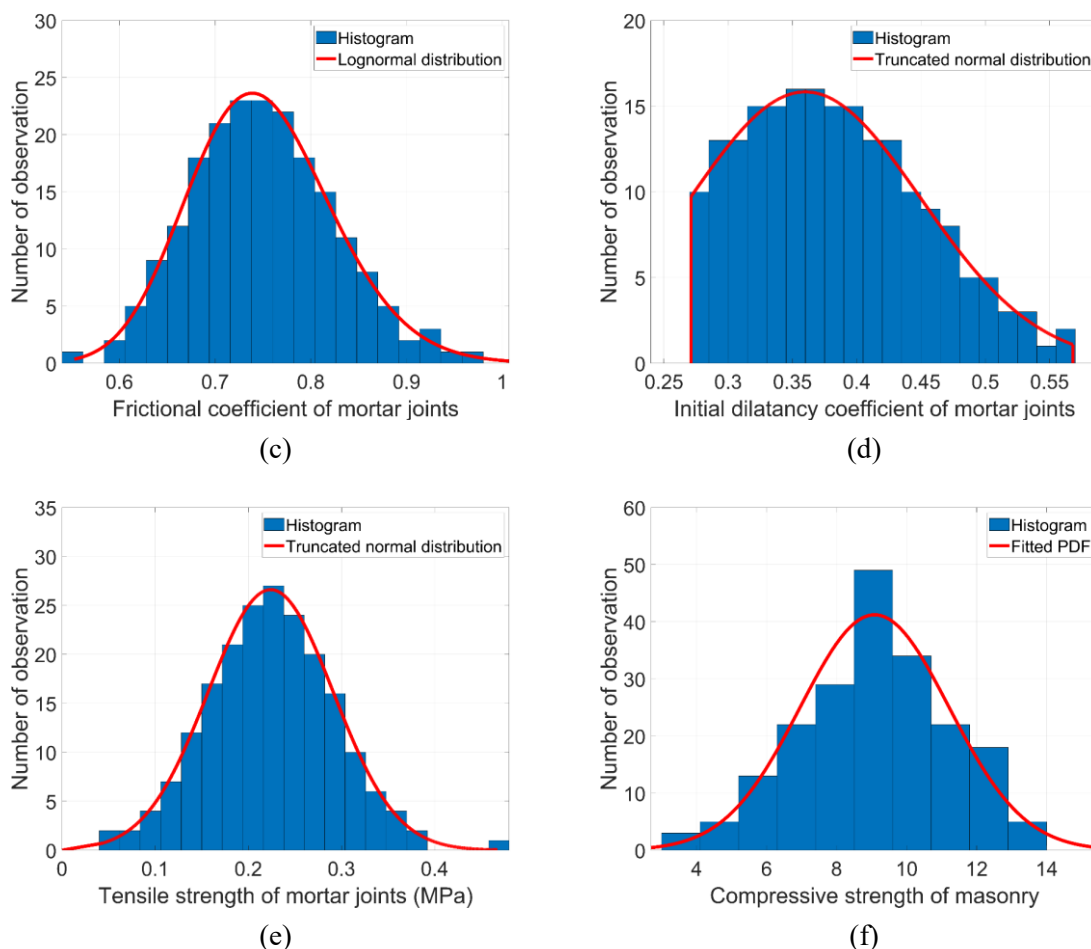


Figure 8-2. Histograms and probability distributions of random variables: (a) compressive strength of masonry units f'_c , (b) tensile strength of mortar joints f_t , (c) frictional coefficient $\tan \psi$, (d) initial dilation coefficient $\tan \psi_0$, (e) peak cohesion c_0 , and (f) compressive strength of masonry f'_m

Due to material variations, the 200 simulated walls exhibit the three typical failure modes, i.e., diagonal tension cracking (DT) for 117 walls (i.e., 58.5%), shear sliding (SS) for 61 walls (i.e., 30.5%), and flexural rocking failure (FR) for 22 walls (i.e., 11.0%). Empirical cumulative probability functions (CDFs) of IP resistances of URM walls governed by each failure mode are depicted in Figure 8-3, along with the CDF of IP resistance of URM walls irrespective of the failure modes. It is observed that, walls failing in FR show higher IP resistance, whereas those failing in

SS show lower IP resistance, but both with less dispersion, compared to those failing in DT. Overall, the IP resistances of the 200 walls range between 53.50 kN and 101.89 kN, with a mean of 76.03 kN and a sample standard deviation of 10.1 kN. Note that the tested wall, assumed to have mean properties, experienced failure in DT with an IP resistance of 72.46 kN.

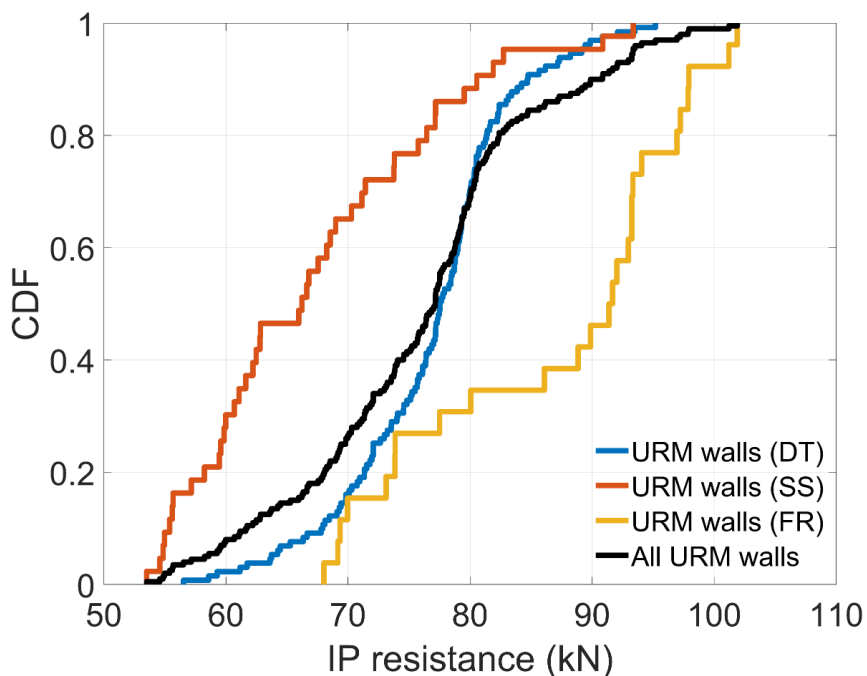


Figure 8-3. Empirical cumulative probability functions of IP resistances for the URM wall considered

The comparison of IP resistances between the design-code and FE predictions obtained from the pilot sample is shown in Figure 8-4 for each failure mode. As depicted in Figure 8-4 (a), the design code tends to underestimate the IP resistances (i.e., the flexural capacities) for walls failing in FR, when compared to the FE predictions. This difference can be primarily attributed to the zero tensile strength assumption for masonry in the design-code model. Similarly, Figure 8-4(c) shows that the design code tends to underestimate the IP resistance (i.e., sliding capacity) compared to the FE predictions, primarily because the design-code model only accounts for the

frictional resistance in mortar joints while neglecting the contribution of cohesion. Regarding the URM walls governed by DT, the design-code model predictions are more consistent with the FE model predictions, as shown in Figure 8-4 (b).

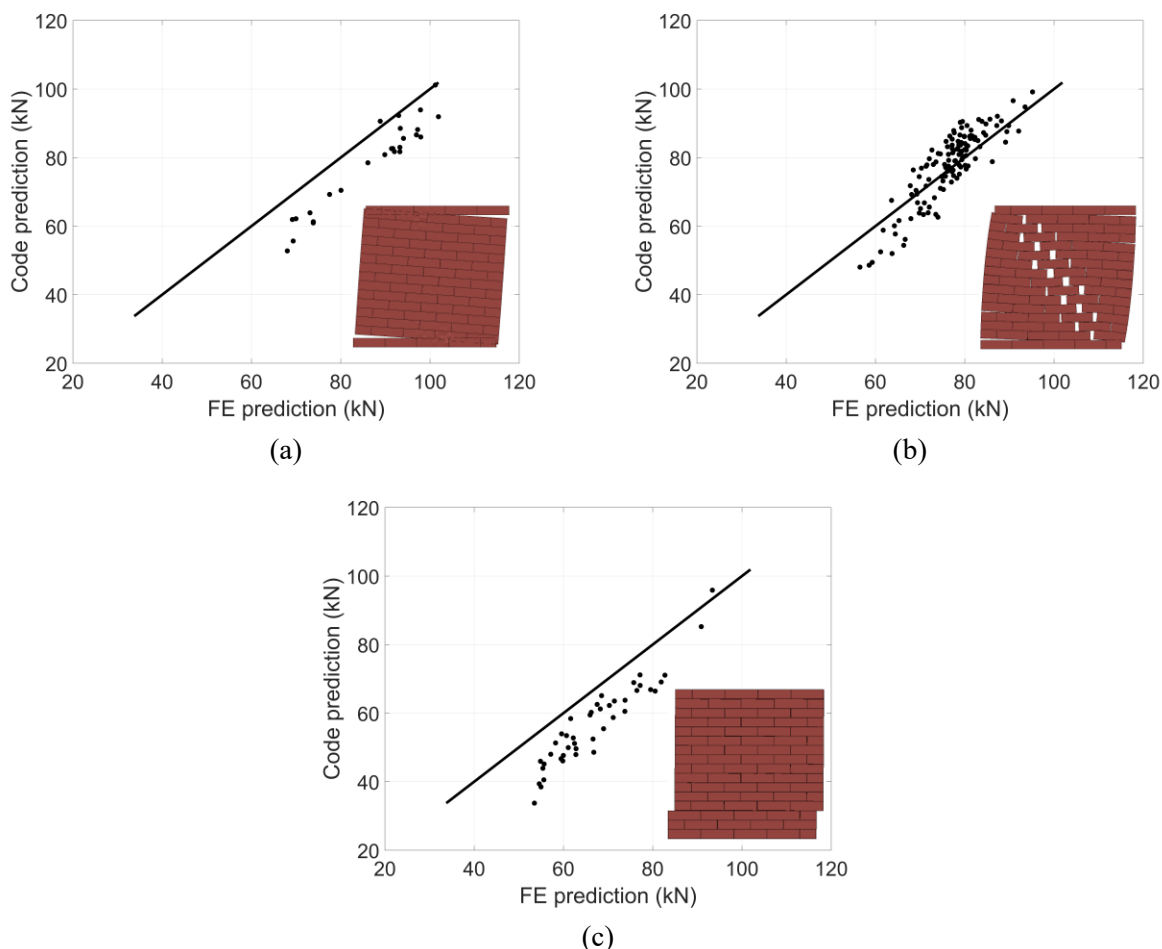


Figure 8-4. Comparison of IP resistances obtained by FE model and design-code model for URM walls governed by (a) flexural rocking, (b) diagonal tension cracking, and (c) shear sliding failure

Despite the discrepancy between design-code predictions and FE predictions, strong correlation exists between them. Thus, the quality of the proposed mean estimator $\hat{\mathbb{E}}_{\text{IM}}$ can be guaranteed because it is only dependent on the squared Pearson correlation coefficient ρ^2 for a given computational cost ratio $w_{\text{CSA}} / w_{\text{FE}}$, as indicated by Eq. (8-18). In this study, computational

costs are measured as multiples of the CPU time for one FE model evaluation, leading to $w_{FE} = 1.0$ and $w_{CSA} = 0.0000047$. The Pearson correlation coefficient ρ estimated by different sample sizes ($N = 20, 50, 100, 150, 200$), ranges from 0.85 to 0.90 as reported in Table 8-2. It can be inferred that the Pearson correlation coefficient does not exhibit significant variation with different sample sizes for the problem considered in this study. and a potentially optimum MSE reduction according to Eq. (8-18) is $e = 75\%$ for the URM wall considered, which is denoted by the green solid circle in Figure 8-5.

Table 8-2. Pearson correlation coefficient ρ between design-code model and FE model for the IP resistance prediction for the URM wall considered

Sample size (N)	Pearson correlation coefficient ρ
20	0.8940
50	0.8562
100	0.8647
150	0.8688
200	0.8770

To gain more insight into the MSE reduction, Figure 8-5 shows the relationship between the MSE ratio $e = \text{MSE}(\hat{\mathbb{E}}_{IM}) / \text{MSE}(\hat{\mathbb{E}}_{FE})$ and different values of Pearson correlation coefficient ρ and different values of w_{CSA} / w_{FE} , assuming the same computational budget. The red line in Figure 8-5 serves as a reference denoting that the estimators $\hat{\mathbb{E}}_{FE}$ and $\hat{\mathbb{E}}_{IM}$ achieve the same level of accuracy. The parametric study based on Eq. (8-18) reveals that when the design-code model is significantly more efficient than FE model (e.g., $w_{CSA} / w_{FE} = 0.0000047$ and 0.00047), an increase in the correlation coefficient leads to a greater accuracy of $\hat{\mathbb{E}}_{IM}$. However, if design-code and FE models exhibit comparable levels of computational cost (e.g., $w_{CSA} / w_{FE} = 0.47$ and 0.047), the proposed estimator only outperforms the FE model-based estimator only in highly correlated cases.

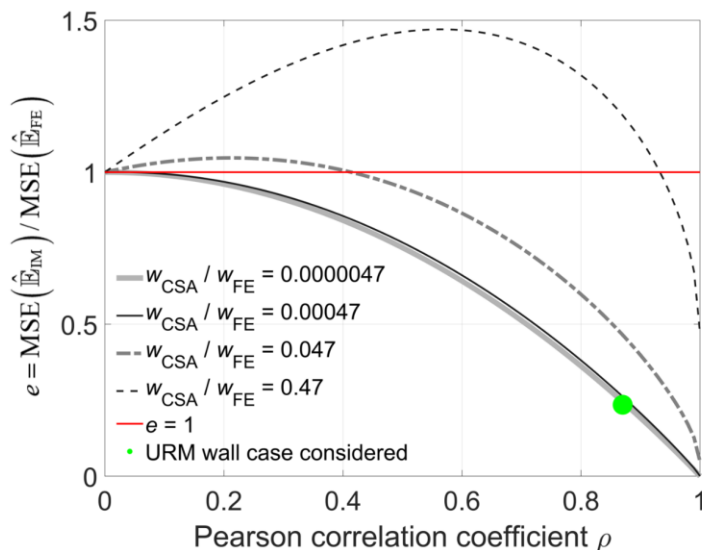


Figure 8-5. Relationship between MSE reduction e and Pearson correlation coefficient ρ with different computational cost ratios w_{CSA} / w_{FE}

To illustrate the effect of computational budget, six different levels for p , ranging from 5 to 30, are considered as summarized in Table 8-3. The computational budget can be purely used for p FE simulations, or $p / 0.0000047$ design-code evaluations in crude Monte Carlo estimators. Alternatively, the computational budget is distributed between FE simulations and design-code evaluations (m_{FE} and m_{CSA}) with the value for coefficient α for the proposed estimator. To fully leverage the 200 FE models already completed, the selection of FE samples for the construction of the proposed estimator will be restricted only to this pre-computed dataset, as suggested by Yao et al. (2022). A reference mean value of IP resistance of 75.97 kN is derived using the proposed estimator with a significantly large computational budget, wherein samples are randomly selected from the pre-computed 200 samples. It is important to acknowledge that the proposed estimator \hat{E}_{IM} is rigorously guaranteed to be unbiased, and therefore using the proposed estimator with a large computational budget to determine the reference mean value is justifiable.

Table 8-3. Model evaluation numbers (m_{FE} and m_{CSA}) and coefficient α for the mean estimation of IP resistance for the URM wall considered

Computational cost p	Crude MC estimators		Proposed estimator		
	FE model	Design-code model	m_{FE}	m_{CSA}	α
	m_{FE}	m_{CSA}			
5	5	1063829	4	4193	0.62
10	10	2127659	9	8386	0.62
15	15	3191489	14	12580	0.62
20	20	4255318	19	16773	0.62
25	25	5319145	24	20967	0.62
30	30	6382974	29	25160	0.62

Figure 8-6 reports the MSE of three estimators (i.e., $\hat{\mathbb{E}}_{CSA}$, $\hat{\mathbb{E}}_{FE}$, $\hat{\mathbb{E}}_{IM}$) used for prediction of the mean value of IP resistance for the URM wall considered, relative to the reference mean value through 500 replicate runs. Notably, the MSE of $\hat{\mathbb{E}}_{CSA}$ levels off at a very early stage, even for the minimum computational budget ($p = 5$) considered, since a large number of design-code model evaluations are used, as illustrated in Table 8-3. This also highlights the inherent bias in the mean estimator when exclusively relying on the design-code model. For the same computational budget, the crude MC estimator $\hat{\mathbb{E}}_{FE}$ derived based on the FE model alone outperform $\hat{\mathbb{E}}_{CSA}$ only when the sufficient number of FE evaluations is used with a relatively large computation budget (say $p > 15$). In contrast, the proposed estimator $\hat{\mathbb{E}}_{IM}$ achieves an MSE that is more than 70% lower than the crude MC estimator $\hat{\mathbb{E}}_{FE}$ derived based on the FE model alone when the same computation budget is used. As the available computational budget increases, the MSE of $\hat{\mathbb{E}}_{IM}$ decreases, suggesting the “unbiasedness” of proposed estimator. The same accuracy (or MSE) level, the proposed estimator needs much less computation budget, and this is because the efficient design-code model is employed to obtain speedups.

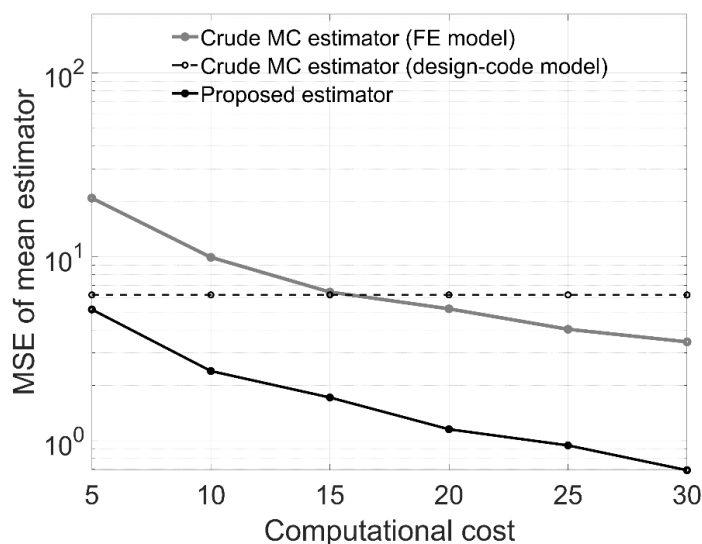


Figure 8-6. MSE of FE model-based crude MC estimator, design-code model-based crude MC estimator, and proposed estimator for the mean value of IP resistance for the URM wall considered

The histograms of \hat{E}_{FE} and \hat{E}_{IM} from 500 replicate runs are shown in Figure 8-7, from which similar conclusions can be obtained. It is worth mentioning that the design-code model-based estimator exhibits nearly zero variance, but significantly deviates from the reference mean value, as shown in Figure 8-7. Notably, the proposed estimator exhibits a smaller variance compared to the FE model-based crude MC estimator when the same computational budget is allocated.

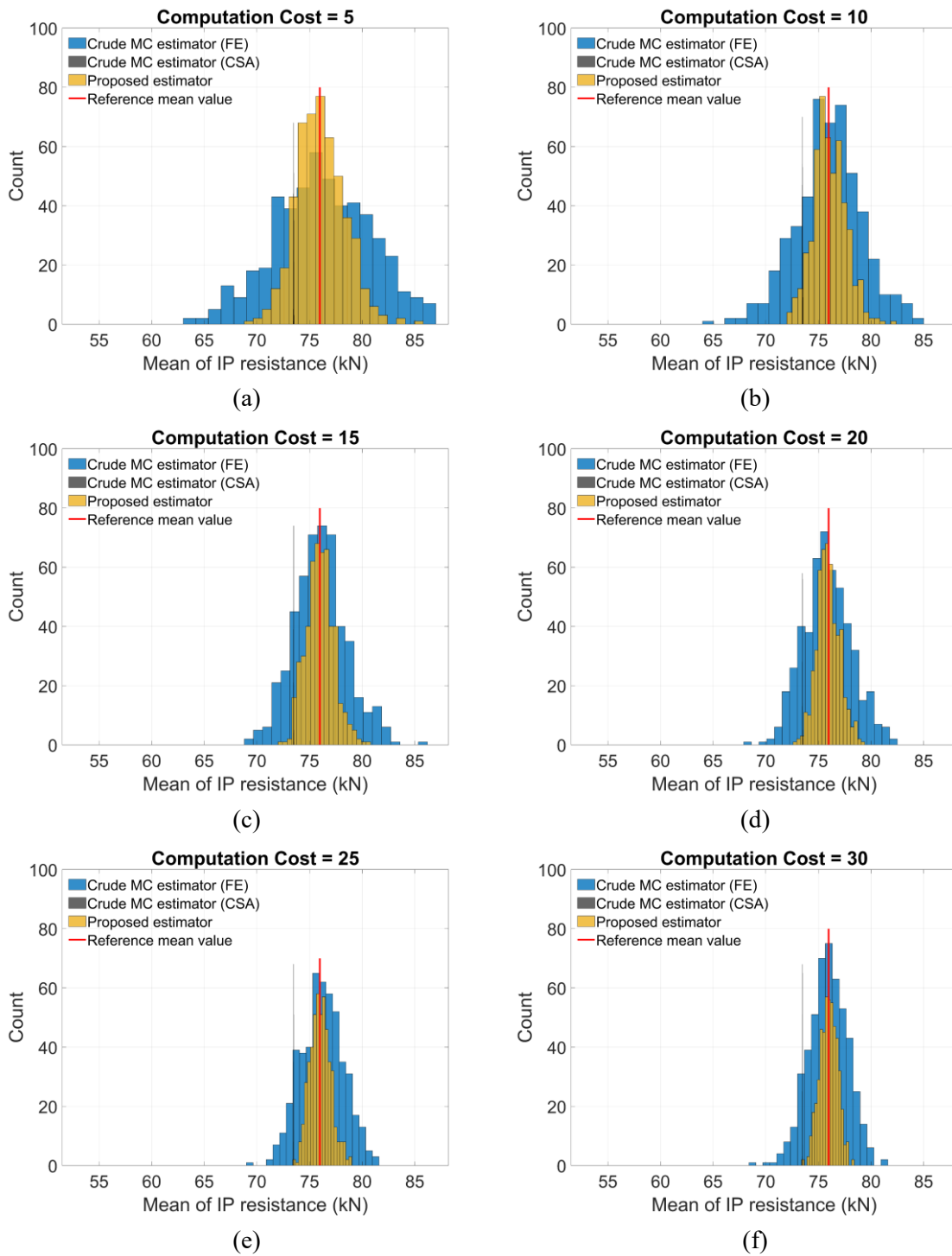


Figure 8-7. Distributions of FE model-based crude MC mean estimator and proposed mean estimator obtained by 500 replicates with different computational costs

The variance estimation is more intricate, owing to the involvement of higher-order moments in the evaluation procedure. As previously discussed, there exists two approaches to determine the model evaluation numbers (m_{FE} and m_{CSA}) and coefficient β . The first approach, also suggested in studies (Qian et al. 2018; Yao et al. 2022), employs a mean-optimal strategy. m_{FE} , m_{CSA} and β obtained following this approach are detailed in Table 8-3. On the other hand, the second approach aims to obtain these quantities by minimizing the MSE of the proposed variance estimator, i.e., Eq. (8-20), with the corresponding values for m_{FE} , m_{CSA} and β presented in Table 8-4. A comparison of Table 8-3 and Table 8-4 reveals the significant differences in m_{FE} , m_{CSA} and β . The primary reason is that in the mean-optimal strategy, more design-code model evaluations would be distributed due to their high correlation between the FE model. However, in the variance-optimal strategy, these quantities are also influenced by the higher-order moments.

Table 8-4. Model evaluation numbers (m_{FE} and m_{CSA}) and coefficient β for the variance estimation of IP resistance for the URM wall considered

Computational cost p	Proposed estimator (variance-optimal strategy)		
	m_{FE}	m_{CSA}	β
5	4	1960	0.40
10	9	4375	0.41
15	14	6832	0.41
20	19	9197	0.41
25	24	11601	0.41
30	29	14009	0.41

To facilitate the discussion, the proposed variance estimators based on the mean-optimal and variance-optimal strategies are denoted as $\hat{V}_{IM,mean}$ and $\hat{V}_{IM,var}$, respectively. Figure 8-8 presents the MSE of different variance estimators, including \hat{V}_{CSA} , \hat{V}_{FE} , $\hat{V}_{IM,mean}$ and $\hat{V}_{IM,var}$. Similarly, the

MSE of the design-code model-based estimator stabilizes around a much larger value due to its inherent bias. The estimator $\hat{V}_{IM,var}$ exhibits the lowest MSE among them. It should be noted that both $\hat{V}_{IM,mean}$ and $\hat{V}_{IM,var}$ outperform the estimator \hat{V}_{FE} , for the URM wall considered in this study. This is significant as it implies that even without optimizing the model evaluation numbers and coefficient for minimizing the MSE, the resultant variance estimators still surpass the crude MC estimator that solely relies on the FE model when the same computation budget is allocated.

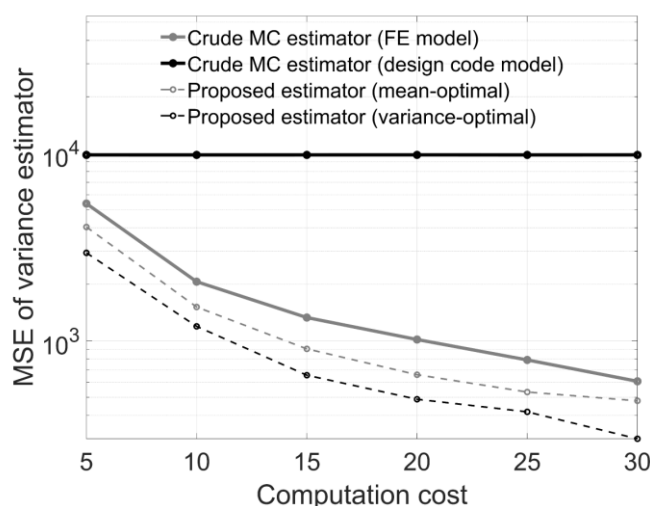
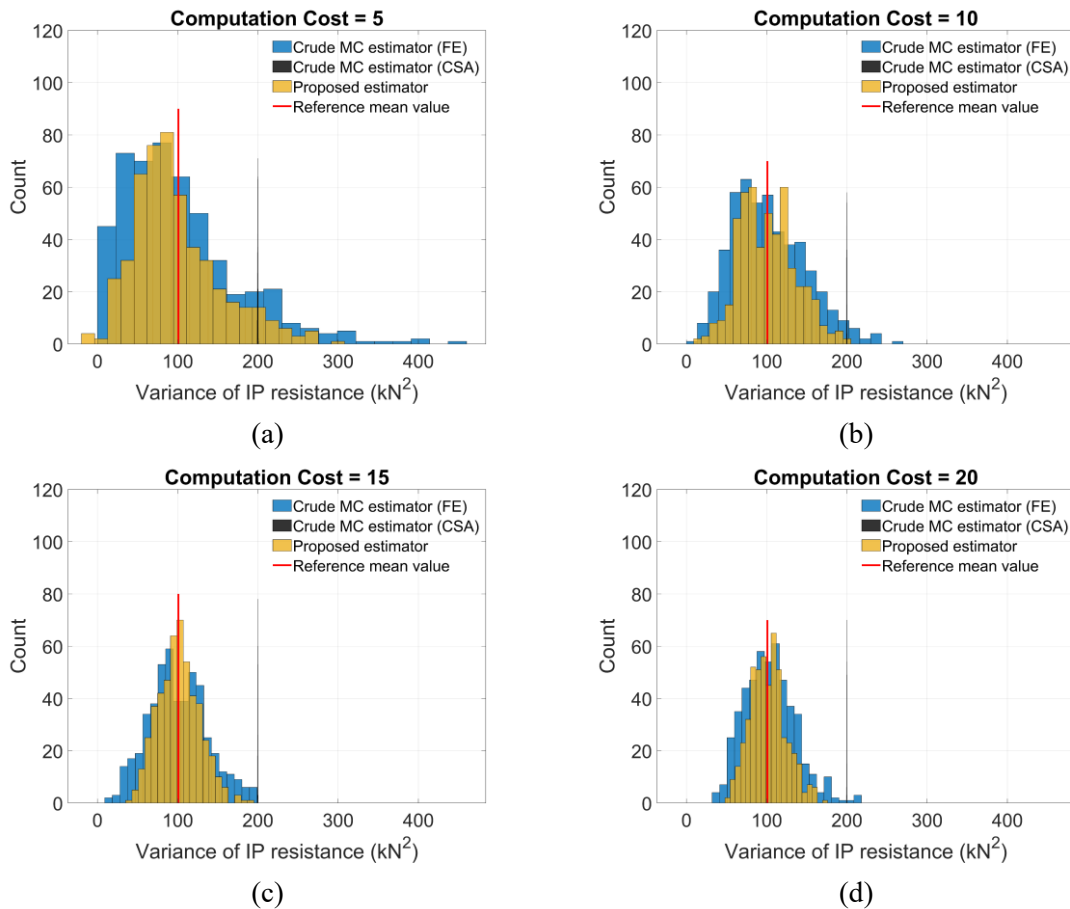


Figure 8-8. MSE of crude MC estimators, and proposed estimators (mean-optimal and variance-optimal) for the variance of IP resistance for the URM wall considered

An additional important observation from Figure 8-8 is that with the increase in the computational budget, the MSEs of estimator $\hat{V}_{IM,mean}$ and $\hat{V}_{IM,var}$ also decrease. This further confirms the “unbiasedness” of the proposed variance estimator, irrespective of the model evaluation numbers and the value of coefficient. However, it should be noted that the MSE of estimator $\hat{V}_{IM,var}$ (i.e., 300.35) achieves an approximate reduction of 50% compared to the estimator \hat{V}_{FE} (i.e., 608.47) at a computational budget of 30. This reduction is smaller than that in the mean

estimation (i.e., around 75%). This is expected, as higher-order moments are more sensitive to the pilot sample size, thus affecting the determination of model evaluation numbers and coefficient. This can also be reflected in the distribution plots shown in Figure 8-9, where a less pronounced variance reduction is observed compared to that in the mean estimation illustrated in Figure 8-7, and the design code model-based variance estimator has almost zero variance due to a large number of samples available, but involves high bias with respect to the reference value.



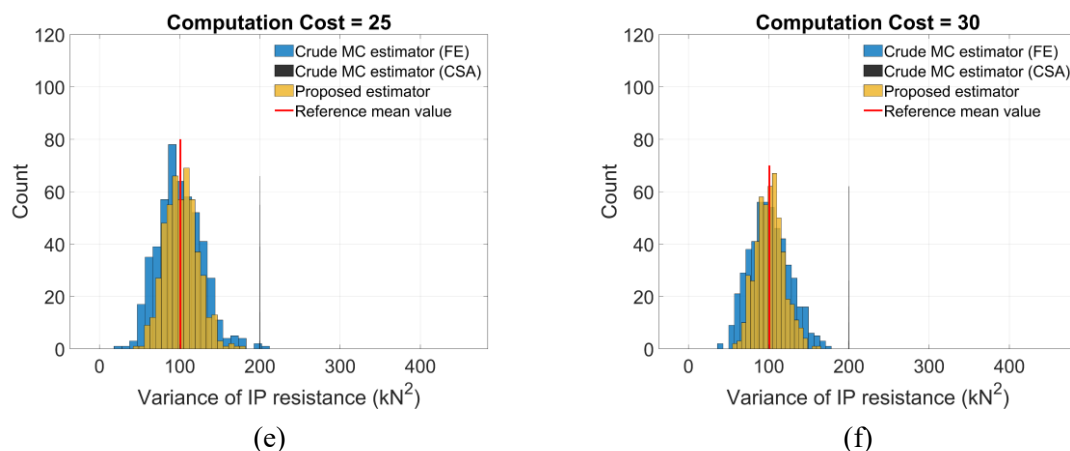


Figure 8-9. Distributions of FE model-based crude MC variance estimator and proposed variance estimator (variance-optimal) obtained by 500 replicates with different computational costs

8.5. MEAN AND VARIANCE ESTIMATORS FOR IP RESISTANCE OF RM WALLS

Variability in the material properties of masonry could result in different failure modes for the URM wall previously discussed. However, this is not the case for RM wall considered. Compared to URM walls, the failure modes of RM walls are less influenced by the material properties of masonry but more significantly by the vertical-to-horizontal reinforcement ratios (Kingsley et al. 2014a), which generally exhibits limited material variability for a RM wall compared with the material variability in masonry and is commonly considered as deterministic in uncertainty analyses (Metwally et al. 2022). To show the applicability of the proposed estimators for RM walls with different failure modes, two RM walls, one failing in diagonal tension cracking and the other in flexure rocking are considered in this section. It is worth noting that shear sliding is rarely observed in engineering practices, given sufficient frictional resistance and dowel forces, and therefore is not considered in this study.

8.5.1. Shear-governed RM wall

8.5.1.1 Wall configuration

The fully grouted RM wall tested by Seif Eldin (2016) is utilized as an example in this section. The wall was designed to fail in diagonal tension cracking and was tested in a cantilever condition with a pre-compression load of 1.0 MPa. For the subsequent analysis and discussion, this wall is denoted as ‘RM shear wall’. The RM shear wall’s dimensions were 1.8 m (length) \times 1.6 m (height) \times 0.19 m (thickness), as illustrated in Figure 8-10. The concrete masonry units conformed to the standard dimensions of 390 mm \times 190 mm \times 190 mm. The vertical reinforcements consisted of 20M bars (with a 300 mm² cross sectional area) in every cell, while the horizontal reinforcements featured uniformly distributed 10M bars (with a 100 mm² cross-sectional area) spaced at 400 mm. The corresponding horizontal and vertical reinforcement ratios were 0.13% and 0.79%, respectively.

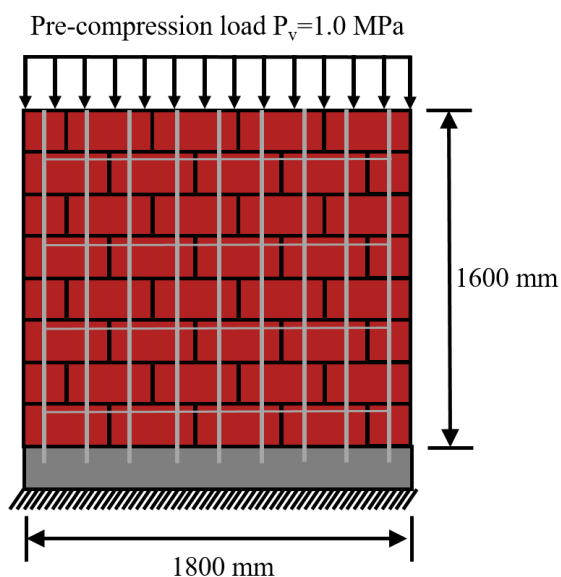


Figure 8-10. RM shear wall considered for the case study

Regarding the material parameters, six statistically independent variables are considered: tensile strength f_t , frictional coefficient $\tan\phi$ and initial dilatancy coefficient $\tan\psi_0$ of interfaces (mortar joints), compressive strength of units f_c^u , compressive strength of grouts f_c^g , and yield strength of reinforcements f_y . Other required material parameters treated as derived random variables using well-established relationships, as summarized in Table 8-5.

Table 8-5. Statistical characterization of material parameters for the RM shear wall

Parameters	Mean	Distribution	COV	Reference
Masonry Units				
Compressive strength f_c^u (MPa)	16.7	Truncated Normal ^(a)	0.048	(Seif Eldin 2016)
Tensile strength f_t^u (MPa)	1.50 ($f_t^u = 0.09f_c^u$)	Truncated Normal	0.048	(Barbosa et al. 2010)
Elastic modulus E_u (MPa)	15665 ($E_u = 938f_c^u$)	Truncated Normal	0.048	(Barbosa et al. 2010)
Grouts				
Compressive strength f_c^g (MPa)	29.4	Truncated Normal ^(a)	0.073	(Seif Eldin 2016)
Elastic modulus E_g (MPa)	14700 ($E_g = 500f_c^g$)	Truncated Normal	0.073	(TMS 2016)
Tensile strength f_t^g (MPa)	7.056 ($f_t^g = 0.24f_c^g$)	Truncated Normal	0.073	(Calderón et al. 2019)
Reinforcements				
Yield strength f_y (MPa)	430	Normal	0.032	(Seif Eldin 2016)
Elastic modulus E_y (MPa)	196080 ($E_y = 456f_y$)	Normal	0.032	(Seif Eldin 2016)
Ultimate strength f_u (MPa)	516 ($f_u = 1.2f_y$)	Normal	0.032	(Seif Eldin 2016)
Mortar joints (interfaces)				
Tensile strength f_t (MPa)	0.6	Truncated Normal ^(a)	0.095	(Seif Eldin 2016)
Mode I fracture energy G_I (N/mm)	0.0099 ($G_I = 0.01571f_t + 0.0004882$)	Truncated Normal	0.09	(Isfeld et al. 2021; Li et al. 2014)
Peak cohesion c_0 (MPa)	0.84 ($c_0 = 1.4f_t$)	Truncated Normal	0.095	(Isfeld et al. 2021; Li et al. 2014)
Frictional coefficient $\tan \psi$	0.7	Lognormal	0.1	(Canadian Standards Association 2014; Pluijm 1999)
Mode II fracture energy when the normal stress is equal to zero G_{II}^0 (N/mm)	0.099 ($G_{II}^0 = 10G_I$)	Truncated Normal	0.09	(Lotfi and Shing 1994)
Initial dilation coefficient $\tan \psi_0$	0.36	Truncated Normal ^(a)	0.25	(Pluijm 1999)
Compressive strength of masonry f_m' (MPa)	$f_m' = 18.46 \ln(f_c^u) - 37.71$	Derived	Derived	(Fortes et al. 2015)
Stiffness constants k_{nn}, k_{ss}, k_{tt} (N/mm ³)	$k_{nn} = \frac{E_u E_m}{h_m (E_u - E_m)}$; $k_{ss} = k_{tt} = \frac{k_{nn}}{2(1 + 0.15)}$	Derived	Derived	(Nazir 2015)

^(a) f_c^u , f_c^g , and f_t have a lower bound of 0.0, $\tan \psi_0$ has lower and upper bounds of 0.27 and 0.57, respectively.

8.5.1.2 Statistics estimations

Similar to the URM case, a pilot run consisting of 200 MC samples on the RM shear wall is first conducted to evaluate the model statistics. Figure 8-11 shows the empirical CDF obtained from

the FE simulations. The IP resistances range between 396.7 kN and 451.4 kN with a mean of 424.9 kN and a standard derivation of 10.87 kN, compared to the IP resistance of 418 kN experimentally reported in (Seif EIDin and Galal 2017). Figure 8-12 illustrates the comparison between the FE model and code predictions obtained from the pilot sample. The FE simulation results reconfirm that the material variability does not affect the failure mode for the RM shear wall considered in this study, i.e., all 200 walls exhibit diagonal tension cracking. Apparently, code predictions are consistently lower than those of the FE model, showing the conservatism of design provisions. This is consistent with the findings presented in (Seif EIDin et al. 2019), in which predictions from CSA S304-14 are consistently lower than the experimental results. In addition, a relatively high correlation is observed between the code and FE predictions, with a correlation coefficient of 0.9228. The average computational cost ratio w_{CSA} / w_{FE} is 0.0000022 / 1. Consequently, model evaluation numbers and coefficients can be derived through relevant optimization procedures, with the results detailed in Table 8-6. A comparative analysis of the results in Table 8-3, Table 8-4, and Table 8-6 shows that more design-code model evaluations are leveraged into the proposed estimator for the RM shear wall. This increase is attributable to the higher correlation between FE model and code predictions, along with a diminished computational cost ratio.

Table 8-6. Model evaluation numbers and coefficient for the mean and variance estimations of IP resistance for the RM shear wall

Computational cost p	Crude MC estimators		Proposed estimator (mean-optimal)			Proposed estimator (variance-optimal)		
	FE model	Design-code model	m_{FE}	m_{CSA}	α	m_{FE}	m_{CSA}	β
	m_{FE}	m_{CSA}						
5	5	1063829	4	8045	1.79	4	30098	3.22
10	10	2127659	9	16090	1.79	9	60197	3.23
15	15	3191489	14	24135	1.79	14	90296	3.23
20	20	4255318	19	32180	1.79	19	120395	3.23
25	25	5319145	24	40225	1.79	24	150494	3.23
30	30	6382974	29	48270	1.79	29	180593	3.23

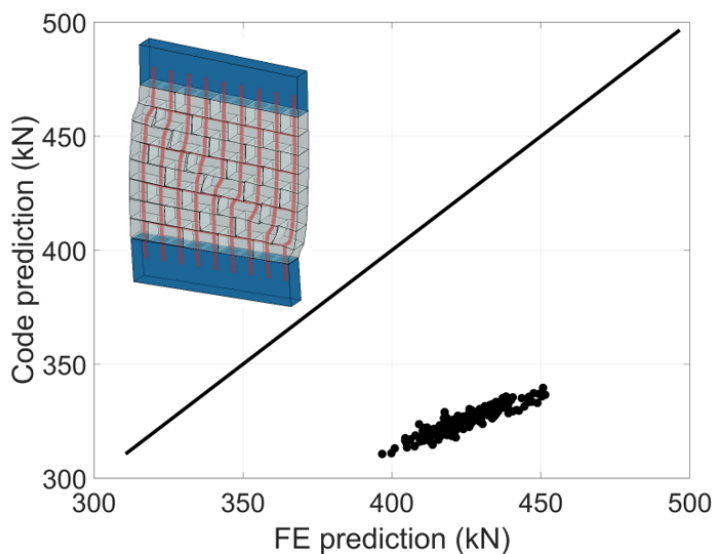


Figure 8-12. Comparison of IP resistance obtained by FE model and design-code model for the RM shear wall

To assess the performance of various estimators (i.e., $\hat{\mathbb{E}}_{CSA}$, $\hat{\mathbb{E}}_{FE}$, and $\hat{\mathbb{E}}_{IM}$ for the mean estimation, and $\hat{\mathbb{V}}_{CSA}$, $\hat{\mathbb{V}}_{FE}$, $\hat{\mathbb{V}}_{IM,mean}$ and $\hat{\mathbb{V}}_{IM,var}$ for the variance estimation), 500 replicate simulations are conducted. Figure 8-13 illustrates the MSEs of these estimators, while their distributions are shown in Figure 8-14 and Figure 8-15. It is worth mentioning that the design-code model-based estimators are excluded in Figure 8-14 and Figure 8-15 since they exhibit nearly

zero variance and involve significant bias, as can be seen in Figure 8-13. The proposed estimators demonstrate consistent decreases in MSE with increased computational cost, and exhibits lower MSE and variances compared to the other estimators examined. At a computational cost of 30, the MSEs of proposed mean and variance estimators (variance-optimal) are reduced by 85.0% and 67.5%, respectively, compared to the crude MC estimator based on the FE model.

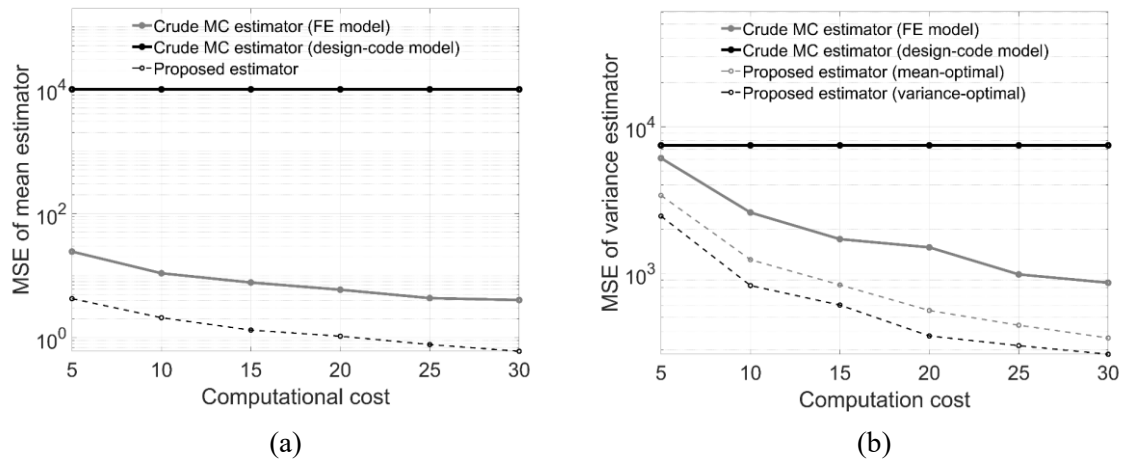


Figure 8-13. MSE of FE model-based crude MC estimator, design code-based crude MC estimator, and proposed estimator for the (a) mean, and (b) variance of IP resistance of the RM shear wall

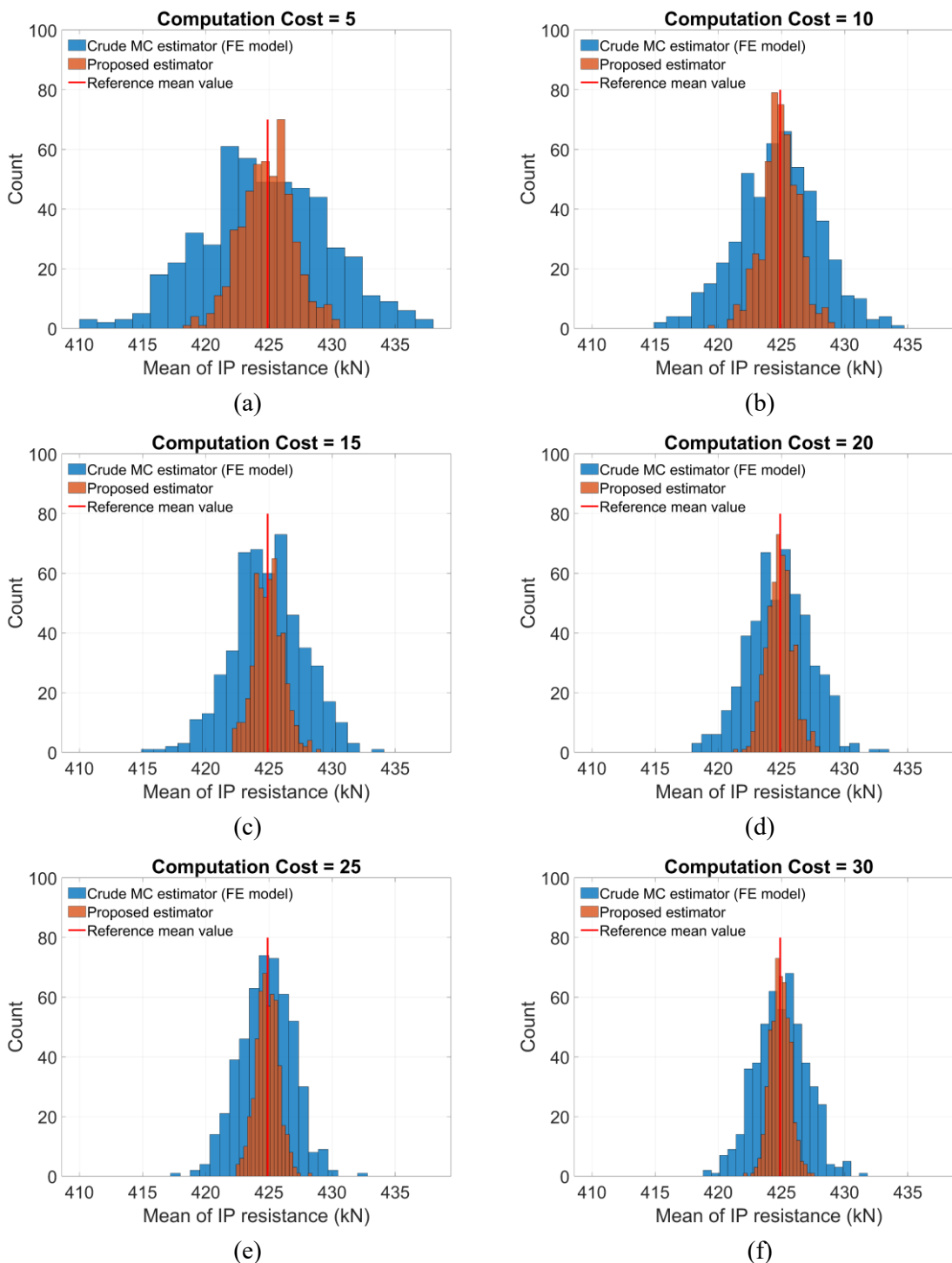


Figure 8-14. Distributions of FE model-based crude MC mean estimator and proposed mean estimator for the IP resistance of the RM shear wall obtained by 500 replicates with different computational costs

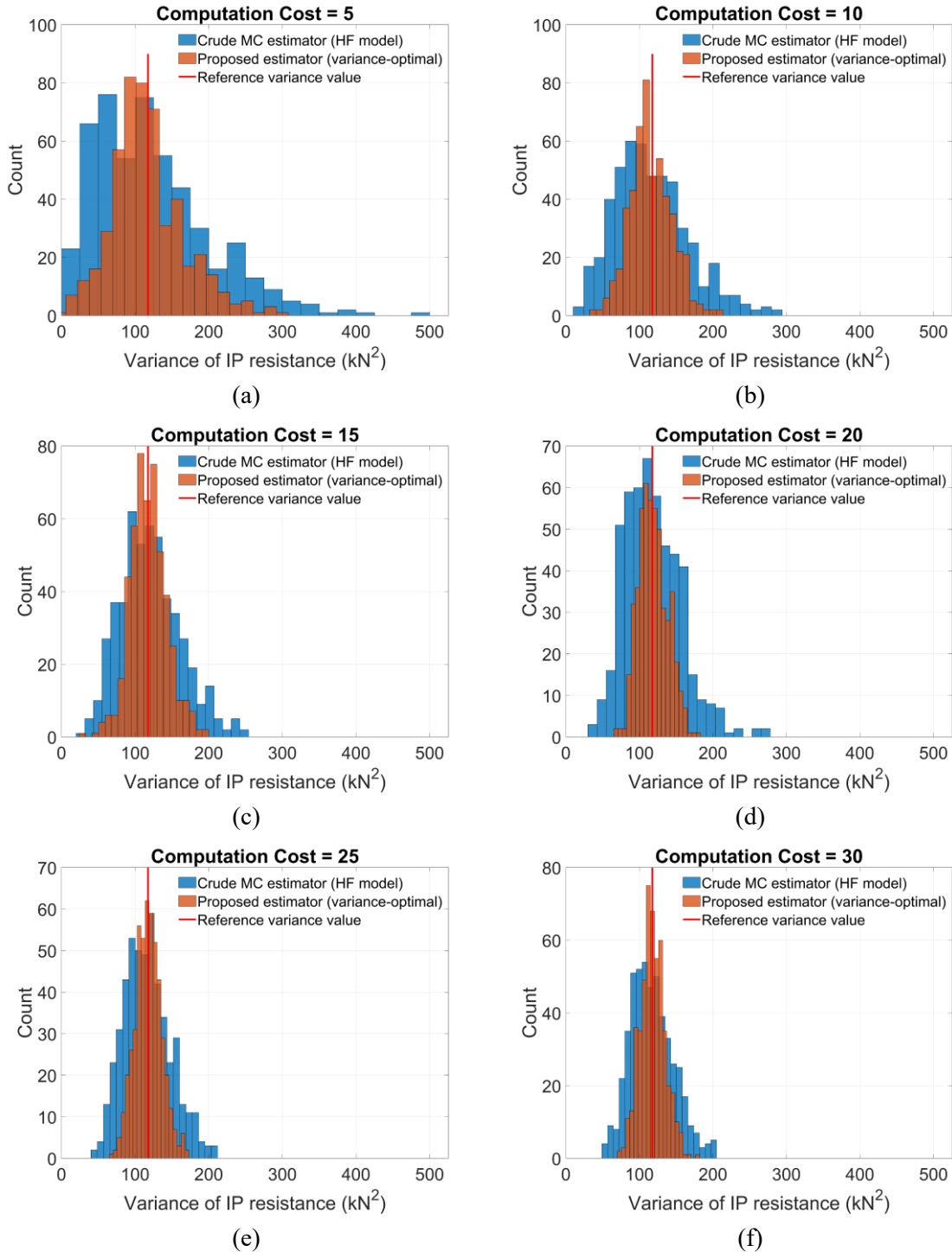


Figure 8-15. Distributions of FE model-based crude MC variance estimator and proposed variance estimator (variance-optimal) obtained by 500 replicates with different computational costs

8.5.2. Flexural-governed RM wall

8.5.2.1 Wall configuration

A flexural-governed RM wall is considered in this section. To facilitate the subsequent discussion, this wall is referred to as ‘RM flexural wall’. The RM flexural wall is designed to have the same geometry, boundary conditions, horizontal reinforcements, and material parameters as the RM shear wall, but differs in the pre-compression load and vertical reinforcements, as shown in Figure 8-16. Specifically, the RM flexural wall is considered without a pre-compression load and is vertically reinforced with three 10M bars, placed at the wall ends and mid-length location. This results in horizontal and vertical reinforcement ratios of 0.13% and 0.88%, respectively.

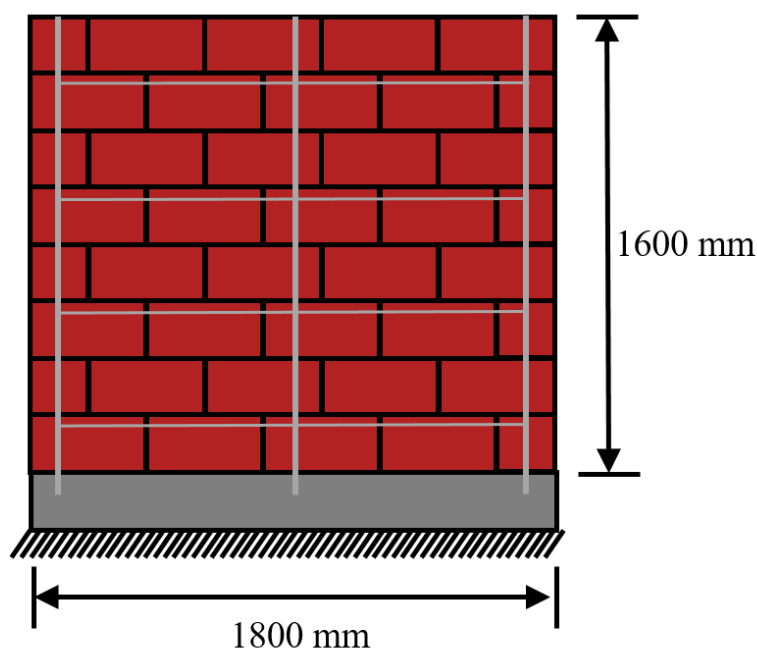


Figure 8-16. RM flexural wall considered for the case study

8.5.2.2 Statistics estimations

The empirical CDF obtained from the pilot run comprising 200 samples is shown in Figure 8-17.

It is observed that the RM flexural wall exhibits lower IP resistance than the RM shear wall. The

RM flexural wall has a mean IP resistance of 52.9 kN, and a standard deviation of 1.48 kN. On the other hand, the comparison between code and FE predictions shown in Figure 8-18 illustrates a significantly high correlation between FE and code predictions with a correlation coefficient of 0.9939. These findings suggest that the sectional analysis method suggested in CSA S304-14 (2014) provides a good representation for the RM flexural wall. As a result, more design-code models are distributed into the proposed estimators, as evidenced by the derived results presented in **Table 8-7**

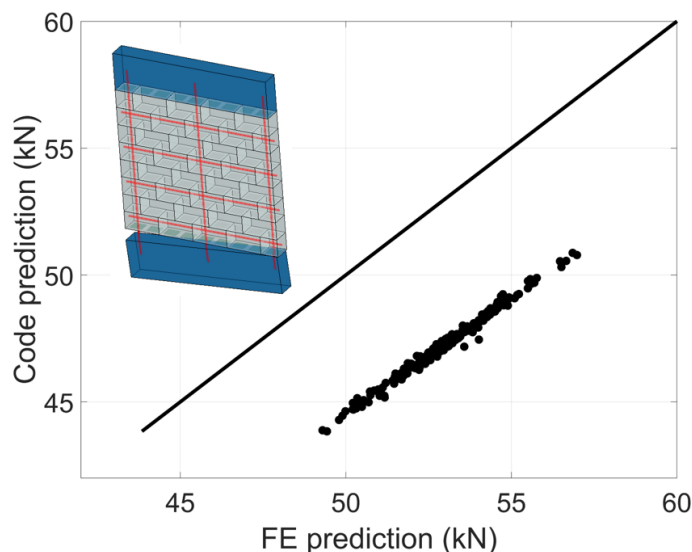


Figure 8-18. Comparison of IP resistance obtained by FE model and design-code model for the RM flexural wall considered

In addition, the design-code model appears to be consistently more conservative than the FE model, showcasing the ‘high-fidelity’ of the FE model. This is supported by various studies comparing the experimental results and code prediction regarding the flexural capacity of RM structures. For instance, Samy et al. (2012) compiled an experimental database of 173 flexural tests on RM beams and walls, and it was concluded that the mean value of experimental to predicted ratio in terms of the flexural strength is 1.13. For the 200 RM walls investigated in the

study, this ratio is calculated as $52.99 \text{ kN} / 47.26 \text{ kN} = 1.12$. This consistency reaffirms the accuracy of the FE model for the prediction of IP flexural capacity of RM walls.

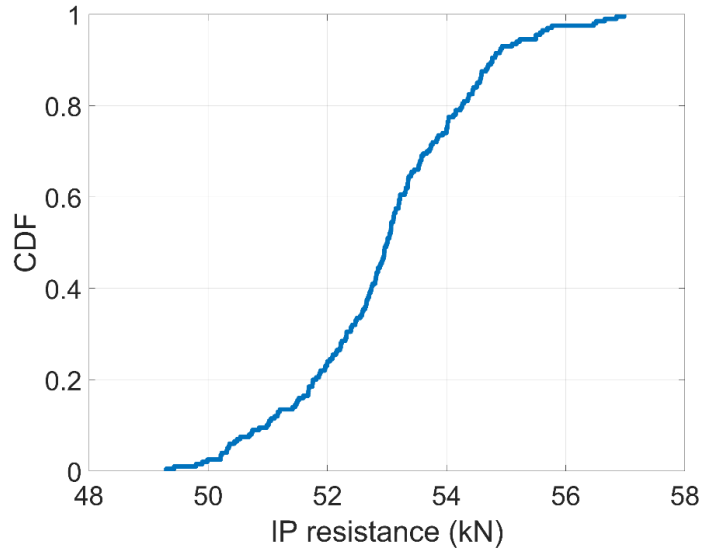


Figure 8-17. Empirical cumulative probability function of IP resistance for the RM flexural wall considered

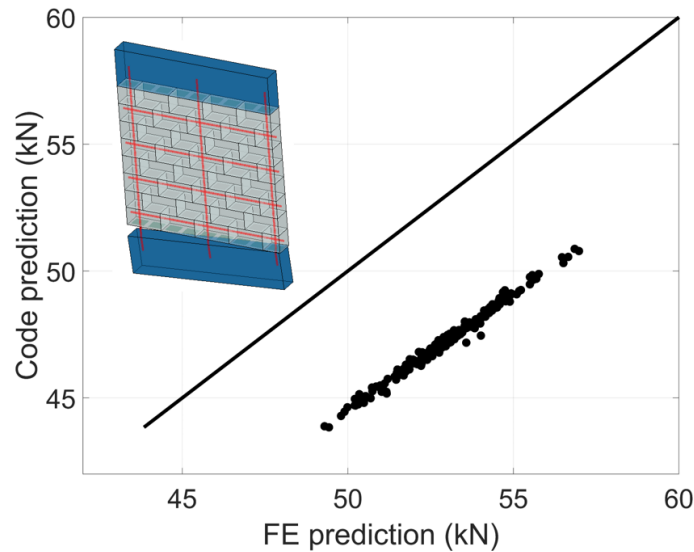


Figure 8-18. Comparison of IP resistance obtained by FE model and design-code model for the RM flexural wall considered

Table 8-7. Model evaluation numbers and coefficients for the mean and variance estimations of IP resistance for the RM flexural wall

Computational cost p	Proposed estimator (mean-optimal)			Proposed estimator (variance-optimal)		
	m_{FE}	m_{CSA}	α	m_{FE}	m_{CSA}	β
5	4	30098	1.08	4	30098	1.16
10	9	60197	1.08	9	60197	1.16
15	14	90296	1.08	14	90296	1.16
20	19	120395	1.08	19	120395	1.16
25	24	150494	1.08	240	150494	1.16
30	29	180593	1.08	29	180593	1.16

Due to the significantly high correlation between FE model and design-code model, the proposed mean and variance estimators achieve a accuracy improvement at almost 2 orders and 1 order in terms of the MSE, respectively, as shown in Figure 8-19.

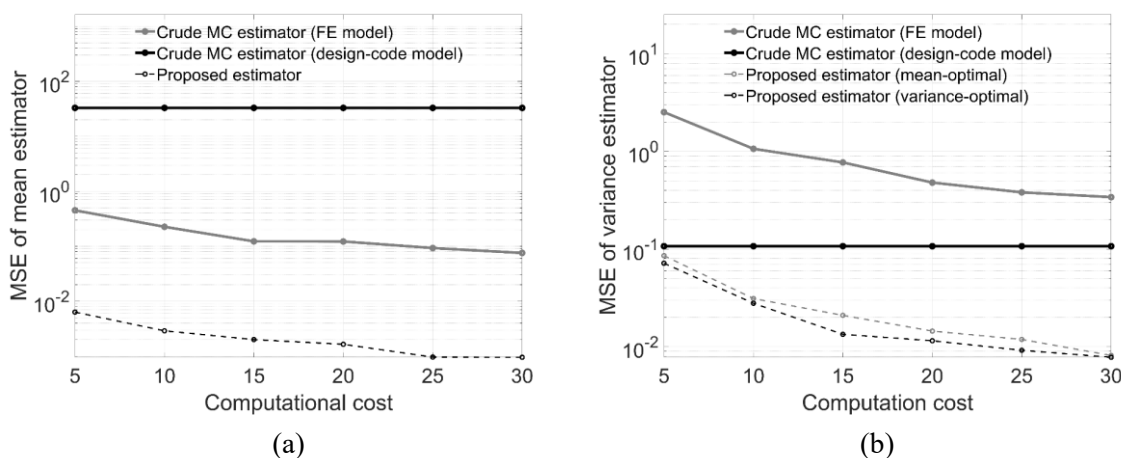


Figure 8-19. MSE of FE model-based crude MC estimator, design code-based crude MC estimator, and proposed estimator for the (a) mean, and (b) variance of IP resistance of the RM flexural wall

At a computational cost of 30, the MSEs of proposed mean and variance estimations are reduced by 98.7% and 97.7% compared to the FE-based crude MC estimators. In addition, the variance of proposed estimators is significantly lower than others, as evidenced by the distribution plots shown in Figure 8-20 and Figure 8-21, for mean and variance estimators, respectively.

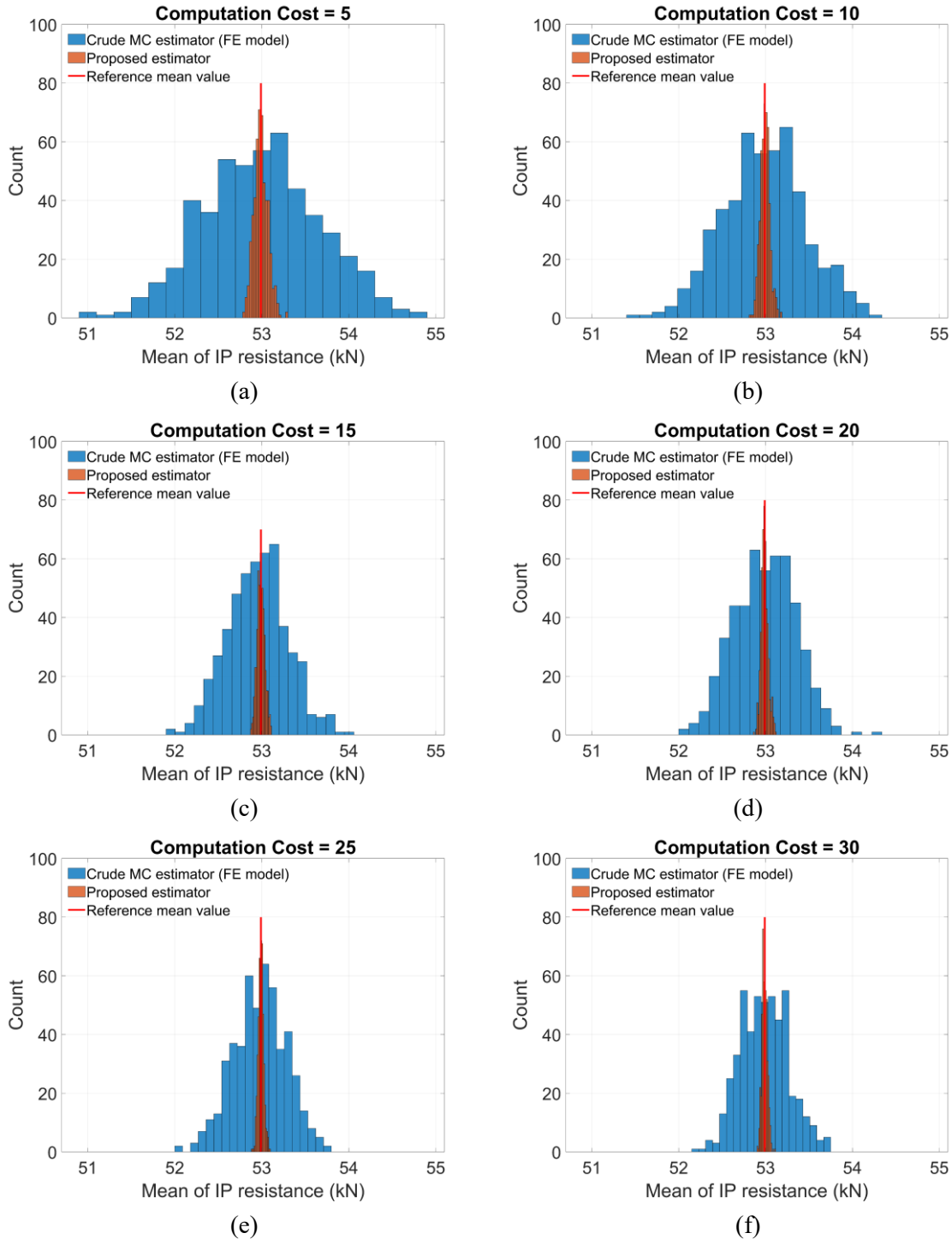


Figure 8-20. Distributions of FE model-based crude MC mean estimator and proposed mean estimator for the IP resistance of the RM flexural wall obtained by 500 replicates with different computational costs

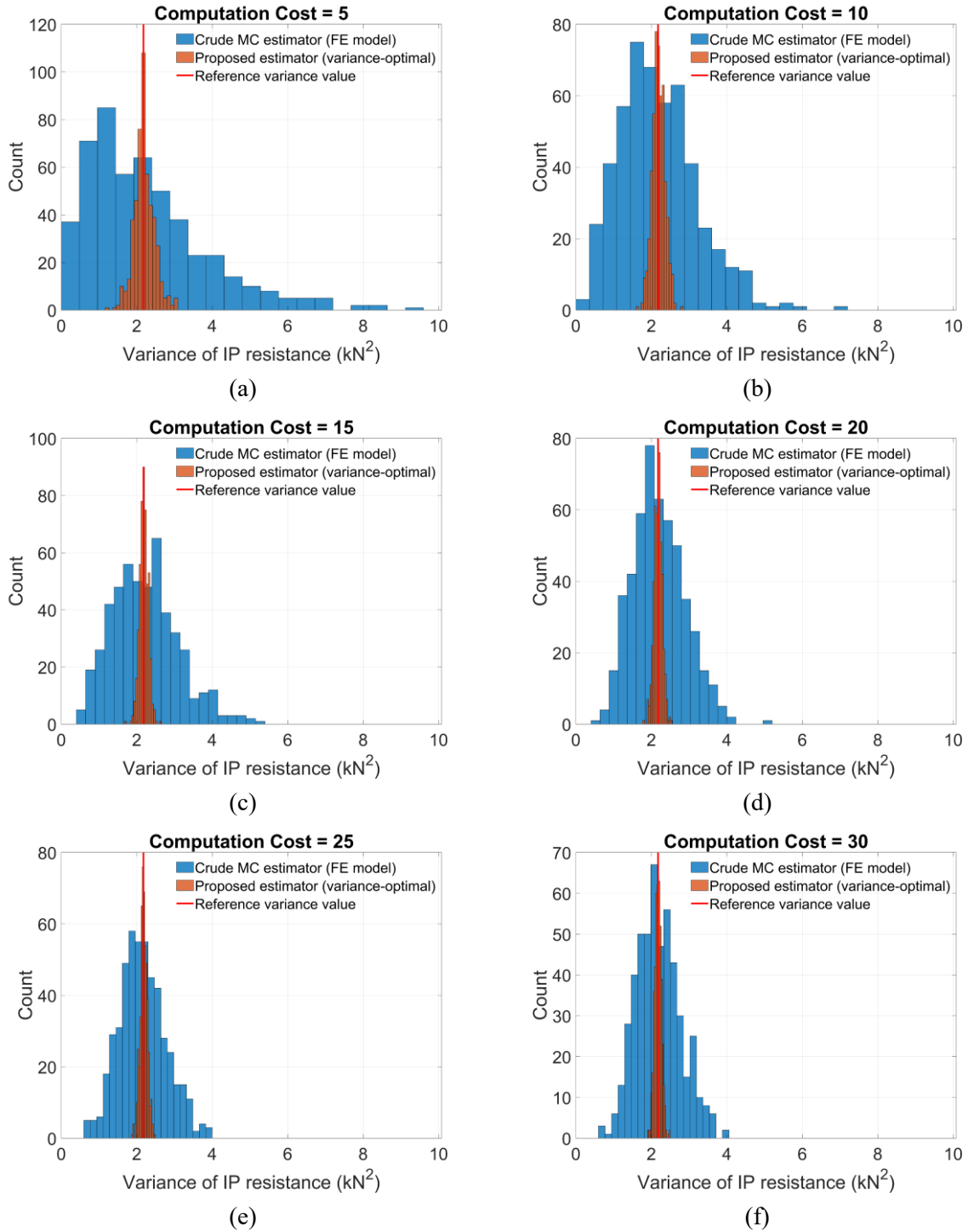


Figure 8-21. Distributions of FE model-based crude MC variance estimator and proposed variance estimator (variance-optimal) obtained by 500 replicates with different computational costs

8.6. CHAPTER CONCLUSIONS

In this chapter, an improved statistic (i.e., mean and variance) estimation for the in-plane (IP) resistance of masonry walls, including unreinforced masonry (URM) walls and reinforced masonry (RM) walls, was presented. The estimators leveraged the advantages of both finite element (FE) model and design code-based model, e.g., Canadian masonry design code CSA S304-14. Although FE model generally provided greater accuracy, they were computationally intensive. Conversely, design code-based model offered efficiency but its accuracy could be compromised by their inherent simplifications. The FE model utilized in this study was developed based on the simplified micro modeling strategy, in which individual components were explicitly represented. The detailed failure modes and associated IP resistances could be accurately captured through this approach.

The proposed estimators were formulated based on a classical variance reduction technique, specifically the control variate method (Nelson 1987, 1990). A large number of design code model evaluations were integrated in the proposed estimators to improve the computational efficiency, while only a limited number of FE model evaluations are involved to ensure the accuracy (i.e., unbiasedness). The construction of proposed statistics estimators for the IP resistance of masonry walls, including the determination of model evaluation numbers and coefficients, was detailed.

The outperformances of proposed estimators were demonstrated by comparing them to the crude Monte Carlo (MC) estimators that relied exclusively on either the FE or design-code model. The analysis results indicated that the design-code model could introduce significant biases, suggesting that relying solely on the design code-based model for uncertainty analysis is not advisable, despite their computational efficiency. The FE model-based crude MC estimator

exhibits large variances, primarily due to its high computational demands. Notably, the proposed estimations displayed the least error and variance, confirming their outperformance.

Chapter 9. STATISTICS ESTIMATION OF OUT-OF-PLANE LOAD RESISTANCE OF MASONRY WALLS USING ANALYTICAL MODELS AND MECHANICS-BASED FINITE ELEMENT MODELS

The susceptibility of masonry walls to out-of-plane (OOP) failure under seismic loading is a critical concern. Adhering to the modern limit state design philosophy, it is imperative to accurately estimate statistics such as the mean and variance of OOP resistance. To achieve this, two deterministic models are often considered within the Monte Carlo (MC) simulation framework: design-code models, known for their computational efficiency but potential for significant model error, and mechanics-based finite element (FE) models, noted for its accuracy but computational intensity. Relying solely on one model for statistical estimation presents challenges due to their respective inherent limitations. This study introduces a strategy that synergizes the strengths of both models, resulting in enhanced statistics estimators for the OOP resistance of masonry walls. The approach involves integrating numerous design-code model evaluations to boost computational efficiency, alongside a limited number of FE model evaluations to maintain accuracy by using the control variate method (Nelson 1987, 1990). Theoretical derivations confirm the accuracy of these proposed estimators in comparison to the crude MC estimator. A key benefit of these estimators is their unbiased nature; and their accuracy is not compromised by the discrepancies between the FE model and the design-code model. To demonstrate the practicality of these estimators, two case studies are illustrated: one focusing on unreinforced masonry (URM) walls and the other on reinforced masonry (RM) walls. The findings reveal that the newly proposed estimators excel in both accuracy and efficiency compared to those relying solely on the FE or design-code models.

9.1. INTRODUCTION

Out-of-plane (OOP) failure is recognized as one of the predominant failure modes of masonry walls under seismic loading, as evidenced by recent post-earthquake surveys (Graziotti et al. 2019; Moon et al. 2014; Vlachakis et al. 2020) and laboratory tests (El-Hashimy et al. 2020; Hamid et al. 1990b; Salem et al. 2019; Sparling and Palermo 2023). Accurate assessment of wall resistances against OOP loads is crucial in design practices. Nevertheless, compared to other construction materials such as steel and concrete, this is more challenging for masonry, primarily due to its heterogeneity (Ferreira et al. 2015; Zeng et al. 2021).

Current design codes largely rely on simplified analytical methods, treating masonry as a homogeneous material. For example, the Canadian masonry design code CSA S304-14 (Canadian Standards Association 2014) advocates the use of linear elastic beam bending theory for assessing the OOP resistance of vertically spanning unreinforced masonry (URM) walls. For reinforced masonry (RM) walls, OOP resistance is determined using section-level equilibrium equations. However, this approach overlooks masonry's tensile strength as well as compressive forces in reinforcing bars. While these assumptions and simplifications facilitate wide applications in industry, they may lead to overly biased predictions (Isfeld et al. 2019; Liu and Hu 2007).

The challenge of accurately assessing the OOP resistance of masonry walls is further intensified by the material's inherent variability (Sahu et al. 2019; Sherafati and Sohrabi 2016b). This variability introduces substantial uncertainties in OOP resistance evaluations, necessitating a shift from deterministic methodologies to probabilistic ones. Uncertainty analysis not only forms the basis of modern limit-state design philosophy but also aligns with the industry's embracement of next-generation probabilistic performance-based design. In this context, the evaluation of

statistical properties, such as the mean and variance of OOP resistance for masonry walls, is of utmost importance.

For this purpose, deterministic models are often utilized in conjunction with stochastic sampling approaches. One of the most widely-used methods is Monte Carlo (MC) simulation method (Metropolis and Ulam 1949) due to its non-intrusive nature and insensitivity to the curse of dimensionality. In the uncertainty analysis of masonry walls, design-code models (e.g., CSA S304-14) are frequently used for their efficiency (Hosseinzadeh and Galal 2021; Moosavi and Korany 2014). However, sole reliance on design-code models is problematic due to potential biases and inaccuracies arising from model assumptions and simplifications. It is essential to quantify model errors using high-quality experimental data prior to their applications (Metwally et al. 2022; Zhai et al. 2012). However, the availability and heterogeneity of such data from various experimental sources pose challenges.

As a complement to design-code models, advanced computational models, such as mechanics-based finite element (FE) models, have been developed to facilitate the prediction of OOP resistances of masonry walls. A representative FE models for masonry is developed based on the micro modeling approach (Lourenço et al. 1995b), in which each component of masonry (i.e., units, mortar, grouts, reinforcements) and their interactions are explicitly simulated. This modeling strategy has been thoroughly studied and validated for the prediction of OOP behavior of masonry walls (Chen et al. 2023; Zeng et al. 2021). Although it is generally perceived to be more reliable in terms of the OOP resistance prediction than design-code models (Metwally et al. 2022), a noticeable obstacle associated with FE model-based statistics estimation is the

unaffordable computational cost, particularly when numerous high-fidelity model evaluations are required.

To summarize, within the MC simulation framework, two types of deterministic models are used for estimating the statistics of OOP resistance in masonry walls: design-code models and FE models. FE models offer greater accuracy but require considerable computational resources. In contrast, design-code models are recognized for their efficiency and ease of access, though they tend to have larger model errors. To mitigate these limitations, the control variate method (Nelson 1987, 1990) was used for the statistics estimation that combined the strengths of both design-code models and FE models. This method entails integrating a limited number of expensive FE model evaluations and a large number of design-code model evaluations to enhance both precision and efficiency. The focus of this chapter is on estimating the mean and variance of OOP resistance for both URM and RM walls. This approach promises more accurate results than reliance on either model alone, offering a new pathway for advancing computational models in masonry design. The effectiveness of this methodology is demonstrated through two case studies on URM and RM walls, highlighting the superior performance of the proposed statistics estimators.

9.2. CRUDE MONTE CARLO STATISTICS ESTIMATION

This section commences with a brief introduction to the FE model and the design-code model utilized for the deterministic prediction of OOP resistance in URM and RM walls. Following this, crude MC estimators relying solely on the FE model or design-code model are presented, and then the quality measures of these estimators are discussed.

9.2.1. Finite element model

FE models for predicting OOP resistances of masonry walls are developed in the general-purpose FE package ABAQUS (Dassault Systemes 2017), adopting the simplified micro modeling approach. This approach was initially introduced for URM walls by Page (1978). For the modeling of RM walls, the simplified micro modeling approach is refined by integrating the reinforcing bars in a discrete manner. Mortar joints are simulated using the zero-thickness interface element COH3D8, in conjunction with a multi-yield surfaces constitutive model recently developed by the authors (Li and Zeng 2023). This model effectively captures various failure modes such as tensile cracking, shear sliding, and compressive crushing. Fully integration element (C3D8) is used for the modeling of concrete blocks and grouts, with their material properties described by the Concrete Damage Plasticity (CDP) model (Lee and Fenves 1998). Reinforcing bars are represented by the truss element T3D2 with the von Mises plasticity model and a bilinear hardening law. A perfect bond is assumed for grout-reinforcement and grout-concrete unit contacts. The effectiveness of this modeling strategy was validated on both small-scale masonry specimens (e.g., unit-mortar-unit assemblages) and large-scale URM and RM walls under OOP loadings (Li and Zeng 2023).

9.2.2. Design-code Model

The loading and boundary conditions for masonry walls considered in this study is a one-way vertical bending with a pin-roller boundary condition, typical for low-to-medium rising buildings. The structural behavior of masonry walls in such condition closely resembles that of a simply supported beam under transverse loading. The OOP resistances of URM and RM walls predicted by the design-code models are elaborated in Appendix E and Appendix F.

9.2.3. Mean and variance estimations based on crude MC simulation

The aforementioned FE and design-code models are integrated into the MC simulation framework for statistics estimation. Suppose that the OOP resistance of a masonry wall is denoted as $f(\mathbf{x})$, where \mathbf{x} represents a vector of random variables, such as the properties of masonry or its constituents. The probability density function associated with \mathbf{x} is denoted by $g(\mathbf{x})$. The objective of this study is to estimate mean (i.e., expectation) and variance, defined as Eq. (9-1) and Eq. (9-2), respectively:

$$\mathbb{E}[f(\mathbf{x})] = \int f(\mathbf{x}) g(\mathbf{x}) d\mathbf{x} \quad (9-1)$$

$$\mathbb{V}[f(\mathbf{x})] = \int [f(\mathbf{x}) - \mathbb{E}[f(\mathbf{x})]]^2 g(\mathbf{x}) d\mathbf{x} \quad (9-2)$$

Here, $\mathbb{E}[\cdot]$ and $\mathbb{V}[\cdot]$ represent the expectation and variance operators, respectively. The model $f(\mathbf{x})$ can be specified as either FE model $f_{FE}(\mathbf{x})$ or design-code model $f_{CSA}(\mathbf{x})$. The integrals in Eq. (9-1) and Eq. (9-2) are estimated using MC simulation. By substituting the models $f_{FE}(\mathbf{x})$ and $f_{CSA}(\mathbf{x})$, crude MC estimators are expressed in Eqs. (9-3)(9-4)(9-5)(9-6):

$$\hat{\mathbb{E}}_{FE} = \frac{1}{m_{FE}} \sum_{i=1}^{m_{FE}} f_{FE}(\mathbf{x}_i) \quad (9-3)$$

$$\hat{\mathbb{V}}_{FE} = \frac{1}{m_{FE} - 1} \sum_{i=1}^{m_{FE}} (f_{FE}(\mathbf{x}_i) - \hat{\mathbb{E}}_{FE})^2 \quad (9-4)$$

$$\hat{\mathbb{E}}_{CSA} = \frac{1}{m_{CSA}} \sum_{i=1}^{m_{CSA}} f_{CSA}(\mathbf{x}_i) \quad (9-5)$$

$$\hat{V}_{\text{CSA}} = \frac{1}{m_{\text{CSA}} - 1} \sum_{i=1}^{m_{\text{CSA}}} \left(f_{\text{CSA}}(\mathbf{x}_i) - \hat{\mathbb{E}}_{\text{CSA}} \right)^2 \quad (9-6)$$

where $\hat{\mathbb{E}}_{\text{FE}}$ and \hat{V}_{FE} are the crude MC estimator for the mean and variance based on the FE model; $\hat{\mathbb{E}}_{\text{CSA}}$ and \hat{V}_{CSA} are the estimators relying on the design-code model; \mathbf{x}_i ($i = 1, 2, \dots, m_{\text{CSA}}$ or m_{FE}) are independent identically distributed samples drawn from $g(\mathbf{x})$, with m_{FE} and m_{CSA} representing sample sizes, i.e., mode evaluation numbers of FE model and design-code model, respectively.

9.2.4. Quality measure of Monte Carlo estimators

The quality of MC estimators is evaluated by the mean square error (MSE) relative to the true value. In this study, the true values of expectation and variance are assumed to be derived by the high-fidelity FE model, i.e., $\mathbb{E}[f_{\text{FE}}(\mathbf{x})]$ and $\mathbb{V}[f_{\text{FE}}(\mathbf{x})]$, considering that true values are typically unavailable. Therefore, MSEs of $\hat{\mathbb{E}}_{\text{FE}}$ and \hat{V}_{FE} are equal to their variances, as shown in Eq. (9-7) and Eq. (9-8), respectively:

$$\text{MSE}(\hat{\mathbb{E}}_{\text{FE}}) = \mathbb{V}[\hat{\mathbb{E}}_{\text{FE}}] = \mathbb{E} \left[\left(\mathbb{E}[f_{\text{FE}}(\mathbf{x})] - \hat{\mathbb{E}}_{\text{FE}} \right)^2 \right] = \frac{\mathbb{V}[f_{\text{FE}}(\mathbf{x})]}{m_{\text{FE}}} \quad (9-7)$$

$$\text{MSE}(\hat{V}_{\text{FE}}) = \mathbb{V}[\hat{V}_{\text{FE}}] = \mathbb{E} \left[\left(\mathbb{V}[f_{\text{FE}}(\mathbf{x})] - \hat{V}_{\text{FE}} \right)^2 \right] = \frac{1}{m_{\text{FE}}} \left[\mu_4[f_{\text{FE}}(\mathbf{x})] - \frac{m_{\text{FE}} - 3}{m_{\text{FE}} - 1} \mathbb{V}[f_{\text{FE}}(\mathbf{x})]^2 \right] \quad (9-8)$$

It should be noted that the crude MC estimators $\hat{\mathbb{E}}_{\text{FE}}$ and \hat{V}_{FE} are unbiased with respect to the true values: $\mathbb{E}[\hat{\mathbb{E}}_{\text{FE}}] = \mathbb{E}[f_{\text{FE}}(\mathbf{x})]$ and $\mathbb{E}[\hat{V}_{\text{FE}}] = \mathbb{V}[f_{\text{FE}}(\mathbf{x})]$. In Eq. (9-8), $\mu_4[f_{\text{FE}}(\mathbf{x})]$ is the fourth central moment of $f_{\text{FE}}(\mathbf{x})$. It can be observed from Eq. (9-7) and Eq. (9-8) that a large

value of m_{FE} is required to achieve reasonable accuracy for $\mathbb{E}[f_{FE}(\mathbf{x})]$ and $\mathbb{V}[f_{FE}(\mathbf{x})]$. However, this is generally impractical since the evaluation of FE models is expensive. Conversely, design-code model-based estimators $\hat{\mathbb{E}}_{CSA}$ and $\hat{\mathbb{V}}_{CSA}$ heavily rely on the relative bias $|f_{CSA}(\mathbf{x}) - f_{FE}(\mathbf{x})|$, as will be demonstrated in the subsequent case studies.

9.3. IMPROVED MEAN AND VARIANCE ESTIMATORS

The underlying principle of the proposed estimators is the control variate (CV) method, a classical variance reduction technique in statistics (Nelson 1987). The proposed estimators leverage the estimations from a very limited number of FE evaluations for enhanced accuracy and a large number of design code evaluations (i.e., $m_{CSA} \gg m_{FE}$) to improve the efficiency. In other words, design-code model serves as a control variate of FE model. The improved estimators for mean and variance for the OOP resistance of masonry walls are described as follows.

9.3.1. Mean estimator

The proposed mean estimator for the OOP resistance of masonry walls, denoted as $\hat{\mathbb{E}}_{IM}$, is formulated as per Eq. (9-9) based on the control variate method (Nelson 1987, 1990):

$$\hat{\mathbb{E}}_{IM} = \frac{1}{m_{FE}} \sum_{i=1}^{m_{FE}} f_{FE}(\mathbf{x}_i) + \alpha \left(\frac{1}{m_{CSA}} \sum_{i=1}^{m_{CSA}} f_{CSA}(\mathbf{x}'_i) - \frac{1}{m_{FE}} \sum_{i=1}^{m_{FE}} f_{CSA}(\mathbf{x}''_i) \right) \quad (9-9)$$

Here, α is a coefficient that weights the differences of the MC estimates obtained from design-code model with different sample sizes; the samples \mathbf{x}_i , \mathbf{x}' , and \mathbf{x}'' are independently and randomly generated. It can be seen that the formulation of $\hat{\mathbb{E}}_{IM}$ integrates both design-code and FE models: the first term on the right-hand side (RHS) relates to the FE estimation, and the latter two terms are based on the design-code predictions. A significant advantage of the proposed mean

estimator is its unbiasedness with respect to $\mathbb{E}[f_{FE}(\mathbf{x})]$, even though the design-code model is integrated:

$$\mathbb{E}[\hat{\mathbb{E}}_{IM}] = \mathbb{E}[f_{HF}(\mathbf{x})] \quad (9-10)$$

Eq. (9-10) can be readily justified by the linearity of expectation. This characteristic of unbiasedness offers a distinct advantage over the design-code model-based estimator due to its nature as an approximation. As such, MSE of $\hat{\mathbb{E}}_{IM}$ with respect to the true value is equal to its variance, as shown in Eq. (9-11):

$$\text{MSE}(\hat{\mathbb{E}}_{IM}) = \frac{\mathbb{V}[f_{FE}(\mathbf{x})]}{m_{FE}} + \left(\frac{1}{m_{FE}} - \frac{1}{m_{CSA}} \right) \left(\alpha^2 \mathbb{V}[f_{CSA}(\mathbf{x})] - 2\alpha\rho\sqrt{\mathbb{V}[f_{FE}(\mathbf{x})]\mathbb{V}[f_{CSA}(\mathbf{x})]} \right) \quad (9-11)$$

Here, ρ is the Pearson correlation coefficient between the FE model and design-code model. Based on Eq. (9-11), it can be observed that $\text{MSE}(\hat{\mathbb{E}}_{IM})$ is highly dependent on the three factors: model evaluation numbers m_{FE} and m_{CSA} , and the coefficients α . They are determined by minimizing $\text{MSE}(\hat{\mathbb{E}}_{IM})$ given a specific computational cost. By assigning the computational costs of one single FE and design-code evaluations as ω_{HF} and ω_{LF} , respectively, and available computational budget as p , the following optimization problem is formulated:

$$\begin{aligned} & \arg \min_{m_{FE}, m_{CSA}, \alpha} \text{MSE}(\hat{\mathbb{E}}_{IM}) \\ & \text{subject to } m_{FE}\omega_{FE} + m_{CSA}\omega_{CSA} \leq p \end{aligned} \quad (9-12)$$

In this study, the close-form solution for the aforementioned optimization problem derived by Peherstorfer et al. (2016b) is used, as shown in Eqs. (9-13)(9-14)(9-15):

$$\alpha = \rho \sqrt{\frac{\mathbb{V}[f_{FE}(\mathbf{x})]}{\mathbb{V}[f_{CSA}(\mathbf{x})]}} \quad (9-13)$$

$$m_{FE} = \frac{p}{w_{FE} + w_{CSA}r_{CSA}} \quad (9-14)$$

$$m_{CSA} = m_{FE}r_{CSA} \quad (9-15)$$

where $r_{CSA} = \sqrt{\frac{w_{FE}\rho^2}{w_{CSA}(1-\rho^2)}}$; ρ is the Pearson correlation coefficient ρ between the FE

model and design-code model, which is expressed in Eq. (9-16):

$$\rho = \frac{\text{Cov}[f_{FE}(\mathbf{x}), f_{CSA}(\mathbf{x})]}{\sqrt{\mathbb{V}[f_{FE}(\mathbf{x})]\mathbb{V}[f_{CSA}(\mathbf{x})]}} \quad (9-16)$$

where $\text{Cov}[\cdot]$ is the covariance operator. Given a dataset with sample size N , Pearson correlation coefficient estimate $\hat{\rho}$ is calculated as Eq. (9-17):

$$\hat{\rho} = \frac{\sum_{i=1}^N [f_{FE}(\mathbf{x}_i) - \overline{f_{FE}(\mathbf{x})}] [f_{CSA}(\mathbf{x}_i) - \overline{f_{CSA}(\mathbf{x})}]}{\sqrt{\sum_{i=1}^N [f_{FE}(\mathbf{x}_i) - \overline{f_{FE}(\mathbf{x})}]^2} \sqrt{\sum_{i=1}^N [f_{CSA}(\mathbf{x}_i) - \overline{f_{CSA}(\mathbf{x})}]^2}} \quad (9-17)$$

Here, $\overline{f_{FE}(\mathbf{x})}$ and $\overline{f_{CSA}(\mathbf{x})}$ are the sample mean: $\overline{f_{FE}(\mathbf{x})} = \sum_{i=1}^N f_{FE}(\mathbf{x}_i)$ and $\overline{f_{CSA}(\mathbf{x})} = \sum_{i=1}^N f_{CSA}(\mathbf{x}_i)$.

By incorporating Eqs. (9-13)(9-14)(9-15) into Eq. (9-11), the MSE of proposed mean estimator $\hat{\mathbb{E}}_{IM}$ can be updated. The performance of $\hat{\mathbb{E}}_{IM}$ relative to the crude FE model-based

estimator is derived through the comparison of MSE ratio e : $e = \text{MSE}(\hat{\mathbb{E}}_{\text{IM}}) / \text{MSE}(\hat{\mathbb{E}}_{\text{FE}})$. In this context, by assuming the identical computational cost p , the FE model evaluation number in the FE model-based estimator is p / w_{FE} . Thus, the ratio e can be derived as Eq. (9-18):

$$e = \frac{\text{MSE}(\hat{\mathbb{E}}_{\text{IM}})}{\text{MSE}(\hat{\mathbb{E}}_{\text{FE}})} = \left(\sqrt{(1 - \rho^2)} + \sqrt{\frac{w_{\text{CSA}} \rho^2}{w_{\text{FE}}}} \right)^2 \quad (9-18)$$

Eq. (9-18) quantifies the MSE reduction achieved by the proposed estimator for a given computational cost compared to $\hat{\mathbb{E}}_{\text{FE}}$. Notably, this ratio only depends on the square of Pearson correlation coefficient ρ^2 and the computational cost ratio $w_{\text{CSA}} / w_{\text{FE}}$. Conversely, it remains unaffected by the discrepancy between the FE and design-code predictions (i.e., $|f_{\text{FE}}(\mathbf{x}_i) - f_{\text{CSA}}(\mathbf{x}_i)|$) and the computational budget p . As $w_{\text{CSA}} / w_{\text{FE}}$ decreases, a greater MSE reduction is realized. Moreover, as the squared correlation coefficient ρ^2 increases, the ratio in Eq. (9-18) becomes smaller if design-code model is significantly more computationally efficient than the FE model, i.e., $\frac{w_{\text{LF}} \rho^2}{w_{\text{HF}}} \ll (1 - \rho^2)$, while is indeed the case considered in this study.

9.3.2. Variance estimator

The proposed variance estimator $\hat{\mathbb{V}}_{\text{IM}}$ is formulated analogously to the mean estimator as detailed in Eq. (9-19) based on the control variate method (Nelson 1987, 1990):

$$\hat{\mathbb{V}}_{\text{IM}} = \frac{1}{m_{\text{FE}} - 1} \sum_{i=1}^{m_{\text{HF}}} \left[f_{\text{FE}}(\mathbf{x}_i) - \frac{1}{m_{\text{FE}}} \sum_{i=1}^{m_{\text{FE}}} f_{\text{FE}}(\mathbf{x}_i) \right]^2 + \beta \left[\frac{1}{m_{\text{CSA}} - 1} \sum_{i=1}^{m_{\text{CSA}}} \left(f_{\text{CSA}}(\mathbf{x}'_i) - \frac{1}{m_{\text{CSA}}} \sum_{i=1}^{m_{\text{CSA}}} f_{\text{CSA}}(\mathbf{x}'_i) \right)^2 - \frac{1}{m_{\text{FE}} - 1} \sum_{i=1}^{m_{\text{FE}}} \left(f_{\text{CSA}}(\mathbf{x}''_i) - \frac{1}{m_{\text{FE}}} \sum_{i=1}^{m_{\text{FE}}} f_{\text{CSA}}(\mathbf{x}''_i) \right)^2 \right] \quad (9-19)$$

where β is a coefficient. Note that \hat{V}_{IM} is also unbiased relative to $\mathbb{V}[f_{FE}(\mathbf{x})]$, i.e., $\mathbb{E}[\hat{V}_{IM}] = \mathbb{V}[f_{FE}(\mathbf{x})]$. Consequently, the MSE of \hat{V}_{IM} is equal to its variance $\mathbb{V}[\hat{V}_{IM}]$. The variance of a sum of random variables is computed by summing the variances of each variable and twice the sum of their pairwise covariances. Accordingly, the MSE of \hat{V}_{IM} with respect to the true value $\mathbb{V}[f_{FE}(\mathbf{x})]$ can be shown in Eq. (9-20):

$$\begin{aligned} \text{MSE}[\hat{V}_{IM}] = & \frac{1}{m_{HF}} \left(\mu_4[f_{FE}(\mathbf{x})] - \frac{m_{FE}-3}{m_{FE}-1} \mathbb{V}[f_{FE}(\mathbf{x})]^2 \right) \\ & + \beta^2 \left(\frac{1}{m_{CSA}} \left(\mu_4[f_{CSA}(\mathbf{x})] - \frac{m_{FE}-3}{m_{FE}-1} \mathbb{V}[f_{CSA}(\mathbf{x})]^2 \right) - \frac{1}{m_{CSA}} \left(\mu_4[f_{CSA}(\mathbf{x})] - \frac{m_{CSA}-3}{m_{CSA}-1} \mathbb{V}[f_{CSA}(\mathbf{x})]^2 \right) \right) \\ & + 2\beta \left(\frac{1}{m_{CSA}} \left(\text{Cov}[\mathbb{V}[f_{CSA}(\mathbf{x})], \mathbb{V}[f_{CSA}(\mathbf{x})]] + \frac{2}{m_{CSA}-1} (\text{Cov}[f_{FE}(\mathbf{x}), f_{CSA}(\mathbf{x})])^2 \right) \right. \\ & \left. - \frac{1}{m_{FE}} \left(\text{Cov}[\mathbb{V}[f_{CSA}(\mathbf{x})], \mathbb{V}[f_{CSA}(\mathbf{x})]] + \frac{2}{m_{FE}-1} (\text{Cov}[f_{FE}(\mathbf{x}), f_{CSA}(\mathbf{x})])^2 \right) \right) \end{aligned} \quad (9-20)$$

The effectiveness of the proposed variance estimator can be deduced by comparing $\text{MSE}[\hat{V}_{IM}]$ and Eq. (9-8). Regarding the determination of model evaluation numbers m_{FE} and m_{CSA} , and coefficient β , the first approach assumes that these quantities be assumed to be identical to those in the mean-optimal model management scheme, as referenced in Eqs. (9-13)(9-14)(9-15). The second approach is to determine these quantities by minimizing $\text{MSE}[\hat{V}_{IM}]$ with a given computational budget p within a numerical optimization procedure, as shown in Eq. (9-21). In this study, these two schemes are used and compared based on the estimation results for the study cases considered later.

$$\begin{aligned} & \arg \min_{m_{FE}, m_{CSA}, \beta} \text{MSE}(\hat{V}_{IM}) \\ & \text{subject to } m_{FE} \omega_{FE} + m_{CSA} \omega_{CSA} \leq p \end{aligned} \quad (9-21)$$

9.4. MEAN AND VARIANCE ESTIMATION OF OOP RESISTANCE OF MASONRY WALLS

This section integrates the previously introduced design-code and FE models into the proposed estimators for predicting the OOP resistances of masonry walls. The effectiveness of these proposed estimators is demonstrated through two case studies: one focusing on a URM wall and the other on an RM wall. For the purpose of comparison, three types of estimators are compared: estimators based exclusively on the design-code model (\hat{E}_{CSA} , \hat{V}_{CSA}), estimators relying solely on the FE model (\hat{E}_{FE} , \hat{V}_{FE}), and the newly proposed estimators (\hat{E}_{IM} , \hat{V}_{IM}). This comparative analysis aims to ascertain the relative accuracy and efficacy of each estimator in predicting the mean and variance OOP resistances, providing valuable insights into their practical applications.

9.4.1. Case study: URM wall

9.4.1.1 Wall configuration and material uncertainties

The URM wall considered in this study was experimentally investigated by Raijmakers (1992). It was constructed using solid clay bricks (210 mm × 52 mm × 100 mm) and 10 mm-thick mortar layers. The wall was 1000 mm high, 990 mm long, and 100 mm thick, as shown in Figure 9-1. The wall was subjected to a pre-compression load of 1.2 MPa. It should be noted that this URM wall was tested in the IP loading scenario. However, it was selected in this study due to its well documented material parameter and corresponding statistical information.

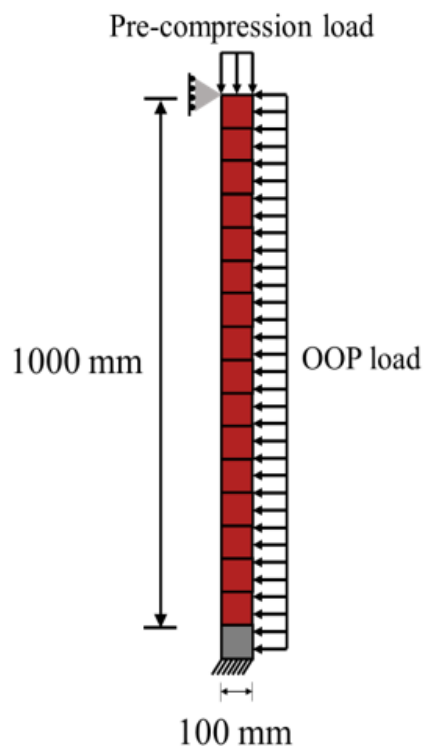


Figure 9-1. URM wall considered for the case study

In the analysis of the URM wall, four statistically independent variables are considered: compressive strength of brick units f_u^c , tensile strength f_t , frictional coefficient $\tan \phi$ and initial dilatancy coefficient $\tan \psi_0$ of interfaces (mortar joints). The mean values of these parameters are assumed to be those reported by Raijmakers (1992). The probability distributions and coefficient of variations (COVs) for these variables are established based on either field tests (Li et al. 2014) or laboratory tests (Pluijm 1999). Other variables are determined based on the deterministic empirical relationships as prescribed in public literature, as shown in Table 8-1.

9.4.1.2 Statistics estimation

To construct the proposed estimator as specified in Eq. (9-9) and Eq. (9-19), it is necessary to determine specific model evaluation numbers m_{FE} and m_{CSA} and the coefficients (α and β for mean and variance estimators, respectively). Optimally defining these quantities involves the calculation of model statistics, such as variance and the fourth central moment, along with the Pearson correlation coefficient. A pilot run on 200 MC samples is performed for this purpose.

Empirical cumulative probability function (CDF) of OOP resistance for the studied URM wall obtained by the pilot run is depicted in Figure 9-2, in which a representative deformed shape of a URM wall under OOP loading is also included. In such scenarios, the moments developed along the wall section would lead to crack opening at the base section and approximately mid-height position. The flexural stresses normal to the bed joints eventually result in tensile failure (e.g., cracking opening) when cracks occur along a course of bed joints. The analysis of the 200 URM walls in the pilot run reveals OOP resistances ranging between 63.09 kPa and 72.35 kPa, with a mean of 67.55 kPa and a sample standard deviation of 1.74 kPa.

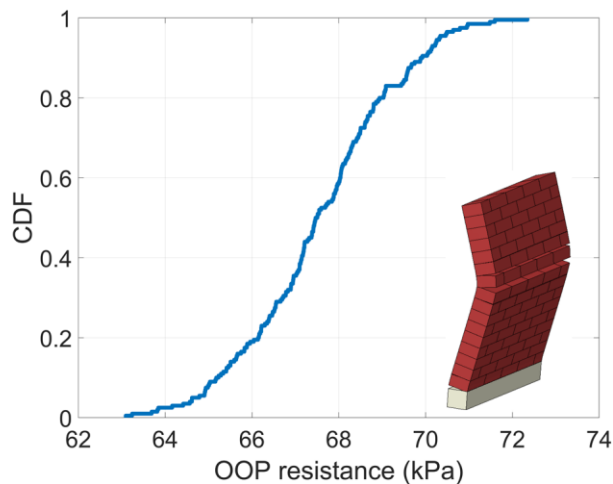


Figure 9-2. Empirical cumulative probability functions of OOP resistances for the URM wall considered

Figure 9-3 presents a comparison of the OOP resistance between the design-code and FE predictions obtained from the pilot sample. It is evident that the design-code model tends to significantly underestimate the OOP resistances compared to the FE predictions. For the same 200 URM walls considered, the design-code predictions showed a mean OOP resistance of 23.08 kPa and a standard deviation of 0.81 kPa, respectively. This tendency of underestimation is anticipated. For URM walls under OOP load and pre-compression load, after the cracking of the base, the counteracting moment due to eccentricity of the base reaction further increases the lateral load that must be applied to cause cracking near mid-height. The design approach inherently incorporates the assumption of zero eccentricity of the reaction at the base and, thus, ignores the significant increase in OOP capacity due to counteracting moment (Drysdale and Hamid 2005).

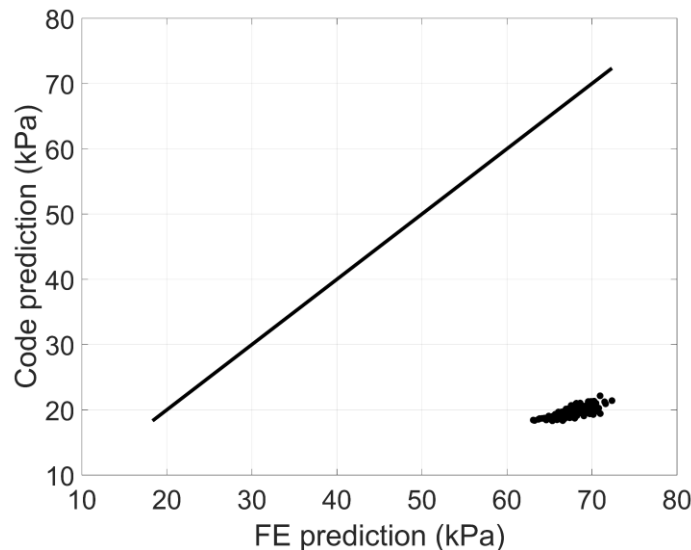


Figure 9-3. Comparison of OOP resistances obtained by the FE model and design-code model for URM walls

Despite the notable discrepancy between design-code and FE model predictions, there exists a strong correlation exists between them, as evidenced by a Pearson correlation coefficient ρ of 0.7902 obtained from the pilot run. Consequently, the quality of the proposed mean estimator

$\hat{\mathbb{E}}_{\text{IM}}$ is guaranteed because it is only dependent on the squared Pearson correlation coefficient ρ^2 for a given computational cost ratio $w_{\text{CSA}} / w_{\text{FE}}$, as indicated by Eq. (9-18). In this study, computational costs are measured as multiples of the CPU time required for a FE model evaluation, leading to $w_{\text{FE}} = 1.0$ and $w_{\text{CSA}} = 0.0000024$. By substituting the values of computational cost ratio $w_{\text{CSA}} / w_{\text{FE}}$ and Pearson correlation coefficient ρ into the MSE reduction ratio in Eq. (9-18), the MSE reduction ratio achieved by the proposed estimator is calculated to be optimally around 63%, compared to the crude FE model-based MC estimator.

To illustrate the effect of computational budget, six different levels for p , ranging from 5 to 30, are considered. Optimization procedures for the determination of model evaluation numbers and coefficients are performed, and corresponding results are presented in **Table 9-1**. As an example, at a computational budget of 5, this budget is exclusively allocated for 5 FE simulations or 2.08×10^7 (calculated as $5 / 0.0000024$) design-code evaluations in the crude MC estimators. Alternatively, in the proposed estimator, this budget is allocated for 4 FE model and 4152 design-code model evaluations. To fully leverage the pre-computed 200 FE models, the selection of FE samples for the construction of the proposed estimator is restricted only to this dataset, as suggested by Yao et al. (2022). A reference mean value of 67.55 kN for OOP resistance is derived using the proposed estimator with a significantly large computational budget, wherein samples are randomly selected from the pre-computed 200 samples. It is critical to acknowledge that the proposed estimator $\hat{\mathbb{E}}_{\text{IM}}$ is rigorously guaranteed to be unbiased, and therefore using the proposed estimator with a large computational budget to determine the reference mean value is justifiable.

Table 9-1. Model evaluation numbers (m_{FE} and m_{CSA}) and coefficient α for the mean estimation of OOP resistance for the URM wall considered

Computational cost p	Crude MC estimators		Proposed estimator		
	FE model	Design-code model	m_{FE}	m_{CSA}	α
	m_{FE}	m_{CSA}			
5	5	2.08×10^7	4	4152	1.70
10	10	4.16×10^7	9	8305	1.70
15	15	6.25×10^7	14	12458	1.70
20	20	8.33×10^7	19	16611	1.70
25	25	1.04×10^8	24	20763	1.70
30	30	1.25×10^8	29	24916	1.70

Figure 9-4 presents the MSE for three estimators (i.e., \hat{E}_{CSA} , \hat{E}_{FE} , \hat{E}_{IM}) in estimating the mean value of OOP resistance for the URM wall considered, relative to the reference mean value through 500 replicates. It is evident that the MSE of \hat{E}_{CSA} reaches a plateau even at the minimum computational budget ($p = 5$) considered, since a large number of design-code model evaluations are available. This finding underscores the inherent bias in the mean estimator when solely relying on the design-code model. The design-code model-based MC estimator exhibits a considerably higher MSE compared to the other two estimators. On the other hand, for all computational budgets considered, the proposed estimator \hat{E}_{IM} achieves an MSE more than 60% lower than \hat{E}_{FE} when the same computation budget is used. As the available computational budget increases, the MSE of \hat{E}_{IM} decreases, indicating its “unbiasedness” of proposed estimator.

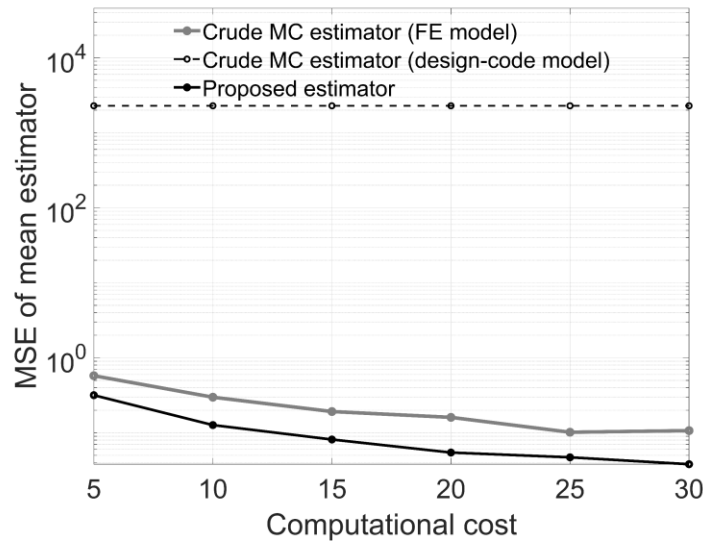


Figure 9-4. MSE of FE model-based crude MC estimator, design-code model-based crude MC estimator, and proposed estimator for the mean value of OOP resistance for the URM wall considered

Figure 9-5 displays the distributions of $\hat{\mathbb{E}}_{FE}$ and $\hat{\mathbb{E}}_{IM}$ from 500 replicates, from which similar conclusions can be drawn. It is important to note that the design-code model-based estimator is excluded in Figure 9-5 since it exhibits nearly zero variance, but significantly deviates from the reference mean value. Notably, the proposed estimator demonstrates a smaller variance compared to the FE model-based crude MC estimator when allotted the same computational budget.

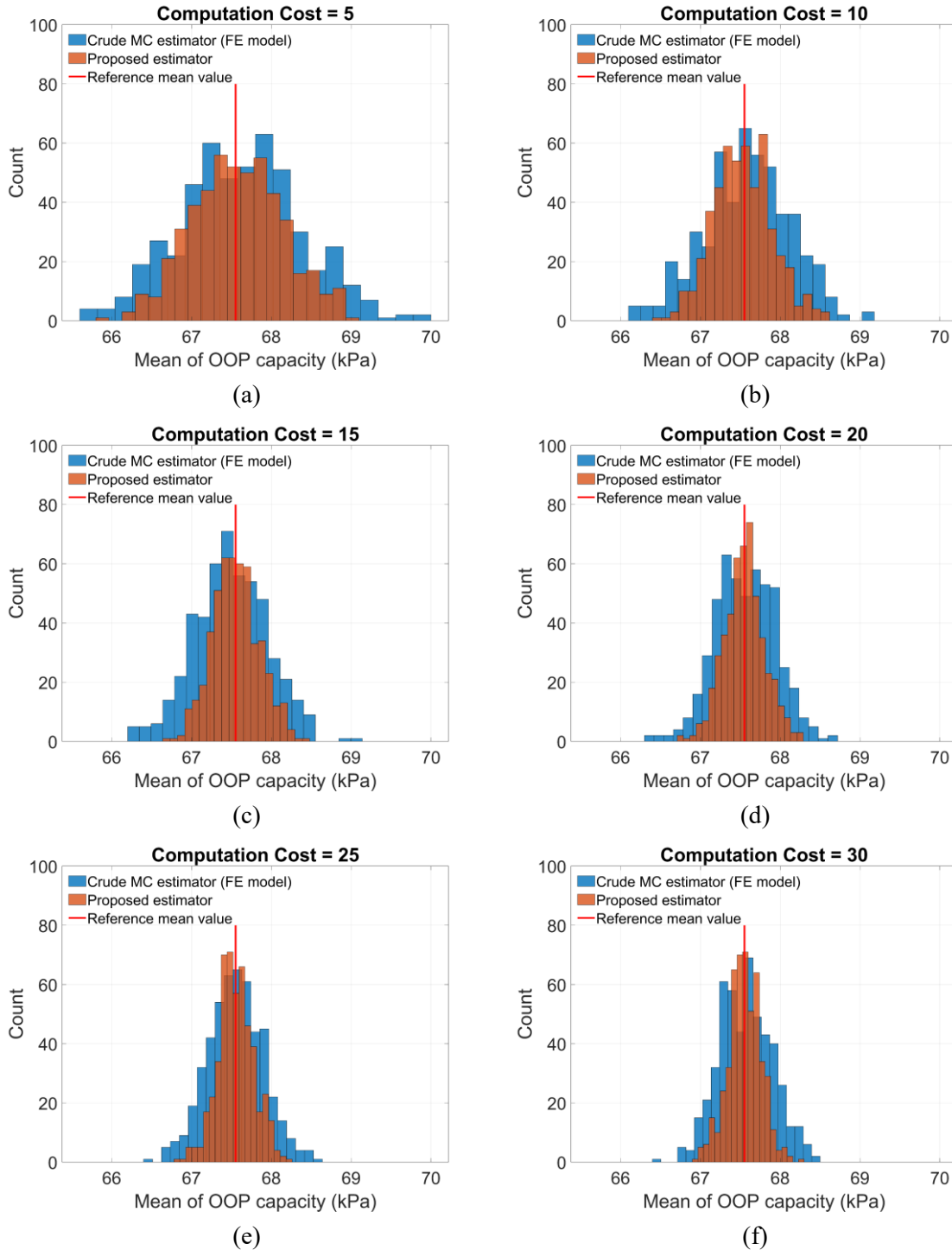


Figure 9-5. Distributions of FE model-based crude MC mean estimator and proposed mean estimator obtained by 500 replicates with different computational costs

Estimating variance in this research is notably challenging due to the involvement of higher-order moments. As previously discussed, two methodologies are identified for calculating model evaluation numbers (m_{FE} and m_{CSA}) and coefficient β . The first method, also suggested in studies (Qian et al. 2018; Yao et al. 2022), adopts a mean-optimal strategy, and corresponding results following this approach are detailed in Table 9-1. Alternatively, the second method focuses on minimizing the MSE of the proposed variance estimator, as indicated in Eq. (9-21), with the corresponding values for m_{FE} , m_{CSA} and β presented in Table 9-2. A comparison of Table 9-1 and Table 9-2 reveals the significant differences in m_{FE} , m_{CSA} and β . This discrepancy primarily results from the mean-optimal strategy's tendency to assign more evaluations to design-code models due to their strong correlation with the FE model. However, the variance-optimal strategy also takes into account the influence of higher-order moments.

Table 9-2. Model evaluation numbers (m_{FE} and m_{CSA}) and coefficient β for the variance estimation of OOP resistance for the URM wall considered

Computational cost p	Proposed estimator (variance-optimal strategy)		
	m_{FE}	m_{CSA}	β
5	4	1576	2.77
10	9	8305	2.75
15	14	12458	2.75
20	19	16611	2.74
25	24	20763	2.74
30	29	24916	2.74

To facilitate the discussion, the proposed variance estimators developed from the mean-optimal and variance-optimal strategies are denoted as $\hat{V}_{IM,mean}$ and $\hat{V}_{IM,var}$, respectively. Figure 9-6 illustrates the MSE of these different variance estimators. Similarly, the MSE of the design-code model-based estimator remains significantly higher due to inherent bias. Among all estimator

evaluated, $\hat{V}_{IM,var}$ exhibits the lowest MSE among them. It should be noted that both $\hat{V}_{IM,mean}$ and $\hat{V}_{IM,var}$ outperform the estimator \hat{V}_{FE} , for the URM wall considered in this study. This finding is crucial as it suggests that even without specific optimization of model evaluation numbers and the coefficient for MSE minimization, the resulting variance estimators are superior to the crude MC estimator, which depends solely on the FE model, given an equivalent computational budget.

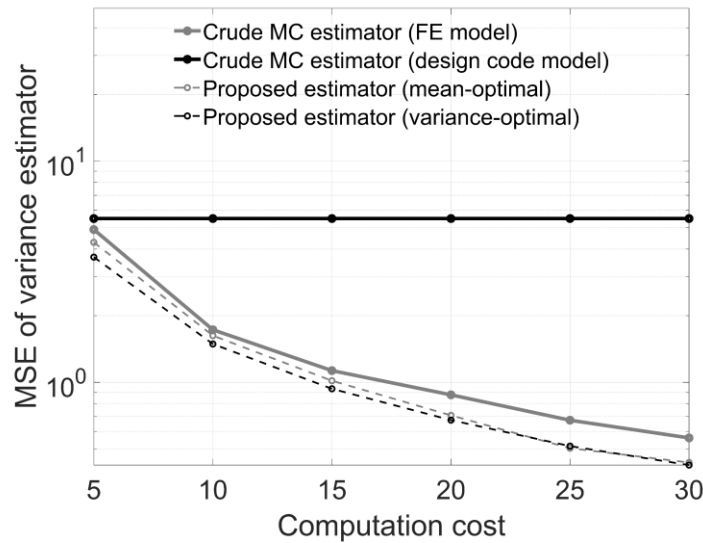


Figure 9-6. MSE of FE-based crude MC estimator, design code-based crude MC estimator, and proposed estimators (mean-optimal and variance-optimal) for the variance of OOP resistance for the URM wall considered

Another key insight from Figure 9-6 is the observation that with an increased computational budget, the MSEs of both estimators $\hat{V}_{IM,mean}$ and $\hat{V}_{IM,var}$ decrease, re-confirming the “unbiasedness” of the proposed variance estimator irrespective of the model evaluation numbers and the value of coefficient. However, it is important to recognize that the MSE of estimator $\hat{V}_{IM,var}$ (i.e., 0.4227) shows an approximate 25% reduction compared to estimator \hat{V}_{FE} (i.e., 0.5608) at a computational budget of 30. This reduction is less pronounced than that observed

in mean estimation, which aligns with expectations since higher-order moments are typically more susceptible to the size of the pilot sample. This aspect influences the determination of model evaluation numbers and the coefficient. This phenomenon is also reflected in the distribution plots in Figure 9-7, where the variance reduction is less marked compared to the mean estimation depicted in Figure 9-5.

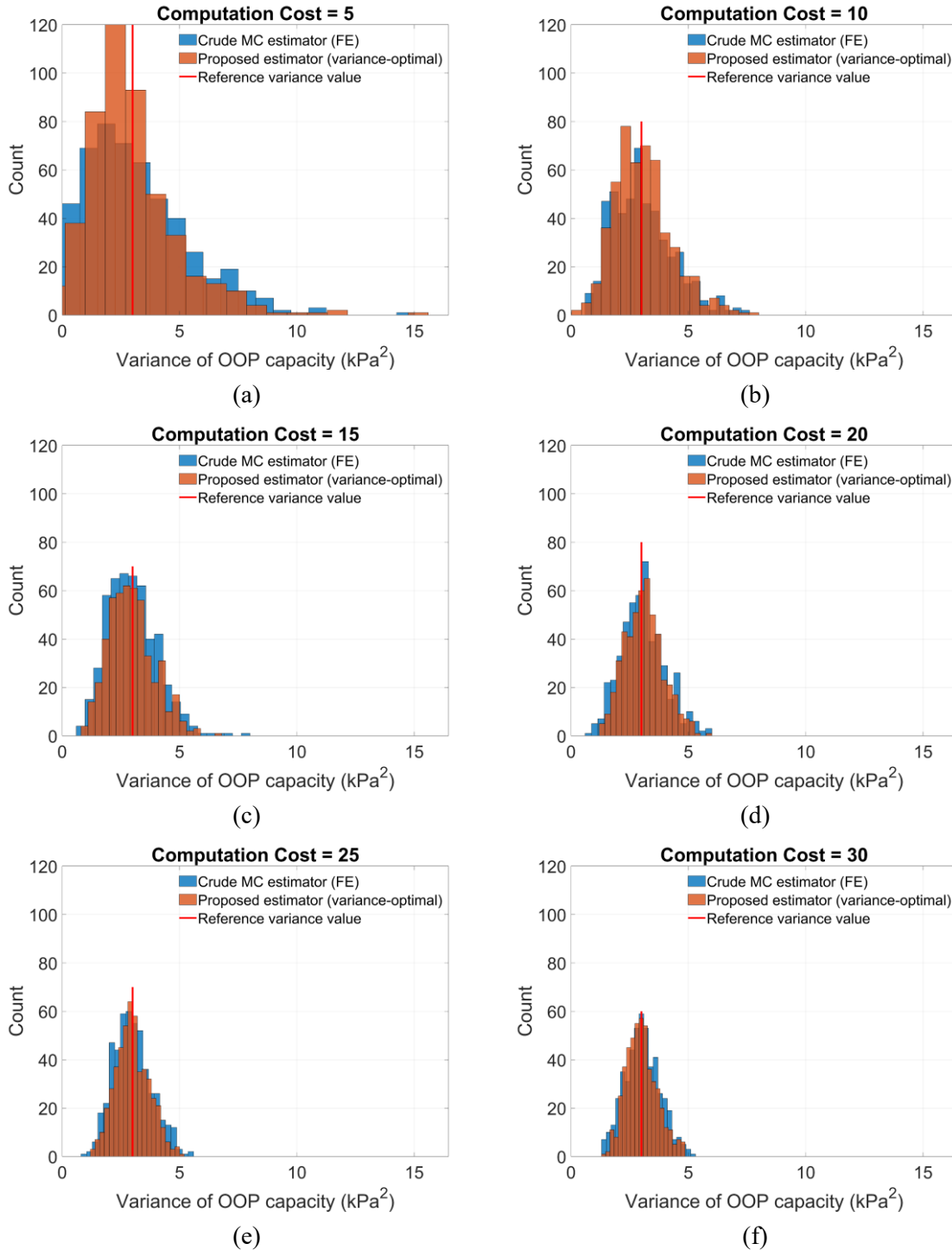


Figure 9-7. Distributions of FE model-based crude MC variance estimator and proposed variance estimator (variance-optimal) obtained by 500 replicates with different computational costs

9.4.2. Case study: RM wall

9.4.2.1 Wall configuration and material uncertainties

The fully grouted RM wall tested by Seif Eldin (2016) is utilized as a case study. This wall is chosen for its well-documented material parameters. The wall's dimensions were 1.8 m in length, 1.6 m in height, 0.19 m in thickness. The concrete masonry units used for the construction of the tested RM wall adhered to the standard dimensions of 390 mm \times 190 mm \times 190 mm. The vertical reinforcements consisted of 20M bars (with a 300 mm² cross sectional area) in every cell, while the horizontal reinforcements comprised the uniformly distributed 10M bars (with a 100 mm² cross-sectional area) spaced at 400 mm. Corresponding horizontal and vertical reinforcement ratios were 0.13% and 0.79%, respectively. A constant pre-compression load of 1.0 MPa was applied to the wall.

In terms of the material parameters, six statistically independent variables are considered: tensile strength f_t , frictional coefficient $\tan \varphi$ and initial dilatancy coefficient $\tan \psi_0$ of interfaces (mortar joints), compressive strength of units f_c^u , compressive strength of grouts f_c^g , and yield strength of reinforcements f_y . Other required material parameters treated as derived random variables using well-established relationships, as summarized in Table 8-5.

9.4.2.2 Statistics estimation

Similar to the URM case, a pilot run on 200 MC samples is first performed. The empirical CDF obtained from the pilot run is shown in Figure 9-8, with the OOP resistance ranging between 0.197 MPa and 0.231 MPa with a mean of 0.213 MPa and a standard derivation of 0.0064 MPa. On the other hand, the comparison of code and FE predictions shown in Figure 9-9 illustrates a significantly high correlation between FE and code predictions with a high correlation coefficient

of 0.8466. This finding suggests that the sectional analysis method suggested in CSA S304-14 (Canadian Standards Association 2014) provides a good representation for the OOP flexural capacity of RM walls. In addition, the design-code model appears to be consistently more conservative than the FE model. This is attributed to the reason that the tensile forces of masonry and the compressive forces of reinforcement bars are ignored in the equilibrium equation. The average computational cost ratio w_{CSA} / w_{FE} is $0.0000019 / 1$. Consequently, model evaluation numbers and coefficients can be derived through mean-optimal and variance-optimal optimization schemes. with the results detailed in Table 9-3. It is evident for the RM wall considered in this study, two optimization schemes lead to identical results for model evaluation numbers, but with different coefficients. In addition, compared to results for URM case shown in Table 9-1 and Table 9-2, more design-code model evaluations are leveraged into the proposed estimator for the RM wall. This increase is attributable to the higher correlation between FE model and code predictions.

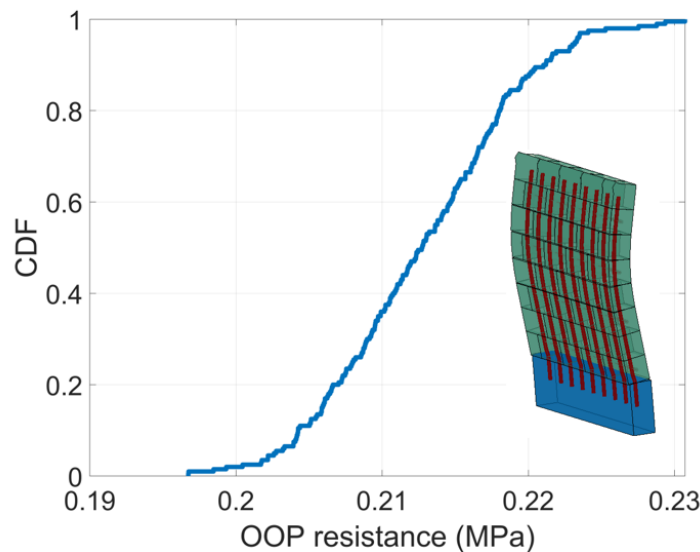


Figure 9-8. Empirical cumulative probability function of OOP resistance for the RM wall

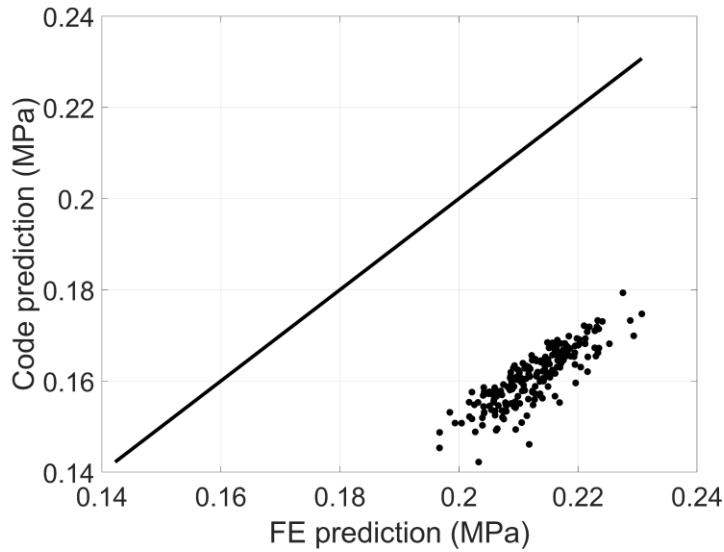


Figure 9-9. Comparison of OOP capacity obtained by design-code and FE models for RM walls

Table 9-3. Model evaluation numbers and coefficient for the mean and variance estimations of OOP resistance for the RM wall

Computational cost p	Crude MC estimators		Proposed estimator (mean-optimal)			Proposed estimator (variance-optimal)		
	FE model	Design-code model	m_{FE}	m_{CSA}	α	m_{FE}	m_{CSA}	β
	m_{FE}	m_{CSA}						
5	5	2.63×10^6	4	5717	0.86	4	5717	0.97
10	10	5.26×10^6	9	11514	0.86	9	11514	0.97
15	15	7.89×10^6	14	17272	0.86	14	17272	0.97
20	20	1.05×10^7	19	23029	0.86	19	23029	0.97
25	25	1.32×10^7	24	28786	0.86	24	28786	0.97
30	30	1.58×10^7	29	34544	0.86	29	34544	0.97

To assess the performance of various estimators (i.e., $\hat{\mathbb{E}}_{CSA}$, $\hat{\mathbb{E}}_{FE}$, and $\hat{\mathbb{E}}_{IM}$ for the mean estimation, and $\hat{\mathbb{V}}_{CSA}$, $\hat{\mathbb{V}}_{FE}$, $\hat{\mathbb{V}}_{IM,mean}$ and $\hat{\mathbb{V}}_{IM,var}$ for the variance estimation), 500 replicates are conducted. Figure 9-10 (a-b) illustrate the MSEs of mean and variance estimators, respectively. Regarding the mean estimation, the proposed estimator $\hat{\mathbb{E}}_{IM}$ achieves a MSE reduction of 70% compared to the FE-based crude MC estimator $\hat{\mathbb{E}}_{FE}$. Similarly, design-code model-based estimator exhibits the highest largest MSE due to its bias. However, for the variance estimation shown in Figure 9-10 (b), the design-code model-based estimator exhibits the smallest MSE for

the computational budgets considered. However, it is expected that with the increase of computational budget, the MSE of $\hat{\mathbb{E}}_{FE}$ and $\hat{\mathbb{E}}_{IM}$ would continue to decrease due to their unbiasedness. By comparing $\hat{\mathbb{E}}_{FE}$ and $\hat{\mathbb{E}}_{IM}$, two modeling management schemes lead to highly identical results. This is also reflected in Table 9-3, in which the model evaluations numbers obtained by two schemes are same and the values of coefficients are close.

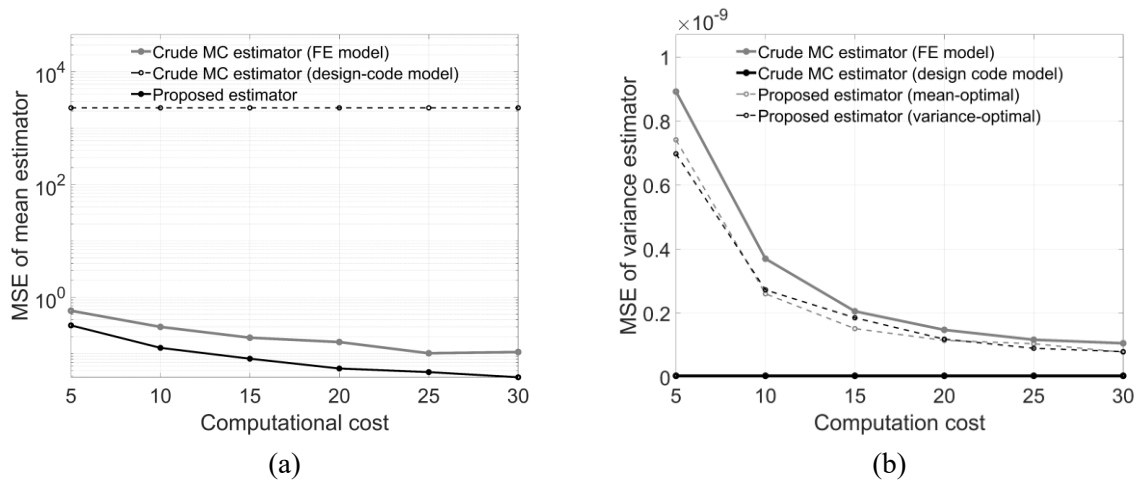


Figure 9-10. MSE of FE model-based crude MC estimator, design code-based crude MC estimator, and proposed estimator for the (a) mean, and (b) variance of OOP resistance of the RM wall

The estimator distributions through 500 replicates are shown in Figure 9-11 and Figure 9-12. The design-code model-based estimators are excluded since they exhibit nearly zero variance. Notably, the proposed estimators demonstrate a smaller variance compared to the FE model-based crude MC estimator when allotted the same computational budget. In addition, the variance reduction is more pronounced in the mean estimator than the variance estimator.

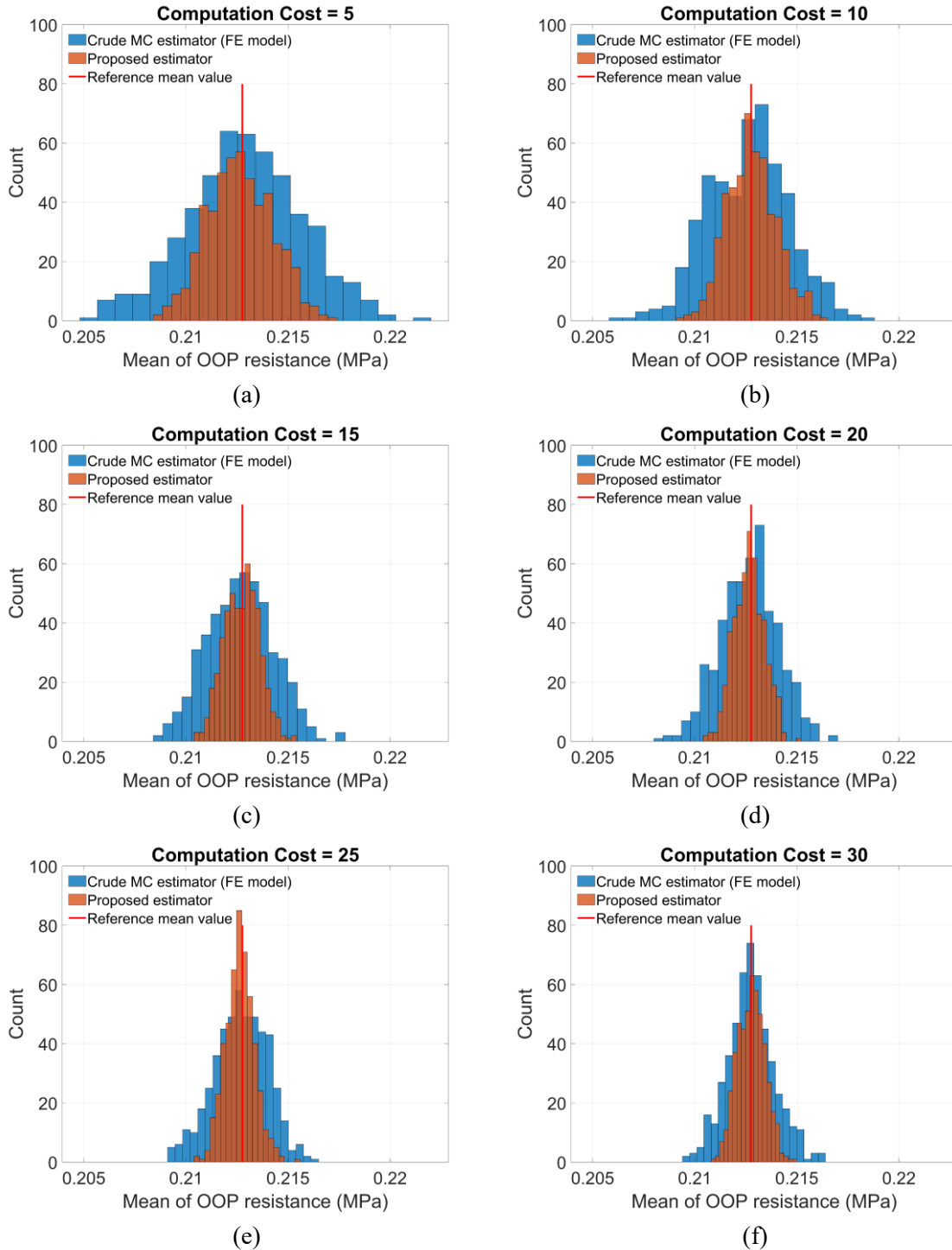


Figure 9-11. Distributions of FE model-based crude MC mean estimator and proposed mean estimator obtained by 500 replicates with different computational costs

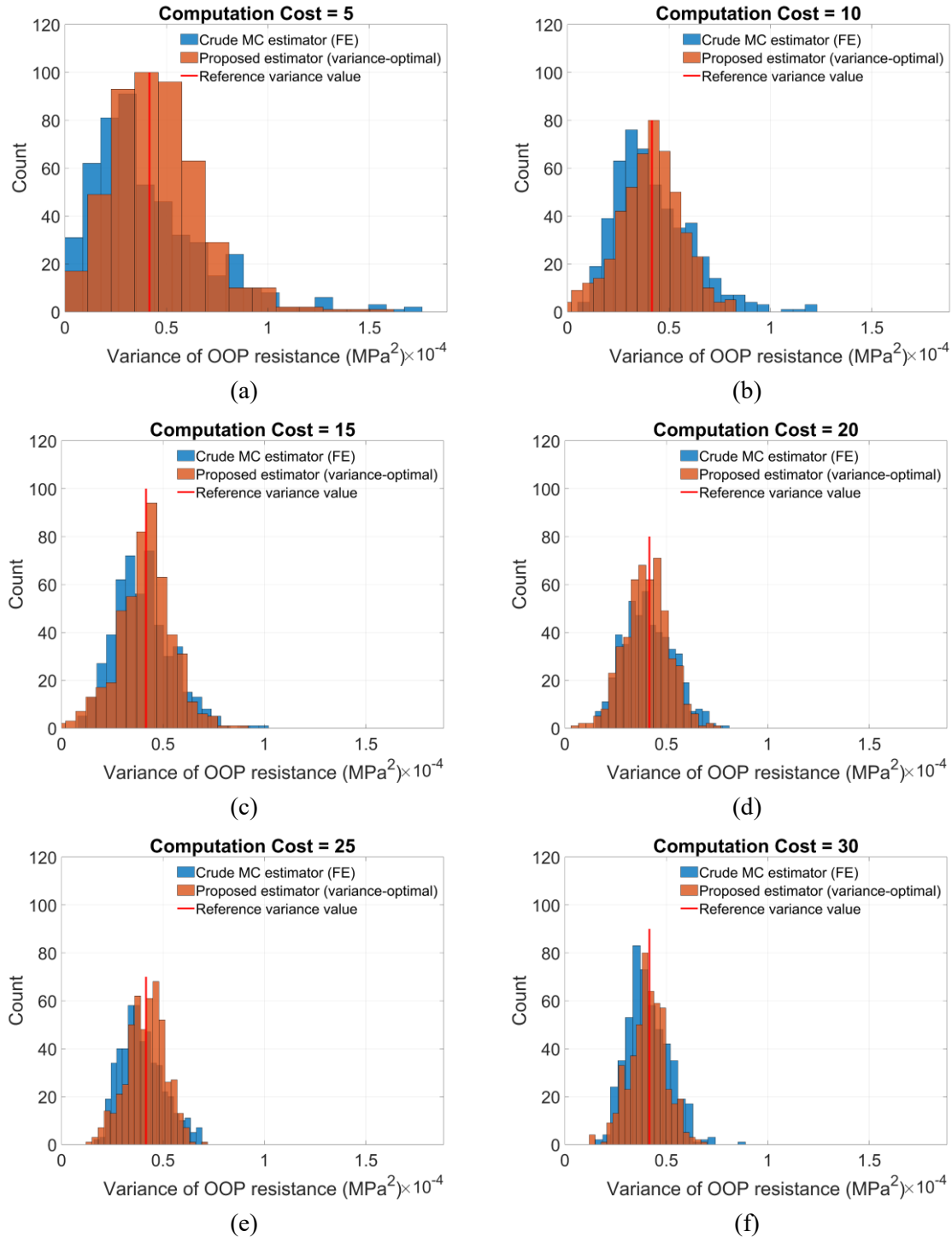


Figure 9-12. Distributions of FE model-based crude MC variance estimator and proposed variance estimator (variance-optimal) obtained by 500 replicates with different computational costs

9.5. CHAPTER CONCLUSION

This chapter presented an improved methodology for estimating the mean and variance of the out-of-plane (OOP) resistance of masonry walls, encompassing both unreinforced masonry (URM) and reinforced masonry (RM) walls. The estimators developed herein adeptly combined the accuracy of mechanics-based finite element (FE) models and the efficiency of Canadian masonry design code-based models. The proposed estimators were formulated using the control variate method, a classical variance reduction technique (Nelson 1987, 1990). A large number of design code model evaluations were integrated in the proposed estimators to improve computational efficiency, while only a limited number of FE model evaluations are involved to ensure accuracy. The methodology for constructing these estimators, especially the determination of model evaluation numbers and coefficients for the OOP resistance of masonry walls, was elucidated in detail.

The proposed statistics estimators had two main advantages: 1) they are strictly unbiased with respect to the true value, irrespective the discrepancy between the FE and design-code models; 2) they potentially could achieve significant variance reductions providing that the higher correlation between the FE and design-code models. Two case studies were provided to illustrate the outperformance of the proposed estimators: one on a URM wall, and the other one on a RM wall. The proposed mean estimator, in particular, shows significantly greater accuracy compared to those based solely on either the FE model or design-code model. Although the variance estimator's superiority is less pronounced than that of the mean estimator, it still exhibits enhanced performance except in the assessment of OOP resistance of an RM wall. This exception is largely due to the maximum computational budget set in this study, limited to 30 FE model runs. It is

expected that with the increase of computational budgets, the proposed estimator would achieve higher accuracy than the design-code model.

Chapter 10. NOVEL STRUCTURAL RELIABILITY METHODS USING MULTI-FIDELITY MODELS THROUGH CROSS-ENTROPY IMPORTANCE SAMPLING AND CONTROL VARIATE TECHNIQUES WITH APPLICATIONS ON MASONRY WALLS

In the realm of reliability assessment for complex real-world structures, the need of using high-fidelity (HF) models (e.g., advanced computational models) in defining limit-state functions (LSFs) poses a significant challenge, due to the high computational costs in sampling-based reliability analysis. To address this challenge, this paper presents a novel multi-fidelity (MF) approach that harmoniously integrates HF and low-fidelity (LF) models to enhance the efficiency and accuracy of reliability analysis. The proposed method involves a two-step leveraging process. Initially, a large number of cost-effective LF models are evaluated, and a biasing probability density is constructed, and an inaccurate LF model-based reliability estimation is obtained through the cross-entropy adaptive sampling strategy. Subsequently, the biasing probability density constructed relying on the LF model is leveraged as an “importance” sampling function in the HF model-based reliability estimation. Lastly, the LF model-based reliability estimation is integrated with the HF model-based reliability estimation through the control variate (CV) technique, leading to a further variance reduction. The additional advantage of the proposed method is its flexibility in integrating any form of LF models, such as data-fit interpolation and regression models or simplified models based on physics, like many design-code models in civil engineering, or FE models with coarse mesh. To illustrate the performance of the proposed multi-fidelity reliability method, four numerical examples are used with comparison to sampling-based reliability estimators.

10.1. INTRODUCTION

The primary goal of structural reliability analysis is to evaluate the probability that a structure fails to fulfill its desired performance after considering pertinent uncertainties, arising from uncertain material properties, structural geometries, external forces, etc. In structural engineering, deterministic response prediction has advanced remarkably, as evidenced by the popularity of high-fidelity (HF) simulation using finite element models, which are unarguably more reliable than oversimplified analytical models with severe restrictions or approximations. However, the direct use of high-fidelity models for probabilistic response prediction or reliability analysis is limited in the field of structural engineering.

Consider a structural system described by a response prediction model $Y = f(\mathbf{X})$, where \mathbf{X} represents a vector of random variables with outcomes or realizations denoted by \mathbf{x} , characterized by a joint probability density function $p(\mathbf{x})$. The structural performance is mathematically described by a performance function or limit state function (LSF), denoted as $g(\mathbf{x})$, defined such that $g(\mathbf{x}) \leq 0$ indicates the failure or unsatisfactory performance of a structural system. The evaluation of $g(\mathbf{x})$ relies on the structural response prediction model $f(\mathbf{x})$, which is typically implicit for complex structural systems. The objective of reliability analysis is to compute the probability of failure P_f , as formulated in Eq. (10-1) (Lemaire 2013):

$$P_f = \int_{g(\mathbf{x}) \leq 0} p(\mathbf{x}) d\mathbf{x} = \int \mathbb{I}(\mathbf{x}) p(\mathbf{x}) d\mathbf{x} \quad (10-1)$$

Here, $\mathbb{I}(\mathbf{x})$ is the indicator function, as given in Eq. (10-2):

$$\mathbb{I}(\mathbf{x}) = \begin{cases} 1 & g(\mathbf{x}) \leq 0 \\ 0 & g(\mathbf{x}) > 0 \end{cases} \quad (10-2)$$

The integral in Eq. (10-1) often becomes analytically intractable when advanced computational models (e.g., nonlinear FE models) are used for $Y = f(\mathbf{X})$. To overcome this, several approximation approaches have been introduced, such as the first-order reliability method (FORM) (Hasofer and Lind 1974; Rackwitz and Flessler 1978; Zhao and Ono 1999) and other methods developed based on FORM. These methods include second-order reliability methods (SORM) (Kiureghian et al. 1987; Zhao and Ono 1999), and response surface methods (RSM) (Bucher and Bourgund 1990; Rajashekhar and Ellingwood 1993), which attempt to approximate the true LSFs in an iterative manner. In the case of highly nonlinear LSFs, the linear approximation employed by FORM can lead to significant errors. This is because a linear representation is incapable of capturing the intricate behavior of a nonlinear function, especially in regions where the function exhibits sharp changes or curvature. As a result, the failure probability estimated by FORM may deviate substantially from the true value, leading to unreliable or even misleading conclusions about the system's reliability. SORM, with its inclusion of second-order terms, offers a more accurate approximation than FORM for moderately nonlinear problems. However, for LSFs with severe nonlinearity or complex behavior, the second-order approximation may still fall short. The accuracy of SORM is heavily dependent on the adequacy of the quadratic approximation to represent the true LSF. In cases where the LSF has higher-order nonlinearities or discontinuities, SORM's performance can deteriorate, resulting in inaccurate reliability estimates.

The challenges posed by high-dimensional problems are multifaceted. Both FORM and SORM rely on the identification of a design point or most probable point in the standard normal

space, which becomes increasingly difficult as the dimensionality of the problem grows. The computational cost associated with the iterative search for the design point escalates rapidly with the number of random variables, making these methods less feasible for large-scale problems. Additionally, the curse of dimensionality affects the accuracy of the linear and quadratic approximations. In high-dimensional spaces, the volume of the region where the approximation is valid diminishes relative to the entire space, leading to a decrease in the overall effectiveness of FORM and SORM, as indicated by relevant studies (Geyer et al. 2019; Kurtz and Song 2013; Song and Kawai 2023). Note that there is another family of approximate methods, i.e., moment-based methods (Cornell n.d.; Shun Li and Lumb 1985; Tichý 1994; Zhao and Ono 2001), which attempt to approximate the probability distribution function based on a few probability moments of the LSF. These methods are practical in the sense that no probability distribution functions of basic random variables are needed, but their use is restricted by their applicability range.

As an alternative to approximation methods, sampling-based approaches, such as the crude Monte Carlo Simulation (MCS) (Metropolis and Ulam 1949), have gained prominence due to their robustness against the complexity of LSFs and their asymptotic accuracy. Crude MCS aims at estimating the probability of failure by sampling the basic random variables, evaluating the LSF $g(\mathbf{x})$ repeatedly, and quantifying the proportion that $g(\mathbf{x}) \leq 0$. As such, crude MCS is particularly attractive when $g(\mathbf{x})$ involves a ‘black-box’ model $f(\mathbf{x})$. However, the accuracy of crude MCS is contingent upon a large sample size due to its low convergence rate when the probability of failure is low for rare event evaluation. This becomes an obstacle when evaluating the LSF is computationally expensive, for example, when high-fidelity models are used for $f(\mathbf{x})$.

To address this issue, researchers have devoted considerable efforts to developing MCS variants to enhance the computational efficiency through variance reduction techniques such as importance sampling (IS) (Ibrahim 1991; Tokdar and Kass 2010), subset simulation (Au et al. 2007; Au and Beck 2001), directional simulation (DS) (Bjerager 1988; Nie and Ellingwood 2000), line sampling (LS) (Koutsourelakis 2004; Koutsourelakis et al. 2004), Quasi-Monte Carlo methods (Nie and Ellingwood 2004a; b), and others as reported in recent literature reviews (Song and Kawai 2023; Tabandeh et al. 2022; Zhang 2021). IS, for instance, targets regions of the input space that significantly influence the quantity of interest, with its efficacy reliant on the selection of the importance sampling distribution. Subset Simulation, on the other hand, partitions the original rare event probability estimation problem into a sequence of more tractable problems with higher probabilities. Its performance hinges on the optimal selection of intermediate failure thresholds, a task that can prove challenging. Although it diminishes the computational burden compared to crude MCS, it may still demand considerable computational resources for problems characterized by very low failure probabilities or high-dimensional input spaces. DS navigates the input space along specific directions, typically dictated by the gradient of the limit state function. Its performance is contingent upon the appropriate choice of directions for simulation, a process that can be complex in problems with intricate failure regions. DS might not be well-suited for scenarios where the failure region does not align well with any particular direction. Lastly, LS aims to simplify the problem by converting it into one-dimensional integrals along chosen lines in the input space. However, this reduction may not fully encapsulate the complexity of the limit state function in high-dimensional scenarios. The effectiveness of LS is dependent on the judicious selection of lines for sampling, a task that can be arduous in problems with irregular failure regions.

To sum up, these sampling-based methods might still be ineffective when the LSF evaluation is computationally intensive. Although they prove to be more efficient than the crude MCS (Song and Kawai 2023), they still necessitate a relatively large number of LSF evaluations, rendering them less feasible for reliability analysis based on HF models that are perceived to be more precise in characterizing the structural response.

On the other hand, more readily accessible low-fidelity (LF) models, such as engineering models prescribed in design codes, analytical models characterized by assumptions or deliberate simplifications in structural complexities, surrogate models trained by data, serve as cost-effective alternatives. These LF models remain essential for practical use by providing efficient evaluations when model accuracy is non-critical. It is imperative to note, however, that LF models often suffer from relatively large inaccuracies, and thus reliability assessments based on LF models without considering model uncertainty may involve substantial errors in the reliability results (Gallimard 2011; Hamdia and Ghasemi 2023; Rashki et al. 2018).

Recognizing the strengths and limitations of HF and LF models, researchers have turned to multi-fidelity (MF) methods integrating both types of models in structural engineering, particularly for response prediction and uncertainty analysis (Hamdia and Ghasemi 2023; Patsialis et al. 2022; Patsialis and Taflanidis 2021; Rashki et al. 2018). These methods include Multi-Level (ML) and Multi-Fidelity (MF) methods. Both ML and MF methods employ HF and LF models. The former is typically limited to a hierarchy of LF models that are derived from the HF model by varying a parameter (e.g., discretization size), while MF methods are less restrictive in terms of the LF models (Peherstorfer et al. 2018b; Zhang 2021). As such, MF methods offer more flexibilities in the selection of LF models. For example, Rashki et al. (2018) and Hamdia and

Ghasemi (2023) used multi-level refinement on a hierarchy of computational models for reliability analysis. Patsialis and Taflanidis (2022; 2021) utilized the reduced order models as LF models for the investigation of seismic behavior of planar moment-resisting frame (MRF) structural systems. Peherstorfer et al. (2016a) used projection-based reduced models as LF models for a clamped plate in bending. It is worth noting that design-code models, which exist widely in structural engineering, can also be alternative LF models in MF methods. For instance, Liu et al. (2023b) used five concrete structure and bridge design-code models as LF models for the shear strength predictions of prestressed concrete girders.

The key component of the MF method is the model management strategy. This involves how the outputs from LF and HF models are used to formulate the statistic estimators of interest, i.e., mean, variance, and probability of failure. In contrast to the correction approach, as used in (Liu et al. 2023b; a) where correction terms to LF models are learned using HF data, HF and LF information can be integrated by fusion or filtering (Peherstorfer et al. 2018b). More specifically, in the realm of reliability analysis, two common approaches to fuse LF and HF information are control variates (Abdollahi et al. 2020; Rashki et al. 2018) and co-kriging (Skandalos et al. 2022; Zhang et al. 2022), by exploiting the correlation between HF and LF models directly, where both HF and LF can be evaluated in parallel (Proppe and Kaupp 2022). In contrast, in the filtering approach, HF model is evaluated selectively in a way guided by LF information, only when meeting some criteria defined based on the LF evaluation (Li and Xiu 2010) or sampling according to a biasing distribution that is constructed with a LF model (Peherstorfer et al. 2016a, 2017). Note that in (Peherstorfer et al. 2016a, 2017), the failure domain is captured using cheap LF models via an expectation-maximization method, which still requires a relatively large number of HF

evaluations, especially for rare event analyses (i.e., P_f is small). Pham and Gorodetsky (2022) developed an approximate control variate estimator for the reliability estimation. The proposed approach leveraged the importance sampling method and variance reduction technique. Moreover, the lower bounds on the number of samples required to guarantee variance reduction were derived. The analysis results indicated that the proposed approximate control variate can further reduce the variance compared to the estimator presented in (Peherstorfer et al. 2016a, 2017). In this research, the developed estimator unexpectedly aligns with an idea previously proposed by Pham and Gorodetsky (2022). However, the primary motivation behind this estimator is to leverage finite element models commonly employed in research and design-code models for reliability analysis, as outlined in this chapter. Consequently, the assessment of this estimator's effectiveness in estimating the probability of a rare event is undertaken through a comparison with estimators reliant on Monte Carlo simulations utilizing one or more models, rather than juxtaposing it against other reliability methods such as FORM.

To further contribute to the field of MF reliability analysis, this paper presents a new MF approach that synergistically integrates the advantages of HF and LF models for reliability analyses using both information fusing (e.g., control variate) and filtering (e.g., importance sampling). As such, the proposed method involves a two-phase leveraging process using HF and LF models. Initially, a great number of cost-effective LF models (or LSFs based on LF models) are evaluated, and an 'importance' sampling density (i.e., a biasing density that allows more samples in the failure domain) is constructed and an inaccurate LF model-based reliability estimation is obtained. This procedure is realized through the cross-entropy adaptive importance sampling strategy (Geyer et al. 2019; Kurtz and Song 2013). Subsequently, the biasing density

constructed relied on the LF model is leveraged in the HF model-based IS reliability estimation, leading to a HF model-based reliability estimator. The computational saving is thus achieved by avoiding running resource-intensive HF models for the construction of biasing density. Lastly, the LF model-based reliability estimation is integrated into the HF model-based reliability estimation through the control variate (CV) technique, leading to a further variance reduction. In what follows, Section 10.2 introduces the proposed approach, including the mathematical fundamentals of cross-entropy based importance sampling and control variate approach in the context of MF framework. Section 10.3 demonstrates the efficacy of the new estimator through four structural engineering case studies, along with comparison to several other estimators in Section 10.3. Section 10.4 provides two application examples on RM walls: one is under IP loading and the other one focuses on the OOP loading scenario.

10.2. MULTI-FIDELITY RELIABILITY ANALYSIS

This section presents the cross-entropy (CE) strategy utilized in importance sampling-based reliability analysis in the context of MFMC. As such, the probability of failure in Eq. (10-1) is reformulated by introducing HF model $f_H(\mathbf{x})$ and LF model $f_L(\mathbf{x})$. Note that both models are dependent on the same set of random variables \mathbf{x} associated with PDF $p(\mathbf{x})$. The objective is to evaluate the probability of failure $P_{f,H}$, i.e., the probability of violating the limit state described by the HF model, $g_H(\mathbf{x}) \leq 0$, as shown in Eq. (10-3):

$$P_{f,H} = \int_{g_H(\mathbf{x}) \leq 0} \mathbb{I}_H(\mathbf{x}) p(\mathbf{x}) d\mathbf{x} \quad (10-3)$$

where $\mathbb{I}_H(\mathbf{x})$ is the indicator function associated with the HF model, defined as

$$\mathbb{I}_H(\mathbf{x}) = \begin{cases} 1 & g_H(\mathbf{x}) < 0 \\ 0 & g_H(\mathbf{x}) \geq 0 \end{cases}$$

10.2.1. Importance sampling (IS)

IS is a variance reduction technique commonly used in computational statistics (Kloek and van Dijk 1978). By introducing a biasing density $q_H(\mathbf{x})$, $P_{f,H}$ can be reformulated as Eq. (10-4):

$$P_{f,H} = \int_{g_H(\mathbf{x}) \leq 0} \frac{\mathbb{I}_H(\mathbf{x}) p(\mathbf{x})}{q_H(\mathbf{x})} q_H(\mathbf{x}) d\mathbf{x} \quad (10-4)$$

In MCS framework, the integral in Eq. (10-4) is estimated as:

$$P_{f,H} \approx \hat{P}_{f,H}^{\text{IS}} = \frac{1}{N} \sum_{i=1}^N \frac{\mathbb{I}_H(\mathbf{x}_i) p(\mathbf{x}_i)}{q_H(\mathbf{x}_i)} \quad (10-5)$$

$\hat{P}_{f,H}^{\text{IS}}$ denotes the IS estimator of $P_{f,H}$, and samples \mathbf{x}_i ($i=1,2,\dots,N$) are drawn in accordance with the biasing density $q_H(\mathbf{x})$, instead of the original one $p(\mathbf{x})$. IS aims to selectively samples more frequently from regions where the failure is more likely, thus improving efficiency by using fewer samples than crude MCS. The effectiveness of the IS estimator is significantly influenced by the choice of biasing density. Theoretically, an optimal biasing density $q_H^*(\mathbf{x})$ exists as shown in Eq. (10-6), such that IS estimator would yield a zero-variance estimate (Fryer and Rubinstein 1983):

$$q_H^*(\mathbf{x}) = \frac{\mathbb{I}_H(\mathbf{x}) p(\mathbf{x})}{\int \mathbb{I}_H(\mathbf{x}) p(\mathbf{x}) d\mathbf{x}} \quad (10-6)$$

However, $q_H^*(\mathbf{x})$ is not directly attainable as the denominator involves the probability of failure $P_{f,H}$ that is being estimated. To address this, numerous sampling methods have been proposed to obtain a near-optimal biasing density (Tabandeh et al. 2022). Nonetheless, these sampling methods still require a relatively large number of HF model evaluations, which is proved to be computationally demanding. To alleviate this issue for MFMC, this study approximates the biasing density $q_H^*(\mathbf{x})$ using the information obtained from LF models. More specifically, the biasing density is derived utilizing an adaptive cross entropy (CE) technique, which will be thoroughly detailed in the subsequent section.

10.2.2. Cross entropy-based importance sampling (CEIS)

Suppose there exists a LF model $f_L(\mathbf{x})$, which is less accurate for the estimation of quantity of interest but more computationally efficient than $f_H(\mathbf{x})$. Thus, a large number of evaluations of the LF model $f_L(\mathbf{x})$, or LSF pertinent to the LF model $g_L(\mathbf{x})$, are much more accessible. The indicator function $\mathbb{I}_L(\mathbf{x})$ for the LF model can be defined as Eq. (10-7):

$$\mathbb{I}_L(\mathbf{x}) = \begin{cases} 1 & g_L(\mathbf{x}) \leq 0 \\ 0 & g_L(\mathbf{x}) > 0 \end{cases} \quad (10-7)$$

Notably, it is anticipated that the failure domains of HF model $\Omega_H(\mathbf{x} \in \Omega_H : g_H(\mathbf{x}) \leq 0)$ and LF model $\Omega_L(\mathbf{x} \in \Omega_L : g_L(\mathbf{x}) \leq 0)$ would exhibit a certain level of overlap, which depends on the closeness between the true failure boundary defined by $g_H(\mathbf{x}) = 0$ and the approximate failure boundary defined by $g_L(\mathbf{x}) = 0$. Analogous to Eq. (10-6), the optimal biasing density $q_L^*(\mathbf{x})$ for the LF model is presented in Eq. (10-8):

$$q_L^*(\mathbf{x}) = \frac{\mathbb{I}_L(\mathbf{x}) p(\mathbf{x})}{\int_{g_L(\mathbf{x}) \leq 0} \mathbb{I}_L(\mathbf{x}) p(\mathbf{x}) d\mathbf{x}} = \frac{\mathbb{I}_L(\mathbf{x}) p(\mathbf{x})}{P_{f,L}} \quad (10-8)$$

The CE method seeks to adjust a parametric family of probability distributions to minimize the Kullback-Leibler (KL) divergence (also referred to as ‘cross-entropy’ or ‘relative entropy’) between $q_L^*(\mathbf{x})$ and the near-optimal density $q_L(\mathbf{x}, \boldsymbol{\nu})$ (Rubinstein and Kroese 2008). Here, $\boldsymbol{\nu}$ denotes the statistical parameter. The KL divergence $D_{\text{KL}}[q_L^*(\mathbf{x}), q_L(\mathbf{x}, \boldsymbol{\nu})]$ is a measure of the ‘distance’ between two PDFs $q_L^*(\mathbf{x})$ and $q_L(\mathbf{x}, \boldsymbol{\nu})$, as defined in Eq. (10-9):

$$D_{\text{KL}}[q_L^*(\mathbf{x}), q_L(\mathbf{x}, \boldsymbol{\nu})] = \int_{g_L(\mathbf{x}) \leq 0} q_L^*(\mathbf{x}) \ln[q_L^*(\mathbf{x})] d\mathbf{x} - \int_{g_L(\mathbf{x}) \leq 0} q_L^*(\mathbf{x}) \ln[q_L(\mathbf{x}, \boldsymbol{\nu})] d\mathbf{x} \quad (10-9)$$

It is noted that the first term in the right-hand side (RHS) of Eq. (10-9) is invariant with respect to $\boldsymbol{\nu}$. Thus, to seek a suitable $\boldsymbol{\nu}$ to minimize $D_{\text{KL}}[q_L^*(\mathbf{x}), q_L(\mathbf{x}, \boldsymbol{\nu})]$, it is equivalent to maximize the second term $\int q_L^*(\mathbf{x}) \ln[q_L(\mathbf{x}, \boldsymbol{\nu})] d\mathbf{x}$. Substituting $q_L^*(\mathbf{x})$ from Eq. (10-8) into Eq. (10-9), and considering that denominator of Eq. (10-8) is a constant, one can obtain:

$$\arg \min_{\boldsymbol{\nu}} D_{\text{KL}}[q_L^*(\mathbf{x}), q_L(\mathbf{x}, \boldsymbol{\nu})] = \arg \max_{\boldsymbol{\nu}} \int_{g_L(\mathbf{x}) \leq 0} \mathbb{I}_L(\mathbf{x}) p(\mathbf{x}) \ln[q_L(\mathbf{x}, \boldsymbol{\nu})] d\mathbf{x} \quad (10-10)$$

In Eq. (10-10), estimating the integral $\int_{g_L(\mathbf{x}) \leq 0} \mathbb{I}_L(\mathbf{x}) p(\mathbf{x}) \ln[q_L(\mathbf{x}, \boldsymbol{\nu})] d\mathbf{x}$ requires samples to be located within the failure domain. Such a procedure typically requires a large number of samples. To facilitate this, IS is re-used by introducing another sampling density $w_L(\mathbf{x}, \mathbf{u})$, with \mathbf{u} representing the statistical parameter. Consequently, Eq. (10-10) is re-written as Eq. (10-11):

$$\arg \min_{\boldsymbol{\nu}} D_{\text{KL}}[q_L^*(\mathbf{x}), q_L(\mathbf{x}, \boldsymbol{\nu})] = \arg \max_{\boldsymbol{\nu}} \int_{g_L(\mathbf{x}) \leq 0} \frac{\mathbb{I}_L(\mathbf{x}) p(\mathbf{x}) \ln[q_L(\mathbf{x}, \boldsymbol{\nu})] w_L(\mathbf{x}, \mathbf{u})}{w_L(\mathbf{x}, \mathbf{u})} d\mathbf{x} \quad (10-11)$$

By defining the likelihood ratio $W_L(\mathbf{x}, \mathbf{u}) = \frac{p(\mathbf{x})}{w_L(\mathbf{x}, \mathbf{u})}$, the RHS of Eq. (10-11) can be

estimated using MCS, as shown in Eq. (10-12):

$$\arg \min_{\mathbf{v}} D_{\text{KL}} [q_L^*(\mathbf{x}), q_L(\mathbf{x}, \mathbf{v})] \approx \arg \max_{\mathbf{v}} \frac{1}{M} \sum_{i=1}^M \mathbb{I}_L(\mathbf{x}_i) \ln [q_L(\mathbf{x}_i, \mathbf{v})] W_L(\mathbf{x}_i, \mathbf{u}) \quad (10-12)$$

In Eq. (10-12), samples \mathbf{x}_i ($i=1,2,\dots,M$) are generated according to the newly introduced density $w_L(\mathbf{x}, \mathbf{u})$, and M is the sample size. Note that statistical parameter \mathbf{u} is distinct from \mathbf{v} , and thus, the updating of \mathbf{u} and \mathbf{v} can be decoupled in the optimization procedure. For most applications, the RHS of Eq. (10-12) is concave and differentiable with respect to \mathbf{v} (Geyer et al. 2019; Kurtz and Song 2013; Rubinstein and Kroese 2004). Therefore, the optimization problem in Eq. (10-12) can be solved by letting the gradient equal to zero, as shown in Eq. (10-13):

$$\arg \max_{\mathbf{v}} \frac{1}{M} \sum_{i=1}^M \mathbb{I}_L(\mathbf{x}_i) \nabla_{\mathbf{v}} \ln [q_L(\mathbf{x}_i, \mathbf{v})] W_L(\mathbf{x}_i, \mathbf{u}) \quad (10-13)$$

However, one should notice that evaluating Eq. (10-13) requires a substantial number of samples to be sampled in the failure domain such that $\mathbb{I}_L(\mathbf{x}_i)=1$ for these samples \mathbf{x}_i . To overcome this, the CE method (Geyer et al. 2019) introduces a series of intermediate failure events, using the concepts of importance splitting as similarly used in subset simulation (Propper and Kaupp 2022). The intermediate failure event is defined such that $\rho \cdot M$ samples are located in its failure domain, and ρ is a chosen value in the interval $[0, 1]$. The indicator function at the t^{th} intermediate level, denoted as $\mathbb{I}_{L,t}(\mathbf{x})$, can be defined as Eq. (10-14):

$$\mathbb{I}_{L,t}(\mathbf{x}) = \begin{cases} 1 & g_L(\mathbf{x}) \leq \zeta^{(t)} \\ 0 & g_L(\mathbf{x}) > \zeta^{(t)} \end{cases} \quad (10-14)$$

Here, $\zeta^{(t)}$ is a non-negative value, which is calculated as the lower ρ -quantile of the LSF values from all M samples at the intermediate level t . The optimization problem in Eq. (10-13) is reformulated at the intermediate level t , as shown in Eq. (10-15):

$$\arg \min_{\mathbf{v}} D_{\text{KL}}[q_{L,t}^*(\mathbf{x}), q_{L,t}(\mathbf{x}, \mathbf{v})] \approx \arg \max_{\mathbf{v}} \frac{1}{M} \sum_{i=1}^M \mathbb{I}_{L,t}(\mathbf{x}_i) \ln[q_L(\mathbf{x}_i, \mathbf{v})] \mathcal{W}_L(\mathbf{x}_i, \mathbf{u}_t) \quad (10-15)$$

where $q_{L,t}^*(\mathbf{x})$, $q_{L,t}(\mathbf{x}, \mathbf{v})$, and \mathbf{u}_t are written with the subscript ‘ t ’, to reflect the intermediate level. Similarly, one can set the gradient of Eq. (10-15) as zero with respect to \mathbf{v} , to find a near-optimal density $q_{L,t}(\mathbf{x}, \mathbf{v})$. By focusing on the derivative of RHS of Eq. (10-15), if a Gaussian distribution is chosen as the parametric family comprising the mean vector $\boldsymbol{\mu}$ and covariance matrix $\boldsymbol{\Sigma}$, i.e., $\mathbf{v} = \mathbf{v}(\boldsymbol{\mu}, \boldsymbol{\Sigma})$, an explicit updating rule for parameters $\boldsymbol{\mu}$ and $\boldsymbol{\Sigma}$ at the intermediate level $t + 1$ can be derived (Kroese et al. 2013):

$$\boldsymbol{\mu}_{t+1} = \frac{\sum_{i=1}^M \mathbb{I}_{L,t}(\mathbf{x}_i) \mathcal{W}_L(\mathbf{x}_i, \mathbf{u}_t) \mathbf{x}_i}{\sum_{i=1}^M \mathbb{I}_{L,t}(\mathbf{x}_i) \mathcal{W}_L(\mathbf{x}_i, \mathbf{u}_t)} \quad (10-16)$$

$$\boldsymbol{\Sigma}_{t+1} = \frac{\sum_{i=1}^M \mathbb{I}_{L,t}(\mathbf{x}_i) \mathcal{W}_L(\mathbf{x}_i, \mathbf{u}_t) (\mathbf{x}_i - \boldsymbol{\mu}_{t+1})(\mathbf{x}_i - \boldsymbol{\mu}_{t+1})^T}{\sum_{i=1}^M \mathbb{I}_{L,t}(\mathbf{x}_i) \mathcal{W}_L(\mathbf{x}_i, \mathbf{u}_t)} \quad (10-17)$$

For the initialization of the abovementioned iterative procedure (i.e., when $t = 0$), the sampling density for $w_L(\mathbf{x}, \mathbf{u}_t)$ is set as the original PDF $p(\mathbf{x})$. Subsequently (when $t > 0$),

$w_L(\mathbf{x}, \mathbf{u}_t)$ is determined as the density with statistical parameters derived following Eq. (10-16) and Eq. (10-17) at the previous level, i.e., $w_{L,t+1}(\mathbf{x}, \mathbf{u}) = q_{L,t}(\mathbf{x}, \mathbf{v})$. The near-optimal density $q_L(\mathbf{x}, \mathbf{v})$ is obtained through several rounds of adaptive sampling until lower ρ - quantile of the LSF values is less or equal than 0. Notably, the LSF at the last iteration becomes the original LSF $\mathbb{I}_L(\mathbf{x})$. Accordingly, the probability of failure based on the cross-entropy importance sampling method (CEIS) $\hat{P}_{f,L}^{\text{CEIS}}$ can be approximated as Eq. (10-18):

$$\hat{P}_{f,L}^{\text{ISCE}} = \frac{1}{M} \sum_{i=1}^M \frac{\mathbb{I}_L(\mathbf{x}_i) p(\mathbf{x}_i)}{q_L(\mathbf{x}_i, \mathbf{v})} \quad (10-18)$$

10.3. MULTI-FIDELITY RELIABILITY ANALYSIS

The cross-entropy importance sampling (CEIS), as discussed in Section 2, yields two essential outputs: a biasing density $q_L(\mathbf{x}, \mathbf{v})$ and a probability of failure estimate $\hat{P}_{f,L}^{\text{CEIS}}$ based on the LF model using the CEIS method. These outputs are integrated into the proposed multi-fidelity (MF) reliability analysis method through control variate (CV) method. In this section, the mathematical preliminary of CV method is first introduced, and subsequently the proposed methodology for reliability assessment is detailed.

10.3.1. Mathematical preliminary of control variate (CV) method

The CV method is another variance reduction technique widely used in the MCS (Song and Kawai 2023). Consider a mean estimator \hat{Y} for a quantity of interest Y and suppose there exists another variable X which is correlated with Y , also known as a control variate, and its expected value is μ . The CV estimator for the mean estimation of Y is written as Eq. (10-19) (Nelson 1987):

$$\hat{Y}_{CV} = Y + \alpha(\hat{X} - \mu) \quad (10-19)$$

where \hat{X} is a mean estimate of X ; and α is a coefficient chosen to minimize the variance of \hat{Y}_{CV} , which can be derived as Eq. (10-20):

$$\mathbb{V}[\hat{Y}_{CV}] = \mathbb{V}[Y] + \alpha^2 \mathbb{V}[\hat{X}] + 2\alpha \cdot \text{COV}[X, \hat{X}] \quad (10-20)$$

In Eq. (10-20), $\mathbb{V}[\cdot]$ is the variance operator; $\text{COV}[\cdot]$ is the covariance operator, $\text{COV}[X, Y] = \mathbb{E}[X - \mathbb{E}(X)][Y - \mathbb{E}(Y)]$; $\mathbb{E}[\cdot]$ is the expectation operator. To seek an optimal α^* , the derivative of $\mathbb{V}(\hat{Y}_{CV})$ with respect to α is set as zero, leading to the result shown in Eq. (10-21):

$$\alpha^* = -\frac{\text{COV}[\hat{X}, Y]}{\mathbb{V}[\hat{X}]} \quad (10-21)$$

The resultant variance of CV estimator $\mathbb{V}[\hat{Y}_{CV}]$, using the optimal α^* , is calculated as per Eq. (10-22):

$$\mathbb{V}[\hat{Y}_{CV}] = \mathbb{V}[Y] - \frac{[\text{COV}[\hat{X}, Y]]^2}{\mathbb{V}[\hat{X}]} = \mathbb{V}[Y](1 - \rho^2) \quad (10-22)$$

where ρ is the correlation coefficient, defined as $\rho = \frac{\text{COV}[\hat{X}, Y]}{\sqrt{\mathbb{V}[\hat{X}]\mathbb{V}[Y]}}$. It is evident that a

higher correlation between \hat{X} and \hat{Y} would lead to a variance reduction.

10.3.2. Multi-fidelity (MF) reliability estimator

The proposed MF reliability analysis method incorporates HF and LF model information based on the aforementioned CV technique. Initially, considering that failure regions of HF and LF models exhibit a certain level of overlap, the biasing density $q_L(\mathbf{x}, \mathbf{v})$ constructed from LF model data is used for IS estimation on the HF model. The corresponding estimator is denoted as $\hat{P}_{f, \text{MH}}^{\text{CEIS}}$. Assuming that the sample size is N_H at each intermediate level in the CEIS-based biasing density construction procedure, i.e., M in Eq. (10-15), $\hat{P}_{f, \text{MH}}^{\text{CEIS}}$ can be estimated as Eq. (10-23):

$$\hat{P}_{f, \text{MH}}^{\text{CEIS}} = \frac{1}{N_H} \sum_{i=1}^{N_H} \frac{\mathbb{I}_H(\mathbf{x}_i) p(\mathbf{x}_i)}{q_L(\mathbf{x}_i, \mathbf{v})} \quad (10-23)$$

It is anticipated that N_H is not large considering the fact that evaluating the HF model is generally much more expensive than evaluating the LF model. Meanwhile, another LF model-based reliability estimator $\hat{P}_{f, \text{L}}$ is introduced. Due to the LF model's cost-effectiveness, a much larger sample size is feasible than the sample used for the estimation of $\hat{P}_{f, \text{MH}}^{\text{CEIS}}$. This estimator can be computed by using methods such as IS, SubSim, DS, or LS mentioned previously. In this study, the CEIS approach from Section 10. 2 is employed for this purpose. With a large sample size, $\hat{P}_{f, \text{L}}$ would have significantly lower variance than $\hat{P}_{f, \text{L}}^{\text{CEIS}}$. Finally, the proposed reliability estimation $\hat{P}_f^{\text{CEIS}\alpha}$ is formulated as Eq. (10-24):

$$\hat{P}_f^{\text{CEIS}\alpha} = P_{f, \text{MH}}^{\text{CEIS}} + \hat{\alpha}^* \left(\hat{P}_{f, \text{L}}^{\text{CEIS}} - P_{f, \text{L}} \right) \quad (10-24)$$

In a sample version, $\hat{P}_f^{\text{CEIS}\alpha}$ is expressed as Eq. (10-25):

$$\hat{P}_f^{\text{ISCE}\alpha} = \left[\frac{1}{N_H} \sum_{i=1}^{N_H} \frac{\mathbb{I}_H(\mathbf{x}_i) p(\mathbf{x}_i)}{q_L(\mathbf{x}_i, \mathbf{v})} \right] + \hat{\alpha}^* \left[\frac{1}{N_H} \sum_{i=1}^{N_H} \frac{\mathbb{I}_L(\mathbf{x}_i) p(\mathbf{x}_i)}{q_L(\mathbf{x}_i, \mathbf{v})} - P_{f,L} \right] \quad (10-25)$$

According to Eq. (10-21), the coefficient $\hat{\alpha}^*$ is approximated, as shown in Eq. (10-26):

$$\hat{\alpha}^* = - \frac{\frac{1}{N_H} \sum_{i=1}^{N_H} \left[\frac{\mathbb{I}_H(\mathbf{x}_i) p(\mathbf{x}_i)}{q_L(\mathbf{x}_i, \mathbf{v})} - \frac{1}{N_H} \sum_{i=1}^{N_H} \frac{\mathbb{I}_H(\mathbf{x}_i) p(\mathbf{x}_i)}{q_L(\mathbf{x}_i, \mathbf{v})} \right] \left[\frac{\mathbb{I}_L(\mathbf{x}_i) p(\mathbf{x}_i)}{q_L(\mathbf{x}_i, \mathbf{v})} - \frac{1}{N_H} \sum_{i=1}^{N_H} \frac{\mathbb{I}_L(\mathbf{x}_i) p(\mathbf{x}_i)}{q_L(\mathbf{x}_i, \mathbf{v})} \right]}{\frac{1}{N_H - 1} \left[\frac{\mathbb{I}_L(\mathbf{x}_i) p(\mathbf{x}_i)}{q_L(\mathbf{x}_i, \mathbf{v})} - \frac{1}{N_H} \sum_{i=1}^{N_H} \frac{\mathbb{I}_L(\mathbf{x}_i) p(\mathbf{x}_i)}{q_L(\mathbf{x}_i, \mathbf{v})} \right]^2} \quad (10-26)$$

It is emphasized here, samples \mathbf{x}_i ($i=1,2,\dots,N_H$) are drawn based on the biasing density $q_L(\mathbf{x}, \mathbf{v})$. To summarize, the proposed reliability analysis method is stated as follows:

Step #1: Construct the biasing density $q_L(\mathbf{x}, \mathbf{v})$ based on the LF model following CEIS strategy detailed in Section 10.2.2, and a corresponding reliability estimate $\hat{P}_{f,L}^{\text{CEIS}}$ is obtained by using the LF model.

Step #2: The biasing density $q_L(\mathbf{x}, \mathbf{v})$ is used for the HF model, and a corresponding HF model-based IS reliability estimate $\hat{P}_{f,MH}^{\text{CEIS}}$ is obtained as per Eq. (10-23), and the coefficient $\hat{\alpha}^*$ can be computed using Eq. (10-26).

Step #3: Compute the LF model-based estimate $\hat{P}_{f,L}$ with a large number of LF models.

Step #4: Leverage $\hat{P}_{f,L}^{\text{CEIS}}$, $\hat{P}_{f,MH}^{\text{CEIS}}$, $\hat{P}_{f,L}$, and $\hat{\alpha}^*$ using the CV technique, leading to the proposed reliability estimate $\hat{P}_f^{\text{CEIS}\alpha} = P_{f,MH}^{\text{CEIS}} + \hat{\alpha}^* \left(\hat{P}_{f,L}^{\text{CEIS}} - P_{f,L} \right)$.

The flowchart of the proposed reliability analysis method is schematically shown in Figure 10-1.

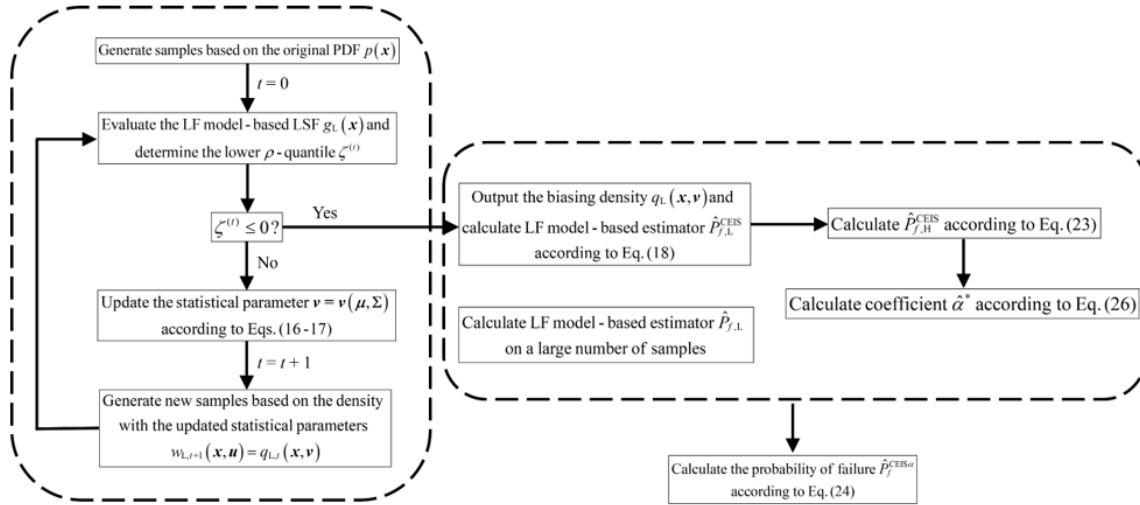


Figure 10-1. Flowchart of the proposed reliability analysis method

10.4. NUMERICAL EXAMPLES

In this section, four numerical examples are illustrated to show the performance of the proposed reliability analysis method. To show the generalization of the proposed method, LF models considered in this study include various commonly used simplified models in structural engineering applications, including finite element (FE) model with coarse mesh, data-based regression model, and structural analysis model with simplified physics. The proposed MF reliability estimation strategy is compared with following methods:

(1) HF-MCS $\hat{P}_{f,H}^{MCS}$: HF model-based crude MCS method $\hat{P}_{f,H}^{MCS} = \frac{1}{N} \sum_{i=1}^N \mathbb{I}_H(\mathbf{x}_i)$

(2) LF-MCS $\hat{P}_{f,L}^{MCS}$: LF model-based crude MCS method $\hat{P}_{f,L}^{MCS} = \frac{1}{N} \sum_{i=1}^N \mathbb{I}_L(\mathbf{x}_i)$

(3) HF-CEIS $\hat{P}_{f,H}^{\text{CEIS}}$: HF model-based cross-entropy importance sampling method

$$\hat{P}_{f,H}^{\text{CEIS}} = \frac{1}{N} \sum_{i=1}^N \frac{\mathbb{I}_H(\mathbf{x}_i) p(\mathbf{x}_i)}{q_H(\mathbf{x}_i, \mathbf{v})}$$

(4) MF-CEIS: Cross-entropy importance sampling method without control variate

$$\hat{P}_{f,MH}^{\text{CEIS}} = \frac{1}{N_H} \sum_{i=1}^{N_H} \frac{\mathbb{I}_H(\mathbf{x}_i) p(\mathbf{x}_i)}{q_L(\mathbf{x}_i, \mathbf{v})}, \text{ i.e., Eq. (10-24).}$$

(5) MF-CEIS α (proposed in this study): Multi-fidelity cross entropy importance sampling

estimator with control variate, i.e., $\hat{P}_f^{\text{CEIS}\alpha} = P_{f,MH}^{\text{CEIS}} + \hat{\alpha}^* (P_{f,L}^{\text{CEIS}} - P_{f,L})$.

500 replicate runs are performed for each numerical example. The quality of estimators is evaluated in terms of the root mean square error (RMSE), relative absolute error (ε), and coefficient of variation (COV). By assuming the reference probability of failure is P_f , and the one single estimation obtained from replicate runs is denoted as \hat{P}_f^i ($i = 1, 2, \dots, 500$), RMSE, ε , and COV are calculated as Eqs. (10-27)(10-28)(10-29):

$$\text{RMSE} = \sqrt{\frac{1}{N_{rep}} \sum_{i=1}^{N_{rep}} (\hat{P}_f^i - P_f)^2} \quad (10-27)$$

$$\varepsilon = \left| \frac{\bar{\hat{P}}_f - P_f}{P_f} \right| \quad (10-28)$$

$$\text{COV} = \frac{\sqrt{\frac{1}{N_{rep} - 1} \sum_{i=1}^{N_{rep}} (\hat{P}_f^i - \bar{\hat{P}}_f)^2}}{\bar{\hat{P}}_f} \quad (10-29)$$

where $N_{rep} = 500$; and \bar{P}_f is the mean of replicate estimates: $\bar{P}_f = \frac{1}{N_{rep}} \sum_{i=1}^{N_{rep}} P_f^i$

10.4.1. Example #1: Cantilever beam

This section examines an isotropic linear elastic cantilever beam. This example was inspired by the example presented in Ferreira (2009), and the reliability problem was formulated to have a probability of failure of interest. The beam has dimensions of 5 m in length and 1 m in height. It is subjected to a concentrated load (P) at the free end. The elastic modulus (E) of the beam and the magnitude of external load (P) are considered as random variables, with their probability distributions and statistical properties detailed in Table 10-1. The structural analysis is conducted using a Finite Element software package implemented in MATLAB (Ferreira 2009). A 2D four-node plane stress quadrilateral element is used for the modeling of the beam. The HF model employs a finer mesh size of 50×10 shown in Figure 10-2(a), while a coarser mesh size of 10×2 is used for the LF model, as illustrated in Figure 10-2(b). The failure is defined when the vertical deflection at the free end exceeds 8 mm, and the associated LSF is specified in Eq. (10-30):

$$g_H(\mathbf{x}) = 8 - \Delta \quad (10-30)$$

Table 10-1. Statistics of random variables for the cantilever beam in Example #1

Variable	Distribution	Mean	Standard deviation
E (Pa)	Normal	3e10	7.5e9
P (N)	Normal	1e5	1e4

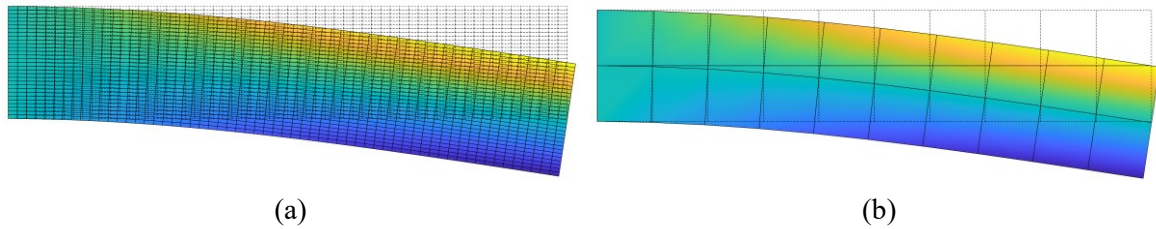


Figure 10-2. Cantilever beam under a concentrated vertical load at the free end: (a) HF model with a finer mesh, and (b) LF model with a coarser mesh

The reference solution for the probability of failure, obtained through crude MCS with a sample size of 10^6 on the HF model, is 7.691×10^{-4} . In comparison, the probability of failure estimated by the LF model using the same sample size is 5.519×10^{-4} , indicating an absolute relative error of 28.2%. This significant discrepancy highlights the influence of mesh density on the reliability analysis for the problem considered.

To provide further insights into the proposed methodology, a specific case is illustrated in Figure 10-3. In Step #1, the samples generated via the CEIS method are depicted in Figure 10-3 (a). For this example, the quantile ratio ρ is determined as 0.1. And correspondingly, five intermediate levels are needed to establish the final biasing density $q_L(\mathbf{x}, \mathbf{v})$, resulting in a total of 40000 LF model evaluations (with 8000 evaluations at each level). The PDFs of beam deflection at various intermediate failure levels are shown in Figure 10-3 (b), demonstrating an increased concentration of sampling points in the failure region as the statistical parameters of the biasing density are adapted. After five iterations, the established density $q_L(\mathbf{x}, \mathbf{v})$ serves as the IS biasing density for the HF model, with the estimated PDF represented by a black line shown in Figure 10-3 (b). Subsequently, the CV coefficient $\hat{\alpha}^*$ can be evaluated based on the PDFs corresponding to two cases ‘LF: $t = 5$ ’ and ‘HF: $t = 5$ ’ shown in Figure 10-3 (b). In Step #3, a large sample size

of 3×10^5 (10 times greater than that used in Step #1) is employed to estimate $\hat{P}_{f,L}$. Finally, the proposed estimator is evaluated in Step #4 by integrating results in the previous three steps, as previously detailed.

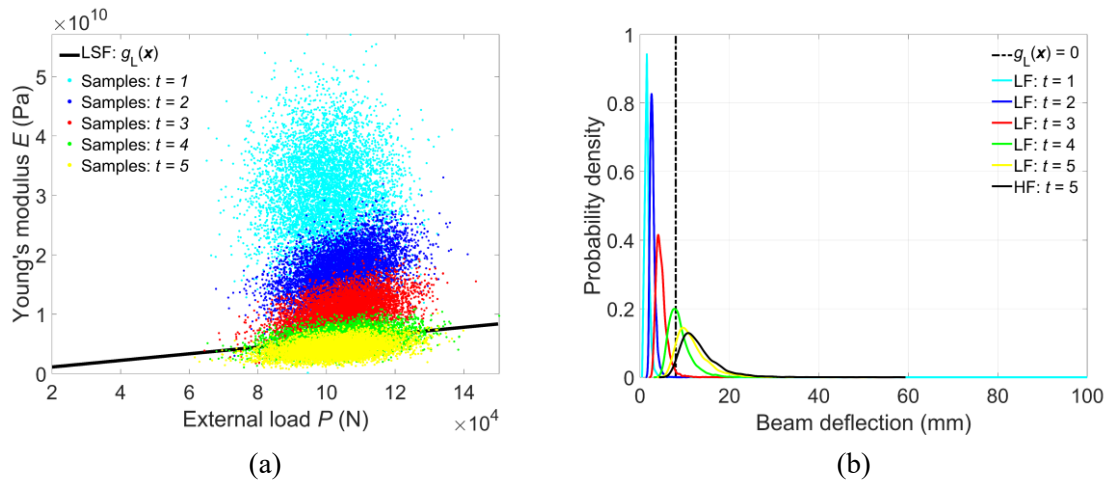


Figure 10-3. Illustration of proposed method: (a) generated samples on the LF model at different intermediate levels, and (b) corresponding probability densities of beam deformation at different intermediate levels for LF and HF models in Example #1

Table 10-2 presents the COV and ε obtained by replicate runs using different methods, with sample size for the HF and LF models evaluated. Notably, for the proposed method MF-CEIS α , the sample size on HF model is identical to MF-CEIS. However, the LF model is 10 times greater than that of MF-CEIS, due to the integration of LF model-based estimator $\hat{P}_{f,L}$. By comparing the results in Table 10-2, it is evident that MF-ISCE α achieves the smallest COV and ε among all methods evaluated. Notably, much fewer samples are required compared to HF-MCS, LF-MCS, HF-CEIS, MF-CEIS α , while more LF models are needed relative to MF-CEIS. However, the influence of more LF model evaluations is limited to the overall computational burden, which will be detailed subsequently.

Table 10-2. Reliability analysis results for Example #1

Method	Sample size (HF+ LF)	\bar{P}_f	COV (%)	ε (%)	
HF-MCS	10^6	7.691×10^{-4}	3.60	-	
LF-MCS	10^6	5.519×10^{-4}	4.24	28.2	
HF-CEIS	4×10^4	7.630×10^{-4}	19.9	5.78	
MF-CEIS	$8 \times 10^3 + 4 \times 10^4$	7.579×10^{-4}	4.77	1.46	
MF-CEISα	$8 \times 10^3 + 4.4 \times 10^5$	7.657×10^{-4}	2.03	0.44	further

To elucidate the superiority of MF-ISCE α , Figure 10-4 provides a comparative analysis of RMSE and COV at varying computational costs. The computational costs here are defined in relation to the sample size and computational time used for the model running. One single evaluation for the HF and LF models are normalized to 1 and 6.5×10^{-4} , respectively, based on their proportional CPU time requirements (32.3 seconds for the HF model and 0.021 seconds for the LF model). For instance, for the MF-ISCE α estimation shown in Table 10-2, the total computational cost is calculated as $8000 + 4.4 \times 10^5 \times 6.5 \times 10^{-4} \approx 8286$. It can be seen that more LF model evaluations do not lead to a significant increase in the computational cost due to its cost-effectiveness. The LF model-based reliability estimation is excluded in Figure 10-4 as it involves a substantial inherent bias. As illustrated in Figure 10-3 (a), MF-ISCE α demonstrates exceptional performance, providing the lowest RMSE at any given computational cost, signifying its capacity to deliver accurate estimations efficiently. Figure 10-3 (b) further exhibits the advantages of MF-ISCE α , where a marked reduction in COV is observed with increasing computational effort, reaffirming its precision and reliability.

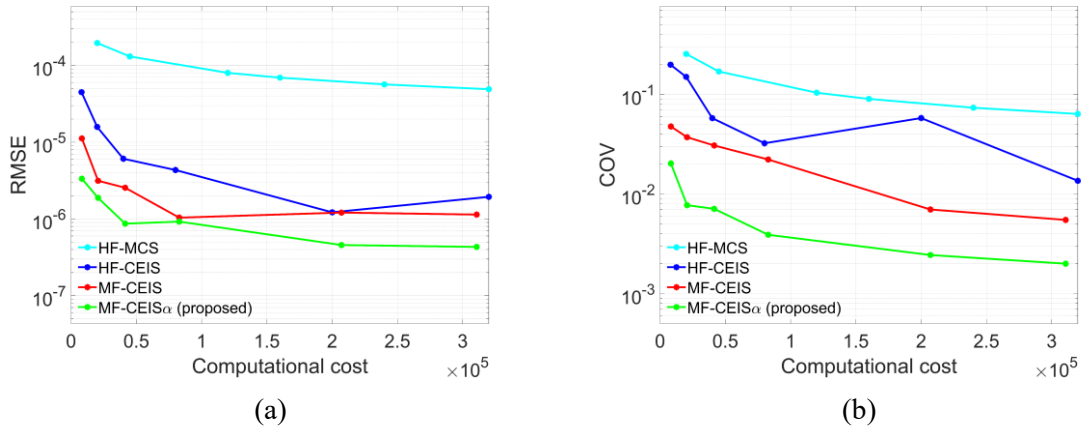


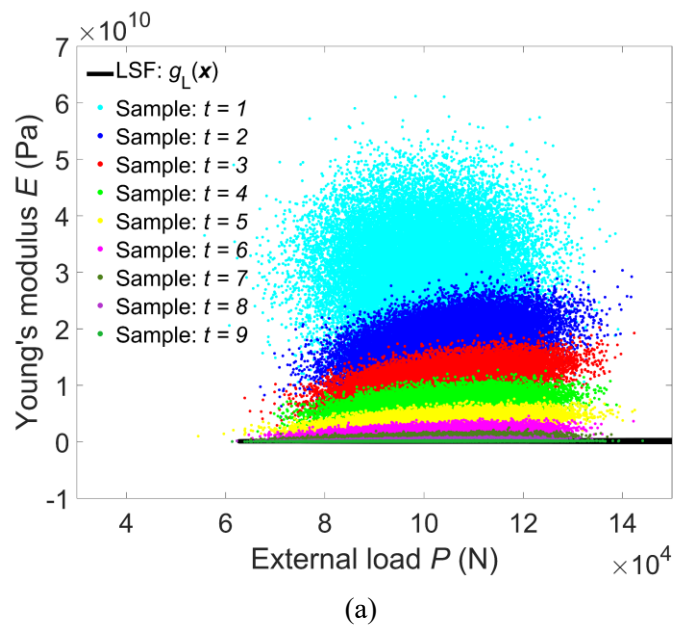
Figure 10-4. Comparison of reliability analysis results for Example #1 in terms of: (a) RMSE, and (b) COV

10.4.2. Example #2: Cantilever beam (rare event analysis)

The example discussed in Section 10.4.1 is revisited here. The main purpose is to investigate the applicability of MF-ISCE α to the problem with small probability of failure, i.e., rare event analysis. This analysis maintains the same parameters as Example #1, except for the definition of LSF. In this case, the maximum allowable deflection is set as 300 mm. Thus, corresponding LSF is re-defined as $g_H(x) = 300 - \Delta$. A crude MCS with a sample size of 10^9 on the HF model is performed to get the reference solution for the probability of failure 3.120×10^{-6} , while this estimate is 2.773×10^{-6} by relying on the LF model.

Given the nature of rare event analysis, a larger sample size is anticipated to be required to obtain a reasonable estimate. Therefore, at each intermediate level, a sample size of 3×10^4 is utilized for both MF-CEIS and MF-CEIS α , with the quantile ratio ρ being 0.1. The analysis results indicate that nine intermediate levels are needed to establish the final biasing density. This leads to a total of 2.7×10^5 LF model evaluations, with the generated samples and corresponding PDFs of beam deflection shown in Figure 10-5 (a) and (b), respectively. Moreover, 2.7×10^6 samples

are used for the estimation of $\hat{P}_{f,L}$, and the equivalent computational cost for these LF model evaluations is approximately only 1755 HF model runs. Again, the results summarized in Table 10-3 shows the significant outperformance of proposed estimator in terms of both COV and ε for the rare event analysis than other methods evaluated in this study. The relationships of RMSE (COV) and computational cost are shown in Figure 10-6, revealing the efficiency of MF-ISCE α in yielding accurate estimations in scenarios with low probability of failure.



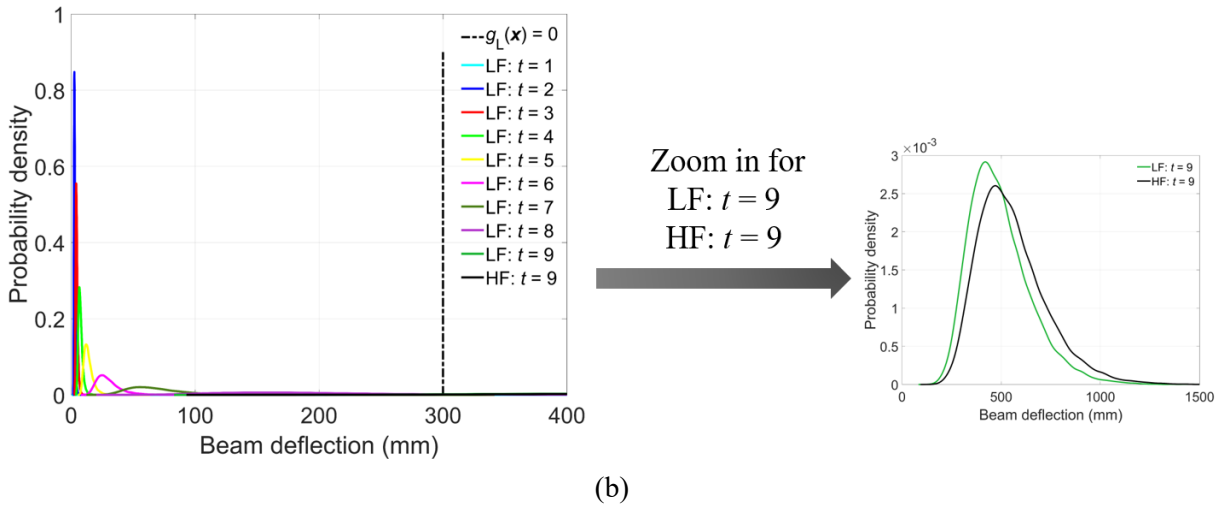


Figure 10-5. Illustration of proposed method: (a) generated samples on the LF model at different intermediate levels, and (b) corresponding probability densities of beam deformation on LF and HF models in Example #2

Table 10-3. Reliability analysis results of the cantilever beam in Example #2

Method	Sample size (HF + LF)	\hat{P}_f	COV (%)	ε (%)
HF-MCS	10^9	3.120×10^{-6}	1.79	-
LF-MCS	10^9	2.773×10^{-6}	1.90	11.1
HF-CEIS	3×10^5	2.967×10^{-6}	11.4	4.90
MF-CEIS	$3 \times 10^4 + 2.7 \times 10^5$	2.994×10^{-6}	8.39	4.04
MF-CEISα	$3 \times 10^4 + 2.97 \times 10^6$	3.115×10^{-6}	0.62	0.15

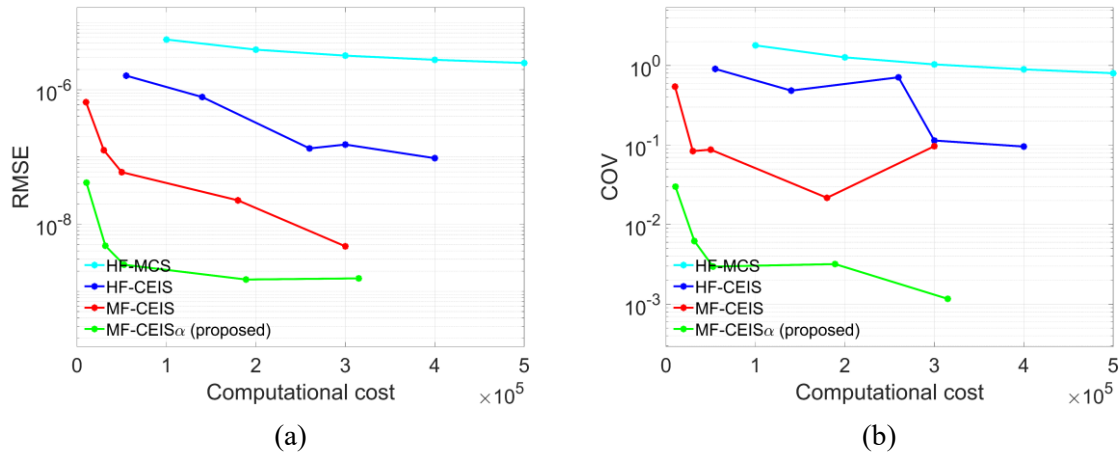


Figure 10-6. Comparison of reliability analysis results for Example #2 in terms of: (a) RMSE, and (b) COV

10.4.3. Example #3: A ten-bar truss structures

In this section, a ten-bar truss structure (Wei and Rahman 2007) is examined, as shown in Figure 10-7. The truss structure is subjected to two identical concentrated loads, each with a magnitude of 445 kN (100000 lb). Each of the ten bars has a Young's modulus of 69 GPa (10^7 psi). The random variables considered are the cross-sectional areas for each bar, and thus a total of 10 variables are considered. They are statistically independent, following a normal distribution truncated at 0 mm², with a mean of 1613 mm² (2.5 inch²) and a standard derivation of 323 mm² (0.5 inch²). The performance function is defined by the vertical displacement at point 'A', denoted as Δ_A . The maximum allowable vertical displacement is 590 mm (22.4 inch), and the LSF for the ten-bar truss structure is defined as per Eq. (10-31):

$$g_H(\mathbf{x}) = 590 - \Delta_A \quad (10-31)$$

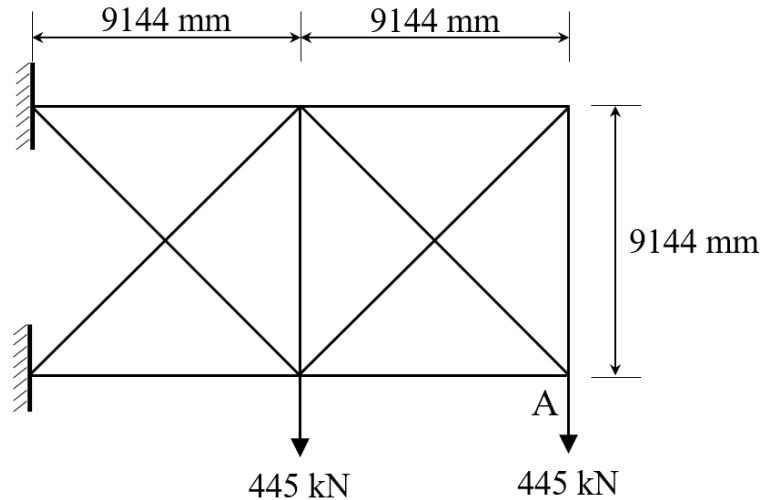


Figure 10-7. A ten-bar truss structure

The HF model is evaluated using CALFEM (Dahlblom et al. 1986), a linear elastic structural analysis program implemented in MATLAB (2021). A reference solution of $P_f = 1.002 \times 10^{-3}$ is obtained through the crude MCS by running 10^6 HF models. The LF model used in this numerical example is a data-fitted model, which is constructed using a multivariate polynomial regression analysis of 5th degree. A dataset comprising 2000 HF samples, generated through the space-filled sampling technique, i.e., Halton' Sequence Sampling (Halton 1994), is employed to construct the LF model. The probability of failure obtained through the LF model is 9.551×10^{-4} . The normalized computational costs for one single HF and LF evaluation are 1 and 4.141×10^{-5} , respectively.

Table 10-4 details the reliability analysis results from various methods and the corresponding sample sizes used. Notably, MF-CEIS α achieves an accurate estimate with only 4000 HF model and 88000 LF model runs and exhibits the smallest ϵ . It is worth mentioning that the training dataset (2000 HF samples) used for the construction of the LF model is also counted in the sample size. Thus, only 2000 HF models are effectively used in the reliability analysis

procedure. By comparison, HF-CEIS achieves a similar level of accuracy with 8000 HF model runs, while MF-CEIS requires 80000 fewer LF model runs to achieve a comparable ε . However, both HF-CEIS and MF-CEIS predictions show significantly higher variance, as evidenced by the COV in Table 10-4. Figure 10-8 presents the variation of RMSE and COV in relation to the computational costs. It is observed that with increased computational cost, MF-CEIS and MF-CEIS α exhibit similar RMSE, but MF-CEIS demonstrates much higher variance at the same computational cost.

Table 10-4. Reliability analysis results for the ten-bar truss structure in Example #3

	Sample size (HF + LF)	\bar{P}_f	COV (%)	ε (%)
HF-MCS	10^6	1.002×10^{-3}	3.14	-
LF-MCS	10^6	9.551×10^{-4}	6.83	4.68
HF-CEIS	8000	9.968×10^{-4}	45.8	0.52
MF-CEIS	4000* + 8000	9.957×10^{-4}	26.7	0.63
MF-CEIS α	4000* + 88000	9.970×10^{-4}	7.19	0.49

*: 2000 HF samples used for the construction of LF model is included in the sample size. Thus, only 2000 HF samples are used in the reliability evaluation procedure.

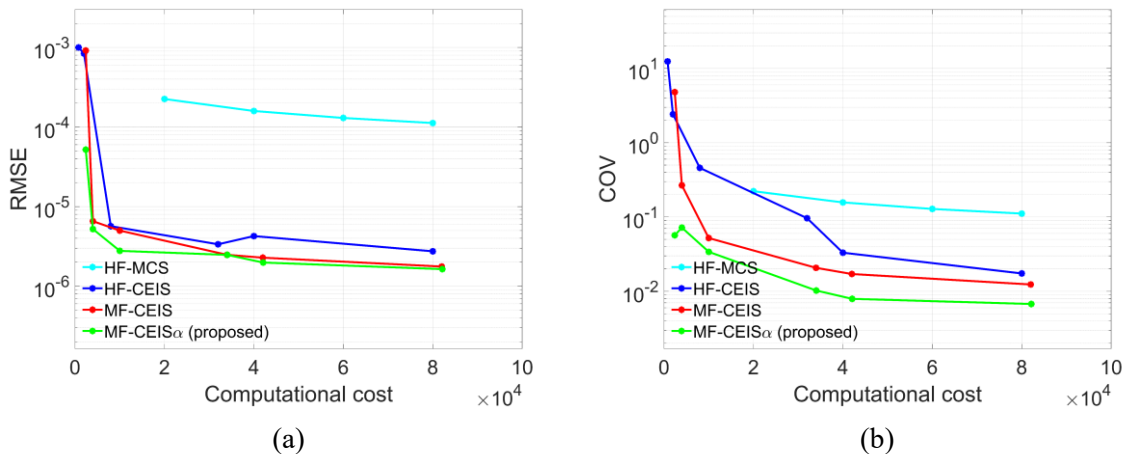


Figure 10-8. Comparison of reliability analysis results for Example #3 in terms of: (a) RMSE, and (b) COV

10.4.4. Example #4: A three-bay three-story frame structure

A three-bay by three-story steel frame investigated in (Haukaas and Scott 2006) is studied in this section. The frame structure is subjected to lateral loads as shown in Figure 10-9. The material model of each member is represented by a uniaxial bilinear hardening model shown in Figure 10-10. This model is characterized by a Young's modulus E , a yield strength f_y , an ultimate strength f_u and an ultimate strain ϵ_u .

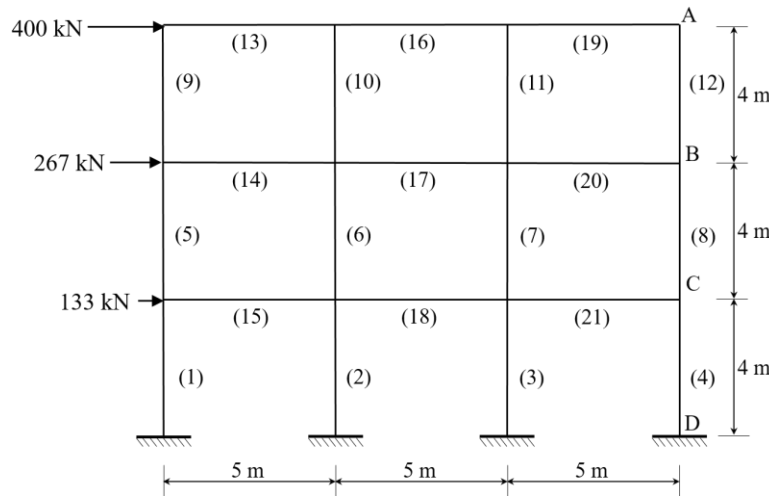


Figure 10-9. A three-bay by three-story frame structure

The frame structure comprises 21 members, and the member IDs are shown in Figure 10-9. All members feature a rectangular section with a length B and a height H . In this example, beam members at the same height and within the same bay possess identical material property. To be specific, members (1) ~ (4), (5) ~ (8), (9) ~ (12), (13) ~ (15), (16) ~ (18), and (19) ~ (21) have identical properties. Young's modulus E , width B , and height H are considered as independent random variables for each group of members. Corresponding statistical information is detailed in Table 10-5. Thus, a total of $6 \times 3 = 18$ random variables are considered. The yield strength f_y is considered to be correlated deterministically with Young's modulus $f_y = 500 \cdot E$, and the ultimate

strength f_u is assumed to be $f_u = 1.2 f_y$, and the corresponding ultimate strain ϵ_u is assumed to be 0.2. The HF model is developed in the general Finite Element (FE) software package ABAQUS (Dassault Systemes 2017) using two-dimensional Timoshenko beam elements through which the shear deformation could be accounted for. Additionally, geometrical nonlinearity is considered. Each structural member is discretized as 5 elements, leading to a relatively finer mesh configuration.

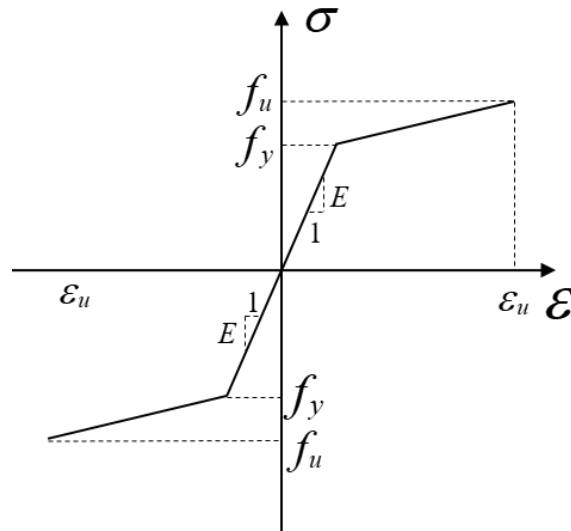


Figure 10-10. Stress-strain curve for the steel member considered in Example #4

Table 10-5. Statistics of the random variables for the plastic frame in Example #4

Variable	Distribution	Mean	Standard deviation
B_i (mm)*	Truncated Normal	100	2
H_i (mm)*	Truncated Normal	250	5
$f_{y,i}$ (MPa)*	Truncated Normal	400	20

* Subscript 'i' ($i = 1, 2, 3, 4, 5, 6$) represents the each group of random variables.

In the LF model, a two-dimensional Euler-Bernoulli beam element is used, with only 2 elements considered for each member, and the geometrical nonlinearity is neglected. The material parameters and corresponding statistics are identical to those in the HF model. The LSF considered for the steel frame structure is related to the interstory drift ratio (IDR). By assuming the maximum

allowable IDR equal to 0.25%, and denoting the horizontal displacements at points ‘A’, ‘B’, and ‘C’ as Δ_A , Δ_B , and Δ_C , respectively, the LSF is defined as per Eq. (10-32):

$$g_H(\mathbf{x}) = 0.25\% - \max(\Delta_A - \Delta_B, \Delta_B - \Delta_C, \Delta_C) / H \quad (10-32)$$

where H is the story height, equal to 4 m.

A crude MCS with a HF sample size of 10^6 leads to a reference solution for probability of failure equal to 1.337×10^{-3} . In comparison, the LF model-based estimation by using the same sample size is 9.150×10^{-4} . The reliability analysis results with certain sample sizes are shown in Table 10-6. Similarly, more LF samples leveraged in the MF-CEIS α contributes the accuracy improvement in predicting the probability of failure, and the variance is significantly reduced compared to MF-CEIS. While HF-CEIS estimation relying on 20000 HF samples exhibits much larger error and variance. The relationship between RMSE (COV) and computational costs are shown in Figure 10-11. Again, MF-CEIS α demonstrates superior performance in both RMSE and COV. With fewer samples, MF-CEIS α exhibits smaller error and variance.

Table 10-6. Reliability analysis results for the steel frame in Example #4

	Sample size (HF + LF)	\bar{P}_f	COV (%)	ε (%)
HF-MCS	10^6	1.337×10^{-3}	2.73	-
LF-MCS	10^6	9.150×10^{-4}	3.33	31.6
HF-CEIS	20000	1.103×10^{-3}	46.5	17.5
MF-CEIS	15000 + 75000	1.313×10^{-3}	15.4	1.80
MF-CEISα	15000 + 825000	1.320×10^{-3}	4.67	1.27

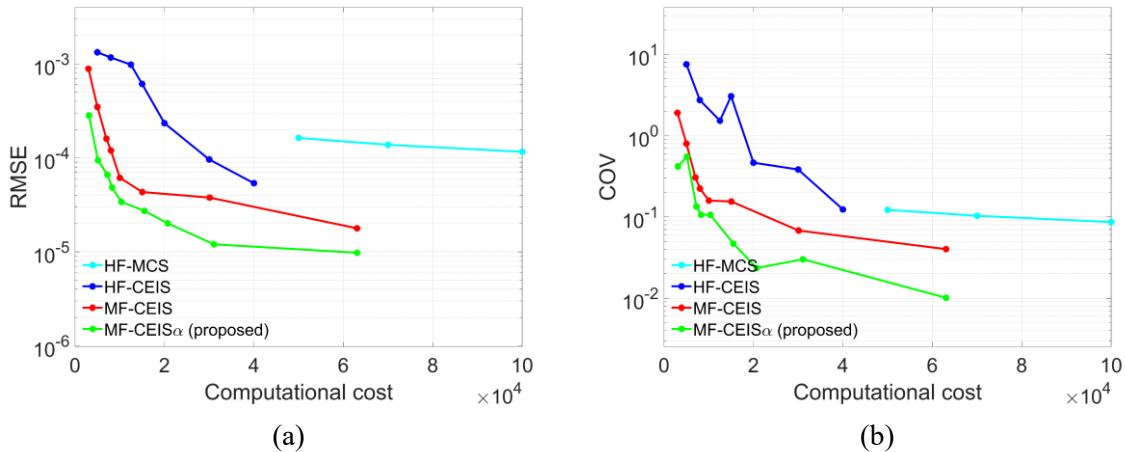


Figure 10-11. Comparison of reliability analysis results for Example #4 in terms of: (a) RMSE, and (b) COV

10.5. RELIABILITY ANALYSIS OF REINFORCED MASONRY WALLS UNDER OUT-OF-PLANE LOADING

10.5.1. Details of the RM wall

The studied RM wall is fully grouted with the height of 3000 mm and the thickness of 190 mm. Concrete masonry units have standard dimensions of 390 mm \times 190 mm \times 190 mm, and the thickness of mortar layer is 10 mm. Reinforcing bars are located at the mid-thickness of the wall, with a reinforcement ratio of 0.0019 and a spacing at 200 mm. This reinforcement ratio intends to ensure the simultaneous yielding of the bars and the critical fiber in the cross-section reaching the crushing strain for the pure-bending case (Moosavi 2017). The RM wall is subjected to an eccentric axial load ratio of 1, and pinner-roller boundary condition (i.e., one-way vertically spanning). The eccentric axial load is applied with an eccentric-to-thickness ratio of 1.0.

10.5.1.1 HF model

The high-fidelity (HF) model utilized in this example is developed using a macro element approach, which is sufficiently accurate for RM walls under OOP loading. To simulate the RM wall, a fiber-based beam element technique available in OpenSees (McKenna et al. 2000) is

employed. The considered RM wall is modeled using displacement-based fiber beam elements, and four integration points are considered for each element. Each integration is assigned with a generalized fiber section consisting of masonry and steel. This methodology enables the integration of the nonlinear behavior of RM sections, considering the distinct nonlinear constitutive properties of each fiber. In this configuration, masonry fibers are modeled using the *Concrete02* model, while steel fibers are depicted using the *Steel01* model. The applicability of this model in reproducing the OOP behavior of masonry walls is well validated in relevant studies (Metwally et al. 2022). In the HF model, the eccentric loading is applied through a rigid beam with a length equals to the load eccentricity.

10.5.1.2 LF model

In this example, LF model is developed following the guidelines of the Canadian design code CSA S304-14 (2014). It should be noted that the OOP capacity of RM walls in this context is determined based on the moment magnifier method, considering the fact that studied RM wall exhibits a slenderness ratio of 18. In the moment magnified method, the maximum moment demand is magnified by a factor. More details about the calculation of OOP capacity based on CSA S304-14 and associated consideration of slenderness effects are detailed in Appendix F.

10.5.2. Demand and resistance calculation

10.5.2.1 Uncertainty in the resistance

The independent material properties considered include the compressive strength of masonry f_m , the yield strength f_y and the Young's modulus E of reinforcements, the location of reinforcements d . The nominal values of these parameters are shown in Table 10-7.

Table 10-7. Nominal values of material parameter considered for the RM wall

Compressive strength of masonry $f_{m,n}$ (MPa)	Yield strength of reinforcements $f_{y,n}$ (MPa)	Young's modulus of reinforcements E_n (MPa)	Reinforcement location d_n (mm)
10	400	200000	95

Other material parameters required in the HF model are assumed to be deterministic or are derived from properties shown in Table 10-7. To be specific, the peak strain (i.e., strain at compressive strength) is assumed to be 0.002. The residual compressive strength of masonry and corresponding strain are determined based on the empirical relationships proposed by Priestley and Elder (1983) for homogeneous masonry. The ultimate tensile strain is set as 0.004 (Wang et al. 1997). The strain hardening ratio of reinforcements is taken as 0.01. The statistical characterization of material parameters is derived according to their nominal values, as detailed in Table 10-8.

Table 10-8. Statistical characterization of random variables considered for the RM wall under OOP loading

Random variable	Mean	Coefficient of variation	Probability distribution	Reference
f_m	$1.6 f_{m,nominal}$	0.24	Gumbel	(Moosavi and Korany 2014) (Moosavi 2017)
f_y	$1.14 f_{y,nominal}$	0.07	Normal	(Moosavi 2017)
E	$E_{nominal}$	0.033	Normal	(Metwally et al. 2022)
d	$d_{nominal}$	$4 / d_{nominal}$	Normal	(Moosavi 2017)

10.5.2.2 Uncertainty in the load effects

The load combination considered in this example is determined according to CSA S304-14 (2014):

$$Load = 1.25DL_n + 1.5LL_n + 0.5SL_n \quad (10-33)$$

where DL_n , LL_n , SL_n denote the nominal values of dead load, live load, and snow load, respectively. The ratios between the dead load and the live load (as well as the snow load)

considered, i.e., $\alpha_{PL} = DL_n / LL_n$ and $\alpha_{PS} = DL_n / SL_n$, are 1.25, as was used for the ultimate strength design of concrete buildings (Bartlett et al. 2003).

The nominal material properties are used to calculate the design resistance $P_{r,design}$. Considering that HF model (i.e., macro element model) generally exhibited higher accuracy than the design code, the design resistance $P_{r,design}$ is obtained by the HF model. Notably, for a RM wall subjected to an eccentric loading with a deterministic eccentricity, the limit state is reached in the design process when the factored axial load is equal to the factored axial load capacity, i.e., design resistance. Subsequently, the nominal load effects can be calculated based on the design resistance. Following the load combination shown in Eq. (10-33), the nominal value of the dead load is determined as per Eq. (10-34):

$$DL_n = \frac{P_{r,design}}{1.25 + 1.5\alpha_{PL} + 0.5\alpha_{PS}} \quad (10-34)$$

where α_{PL} and α_{PS} are the load ratios. The nominal load values are used with the statistical characteristics outlined by Bartlett (2003), as shown in Table 10-9, to determine the probabilistic load effects.

Table 10-9. Statistical parameters for loads (Bartlett et al. 2003)

Load Type		Mean	Coefficient of variation	Distribution
Dead		$1.05DL_n$	0.10	Normal
Live	50-year maximum load	$0.90LL_n$	0.17	Gumbel
	Point-in-time load	$0.27LL_n$	0.68	Weibull
	Transformation to load effects	1.00	0.21	Normal
Snow	50-year maximum load	$1.10SL_n$	0.20	Gumbel
	Point-in-time load	$0.20SL_n$	0.89	Weibull
	Transformation to load effects	0.60	0.42	Lognormal

10.5.3. Reliability analysis

For the RM wall under an eccentric axial loading, the limit state function is established by comparing the applied axial load and axial load capacity. A reference solution for the probability of failure for this example is 1.763×10^{-4} . The solution is obtained through running 5×10^6 HF samples using the crude MCS, with the probabilistic demands and resistances shown in Figure 10-12. In comparison, when utilizing the LF model (i.e., design-code model) with an identical sample size, the reliability analysis yields a probability of failure of 3.674×10^{-4} , indicating a relative error of 108.4%.

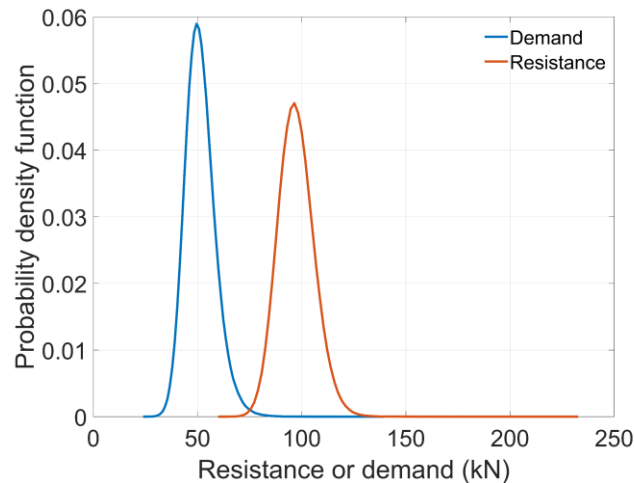


Figure 10-12. Probabilistic load effects and resistance of RM wall under OOP loading using crude MCS on the HF model

Table 10-10 displays the results of reliability analysis using various methodologies. For HF-CEIS, MF-CEIS, and MF-CEIS α , a sample size of 1000 is utilized at each intermediate level, with the quantile ratio ρ being 0.2. This setup necessitates five intermediate levels to achieve a converged biasing PDF. Regarding the four material parameters detailed in Table 10-8, their adaptive probability densities are graphically illustrated in Figure 10-13. Evidently, the probability distributions for the yield strength of reinforcements and the reinforcement location are subject to

more substantial adjustments compared to others, e.g., Young's modulus of reinforcements. From this, it can be inferred that the OOP resistances are particularly sensitive to the yield strength of reinforcements and the reinforcement location.

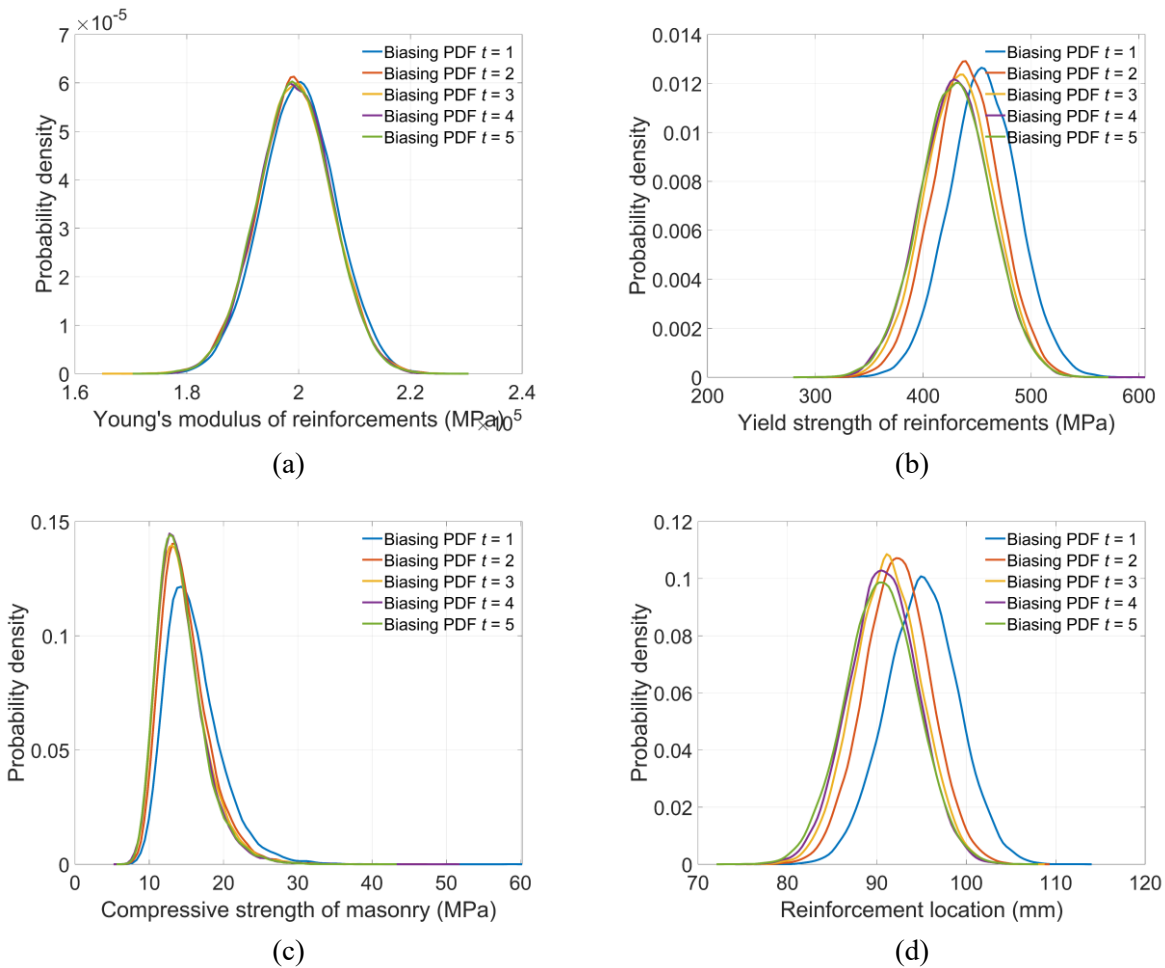


Figure 10-13. Biasing PDFs at intermediate levels in the cross-entropy adaptive sampling procedure for the RM wall under OOP loading: (a) Young's modulus of reinforcements, (b) yield strength of reinforcements, (c) compressive strength of masonry, and (d) reinforcement location

Table 10-10 reveals that the HF-CEIS method, with 5000 HF samples, leads to a solution characterized by a significant high COV, in contrast, MF-CEIS α achieves the smallest COV and ε . To illustrate the influence of sample size, the computational cost for one single evaluation of HF and LF models are normalized to 1 and 5.4×10^{-5} , respectively, based on their proportional CPU

time requirements (3.3 seconds for the HF model and 0.00018 seconds for the LF model). As illustrated in Figure 10-14 (a), MF-ISCE α demonstrates superior performance, providing the lowest RMSE at any given computational cost, especially with a relatively smaller sample size. Figure 10-14 (b) further highlights the benefits of MF-ISCE α , where a smaller COV is observed compared to other methods, reaffirming its precision and reliability.

Table 10-10. Reliability analysis results for the RM wall under OOP loading

	Sample size (HF + LF)	\bar{P}_f	COV (%)	ε (%)
HF-MCS	5×10^6	1.763×10^{-4}	7.53	-
LF-MCS	5×10^6	3.674×10^{-4}	5.22	108.4
HF-CEIS	5000	2.254×10^{-4}	577	27.9
MF-CEIS	1000 + 5000	1.674×10^{-4}	6.48	5.05
MF-CEISα	1000 + 55000	1.681×10^{-4}	2.35	4.65

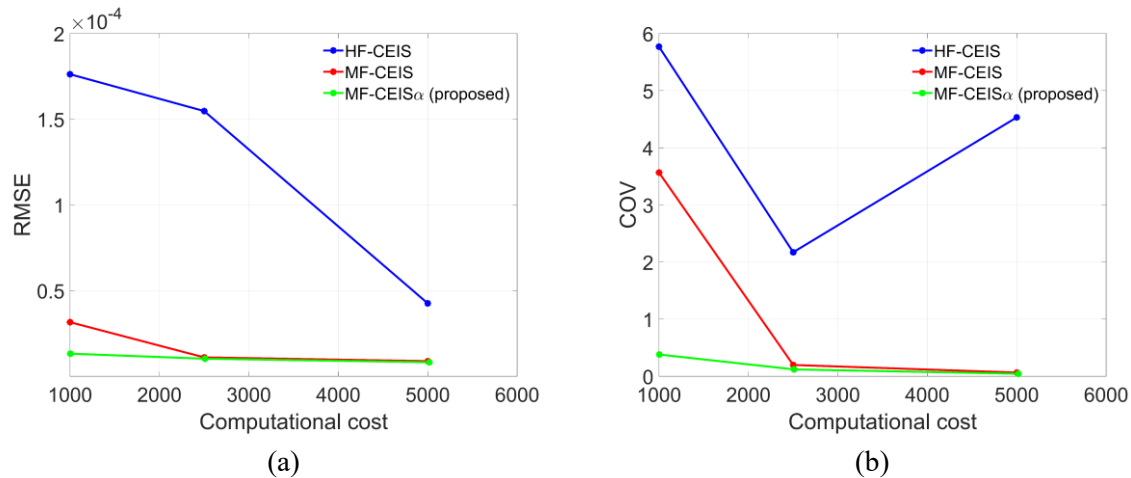


Figure 10-14. Comparison of reliability analysis results for the RM wall under OOP loading in terms of: (a) RMSE, and (b) COV

10.6. RELIABILITY ANALYSIS OF REINFORCED MASONRY WALLS UNDER IN-PLANE LOADING

10.6.1. Details of the RM wall

In this section, a fully grouted RM wall tested by Seif Eldin (2016) is utilized as an application example. The wall was designed to fail in a diagonal tension cracking mode and was tested in a

cantilever condition with a pre-compression load of 1.0 MPa. The tested RM shear wall's dimensions were 1.8 m (length) \times 1.6 m (height) \times 0.19 m (thickness). The concrete masonry units conformed to the standard dimensions of 390 mm \times 190 mm \times 190 mm. The vertical reinforcements consisted of 20M bars (with a 300 mm² cross sectional area) in every cell, while the horizontal reinforcements featured uniformly distributed 10M bars (with a 100 mm² cross-sectional area) spaced at 400 mm. The corresponding horizontal and vertical reinforcement ratios were 0.13% and 0.79%, respectively.

10.6.1.1 HF model

HF model for the RM wall is developed based on the simplified micro modeling strategy (Page 1978). Within this approach, the mortar layer plus its associated unit-mortar interactions is lumped into a single zero-thickness interface. Mortar joints are simulated using zero-thickness interface elements COH3D8 in ABAQUS (Dassault Systemes 2017), in conjunction with a recently developed constitutive model by the authors (Li and Zeng 2023). This newly developed constitutive model is characterized by two yield surfaces (i.e., tension-shear yield surface f_1 and compression cap surface f_2) and is capable of capturing various failure modes, including tensile cracking, shear sliding, and compressive crushing. Concrete blocks and grouts are modeled using the C3D8 element plus the nonlinear behaviors represented via the Concrete Damage Plasticity (CDP) model (Lee and Fenves 1998), in which tensile cracking and compressive crushing can be well described using different parameters for concrete units and grouts. Reinforcing bars in RM walls are modeled using the truss element T3D2 with the von Mises plasticity model and a bilinear hardening law. A perfect bond is assumed for grout and steel reinforcement in RM walls.

10.6.1.2 LF model

The LF model for the calculation of IP resistance of RM walls is based on the Canadian masonry design code CSA S304-14 (2014). RM walls under IP loading may exhibit three different failure modes: flexural rocking, diagonal tension cracking, and shear sliding. In design practices, IP resistance corresponding to each of these three failure modes is evaluated individually based on (semi-) empirical or simplified analytical models/methods, with the one presenting the lowest value being the governing failure mode. In CSA S304-14 (2014), shear sliding resistance is evaluated based on the Mohr-Coulomb relationship, and the IP resistance of masonry walls governed by diagonal tension cracking is assessed using a semi-empirical relationship. On the other hand, the flexural capacity is evaluated based on the cross-sectional capacity, using the equivalent rectangular block by assuming zero tensile strength of masonry. The code provisions of CSA S304-14 for the prediction of IP resistances of RM walls are detailed in Appendix D.

10.6.2. Reliability analysis

Material parameters considered in this application example include six statistically independent variables: tensile strength f_t and frictional coefficient $\tan\phi$ of interfaces (mortar joints), compressive strength of units f_c^u , compressive strength of grouts f_c^g , and yield strength of reinforcements f_y . The nominal values of these parameters are detailed in Table 10-11. Other required material parameters are correlated with these four parameters, using well-established relationships, as summarized in Table 10-12. Accordingly, the randomness of material parameters is related to the nominal values, with the information summarized in Table 10-13.

Table 10-11. Statistical characterization of material parameters for the RM wall under IP loading

Parameters	Nominal value
------------	---------------

Compressive strength of units $f_{c,n}^u$ (MPa)	15
Compressive strength of grouts $f_{c,n}^g$ (MPa)	30
Yield strength of reinforcements $f_{y,n}$ (MPa)	400
Tensile strength of mortar joints $f_{t,n}$ (MPa)	0.3
Frictional coefficient of mortar joints $\tan \varphi_n$	0.7

Table 10-12. Empirical relationships of material parameters for the RM wall under IP loading

Parameters	Relationship
Masonry Units	
Tensile strength f_t^u (MPa)	$f_t^u = 0.09 f_c^u$
Elastic modulus E_u (MPa)	$E_u = 938 f_c^u$
Grouts	
Elastic modulus E_g (MPa)	$E_g = 500 f_c^g$
Tensile strength f_t^g (MPa)	$f_t^g = 0.24 f_c^g$
Reinforcements	
Elastic modulus E_y (MPa)	$E_y = 456 f_y$
Ultimate strength f_u (MPa)	$f_u = 1.2 f_y$
Mortar joints (interfaces)	
Mode I fracture energy G_I (N/mm)	$G_I = 0.01571 f_t + 0.0004882$
Peak cohesion c_0 (MPa)	$c_0 = 1.4 f_t$
Mode II fracture energy when the normal stress is equal to zero G_{II}^0 (N/mm)	$G_{II}^0 = 10 G_I$
Compressive strength of masonry f_m' (MPa)	$f_m' = 18.46 \ln(f_c^u) - 37.71$
Stiffness constants k_m, k_{ss}, k_u (N/mm ³)	$k_m = \frac{E_u E_m}{h_m (E_u - E_m)}$ $k_{ss} = k_u = \frac{k_{nn}}{2(1 + 0.15)}$

Table 10-13. Statistical characterization of material parameters for the RM wall under IP loading

Random variable	Mean	Coefficient of variation	Probability distribution	Reference
Compressive strength of units f_c^u (MPa)	1.41 $f_{c,n}^u$	0.16	Normal	(Kazemi et al. 2011)
Compressive strength of grouts f_c^g (MPa)	1.4 $f_{c,n}^g$	0.20	Normal	Assumed
Yield strength of reinforcements f_y (MPa)	1.14 $f_{y,n}$	0.07	Normal	(Moosavi 2017)
Tensile strength of mortar joints f_t (MPa)	$f_{t,n}$	0.3	Normal	(Li et al. 2014)
Frictional coefficient of mortar joints $\tan \varphi$	$\tan \varphi_n$	0.1	Lognormal	Assumed

The load combination is considered as identical as the OOP case discussed in Section 10.6.1, with the nominal load effects derived from the nominal material parameters. For the RM wall under IP loading considered in this study, the limit state function is established by comparing the applied IP load and IP capacity. The IP load is applied horizontally at the top of the wall. For the application of the proposed reliability analysis algorithm, the LF model (i.e., Canadian masonry design code) is firstly evaluated. At each level in the CEIS procedure, 500 LF models are evaluated. This necessitates a total of five levels to reach the ultimate biasing PDF. The probability distributions of uncertain parameters at each level are shown in Figure 10-15. It should be noted that the true value for this application example is unavailable since evaluating a large number of HF models is impractical. Thus, the reliability analysis results obtained by LF-MCS, MF-CEIS and MF-CEIS α are presented here only to show the difference, or the possible improvement achieved by the proposed approach. Notably, for MF-CEIS, a total of 2500 LF samples are used (with 500 at each intermediate level). For the proposed estimator MF-CEIS α , an additional 25000 LF samples are used, leading to a total of 27500 LF model evaluations. Corresponding results are presented in Table 10-14, with the probability of failure predicted by the proposed method is 0.0078.

Table 10-14. Reliability analysis results for the RM wall under OOP loading

	Sample size (HF + LF)	\bar{P}_f
LF-MCS	1×10^6	0.0109
MF-CEIS	500 + 2500	0.0098
MF-CEISα	500 + 27500	0.0078

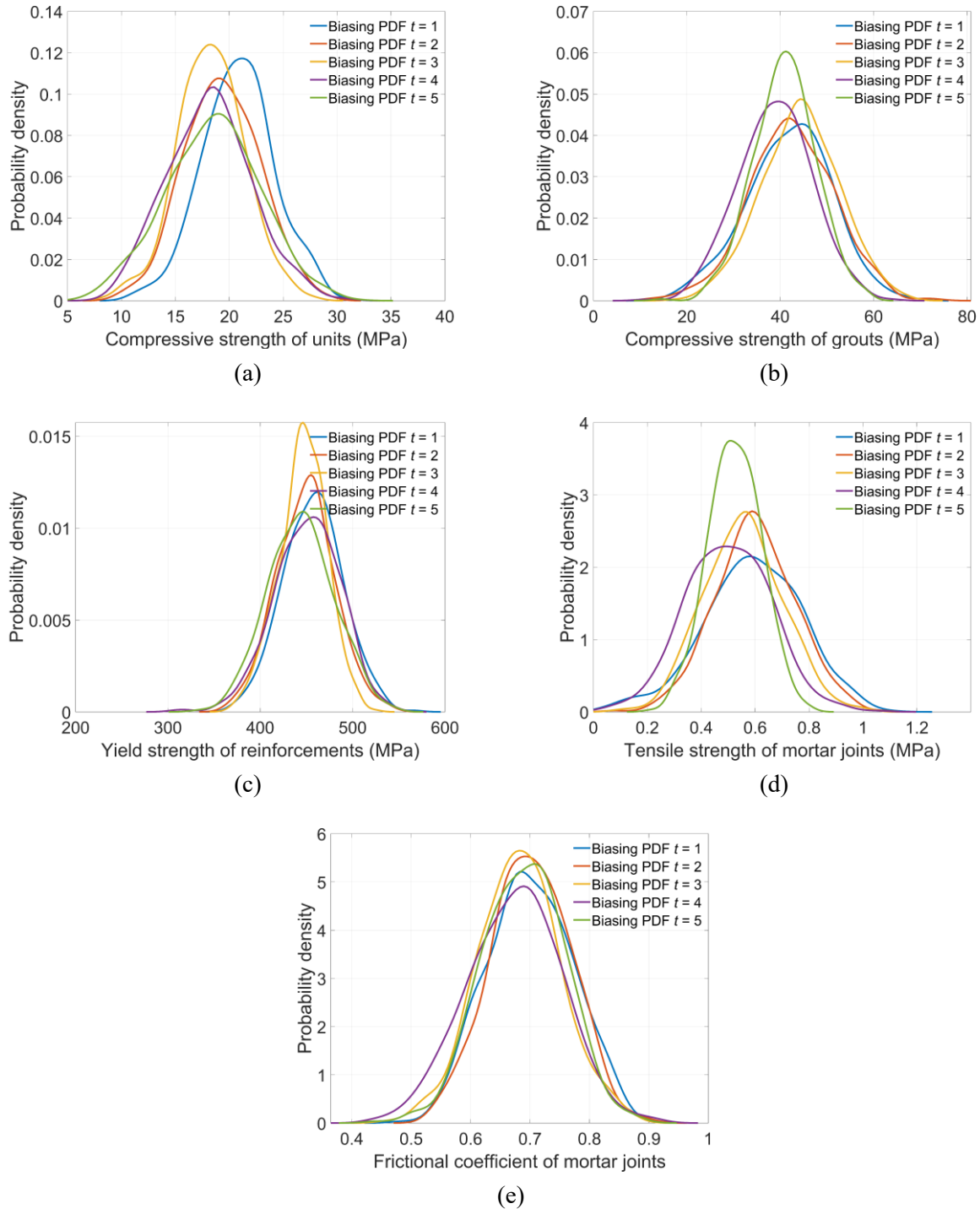


Figure 10-15. Biasing PDFs at intermediate levels in the cross-entropy adaptive sampling procedure for the RM wall under IP loading: (a) Young’s modulus of reinforcements, (b) yield strength of reinforcements, (c) compressive strength of masonry, and (d) reinforcement location

10.7. CONCLUSIONS

This chapter has presented a multi-fidelity (MF) methodology to structural reliability analysis through the integration of high-fidelity (HF) and low-fidelity (LF) models. The proposed method, underpinned by a two-step leveraging process, harmonizes the accuracy of HF models with the computational efficiency of LF models, addressing the challenges traditionally associated with reliability assessments in structural engineering. The proposed MF approach effectively navigates these challenges. Initially, it involves assessing a large number of LF models to construct a biasing density that emphasizes the failure domain. This process, facilitated by the cross-entropy adaptive importance sampling strategy, allows for a preliminary, albeit less precise, LF model-based reliability estimation. The subsequent step leverages this biasing density in an HF model-based IS reliability estimation, leading to a more accurate reliability estimator. This integration not only enhances the precision of reliability assessments but also achieves significant computational savings by reducing dependence on resource-intensive HF model evaluations. Additionally, the incorporation of the control variate (CV) technique furthers the reduction of variance in our estimates. Notably, our methodology demonstrates flexibility in the choice of LF models, including data-fit interpolation, regression models, or FE models with simplified physics.

Through detailed discussions and structural engineering examples, we have demonstrated the efficacy of our proposed method in comparison with other approaches. The results underscore the advantages of the MF approach in accurately estimating the probability of failure while mitigating computational costs and complexities.

In conclusion, this research contributes a significant advancement in the field of structural reliability analysis. By synergistically combining HF and LF models, our MF approach addresses

both accuracy and efficiency, paving the way for more resilient and performance-based designs in structural engineering. Future work may explore the extension of this methodology to a broader range of applications, further enhancing its adaptability and applicability in the ever-evolving landscape of structural engineering.

Chapter 11. CONCLUSIONS AND RECOMMENDATIONS

11.1. SUMMARY AND CONCLUSIONS

This thesis is dedicated to developing strategies to facilitate the understanding and prediction of the structural behaviors of masonry walls in both deterministic and probabilistic manners. The following summarizes the research conducted in this thesis and the conclusions derived in response to the stated research objectives:

(1) Sub-objective #1: Development of 3D constitutive models for mortar joints to facilitate the high-fidelity modeling of masonry walls

Two novel 3D multi-yield surface constitutive models for masonry mortar joints were developed. The first model, based on a computational plasticity framework, featured two hyperbolic yield surfaces adept at capturing various failure modes, including tensile cracking, shear sliding, and compressive crushing within mortar joints. In addition, an unassociated flow rule was incorporated in conjunction with a dilatancy-softening model in the proposed model to accurately capture the ‘dilatancy’ phenomenon within mortar joints. An implicit Euler backward integration algorithm, combined with a local-global Newton-Raphson (NR) solver, was adopted to achieve the predictor-corrector return mapping in the numerical formulation. The error-based auto-adaptive sub-stepping algorithm was employed to achieve robustness and efficiency in the integration procedure. Numerical validations at the masonry assemblage level showed that the developed model effectively captured stress-displacement responses, volume increases, and specimen uplift. At the structural level, the numerical-experimental comparison demonstrated reasonable agreement in terms of initial stiffness, in-plane/out-of-plane capacity, post-peak behavior, and crack patterns of

masonry walls. Notably, the study highlighted the impact of the dilatancy model on load-displacement curves, indicating that neglecting dilatancy softening led to a significant overestimation of the in-plane or out-of-plane capacity of masonry walls, whereas constant zero dilatancy tended to underestimate wall capacities. In contrast, the simulation results obtained by the proposed model with dilatancy softening had the best predictability when compared with the experimental results.

The second model, formulated within a damage-plasticity framework, focuses on the cyclic behavior of masonry mortar joints. Extending the features of the monotonic model, the cyclic model additionally included two damage scalars for the description of stiffness degradation. Additionally, two damage functions were integrated into the constitutive model formulation to describe the (tensile/cohesion/compressive) strength softening. The reliability of the proposed model was validated through simulations of various experimental tests available in the public literature, such as an indirect tensile test on a mortar jointed cylinder specimen and three masonry couplets under compression-shear loading. The validation results showed precise representations of peak capacity, strength softening, and stiffness degradation. At the structural level, two unreinforced masonry walls with different aspect ratios were simulated to assess the capability of the developed model to capture different failure modes of masonry walls (i.e., diagonal tension cracking and flexural rocking) and associated characteristics in the load deformation behaviors. The validation results indicated that using the proposed model could well predict different failure modes of masonry walls.

In conclusion, these two newly developed models have demonstrated their effectiveness in accurately predicting failure modes and load-deformation behavior of masonry walls and can be

used to simulate masonry wall behaviors with high fidelity under complex loading scenarios (e.g., under combined IP and OOP loading).

(2) Sub-objective #2: Investigation of IP-OOP interaction behavior of unreinforced and reinforced masonry walls

The structural behaviors of unreinforced masonry (URM) and reinforced masonry (RM) walls under combined IP and OOP loading were studied. This study specifically investigated the influence of aspect ratio (AR), slenderness ratio (SR), and pre-compression load (P_v) on the IP-OOP interaction behaviors in both wall types, with particular attention to the failure modes, load-deformation behaviors, and capacity interaction curves.

For URM walls, the simulation results revealed a significant reduction in IP capacity due to the presence of OOP loading, particularly in longer walls with smaller ARs and in highly slender walls. For instance, for the wall with an AR of 0.75 and SR of 9.92 without pre-compression load, when the pre-applied OOP load is at 80% of the OOP capacity, the IP capacity experienced a 37% reduction in the IP capacity. Among all the walls studied, the most substantial interaction effect was observed in the wall with the highest SR and a pre-compression load of 0.0 MPa: the IP capacity of the wall with an aspect ratio of 1.00 and a slenderness ratio of 32.24 was reduced by 61.5% when the pre-applied OOP load reached 80% of its pure OOP capacity. It should be noted that this reduction surpassed the 58% reduction suggested in ASCE 41-17 for masonry infill walls. Another notable observation was that lower values of P_v mitigated the IP-OOP interaction effects given its positive role in enhancing the sliding resistance, while higher values of P_v intensified the interaction effects. To facilitate the practical consideration of IP-OOP interaction effects of URM walls, an analytical model was proposed based on the FE simulation results. This model efficiently

predicted the IP and OOP capacity interaction curves by accounting for the influence of AR, SR, and P_v and showed superior performance compared to existing models in the public literature.

In the case of RM walls, OOP loading also led to substantial IP capacity reductions, particularly in flexural governed walls with larger ARs and lower levels of P_v . The interaction effects in flexural governed walls were less sensitive to geometrical parameters (i.e., AR, SR) and P_v compared to shear governed walls. Similar to URM walls, the most significant interaction occurred in highly slender walls without pre-compression loads, leading to a 45% reduction in IP capacity when OOP loading reached 80% of its capacity. This notable reduction was attributed to OOP instability, and it was observed that increasing P_v could effectively mitigate IP-OOP effects. The IP-OOP interaction in RM walls was less pronounced than that specified for masonry infill walls in the ASCE 41-17 design provision.

A comparative study was performed between URM and RM walls in terms of the IP-OOP capacity interaction curves. Three representative walls were studied: the most ‘flexural’ wall (AR = 2.00, SR = 8.42, and $P_v = 0.0$ MPa), the most ‘shear’ wall (AR = 0.67, SR = 8.42, and $P_v = 2.5$ MPa), and the slenderest wall with the most IP-OOP interaction (AR = 1.33, SR = 29.47, and $P_v = 0.0$ MPa). The analysis results reveal that all three representative RM walls exhibited a lower capacity reduction in comparison to their URM counterparts. Additionally, it was also noted that the interaction curve derived for the URM wall with the strongest interaction was relatively well correlated with the one suggested in ASCE 41-17 for masonry infill walls.

(3) Sub-objective #3: Using the control variate method for statistics estimation and its application on the IP and OOP resistances of masonry walls with uncertain material properties

This sub-objective tackles the first of two primary goals in the uncertainty quantification aspect of this research: statistics estimation. In this context, two statistics estimators, one for the mean and the other for the variance, were formulated by using the control variate method. The proposed estimators used a multi-fidelity approach to capitalize on the strengths of both high-fidelity (HF) models (e.g., the FE model developed in Sub-objective #1) and design code-based models. While FE models offer higher accuracy, their computational intensity is notable. In contrast, design code-based models provide efficiency but may suffer accuracy limitations (e.g., large bias) due to inherent simplifications. The multi-fidelity approach involves integrating numerous evaluations of the design code model to enhance computational efficiency while involving only a limited number of FE model evaluations to ensure accuracy and unbiasedness.

Three case studies were presented for the statistics estimation of IP resistances of masonry walls: one on URM walls and two on RM walls. Furthermore, two case studies were presented for OOP resistance prediction, respectively. The results indicated that the proposed estimators for mean and variance outperform the estimators that rely solely on the FE and design-code models regarding accuracy and efficiency. The results underscored the potential for significant biases when relying exclusively on design code-based models for statistics estimation. On the other hand, the FE model-based crude MC estimators were associated with large variances when a small number of simulations were used, primarily attributable to the high computational demands of the FE model. For the URM wall considered in the case study, the mean and standard derivation of the IP resistance were 76.03 kN and 10.1 kN, respectively, indicating a coefficient of variation (COV) of 14.1%. In contrast, the value of COV is lower for RM walls: 2.6% and 2.8% for flexural and shear governed RM walls, respectively. Moreover, this statistics estimation method could be

further used for the evaluation of mean and mean minus one standard deviation of IP and OOP capacities of masonry walls. Such quantities are critically important for the next-generation performance-based design, as specified in ASCE 41-17.

(4) Sub-objective #4: Development of multi-fidelity reliability analysis algorithm and its application to masonry walls with uncertain material properties

The last sub-objective addressed the second goal of the uncertainty quantification part of this thesis: reliability analysis. A multi-fidelity (MF) reliability analysis algorithm was proposed, underpinned by a two-step information leveraging procedure that effectively integrated models of varying fidelities. The proposed method balanced the precision of high-fidelity (HF) models with the computational efficiency of low-fidelity (LF) models, effectively tackling the common challenges in reliability assessments within the realm of structural engineering. The distinct advantage of this method, as compared to other approaches, was demonstrated through comprehensive discussions and four examples in structural engineering. These illustrative examples highlighted the fact that the proposed MF approach was capable of accurately estimating failure probabilities while concurrently addressing computational constraints and complexities.

The practical application of this newly developed reliability analysis algorithm was then broadened to encompass the reliability assessment of masonry walls under both in-plane (IP) and out-of-plane (OOP) loading conditions. Two application examples are presented, each corresponding to one of the loading scenarios, demonstrating the algorithm's applicability to real-world applications in masonry wall analysis. As such, it can be used for reliability analysis of masonry walls designed based on limit-state design approaches, leading to more convincing evaluations than those using design-code models without considering model uncertainty. From a

scientific perspective, this component of this research represents a contribution to the field of structural reliability analysis. By synergistically combining HF and LF models, the proposed MF approach strikes a balance between computational accuracy and efficiency. This is instrumental in fostering the development of reliability-based design and maintenance not only within the masonry community, but also more broadly in the field of structural engineering.

11.2. CONTRIBUTIONS AND DELIVERABLES

The primary contributions and deliverables of this thesis, focusing on the development and application of computational techniques and uncertainty quantification algorithms for masonry walls, are outlined below:

- (1) This research presents two novel constitutive models for masonry mortar joints developed within the computational plasticity and damage plasticity frameworks for the simulation of monotonic and cyclic behaviors, respectively. The numerical validation examples demonstrated their great applicability in predicting the structural behavior (e.g., load-deformation behavior, crack propagation, failure modes) of masonry walls under IP and/or OOP loading conditions. As such, the developed models enhance the capabilities of the general-purpose Finite Element (FE) software ABAQUS (Dassault Systemes 2017). The implementation comprises two Fortran-based subroutines:

- ***Monotonic.for***: A subroutine of the constitutive model to simulate the monotonic behavior of masonry mortar joints
- ***Cyclic.for***: A subroutine of the constitutive model to simulate the cyclic behavior of masonry mortar joints

- (2) The study of masonry walls under combined in-plane (IP) and out-of-plane (OOP) loading conditions reveals critical insights for practical design considerations, suggesting that IP-OOP capacity interaction effects should be rigorously considered. Notably, walls with higher slenderness ratios (i.e., height-to-thickness ratios) exhibit significant IP capacity reductions due to OOP loading. In addition, such interaction effects (i.e., IP capacity reduction due to the presence of the OOP load) are generally more substantial in URM walls than in RM walls. A newly developed simplified analytical model, considering the impacts of aspect ratio, slenderness ratio, and pre-compression load, offers a valuable tool for addressing the IP-OOP capacity interaction effects of URM walls.
- (3) To streamline the micro modeling strategy of masonry walls, two Python-based automated tools were developed and integrated into the general-purpose Finite Element (FE) software ABAQUS. These tools offer a user-friendly environment for simulating masonry walls using micro modeling strategies with different boundary (e.g., cantilever, double-fixed, pin-roller) and loading conditions (e.g., IP loading, OOP loading, combined IP and OOP loadings):
- ***URM.py***: A tool for the modeling of unreinforced masonry wall
 - ***RM.py***: A tool for the modeling of fully grouted reinforced masonry wall
- (4) To enable efficient estimation of the IP and OOP resistances of masonry walls in accordance with CSA S304-14, four MATLAB functions were implemented:
- ***IP_URM.m***: A toolbox for evaluating the IP capacity of unreinforced masonry walls
 - ***IP_RM.m***: A toolbox for evaluating the IP capacity of reinforced masonry walls
 - ***OOP_URM.m***: A toolbox for evaluating the OOP capacity of unreinforced masonry walls, applicable for both eccentric axial loading and uniform lateral pressure loading scenarios (slenderness effects are considered through the moment magnifier method)

- ***OOP_RM.m***: a toolbox for evaluating the OOP capacity of fully grouted reinforced masonry, applicable for both eccentric axial loading and uniform lateral pressure loading scenarios (slenderness effects are considered through the moment magnifier method)
- (5) The MF reliability analysis method for the masonry walls presented in this thesis was implemented in MATLAB, and this toolbox allows the flexible integration of high-fidelity FE models and design code models (e.g., m-file, function handle) for the reliability analysis of masonry walls. Beyond the statistics estimation, this will advance the masonry community by laying the foundation for reliability-based code calibration and moment-based reliability analysis method. Accordingly, two MATLAB functions were implemented:
- ***MF_MEAN.m***: A toolbox for estimating the mean using the control variate-based multi-fidelity approach
 - ***MF_VAR.m***: A toolbox for estimating the variance using the control variate-based multi-fidelity approach
- (6) The MF reliability analysis algorithm developed in this thesis was implemented in MATLAB, and this toolbox allows the flexible integration of various high-fidelity and low-fidelity models (e.g., m-file, function handle). Note that the toolbox implemented allows for any type of model incorporated (e.g., FE model, analytical model), thus allowing for a wide range of applications. This will lay the basis and open the new door for reliability analysis/fragility analysis using high-fidelity expensive computational models in structural engineering.
- ***MF_RA.m***: A toolbox that performs the MF reliability analysis

These contributions and deliverables are collectively summarized in Figure 11-1.

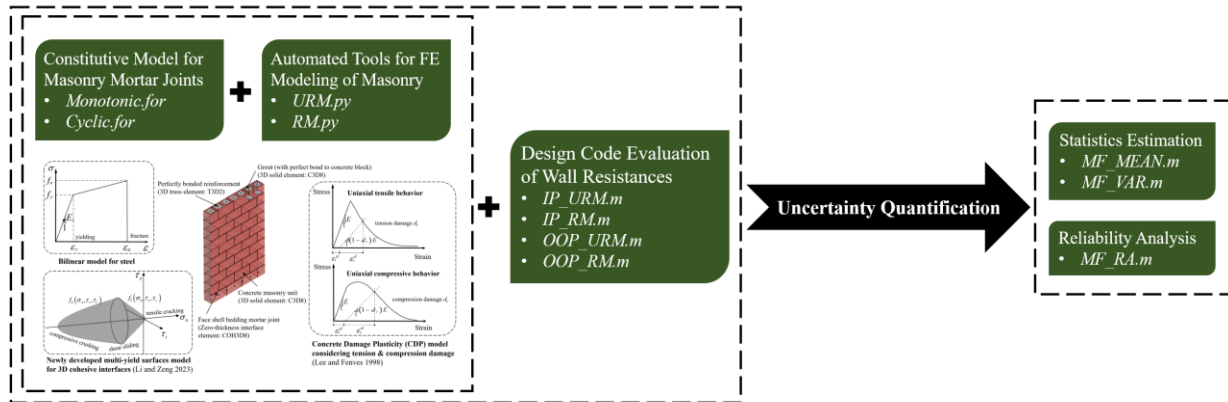


Figure 11-1. Contribution and deliverables of this research work

11.3. LIMITATIONS AND RECOMMENDATIONS FOR FUTURE WORK

This research work develops innovative constitutive models for mortar joints that enhance high-fidelity modeling and introduces sophisticated uncertainty quantification algorithms for masonry walls. Despite these advancements, the study identifies certain limitations that offer directions for future research. In the first part of this thesis, which focuses on computational modeling of masonry walls and their application in the IP-OOP interaction effects, the main limitations and recommendations are as follows:

- (1) A limitation in the FE modeling of reinforced masonry (RM) walls is the absence of a nonlinear bond-slip relationship between grouts and reinforcements. Additionally, bar buckling is neglected in the proposed modeling strategy. This should be addressed in future studies.
- (2) In numerical investigations into studying the IP-OOP interaction behavior of masonry walls, material parameters were considered constants without variations. However, some critical parameters (e.g., tensile strength of mortar joints, compressive strength of masonry) could potentially influence the failure modes of masonry walls under combined IP and

OOP loading, thus further impacting the IP-OOP capacity interaction effects. In this regard, such influence needs to be investigated.

For the second part of this study on uncertainty analysis, the main limitations and recommendations for future work are:

- (1) The primary limitation associated with the second part of this thesis is the assumption of taking the finite element model as the high-fidelity model. While this is reasonable when compared to design-code models, it is important to note that no model is error-free. Future research should aim to integrate experimental results into the proposed methodologies.
- (2) In the numerical examples for masonry walls, spatial variability is neglected. However, for masonry materials, spatial variability is widely observed. Future research work should incorporate such variability.
- (3) While the proposed reliability analysis algorithm performs well in the numerical examples provided, future work should include mathematical derivations of the quality of the proposed MF reliability estimator, such as variance and mean square error relative to the true value. Correspondingly, a model management scheme is anticipated to determine the model evaluation numbers for both high-fidelity and low-fidelity models, similar to what was done in the statistics estimation.
- (4) A finite element reliability-based code calibration for contemporary masonry design standards in North America is suggested for future research. This can be achieved by the MF reliability analysis algorithm developed in this study.

REFERENCE

- Abdellatif, A., M. Shedid, H. Okail, and A. Abdelrahman. 2019. “Numerical modeling of reinforced masonry walls under lateral loading at the component level response as opposed to system level response.” *Ain Shams Eng. J.*, 10 (2): 435–451. Ain Shams University. <https://doi.org/10.1016/j.asej.2018.12.003>.
- Abdollahi, A., M. Azhdary Moghaddam, S. A. Hashemi Monfared, M. Rashki, and Y. Li. 2020. “A refined subset simulation for the reliability analysis using the subset control variate.” *Struct. Saf.*, 87 (August): 102002. Elsevier. <https://doi.org/10.1016/j.strusafe.2020.102002>.
- Abdulla, K. F., L. S. Cunningham, and M. Gillie. 2017. “Simulating masonry wall behaviour using a simplified micro-model approach.” *Eng. Struct.*, 151: 349–365. Elsevier Ltd. <https://doi.org/10.1016/j.engstruct.2017.08.021>.
- Addressi, D., D. Liberatore, and R. Masiani. 2015. “Force-based beam finite element (FE) for the pushover analysis of masonry buildings.” *Int. J. Archit. Herit.*, 9 (3): 231–243. Taylor & Francis. <https://doi.org/10.1080/15583058.2013.768309>.
- Addressi, D., A. Mastrandrea, and E. Sacco. 2014. “An equilibrated macro-element for nonlinear analysis of masonry structures.” *Eng. Struct.*, 70: 82–93. Elsevier Ltd. <https://doi.org/10.1016/j.engstruct.2014.03.034>.
- Addressi, D., P. Di Re, C. Gatta, and E. Sacco. 2021. “Multiscale analysis of out-of-plane masonry elements using different structural models at macro and microscale.” *Comput. Struct.*, 247: 106477. Pergamon. <https://doi.org/10.1016/j.compstruc.2020.106477>.
- Agnihotri, P., V. Singhal, and D. C. Rai. 2013. “Effect of in-plane damage on out-of-plane strength of unreinforced masonry walls.” *Eng. Struct.*, 57: 1–11. Elsevier. 402

<https://doi.org/10.1016/j.engstruct.2013.09.004>.

Aguilar, V., C. Sandoval, J. M. Adam, J. Garzón-Roca, and G. Valdebenito. 2016. “Prediction of the shear strength of reinforced masonry walls using a large experimental database and artificial neural networks.” *Struct. Infrastruct. Eng.*, 12 (12): 1661–1674. Taylor & Francis. <https://doi.org/10.1080/15732479.2016.1157824>.

Alexandrov, N. M., R. M. Lewis, C. R. Gumbert, L. L. Green, and P. A. Newman. 2001. “Approximation and model management in aerodynamic optimization with variable-fidelity models.” *J. Aircr.*, 38 (6): 1093–1101. <https://doi.org/10.2514/2.2877>.

Algoji, B. 2013. “An Experimental and Numerical Study of Retrofitted Masonry Walls under Cyclic Loading [Ph.D thesis].” King Fahd University of Petroleum and Minerals.

Almeida, J. A. P. P., D. Bordigoni, E. B. Pereira, J. A. O. Barros, and A. Aprile. 2016. “Assessment of the properties to characterise the interface between clay brick substrate and strengthening mortar.” *Constr. Build. Mater.*, 103: 47–66. Elsevier Ltd. <https://doi.org/10.1016/j.conbuildmat.2015.11.036>.

Álvarez-Pérez, J., J. H. Chávez-Gómez, B. T. Terán-Torres, M. Mesa-Lavista, and R. Balandrano-Vázquez. 2020. “Multifactorial behavior of the elastic modulus and compressive strength in masonry prisms of hollow concrete blocks.” *Constr. Build. Mater.*, 241: 118002. Elsevier. <https://doi.org/10.1016/j.conbuildmat.2020.118002>.

Amadei, B., S. Sture, S. Saeb, and R. H. Atkinson. 1989. “An evaluation of masonry joint shear strength in existing buildings.” *Rep. Prep. NSF*.

Anand, S. C., and K. K. Yalamanchili. 1996. “Three-Dimensional Failure Analysis of Composite Masonry Walls.” *J. Struct. Eng.*, 122 (9): 1031–1039. [https://doi.org/10.1061/\(asce\)0733-](https://doi.org/10.1061/(asce)0733-)

9445(1996)122:9(1031).

Andreotti, G., F. Graziotti, and G. Magenes. 2019. “Expansion of mortar joints in direct shear tests of masonry samples: implications on shear strength and experimental characterization of dilatancy.” *Mater. Struct.*, 52 (4): 1–16. Springer Netherlands. <https://doi.org/10.1617/s11527-019-1366-5>.

Anthoine, A., and G. Magonette. 1995. “Shear-compression testing and analysis of brick masonry walls.” *Proc. 10th Eur. Conf. Earthq. Eng.*, 1–6. Central Institute for Meteorology and Geodynamics Vienna, Austria.

Anthoine, A., G. Magonette, and G. Magenes. 1994. “Shear-compression testing and analysis of brick masonry walls.” *Proc. 10th Eur. Conf. Earthq. Eng.*

Applied Technology Council. 1997. “NEHRP guidelines for the seismic rehabilitation of buildings: FEMA 273.” *Fed. Emerg. Manag. Agency*, (October): 435.

Aref, A. J., and K. M. Dolatshahi. 2013. “A three-dimensional cyclic meso-scale numerical procedure for simulation of unreinforced masonry structures.” *Comput. Struct.*, 120: 9–23. Elsevier Ltd. <https://doi.org/10.1016/j.compstruc.2013.01.012>.

AS3700. 2018. *Australian Standard of Masonry Structures*.

ASCE. 2017. *Seismic Evaluation and Retrofit of Existing Buildings. Seism. Eval. Retrofit Exist. Build.* American Society of Civil Engineers.

Astroza, M., O. Moroni, S. Brzev, and J. Tanner. 2012. “Seismic performance of engineered masonry buildings in the 2010 Maule earthquake.” *Earthq. Spectra*, 28 (SUPPL.1): 385–406. <https://doi.org/10.1193/1.4000040>.

Atkinson, R. H., B. P. Amadei, S. Saeb, and S. Sture. 1989. “Response of masonry bed joints in

- direct shear.” *J. Struct. Eng.*, 115 (9): 2276–2296. [https://doi.org/10.1061/\(ASCE\)0733-9445\(1989\)115:9\(2276\)](https://doi.org/10.1061/(ASCE)0733-9445(1989)115:9(2276)).
- Atkinson, R. H., G. R. Kingsley, S. Saeb, B. Amadei, and S. Sture. 1988. “A laboratory and in situ study of the shear strength of masonry bed joints.” *Proc. Eighth Int. Brick Block Mason. Conf.*, 261–271.
- Au, S. K., and J. L. Beck. 2001. “Estimation of small failure probabilities in high dimensions by subset simulation.” *Probabilistic Eng. Mech.*, 16 (4): 263–277. [https://doi.org/10.1016/S0266-8920\(01\)00019-4](https://doi.org/10.1016/S0266-8920(01)00019-4).
- Au, S. K., J. Ching, and J. L. Beck. 2007. “Application of subset simulation methods to reliability benchmark problems.” *Struct. Saf.*, 29 (3): 183–193. Elsevier. <https://doi.org/10.1016/J.STRUSAFE.2006.07.008>.
- Barbosa, C. S., P. B. Lourenço, and J. B. Hanai. 2010. “On the compressive strength prediction for concrete masonry prisms.” *Mater. Struct. Constr.*, 43 (3): 331–344. <https://doi.org/10.1617/s11527-009-9492-0>.
- Bartlett, F. M., H. P. Hong, and W. Zhou. 2003. “Load factor calibration for the proposed 2005 edition of the National Building Code of Canada : Statistics of loads and load effects.” *Can. J. Civ. Eng.*, 30 (2): 429–439. <https://doi.org/10.1139/L02-087>.
- Bartoli, G., M. Betti, P. Biagini, A. Borghini, A. Ciavattone, M. Girardi, G. Lancioni, A. M. Marra, B. Ortolani, B. Pintucchi, and L. Salvatori. 2017. “Epistemic Uncertainties in Structural Modeling: A Blind Benchmark for Seismic Assessment of Slender Masonry Towers.” *J. Perform. Constr. Facil.*, 31 (5): 1–18. [https://doi.org/10.1061/\(asce\)cf.1943-5509.0001049](https://doi.org/10.1061/(asce)cf.1943-5509.0001049).
- Berto, L., A. Saetta, R. Scotta, and R. Vitaliani. 2002. “An orthotropic damage model for masonry

- structures.” *Int. J. Numer. Methods Eng.*, 55 (2): 127–157. <https://doi.org/10.1002/nme.495>.
- Berto, L., A. Saetta, R. Scotta, and R. Vitaliani. 2004. “Shear behaviour of masonry panel: Parametric FE analyses.” *Int. J. Solids Struct.*, 41 (16–17): 4383–4405. <https://doi.org/10.1016/j.ijsolstr.2004.02.046>.
- Biye, W., D. Junwu, B. Wen, and Y. Yongqiang. 2022. “Triaxial elastoplastic damage constitutive model of unreinforced clay brick masonry wall.” *Earthq. Eng. Eng. Vib.* <https://doi.org/10.1007/s11803-023-2151-6>.
- Bjerager, P. 1988. “Probability Integration by Directional Simulation.” *J. Eng. Mech.*, 114 (8): 1285–1302. [https://doi.org/10.1061/\(asce\)0733-9399\(1988\)114:8\(1285\)](https://doi.org/10.1061/(asce)0733-9399(1988)114:8(1285)).
- Bolhassani, M., A. A. Hamid, C. Johnson, and A. E. Schultz. 2016. “Shear strength expression for partially grouted masonry walls.” *Eng. Struct.*, 127: 475–494. Elsevier Ltd. <https://doi.org/10.1016/j.engstruct.2016.09.001>.
- Bracchi, S., A. Galasco, and A. Penna. 2021. “A novel macroelement model for the nonlinear analysis of masonry buildings. Part 1: Axial and flexural behavior.” *Earthq. Eng. Struct. Dyn.*, 50 (8): 2233–2252. <https://doi.org/10.1002/eqe.3445>.
- Bracchi, S., and A. Penna. 2021. “A novel macroelement model for the nonlinear analysis of masonry buildings. Part 2: Shear behavior.” *Earthq. Eng. Struct. Dyn.*, 50 (8): 2212–2232. <https://doi.org/10.1002/eqe.3444>.
- Bucher, C. G., and U. Bourgund. 1990. “A fast and efficient response surface approach for structural reliability problems.” *Struct. Saf.*, 7 (1): 57–66. [https://doi.org/10.1016/0167-4730\(90\)90012-E](https://doi.org/10.1016/0167-4730(90)90012-E).
- De Buhan, P., and G. De Felice. 1997. “A homogenization approach to the ultimate strength of

- brick masonry.” *J. Mech. Phys. Solids*, 45 (7): 1085–1104. [https://doi.org/10.1016/S0022-5096\(97\)00002-1](https://doi.org/10.1016/S0022-5096(97)00002-1).
- Caballero, A., K. J. Willam, and I. Carol. 2008. “Consistent tangent formulation for 3D interface modeling of cracking/fracture in quasi-brittle materials.” *Comput. Methods Appl. Mech. Eng.*, 197 (33–40): 2804–2822. North-Holland. <https://doi.org/10.1016/j.cma.2008.01.011>.
- Calderini, C., S. Cattari, and S. Lagomarsino. 2009. “In-plane strength of unreinforced masonry piers.” *Earthq. Eng. Struct. Dyn.*, 38: 243–267. <https://doi.org/10.1002/eqe>.
- Calderini, C., S. Cattari, and S. Lagomarsino. 2010. “The use of the diagonal compression test to identify the shear mechanical parameters of masonry.” *Constr. Build. Mater.*, 24 (5): 677–685. Elsevier Ltd. <https://doi.org/10.1016/j.conbuildmat.2009.11.001>.
- Calderini, C., and S. Lagomarsino. 2008. “Continuum Model for In-Plane Anisotropic Inelastic Behavior of Masonry.” *J. Struct. Eng.*, 134 (2): 209–220. [https://doi.org/10.1061/\(asce\)0733-9445\(2008\)134:2\(209\)](https://doi.org/10.1061/(asce)0733-9445(2008)134:2(209)).
- Calderón, S., O. Arnau, and C. Sandoval. 2019. “Detailed micro-modeling approach and solution strategy for laterally loaded reinforced masonry shear walls.” *Eng. Struct.*, 201 (October): 109786. Elsevier. <https://doi.org/10.1016/j.engstruct.2019.109786>.
- Calderón, S., G. Milani, and C. Sandoval. 2021a. “Simplified micro-modeling of partially-grouted reinforced masonry shear walls with bed-joint reinforcement: Implementation and validation.” *Eng. Struct.*, 234 (January). <https://doi.org/10.1016/j.engstruct.2021.111987>.
- Calderón, S., C. Sandoval, and O. Arnau. 2017. “Shear response of partially-grouted reinforced masonry walls with a central opening: Testing and detailed micro-modelling.” *Mater. Des.*, 118: 122–137. Elsevier Ltd. <https://doi.org/10.1016/j.matdes.2017.01.019>.

- Calderón, S., C. Sandoval, G. Milani, and O. Arnau. 2021b. “Detailed micro-modeling of partially grouted reinforced masonry shear walls: extended validation and parametric study.” *Arch. Civ. Mech. Eng.*, 21 (3). Springer London. <https://doi.org/10.1007/s43452-021-00237-z>.
- Canadian Standards Association. 2004. “CSA S304. 1-04: Design of masonry structures.” Mississauga, ON, Canada.
- Canadian Standards Association. 2014. “CSA S304-14: Design of Masonry Structures.” Mississauga, Ontario, Canada.
- Carol, I., C. M. López, and O. Roa. 2001. “Micromechanical analysis of quasi-brittle materials using fracture-based interface elements.” *Int. J. Numer. Methods Eng.*, 52 (1–2): 193–215. <https://doi.org/10.1002/nme.277>.
- Carol, I., P. C. Prat, and C. M. López. 1997. “Normal/Shear Cracking Model: Application to Discrete Crack Analysis.” *J. Eng. Mech.*, 123 (8): 765–773. [https://doi.org/10.1061/\(asce\)0733-9399\(1997\)123:8\(765\)](https://doi.org/10.1061/(asce)0733-9399(1997)123:8(765)).
- Casapulla, C., and F. Portioli. 2016. “Experimental tests on the limit states of dry-jointed tuff blocks.” *Mater. Struct. Constr.*, 49 (3): 751–767. Springer Netherlands. <https://doi.org/10.1617/s11527-015-0536-3>.
- Casapulla, C., F. Portioli, A. Maione, and R. Landolfo. 2013. “A macro-block model for in-plane loaded masonry walls with non-associative Coulomb friction.” *Meccanica*, 48 (9): 2107–2126. <https://doi.org/10.1007/s11012-013-9728-5>.
- Celano, T., L. U. Argiento, F. Ceroni, and C. Casapulla. 2021. “Literature review of the in-plane behavior of masonry walls: Theoretical vs. experimental results.” *Materials (Basel)*, 14 (11). <https://doi.org/10.3390/ma14113063>.

- Chaimoon, K., and M. M. Attard. 2007. "Modeling of unreinforced masonry walls under shear and compression." *Eng. Struct.*, 29 (9): 2056–2068. Elsevier. <https://doi.org/10.1016/j.engstruct.2006.10.019>.
- Chen, C., Y. Yang, H. Hou, C. Peng, and W. Xu. 2022. "Real-time hybrid simulation with multi-fidelity Co-Kriging for global response prediction under structural uncertainties." *Earthq. Eng. Struct. Dyn.*, 51 (11): 2591–2609. Wiley Online Library.
- Chen, D., H. Wu, and Q. Fang. 2023. "Simplified micro-model for brick masonry walls under out-of-plane quasi-static and blast loadings." *Int. J. Impact Eng.*, 174 (December 2022). <https://doi.org/10.1016/j.ijimpeng.2023.104529>.
- Chen, S. Y., F. L. Moon, and T. Yi. 2008. "A macroelement for the nonlinear analysis of in-plane unreinforced masonry piers." *Eng. Struct.*, 30 (8): 2242–2252. Elsevier. <https://doi.org/10.1016/J.ENGSTRUCT.2007.12.001>.
- Cheng, J., and P. B. Shing. 2022a. "A beam-column element for modeling nonlinear flexural and shear behaviors of reinforced masonry walls." *Earthq. Eng. Struct. Dyn.*
- Cheng, J., and P. B. Shing. 2022b. "Practical Nonlinear Analysis Methods for Flexure-Dominated Reinforced Masonry Shear Walls." *J. Struct. Eng.*, 148 (8): 1–19. [https://doi.org/10.1061/\(asce\)st.1943-541x.0003429](https://doi.org/10.1061/(asce)st.1943-541x.0003429).
- Chisari, C., L. Macorini, and B. A. Izzuddin. 2023. "An anisotropic plastic-damage model for 3D nonlinear simulation of masonry structures." *Int. J. Numer. Methods Eng.*
- Citto, C. 2008. "Two-dimensional interface model applied to masonry structures [MS.c thesis]." University of Bologna.
- Clermont, P., and B. Sudret. 2007. "Uncertainty Propagation and Sensitivity Analysis in

Mechanical Models.” *English*.

- Comi, C., and U. Perego. 2001. “Fracture energy based bi-dissipative damage model for concrete.” *Int. J. Solids Struct.*, 38 (36–37): 6427–6454. Pergamon. [https://doi.org/10.1016/S0020-7683\(01\)00066-X](https://doi.org/10.1016/S0020-7683(01)00066-X).
- Cornell, C. A. n.d. “A Probability-Based Structural Code*.” *ACI J. Proc.*, 66 (12). <https://doi.org/10.14359/7446>.
- D’Altri, A. M., F. Messali, J. Rots, G. Castellazzi, and S. de Miranda. 2019. “A damaging block-based model for the analysis of the cyclic behaviour of full-scale masonry structures.” *Eng. Fract. Mech.*, 209: 423–448. Elsevier Ltd. <https://doi.org/10.1016/j.engfracmech.2018.11.046>.
- D’Altri, A. M., S. de Miranda, G. Castellazzi, and V. Sarhosis. 2018. “A 3D detailed micro-model for the in-plane and out-of-plane numerical analysis of masonry panels.” *Comput. Struct.*, 206: 18–30. Elsevier Ltd. <https://doi.org/10.1016/j.compstruc.2018.06.007>.
- D’Altri, A. M., V. Sarhosis, G. Milani, J. Rots, S. Cattari, S. Lagomarsino, E. Sacco, A. Tralli, G. Castellazzi, and S. de Miranda. 2020. “Modeling Strategies for the Computational Analysis of Unreinforced Masonry Structures: Review and Classification.” *Arch. Comput. Methods Eng.*, 27 (4): 1153–1185. Springer Netherlands. <https://doi.org/10.1007/s11831-019-09351-x>.
- Dahlblom, O., A. Peterson, and H. Petersson. 1986. “Calfem — a program for computer-aided learning of the finite element method.” *Eng. Comput.*, 3 (2): 155–160. MCB UP Ltd. <https://doi.org/10.1108/eb023653>.
- Dashti, F., R. P. Dhakal, and S. Pampanin. 2018. “Evolution of out-of-plane deformation and

- subsequent instability in rectangular RC walls under in-plane cyclic loading: Experimental observation.” *Earthq. Eng. Struct. Dyn.*, 47 (15): 2944–2964. <https://doi.org/10.1002/eqe.3115>.
- Dassault Systemes. 2017. “Abaqus/Standard 2017.” *Dassault Syst. SIMULIA, Provid. RI*.
- Deng, J., D. Gu, X. Li, and Z. Q. Yue. 2005. “Structural reliability analysis for implicit performance functions using artificial neural network.” *Struct. Saf.*, 27 (1): 25–48. <https://doi.org/10.1016/j.strusafe.2004.03.004>.
- Dey, S., S. Chakraborty, and S. Tesfamariam. 2021. “Multi-fidelity approach for uncertainty quantification of buried pipeline response undergoing fault rupture displacements in sand.” *Comput. Geotech.*, 136: 104197. Elsevier. <https://doi.org/10.1016/J.COMPGEO.2021.104197>.
- Dhanasekar, M., and W. Haider. 2008. “Explicit finite element analysis of lightly reinforced masonry shear walls.” *Comput. Struct.*, 86 (1–2): 15–26. Pergamon. <https://doi.org/10.1016/j.compstruc.2007.06.006>.
- Dizhur, D., J. Ingham, L. Moon, M. Griffith, A. Schultz, I. Senaldi, G. Magenes, J. Dickie, S. Lissel, J. Centeno, C. Ventura, J. Leite, and P. Lourenco. 2011. “Performance of masonry buildings and churches in the 22 February 2011 Christchurch earthquake.” *Bull. New Zeal. Soc. Earthq. Eng.*, 44 (4): 279–296. <https://doi.org/10.5459/bnzsee.44.4.279-296>.
- Doherty, K., M. C. Griffith, N. Lam, and J. Wilson. 2002. “Displacement-based seismic analysis for out-of-plane bending of unreinforced masonry walls.” *Earthq. Eng. Struct. Dyn.*, 31 (4): 833–850. <https://doi.org/10.1002/eqe.126>.
- Dolatshahi, K. M. 2012. “Computational, Analytical and Experimental Modeling of Masonry

- Structures [Ph.D thesis].” State University of New York at Buffalo.
- Dolatshahi, K. M., and A. J. Aref. 2011. “Two-dimensional computational framework of meso-scale rigid and line interface elements for masonry structures.” *Eng. Struct.*, 33 (12): 3657–3667. Elsevier. <https://doi.org/10.1016/j.engstruct.2011.07.030>.
- Dolatshahi, K. M., and A. J. Aref. 2016. “Multi-directional response of unreinforced masonry walls: experimental and computational investigations.” *Earthq. Eng. Struct. Dyn.*, 45 (9): 1427–1449. <https://doi.org/10.1002/eqe.2714>.
- Dolatshahi, K. M., A. J. Aref, and A. S. Whittaker. 2015. “Interaction curves for in-plane and out-of-plane behaviors of unreinforced masonry walls.” *J. Earthq. Eng.*, 19 (1): 60–84. <https://doi.org/10.1080/13632469.2014.946571>.
- Dolatshahi, K. M., and M. Yekrangnia. 2015. “Out-of-plane strength reduction of unreinforced masonry walls because of in-plane damages.” *Earthq. Eng. Struct. Dyn.*, 44: 2157–2176. <https://doi.org/10.1002/eqe>.
- Drougkas, A., P. Roca, and C. Molins. 2019. “Experimental analysis and detailed micro-modeling of masonry walls subjected to in-plane shear.” *Eng. Fail. Anal.*, 95 (February 2018): 82–95. Elsevier. <https://doi.org/10.1016/j.engfailanal.2018.08.030>.
- Drucker, D. C., and W. Prager. 1952. “Soil mechanics and plastic analysis or limit design.” *Q. Appl. Math.*, 10 (2): 157–165.
- Drysdale, R. G., and A. A. Hamid. 2005. *Masonry Structures: Behaviour and Design, Canadian Edition*. Mississauga, ON: Canada Masonry Design Centre.
- Dymiotis, C., and B. M. Gutleiderer. 2002. “Allowing for uncertainties in the modelling of masonry compressive strength.” *Constr. Build. Mater.*, 16 (8): 443–452. Elsevier.

- [https://doi.org/10.1016/S0950-0618\(02\)00108-3](https://doi.org/10.1016/S0950-0618(02)00108-3).
- El-Dakhakhni, W., and A. Ashour. 2017. “Seismic Response of Reinforced-Concrete Masonry Shear-Wall Components and Systems: State of the Art.” *J. Struct. Eng.*, 143 (9): 1–25. [https://doi.org/10.1061/\(asce\)st.1943-541x.0001840](https://doi.org/10.1061/(asce)st.1943-541x.0001840).
- El-Hashimy, T., M. Ezzeldin, W. El-Dakhakhni, and M. Tait. 2020. “Behavior of Seismically Detailed Reinforced Concrete Block Shear Walls with Boundary Elements under Out-of-Plane Loading.” *J. Struct. Eng.*, 146 (3): 1–17. [https://doi.org/10.1061/\(asce\)st.1943-541x.0002478](https://doi.org/10.1061/(asce)st.1943-541x.0002478).
- El-Hashimy, T., M. Ezzeldin, M. Tait, and W. El-Dakhakhni. 2019. “Out-of-Plane Performance of Reinforced Masonry Shear Walls Constructed with Boundary Elements.” *J. Struct. Eng.*, 145 (8): 1–14. [https://doi.org/10.1061/\(asce\)st.1943-541x.0002337](https://doi.org/10.1061/(asce)st.1943-541x.0002337).
- Ellingwood, B., and A. Tallin. 1985. “Limit States Criteria for Masonry Construction.” *J. Struct. Eng.*, 111 (1): 108–122. [https://doi.org/10.1061/\(asce\)0733-9445\(1985\)111:1\(108\)](https://doi.org/10.1061/(asce)0733-9445(1985)111:1(108)).
- Elvin, A., and H. Uzoegbo. 2011. “Response of a full-scale dry-stack masonry structure subject to experimentally applied earthquake loading.” *J. South African Inst. Civ. Eng.*, 53 (1): 22–32.
- European Committee for Standardization (CEN). 2005. “Design of masonry structures—Part 1-1: General rules for reinforced and unreinforced masonry structures.” Eurocode 6, CEN, Brussels, Belgium.
- Ferreira, A. J. M. 2009. *MATLAB codes for finite element analysis*. Springer.
- Ferreira, T. M., A. A. Costa, and A. Costa. 2015. “Analysis of the Out-Of-Plane Seismic Behavior of Unreinforced Masonry: A Literature Review.” *Int. J. Archit. Herit.*, 9 (8): 949–972. Taylor & Francis. <https://doi.org/10.1080/15583058.2014.885996>.

- Ferretti, F., C. Mazzotti, R. Esposito, and J. G. Rots. 2018. "Shear-sliding behavior of masonry: Numerical micro-modeling of triplet tests." *Comput. Model. Concr. Struct. - Proc. Conf. Comput. Model. Concr. Concr. Struct. EURO-C 2018*, 941–954. <https://doi.org/10.1201/9781315182964-109>.
- Forrester, A. I. J., N. W. Bressloff, and A. J. Keane. 2006. "Optimization using surrogate models and partially converged computational fluid dynamics simulations." *Proc. R. Soc. A Math. Phys. Eng. Sci.*, 462 (2071): 2177–2204. <https://doi.org/10.1098/rspa.2006.1679>.
- Fortes, E. S., G. A. Parsekian, and F. S. Fonseca. 2015. "Relationship between the Compressive Strength of Concrete Masonry and the Compressive Strength of Concrete Masonry Units." *J. Mater. Civ. Eng.*, 27 (9): 04014238. [https://doi.org/10.1061/\(asce\)mt.1943-5533.0001204](https://doi.org/10.1061/(asce)mt.1943-5533.0001204).
- Fouchal, F., F. Lebon, and I. Titeux. 2009. "Contribution to the modelling of interfaces in masonry construction." *Constr. Build. Mater.*, 23 (6): 2428–2441. Elsevier. <https://doi.org/10.1016/j.conbuildmat.2008.10.011>.
- Fryer, M. J., and R. Y. Rubinstein. 1983. *Simulation and the Monte Carlo Method*. *J. R. Stat. Soc. Ser. A*. John Wiley & Sons.
- Gaetani, A., P. B. Lourenço, G. Monti, and G. Milani. 2017. "A parametric investigation on the seismic capacity of masonry cross vaults." *Eng. Struct.*, 148: 686–703. Elsevier Ltd. <https://doi.org/10.1016/j.engstruct.2017.07.013>.
- Gallimard, L. 2011. "Error bounds for the reliability index in finite element reliability analysis." *Int. J. Numer. Methods Eng.*, (February): 781–794. <https://doi.org/10.1002/nme>.
- Gambarotta, L., and S. Lagomarsino. 1997a. "Damage models for the seismic response of brick masonry shear walls. Part I: The mortar joint model and its applications." *Earthq. Eng. Struct.*

- Dyn.*, 26 (4): 423–439. [https://doi.org/10.1002/\(sici\)1096-9845\(199704\)26:4<423::aid-eqe650>3.0.co;2-%23](https://doi.org/10.1002/(sici)1096-9845(199704)26:4<423::aid-eqe650>3.0.co;2-%23).
- Gambarotta, L., and S. Lagomarsino. 1997b. “Damage models for the seismic response of brick masonry shear walls. Part II: The continuum model and its applications.” *Earthq. Eng. Struct. Dyn.*, 26 (4): 423–439. [https://doi.org/10.1002/\(sici\)1096-9845\(199704\)26:4<423::aid-eqe650>3.0.co;2-%23](https://doi.org/10.1002/(sici)1096-9845(199704)26:4<423::aid-eqe650>3.0.co;2-%23).
- Gatta, C., D. Addessi, and F. Vestroni. 2018. “Static and dynamic nonlinear response of masonry walls.” *Int. J. Solids Struct.*, 155: 291–303. Elsevier Ltd. <https://doi.org/10.1016/j.ijsolstr.2018.07.028>.
- Geyer, S., I. Papaioannou, and D. Straub. 2019. “Cross entropy-based importance sampling using Gaussian densities revisited.” *Struct. Saf.*, 76 (July 2018): 15–27. Elsevier. <https://doi.org/10.1016/j.strusafe.2018.07.001>.
- Ghiassi, B., and G. Milani. 2019. *Numerical modeling of masonry and historical structures: from theory to application*. Woodhead Publishing.
- Giambanco, G., and L. Di Gati. 1997. “A cohesive interface model for the structural mechanics of block masonry.” *Mech. Res. Commun.*, 24 (5): 503–512. Pergamon. [https://doi.org/10.1016/s0093-6413\(97\)00055-4](https://doi.org/10.1016/s0093-6413(97)00055-4).
- Giambanco, G., E. La Malfa Ribolla, and A. Spada. 2018. “Meshless meso-modeling of masonry in the computational homogenization framework.” *Meccanica*, 53 (7): 1673–1697. Springer Netherlands. <https://doi.org/10.1007/s11012-017-0664-7>.
- Giambanco, G., S. Rizzo, and R. Spallino. 2001. “Numerical analysis of masonry structures via interface models.” *Comput. Methods Appl. Mech. Eng.*, 190 (49–50): 6493–6511. North-

- Holland. [https://doi.org/10.1016/S0045-7825\(01\)00225-0](https://doi.org/10.1016/S0045-7825(01)00225-0).
- Gianluca, G., M. S. Eldred, and G. Iaccarino. 2017. “A multifidelity multilevel Monte Carlo method for uncertainty propagation in aerospace applications.” *19th AIAA Non-Deterministic Approaches Conf. 2017*, 1–24. <https://doi.org/10.2514/6.2017-1951>.
- Giaretton, M., D. Dizhur, F. da Porto, and J. M. Ingham. 2016. “Construction Details and Observed Earthquake Performance of Unreinforced Clay Brick Masonry Cavity-walls.” *Structures*, 6: 159–169. Elsevier B.V. <https://doi.org/10.1016/j.istruc.2016.04.004>.
- Gilbert, M., C. Casapulla, and H. M. Ahmed. 2006. “Limit analysis of masonry block structures with non-associative frictional joints using linear programming.” *Comput. Struct.*, 84 (13–14): 873–887. <https://doi.org/10.1016/j.compstruc.2006.02.005>.
- Giles, M. B. 2008. “Multilevel Monte Carlo path simulation.” *Oper. Res.*, 56 (3): 607–617. <https://doi.org/10.1287/opre.1070.0496>.
- Giles, M. B. 2015. “Multilevel Monte Carlo methods.” *Acta Numer.*, 24: 259–328. <https://doi.org/10.1017/S096249291500001X>.
- Godio, M., and K. Beyer. 2019. “Trilinear Model for the Out-of-Plane Seismic Assessment of Vertically Spanning Unreinforced Masonry Walls.” *J. Struct. Eng.*, 145 (12): 04019159. [https://doi.org/10.1061/\(asce\)st.1943-541x.0002443](https://doi.org/10.1061/(asce)st.1943-541x.0002443).
- Gonen, S., B. Pulatsu, E. Erdogmus, P. B. Lourenço, and S. Soyoz. 2022. “Effects of spatial variability and correlation in stochastic discontinuum analysis of unreinforced masonry walls.” *Constr. Build. Mater.*, 337 (September 2021): 127511. Elsevier Ltd. <https://doi.org/10.1016/j.conbuildmat.2022.127511>.
- Gonen, S., B. Pulatsu, S. Soyoz, and E. Erdogmus. 2021. “Stochastic discontinuum analysis of

- unreinforced masonry walls: Lateral capacity and performance assessments.” *Eng. Struct.*, 238 (March): 112175. Elsevier Ltd. <https://doi.org/10.1016/j.engstruct.2021.112175>.
- Gooch, L. J., M. J. Masia, and M. G. Stewart. 2021. “Application of stochastic numerical analyses in the assessment of spatially variable unreinforced masonry walls subjected to in-plane shear loading.” *Eng. Struct.*, 235 (February): 112095. Elsevier Ltd. <https://doi.org/10.1016/j.engstruct.2021.112095>.
- Goodman, R. E., R. L. Taylor, and T. L. Brekke. 1968. “A Model for the Mechanics of Jointed Rock.” *J. Soil Mech. Found. Div.*, 94 (3): 637–659. <https://doi.org/10.1061/jsfeaq.0001133>.
- Gopalaratnam, V. S., and S. P. Shah. 1985. “Softening Response of Plain Concrete in Direct Tension.” *J. Am. Concr. Inst.*, 82 (3): 310–323. [https://doi.org/10.1016/0148-9062\(86\)91965-0](https://doi.org/10.1016/0148-9062(86)91965-0).
- Grassl, P., and R. Rempling. 2008. “A damage-plasticity interface approach to the meso-scale modelling of concrete subjected to cyclic compressive loading.” *Eng. Fract. Mech.*, 75 (16): 4804–4818. Pergamon. <https://doi.org/10.1016/j.engfracmech.2008.06.005>.
- Grassl, P., D. Xenos, U. Nyström, R. Rempling, and K. Gylltoft. 2013. “CDPM2: A damage-plasticity approach to modelling the failure of concrete.” *Int. J. Solids Struct.*, 50 (24): 3805–3816. Pergamon. <https://doi.org/10.1016/j.ijsolstr.2013.07.008>.
- Graziotti, F., A. Penna, and G. Magenes. 2019. “A comprehensive in situ and laboratory testing programme supporting seismic risk analysis of URM buildings subjected to induced earthquakes.” *Bull. Earthq. Eng.*, 17 (8): 4575–4599. Springer Netherlands. <https://doi.org/10.1007/s10518-018-0478-6>.
- Greco, F., L. Leonetti, R. Luciano, and P. Nevone Blasi. 2016. “An adaptive multiscale strategy

- for the damage analysis of masonry modeled as a composite material.” *Compos. Struct.*, 153: 972–988. Elsevier Ltd. <https://doi.org/10.1016/j.compstruct.2016.06.066>.
- Gruber, A., M. Gunzburger, L. Ju, and Z. Wang. 2023. “A Multifidelity Monte Carlo Method for Realistic Computational Budgets.” *J. Sci. Comput.*, 94 (1): 1–18. Springer US. <https://doi.org/10.1007/s10915-022-02051-y>.
- Gupta, A., U. M. Krishnan, R. Chowdhury, and A. Chakrabarti. 2020. “An auto-adaptive substepping algorithm for phase-field modeling of brittle fracture.” *Theor. Appl. Fract. Mech.*, 108: 102622. Elsevier B.V. <https://doi.org/10.1016/j.tafmec.2020.102622>.
- Gupta, S., and C. S. Manohar. 2004. “An improved response surface method for the determination of failure probability and importance measures.” *Struct. Saf.*, 26 (2): 123–139. [https://doi.org/10.1016/S0167-4730\(03\)00021-3](https://doi.org/10.1016/S0167-4730(03)00021-3).
- Haach, V. G. 2009. “Development of a design method for reinforced masonry subjected to in-plane loading based on experimental and numerical analysis [Ph.D thesis].”
- Haach, V. G., G. Vasconcelos, and P. B. Lourenço. 2013. “Proposal of a Design Model for Masonry Walls Subjected to In-Plane Loading.” *J. Struct. Eng.*, 139 (4): 537–547. [https://doi.org/10.1061/\(asce\)st.1943-541x.0000636](https://doi.org/10.1061/(asce)st.1943-541x.0000636).
- Haider, W. 2007. “Inplane response of wide spaced reinforced masonry shear walls [Ph.D thesis].” Central Queensland University.
- Halton, J. H. 1994. “Sequential monte carlo techniques for the solution of linear systems.” *J. Sci. Comput.*, 9 (2): 213–257. <https://doi.org/10.1007/BF01578388>.
- Hamdia, K. M., and H. Ghasemi. 2023. “Reliability analysis of the stress intensity factor using multilevel Monte Carlo methods.” *Probabilistic Eng. Mech.*, 74 (August): 103497. Elsevier

- Ltd. <https://doi.org/10.1016/j.pro bengmech.2023.103497>.
- Hamid, A. A., and B. E. Abboud. 1989. "Response of Reinforced Block Masonry Walls to Out-of-Plane Static Loads." *U.S.-Japan Coord. Progr. Mason. Build. Rep. No. 3.2(a)*. Pennsylvania: Department of Civil and Architectural Engineering, Drexel University.
- Hamid, A. A., B. E. Abboud, M. Farah, and H. G. Harris. 1990a. "Flexural behavior of vertically spanned reinforced concrete block masonry walls." *Proc., 5th Can. Mason. Symp.*, 209–218.
- Hamid, A. A., M. K. Hatem, H. G. Harris, and B. E. Abboud. 1990b. "Hysteretic response and ductility of reinforced concrete masonry walls under out-of-plane loading." *Proc., 5th North Am. Mason. Conf*, 397–405.
- Hasofer, A. M., and N. C. Lind. 1974. "Exact and Invariant Second-Moment Code Format." *ASCE J Eng Mech Div*, 100 (EM1): 111–121. <https://doi.org/10.1061/jmcea3.0001848>.
- Haukaas, T., and M. H. Scott. 2006. "Shape sensitivities in the reliability analysis of nonlinear frame structures." *Comput. Struct.*, 84 (15–16): 964–977. <https://doi.org/10.1016/j.compstruc.2006.02.014>.
- Heffler, L., M. Stewart, M. Masia, and M. Correa. 2008. "Statistical Analysis and Spatial Correlation of Flexural Bond Strength for Masonry Walls." *Mason. Int.*, (September).
- Hong, L., H. Li, and J. Fu. 2022. "Novel Kriging-Based Variance Reduction Sampling Method for Hybrid Reliability Analysis with Small Failure Probability." *ASCE-ASME J. Risk Uncertain. Eng. Syst. Part A Civ. Eng.*, 8 (2): 1–12. <https://doi.org/10.1061/ajrua6.0001231>.
- Hosseinzadeh, S., and K. Galal. 2021. "Probabilistic seismic resilience quantification of a reinforced masonry shear wall system with boundary elements under bi-directional horizontal excitations." *Eng. Struct.*, 247 (September): 113023. Elsevier Ltd.

- <https://doi.org/10.1016/j.engstruct.2021.113023>.
- Hwang, S. H., S. Kim, and K. H. Yang. 2022. “In-plane lateral load transfer capacity of unreinforced masonry walls considering presence of openings.” *J. Build. Eng.*, 47 (August 2021): 103868. Elsevier Ltd. <https://doi.org/10.1016/j.jobbe.2021.103868>.
- Iannacone, L., M. Andreini, P. Gardoni, and M. Sassu. 2021. “Probabilistic Models and Fragility Estimates for Unreinforced Masonry Walls Subject to In-Plane Horizontal Forces.” *J. Struct. Eng.*, 147 (6): 1–13. [https://doi.org/10.1061/\(asce\)st.1943-541x.0003006](https://doi.org/10.1061/(asce)st.1943-541x.0003006).
- Ibrahim, Y. 1991. “Observations on applications of importance sampling in structural reliability analysis.” *Struct. Saf.*, 9 (4): 269–281. [https://doi.org/10.1016/0167-4730\(91\)90049-F](https://doi.org/10.1016/0167-4730(91)90049-F).
- Isfeld, A. C., A. L. Müller, M. Hagel, and N. G. Shrive. 2019. “Analysis of safety of slender concrete masonry walls in relation to CSA S304-14.” *Can. J. Civ. Eng.*, 46 (5): 424–438. <https://doi.org/10.1139/cjce-2018-0210>.
- Isfeld, A. C., M. G. Stewart, and M. J. Masia. 2021. “Stochastic finite element model assessing length effect for unreinforced masonry walls subjected to one-way vertical bending under out-of-plane loading.” *Eng. Struct.*, 236 (January): 112115. Elsevier Ltd. <https://doi.org/10.1016/j.engstruct.2021.112115>.
- Isfeld, A. C., M. G. Stewart, and M. J. Masia. 2023. “Structural reliability and partial safety factor assessment of unreinforced masonry in vertical bending.” *Aust. J. Struct. Eng.*, 24 (3): 191–205. Taylor & Francis. <https://doi.org/10.1080/13287982.2023.2173868>.
- Izquierdo, K. 2021. “Statistical prediction methods for the in-plane shear strength of partially grouted masonry walls [MS.c. thesis].” University of Alberta.
- Jafari, S., J. G. Rots, and R. Esposito. 2020. “Core testing method to assess nonlinear shear-sliding

- behaviour of brick-mortar interfaces: A comparative experimental study.” *Constr. Build. Mater.*, 244: 118236. Elsevier. <https://doi.org/10.1016/J.CONBUILDMAT.2020.118236>.
- Jason, L., A. Huerta, G. Pijaudier-Cabot, and S. Ghavamian. 2006. “An elastic plastic damage formulation for concrete: Application to elementary tests and comparison with an isotropic damage model.” *Comput. Methods Appl. Mech. Eng.*, 195 (52): 7077–7092. North-Holland. <https://doi.org/10.1016/j.cma.2005.04.017>.
- Jefferson, A. D., and N. R. Mills. 1998. “Fracture and shear properties of concrete construction joints from core samples.” *Mater. Struct. Constr.*, 31 (9): 595–601. <https://doi.org/10.1007/bf02480609>.
- Kaminosono, T., M. Teshigawara, H. Haraishi, M. Fujiissawa, and A. Nakaoka. 1988. “Experimental study on seismic performance of reinforced masonry walls.” *Proceeding ninth world Conf. Earthq. Eng.*, VI-109-VI-114.
- Karapitta, L., H. Mouzakis, and P. Carydis. 2011. “Explicit finite-element analysis for the in-plane cyclic behavior of unreinforced masonry structures.” *Earthq. Eng. Struct. Dyn.*
- Kaushik, H. B., D. C. Rai, and S. K. Jain. 2007. “Stress-strain characteristics of clay brick masonry under uniaxial compression.” *J. Mater. Civ. Eng.*, 19 (9): 728–739. [https://doi.org/10.1061/\(ASCE\)0899-1561\(2007\)19:9\(728\)](https://doi.org/10.1061/(ASCE)0899-1561(2007)19:9(728)).
- Kazemi, S., M. Mahoutian, H. Moosavi, and Y. Korany. 2011. “Reliability analysis of masonry members under compression.” *Struct. Congr. 2011 - Proc. 2011 Struct. Congr.*, 605–615. [https://doi.org/10.1061/41171\(401\)53](https://doi.org/10.1061/41171(401)53).
- Kennedy, M. C., and A. O’Hagan. 2000. “Predicting the output from a complex computer code when fast approximations are available.” *Biometrika*, 87 (1): 1–13.

<https://doi.org/10.1093/biomet/87.1.1>.

Kesavan, P., and A. Menon. 2022. “Investigation of in-plane and out-of-plane interaction in unreinforced masonry piers by block-based micro-modeling.” *Structures*, 46 (July): 1327–1344. Elsevier Ltd. <https://doi.org/10.1016/j.istruc.2022.10.105>.

Kesavan, P., and A. Menon. 2023. “A macro-element with bidirectional interaction for seismic analysis of unreinforced masonry walls.” *Earthq. Eng. Struct. Dyn.* <https://doi.org/10.1002/eqe.3841>.

Khansefid, A., S. M. Yadollahi, G. Müller, F. Taddei, and A. Kumawat. 2022. “Seismic performance assessment of a masonry building under earthquakes induced by geothermal power plants operation.” *J. Build. Eng.*, 48: 103909. Elsevier Ltd. <https://doi.org/10.1016/j.jobbe.2021.103909>.

Kingsley, G. R., P. B. Shing, T. Gangel, and NIST. 2014a. *Seismic Design of Special Reinforced Masonry Shear Walls: A Guide for Practicing Engineers*.

Kingsley, G., P. B. Shing, and T. Gangel. 2014b. “NEHRP Seismic Design Technical Brief No. 9: Seismic Design of Special Reinforced Masonry Shear Walls.” *Grant/Contract Reports - 14-917-31*. Grant/Contract Reports (NISTGCR), National Institute of Standards and Technology, Gaithersburg, MD.

Kiureghian, A. Der, and O. Ditlevsen. 2009. “Aleatory or epistemic? Does it matter?” *Struct. Saf.*, 31 (2): 105–112. Elsevier Ltd. <https://doi.org/10.1016/j.strusafe.2008.06.020>.

Kiureghian, B. A. Der, M. Asce, H. Lin, and S. Hwang. 1987. “Second-order reliability approximations.” *J. Eng. Mech.*, 113 (8): 1208–1225.

Kloek, T., and H. K. van Dijk. 1978. “Bayesian Estimates of Equation System Parameters: An

- Application of Integration by Monte Carlo.” *Econometrica*, 46 (1): 1.
<https://doi.org/10.2307/1913641>.
- Koutras, A. 2019. “Assessment of the Seismic Behavior of Fully and Partially Grouted Reinforced Masonry Structural Systems through Finite Element Analysis and Shake-Table Testing [Ph.D. thesis].” University of California, San Diego.
- Koutras, A. A., and P. B. Shing. 2021a. “Finite-element modeling of the seismic response of reinforced masonry wall structures.” *Earthq. Eng. Struct. Dyn.*
- Koutras, A. A., and P. B. Shing. 2021b. “Numerical and Experimental Assessment of an Improved Design Detail for Partially Grouted Reinforced Masonry Wall Structures.” *J. Struct. Eng.*, 147 (8): 1–20. [https://doi.org/10.1061/\(asce\)st.1943-541x.0003081](https://doi.org/10.1061/(asce)st.1943-541x.0003081).
- Koutromanos, I., and P. B. Shing. 2012. “Cohesive crack model to simulate cyclic response of concrete and masonry structures.” *ACI Struct. J.*, 109 (3): 349–358.
<https://doi.org/10.14359/51683748>.
- Koutsourelakis, P. S. 2004. “Reliability of structures in high dimensions. Part II. Theoretical validation.” *Probabilistic Eng. Mech.*, 19 (4): 419–423.
<https://doi.org/10.1016/j.pro bengmech.2004.05.002>.
- Koutsourelakis, P. S., H. J. Pradlwarter, and G. I. Schuëller. 2004. “Reliability of structures in high dimensions, part I: Algorithms and applications.” *Probabilistic Eng. Mech.*, 19 (4): 409–417.
<https://doi.org/10.1016/j.pro bengmech.2004.05.001>.
- Krishnachandran, S., and A. Menon. 2023. “Effect of out-of-plane displacements on the in-plane capacity of lightly precompressed rocking unreinforced masonry piers.” *Eng. Struct.*, 281 (February 2022): 115756. Elsevier Ltd. <https://doi.org/10.1016/j.engstruct.2023.115756>.

- Kroese, D. P., R. Y. Rubinstein, and P. W. Glynn. 2013. "The cross-entropy method for estimation." *Handb. Stat.*, 19–34. Elsevier.
- Kumar, N., R. Amirtham, and M. Pandey. 2014. "Plasticity based approach for failure modelling of unreinforced masonry." *Eng. Struct.*, 80: 40–52. Elsevier Ltd. <https://doi.org/10.1016/j.engstruct.2014.08.021>.
- Kumar, N., and M. Barbato. 2019. "New Constitutive Model for Interface Elements in Finite-Element Modeling of Masonry." *J. Eng. Mech.*, 145 (5): 1–15. [https://doi.org/10.1061/\(ASCE\)EM.1943-7889.0001592](https://doi.org/10.1061/(ASCE)EM.1943-7889.0001592).
- Kumar, N., A. Rajagopal, and M. Pandey. 2015. "A rate independent cohesive zone model for modeling failure in quasi-brittle materials." *Mech. Adv. Mater. Struct.*, 22 (8): 681–696. <https://doi.org/10.1080/15376494.2013.855852>.
- Kurtz, N., and J. Song. 2013. "Cross-entropy-based adaptive importance sampling using Gaussian mixture." *Struct. Saf.*, 42: 35–44. <https://doi.org/10.1016/j.strusafe.2013.01.006>.
- Lawrence, S. J., and M. G. Stewart. 2015. "Reliability-Based Calibration of the Capacity Reduction Factor for Design of Masonry in Compression to AS3700." *Aust. J. Struct. Eng.*, 9 (2). <https://doi.org/10.1080/13287982.2009.11465013>.
- Le, L. A., G. D. Nguyen, H. H. Bui, A. H. Sheikh, and A. Kotousov. 2018. "Localised failure mechanism as the basis for constitutive modelling of geomaterials." *Int. J. Eng. Sci.*, 133: 284–310. Elsevier Ltd. <https://doi.org/10.1016/j.ijengsci.2018.09.004>.
- Le, L. A., G. D. Nguyen, H. H. Bui, A. H. Sheikh, A. Kotousov, and A. Khanna. 2017. "Modelling jointed rock mass as a continuum with an embedded cohesive-frictional model." *Eng. Geol.*, 228 (August): 107–120. Elsevier. <https://doi.org/10.1016/j.enggeo.2017.07.011>.

- Lee, J., and G. L. Fenves. 1998. "Plastic-damage model for cyclic loading of concrete structures." *J. Eng. Mech.*, 124 (8): 892–900. [https://doi.org/10.1061/\(ASCE\)0733-9399\(1998\)124:8\(892\)](https://doi.org/10.1061/(ASCE)0733-9399(1998)124:8(892)).
- Lemaire, M. 2013. *Structural reliability*. John Wiley & Sons.
- Lemos, J. V. 2017. "Contact representation in rigid block models of masonry." *Int. J. Mason. Res. Innov.*, 2 (4): 321–334. Inderscience Publishers (IEL).
- Li, J., M. J. Masia, and M. G. Stewart. 2017. "Stochastic spatial modelling of material properties and structural strength of unreinforced masonry in two-way bending." *Struct. Infrastruct. Eng.*, 13 (6): 683–695. Taylor & Francis. <https://doi.org/10.1080/15732479.2016.1188125>.
- Li, J., M. J. Masia, M. G. Stewart, and S. J. Lawrence. 2014. "Spatial variability and stochastic strength prediction of unreinforced masonry walls in vertical bending." *Eng. Struct.*, 59: 787–797. Elsevier Ltd. <https://doi.org/10.1016/j.engstruct.2013.11.031>.
- Li, J., M. G. Stewart, M. J. Masia, and S. J. Lawrence. 2016. "Spatial Correlation of Material Properties and Structural Strength of Masonry in Horizontal Bending." *J. Struct. Eng.*, 142 (11): 1–11. [https://doi.org/10.1061/\(asce\)st.1943-541x.0001488](https://doi.org/10.1061/(asce)st.1943-541x.0001488).
- Li, J., and D. Xiu. 2010. "Evaluation of failure probability via surrogate models." *J. Comput. Phys.*, 229 (23): 8966–8980. Elsevier Inc. <https://doi.org/10.1016/j.jcp.2010.08.022>.
- Li, M., and G. Jia. 2020. "Multifidelity Gaussian Process Model Integrating Low- and High-Fidelity Data Considering Censoring." *J. Struct. Eng.*, 146 (3): 1–15. [https://doi.org/10.1061/\(asce\)st.1943-541x.0002531](https://doi.org/10.1061/(asce)st.1943-541x.0002531).
- Li, P., and Y. Wang. 2021. "Development of an Efficient Response Surface Method for Highly Nonlinear Systems from Sparse Sampling Data Using Bayesian Compressive Sensing."

-
- ASCE-ASME J. Risk Uncertain. Eng. Syst. Part A Civ. Eng.*, 7 (4): 1–14.
<https://doi.org/10.1061/ajrua6.0001155>.
- Li, T., and S. Atamturktur. 2014. “Fidelity and Robustness of Detailed Micromodeling, Simplified Micromodeling, and Macromodeling Techniques for a Masonry Dome.” *J. Perform. Constr. Facil.*, 28 (3): 480–490. [https://doi.org/10.1061/\(asce\)cf.1943-5509.0000440](https://doi.org/10.1061/(asce)cf.1943-5509.0000440).
- Li, Y., and B. Zeng. 2023. “Modeling of masonry structures using a new 3D cohesive interface material model considering dilatancy softening.” *Eng. Struct.*, 277 (December 2022): 115466. Elsevier Ltd. <https://doi.org/10.1016/j.engstruct.2022.115466>.
- Liberatore, D., and D. Addessi. 2015. “Strength domains and return algorithm for the lumped plasticity equivalent frame model of masonry structures.” *Eng. Struct.*, 91: 167–181. Elsevier Ltd. <https://doi.org/10.1016/j.engstruct.2015.02.030>.
- Liberatore, L., O. AlShawa, C. Marson, M. Pasca, and L. Sorrentino. 2020. “Out-of-plane capacity equations for masonry infill walls accounting for openings and boundary conditions.” *Eng. Struct.*, 207: 110198. Elsevier Ltd. <https://doi.org/10.1016/j.engstruct.2020.110198>.
- Liu, J., J. Alexander, Q. Gu, and Y. Li. 2023a. “Gaussian process regression-based load-carrying capacity models of corroded prestressed concrete bridge girders for fast-screening and reliability-based evaluation.” *Eng. Struct.*, 285 (October 2022): 116040. Elsevier Ltd. <https://doi.org/10.1016/j.engstruct.2023.116040>.
- Liu, J., J. Alexander, and Y. Li. 2023b. “Probabilistic error assessment and correction of design code-based shear strength prediction models for reliability analysis of prestressed concrete girders.” *Eng. Struct.*, 279 (January): 115664. Elsevier Ltd. <https://doi.org/10.1016/j.engstruct.2023.115664>.

- Liu, Y., and K. Hu. 2007. "Experimental study of reinforced masonry walls subjected to combined axial load and out-of-plane bending." *Can. J. Civ. Eng.*, 34 (11): 1486–1494. <https://doi.org/10.1139/L06-167>.
- Livesley, R. K. 1992. "A computational model for the limit analysis of three-dimensional masonry structures." *Meccanica*, 27 (3): 161–172. <https://doi.org/10.1007/BF00430042>.
- Lopez, J., S. Oller, E. Oñate, and J. Lubliner. 1999. "A homogeneous constitutive model for masonry." *Int. J. Numer. Methods Eng.*, 46 (10): 1651–1671. [https://doi.org/10.1002/\(SICI\)1097-0207\(19991210\)46:10<1651::AID-NME718>3.0.CO;2-2](https://doi.org/10.1002/(SICI)1097-0207(19991210)46:10<1651::AID-NME718>3.0.CO;2-2).
- Lotfi, H. R., and P. B. Shing. 1991. "An appraisal of smeared crack models for masonry shear wall analysis." *Comput. Struct.*, 41 (3): 413–425.
- Lotfi, H. R., and P. B. Shing. 1994. "Interface model applied to fracture of masonry structures." *J. Struct. Eng.*, 120 (1): 63–80. [https://doi.org/10.1061/\(ASCE\)0733-9445\(1994\)120:1\(63\)](https://doi.org/10.1061/(ASCE)0733-9445(1994)120:1(63)).
- Lourenço, P. B. 1996. "Computational strategies for masonry structures [Ph.D thesis]." *Delft Univ. Netherlands*. Delft University of Technology.
- Lourenço, P. B. 2000a. "Anisotropic Softening Model for Masonry Plates and Shells." *J. Struct. Eng.*, 126 (9): 1008–1016. [https://doi.org/10.1061/\(asce\)0733-9445\(2000\)126:9\(1008\)](https://doi.org/10.1061/(asce)0733-9445(2000)126:9(1008)).
- Lourenço, P. B. 2000b. "Anisotropic Softening Model for Masonry Plates and Shells." *J. Struct. Eng.*, 126 (9): 1008–1016. [https://doi.org/10.1061/\(asce\)0733-9445\(2000\)126:9\(1008\)](https://doi.org/10.1061/(asce)0733-9445(2000)126:9(1008)).
- Lourenço, P. B., R. De Borst, and J. G. Rots. 1997. "A plane stress softening plasticity model for orthotropic materials." *Int. J. Numer. Methods Eng.*, 40 (21): 4033–4057. [https://doi.org/10.1002/\(SICI\)1097-0207\(19971115\)40:21<4033::AID-NME248>3.0.CO;2-](https://doi.org/10.1002/(SICI)1097-0207(19971115)40:21<4033::AID-NME248>3.0.CO;2-)

0.

- Lourenco, P. B., and L. F. Ramos. 2004. "Characterization of Cyclic Behavior of Dry Masonry Joints." *J. Struct. Eng.*, 130 (5): 779–786. [https://doi.org/10.1061/\(ASCE\)0733-9445\(2004\)130](https://doi.org/10.1061/(ASCE)0733-9445(2004)130).
- Lourenço, P. B., J. Rots, and J. Blaauwendraad. 1995a. "Two approaches for the analysis of masonry structures." *Heron*, 40 (4): 313–340.
- Lourenço, P. B., and J. G. Rots. 1997. "Multisurface Interface Model for Analysis of Masonry Structures." *J. Eng. Mech.*, 123 (7): 660–668. [https://doi.org/10.1061/\(asce\)0733-9399\(1997\)123:7\(660\)](https://doi.org/10.1061/(asce)0733-9399(1997)123:7(660)).
- Lourenço, P. B., J. G. Rots, and J. Blaauwendraad. 1995b. "Two approaches for the analysis of masonry structures - micro and macro-modeling." *Heron*, 40 (4): 313–340. Delft University of Technology.
- Lourenço, P. B., J. G. Rots, and J. Blaauwendraad. 1998. "Continuum Model for Masonry: Parameter Estimation and Validation." *J. Struct. Eng.*, 124 (6): 642–652. [https://doi.org/10.1061/\(asce\)0733-9445\(1998\)124:6\(642\)](https://doi.org/10.1061/(asce)0733-9445(1998)124:6(642)).
- Lu, X., L. Xie, H. Guan, Y. Huang, and X. Lu. 2015. "A shear wall element for nonlinear seismic analysis of super-tall buildings using OpenSees." *Finite Elem. Anal. Des.*, 98: 14–25. Elsevier. <https://doi.org/10.1016/j.finel.2015.01.006>.
- Luccioni, B., S. Oller, and R. Danesi. 1996. "Coupled plastic-damaged model." *Comput. Methods Appl. Mech. Eng.*, 129 (1–2): 81–89. North-Holland. [https://doi.org/10.1016/0045-7825\(95\)00887-X](https://doi.org/10.1016/0045-7825(95)00887-X).
- Lumantarna, R., D. T. Biggs, and J. M. Ingham. 2014. "Compressive, Flexural Bond, and Shear

- Bond Strengths of In Situ New Zealand Unreinforced Clay Brick Masonry Constructed Using Lime Mortar between the 1880s and 1940s.” *J. Mater. Civ. Eng.*, 26 (4): 559–566. [https://doi.org/10.1061/\(asce\)mt.1943-5533.0000685](https://doi.org/10.1061/(asce)mt.1943-5533.0000685).
- Macorini, L., and B. A. Izzuddin. 2011. “A non-linear interface element for 3D mesoscale analysis of brick-masonry structures.” *Int. J. Numer. Methods Eng.*, 85: 1584–1608. <https://doi.org/10.1002/nme.3046>.
- Maleki, M. 2008. “Behaviour of partially grouted masonry shear walls under cyclic reversed loading [Ph.D. thesis].” McMaster University.
- Malomo, D., and M. J. DeJong. 2022. “A Macro-Distinct Element Model (M-DEM) for simulating in-plane/out-of-plane interaction and combined failure mechanisms of unreinforced masonry structures.” *Earthq. Eng. Struct. Dyn.*, 51 (4): 793–811. <https://doi.org/10.1002/eqe.3591>.
- Marfia, S., and E. Sacco. 2012. “Multiscale damage contact-friction model for periodic masonry walls.” *Comput. Methods Appl. Mech. Eng.*, 205–208 (1): 189–203. Elsevier B.V. <https://doi.org/10.1016/j.cma.2010.12.024>.
- Martínez, M., and S. Atamturktur. 2019. “Experimental and numerical evaluation of reinforced dry-stacked concrete masonry walls.” *J. Build. Eng.*, 22 (September 2017): 181–191. Elsevier Ltd. <https://doi.org/10.1016/j.jobe.2018.12.007>.
- Masonry Standards Joint Committee. 2005. “Building Code Requirements for Masonry Structures (ACI 530/ASCE 5/TMS 402).” American Concrete Institute.
- MATLAB, M. 2021. “Version 9.10. 0 (R2021a) The MathWorks Inc.” Natick, MA, USA.
- Matsumura, A. 1988. “Shear strength of reinforced masonry walls.” *9th World Conf. Earthq. Eng.*, 121–126.

- Mavros, M. 2015. “Experimental and Numerical Investigation of the Seismic Performance of Reinforced Masonry Structures [Ph.D thesis].” University of California, San Diego.
- Mazza, F., and A. Donnici. 2022. “In-plane-out-of-plane single and mutual interaction of masonry infills in the nonlinear seismic analysis of RC framed structures.” *Eng. Struct.*, 257 (January): 114076. Elsevier Ltd. <https://doi.org/10.1016/j.engstruct.2022.114076>.
- Mazzoni, S., F. McKenna, M. H. Scott, and G. L. Fenves. 2006. “OpenSees command language manual.” *Pacific Earthq. Eng. Res. Cent.*, 264: 137–158. Berkeley, California, United States.
- McKenna, F., G. L. Fenves, and M. H. Scott. 2000. “Open system for earthquake engineering simulation.” *Univ. California, Berkeley, CA*.
- La Mendola, L., M. Accardi, C. Cucchiara, and V. Licata. 2014. “Nonlinear FE analysis of out-of-plane behaviour of masonry walls with and without CFRP reinforcement.” *Constr. Build. Mater.*, 54: 190–196. Elsevier. <https://doi.org/10.1016/j.conbuildmat.2013.12.068>.
- Mendoza-Puchades, M. 2021. “Masonry brick-to-mortar interface variability, for compressive and tensile strength, under blast actions: Experimental testing, numerical modelling challenges and the application of a framework for the treatment of uncertainties [Ph.D. thesis].” University of Liverpool.
- Messali, F., R. Esposito, G. J. P. Ravenshorst, and J. G. Rots. 2020. “Experimental investigation of the in-plane cyclic behaviour of calcium silicate brick masonry walls.” *Bull. Earthq. Eng.*, 18 (8): 3963–3994. Springer Netherlands. <https://doi.org/10.1007/s10518-020-00835-x>.
- Metropolis, N., and S. Ulam. 1949. “The Monte Carlo Method.” *J. Am. Stat. Assoc.*, 44 (247): 335–341. <https://doi.org/10.1080/01621459.1949.10483310>.
- Metwally, Z., B. Zeng, and Y. Li. 2022. “Probabilistic Behavior and Variance-Based Sensitivity

- Analysis of Reinforced Concrete Masonry Walls Considering Slenderness Effect.” *ASCE-ASME J. Risk Uncertain. Eng. Syst. Part A Civ. Eng.*, 8 (4): 1–12. <https://doi.org/10.1061/ajrua6.0001273>.
- Milani, G., P. Lourenço, and A. Tralli. 2006. “Homogenization Approach for the Limit Analysis of Out-of-Plane Loaded Masonry Walls.” *J. Struct. Eng.*, 132 (10): 1650–1663. [https://doi.org/10.1061/\(ASCE\)0733-9445\(2006\)132:10\(1650\)](https://doi.org/10.1061/(ASCE)0733-9445(2006)132:10(1650)).
- Milani, G., and A. Taliercio. 2016. “Limit analysis of transversally loaded masonry walls using an innovative macroscopic strength criterion.” *Int. J. Solids Struct.*, 81: 274–293. Elsevier Ltd. <https://doi.org/10.1016/j.ijsolstr.2015.12.004>.
- Minga, E., L. Macorini, and B. A. Izzuddin. 2018. “A 3D mesoscale damage-plasticity approach for masonry structures under cyclic loading.” *Meccanica*, 53 (7): 1591–1611. Springer Netherlands. <https://doi.org/10.1007/s11012-017-0793-z>.
- Moon, L., D. Dizhur, I. Senaldi, H. Derakhshan, M. Griffith, G. Magenes, and J. Ingham. 2014. “The demise of the URM building stock in Christchurch during the 2010-2011 Canterbury earthquake sequence.” *Earthq. Spectra*, 30 (1): 253–276. <https://doi.org/10.1193/022113EQS044M>.
- Moosavi, H. 2017. “Structural Reliability of Non-Slender Loadbearing Concrete Masonry Members under Concentric and Eccentric Loads [Ph.D. thesis].” University of Alberta.
- Moosavi, H., and Y. Korany. 2014. “Assessment of the structural reliability of loadbearing concrete masonry designed to the Canadian standard s304.1.” *Can. J. Civ. Eng.*, 41 (12): 1046–1053. <https://doi.org/10.1139/cjce-2013-0498>.
- Mucedero, G., D. Perrone, and R. Monteiro. 2022. “Epistemic uncertainty in poorly detailed

- existing frames accounting for masonry infill variability and RC shear failure.” *Earthq. Eng. Struct. Dyn.*, 51 (15): 3755–3778. <https://doi.org/10.1002/eqe.3748>.
- Muhit, I. B., M. J. Masia, M. G. Stewart, and A. C. Isfeld. 2022. “Spatial variability and stochastic finite element model of unreinforced masonry veneer wall system under Out-of-plane loading.” *Eng. Struct.*, 267 (May): 114674. Elsevier Ltd. <https://doi.org/10.1016/j.engstruct.2022.114674>.
- Mukherjee, D., B. N. Rao, and A. Meher Prasad. 2011. “Global sensitivity analysis of unreinforced masonry structure using high dimensional model representation.” *Eng. Struct.*, 33 (4): 1316–1325. Elsevier Ltd. <https://doi.org/10.1016/j.engstruct.2011.01.008>.
- Müller, D., and C.-A. Graubner. 2021. “Assessment of Masonry Compressive Strength in Existing Structures Using a Bayesian Method.” *ASCE-ASME J. Risk Uncertain. Eng. Syst. Part A Civ. Eng.*, 7 (1). <https://doi.org/10.1061/ajrua6.0001113>.
- Najafgholipour, M. A., M. R. Maheri, and P. B. Lourenço. 2013. “Capacity interaction in brick masonry under simultaneous in-plane and out-of-plane loads.” *Constr. Build. Mater.*, 38: 619–626. Elsevier Ltd. <https://doi.org/10.1016/j.conbuildmat.2012.08.032>.
- Najafgholipour, M. A., M. R. Maheri, and P. B. Lourenço. 2014. “Definition of interaction curves for the in-plane and out-of-plane capacity in brick masonry walls.” *Constr. Build. Mater.*, 55: 168–182. Elsevier Ltd. <https://doi.org/10.1016/j.conbuildmat.2014.01.028>.
- National Research Council of Canada. 2015. *National building code of Canada*. NRCC Ottawa.
- Nazir, S. 2015. “Studies on the failure of unreinforced masonry shear walls [Ph.D thesis].” Queensland University of Technology.
- Nazir, S., and M. Dhanasekar. 2014. “A non-linear interface element model for thin layer high

- adhesive mortared masonry.” *Comput. Struct.*, 144: 23–39. Elsevier Ltd.
<https://doi.org/10.1016/j.compstruc.2014.07.023>.
- Nelson, B. L. 1987. “On control variate estimators.” *Comput. Oper. Res.*, 14 (3): 219–225. Elsevier.
- Nelson, B. L. 1990. “Control variate remedies.” *Oper. Res.*, 38 (6): 974–992. INFORMS.
- Ng, C. L. 1996. “Experimental and theoretical investigation of the behaviour of brickwork cladding panel subjected to lateral loading [Ph.D thesis].” The University of Edinburgh.
- Ng, L. W. T., and K. E. Willcox. 2016. “Monte Carlo information-reuse approach to aircraft conceptual design optimization under uncertainty.” *J. Aircr.*, 53 (2): 427–438.
<https://doi.org/10.2514/1.C033352>.
- Ngo, D., and A. C. Scordelis. 1967. “Finite Element Analysis of Reinforced Concrete Beams.” *ACI J. Proc.*, 64 (3). <https://doi.org/10.14359/7551>.
- Nguyen, G. D. 2005. “A thermodynamic approach to constitutive modelling of concrete using damage mechanics and plasticity theory [Ph.D thesis].” *Thesis*. Trinity College, University of Oxford.
- Nguyen, Q. T., and R. Livaoğlu. 2020. “The effect of the ratio of Λ -shaped shear connectors on the flexural behavior of a reinforced concrete frame.” *Adv. Struct. Eng.*, 23 (12): 2724–2740.
<https://doi.org/10.1177/1369433220920442>.
- Nie, J., and B. R. Ellingwood. 2000. “Directional methods for structural reliability analysis.” *Struct. Saf.*, 22 (3): 233–249. [https://doi.org/10.1016/S0167-4730\(00\)00014-X](https://doi.org/10.1016/S0167-4730(00)00014-X).
- Nie, J., and B. R. Ellingwood. 2004a. “A new directional simulation method for system reliability. Part I: Application of deterministic point sets.” *Probabilistic Eng. Mech.*, 19 (4): 425–436.

- <https://doi.org/10.1016/j.pro bengmech.2004.03.004>.
- Nie, J., and B. R. Ellingwood. 2004b. "A new directional simulation method for system reliability. Part II: Application of neural networks." *Probabilistic Eng. Mech.*, 19 (4): 437–447. <https://doi.org/10.1016/j.pro bengmech.2004.03.005>.
- Nie, Y., A. Sheikh, M. Griffith, and P. Visintin. 2022a. "A damage-plasticity based interface model for simulating in-plane/out-of-plane response of masonry structural panels." *Comput. Struct.*, 260: 106721. Elsevier Ltd. <https://doi.org/10.1016/j.compstruc.2021.106721>.
- Nie, Y., A. Sheikh, P. Visintin, and M. Griffith. 2022b. "An interfacial damage-plastic model for the simulation of masonry structures under monotonic and cyclic loadings." *Eng. Fract. Mech.*, 271 (June): 108645. Elsevier Ltd. <https://doi.org/10.1016/j.engfracmech.2022.108645>.
- Noor-E-Khuda, S., and M. Dhanasekar. 2018a. "Masonry Walls under Combined In-Plane and Out-of-Plane Loadings." *J. Struct. Eng.*, 144 (2): 1–10. [https://doi.org/10.1061/\(ASCE\)ST.1943-541X.0001930](https://doi.org/10.1061/(ASCE)ST.1943-541X.0001930).
- Noor-E-Khuda, S., and M. Dhanasekar. 2018b. "Three sides supported unreinforced masonry walls under multi-directional loading." *Constr. Build. Mater.*, 188: 1207–1220. Elsevier Ltd. <https://doi.org/10.1016/j.conbuildmat.2018.08.144>.
- Noor-E-Khuda, S., and M. Dhanasekar. 2020. "On the out-of-plane flexural design of reinforced masonry walls." *J. Build. Eng.*, 27 (September 2019): 100945. Elsevier Ltd. <https://doi.org/10.1016/j.job.2019.100945>.
- Noor-E-Khuda, S., M. Dhanasekar, and D. P. Thambiratnam. 2016a. "An explicit finite element modelling method for masonry walls under out-of-plane loading." *Eng. Struct.*, 113: 103–

120. Elsevier Ltd. <https://doi.org/10.1016/j.engstruct.2016.01.026>.
- Noor-E-Khuda, S., M. Dhanasekar, and D. P. Thambiratnam. 2016b. “Out-of-plane deformation and failure of masonry walls with various forms of reinforcement.” *Compos. Struct.*, 140: 262–277. Elsevier Ltd. <https://doi.org/10.1016/j.compstruct.2015.12.028>.
- Noor-E-Khuda, S., and D. P. Thambiratnam. 2021. “In-plane and out-of-plane structural performance of fully grouted reinforced masonry walls with varying reinforcement ratio – A numerical study.” *Eng. Struct.*, 248 (May): 113288. Elsevier Ltd. <https://doi.org/10.1016/j.engstruct.2021.113288>.
- Oliveira, D. V. de C. 2003. “Experimental and Numerical Analysis of Blocky Masonry Structures Under Cyclic Loading [Ph.D thesis].” Universidade do Minho.
- Oliveira, D. V., and P. B. Lourenço. 2004. “Implementation and validation of a constitutive model for the cyclic behaviour of interface elements.” *Comput. Struct.*, 82 (17–19): 1451–1461. Pergamon. <https://doi.org/10.1016/j.compstruc.2004.03.041>.
- Page, A. W. 1978. “Finite Element Model for Masonry.” *ASCE J Struct Div*, 104 (8): 1267–1285. <https://doi.org/10.1061/jsdeag.0004969>.
- Paiva, R. M., A. R. D. Carvalho, C. Crawford, and A. Suleman. 2010. “Comparison of surrogate models in a multidisciplinary optimization framework for wing design.” *AIAA J.*, 48 (5): 995–1006. <https://doi.org/10.2514/1.45790>.
- Pantò, B., F. Cannizzaro, I. Calìo, and P. B. Lourenço. 2017. “Numerical and Experimental Validation of a 3D Macro-Model for the In-Plane and Out-Of-Plane Behavior of Unreinforced Masonry Walls.” *Int. J. Archit. Herit.*, 11 (7): 946–964. Taylor & Francis. <https://doi.org/10.1080/15583058.2017.1325539>.

- Pantò, B., C. Casapulla, and I. Calì. 2021. “Discrete rotating links model for the non-linear torsion-shear behaviour of masonry joints.” *Proc. Inst. Civ. Eng. Eng. Comput. Mech.*, 174 (4): 215–235. <https://doi.org/10.1680/jencm.21.00010>.
- Pari, M., A. V. Van de Graaf, M. A. N. Hendriks, and J. G. Rots. 2021. “A multi-surface interface model for sequentially linear methods to analyse masonry structures.” *Eng. Struct.*, 238 (January): 112123. Elsevier Ltd. <https://doi.org/10.1016/j.engstruct.2021.112123>.
- Parrinello, F., B. Failla, and G. Borino. 2009. “Cohesive-frictional interface constitutive model.” *Int. J. Solids Struct.*, 46 (13): 2680–2692. Pergamon. <https://doi.org/10.1016/j.ijsolstr.2009.02.016>.
- Patsialis, D., and A. A. Taflanidis. 2021. “Multi-fidelity Monte Carlo for seismic risk assessment applications.” *Struct. Saf.*, 93: 102129. Elsevier. <https://doi.org/10.1016/J.STRUSAFE.2021.102129>.
- Patsialis, D., A. A. Taflanidis, and D. Vamvatsikos. 2022. *Improving the computational efficiency of seismic building-performance assessment through reduced order modeling and multi-fidelity Monte Carlo techniques*. *Bull. Earthq. Eng.* Springer Netherlands.
- Peherstorfer, B., P. S. Beran, and K. Willcox. 2018a. “Multifidelity monte carlo estimation for large-scale uncertainty propagation.” *AIAA Non-Deterministic Approaches Conf. 2018*, 0 (209969): 0–15. <https://doi.org/10.2514/6.2018-1660>.
- Peherstorfer, B., T. Cui, Y. Marzouk, and K. Willcox. 2016a. “Multifidelity importance sampling.” *Comput. Methods Appl. Mech. Eng.*, 300: 490–509. Elsevier B.V. <https://doi.org/10.1016/j.cma.2015.12.002>.
- Peherstorfer, B., B. Kramer, and K. Willcox. 2017. “Combining multiple surrogate models to

- accelerate failure probability estimation with expensive high-fidelity models.” *J. Comput. Phys.*, 341: 61–75. Elsevier Inc. <https://doi.org/10.1016/j.jcp.2017.04.012>.
- Peherstorfer, B., K. Willcox, and M. Gunzburger. 2016b. “Optimal model management for multifidelity Monte Carlo estimation.” *SIAM J. Sci. Comput.*, 38 (5): A3163–A3194. <https://doi.org/10.1137/15M1046472>.
- Peherstorfer, B., K. Willcox, and M. Gunzburger. 2018b. “Survey of multifidelity methods in uncertainty propagation, inference, and optimization.” *SIAM Rev.*, 60 (3): 550–591. <https://doi.org/10.1137/16M1082469>.
- Pelà, L., M. Cervera, and P. Roca. 2011. “Continuum damage model for orthotropic materials: Application to masonry.” *Comput. Methods Appl. Mech. Eng.*, 200 (9–12): 917–930. <https://doi.org/10.1016/j.cma.2010.11.010>.
- Pelà, L., M. Cervera, and P. Roca. 2013. “An orthotropic damage model for the analysis of masonry structures.” *Constr. Build. Mater.*, 41: 957–967. <https://doi.org/10.1016/j.conbuildmat.2012.07.014>.
- Penelis, G. G. 2006. “An efficient approach for pushover analysis of unreinforced masonry (URM) structures.” *J. Earthq. Eng.*, 10 (3): 359–379. <https://doi.org/10.1080/13632460609350601>.
- Peng, B., D. D. Wang, G. Zong, and S. D. Wei. 2020. “Calculation of reliability index for in-plane shear failure of unreinforced masonry walls based on Gaussian process model.” *Eur. J. Environ. Civ. Eng.*, 0 (0): 1–14. Taylor & Francis. <https://doi.org/10.1080/19648189.2019.1708467>.
- Penna, A., S. Lagomarsino, and A. Galasco. 2014. “A nonlinear macroelement model for the seismic analysis of masonry buildings.” *Earthq. Eng. Struct. Dyn.*, 43: 159–179.

- <https://doi.org/10.1002/eqe>.
- Pérez-Foguet, A., A. Rodríguez-Ferran, and A. Huerta. 2001. “Consistent tangent matrices for substepping schemes.” *Comput. Methods Appl. Mech. Eng.*, 190 (35–36): 4627–4647. North-Holland. [https://doi.org/10.1016/S0045-7825\(00\)00336-4](https://doi.org/10.1016/S0045-7825(00)00336-4).
- Peruch, M., E. Spacone, and G. Camata. 2019a. “Nonlinear analysis of masonry structures using fiber-section line elements.” *Earthq. Eng. Struct. Dyn.*, 48 (12): 1345–1364. <https://doi.org/10.1002/eqe.3188>.
- Peruch, M., E. Spacone, and P. B. Shing. 2019b. “Cyclic Analyses of Reinforced Concrete Masonry Panels Using a Force-Based Frame Element.” *J. Struct. Eng.*, 145 (7): 1–12. [https://doi.org/10.1061/\(asce\)st.1943-541x.0002335](https://doi.org/10.1061/(asce)st.1943-541x.0002335).
- Pham, T., and A. A. Gorodetsky. 2022. “Ensemble Approximate Control Variate Estimators: Applications to MultiFidelity Importance Sampling.” *SIAM-ASA J. Uncertain. Quantif.*, 10 (3): 1250–1292. <https://doi.org/10.1137/21M1412268>.
- Pina-Henriques, J., and P. B. Lourenço. 2003. “Testing and modelling of masonry creep and damage in uniaxial compression.” *WIT Trans. Built Environ.* WIT Press.
- Pirsaheb, H., M. Javad Moradi, and G. Milani. 2020. “A Multi-Pier MP procedure for the non-linear analysis of in-plane loaded masonry walls.” *Eng. Struct.*, 212 (March): 110534. Elsevier. <https://doi.org/10.1016/j.engstruct.2020.110534>.
- Van der Pluijm, R. 1992. “Material properties of masonry and its components under tension and shear.” *Proc. 6th Can. Mason. Symp. 15-17 June 1992, Saskatoon, Canada, 675 - 686*. University of Saskatchewan.
- Van der Pluijm, R. 1993. “Shear behaviour of bed joints.” *6th North Am. Mason. Conf. 6-9 June*

- 1993, Philadelphia, Pennsylvania, USA, 125–136. Technomic Publ. Co.
- Pluijm, R. Van der. 1999. “Out-of-Plane Bending of Masonry: Behaviour and Strength.”
- Portioli, F., and L. Cascini. 2016. “Assessment of masonry structures subjected to foundation settlements using rigid block limit analysis.” *Eng. Struct.*, 113: 347–361. Elsevier Ltd. <https://doi.org/10.1016/j.engstruct.2016.02.002>.
- da Porto, F. 2005. “In-plane cyclic behaviour of thin layer joint masonry walls [Ph.D. thesis].” UNIVERSITA’ DEGLI STUDI DI TRENTO.
- da Porto, F., G. Guidi, E. Garbin, and C. Modena. 2010. “In-Plane Behavior of Clay Masonry Walls: Experimental Testing and Finite-Element Modeling.” *J. Struct. Eng.*, 136 (11): 1379–1392. [https://doi.org/10.1061/\(asce\)st.1943-541x.0000236](https://doi.org/10.1061/(asce)st.1943-541x.0000236).
- da Porto, F., F. Mosele, and C. Modena. 2011. “Cyclic out-of-plane behaviour of tall reinforced masonry walls under P- Δ effects.” *Eng. Struct.*, 33 (2): 287–297. Elsevier Ltd. <https://doi.org/10.1016/j.engstruct.2010.10.004>.
- Priestley, M. J. N., and D. M. Elder. 1983. “Stress-strain curves for unconfined and confined concrete masonry.” *J. Proc.*, 192–201.
- Proppe, C., and J. Kaupp. 2022. “On information fusion for reliability estimation with multifidelity models.” *Probabilistic Eng. Mech.*, 69 (April): 103291. Elsevier Ltd. <https://doi.org/10.1016/j.pro bengmech.2022.103291>.
- Pulatsu, B., S. Gonen, and F. Parisi. 2023. “Effect of Precompression and Material Uncertainty on the In-Plane Behavior of URM Pier–Spandrel Systems.” *Buildings*, 13 (1): 1–12. <https://doi.org/10.3390/buildings13010203>.
- Pulatsu, B., S. Gonen, F. Parisi, E. Erdogmus, K. Tuncay, M. F. Funari, and P. B. Lourenço. 2022.

- “Probabilistic approach to assess URM walls with openings using discrete rigid block analysis (D-RBA).” *J. Build. Eng.*, 61 (August): 105269. Elsevier Ltd. <https://doi.org/10.1016/j.jobe.2022.105269>.
- Qamar, F., and S. Qin. 2021. “Development of Nonlinear Finite Element Models of Mortar-Free Interlocked Single Block Column Subjected to Lateral Loading.” *Arab. J. Sci. Eng.*, (0123456789). Springer Berlin Heidelberg. <https://doi.org/10.1007/s13369-021-05668-7>.
- Qian, E., B. Peherstorfer, D. O’Malley, V. V. Vesselinov, and K. Willcox. 2018. “Multifidelity monte carlo estimation of variance and sensitivity indices.” *SIAM-ASA J. Uncertain. Quantif.*, 6 (2): 683–706. <https://doi.org/10.1137/17M1151006>.
- Rackwitz, R., and B. Flessler. 1978. “Structural reliability under combined random load sequences.” *Comput. Struct.*, 9 (5): 489–494. [https://doi.org/10.1016/0045-7949\(78\)90046-9](https://doi.org/10.1016/0045-7949(78)90046-9).
- Raijmakers, T. M. J. 1992. *Deformation controlled tests in masonry shear walls: report B-92-1156*.
- Raijmakers, T. M. J., and A. T. Vermeltfoort. 1992. *Deformation controlled tests in masonry shear walls. holandés), Rep. B-92-1156, TNO-Bouw, Delft, Países Bajos*.
- Rajashekhar, M. R., and B. R. Ellingwood. 1993. “A new look at the response surface approach.” *Struct. Saf.*, 12 (April 1994): 205–220.
- Rashki, M., A. Ghavidel, H. Ghohani Arab, and S. R. Mousavi. 2018. “Low-cost finite element method-based reliability analysis using adjusted control variate technique.” *Struct. Saf.*, 75: 133–142. Elsevier Ltd. <https://doi.org/10.1016/j.strusafe.2017.11.005>.
- Reinhardt, H. W. 1984. “Fracture Mechanics of an Elastic Softening Material Like Concrete.”

- Heron*, 29 (2): 1–42.
- Remacle, J., J. Lambrechts, and B. Seny. 2012. “Blossom-Quad: A non-uniform quadrilateral mesh generator using a minimum-cost perfect-matching algorithm.” *International*, 85 (February): 1102–1119. <https://doi.org/10.1002/nme>.
- Rinaldin, G., C. Amadio, and L. Macorini. 2016. “A macro-model with nonlinear springs for seismic analysis of URM buildings.” *Earthq. Eng. Struct. Dyn.*
- De Risi, M. T., M. Di Domenico, P. Ricci, G. M. Verderame, and G. Manfredi. 2019. “Experimental investigation on the influence of the aspect ratio on the in-plane/out-of-plane interaction for masonry infills in RC frames.” *Eng. Struct.*, 189 (April): 523–540. Elsevier. <https://doi.org/10.1016/j.engstruct.2019.03.111>.
- Robazza, B. R., S. Brzev, T. Y. Yang, K. J. Elwood, D. L. Anderson, and B. McEwen. 2018. “Out-of-Plane Behavior of Slender Reinforced Masonry Shear Walls under In-Plane Loading: Experimental Investigation.” *J. Struct. Eng.*, 144 (3): 1–16. [https://doi.org/10.1061/\(ASCE\)ST.1943-541X.0001968](https://doi.org/10.1061/(ASCE)ST.1943-541X.0001968).
- Roca, P., C. Molins, and A. Drougkas. 2016. “Micro-mechanical modeling of masonry - Parametric study.” *Struct. Anal. Hist. Constr. Anamn. diagnosis, Ther. Control. - Proc. 10th Int. Conf. Struct. Anal. Hist. Constr. SAHC 2016*, (September): 279–283. <https://doi.org/10.1201/9781315616995-36>.
- Roca, P., C. Molins, and A. R. Marí. 2005. “Strength Capacity of Masonry Wall Structures by the Equivalent Frame Method.” *J. Struct. Eng.*, 131 (10): 1601–1610. [https://doi.org/10.1061/\(asce\)0733-9445\(2005\)131:10\(1601\)](https://doi.org/10.1061/(asce)0733-9445(2005)131:10(1601)).
- Rota, M., A. Penna, and G. Magenes. 2014. “A framework for the seismic assessment of existing

- masonry buildings accounting for different sources of uncertainty.” *Earthq. Eng. Struct. Dyn.*, 43: 1045–1066. <https://doi.org/10.1002/eqe>.
- Rots, J. G. 1991. “Numerical simulation of cracking in structural masonry.” *Heron*.
- Rubinstein, R. Y., and D. P. Kroese. 2004. *The cross-entropy method: a unified approach to combinatorial optimization, Monte-Carlo simulation, and machine learning*. Springer.
- Rubinstein, R. Y., and D. P. Kroese. 2008. *The Cross-Entropy Method. Technometrics*.
- Saatcioglu, M., A. Ghobarah, and I. Nistor. 2006. “Performance of structures in Indonesia during the December 2004 Great Sumatra earthquake and Indian Ocean tsunami.” *Earthq. Spectra*, 22 (SUPPL. 3): 295–319. <https://doi.org/10.1193/1.2209171>.
- Sacco, E., and F. Lebon. 2012. “A damage-friction interface model derived from micromechanical approach.” *Int. J. Solids Struct.*, 49 (26): 3666–3680. Pergamon. <https://doi.org/10.1016/j.ijsolstr.2012.07.028>.
- Sacks, J., W. J. Welch, T. J. Mitchell, and H. P. Wynn. 1989. “Design and Analysis of Computer Experiments.” *Stat. Sci.*, 4 (4): 409–435. <https://doi.org/10.2307/2246134>.
- Sahu, S., P. R. Ravi Teja, P. Sarkar, and R. Davis. 2019. “Variability in the Compressive Strength of Fly Ash Bricks.” *J. Mater. Civ. Eng.*, 31 (2): 1–10. [https://doi.org/10.1061/\(asce\)mt.1943-5533.0002592](https://doi.org/10.1061/(asce)mt.1943-5533.0002592).
- Sahu, S., P. Sarkar, and R. Davis. 2020. “Uncertainty in Bond Strength of Unreinforced Fly-Ash Brick Masonry.” *J. Mater. Civ. Eng.*, 32 (3): 1–10. [https://doi.org/10.1061/\(asce\)mt.1943-5533.0003095](https://doi.org/10.1061/(asce)mt.1943-5533.0003095).
- Salari, M. R., S. Saeb, K. J. Willam, S. J. Patchet, and R. C. Carrasco. 2004. “A coupled elastoplastic damage model for geomaterials.” *Comput. Methods Appl. Mech. Eng.*, 193 (27–

- 29): 2625–2643. North-Holland. <https://doi.org/10.1016/J.CMA.2003.11.013>.
- Salem, S., M. Ezzeldin, W. El-Dakhakhni, and M. Tait. 2019. “Out-of-Plane Behavior of Load-Bearing Reinforced Masonry Shear Walls.” *J. Struct. Eng.*, 145 (11): 1–17. [https://doi.org/10.1061/\(asce\)st.1943-541x.0002403](https://doi.org/10.1061/(asce)st.1943-541x.0002403).
- Salmanpour, A. H. 2017. “Displacement capacity of structural masonry [Ph.D thesis].” ETH Zurich.
- Salmanpour, A. H., N. Mojsilović, and J. Schwartz. 2015. “Displacement capacity of contemporary unreinforced masonry walls: An experimental study.” *Eng. Struct.*, 89: 1–16. <https://doi.org/10.1016/j.engstruct.2015.01.052>.
- Saloustros, S., L. Pelà, M. Cervera, and P. Roca. 2018. “An Enhanced Finite Element Macro-Model for the Realistic Simulation of Localized Cracks in Masonry Structures: A Large-Scale Application.” *Int. J. Archit. Herit.*, 12 (3): 432–447. <https://doi.org/10.1080/15583058.2017.1323245>.
- Samy, B. A., S. R. Sarhat, and E. G. Sherwood. 2012. “Comparing flexural capacity of reinforced masonry members using different codes.” *Proceedings, Annu. Conf. - Can. Soc. Civ. Eng.*, 4 (May): 2648–2657.
- Savalle, N., P. B. Lourenço, and G. Milani. 2022. “Joint Stiffness Influence on the First-Order Seismic Capacity of Dry-Joint Masonry Structures: Numerical DEM Investigations.” *Appl. Sci.*, 12 (4). <https://doi.org/10.3390/app12042108>.
- Schöbi, R., B. Sudret, and S. Marelli. 2017. “Rare Event Estimation Using Polynomial-Chaos Kriging.” *ASCE-ASME J. Risk Uncertain. Eng. Syst. Part A Civ. Eng.*, 3 (2): 1–12. <https://doi.org/10.1061/ajrua6.0000870>.

- Seif Eldin, H. M. 2016. “In-plane Shear Behaviour of Fully Grouted Reinforced Masonry Shear Wall [Ph.D. thesis].” Concordia University.
- Seif Eldin, H. M., N. Aly, and K. Galal. 2019. “In-plane shear strength equation for fully grouted reinforced masonry shear walls.” *Eng. Struct.*, 190 (April): 319–332. Elsevier. <https://doi.org/10.1016/j.engstruct.2019.03.079>.
- Seif Eldin, H. M., and K. Galal. 2017. “In-Plane Seismic Performance of Fully Grouted Reinforced Masonry Shear Walls.” *J. Struct. Eng.*, 143 (7): 1–13. [https://doi.org/10.1061/\(asce\)st.1943-541x.0001758](https://doi.org/10.1061/(asce)st.1943-541x.0001758).
- Senanayake, S. M. C. U., A. Haque, and H. H. Bui. 2022. “An experiment-based cohesive-frictional constitutive model for cemented materials.” *Comput. Geotech.*, 149 (June): 104862. Elsevier Ltd. <https://doi.org/10.1016/j.compgeo.2022.104862>.
- Serpieri, R., M. Albarella, and E. Sacco. 2017. “A 3D microstructured cohesive–frictional interface model and its rational calibration for the analysis of masonry panels.” *Int. J. Solids Struct.*, 122–123: 110–127. Elsevier Ltd. <https://doi.org/10.1016/j.ijsolstr.2017.06.006>.
- Shadlou, M., E. Ahmadi, and M. M. Kashani. 2020. “Micromechanical modelling of mortar joints and brick-mortar interfaces in masonry Structures: A review of recent developments.” *Structures*, 23: 831–844. Elsevier. <https://doi.org/10.1016/j.istruc.2019.12.017>.
- Shedid, M. T., W. W. El-Dakhkhni, and R. G. Drysdale. 2008. “Behavior of Fully Grouted Reinforced Concrete Masonry Shear Walls Failing in Flexure: Experimental Results.” *J. Struct. Eng.*, 134 (11): 1754–1767. <https://doi.org/10.1016/j.engstruct.2009.03.006>.
- Shen, J., X. Ren, Y. Zhang, and J. Chen. 2022. “Slip-enhanced plastic-damage constitutive model for masonry structures.” *Eng. Struct.*, 254 (December 2021). Elsevier Ltd.

<https://doi.org/10.1016/j.engstruct.2021.113792>.

Shen, Y., Y. Tu, T. Li, and Y. Li. 2023. “Experimental and numerical study of resistance of multi-cell L-shaped concrete-filled steel tubular stub columns under biaxial eccentric compressive loading.” *J. Build. Eng.*, 70 (March): 106399. Elsevier Ltd. <https://doi.org/10.1016/j.jobe.2023.106399>.

Sherafati, M. A., and M. R. Sohrabi. 2016a. “Performance of Masonry Walls during Kaki, Iran, Earthquake of April 9, 2013.” *J. Perform. Constr. Facil.*, 30 (3): 1–19. [https://doi.org/10.1061/\(asce\)cf.1943-5509.0000788](https://doi.org/10.1061/(asce)cf.1943-5509.0000788).

Sherafati, M. A., and M. R. Sohrabi. 2016b. “Probabilistic Model for Bed-Joint Shear-Sliding Strength of Clay-Brick Walls Based on Field Test Data.” *ASCE-ASME J. Risk Uncertain. Eng. Syst. Part A Civ. Eng.*, 2 (4): 04016007. <https://doi.org/10.1061/ajrua6.0000879>.

Shing, B., J. Noland, H. Spaeh, E. Klamerus, and M. Schuller. 1991. *Response of Single-Story Reinforced Masonry Shear Walls to In-Plane Lateral Loads*.

Shing, P. B., and L. Cao. 1997. *Analysis of partially grouted masonry shear walls, NIST GCR report*.

Shing, P. B., J. L. Noland, E. Klamerus, and H. Spaeh. 1989a. “Inelastic behaviour of concrete masonry shear walls.” *J. Struct. Eng.*

Shing, P. B., J. L. Noland, E. Klamerus, and H. Spaeh. 1989b. “Inelastic Behavior of Concrete Masonry Shear Walls.” *J. Struct. Eng.*, 115 (9): 2204–2225. [https://doi.org/10.1061/\(asce\)0733-9445\(1989\)115:9\(2204\)](https://doi.org/10.1061/(asce)0733-9445(1989)115:9(2204)).

Shing, P. B., M. Schuller, and V. S. Hoskere. 1990a. “In-Plane Resistance of Reinforced Masonry Shear Walls.” *J. Struct. Eng.*, 116 (3): 619–640. [https://doi.org/10.1061/\(asce\)0733-](https://doi.org/10.1061/(asce)0733-)

- 9445(1990)116:3(619).
- Shing, P. B., M. Schuller, V. S. Houskere, and E. Carter. 1990b. “Flexural and shear response of reinforced masonry walls.” *Struct. J.*, 87 (6): 646–656.
- Shun Li, K., and P. Lumb. 1985. “Reliability analysis by numerical integration and curve fitting.” *Struct. Saf.*, 3 (1): 29–36. [https://doi.org/10.1016/0167-4730\(85\)90005-0](https://doi.org/10.1016/0167-4730(85)90005-0).
- Simo, J. C., and T. J. R. Hughes. 2006. *Computational inelasticity*. Springer Science & Business Media.
- Simo, J. C., and J. W. Ju. 1987a. “Strain- and stress-based continuum damage models-I. Formulation.” *Int. J. Solids Struct.*, 23 (7): 821–840. [https://doi.org/10.1016/0020-7683\(87\)90083-7](https://doi.org/10.1016/0020-7683(87)90083-7).
- Simo, J. C., and J. W. Ju. 1987b. “Strain- and stress-based continuum damage models—II. Computational aspects.” *Int. J. Solids Struct.*, 23 (7): 841–869. Pergamon. [https://doi.org/10.1016/0020-7683\(87\)90084-9](https://doi.org/10.1016/0020-7683(87)90084-9).
- Simo, J. C., J. G. Kennedy, and S. Govindjee. 1988. “Non-smooth multisurface plasticity and viscoplasticity. Loading/unloading conditions and numerical algorithms.” *Int. J. Numer. Methods Eng.*, 26 (10): 2161–2185. <https://doi.org/10.1002/nme.1620261003>.
- Simulia, D. S. 2017. “Abaqus 2017, Documentation.” *Dassault Syst. Waltham, MA, USA*.
- Skandalos, K., S. Chakraborty, and S. Tesfamariam. 2022. “Seismic reliability analysis using a multi-fidelity surrogate model: Example of base-isolated buildings.” *Struct. Saf.*, 97 (October 2020): 102222. Elsevier Ltd. <https://doi.org/10.1016/j.strusafe.2022.102222>.
- Song, C., and R. Kawai. 2023. “Monte Carlo and variance reduction methods for structural reliability analysis: A comprehensive review.” *Probabilistic Eng. Mech.*, 73 (June): 103479.

- Elsevier Ltd. <https://doi.org/10.1016/j.pro bengmech.2023.103479>.
- Sousa, R., J. Guedes, and H. Sousa. 2015. "Characterization of the uniaxial compression behaviour of unreinforced masonry-Sensitivity analysis based on a numerical and experimental approach." *Arch. Civ. Mech. Eng.*, 15 (2): 532–547. Politechnika Wrocławska. <https://doi.org/10.1016/j.acme.2014.06.007>.
- Sousa, R., H. Sousa, and J. Guedes. 2013. "Diagonal compressive strength of masonry samples - Experimental and numerical approach." *Mater. Struct. Constr.*, 46 (5): 765–786. <https://doi.org/10.1617/s11527-012-9933-z>.
- Sparling, A., and D. Palermo. 2023. "Response of Full-Scale Slender Masonry Walls with Conventional and NSM Steel Reinforcement Subjected to Axial and Out-of-Plane Loads." *J. Struct. Eng.*, 149 (1): 1–16. <https://doi.org/10.1061/jsendh.steng-11364>.
- Stankowski, T., K. Runesson, and S. Sture. 1993a. "Fracture and slip of interfaces in cementitious composites II: implementation." *J. Eng. Mech.*, 119 (2): 315–327.
- Stankowski, T., K. Runesson, and S. Sture. 1993b. "Fracture and slip of interface in cementitious composites; I: characteristic." *J. Eng. Mech.*, 119 (2): 292–314.
- Stavridis, A., and P. B. Shing. 2010. "Finite-Element Modeling of Nonlinear Behavior of Masonry-Infilled RC Frames." *J. Struct. Eng.*, 136 (3): 285–296. [https://doi.org/10.1061/\(ASCE\)ST.1943-541X.116](https://doi.org/10.1061/(ASCE)ST.1943-541X.116).
- Stewart, M. G., and S. J. Lawrence. 2007. "Model Error , Structural Reliability and Partial Safety Factors for Structural Masonry in Compression." *Mason. Int.*, 20 (3): 107–116.
- Sudret, B. 2008. "Global sensitivity analysis using polynomial chaos expansions." *Reliab. Eng. Syst. Saf.*, 93 (7): 964–979. Elsevier. <https://doi.org/10.1016/j.ress.2007.04.002>.

- Tabandeh, A., G. Jia, and P. Gardoni. 2022. “A review and assessment of importance sampling methods for reliability analysis.” *Struct. Saf.*, 97 (March): 102216. Elsevier Ltd. <https://doi.org/10.1016/j.strusafe.2022.102216>.
- Tabbakhha, M., and G. Deodatis. 2017. “Effect of Uncertainty of Tensile Strength of Mortar Joints on the Behavior of Masonry Walls under Lateral Loads.” *J. Struct. Eng.*, 143 (2): 1–15. [https://doi.org/10.1061/\(ASCE\)ST.1943-541X.0001640](https://doi.org/10.1061/(ASCE)ST.1943-541X.0001640).
- Takashi, K., I. Hiroshi, Y. Yoshiharu, and K. Ryogo. 1986. “Seismic Capacity of Reinforced Masonry Walls Including Effects of Axial Stress.” *Proc. 4th Can. Mason. Symp.*, 163–174.
- Tariq, H., M. Amir, V. Sarhosis, and G. Milani. 2023. “In-plane strength of masonry wall panels : A comparison between design codes and high-fidelity models.” *Structures*, 47 (December 2022): 1869–1899. Elsevier Ltd. <https://doi.org/10.1016/j.istruc.2022.11.125>.
- Tichý, M. 1994. “First-order third-moment reliability method.” *Struct. Saf.*, 16 (3): 189–200. [https://doi.org/10.1016/0167-4730\(94\)00021-H](https://doi.org/10.1016/0167-4730(94)00021-H).
- TMS. 2016. *Building code requirements and specification for masonry structures (TMS 402/602-16)*. The Masonry Society Boulder, CO.
- Tokdar, S. T., and R. E. Kass. 2010. “Importance sampling: A review.” *Wiley Interdiscip. Rev. Comput. Stat.*, 2 (1): 54–60. <https://doi.org/10.1002/wics.56>.
- Di Trapani, F., P. B. Shing, and L. Cavaleri. 2018. “Macroelement Model for In-Plane and Out-of-Plane Responses of Masonry Infills in Frame Structures.” *J. Struct. Eng.*, 144 (2). [https://doi.org/10.1061/\(ASCE\)ST.1943-541X.0001926](https://doi.org/10.1061/(ASCE)ST.1943-541X.0001926).
- Tubaldi, E., L. Macorini, and B. A. Izzuddin. 2020. “Identification of critical mechanical parameters for advanced analysis of masonry arch bridges.” *Struct. Infrastruct. Eng.*, 16 (2):

- 328–345. Taylor & Francis. <https://doi.org/10.1080/15732479.2019.1655071>.
- Vaculik, J. 2012. “Unreinforced masonry walls subjected to out-of-plane seismic actions [Ph.D thesis].” University of Adelaide.
- Vandoren, B., K. De Proft, A. Simone, and L. J. Sluys. 2013. “Mesoscopic modelling of masonry using weak and strong discontinuities.” *Comput. Methods Appl. Mech. Eng.*, 255: 167–182. Elsevier B.V. <https://doi.org/10.1016/j.cma.2012.11.005>.
- Vanin, F., A. Penna, and K. Beyer. 2020. “A three-dimensional macroelement for modelling the in-plane and out-of-plane response of masonry walls.” *Earthq. Eng. Struct. Dyn.*, 49 (14): 1365–1387. <https://doi.org/10.1002/eqe.3277>.
- Vasconcelos, G., P. B. Lourenço, and D. Oliveira. 2008. “Experimental shear behavior of stone masonry joints.” *Struct. Anal. Hist. Constr. Preserv. Saf. Significance - Proc. 6th Int. Conf. Struct. Anal. Hist. Constr. SAHC08*, 771–779.
- Vermeltfoort, A. T., and T. M. J. Raijmakers. 1993. *Deformation controlled tests in masonry shear walls, Part 2. holandés*, Rep. TUE/BKO/93.08, Eindhoven Univ. Technol. Eindhoven, Países Bajos.
- Vitali, R., R. T. Haftka, and B. V. Sankar. 2002. “Multi-fidelity design of stiffened composite panel with a crack.” *Struct. Multidiscip. Optim.*, 23 (5): 347–356. <https://doi.org/10.1007/s00158-002-0195-1>.
- Vlachakis, G., E. Vlachaki, and P. B. Lourenço. 2020. “Learning from failure: Damage and failure of masonry structures, after the 2017 Lesvos earthquake (Greece).” *Eng. Fail. Anal.*, 117 (July): 104803. Elsevier. <https://doi.org/10.1016/j.engfailanal.2020.104803>.
- Voon, K. C., and J. M. Ingham. 2007. “Design Expression for the In-Plane Shear Strength of

- Reinforced Concrete Masonry.” *J. Struct. Eng.*, 133 (5): 706–713.
[https://doi.org/10.1061/\(asce\)0733-9445\(2007\)133:5\(706\)](https://doi.org/10.1061/(asce)0733-9445(2007)133:5(706)).
- Walsh, K., D. Dizhur, I. Giongo, H. Derakhshan, and J. Ingham. 2018. “Predicted Versus Experimental Out-of-plane Force-displacement Behaviour of Unreinforced Masonry Walls.” *Structures*, 15: 292–306. Elsevier Ltd. <https://doi.org/10.1016/j.istruc.2018.07.012>.
- Wambacq, J., J. Ulloa, G. Lombaert, and S. François. 2022. “A variationally coupled phase field and interface model for fracture in masonry.” *Comput. Struct.*, 264: 106744. Elsevier Ltd. <https://doi.org/10.1016/j.compstruc.2022.106744>.
- Wang, R., A. E. Elwi, and M. A. Hatzinikolas. 1997. “Numerical study of tall masonry cavity walls subjected to eccentric loads.” *J. Struct. Eng.*, 123 (10): 1287–1294. American Society of Civil Engineers.
- Wei, D., and S. Rahman. 2007. “Structural reliability analysis by univariate decomposition and numerical integration.” *Probabilistic Eng. Mech.*, 22 (1): 27–38.
<https://doi.org/10.1016/j.pro bengmech.2006.05.004>.
- Xie, X., Z. Qu, H. Fu, and L. Zhang. 2021a. “Effect of prior in-plane damage on the out-of-plane behavior of masonry infill walls.” *Eng. Struct.*, 226: 111380. Elsevier Ltd. <https://doi.org/10.1016/j.engstruct.2020.111380>.
- Xie, Z., M. Sousamli, F. Messali, and J. G. Rots. 2021b. “A sub-stepping iterative constitutive model for cyclic cracking-crushing-shearing in masonry interface elements.” *Comput. Struct.*, 257: 106654. Pergamon. <https://doi.org/10.1016/j.compstruc.2021.106654>.
- Xu, C., X. Cheng, and L. Bin. 2012. “Modeling of influence of heterogeneity on mechanical performance of unreinforced masonry shear walls.” *Constr. Build. Mater.*, 26 (1): 90–95.

- Elsevier. <https://doi.org/10.1016/j.conbuildmat.2011.05.007>.
- Xu, H., and Z. Liu. 2019. "Control variate multifidelity estimators for the variance and sensitivity analysis of mesostructure-structure systems." *ASCE-ASME J. Risk Uncertain. Eng. Syst. Part B Mech. Eng.*, 5 (2). <https://doi.org/10.1115/1.4042835>.
- Yacila, J., G. Camata, J. Salsavilca, and N. Tarque. 2019. "Pushover analysis of confined masonry walls using a 3D macro-modelling approach." *Eng. Struct.*, 201: 109731. Elsevier Ltd. <https://doi.org/10.1016/j.engstruct.2019.109731>.
- Yao, Y., X. Huan, and J. Capecelatro. 2022. "Multi-fidelity uncertainty quantification of particle deposition in turbulent pipe flow." *J. Aerosol Sci.*, 166 (July): 106065. Elsevier Ltd. <https://doi.org/10.1016/j.jaerosci.2022.106065>.
- Yavartanoo, F., and T. H.-K. Kang. 2022. "Dry-Stack Masonry Wall Modeling Using Finite-Element Method." *J. Struct. Eng.*, 148 (11): 1–14. [https://doi.org/10.1061/\(asce\)st.1943-541x.0003457](https://doi.org/10.1061/(asce)st.1943-541x.0003457).
- Yuen, T. Y. P., T. Deb, H. Zhang, and Y. Liu. 2019. "A fracture energy based damage-plasticity interfacial constitutive law for discrete finite element modelling of masonry structures." *Comput. Struct.*, 220: 92–113. Elsevier Ltd. <https://doi.org/10.1016/j.compstruc.2019.05.007>.
- Zeng, B., and Y. Li. 2023. "Towards Performance-Based Design of Masonry Buildings: Literature Review." *Buildings*, 13 (1534). <https://doi.org/10.3390/buildings13061534>.
- Zeng, B., Y. Li, and C. Cruz Noguez. 2021. "Modeling and parameter importance investigation for simulating in-plane and out-of-plane behaviors of un-reinforced masonry walls." *Eng. Struct.*, 248: 113233. Elsevier. <https://doi.org/10.1016/j.engstruct.2021.113233>.

- Zhai, C., X. Wang, J. Kong, S. Li, and L. Xie. 2017. "Numerical Simulation of Masonry-Infilled RC Frames Using XFEM." *J. Struct. Eng.*, 143 (10): 1–14. [https://doi.org/10.1061/\(ASCE\)ST.1943-541X.0001886](https://doi.org/10.1061/(ASCE)ST.1943-541X.0001886).
- Zhai, X., and M. G. Stewart. 2010. "Structural reliability analysis of reinforced grouted concrete block masonry walls in compression." *Eng. Struct.*, 32 (1): 106–114. Elsevier. <https://doi.org/10.1016/j.engstruct.2009.08.020>.
- Zhai, X., Z. Zhong, and M. Stewart. 2012. "Model error and structural reliability for reinforced concrete block masonry walls in shear." *Adv. Struct. Eng.*, 15 (3): 389–398. <https://doi.org/10.1260/1369-4332.15.3.389>.
- Zhang, C., C. Song, and A. Shafieezadeh. 2022. "Adaptive reliability analysis for multi-fidelity models using a collective learning strategy." *Struct. Saf.*, 94 (August 2021): 102141. Elsevier Ltd. <https://doi.org/10.1016/j.strusafe.2021.102141>.
- Zhang, J. 2021. "Modern Monte Carlo methods for efficient uncertainty quantification and propagation: A survey." *Wiley Interdiscip. Rev. Comput. Stat.*, 13 (5): 1–23. <https://doi.org/10.1002/wics.1539>.
- Zhang, S., N. Richart, and K. Beyer. 2018. "Numerical evaluation of test setups for determining the shear strength of masonry." *Mater. Struct.*, 51 (4): 1–12. Springer Netherlands. <https://doi.org/10.1617/s11527-018-1236-6>.
- Zhang, S., S. M. Taheri Mousavi, N. Richart, J. F. Molinari, and K. Beyer. 2017. "Micro-mechanical finite element modeling of diagonal compression test for historical stone masonry structure." *Int. J. Solids Struct.*, 112: 122–132. Pergamon. <https://doi.org/10.1016/j.ijsolstr.2017.02.014>.

- Zhang, Y., L. Macorini, and B. A. Izzuddin. 2016. “Mesoscale partitioned analysis of brick-masonry arches.” *Eng. Struct.*, 124: 142–166. Elsevier. <https://doi.org/10.1016/J.ENGSTRUCT.2016.05.046>.
- Zhao, Y. G., and T. Ono. 1999. “A general procedure for first/second-order reliability method (FORM/SORM).” *Struct. Saf.*, 21 (2): 95–112. [https://doi.org/10.1016/S0167-4730\(99\)00008-9](https://doi.org/10.1016/S0167-4730(99)00008-9).
- Zhao, Y. G., and T. Ono. 2001. “Moment methods for structural reliability.” *Struct. Saf.*, 23 (1): 47–75. [https://doi.org/10.1016/S0167-4730\(00\)00027-8](https://doi.org/10.1016/S0167-4730(00)00027-8).
- Zhu, F., Q. Zhou, F. Wang, and X. Yang. 2017. “Spatial variability and sensitivity analysis on the compressive strength of hollow concrete block masonry wallettes.” *Constr. Build. Mater.*, 140: 129–138. Elsevier Ltd. <https://doi.org/10.1016/j.conbuildmat.2017.02.099>.
- van Zijl, G. P. A. G. 2004. “Modeling Masonry Shear-Compression: Role of Dilatancy Highlighted.” *J. Eng. Mech.*, 130 (11): 1289–1296. [https://doi.org/10.1061/\(asce\)0733-9399\(2004\)130:11\(1289\)](https://doi.org/10.1061/(asce)0733-9399(2004)130:11(1289)).
- Del Zoppo, M., M. Di Ludovico, G. M. Verderame, and A. Prota. 2017. “Experimental Behavior of Nonconforming RC Columns with Deformed Bars under Constant Axial Load and Fixed Biaxial Bending.” *J. Struct. Eng.*, 143 (11): 1–14. [https://doi.org/10.1061/\(asce\)st.1943-541x.0001892](https://doi.org/10.1061/(asce)st.1943-541x.0001892).
- Zucchini, A., and P. B. Lourenço. 2004. “A coupled homogenisation-damage model for masonry cracking.” *Comput. Struct.*, 82 (11–12): 917–929. Pergamon. <https://doi.org/10.1016/j.compstruc.2004.02.020>.
- Zucchini, A., and P. B. Lourenço. 2007. “Mechanics of masonry in compression: Results from a

homogenisation approach.” *Comput. Struct.*, 85 (3–4): 193–204. Pergamon.
<https://doi.org/10.1016/j.compstruc.2006.08.054>.

Zuhair Murad, Y. 2021. “Predictive model for bidirectional shear strength of reinforced concrete columns subjected to biaxial cyclic loading.” *Eng. Struct.*, 244 (June): 112781. Elsevier Ltd.
<https://doi.org/10.1016/j.engstruct.2021.112781>.

Appendix A. DERIVATION OF JACOBIAN MATRICES IN THE 3D MULTI-YIELD SURFACES PLASTICITY-BASED CONSTITUTIVE MODEL

In the multi-yield surface plasticity integration strategy illustrated in Chapter 4, Jacobian matrices J_1 , J_2 , and J_3 are required in the Implicit Euler Backward integration strategy. They are detailed in Eq. (A-1) to Eq. (A-9):

$$J_1(\boldsymbol{\sigma}, \kappa_1, \kappa_2, \dot{\lambda}_1)_{6 \times 6} = \begin{bmatrix} \mathbf{I} + \dot{\lambda}_1 \mathbf{K} \frac{\partial^2 g_1}{\partial \boldsymbol{\sigma}^2} & \dot{\lambda}_1 \mathbf{K} \frac{\partial^2 g_1}{\partial \boldsymbol{\sigma} \partial \kappa_1} & \dot{\lambda}_1 \mathbf{K} \frac{\partial^2 g_1}{\partial \boldsymbol{\sigma} \partial \kappa_2} & \mathbf{K} \frac{\partial g_1}{\partial \boldsymbol{\sigma}} \\ -\frac{\partial \Delta \kappa_1}{\partial \boldsymbol{\sigma}} & 1 - \frac{\partial \Delta \kappa_1}{\partial \kappa_1} & -\frac{\partial \Delta \kappa_1}{\partial \kappa_2} & -\frac{\partial \Delta \kappa_1}{\partial \dot{\lambda}_1} \\ -\frac{\partial \Delta \kappa_2}{\partial \boldsymbol{\sigma}} & -\frac{\partial \Delta \kappa_2}{\partial \kappa_1} & 1 - \frac{\partial \Delta \kappa_2}{\partial \kappa_2} & -\frac{\partial \Delta \kappa_2}{\partial \dot{\lambda}_1} \\ \frac{\partial f_1}{\partial \boldsymbol{\sigma}} & \frac{\partial f_1}{\partial \kappa_1} & \frac{\partial f_1}{\partial \kappa_2} & 0 \end{bmatrix}, \quad (\text{A-1})$$

$$J_2(\boldsymbol{\sigma}, \kappa_3, \dot{\lambda}_2)_{5 \times 5} = \begin{bmatrix} \mathbf{I} + \dot{\lambda}_2 \mathbf{K} \frac{\partial^2 f_2}{\partial \boldsymbol{\sigma}^2} & \dot{\lambda}_2 \mathbf{K} \frac{\partial^2 f_2}{\partial \boldsymbol{\sigma} \partial \kappa_3} & \mathbf{K} \frac{\partial f_2}{\partial \boldsymbol{\sigma}} \\ -\frac{\partial \Delta \kappa_3}{\partial \boldsymbol{\sigma}} & 1 - \frac{\partial \Delta \kappa_3}{\partial \kappa_3} & -\frac{\partial \Delta \kappa_3}{\partial \dot{\lambda}_2} \\ \frac{\partial f_2}{\partial \boldsymbol{\sigma}} & \frac{\partial f_2}{\partial \kappa_3} & 0 \end{bmatrix} \quad (\text{A-2})$$

$$\mathbf{J}_3(\boldsymbol{\sigma}, \kappa_1, \kappa_2, \kappa_3, \dot{\lambda}_1, \dot{\lambda}_2)_{8 \times 8} = \begin{bmatrix} \mathbf{J}_{3 \times 3}^{11} & \mathbf{J}_{3 \times 1}^{12} & \mathbf{J}_{3 \times 1}^{13} & \mathbf{J}_{3 \times 1}^{14} & \mathbf{J}_{3 \times 1}^{15} & \mathbf{J}_{3 \times 1}^{16} \\ -\frac{\partial \Delta \kappa_1}{\partial \boldsymbol{\sigma}} & 1 - \frac{\partial \Delta \kappa_1}{\partial \kappa_1} & -\frac{\partial \Delta \kappa_1}{\partial \kappa_2} & -\frac{\partial \Delta \kappa_1}{\partial \kappa_3} & -\frac{\partial \Delta \kappa_1}{\partial \dot{\lambda}_1} & -\frac{\partial \Delta \kappa_1}{\partial \dot{\lambda}_2} \\ -\frac{\partial \Delta \kappa_2}{\partial \boldsymbol{\sigma}} & -\frac{\partial \Delta \kappa_2}{\partial \kappa_1} & 1 - \frac{\partial \Delta \kappa_2}{\partial \kappa_2} & -\frac{\partial \Delta \kappa_2}{\partial \kappa_3} & -\frac{\partial \Delta \kappa_2}{\partial \dot{\lambda}_1} & -\frac{\partial \Delta \kappa_2}{\partial \dot{\lambda}_2} \\ -\frac{\partial \Delta \kappa_3}{\partial \boldsymbol{\sigma}} & -\frac{\partial \Delta \kappa_3}{\partial \kappa_1} & -\frac{\partial \Delta \kappa_3}{\partial \kappa_2} & 1 - \frac{\partial \Delta \kappa_3}{\partial \kappa_3} & -\frac{\partial \Delta \kappa_3}{\partial \dot{\lambda}_1} & -\frac{\partial \Delta \kappa_3}{\partial \dot{\lambda}_2} \\ \frac{\partial f_1}{\partial \boldsymbol{\sigma}} & \frac{\partial f_1}{\partial \kappa_1} & \frac{\partial f_1}{\partial \kappa_2} & \frac{\partial f_1}{\partial \kappa_3} & 0 & 0 \\ \frac{\partial f_2}{\partial \boldsymbol{\sigma}} & \frac{\partial f_2}{\partial \kappa_1} & \frac{\partial f_2}{\partial \kappa_2} & \frac{\partial f_2}{\partial \kappa_3} & 0 & 0 \end{bmatrix} \quad (\text{A-3})$$

where the elements in the first row in \mathbf{J}_3 are expressed in Eq. (A-4) to Eq. (A-9):

$$\mathbf{J}_{3 \times 3}^{11} = \mathbf{I} + \dot{\lambda}_1 \mathbf{K} \frac{\partial^2 g_1}{\partial \boldsymbol{\sigma}^2} + \dot{\lambda}_2 \mathbf{K} \frac{\partial^2 f_2}{\partial \boldsymbol{\sigma}^2} \quad (\text{A-4})$$

$$\mathbf{J}_{3 \times 1}^{12} = \dot{\lambda}_1 \mathbf{K} \frac{\partial^2 g_1}{\partial \boldsymbol{\sigma} \partial \kappa_1} + \dot{\lambda}_2 \mathbf{K} \frac{\partial^2 f_2}{\partial \boldsymbol{\sigma} \partial \kappa_1} \quad (\text{A-5})$$

$$\mathbf{J}_{3 \times 1}^{13} = \dot{\lambda}_1 \mathbf{K} \frac{\partial^2 g_1}{\partial \boldsymbol{\sigma} \partial \kappa_2} + \dot{\lambda}_2 \mathbf{K} \frac{\partial^2 f_2}{\partial \boldsymbol{\sigma} \partial \kappa_2} \quad (\text{A-6})$$

$$\mathbf{J}_{3 \times 1}^{14} = \dot{\lambda}_1 \mathbf{K} \frac{\partial^2 g_1}{\partial \boldsymbol{\sigma} \partial \kappa_3} + \dot{\lambda}_2 \mathbf{K} \frac{\partial^2 f_2}{\partial \boldsymbol{\sigma} \partial \kappa_3} \quad (\text{A-7})$$

$$\mathbf{J}_{3 \times 1}^{15} = \mathbf{K} \frac{\partial g_1}{\partial \boldsymbol{\sigma}} \quad (\text{A-8})$$

$$\mathbf{J}_{3 \times 1}^{16} = \mathbf{K} \frac{\partial f_2}{\partial \boldsymbol{\sigma}} \quad (\text{A-9})$$

Expressions for entries of Jacobian matrices are derived as (A-10) - (A-42):

$$\frac{\partial g_1}{\partial \sigma} = \begin{bmatrix} \tan \psi \\ \frac{\tau_s}{\sqrt{\tau_s^2 + \tau_t^2 + (c - \sigma_t \tan \psi)^2}} \\ \frac{\tau_t}{\sqrt{\tau_s^2 + \tau_t^2 + (c - \sigma_t \tan \psi)^2}} \end{bmatrix} \quad (\text{A-10})$$

$$\frac{\partial^2 g_1}{\partial \sigma^2} = \begin{bmatrix} \frac{\partial^2 g}{\partial \sigma_n^2} & 0 & 0 \\ 0 & \frac{\tau_t^2 + (c - \sigma_t \tan \psi)^2}{\left[\tau_s^2 + \tau_t^2 + (c - \sigma_t \tan \psi)^2 \right]^{\frac{3}{2}}} & \frac{-\tau_s \tau_t}{\left[\tau_s^2 + \tau_t^2 + (c - \sigma_t \tan \psi)^2 \right]^{\frac{3}{2}}} \\ 0 & \frac{-\tau_s \tau_t}{\left[\tau_s^2 + \tau_t^2 + (c - \sigma_t \tan \psi)^2 \right]^{\frac{3}{2}}} & \frac{\tau_s^2 + (c - \sigma_t \tan \psi)^2}{\left[\tau_s^2 + \tau_t^2 + (c - \sigma_t \tan \psi)^2 \right]^{\frac{3}{2}}} \end{bmatrix} \quad (\text{A-11})$$

In Eq. (A-11), $\frac{\partial^2 g}{\partial \sigma_n^2}$ is derived as per Eq. (A-12):

$$\frac{\partial^2 g_1}{\partial \sigma_n^2} = \begin{cases} 0 & \sigma_n \geq 0 \\ -\frac{(\tan \psi_0 - \tan \psi_r)}{\sigma_u} \left\langle 1 - \frac{\sqrt{(u_s^p)^2 + (u_t^p)^2}}{u_\tau} \right\rangle & \sigma_u \leq \sigma_n < 0 \\ 0 & \sigma_n < \sigma_u \end{cases} \quad (\text{A-12})$$

$$\frac{\partial \Delta \kappa_1}{\partial \kappa_2} = \begin{cases} \frac{\lambda_1 \left[\frac{\partial g_1}{\partial \sigma_n} \frac{\partial^2 g_1}{\partial \sigma_n \partial \kappa_2} + \left(\frac{G_I}{G_{II}} \times \frac{c_0}{f_t} \right)^2 \left(\frac{\partial g_1}{\partial \tau_s} \frac{\partial^2 g_1}{\partial \tau_s \partial \kappa_2} + \frac{\partial g_1}{\partial \tau_t} \frac{\partial^2 g_1}{\partial \tau_t \partial \kappa_2} \right) \right]}{\sqrt{\left(\frac{\partial g_1}{\partial \sigma_n} \right)^2 + \left(\frac{G_I}{G_{II}} \times \frac{c_0}{f_t} \sqrt{\left(\frac{\partial g_1}{\partial \tau_s} \right)^2 + \left(\frac{\partial g_1}{\partial \tau_t} \right)^2} \right)^2}} & \sigma_n \geq 0 \\ \frac{\lambda_1 \left[\left(\frac{G_I}{G_{II}} \times \frac{c_0}{f_t} \right)^2 \left(\frac{\partial g_1}{\partial \tau_s} \frac{\partial^2 g_1}{\partial \tau_s \partial \kappa_2} + \frac{\partial g_1}{\partial \tau_t} \frac{\partial^2 g_1}{\partial \tau_t \partial \kappa_2} \right) \right]}{\sqrt{\left(\frac{G_I}{G_{II}} \times \frac{c_0}{f_t} \sqrt{\left(\frac{\partial g_1}{\partial \tau_s} \right)^2 + \left(\frac{\partial g_1}{\partial \tau_t} \right)^2} \right)^2}} & \sigma_n < 0 \end{cases} \quad (\text{A-13})$$

$$\frac{\partial \Delta \kappa_1}{\partial \kappa_1} = \begin{cases} \frac{\lambda_1 \left[\frac{\partial g_1}{\partial \sigma_n} \frac{\partial^2 g_1}{\partial \sigma_n \partial \kappa_1} + \left(\frac{G_I}{G_{II}} \times \frac{c_0}{f_t} \right)^2 \left(\frac{\partial g_1}{\partial \tau_s} \frac{\partial^2 g_1}{\partial \tau_s \partial \kappa_1} + \frac{\partial g_1}{\partial \tau_t} \frac{\partial^2 g_1}{\partial \tau_t \partial \kappa_1} \right) \right]}{\sqrt{\left(\frac{\partial g_1}{\partial \sigma_n} \right)^2 + \left(\frac{G_I}{G_{II}} \times \frac{c_0}{f_t} \sqrt{\left(\frac{\partial g_1}{\partial \tau_s} \right)^2 + \left(\frac{\partial g_1}{\partial \tau_t} \right)^2} \right)^2}} & \sigma_n \geq 0 \\ \frac{\lambda_1 \left[\left(\frac{G_I}{G_{II}} \times \frac{c_0}{f_t} \right)^2 \left(\frac{\partial g_1}{\partial \tau_s} \frac{\partial^2 g_1}{\partial \tau_s \partial \kappa_1} + \frac{\partial g_1}{\partial \tau_t} \frac{\partial^2 g_1}{\partial \tau_t \partial \kappa_1} \right) \right]}{\sqrt{\left(\frac{G_I}{G_{II}} \times \frac{c_0}{f_t} \sqrt{\left(\frac{\partial g_1}{\partial \tau_s} \right)^2 + \left(\frac{\partial g_1}{\partial \tau_t} \right)^2} \right)^2}} & \sigma_n < 0 \end{cases} \quad (\text{A-14})$$

$$\frac{\partial^2 g_1}{\partial \boldsymbol{\sigma} \partial \kappa_1} = \begin{bmatrix} 0 \\ \frac{\tau_s (c - \sigma_t \tan \psi) \left(\frac{\partial \sigma_t}{\partial \kappa_1} \tan \psi \right)}{\left[\tau_s^2 + \tau_t^2 + (c - \sigma_t \tan \psi)^2 \right]^{\frac{3}{2}}} \\ \frac{\tau_t (c - \sigma_t \tan \psi) \left(\frac{\partial \sigma_t}{\partial \kappa_1} \tan \psi \right)}{\left[\tau_s^2 + \tau_t^2 + (c - \sigma_t \tan \psi)^2 \right]^{\frac{3}{2}}} \end{bmatrix} \quad (\text{A-15})$$

$$\frac{\partial \sigma_t}{\partial \kappa_1} = -\frac{f_t^2}{G_I} \exp\left(-\frac{f_t}{G_I} \kappa_1\right) \quad (\text{A-16})$$

$$\frac{\partial^2 g_1}{\partial \boldsymbol{\sigma} \partial \kappa_2} = \begin{bmatrix} 0 \\ \frac{-\tau_s (c - \sigma_t \tan \psi) \left(\frac{\partial c}{\partial \kappa_2} \right)}{\left[\tau_s^2 + \tau_t^2 + (c - \sigma_t \tan \psi)^2 \right]^{\frac{3}{2}}} \\ \frac{-\tau_t (c - \sigma_t \tan \psi) \left(\frac{\partial c}{\partial \kappa_2} \right)}{\left[\tau_s^2 + \tau_t^2 + (c - \sigma_t \tan \psi)^2 \right]^{\frac{3}{2}}} \end{bmatrix} \quad (\text{A-17})$$

$$\frac{\partial c}{\partial \kappa_2} = -\frac{c_0^2}{G_{II}} \exp\left(-\frac{c_0}{G_{II}} \kappa_2\right) \quad (\text{A-18})$$

$$\frac{\partial \Delta \kappa_1}{\partial \sigma} = \left\{ \begin{array}{l} \frac{\lambda_1}{\sqrt{\left(\frac{\partial g_1}{\partial \sigma_n}\right)^2 + \left(\frac{G_I}{G_{II}} \times \frac{c_0}{f_t} \sqrt{\left(\frac{\partial g_1}{\partial \tau_s}\right)^2 + \left(\frac{\partial g_1}{\partial \tau_t}\right)^2}\right)^2}} \left\{ \begin{array}{l} \frac{\partial g_1}{\partial \sigma_n} \frac{\partial^2 g_1}{\partial \sigma_n^2} \\ \left(\frac{G_I}{G_{II}^0} \times \frac{c_0}{f_t}\right)^2 \left(\frac{\partial g_1}{\partial \tau_s} \frac{\partial^2 g_1}{\partial \tau_s^2} + \frac{\partial g_1}{\partial \tau_t} \frac{\partial^2 g_1}{\partial \tau_t \partial \tau_s}\right) \\ \left(\frac{G_I}{G_{II}^0} \times \frac{c_0}{f_t}\right)^2 \left(\frac{\partial g_1}{\partial \tau_s} \frac{\partial^2 g_1}{\partial \tau_s \partial \tau_t} + \frac{\partial g_1}{\partial \tau_t} \frac{\partial^2 g_1}{\partial \tau_t^2}\right) \end{array} \right. \sigma_n \geq 0 \\ \\ \frac{G_I}{G_{II}} \times \frac{c_0}{f_t} \frac{\lambda_1}{\sqrt{\left(\frac{\partial g_1}{\partial \tau_s}\right)^2 + \left(\frac{\partial g_1}{\partial \tau_t}\right)^2}} \left\{ \begin{array}{l} \frac{a \left[\left(\frac{\partial g_1}{\partial \tau_s}\right)^2 + \left(\frac{\partial g_1}{\partial \tau_t}\right)^2 \right]}{G_{II}} \\ \frac{\partial g_1}{\partial \tau_s} \frac{\partial^2 g_1}{\partial \tau_s^2} + \frac{\partial g_1}{\partial \tau_t} \frac{\partial^2 g_1}{\partial \tau_t \partial \tau_s} \\ \frac{\partial g_1}{\partial \tau_s} \frac{\partial^2 g_1}{\partial \tau_s \partial \tau_t} + \frac{\partial g_1}{\partial \tau_t} \frac{\partial^2 g_1}{\partial \tau_t^2} \end{array} \right. \sigma_n < 0 \end{array} \right. \quad (\text{A-19})$$

$$\frac{\partial \Delta \kappa_1}{\partial \kappa_1} = \left\{ \begin{array}{l} \frac{\lambda_1 \left[\frac{\partial g_1}{\partial \sigma_n} \frac{\partial^2 g_1}{\partial \sigma_n \partial \kappa_1} + \left(\frac{G_I}{G_{II}} \times \frac{c_0}{f_t}\right)^2 \left(\frac{\partial g_1}{\partial \tau_s} \frac{\partial^2 g_1}{\partial \tau_s \partial \kappa_1} + \frac{\partial g_1}{\partial \tau_t} \frac{\partial^2 g_1}{\partial \tau_t \partial \kappa_1}\right) \right]}{\sqrt{\left(\frac{\partial g_1}{\partial \sigma_n}\right)^2 + \left(\frac{G_I}{G_{II}} \times \frac{c_0}{f_t} \sqrt{\left(\frac{\partial g_1}{\partial \tau_s}\right)^2 + \left(\frac{\partial g_1}{\partial \tau_t}\right)^2}\right)^2}} \sigma_n \geq 0 \\ \\ \frac{\lambda_1 \left[\left(\frac{G_I}{G_{II}} \times \frac{c_0}{f_t}\right)^2 \left(\frac{\partial g_1}{\partial \tau_s} \frac{\partial^2 g_1}{\partial \tau_s \partial \kappa_1} + \frac{\partial g_1}{\partial \tau_t} \frac{\partial^2 g_1}{\partial \tau_t \partial \kappa_1}\right) \right]}{\sqrt{\left(\frac{G_I}{G_{II}} \times \frac{c_0}{f_t} \sqrt{\left(\frac{\partial g_1}{\partial \tau_s}\right)^2 + \left(\frac{\partial g_1}{\partial \tau_t}\right)^2}\right)^2}} \sigma_n < 0 \end{array} \right. \quad (\text{A-20})$$

$$\frac{\partial \Delta \kappa_1}{\partial \kappa_2} = \begin{cases} \frac{\lambda_1 \left[\frac{\partial g_1}{\partial \sigma_n} \frac{\partial^2 g_1}{\partial \sigma_n \partial \kappa_2} + \left(\frac{G_I}{G_{II}} \times \frac{c_0}{f_t} \right)^2 \left(\frac{\partial g_1}{\partial \tau_s} \frac{\partial^2 g_1}{\partial \tau_s \partial \kappa_2} + \frac{\partial g_1}{\partial \tau_t} \frac{\partial^2 g_1}{\partial \tau_t \partial \kappa_2} \right) \right]}{\sqrt{\left(\frac{\partial g_1}{\partial \sigma_n} \right)^2 + \left(\frac{G_I}{G_{II}} \times \frac{c_0}{f_t} \sqrt{\left(\frac{\partial g_1}{\partial \tau_s} \right)^2 + \left(\frac{\partial g_1}{\partial \tau_t} \right)^2} \right)^2}} & \sigma_n \geq 0 \\ \frac{\lambda_1 \left[\left(\frac{G_I}{G_{II}} \times \frac{c_0}{f_t} \right)^2 \left(\frac{\partial g_1}{\partial \tau_s} \frac{\partial^2 g_1}{\partial \tau_s \partial \kappa_2} + \frac{\partial g_1}{\partial \tau_t} \frac{\partial^2 g_1}{\partial \tau_t \partial \kappa_2} \right) \right]}{\sqrt{\left(\frac{G_I}{G_{II}} \times \frac{c_0}{f_t} \sqrt{\left(\frac{\partial g_1}{\partial \tau_s} \right)^2 + \left(\frac{\partial g_1}{\partial \tau_t} \right)^2} \right)^2}} & \sigma_n < 0 \end{cases} \quad (\text{A-21})$$

$$\frac{\partial \Delta \kappa_1}{\partial \lambda_1} = \begin{cases} \sqrt{\left(\frac{\partial g_1}{\partial \sigma_n} \right)^2 + \left(\frac{G_I}{G_{II}} \times \frac{c_0}{f_t} \sqrt{\left(\frac{\partial g_1}{\partial \tau_s} \right)^2 + \left(\frac{\partial g_1}{\partial \tau_t} \right)^2} \right)^2} & \sigma_n \geq 0 \\ \sqrt{\left(\frac{G_I}{G_{II}} \times \frac{c_0}{f_t} \sqrt{\left(\frac{\partial g_1}{\partial \tau_s} \right)^2 + \left(\frac{\partial g_1}{\partial \tau_t} \right)^2} \right)^2} & \sigma_n < 0 \end{cases} \quad (\text{A-22})$$

$$\frac{\partial \Delta \kappa_2}{\partial \sigma} = \begin{cases} \frac{\lambda_1 \left[\frac{\left(\frac{G_{II}^0}{G_I} \times \frac{f_t}{c_0} \right)^2 \frac{\partial g_1}{\partial \sigma_n} \frac{\partial^2 g_1}{\partial \sigma_n^2}}{\left(\frac{G_{II}^0}{G_I} \times \frac{f_t}{c_0} \right)^2 \frac{\partial g_1}{\partial \sigma_n} \frac{\partial^2 g_1}{\partial \sigma_n^2} + \left(\frac{\partial g_1}{\partial \tau_s} \right)^2 + \left(\frac{\partial g_1}{\partial \tau_t} \right)^2} \right]}{\sqrt{\left(\frac{G_{II}^0}{G_I} \times \frac{f_t}{c_0} \times \frac{\partial g_1}{\partial \sigma_n} \right)^2 + \left(\frac{\partial g_1}{\partial \tau_s} \right)^2 + \left(\frac{\partial g_1}{\partial \tau_t} \right)^2}} \begin{cases} \frac{\partial g_1}{\partial \tau_s} \frac{\partial^2 g_1}{\partial \tau_s^2} + \frac{\partial g_1}{\partial \tau_t} \frac{\partial^2 g_1}{\partial \tau_t^2} & \sigma_n \geq 0 \\ \frac{\partial g_1}{\partial \tau_s} \frac{\partial^2 g_1}{\partial \tau_s \partial \tau_t} + \frac{\partial g_1}{\partial \tau_t} \frac{\partial^2 g_1}{\partial \tau_t^2} & \sigma_n < 0 \end{cases} \\ \frac{\lambda_1 \left[\frac{\partial g_1}{\partial \tau_s} \frac{\partial^2 g_1}{\partial \tau_s^2} + \frac{\partial g_1}{\partial \tau_t} \frac{\partial^2 g_1}{\partial \tau_t^2} \right]}{\sqrt{\left(\frac{\partial g_1}{\partial \tau_s} \right)^2 + \left(\frac{\partial g_1}{\partial \tau_t} \right)^2}} \begin{cases} 0 & \sigma_n \geq 0 \\ \frac{\partial g_1}{\partial \tau_s} \frac{\partial^2 g_1}{\partial \tau_s \partial \tau_t} + \frac{\partial g_1}{\partial \tau_t} \frac{\partial^2 g_1}{\partial \tau_t^2} & \sigma_n < 0 \end{cases} \end{cases} \quad (\text{A-23})$$

$$\frac{\partial \Delta \kappa_2}{\partial \kappa_1} = \begin{cases} \frac{\lambda_1 \left[\left(\frac{G_H^0}{G_I} \times \frac{f_t}{c_0} \right)^2 \frac{\partial g_1}{\partial \sigma_n} \frac{\partial^2 g_1}{\partial \sigma_n \partial \kappa_1} + \frac{\partial g_1}{\partial \tau_s} \frac{\partial^2 g_1}{\partial \tau_s \partial \kappa_1} + \frac{\partial g_1}{\partial \tau_t} \frac{\partial^2 g_1}{\partial \tau_t \partial \kappa_1} \right]}{\sqrt{\left(\frac{G_H^0}{G_I} \times \frac{f_t}{c_0} \times \frac{\partial g_1}{\partial \sigma_n} \right)^2 + \left(\frac{\partial g_1}{\partial \tau_s} \right)^2 + \left(\frac{\partial g_1}{\partial \tau_t} \right)^2}} & \sigma_n \geq 0 \\ \frac{\lambda_1 \left[\left(\frac{\partial g_1}{\partial \tau_s} \frac{\partial^2 g_1}{\partial \tau_s \partial \kappa_1} + \frac{\partial g_1}{\partial \tau_t} \frac{\partial^2 g_1}{\partial \tau_t \partial \kappa_1} \right) \right]}{\sqrt{\left(\frac{\partial g_1}{\partial \tau_s} \right)^2 + \left(\frac{\partial g_1}{\partial \tau_t} \right)^2}} & \sigma_n < 0 \end{cases} \quad (\text{A-24})$$

$$\frac{\partial \Delta \kappa_2}{\partial \kappa_2} = \begin{cases} \frac{\lambda_1 \left[\left(\frac{G_H^0}{G_I} \times \frac{f_t}{c_0} \right)^2 \frac{\partial g_1}{\partial \sigma_n} \frac{\partial^2 g_1}{\partial \sigma_n \partial \kappa_2} + \frac{\partial g_1}{\partial \tau_s} \frac{\partial^2 g_1}{\partial \tau_s \partial \kappa_2} + \frac{\partial g_1}{\partial \tau_t} \frac{\partial^2 g_1}{\partial \tau_t \partial \kappa_2} \right]}{\sqrt{\left(\frac{G_H^0}{G_I} \times \frac{f_t}{c_0} \times \frac{\partial g_1}{\partial \sigma_n} \right)^2 + \left(\frac{\partial g_1}{\partial \tau_s} \right)^2 + \left(\frac{\partial g_1}{\partial \tau_t} \right)^2}} & \sigma_n \geq 0 \\ \frac{\lambda_1 \left[\left(\frac{\partial g_1}{\partial \tau_s} \frac{\partial^2 g_1}{\partial \tau_s \partial \kappa_2} + \frac{\partial g_1}{\partial \tau_t} \frac{\partial^2 g_1}{\partial \tau_t \partial \kappa_2} \right) \right]}{\sqrt{\left(\frac{\partial g_1}{\partial \tau_s} \right)^2 + \left(\frac{\partial g_1}{\partial \tau_t} \right)^2}} & \sigma_n < 0 \end{cases} \quad (\text{A-25})$$

$$\frac{\partial \Delta \kappa_2}{\partial \dot{\lambda}_1} = \begin{cases} \sqrt{\left(\frac{G_H^0}{G_I} \times \frac{f_t}{c_0} \times \frac{\partial g_1}{\partial \sigma_n} \right)^2 + \left(\frac{\partial g_1}{\partial \tau_s} \right)^2 + \left(\frac{\partial g_1}{\partial \tau_t} \right)^2} & \sigma_n \geq 0 \\ \sqrt{\left(\frac{\partial g_1}{\partial \tau_s} \right)^2 + \left(\frac{\partial g_1}{\partial \tau_t} \right)^2} & \sigma_n < 0 \end{cases} \quad (\text{A-26})$$

$$\frac{\partial f_1}{\partial \sigma} = \begin{bmatrix} \tan \varphi \\ \frac{\tau_s}{\sqrt{\tau_s^2 + \tau_t^2 + (c - \sigma_t \tan \varphi)^2}} \\ \frac{\tau_t}{\sqrt{\tau_s^2 + \tau_t^2 + (c - \sigma_t \tan \varphi)^2}} \end{bmatrix} \quad (\text{A-27})$$

$$\frac{\partial f_1}{\partial \kappa_1} = -\frac{\partial c}{\partial \kappa_1} + \sigma_n \frac{\partial \tan \varphi}{\partial \kappa_1} + \frac{(c - \sigma_t \tan \varphi) \left(\frac{\partial c}{\partial \kappa_1} - \frac{\partial \sigma_t}{\partial \kappa_1} \tan \varphi - \frac{\partial \tan \varphi}{\partial \kappa_1} \sigma_t \right)}{\sqrt{\tau_s^2 + \tau_t^2 + (c - \sigma_t \tan \varphi)^2}} \quad (\text{A-28})$$

$$\frac{\partial \tan \varphi}{\partial \kappa_1} = \frac{\tan \varphi_0 - \tan \varphi_r}{c_0} \frac{\partial c}{\partial \kappa_1} = 0 \quad (\text{A-29})$$

$$\frac{\partial \sigma_t}{\partial \kappa_1} = -\frac{f_t^2}{G_I} \exp\left(-\frac{f_t}{G_I} \kappa_1\right) \quad (\text{A-30})$$

$$\frac{\partial f_1}{\partial \kappa_2} = -\frac{\partial c}{\partial \kappa_2} + \sigma_n \frac{\partial \tan \varphi}{\partial \kappa_2} + \frac{(c - \sigma_t \tan \varphi) \left(\frac{\partial c}{\partial \kappa_2} - \frac{\partial \sigma_t}{\partial \kappa_2} \tan \varphi - \frac{\partial \tan \varphi}{\partial \kappa_2} \sigma_t \right)}{\sqrt{\tau_s^2 + \tau_t^2 + (c - \sigma_t \tan \varphi)^2}} \quad (\text{A-31})$$

$$\frac{\partial \tan \varphi}{\partial \kappa_2} = \frac{\tan \varphi_0 - \tan \varphi_r}{c_0} \frac{\partial c}{\partial \kappa_2} \quad (\text{A-32})$$

$$\frac{\partial c}{\partial \kappa_2} = -\frac{c_0^2}{G_{II}} \exp\left(-\frac{f_t}{G_{II}} \kappa_2\right) \quad (\text{A-33})$$

$$\frac{\partial \sigma_t}{\partial \kappa_2} = 0 \quad (\text{A-34})$$

$$\frac{\partial f_2}{\partial \sigma} = \begin{bmatrix} -\tan \theta \\ \frac{\tau_s}{\sqrt{\tau_s^2 + \tau_t^2 + (f_c - \sigma_c \tan \theta)^2}} \\ \frac{\tau_t}{\sqrt{\tau_s^2 + \tau_t^2 + (f_c - \sigma_c \tan \theta)^2}} \end{bmatrix} \quad (\text{A-35})$$

$$\frac{\partial^2 f_2}{\partial \sigma^2} = \begin{bmatrix} 0 & 0 & 0 \\ 0 & \frac{\tau_t^2 + (f_c - \sigma_c \tan \theta)^2}{\left[\tau_s^2 + \tau_t^2 + (f_c - \sigma_c \tan \theta)^2 \right]^{\frac{3}{2}}} & \frac{-\tau_s \tau_t}{\left[\tau_s^2 + \tau_t^2 + (f_c - \sigma_c \tan \theta)^2 \right]^{\frac{3}{2}}} \\ 0 & \frac{-\tau_s \tau_t}{\left[\tau_s^2 + \tau_t^2 + (f_c - \sigma_c \tan \theta)^2 \right]^{\frac{3}{2}}} & \frac{\tau_s^2 + (f_c - \sigma_c \tan \theta)^2}{\left[\tau_s^2 + \tau_t^2 + (f_c - \sigma_c \tan \theta)^2 \right]^{\frac{3}{2}}} \end{bmatrix} \quad (\text{A-36})$$

$$\frac{\partial^2 f_2}{\partial \sigma \partial \kappa_3} = \begin{bmatrix} 0 \\ \frac{\tau_s \tan \theta (f_c - \sigma_c \tan \theta) \frac{\partial \sigma_c}{\partial \kappa_3}}{\left[\tau_s^2 + \tau_t^2 + (f_c - \sigma_c \tan \theta)^2 \right]^{\frac{3}{2}}} \\ \frac{\tau_t \tan \theta (f_c - \sigma_c \tan \theta) \frac{\partial \sigma_c}{\partial \kappa_3}}{\left[\tau_s^2 + \tau_t^2 + (f_c - \sigma_c \tan \theta)^2 \right]^{\frac{3}{2}}} \end{bmatrix} \quad (\text{A-37})$$

$$\frac{\partial \sigma_c}{\partial \kappa_3} = \begin{cases} (\sigma_c^p - \sigma_c^i) \left(\frac{2}{\kappa_3^p} - \frac{2\kappa_3}{\kappa_3^p} \right) & 0 \leq \kappa_3 \leq \kappa_p \\ 2(\sigma_c^m - \sigma_c^p) \left(\frac{\kappa_3 - \kappa_3^p}{\kappa_3^m - \kappa_3^p} \right) \left(\frac{1}{\kappa_3 - \kappa_3^p} \right) & \kappa_3^p < \kappa_3 \leq \kappa_3^m \\ 2 \frac{\sigma_c^m - \sigma_c^p}{\kappa_3^m - \kappa_3^p} \exp \left(2 \frac{\sigma_c^m - \sigma_c^p}{\kappa_3^m - \kappa_3^p} \frac{\kappa_3 - \kappa_m}{\sigma_c^m - \sigma_c^r} \right) & \kappa_3 > \kappa_m \end{cases} \quad (\text{A-38})$$

$$\frac{\partial \Delta \kappa_3}{\partial \sigma} = \frac{\dot{\lambda}_2}{\sqrt{\left(\frac{\partial f_2}{\partial \sigma_n} \right)^2 + \left(\frac{\partial f_2}{\partial \tau_s} \right)^2 + \left(\frac{\partial f_2}{\partial \tau_t} \right)^2}} \begin{cases} 0 \\ \frac{\partial f_2}{\partial \tau_s} \frac{\partial^2 f_2}{\partial \tau_s^2} + \frac{\partial f_2}{\partial \tau_t} \frac{\partial^2 f_2}{\partial \tau_t \partial \tau_s} \\ \frac{\partial f_2}{\partial \tau_s} \frac{\partial^2 f_2}{\partial \tau_s \partial \tau_t} + \frac{\partial f_2}{\partial \tau_t} \frac{\partial^2 f_2}{\partial \tau_t^2} \end{cases} \quad (\text{A-39})$$

$$\frac{\partial \Delta \kappa_3}{\partial \kappa_3} = \frac{\dot{\lambda}_2}{\sqrt{\left(\frac{\partial f_2}{\partial \sigma_n} \right)^2 + \left(\frac{\partial f_2}{\partial \tau_s} \right)^2 + \left(\frac{\partial f_2}{\partial \tau_t} \right)^2}} \left(\frac{\partial f_2}{\partial \sigma_n} \frac{\partial^2 f_2}{\partial \sigma_n \partial \kappa_3} + \frac{\partial f_2}{\partial \tau_s} \frac{\partial^2 f_2}{\partial \tau_s \partial \kappa_3} + \frac{\partial f_2}{\partial \tau_t} \frac{\partial^2 f_2}{\partial \tau_t \partial \kappa_3} \right) \quad (\text{A-40})$$

$$\frac{\partial \Delta \kappa_3}{\partial \dot{\lambda}_2} = \frac{\partial}{\partial \dot{\lambda}_2} \sqrt{(\dot{u}_n^p)^2 + (\dot{u}_s^p)^2 + (\dot{u}_t^p)^2} = \sqrt{\left(\frac{\partial f_2}{\partial \sigma_n} \right)^2 + \left(\frac{\partial f_2}{\partial \tau_s} \right)^2 + \left(\frac{\partial f_2}{\partial \tau_t} \right)^2} \quad (\text{A-41})$$

$$\frac{\partial f_2}{\partial \kappa_3} = \frac{-\tan \theta (f_c - \sigma_c \tan \theta) \frac{\partial \sigma_c}{\partial \kappa_3}}{\sqrt{\tau_s^2 + \tau_t^2 + (f_c - \sigma_c \tan \theta)^2}} \quad (\text{A-42})$$

Appendix B. DERIVATION OF TANGENT STIFFNESS MATRIX AND STRESS INCREMENT IN THE 3D MULTI-YIELD SURFACES DAMAGE PLASTICITY-BASED CONSTITUTIVE MODEL

The tangent stiffness \mathbf{K}^{tan} for the plasticity damage-based constitutive model presented in Chapter 5 is formulated as Eq. (B-1):

$$\mathbf{K}^{\text{tan}} = \mathbf{K}_1^{\text{tan}} + \mathbf{K}_2^{\text{tan}} + \mathbf{K}_3^{\text{tan}} \quad (\text{B-1})$$

where $\mathbf{K}_1^{\text{tan}}$, $\mathbf{K}_2^{\text{tan}}$, and $\mathbf{K}_3^{\text{tan}}$ are derived as follows:

$$\mathbf{K}_1^{\text{tan}} = \frac{\partial \boldsymbol{\sigma}}{\partial \mathbf{u}} + \frac{\partial \boldsymbol{\sigma}}{\partial \mathbf{u}^p} \left(\mathbf{P}_1 \frac{\partial \mathbf{g}_1}{\partial \boldsymbol{\sigma}} + \mathbf{P}_2 \frac{\partial \mathbf{g}_2}{\partial \boldsymbol{\sigma}} \right) \quad (\text{B-2})$$

$$\mathbf{K}_2^{\text{tan}} = \frac{\partial \boldsymbol{\sigma}}{\partial D_t} \mathbf{P}_1 (1 - D_t) \sqrt{\left(\frac{\left\langle \alpha \frac{\partial \mathbf{g}_1}{\partial \sigma_n} \right\rangle}{u_{t0}} \right)^2 + \left(\frac{\beta \frac{\partial \mathbf{g}_1}{\partial \sigma_s}}{u_{t0}} \right)^2 + \left(\frac{\beta \frac{\partial \mathbf{g}_1}{\partial \sigma_t}}{u_{t0}} \right)^2} \quad (\text{B-3})$$

$$\mathbf{K}_3^{\text{tan}} = \frac{\partial \boldsymbol{\sigma}}{\partial D_c} \mathbf{P}_2 (1 - D_2) \sqrt{\left(\frac{\gamma \frac{\partial \mathbf{g}_2}{\partial \sigma_n}}{u_{c0}} \right)^2} \quad (\text{B-4})$$

\mathbf{P}_1 and \mathbf{P}_2 are defined as Eq.(B-5) and Eq. (B-6), respectively:

$$\mathbf{P}_1 = \frac{-\frac{\partial f_1}{\partial \boldsymbol{\sigma}} \frac{\partial \boldsymbol{\sigma}}{\partial \mathbf{u}} \dot{\mathbf{u}}}{\frac{\partial f_1}{\partial \boldsymbol{\sigma}} \frac{\partial \boldsymbol{\sigma}}{\partial \mathbf{u}^p} \frac{\partial \mathbf{g}_1}{\partial \boldsymbol{\sigma}} + \sqrt{\left(\frac{\left\langle \alpha \frac{\partial \mathbf{g}_1}{\partial \sigma_n} \right\rangle}{u_{t0}} \right)^2 + \left(\frac{\beta \frac{\partial \mathbf{g}_1}{\partial \sigma_s}}{u_{t0}} \right)^2 + \left(\frac{\beta \frac{\partial \mathbf{g}_1}{\partial \sigma_t}}{u_{t0}} \right)^2} \left[\frac{\partial f_1}{\partial \boldsymbol{\sigma}} \frac{\partial \boldsymbol{\sigma}}{\partial D_t} (1 - D_t) + \frac{\partial f_1}{\partial D} (1 - D_t) \right] \quad (\text{B-5})$$

$$\mathbf{P}_2 = \frac{-\frac{\partial f_2}{\partial \boldsymbol{\sigma}} \frac{\partial \boldsymbol{\sigma}}{\partial \mathbf{u}} \dot{\mathbf{u}}}{\frac{\partial f_2}{\partial \boldsymbol{\sigma}} \frac{\partial \boldsymbol{\sigma}}{\partial \mathbf{u}^p} \frac{\partial g_2}{\partial \boldsymbol{\sigma}} + \sqrt{\left(\frac{\langle -\gamma \frac{\partial g_2}{\partial \boldsymbol{\sigma}_n} \rangle}{u_{c0}} \right)^2} \left[\frac{\partial f_2}{\partial \boldsymbol{\sigma}} \frac{\partial \boldsymbol{\sigma}}{\partial D_c} (1-D_c) + \frac{\partial f_2}{\partial D_c} (1-D_c) \right]} \quad (\text{B-6})$$

The expressions for the individual terms involved in previous equations are derived as follows:

$$\frac{\partial \boldsymbol{\sigma}}{\partial \mathbf{u}} = \begin{cases} \begin{bmatrix} k_{nn}(1-D) & 0 & 0 \\ 0 & k_{ss}(1-D) & 0 \\ 0 & 0 & k_{tt}(1-D) \end{bmatrix} & \sigma_n \geq 0 \\ \begin{bmatrix} k_{nn}(1-D) & 0 & 0 \\ 0 & k_{ss} & 0 \\ 0 & 0 & k_{tt} \end{bmatrix} & \sigma_n < 0 \end{cases} \quad (\text{B-7})$$

$$\frac{\partial \boldsymbol{\sigma}}{\partial \mathbf{u}^p} = \begin{cases} \begin{bmatrix} -k_{nn}(1-D) & 0 & 0 \\ 0 & -k_{ss}(1-D) & 0 \\ 0 & 0 & -k_{tt}(1-D) \end{bmatrix} & \sigma_n \geq 0 \\ \begin{bmatrix} -k_{nn}(1-D) & 0 & 0 \\ 0 & -k_{ss} & 0 \\ 0 & 0 & -k_{tt} \end{bmatrix} & \sigma_n < 0 \end{cases} \quad (\text{B-8})$$

$$\frac{\partial g_1}{\partial \boldsymbol{\sigma}} = \begin{bmatrix} \tan \psi \\ \frac{\tau_s}{\sqrt{\tau_s^2 + \tau_t^2 + [c_0 \xi_t - f_t \xi_t \tan \psi]^2}} \\ \frac{\tau_t}{\sqrt{\tau_s^2 + \tau_t^2 + [c_0 \xi_t - f_t \xi_t \tan \psi]^2}} \end{bmatrix} \quad (\text{B-9})$$

$$\frac{\partial g_2}{\partial \sigma} = \begin{bmatrix} -\tan \theta \\ \frac{\sigma_s}{\sqrt{\sigma_s^2 + \sigma_t^2 + [f_c - ((f_c - f_r)\xi_c(D_c) + f_r)\tan \theta]^2}} \\ \frac{\sigma_t}{\sqrt{\sigma_s^2 + \sigma_t^2 + [f_c - ((f_c - f_r)\xi_c(D_c) + f_r)\tan \theta]^2}} \end{bmatrix} \quad (\text{B-10})$$

$$\frac{\partial f_1}{\partial \sigma} = \begin{bmatrix} \tan \varphi \\ \frac{\tau_s}{\sqrt{\tau_s^2 + \tau_t^2 + [c_0\xi_t - f_t\xi_t \tan \varphi]^2}} \\ \frac{\tau_t}{\sqrt{\tau_s^2 + \tau_t^2 + [c_0\xi_t - f_t\xi_t \tan \varphi]^2}} \end{bmatrix} \quad (\text{B-11})$$

$$\frac{\partial f_2}{\partial \sigma} = \begin{bmatrix} -\tan \theta \\ \frac{\sigma_s}{\sqrt{\sigma_s^2 + \sigma_t^2 + [f_c - ((f_c - f_r)\xi_c(D_c) + f_r)\tan \theta]^2}} \\ \frac{\sigma_t}{\sqrt{\sigma_s^2 + \sigma_t^2 + [f_c - ((f_c - f_r)\xi_c(D_c) + f_r)\tan \theta]^2}} \end{bmatrix} \quad (\text{B-12})$$

$$\frac{\partial \sigma}{\partial D_t} = \begin{cases} \begin{cases} -k_{nn}(u_n - u_n^p) \\ -k_{ss}(u_s - u_t^p) \\ -k_{tt}(u_t - u_t^p) \end{cases} & \sigma_n \geq 0 \\ \begin{cases} -(1 - \omega_c)k_{nn}(u_n - u_n^p) \\ 0 \\ 0 \end{cases} & \sigma_n < 0 \end{cases} \quad (\text{B-13})$$

$$\frac{\partial \boldsymbol{\sigma}}{\partial D_c} = \begin{cases} \begin{cases} -(1-\omega_t)k_{nn}(u_n - u_n^p) \\ -k_{ss}(u_s - u_t^p) \\ -k_{tt}(u_t - u_t^p) \end{cases} & \sigma_n \geq 0 \\ \begin{cases} -k_{nn}(u_n - u_n^p) \\ 0 \\ 0 \end{cases} & \sigma_n < 0 \end{cases} \quad (\text{B-14})$$

Appendix C. IN-PLANE RESISTANCE PREDICTION OF UNREINFORCED MASONRY WALLS BASED ON CSA S304-14

In the Canadian masonry design code CSA S304-14, the in-plane (IP) resistances of unreinforced masonry walls corresponding to three failure modes (i.e., diagonal tension cracking, shear sliding, flexural rocking) are denoted as V_{dt} , V_{ss} , and V_{fr} . They are expressed in Eqs. (C-1)(C-2)(C-3), respectively:

$$V_{dt} = (v_m d_v t + 0.25 P_d) \gamma_g \leq 0.4 \sqrt{f'_m} t d_v \gamma_g \quad (C-1)$$

$$V_{ss} = \min(0.16 \sqrt{f'_m} l t + \mu P_d, \mu P_1) \quad (C-2)$$

$$V_{fr} = \frac{P_d l}{h} \left(1 - \frac{P_d}{0.85 f'_m l t} \right) \quad (C-3)$$

where $v_m = 0.16 \left(2 - \frac{M}{V d_v} \right) \sqrt{f'_m}$, M and V are the IP moment and shear force, respectively. d_v is the effective shear depth. h , l , and t are the wall height, length and thickness, respectively. f'_m is the compressive strength of masonry. P_d is the pre-compression load applied on the wall. γ_g is a grouting factor, taken as 1.0 for URM walls constructed with solid brick units. μ is the friction coefficient, P_1 is the compressive force acting normal to the sliding place, normally taken as P_d plus the tensile force at yield of the vertical dowels crossing the sliding plane.

The IP resistance of a specific URM wall V_{ip} is then determined as the minimum one:

$$V_{IP} = \min(V_{dt}, V_{ss}, V_{fr}) \quad (C-4)$$

Appendix D. IN-PLANE RESISTANCE PREDICTION OF REINFORCED MASONRY WALLS BASED ON CSA S304-14

IP resistances of RM walls corresponding to the diagonal tension cracking V_{dt} and sliding failure V_{ss} specified by CSA S304-14 are given by:

$$V_{dt} = (v_m d_v t + 0.25 P_d) \gamma_g + 0.60 A_{sh} f_{yh} \frac{d_v}{s} \leq 0.4 \sqrt{f'_m} t d_v \gamma_g \left(2 - \frac{h}{l} \right) \quad (D-1)$$

$$V_{ss} = \mu (P_d + T_y) \quad (D-2)$$

where V_m is the shear strength of masonry, defined as a function of compressive strength of masonry f'_m and shear span to depth ratio $\frac{M}{Vd_v}$: $v_m = 0.16 \left(2 - \frac{M}{Vd_v} \right) \sqrt{f'_m}$. d_v is the effective wall depth. M and V are the moment and horizontal shear force. γ_g is a grouting factor, taken as 1.0 for fully grouted RM walls. f_{yh} , A_{sh} and s are the yield strength, area, and spacing of horizontal reinforcements. l , t , and h are the length, thickness, and height of the wall, P_d is the pre-compression load applied on the wall. μ is the frictional coefficient. T_y is the tensile force at the yielding of vertical reinforcements, determined as $T_y = f_{yv} A_{sv}$. f_{yv} is the yield strength of vertical reinforcements. For the Conventional Construction shear walls and Moderately Ductile shear walls, A_{sv} denotes the total area of vertical reinforcement crossing the sliding plane.

To evaluate the IP flexural capacity V_{fr} , the equilibrium equations can be established as per Eq. (D-3), by ignoring the tensile forces of masonry and compressive forces of reinforcements:

$$C_m = \sum T_{s,i} + P_d \quad (D-3)$$

where P_d is the pre-compression load applied on the wall, C_m and $\sum T_{s,i}$ are the total forces in masonry and reinforcement, calculated based on Eq. (D-4) and Eq. (D-5):

$$C_m = 0.85 f'_m b \beta_1 c \quad (D-4)$$

$$T_{r,i} = \begin{cases} A_{s,i} f_{y,i} & \text{for bars that yield} \\ A_{s,i} \varepsilon_{mu} \frac{d_i - c}{c} E_{s,i} & \text{for bars that do not yield} \end{cases} \quad (D-5)$$

$A_{s,i}$, $E_{s,i}$, and $f_{y,i}$ are the cross-section area, Young's modulus and yield strength of i -th reinforcement bar; ε_{mu} is the ultimate strain of masonry, taken as 0.0025; d_i is the distance from the extreme compression fiber to centroid of tension reinforcement; c is the neutral axis depth.

An iterative procedure is employed to solve the neutral axis depth c . Subsequently, the moment capacity of a RM wall can then be determined as Eq. (D-6):

$$M_r = C_m \left(\frac{l}{2} - \frac{\beta c}{2} \right) + \sum T_{r,i} \left(d_i - \frac{l}{2} \right) \quad (D-6)$$

Here, l is the wall length. The quantities in parentheses denote the moment arms of each (compressive or tensile) force. For the cantilever wall considered, the IP flexural capacity V_{fr} can be evaluated as:

$$V_{fr} = M_r / h \quad (D-7)$$

The IP resistance of a specific RM wall V_{IP} is then determined as the minimum one:

$$V_{IP} = \min(V_{dt}, V_{ss}, V_{fr}) \quad (D-8)$$

Appendix E. OUT-OF-PLANE RESISTANCE PREDICTION OF UNREINFORCED MASONRY WALLS BASED ON CSA S304-14

Given the limited tensile strength and brittleness of URM structures, CSA S304-14 recommends the use of elastic bending beam theory to determine the OOP resistance of URM walls V_{OOP} . It is noted that the OOP resistance V_{OOP} refers to the capacity to resist lateral load pressure. For unreinforced masonry walls that need to remain uncracked, the underlying principle in the design provision is to equate the maximum bending moment at the wall's mid-height with the sectional moment capacity. The sectional moment capacity is calculated based on the tensile strength of masonry f_{tm} or the compressive strength of masonry f_{cm} plus the contribution of uniform axial compression P_d , as shown in Eq. (E-1):

$$V_{OOP,t} = \left(f_{tm} + \frac{P_d}{lt} \right) \frac{8S_e}{h^2} \quad (\text{E-1})$$

$$V_{OOP,c} = \left(f_{cm} - \frac{P_d}{lt} \right) \frac{8S_e}{h^2} \quad (\text{E-2})$$

where l and t are the wall's length and thickness; and S_e is the section modulus.

Appendix F. OUT-OF-PLANE RESISTANCE PREDICTION OF REINFORCED MASONRY WALLS BASED ON CSA S304-14

To evaluate the OOP resistance of RM walls, section P-M interaction diagram is derived first. For a given axial load, the section moment capacity of RM wall can be calculated using the equilibrium condition, assuming no tensile force contributions from masonry and no compressive force contribution from the reinforcing bars. The equilibrium equation is expressed as Eq. (F-1):

$$C_m = P_d + T_r \quad (\text{F-1})$$

where P_d is the pre-compression load; C_m and T_r are the compressive forces in masonry and tensile forces in steel, respectively. By assuming that the reinforcing bars experiencing the yielding and the masonry is experiencing the crushing, C_m can be calculated by assuming the compressive block $C_m = 0.85 f'_m b \beta_1 c$, in which $b = \min(4t, s)$ and s is the bar spacing; $\beta_1 c$ is the depth of compressive block. The tensile forces of steel T_r is determined as $T_r = A_{sv} f_{yv}$ where f_{yv} is the yield strength of reinforcements, Based on the equilibrium equation shown in Eq. (F-1), the compressive block depth is calculated as per Eq. (F-2):

$$\beta_1 c = \frac{A_{sv} f_{yv} + P_d}{0.85 f'_m b} \quad (\text{F-2})$$

The moment resistance of a RM wall can then be calculated by Eq. (F-3):

$$M_r = 0.85 f'_m b \beta_1 c \left(d - \frac{\beta_1 c}{2} \right) \quad (\text{F-3})$$

where d is the effective depth, i.e., the distance from the extreme compression fiber to the centroid of the reinforcing bars. For the walls in which the reinforcements are placed in the center of the wall, $d = t / 2$. As such, the OOP resistance against the lateral pressure load is evaluated based on the moment capacity M_r :

$$V_{oop} = \frac{8M_r}{h^2} \quad (\text{F-4})$$

Above equations are derived by assuming the steel bar experiences the yielding, and this needs to be checked. According to the strain compatibility, strain ε_s in the reinforcement bars is calculated as:

$$\varepsilon_s = \frac{0.003 \times (d - c)}{c} \quad (\text{F-5})$$

If $\varepsilon_s \geq \varepsilon_y = \frac{f_{sv}}{E_s}$, here ε_y is the yield strain, and E_s is the Young's modulus of reinforcements, the assumption of steel bar yielding is correct. Otherwise, the compressive block depth needs to be re-calculated as per Eq. (F-6):

$$\beta_1 c = \frac{A_{sv} f_{sv} + P_d}{0.85 f'_m b} \quad (\text{F-6})$$

where f_{sv} is the stress (less than the yield strength) of reinforcements, determined as Eq. (F-7) according to strain compatibility:

$$f_{sv} = \frac{0.003(d - c)}{c} \quad (\text{F-7})$$

One can solve Eq. (F-6) and Eq. (F-7) to obtain $\beta_1 c$. Following this, the section moment capacity and OOP capacity against the lateral load pressure can be calculated as Eq. (F-3) and Eq. (F-4).

To account for the second-order effects, CSA S304-14 suggests the moment magnifier method. In that sense, the moment applied on the RM wall is magnified by a factor, as given in Eq. (F-8). P_{cr} is the Euler buckling load of the wall defined as per Eq. (F-9):

$$\psi = \frac{C_m}{1 - \frac{P_d}{P_{cr}}} \quad (\text{F-8})$$

where C_m is a factor relating actual moment diagram to an equivalent uniform moment diagram, determined as $C_m = 0.6 + 0.4 M_1/M_2$ where M_1 and M_2 are the end moments, P_d is the axial load acting on the wall, P_{cr} is Euler buckling load of the wall. P_{cr} is related to effective flexural rigidity EI_{eff} . They are calculated according to Eq. (F-9) and Eq. (F-10):

$$P_{cr} = \pi^2 EI_{eff} (kh)^2 \quad (\text{F-9})$$

$$EI_{eff} = E_m I_{cr} \leq E_m \left[0.25 I_o - (0.25 I_o - I_{cr}) \left(\frac{e - e_k}{2e_k} \right) \right] \leq 0.25 E_m I_o \quad (\text{F-10})$$

In Eq. (F-9), k is the effective length depending on the boundary conditions (e.g., $k = 1.0$ for simply supported), and h is the unsupported wall length. In Eq. (F-10), E_m is the masonry modulus of elasticity, I_{cr} is the cracked moment of inertia, I_o is the gross moment of inertia, e is the eccentricity which is defined as the ratio between the applied moment and the axial load, and e_k is the kern eccentricity which is defined between the ratio between the section modulus S_e and the effective cross-section area. The cracked moment of inertia I_{cr} is calculated as per Eq. (F-11):

$$I_{cr} = \frac{bc^3}{3} + nA_s(d-c)^2 \quad (\text{F-11})$$

All the quantities are available for the calculation of moment magnifier factor. The moment capacity of a wall with the consideration of slenderness effects is equal to the section moment capacity, i.e., shown in Eq. (F-3), reduced by this factor.

Appendix G. PYTHON-BASED TOOLS FOR MODELING MASONRY WALLS BASED ON MICRO MODELING STRATEGY

To streamline the micro modeling strategy of masonry walls, two Python-based automated tools, namely *URM.py* and *RM.py*, were developed and integrated into the general-purpose Finite Element (FE) software ABAQUS. These tools offer a user-friendly environment for simulating masonry walls using micro modeling strategies with different boundary (e.g., cantilever, double-fixed, pin-roller) and loading conditions (e.g., IP loading, OOP loading, combined IP and OOP loadings). The following inputs are needed to run the codes:

- Working directory (default: C:\temp)
- Geometry: dimensions of units (height, thickness, and length), and dimensions of walls (height, thickness, and length)
- Material parameters of units and grouts (Concrete Damage Plasticity model): Young's modulus, Poisson's ratio, tensile strength, compressive strength, dilation angle, flow potential eccentricity (default: 0.1), the ratio between the biaxial initial compressive strength and the initial uniaxial compressive strength (default: 1.16), the ratio of the second stress invariant on the tensile meridian to that on the compressive meridian (default: 0.67), and viscosity parameter (default: 0.0002)
- Material parameters of reinforcements (only for reinforcement masonry walls): Young's modulus, Poisson's ratio, yield stress vs plastic strain, cross section area, locations for horizontal reinforcements (indicate all reinforcements), and locations for vertical reinforcements (indicate all reinforcements)
- Material parameters of mortar joints

- For the monotonic model: Elastic stiffness constants (k_{nn} , k_{ss} , and k_{tt}), tensile strength, peak cohesion, initial/residual frictional coefficients, initial/residual dilatancy coefficients, mode I fracture energy, mode II fracture energy when the normal stress is zero, coefficient for mode II fracture energy (considering the influence of compressive stress on the mode II fracture energy), compressive strength of masonry, displacement corresponding to the compressive strength, and initial/residual compressive yield stress
- For the cyclic model (in addition to the parameters required for the monotonic model): compression-to-tension stiffness recovery factor, tension-to-compression stiffness recovery factor, ratios between stiffness degradation and strength softening or tension and compression (default: 1.0), and non-physical parameters (α , β , and γ)
- Numerical integration option (for monotonic model)
 - Activation of yield surfaces: 1 = active tension-shear yield surface, 2 = active compression cap yield surface, and 3 = active both yield surfaces
 - Error-based Sub-stepping integration strategy: 0 = off, and 1 = on (default)
 - Plasticity integration solver: 0 = modified Newton-Raphson method, and 1 = Newton-Raphson method (default)
 - Error-based sub-stepping integration factor (default: 0.2)
 - Initial sub-stepping incremental size (default: 0.001)
 - Maximum iterations in Newton-Raphson method (default: 100)
 - Tolerance for Newton-Raphson method (default: 1e-4)

- Mesh size and element type
- Loading condition: 1 = in-plane loading (applied at the top beam along the horizontal direction), 2 = out-of-plane loading (applied as a uniform pressure at the outer surface of the wall), 3 = combined in-plane and out-of-plane loading. More options are available:
 - In-plane loading: “fixed_IP” for double fixed end condition, and “cantilever_IP” for cantilever condition
 - Out-of-plane loading: “pin_pin” for pin-pin condition (one-way vertical bending), “fixed_fixed” for fixed-fixed condition (one-way vertical bending)
 - When combined in-plane and out-of-plane loading conditions are selected, the aforementioned options can also be used.

After inputting all necessary parameters, *URM.py* and *RM.py* could be run in Windows command batch mode or in ABAQUS CAE GUI mode.